Solar Cells
Thin-Film Technologies

Edited by Leonid A. Kosyachenko

SOLAR CELLS – THIN-FILM TECHNOLOGIES

Edited by **Leonid A. Kosyachenko**

Notice

Statements and opinions expressed in the chapters are these of the individual contributors and not necessarily those of the editors or publisher. No responsibility is accepted for the accuracy of information contained in the published chapters. The publisher assumes no responsibility for any damage or injury to persons or property arising out of the use of any materials, instructions, methods or ideas contained in the book.

We are IntechOpen,
the world's leading publisher of Open Access books
Built by scientists, for scientists

4,000+
Open access books available

116,000+
International authors and editors

120M+
Downloads

151
Countries delivered to

Our authors are among the

Top 1%
most cited scientists

12.2%
Contributors from top 500 universities

CLARIVATE ANALYTICS

BOOK CITATION INDEX

INDEXED

WEB OF SCIENCE™

Selection of our books indexed in the Book Citation Index
in Web of Science™ Core Collection (BKCI)

Interested in publishing with us?
Contact book.department@intechopen.com

Numbers displayed above are based on latest data collected.
For more information visit www.intechopen.com

Meet the editor

Dr. Leonid A. Kosyachenko is professor of National University of Chernivtsi, Ukraine. After receiving his Doctor of Sciences Degree in Physics and Mathematics in 1983, he founded and became a head of Optoelectronics Department – the first department of this kind at Ukrainian universities. About twenty of his pupils have performed work to obtain the degrees of Candidate (Ph.D.) and Doctor of Sciences. His research interests have been in physics and technology of solar cells, semiconductor X-ray and γ-ray detectors, light-emitting and photosensitive devices. He is author (co-author) of several books and numerous scientific articles; presented reports at international scientific conferences and meetings in Germany, Italy, England, Japan, China, Greece, Spain, Belgium, Russia. He was the leader of several collaborative projects with the institutions of Russia, Belorussia and is one of the leaders of the long-term projects of the European Commission. Prof. L.A. Kosyachenko is a member of the Ukrainian Physical Society and the guest editor of journal "Solar Energy Materials and Solar Cells".

Contents

Preface

Solar cells are optoelectronic devices that convert the energy of solar radiation directly into electricity by the photovoltaic (PV) effect. Assemblies of cells electrically connected together are known as PV modules, or solar panels. The photovoltaic effect was first recognized in the 19th century but the modern PV cells were developed in the mid-1950s. The practical application of photovoltaics started to provide energy for orbiting satellites. Today PV installations may be ground-mounted or built into the roof or walls of buildings, and are used for electric power in boats, cars, water pumps, radio stations, and more. The majority of PV modules are used for grid connected power generation. More than 100 countries use photovoltaics. Solar power is pollution-free during use. Due to the growing demand for renewable energy sources, the manufacturing of solar cells and PV arrays has advanced considerably in recent years.

Solar cells and modules based on crystalline and polycrystalline silicon wafers, the representatives of the so-called first generation of solar cells, dominate the photovoltaic today and demonstrate high growth rates in the entire energy sector. Nevertheless, despite the relatively high annual growth, the contribution of photovoltaics in the global energy system is small. The reason for this lies in a large consumption of materials and energy, high labor intensiveness and, as a consequence, a low productivity and high cost of modules with acceptable PV conversion efficiency for mass production. Driven by advances in technology and increases in manufacturing scale, the cost of photovoltaics has declined steadily since the first solar cells were manufactured. For decades, an intensive search for cheaper production technology of silicon solar cells is underway. In many laboratories around the world, extensive research to improve the efficiency of solar cells and modules without increasing the cost of production are carried out. A large variety of solar cells, which differ depending on the materials used, PV structure, design and even the principle of PV conversion are designed to date. Among the radical ways to reduce the cost of solar modules and to increase drastically the volume of their production is the transition to thin-film technology and the use of a cheap large-area substrate (glass, metal foil, plastic).

Amorphous silicon (a-Si) was the first material for commercial thin-film solar cells with all their attractiveness to reduce consumption of absorbing material, increase in

area and downturn in price of modules. Quite common in commercial solar cells are the multi-layer structures based on a-Si. It seemed that the tandem structure, a representative of the third generation of solar cells, opened the prospect of developing efficient and low-cost solar cells. Special place in the thin-film photovoltaics is the so-called micromorph solar cells, which are closely related to the a-Si. However, the use of a-Si and micromorph solar cells is limited preferably to areas, where low cost is more important than the efficiency of photoelectric conversion such as consumer electronics and building-integrated photovoltaics (BIPV).

Unquestionable leaders in thin-film technologies are solar cells on $CuIn_xGa_{1-x}Se_2$ (CIGS) and CdTe, the representatives of the so-called second generation photovoltaics. For a long time, CIGS have been considered as promising material for high-performance thin-film solar cells and fabrication of monolithically interconnected modules intended for cost-effective power generation. As a result of research, aimed to reducing the cost of CIGS solar modules, several companies developed the commercial CIGS solar modules and initiated their large-scale production. In the early years of the 21st century, the technology and manufacturing of solar modules based on CdTe, which could compete with silicon counterparts, was also developed. It should be emphasized that the growth rates of CdTe module production over the last decade are the highest in the entire solar energy sector.

Dye-sensitized solar cells (DSSCs) are considered to be extremely promising because they are made of low-cost materials with simple inexpensive manufacturing procedures and can be engineered into flexible sheets. Organic solar cells attract the attention also by the simplicity of technology leading to inexpensive, large-scale production for the future. This type of cells as well as multi-junction structures based on a-Si and micromorph silicon can be assigned to the so-called third generation solar photovoltaics. GaAs based multi-junction devices were originally designed for special applications such as satellites and space exploration. To date they are the most efficient solar cells.

Four-volume edition under the joint name of "Solar cells" encompasses virtually all aspects of photovoltaics. Research and development in the field of thin-film solar cells based on CIGS, CdTe, amorphous, micro- and polycrystalline silicon are presented in the first volume with the subtitle "Thin-film technology". The second volume subtitled «Dye-Sensitized Devices» is devoted to the problems of developing high-efficiency solar modules using low-cost materials with simple inexpensive manufacturing processes. The third volume subtitled « Silicon Wafer-Based Technologies» includes the chapters that present the results of research aimed ultimately to reduce consumption of materials, energy, labor and hence cost of silicon solar modules on wafer or ribbon silicon. Chapters that present new scientific ideas and technical solutions of photovoltaics, new methods of research and testing of solar cells and modules have been collected in the forth volume subtitled «New Aspects and Solutions».

It is hoped that readers will find many interesting and useful material in all four volumes of «Solar Cells» covering highly topical issues of photovoltaics.

From the above it follows that the first book of this four-volume edition is dedicated to one of the most promising areas of photovoltaics, which has already reached a large-scale production of the second-generation thin-film solar modules and has resulted in building the powerful solar plants in several countries around the world. Thin-film technologies using direct-gap semiconductors such as CIGS and CdTe offer the lowest manufacturing costs and are becoming more prevalent in the industry allowing to improve manufacturability of the production at significantly larger scales than for wafer or ribbon Si modules. It is only a matter of time before thin films like CIGS and CdTe would replace wafer-based silicon solar cells as the dominant photovoltaic technology. Photoelectric efficiency of thin-film solar modules is still far from the theoretical limit. The scientific and technological problems of increasing this key parameter of the solar cell are discussed in several chapters of this volume.

The editor addresses special thanks to the contributors for their initiative and high quality work, and to the technical editors that conveyed the submitted chapters into a qualitative and pleasant presentation.

Professor, Doctor of Sciences, Leonid A. Kosyachenko
National University of Chernivtsi
Ukraine

Thin-Film Photovoltaics
as a Mainstream of Solar Power Engineering

Leonid A. Kosyachenko
Chernivtsi National University
Ukraine

1. Introduction

Provision of energy is one of the most pressing problems facing humanity in the 21st century. Without energy, it is impossible to overcome the critical issues of our time. Industrial world suggests continuous growth in energy consumption in the future.

According to the U.S. Department of Energy, the world's generating capacity is now close to 18 TW. The main source of energy even in highly developed countries is fossil fuel, i.e. coal, oil and natural gas. However, resources of fossil fuel are limited, and its production and consumption irreversibly affect the environmental conditions with the threat of catastrophic climate change on Earth. Other energy sources, particularly *nuclear* energy, are also used that would fully meet *in principle* the energy needs of mankind. Capacity of existing nuclear reactors (nearly 450 in the world) is ~ 370 GW. However, increasing their capacity up to ~ 18 TW or about 50 times (!), is quite problematic (to provide humanity with *electric* energy, the capacity of nuclear power should be increased about 10 times). Resources of hydroelectric, geothermal, wind energy, energy from biofuels are also limited. At the same time, the power of solar radiation of the Earth's surface exceeds the world's generating capacity by more than 1000 times. It remains only to master this accessible, inexhaustible, gratuitous and nonhazardous source of energy in an environmentally friendly way.

Solar energy can be converted into heat and electricity. Different ways of converting sunlight into electricity have found practical application. The power plants, in which water is heated by sunlight concentrating devices resulting in a high-temperature steam and operation of an electric generator, are widespread. However, solar cells are much more attractive due to the *direct* conversion of solar radiation into electricity. This is the so-called *photovoltaics.* Under the conditions of the growing problems of global warming, photovoltaics is the most likely candidate to replace fossil fuels and nuclear reactors.

2. Silicon solar cells

Over the decades, solar modules (panels) based on single-crystalline (mono-crystalline, c-Si), polycrystalline (multi-crystalline, mc-Si), ribbon (ribbon-Si) and amorphous (a-Si) silicon are dominant in photovoltaics (Fig. 1).

In recent years, photovoltaics demonstrates high growth rates in the entire energy sector. According to the European Photovoltaic Industry Association , despite the global financial and economic crisis, the capacity of installed solar modules in the world grew by 16.6 GW in
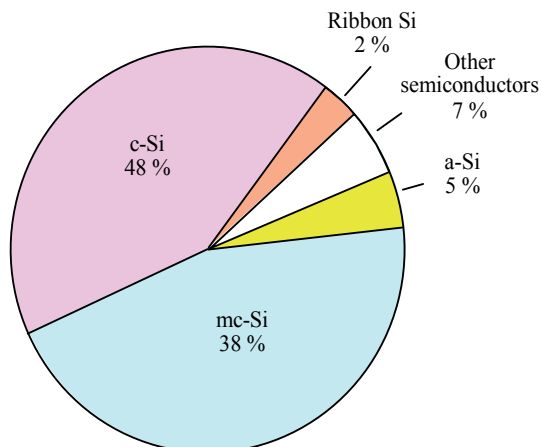
Fig. 1. Distribution of capacity of photovoltaic energy in the world.

2010, and their total capacity reached ~ 40 GW, that is almost 8 times more than in 2005. The growth rate of the photovoltaic energy for the next 4-5 years is expected to be quite high. In 2014, capacity of installed modules will be about 14 GW and 30 GW according to the pessimistic and optimistic forecast, respectively. Nevertheless, despite the relatively high annual growth, the contribution of semiconductor solar cells in the global energy system is small (less than 0.3%!), and the prospects for *desired rapid* development of photovoltaics are not reassuring (Fig. 2). The contribution of Si photovoltaic solar power plants in generation capacity in the world will reach ~ 1% only in the years 2018-2020, and may exceed 10% in the years 2045-2050 (EPIA, 2011; EUR 24344 PV, 2010; Jager-Waldau, 2010). Analysts do not accept the development of the PV scenario shown by the dashed line in Fig. 2. Thus, solving the energy problems by developing Si photovoltaics seems too lengthy.[1]

The reason for the slow power growth of traditional silicon solar modules lies in a large consumption of materials and energy, high labor intensiveness and, as a consequence, a low productivity and high cost of modules with acceptable photovoltaic conversion efficiency for mass production (16-17 and 13-15% in the case of single-crystalline and polycrystalline material, respectively) (Szlufcik et al., 2003; Ferrazza, 2003).[2] The problem is fundamental and lies in the fact that silicon is an i*ndirect* semiconductor and therefore the *total* absorption needs its significant thickness (up to 0.5 mm and more). As a result, to collect the charge photogenerated in a thick absorbing layer, considerable diffusion length of minority carriers (long lifetime and high mobility) and, therefore, high quality material with high *carrier diffusion length of hundreds of micrometers* are required.

Estimating the required thickness of the semiconductor in solar cells, one is often guided by an effective penetration depth of radiation into the material α^{-1}, where α is the absorption coefficient in the region of electronic interband transitions. However, the value of α varies

---

[1] In the European Union, these rates are much higher. Now the cumulative power of solar modules is 1.2% and, by 2015 and 2020, will rise to 4-5% and 6-12% of the EU's electricity demand, respectively.

[2] A lot of effort has been undertaken to increase the efficiency of silicon solar cells above 20-24% but improvements are reached only with the help of cost-intensive processes, which usually cannot be implemented into industrial products (Koch et al., 2003).
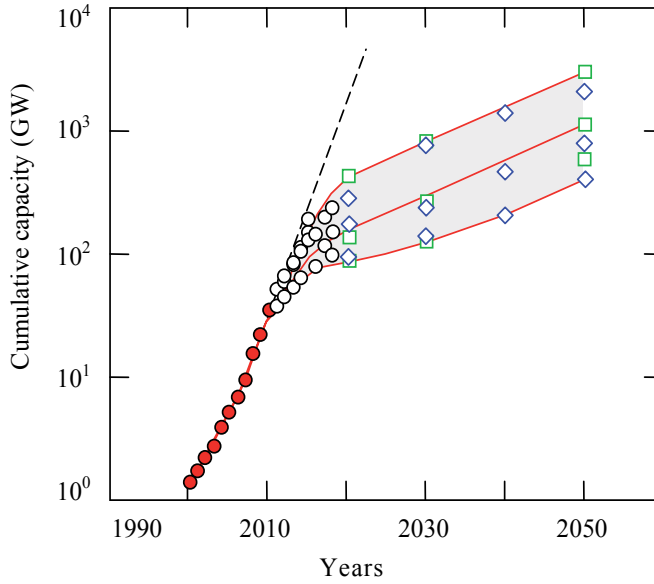
Fig. 2. Evolution of world cumulative installed PV capacity until 2050: ● historical data, ○, □, ◇ forecasts (EPIA, 2011; EUR 24344 PV, 2010; Hegedus & Luque, 2011).

rather widely, especially in the indirect semiconductor, and solar radiation is distributed over the spectrum in a complicated manner (Fig. 3(a)). Therefore, the absorptive capacity (absorptivity) of the material, used in solar cell, can be described by a certain *integral* characteristic, which takes into account the absorption spectrum of the material and the spectral distribution of solar radiation. For a structure with flat surfaces, the integral absorption ability of the radiation, which has penetrated into the material (certain part of radiation is reflected from the front surface), can be represented as

$$A(d) = \frac{\sum_i \frac{\Phi_i + \Phi_{i-1}}{2}\left[1 - \exp\left(-\frac{\alpha_i + \alpha_{i-1}}{2}d\right)\right]\Delta\lambda_i}{\sum_i \frac{\Phi_i + \Phi_{i-1}}{2}\Delta\lambda_i} \, , \tag{1}$$

where Φ_i is the spectral power density of solar radiation at the wavelength λ_i under standard solar irradiation AM1.5 shown in Fig. 3(a), $\Delta\lambda_i$ is the spacing between neighboring wavelengths in Table 9845-1 of the International Organization for Standardization (Standard ISO, 1992), and α_i is the absorption coefficient at wavelength λ_i. The summation in Eq. (1) is made from $\lambda \approx 300$ nm to $\lambda = \lambda_g = hc/E_g$, since at wavelengths λ shorter than 300 nm, terrestrial radiation of the Sun is virtually absent, and when $\lambda > \lambda_g$, radiation is not absorbed in the material with the generation of electron-hole pairs.

Fig. 3(b) shows the dependences of absorptivity of solar radiation A of single-crystalline silicon on the thickness of the absorber layer d calculated by Eq. (1).

As seen in Fig. 3(b), in crystalline silicon, the total absorption of solar radiation in the fundamental absorption region ($h\nu \geq E_g$) occurs when d is close to 1 cm (!), and 95% of the radiation is absorbed at a thickness of about 300 μm. More absorption can be achieved by using the reflection of light from the rear surface of the solar cell, which is usually completely

(a)

(b)
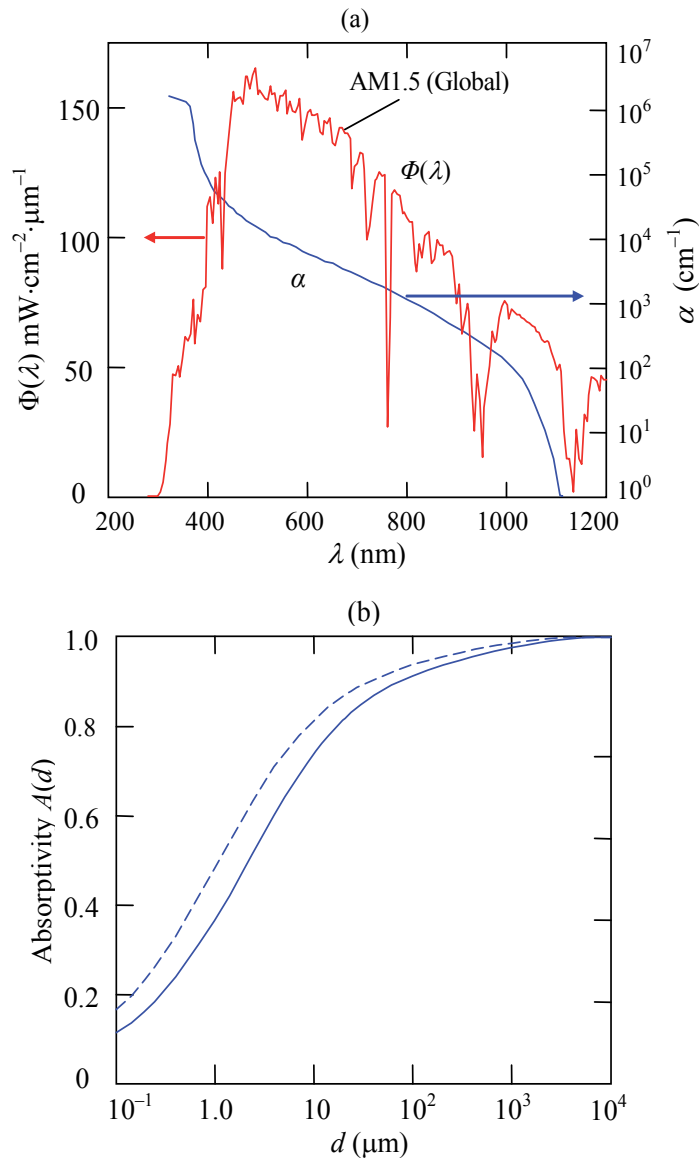
Fig. 3. (a) – Power spectral density of the total solar radiation Φ under AM1.5 conditions and the absorption curve $\alpha(\lambda)$ for crystalline silicon. (b) – Dependence of absorptivity of solar radiation in the $h\nu \geq E_g$ spectral range on the absorber layer thickness d for crystalline silicon. The dashed line shows the absorptivity of a silicon wafer taking into account 100% reflection from its rear surface.

covered with metal. If in the ideal case, the reflectivity of light from the rear surface is unity, the absorption of the plate will be such as if its thickness is twice as much. In this case, 95% of the radiation is absorbed by the plate of 150 µm thickness.

Of course, it has to be rejected to use silicon wafers of thickness a few millimeters, so that the absorption of solar radiation was complete. Many companies producing silicon modules

agreed on a compromise thickness of 150-250 μm, when about 93% of solar radiation with photon energy $h\nu \geq E_g$ is absorbed or about 94% when the rear surface of the solar cell is mirror (Szlufcik et al., 2003; Ferrazza, 2003).[3] Deficiency of absorption in the material offsets by the creation of a special profile on surfaces (texturing) and by other ways. Needless to say, an anti-reflective coating is applied to reduce significantly the reflection from the front surface because over 30% of the radiation is reflected from a flat silicon surface.

Production of solar modules based on silicon wafers involves a lot of stages (Hegedus & Luque, 2011). The so-called metallurgical grade (MG) silicon is obtained from quarzite (SiO_2) with charcoal in a high-temperature arc furnace. Then MG silicon is highly purified commonly by a method developed by the Siemens Company consisting of the fractional distillation of chlorosilanes. Finally, chlorosilanes are reduced with hydrogen at high temperatures to produce the so-called semiconductor grade (SG) silicon. By recrystallizing such polycrystalline silicon, single-crystalline Si ingots are often grown by the Czochralski (Cz) or the floating-zone (FZ) techniques adapted from the microelectronics industry. This is followed by cutting (slicing) the ingot into wafers, of course, with considerable waste. It should be noted that the cost of silicon purification, production of ingots, slicing them into wafers constitute up to 40-55% of the cost of solar module.

Manufacture of conventional silicon solar cell also includes a number of other operations. Among them, (i) chemical etching wafers to provide removal of the layer damaged during slicing and polishing; (ii) high-temperature diffusion to create a p-n junction; (iii) anisotropic etching to build a surface structure with random pyramids that couples the incoming light more effectively into the solar cell; (iv) complicated procedure of applying full area and grid-like ohmic contacts to p- and n-type regions provided a minimum of electrical and recombination losses (contacts in silicon solar cells are often made by screen-printing metal paste, which is then annealed at several hundred degrees Celsius to form metal electrodes), etc. (Mauk, et al., 2003). Once the cells are manufactured they are assembled into modules either in the cell factories or in module assembly factories that purchase cells from variety cell factories (Hegedus & Luque, 2011). All that complicates the manufacturing technology and, hence, reduces the productivity and increases the cost of solar modules.

Summing up, one should again emphasize that single-crystalline Si modules are among the most efficient but at the same time the most expensive since they require the highest purity silicon and involve a lot of stages of complicated processes in their manufacture.

For decades, an intensive search for cheaper production technology of silicon solar cells is underway. Back in the 1980's, a technology of material solidification processes for production of large silicon ingots (blocks with weights of 250 to 300 kg) of **polycrystalline (multicrystalline) silicon** (mc-Si) has been developed (Koch et al., 2003). In addition to lower cost manufacturing process, an undoubted advantage of mc-Si is the rational use of the material in the manufacture of solar cells due to the rectangular shape of the ingot. In the case of a single-crystalline ingot of cylindrical form, the so-called "pseudo-square" wafers with rounded corners are used, i.e. c-Si modules have some gaps at the four corners of the cells).

Polycrystalline silicon is characterized by defects caused by the presence of random grains of crystalline Si, a significant concentration of dislocations and other crystal defects (impurities). These defects reduce the carrier lifetime and mobility, enhance recombination of carriers and ultimately decrease the solar cells efficiency. Thus, polysilicon-based cells

---

[3] Further thinning of silicon is also constrained by the criteria of mechanical strength of a wafer as well as the handling and processing techniques (silicon is brittle).

are less expensive to produce single-crystalline silicon cells but are less efficient. As a result, cost per unit of generated electric power ("specific" or "relative" cost) for c-Si and mc-Si modules is practically equal (though the performance gap has begun to close in recent years). The polysilicon-based cells are the most common solar modules on the market being less expensive than single-crystalline silicon.

A number of methods for growing the so-called **ribbon-Si**, i.e. a polycrystalline silicon in the form of thin sheets, is also proposed. The advantages of ribbon silicon are obvious, as it excludes slicing the ingot into thin wafers, allowing material consumption to reduce roughly *halved*. However, the efficiency of ribbon-Si solar cells is not as high as of mc-Si cells because the need of high quality material with the thickness of the absorber layer of 150-250 μm and, hence, with high carrier diffusion lengths of hundreds of micrometers remains (Hegedus & Luque, 2011). Nevertheless, having a lower efficiency, ribbon-Si cells save on production costs due to a great reduction in waste because slicing silicon crystal into the thin wafers results in losses (of about 50%) of expensive pure silicon feedstock (Koch et al., 2003). Some of the manufacturing technologies of silicon ribbons are introduced into production, but their contribution to the Si-based solar energy is negligible (Fig. 1). The cost of ribbon-Si modules, as well as other types of silicon solar modules, remains quite high.

Many companies are developing solar cells that use lenses or/and mirrors to concentrate a large amount of sunlight onto a small area of photovoltaic material to generate electricity. This is the so-called **concentrated photovoltaics**. The main gain that is achieved through the involvement of concentrators is to save material. This, however, does not too reduce the cost of the device, because a number of factors lead to higher prices. (i) For the concentration of radiation, an optical system is necessarily required, which should maintain a solar cell in focus by the hardware when the sun moves across the sky. (ii) With a significant increase in the intensity of the radiation, the photocurrent also increases significantly, and the electrical losses rapidly increase due to voltage drop across the series-connected resistance of the bulk of the diode structure and contacts. (iii) For the removal of heat generated by irradiation that decreases the efficiency of photovoltaic conversion, it is necessary to use copper heatsinks. (iv) The requirements to quality of the solar cell used in the concentrator considerably increase. (v) Using concentrators, only direct beam of solar radiation is used, which leads to losing about 15% efficiency of solar module.

Nevertheless, today the efficiency of solar concentrators is higher compared to conventional modules, and this trend will intensify in the application of more efficient solar devices. In 2009, for example, the power produced in the world using solar energy concentration did not exceed 20-30 MW, which is ~ 0.1% of silicon power modules (Jager-Waldau, 2010). According to experts, concentrator market share can be expected to remain quite small although increasing by 25% to 35% per year (Von Roedern, 2006).

In general, in this protracted situation, experts and managers of some silicon PV companies have long come to conclusion that there would be limits to growing their wafer (ribbon) silicon business to beyond 1 GW per year by simply expanding further (Von Roedern, 2006). All of these companies are researching wafer-Si alternatives including the traditional *thin-film technologies* and are already offering such commercial thin-film modules.

Concluding this part of the analysis, one must agree, nevertheless, that wafer and ribbon silicon technology provides a fairly high rate of development of solar energy. According to the European Photovoltaic Industry Association (EPIA), the total installed PV capacity in the world has multiplied by a factor of 27, from 1.5 GW in 2000 to 39.5 GW in 2010 – a yearly growth rate of 40% (EPIA, 2011).

Undoubtedly, solar cells of all types on silicon wafers, representatives of the so-called *first generation photovoltaics*, will maintain their market position in the future. In hundreds of companies around the world, one can always invest (with minimal risk) and implement the silicon technology developed for microelectronics with some minor modifications (in contrast, manufacturers of thin-film solar modules had to develop their "own" manufacturing equipment). Monocrystalline and polycrystalline wafers, which are used in the semiconductor industry, can be made into efficient solar cells with full confidence. It is also important that silicon is very abundant, clean, nontoxic and very stable. However, due to limitations in production in large volumes of silicon for solar modules, which are both highly efficient and cost-effective, often-expressed projections for *desirable significant* increase in their contribution to the world energy system in the coming years are highly questionable.

3. Thin-film solar cells

Among the radical ways to reduce the cost of solar modules and to increase drastically the volume of their production is the transition to thin-film technology, the use of direct-gap semiconductors deposited on a cheap large-area substrate (glass, metal foil, plastic).

We start with the fact that the direct-gap semiconductor can absorb solar radiation with a thickness, which is much smaller than the thickness of the silicon wafer. This is illustrated by the results of calculations in Fig. 4 similar to those performed for the single-crystalline silicon shown in Fig. 2. Calculations were carried out for direct-gap semiconductors, which is already used as absorber layers of solar modules: a-Si, CdTe, CuInSe$_2$ and CuGaSe$_2$.

As expected, the absorptivity of solar radiation of direct-gap semiconductors in general is much stronger compared to crystalline silicon but the curves noticeably differ among themselves (in the references, the absorption curves for a-Si are somewhat different). Almost complete absorption of solar radiation by amorphous silicon (a-Si) in the $\lambda \leq \lambda_g = hc/E_g$ spectral range is observed at its thickness $d > 30\text{-}60\ \mu m$, and 95% of the radiation is absorbed at a thickness of 2-6 μm (Fig. 4(a)). These data are inconsistent with the popular belief that in a-Si, as a direct-gap semiconductor, the *total* absorption of solar radiation occurs at a layer thickness of several microns. The total absorption of solar radiation in CdTe occurs if the thickness of the layer exceeds 20-30 μm, and 95% of the radiation is absorbed if the layer is thinner than ~ 1 μm. Absorptivities of the CuInSe$_2$ and CuGaSe$_2$ are even higher. Almost complete absorption of radiation in these materials takes place at a layer thickness of 3-4 μm, and 95% of the radiation is absorbed if the thickness of layer is only 0.4-0.5 μm (!).

Thus, the transition from crystalline silicon to direct-gap semiconductors leads to noncomparable less consumption of photoelectrically active material used in the solar cell.

High absorptivity of a semiconductor has important consequences with respect to other characteristics of the semiconductors used in solar cells. Since the direct-gap semiconductor can absorb solar radiation at its thickness much smaller than the thickness of the silicon wafer (ribbon), the requirements for chemical purity and crystalline perfection of the absorber layer in the solar cell became much weaker.

In fact, to collect photogenerated charge carriers, it is necessary to have a diffusion length of minority carriers in excess of the thickness of the absorbing layer. In the case of crystalline Si, the photogenerated carriers must be collected at a thickness of 1-2 hundred microns and 2 orders of magnitude smaller than in the case of CdTe, CIS or CGS. From this it follows that in the solar cell based on direct-gap semiconductor, the diffusion length L may be about two

(a)

(b)
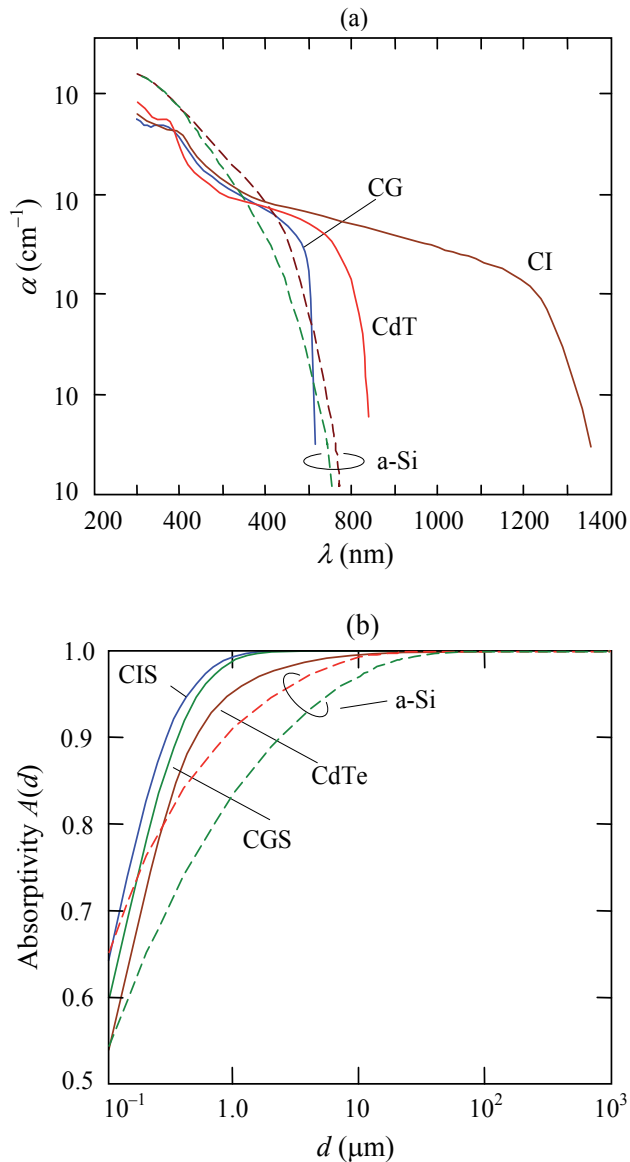
Fig. 4. Absorption curves (a) and dependence of absorptivity of AM1.5 solar radiation in the $h\nu \geq E_g$ spectral range on the absorber layer thickness d (b) for amorphous silicon (a-Si), cadmium telluride (CdTe), copper-indium diselenide (CIS) and copper gallium diselenide (CGS) (Han et al., 2007; Paulson et al., 2003; Gray et al., 1990; http://refractiveindex.info/a-Si).

orders of magnitude smaller, i.e. the carrier lifetime τ can be by 4(!) order shorter ($L \sim \tau^{1/2}$). Thus, the manufacture of thin film solar modules based on the direct-gap semiconductors does not require costly high purification and crystallinity of the material as it is needed in the production of modules based on crystalline, multicrystalline or ribbon silicon.

Thin-film technology has a number of other significant merits. While Si devices are manufactured from wafers or ribbons and then processed and assembled to form a modules,

in thin-film technology many cells are simultaneously made and formed as a module. The layers of solar cells are deposited sequentially on moving substrates in a continuous highly automated production line (conveyor system) and, importantly, at temperatures not exceeding 200-650°C compared with 800-1450°C for the main processes of c-Si. This minimises handling and facilitates automation leading to the so-called *monolithic integration*.[4] Thin-film solar modules offer the lowest manufacturing costs, and are becoming more prevalent in the industry because allow to improve manufacturability of the production at significantly larger scales than for wafer or ribbon Si modules. Therefore, it is generally recognised that the contribution of thin-film technology in solar energy will be to grow from year to year faster. Many analysts believe *that it is only a matter of time before thin films would replace silicon wafer-based solar cells as the dominant photovoltaic technology*.

Unquestionable leaders in thin film technologies are solar cells on **amorphous silicon** (a-Si), **copper-indium-gallium diselenide** ($CuIn_xGa_{1-x}Se_2$) and **cadmium telluride** (CdTe), whose market share is expanding every year (Hegedus & Luque, 2011). The rest of the thin-film technologs are yet too immature to appear in the market but some of them is already reaching the level of industrial production. Below these technologies will first be briefly described, and a more detailed analysis of solar modules based on a-Si, CdTe and CIGS are allocated in separate subsections. Now the most successful non-Si based thin film PV technologies are representatives of the so-called *second generation photovoltaics* $CuIn_xGa_{1-x}Se_2$ and CdTe solar cells. Both of them have been manufactured in large scale and are commercialized.

(i) For a long time, intensive researches on own initiative and within different levels of government programs are carried out on developing **thin-film crystalline Si solar cells**. These devices are opposed to solar cells based on silicon wafers or ribbons because are made by depositing thin silicon layer on a foreign substrate. The thickness of such a layer can vary from a few tens of nanometers to tens of micrometers. Thin-film solar cells based on **crystalline silicon on glass substrate** (**CSG**) occupy a special place in these studies (Basore, 2006; Widenborg & Aberle, 2007). Such devices have the potential to reduce considerably the cost of manufacture of photovoltaic modules due to a significant thinning the absorbing layer and the use of cheap glass substrates. Of course, in a thin layer and a thick wafer of silicon, processes of collection of photogenerated carriers may substantially differ due to differences not only of layer thickness but also the structure of the material and its parameters such as the lifetime of carriers, their mobility and others. Because the mobility and lifetime of charge carriers in thin-film silicon layers are relatively low, the carrier diffusion lengths are generally lower than the penetration depths for the long-wavelength part of the solar spectrum and a narrow p-n junction cannot be employed in the thin-film silicon case. For this reason, one has to use p-i-n diode structures, where the photo-generation takes place in the i-layer and transport and collection are drift-assisted (Shah et al., 2006).

All the same, the thickness of Si layer is of great importance for other reasons. If in a typical case, the Si thickness is less than ~ 2 μm, an effective optical enhancement technique (light trapping) is necessary. Indeed, approximately only half of the solar radiation is absorbed in such layer, even when eliminating the reflection from the front surface of the solar cell (Fig. 3(b)).

---

[4] For example, First Solar manufactures the CdTe-based modules (120 cm × 60 cm, 70-80 W) on high throughput, automated lines from semiconductor deposition to final assembly and test – all in one continuous process. The whole flow, from a piece of glass to a completed solar module, takes less than 2.5 hours.

One effective way to obtain light trapping is to texture the supporting material (glass substrate) prior to the deposition of the Si film. To implement this idea, in particular, a glass aluminium-induced texturing (AIT) method was developed (Widenborg & Aberle, 2007).

On the textured surface, silicon is deposited in amorphous form followed by solid-phase crystallisation and hydrogen passivation. An amorphous silicon is transformed into a polycrystalline layer after a special annealing at 400-600ºC. As a result of the texture, light is transmitted obliquely into the Si film, significantly enhancing the optical pathlength and thus increasing the optical absorption. The effect is further enhanced by depositing a high-quality reflector onto the back surface. Best optical absorption is obtained if the texture and the back surface reflector are optimised such that the total internal reflection occurs both at the front and the rear surface of the Si film, enabling multiple passes of the light through the solar cell. There are other glass texturing methods compatible with producing poly-Si thin-film solar cells, for example, CSG Solar's glass bead method (Ji & Shi, 2002). Apart from the light trapping benefits, the textured substrate also reduces reflection losses at the front surface of the solar cell.

It should be noted again that the development of silicon solar cells on glass substrate is not limited to the problem of light trapping. Fabrication of these modules is also facing serious problems of differences in the thermal expansion coefficients of silicon and substrate, the influence of substrate material on the properties of a silicon thin layer at elevated temperatures and many others.

Despite the efforts of scientists and engineers for about 30 years, the stabilized efficiency of typical CSG devices still does not exceed 9-10%. Nevertheless, large-area CSG modules with such efficiency produce sufficient power to provide installers with a cost-effective alternative to conventional wafer or ribbon Si based products. Because of a low cost of production even with reduced efficiency, large-area CSG modules are attractive for some applications and are in production in factories having a capacity of tens of MW per year (Basore, 2006).

(ii) **Dye-sensitized-solar-cells** (DSSCs), invented by M. Grätzel and coworkers in 1991, are considered to be extremely promising because they are made of low-cost materials with simple inexpensive manufacturing procedures and can be engineered into flexible sheets (O'Regan & Grätzel, 1991; Grätzel, 2003; Chiba et al., 2006).

DSSCs are emerged as a truly new class of energy conversion devices. Mechanism of conversion of solar energy into electricity in these devices is quite peculiar. Unlike a traditional solar cell design, dye molecules in DSSC absorb sunlight, just as it occurs in nature (like the chlorophyll in green leaves). A porous layer of nanocrystalline oxide semiconductor (very often TiO_2) provides charge collection and charge separation, which occurs at the surfaces between the dye, semiconductor and electrolyte. In other words, the natural light harvest in photosynthesis is imitated in DSSC. DSSCs are representatives of the *third generation solar technology*. The dyes used in early solar cells were sensitive only in the short-wavelength region of the solar spectrum (UV and blue). Current DSSCs have much wider spectral response including the long-wavelength range of red and infrared radiation. It is necessary to note that DSSCs can work even in low-light conditions, i.e. under cloudy skies and non-direct sunlight collecting energy from the lights in the house.

The major disadvantage of the DSSC design is the use of the liquid electrolyte, which can freeze at low temperatures. Higher temperatures cause the liquid to expand, which causes problems sealing of the cell. DSSCs with liquid electrolyte can have the less long-term stability due to the volatility of the electrolyte contained organic solvent. Replacing the liquid electrolyte with a solid has been a field of research.

It should be noted that DSSCs can degrade when exposed to ultraviolet radiation. However, it is believed that DSSCs are still at the start of their development stage. Efficiency gain is possible and has recently started to be implemented. These include, in particular, the use of quantum dots for conversion of higher-energy photons into electricity, solid-state electrolytes for better temperature stability, and more.

Although the light-to-electricity conversion efficiency is less than in the best thin film cells, the DSSC price should be low enough to compete with fossil fuel electrical generation. This is a popular technology with some commercial impact forecast especially for some applications where mechanical flexibility is important. As already noted, energy conversion efficiencies achieved are low, however, it has improved quickly in the last few years. For some laboratory dye-sensitized-solar-cells, the conversion efficiency of 10.6% under standard AM 1.5 radiation conditions has been reached (Grätzel, 2004).

 (iii) **Organic solar cells** attract the attention also by the simplicity of technology, leading to inexpensive, large-scale production. In such devices, the organic substances (polymers) are used as thin films of thickness ~ 100 nm. Unlike solar cells based on inorganic materials, the photogenerated electrons and holes in organic solar cells are separated not by an electric field of p-n junction. The first organic solar cells were composed of a single layer of photoactive material sandwiched between two electrodes of different work functions (Chamberlain, 1983). However, the separation of the photogenerated charge carriers was so inefficient that far below 1% power-conversion efficiency could be achieved. This was due to the fact that photon absorption in organic materials results in the production of a mobile excited state (exciton) rather than free electron-hole pairs in inorganic solar cells, and the exciton diffusion length in organic materials is only 5-15 nm (Haugeneder et al., 1999). Too short exciton diffusion length and low mobility of excitons are factors limiting the efficiency of organic solar cell, which is low in comparison with devices based on inorganic materials.

Over time, two dissimilar organic layers (bilayer) with specific properties began to be used in the organic solar cell (Tang, 1986). Electron-hole pair, which arose as a result of photon absorption, diffuses in the form of the exciton and is separated into a free electron and a hole at the interface between two materials. The effectiveness of ~ 7% reached in National Renewable Energy Laboratory, USA can be considered as one of best results for such kind of solar cells (1-2% for modules). However, instabilities against oxidation and reduction, recrystallization and temperature variations can lead to device degradation and lowering the performance over time. These problems are an area in which active research is taking place around the world. Organic photovoltaics have attracted much attention as a promising new thin-film PV technology for the future.

(iv) Of particular note are solar cells based on **III-V group semiconductors such as GaAs** and AlGaAs, GaInAs, GaInP, GaAsP alloys developed in many laboratories. These multi-junction cells consist of multiple thin films of different materials produced using metalorganic vapour phase epitaxy. Each type of semiconductor with a characteristic band gap absorbs radiation over a portion of the spectrum. The semiconductor band gaps are carefully chosen to generate electricity from as much of the solar energy as possible.

GaAs-based multi-junction devices were originally designed for special applications such as satellites and space exploration. To date they are the most efficient solar cells (higher than 41% under solar concentration and laboratory conditions), but the issue of large-scale use of GaAs-based solar cells in order to solve global energy problems is not posed (King, 2008; Guter at al., 2009).

Other solar cells have also been suggested, namely quantum dots, hot carrier cells, etc. However, they are currently studied at the cell-level and have a long way to be utilized in large-area PV modules.

3.1 Amorphous silicon

Amorphous silicon (a-Si) has been proposed as a material for solar cells in the mid 1970's and was the first material for commercial thin-film solar cells with all their attractiveness to reduce consumption of absorbing material, increase in area and downturn in price of modules.

It was discovered that the electrical properties of a-Si deposited from a glow discharge in silane (SiH$_4$) are considerably different from single-crystalline silicon (Deng & Schiff, 2003). When put into silane of a small amount of phosphine (PH$_3$) or boron (B$_2$H$_6$), electrical conduction of a-Si becomes n-type or p-type, respectively (Spear & Le Comber, 1975).

In 1976 Carlson and Wronski reported the creation of a-Si solar cells with efficiency of 2.4% using p-i-n structure deposited from a glow discharge in silane rather than evaporating silicon (Carlson & Wronski, 1976). The maximum efficiency of thin film amorphous silicon solar cells was estimated to be 14–15%.

a-Si is an allotropic form of silicon, in which there is no far order characteristic of a crystal. Due to this, some of a-Si atoms have nonsaturated bonding that appears as imperfection of the material and significantly affects its properties. The concentration of such defects is reduced by several orders due to the presence of hydrogen, which is always present in large quantities when obtained from the silane or at the surface treatment by hydrogen. The hydrogen atoms improve essentially the electronic properties of the plasma-deposited material. This material has generally been known as *amorphous hydrogenated silicon* (a-Si:H) and applied in the majority in practice.

Depending on the gas flow rate and other growth conditions, the optical band gap of a-Si:H varies, but typically ranges from 1.6 to 1.7 eV. Its absorption coefficient is much higher than that of mono-crystalline silicon (Fig. 4). As it has been noted, in the case of a-Si:H, the thickness of 2-6 μm (rather than 300 μm as in the case of c-Si) is sufficient for almost complete (95%) absorption of solar radiation in the $h\nu \geq E_g$ spectral range. It is also important that the technology of a-Si:H is relatively simple and inexpensive compared to the technologies for growing Si crystals. The low deposition temperature (< 300°C) and the application of the monolithic technique for a-Si:H module manufacturing were generally considered as key features to obtain low costs of the devices.

As in the past, the layers of a-Si:H can be deposited on large area (1 m^2 or more) usually by method termed as plasma enhanced chemical vapor deposition (PECVD) on glass coated with transparent conductive oxide (TCO) or on non-transparent substrates (stainless steel, polymer) at relatively low temperatures (a-Si:H can be also deposited roll-to-roll technology). Like the crystalline silicon, a-Si:H can be doped creating p-n junctions, which is widely used in other field of electronics, particularly in thin-film transistors (TFT).

This opens up the possibility of relatively easy to form the desired configuration of the active photodiode structure of the solar cell. To date, p-i-n junction is normally used in solar cells based on a-Si:H. The i-layer thickness is amount to several hundred nanometers, the thickness of frontal p-film, which is served as a "window" layer, is equal to ~ 20 nm, the back n-layer can be even thinner. It is believed that almost all electron-hole pairs are photogenerated in the i-layer, where they are separated by electric field of p-i-n structure. The output power of a-Si:H solar cell can has a *positive temperature coefficient*, i.e. at elevated ambient temperatures the efficiency is higher.
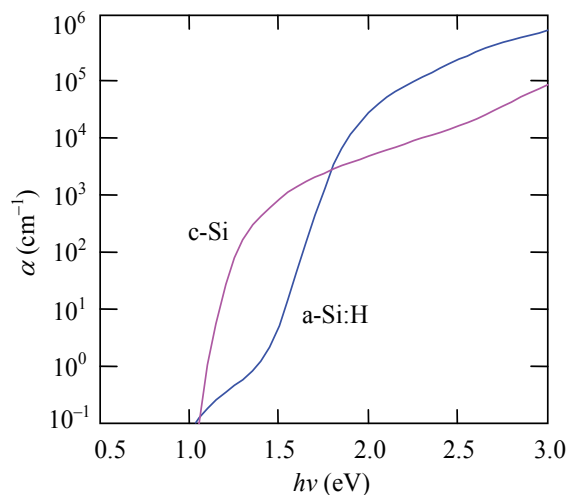
Fig. 5. Spectral dependence of absorption coefficient *a* in the crystalline (c-Si) and amorphous hydrogenated silicon (a-Si: H).

Quite common in commercial solar cells are the **multi-layer structures** based on amorphous silicon and silicon germanium alloys, when the p-i-n photodiode structures (subcells) with different band gap semiconductors are superimposed one layer on another. It seemed that the spectrum splitting tandem structure, a representative of the *third generation of solar cells*, opened the prospect of developing highly efficient and low-cost solar cells (Kuwano et al. 1982).

One of the tandem a-Si:H structures is shown in Fig. 6. This is the so-called superstrate design, when solar radiation enters through the transparent substrate such as glass or polymer (the substrate design with flexible stainless steel foil is also widely used). In the superstrate design, p- , i- and n-layers of a-Si:H are consistently applied on a glass plate coated with a transparent film (ITO, SnO_2). Over them the analogous layers of a-SiGe:H alloy are deposited in the discharge of silane CH_4 together with GeH_4. The frontal 0.5-µm thick layers of p-i-n structure absorb photons with energies larger than ~ 1.9 eV and transmits photons with energies lower than ~ 1.9 eV. The band gap of a-SiGe:H alloy is lower than that of a-Si, therefore the radiation that has passed through a-Si will be absorbed in the a-SiGe layers, where additional electron-hole pairs are generated and solar cell efficiency increases. Even greater effect can be achieved in a triple-junction structure a-Si/a-SiGe/a-SiGe. One of the record efficiency of such solar cell is 14.6% (13.0% stabilized efficiencies) (Yang et al,. 1997). At high content of Ge in $Si_{1-x}Ge_x$ alloy, optoelectronic properties of the material are deteriorated, therefore in multi-junction solar cells, the band gap of the amorphous $Si_{1-x}Ge_x$ layers cannot be less than 1.2-1.3 eV.

The results presented in Fig. 4, show that 10-15% of solar radiation power in the range $h\nu > E_g$ is not absorbed if the thickness of the a-Si layer is 1 µm. Therefore, to improve the power output, back reflector and substrate texturing can be used in a-Si solar cells. Apparently, the light trapping occurs for weakly absorbed light. It was shown that using geometries maximizing enhancement effects, the short circuit current in amorphous silicon solar cell (< 1 µm thick) increases by several mA/cm² (Deckman et al., 1983).

The use of multi-junction solar cells is successful because there is no need for lattice matching of materials, as is required for crystalline heterojunctions.
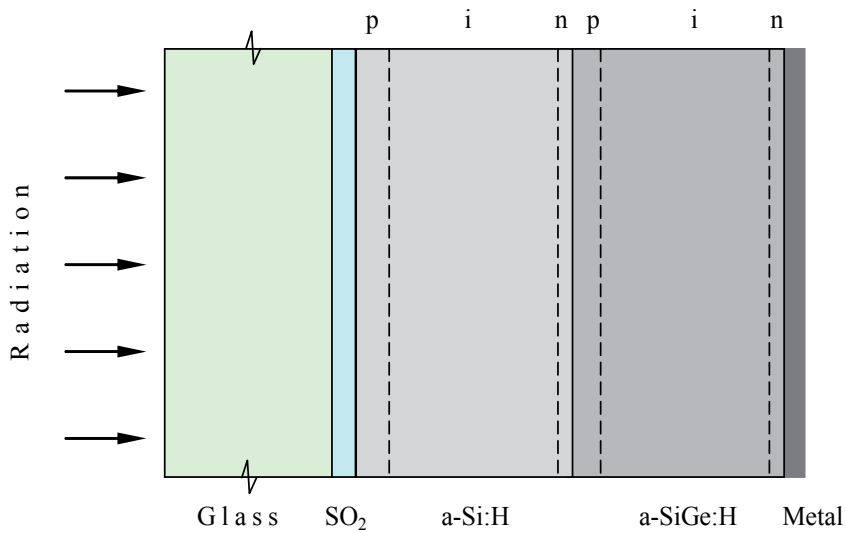
Fig. 6. Tandem solar cell based on a-Si:H and a-SiGe:H (Deng & Schiff, 2003).

Solar cells based on a-Si:H are much cheaper than those produced on silicon wafers or ribbons, but their efficiency in operation under illumination becomes lower during the first few hundred hours and then the degradation process is slowed down considerably (Fig. 7). The degradation of multiple-junction and single-junction solar cells is usually in the range of 10-12 and 20-40%, respectively (20-30% for commercial devices).

Degradation of a-Si:H solar cells, called the Staebler–Wronski effect, is a *fundamental* a-Si property. The same degradation is observed in solar cells from different manufacturers and with different initial efficiencies (Von Roedern et al., 1995). It has been established that stabilization of the degradation occurs at levels that depend on the operating conditions, as well as on the operating history of the modules. After annealing for several minutes at 130-150°C, the solar cell properties can be restored. The positive effect of annealing can also occur
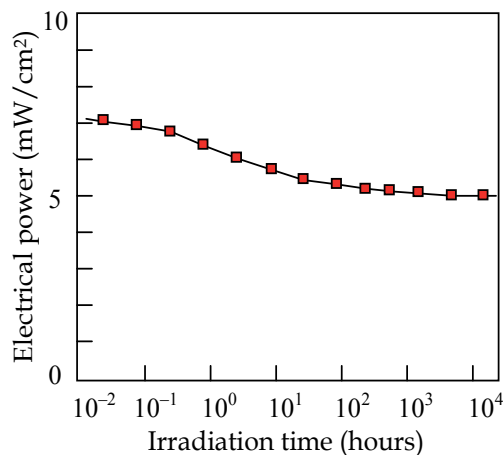
Fig. 7. Decline in power output of solar cell based on a-Si:H in the initial period of irradiation 100mV/sm² (Staebler–Wronski effect) (Deng & Schiff, 2003).

as a result of *seasonal* temperature variations therefore the efficiency of a-Si:H modules in the summer is greater than in winter.

Degradation of a-Si:H solar cells is mostly caused by photostimulated formation of defects (dangling bonds) that act as recombination centers (Staebler & Wronski, 1977). The effect can not be explained by a single degradation mechanism. At least two mechanisms have to be involved: a fast one that can be annealed at typical module operating temperatures, and a slow one that does not recover measurably when annealing temperatures are limited to values below 70°C (Von Roedern et al., 1995; Von Roedern & del Cueto, 2000).

It is important from a practical point of view that a-Si:H reaches a "stabilized" state after extended irradiation. The stabilized a-Si:H arrays show less than 1% degradation per year, which is about the same rate at which crystalline silicon losses power over time. Therefore, still 20 years ago, it was recommended that all a-Si solar cells and modules performances should be reported after stabilization under standard conditions for 1000 hours at 50°C (Von Roedern & del Cueto, 2000).

Along with amorphous silicon, during the same 30 years, the intensive investigations of the possibility of using the glow discharge method for producing **thin-film crystalline silicon** were also carried out (Faraji et al., 1992; Meier et al., 1994). In 1994, using this method thin-film p-i-n solar cells based on hydrogenated **microcrystalline silicon** (**µc-Si**) have been prepared at substrate temperatures as low as ~ 200°C (Meier et al., 1994). Compared with a-Si:H solar cells, an enhanced absorption in the near-infrared (up to 1.1 eV) and an efficiency of 4.6% were obtained. First light-soaking experiments indicate also no degradation for such µc-Si:H cells. Years later, other groups started research activities utilizing this material and naming the microcrystalline silicon as "**nanocrystalline**" (**nc-Si**) or "**policrystalline**" **silicon** (**poly-Si**).

Microcrystalline silicon (µc-Si, nc-Si,poly-Si) has small grains of crystalline silicon (< 50 nm) within the amorphous phase. This is in contrast to multi-crystalline silicon, which consists solely of crystalline silicon grains separated by grain boundaries. Microcrystalline silicon has a number of useful advantages over a-Si, because it can have a higher electron mobility due to the presence of the silicon crystallites. It also shows increased absorption in the red and infrared regions, which makes µc-Si as an important material for use in solar cells. Another important advantages of µc-Si is that it has improved stability over a-Si, one of the reasons being because of its lower hydrogen concentration. There is also the advantage over poly-Si, since the µc-Si can be deposited using conventional low temperature a-Si deposition techniques, such as plasma enhanced chemical vapor deposition.

Special place in the thin-film photovoltaics is the so-called **micromorph solar cells**, which are closely related to the amorphous silicon. The term "micromorph" is used for stacked tandem thin-film solar cells consisting of an a-Si p-i-n junction as the top component, which absorbs the "blue" light, and a µc-Si p-i-n junction as the bottom component, which absorbs the "red" and near-infrared light in the solar spectrum (Fig. 8). This artificial word has first been mentioned by Meier in the late 1990's (Meier et al., 1995; Meier et al., 1998).

A double-junction or tandem solar cell consisting of a microcrystalline silicon solar cell (E_g = 1.1 eV) and an amorphous silicon cell (E_g ≈ 1.75 eV) corresponds almost to the theoretically optimal band gap combination. Using µc-Si:H as the narrow band gap cell instead of a-SiGe cell yields the higher efficiency in the long-wavelength region. At the same time, the stable µc-Si:H bottom cell contributes to usually a better stability of the entire micromorph tandem cell under light-soaking. The stabilized efficiency of such double-junctions solar cells of 11-12% was achieved (Meier et al., 1998).

It was also suggested that the micromorph solar cells open new perspectives for low-temperature thin-film crystalline silicon technology and even has the potential to become for the next third generation of thin-film solar cells (Keppner et al., 1999). However, due to the effect of the indirect band, the µc-Si component of solar cells requires much thicker i-layers to absorb the sunlight (1.5 to 2 µm compared to 0.2 µm thickness of a-SiGe:H absorber). At the same time, the deposition rate for µc-Si:H material is significantly lower compared to that for a-SiGe, so that a much longer time is needed to deposit a thicker µc-Si layer than what is needed for an a-SiGe structure. In addition, advanced light enhancement schemes need to be used because µc-Si has a lower absorption coefficient. Finally, µc-Si solar cell has a lower open-circuit voltage compared to a-SiGe:H cell.

Nevertheless, one should tell again that micromorph tandem solar cells consisting of a microcrystalline silicon bottom cell and an amorphous silicon top cell are considered as one of the promising thin-film silicon solar-cell devices. The promise lies in the hope of simultaneously achieving high conversion efficiencies at relatively low manufacturing costs.
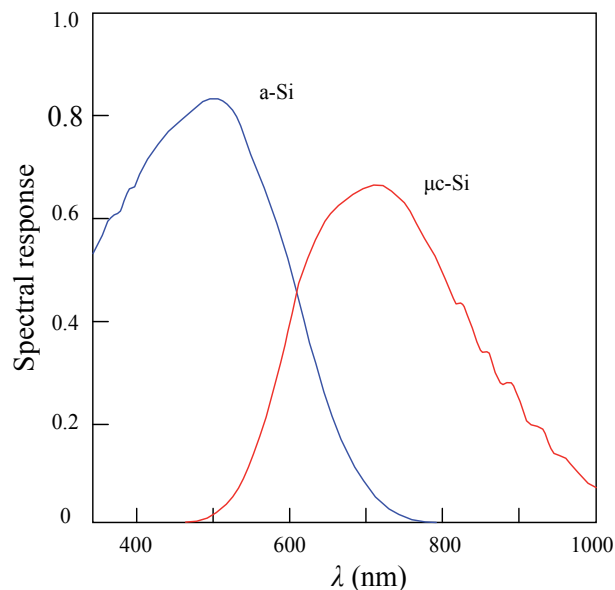
Fig. 8. Spectral response of a double-stacked micromorph tandem solar cell (Keppner et al., 1999).

Concluding the section, one must admit the considerable progress for more than 30 years in improving the efficiency of a-Si and micromorph solar cells. However, despite the persistent efforts of researchers and engineers in various laboratories in many countries, under initiatory researches and government programs, stabilized efficiency of large-area a-Si:H solar modules lies within 8 to 10%. So far, stabilized efficiencies of about 11-12% can be obtained with micromorph solar cells. A number of technological methods allow the efficiency just somewhat to increase using the above alloys of Si-Ge and special multiple-junction structures including the use of µc-Si:H and others.[5] But the cost of such multiple-

---

[5] One of the highest stabilized cell efficiency for a laboratory triple-junction structure is ~ 13.0% (Deng & Schiff, 2003).

junction solar cells always increases markedly. In addition, faster deposition processes need to be developed that is necessary for low-cost and high-throughput manufacturing.

Thus, in the field of amorphous and micromorph silicon photovoltaics, it is succeeded in realizing only part of the benefits of thin-film solar cells, and its share in the global solar energy is quite small (Fig. 1). The use of a-Si:H and micromorph solar cells is limited preferably to areas where low cost is more important than the efficiency of photoelectric conversion (such as consumer electronics). Semitransparent modules are also used as architectural elements or windows and skylights. This is the so-called building-integrated photovoltaics (BIPV), where large building envelope areas can be covered with the PV modules available at the lowest prices per square meter. The advantage of BIPV is also that the initial cost can be offset by reducing the amount spent on building materials. This trend becomes noticeable segment of the photovoltaic industry.

3.2 Copper-indium-gallium diselenide

$CuInSe_2$ (CIS) and $CuGaSe_2$ (CGS), compound semiconductors of elements from groups I, III and VI in the periodic table, are typical representatives of a broad class of substances with different properties, so-called chalcopyrite.[6] $CuInSe_2$ and $CuGaSe_2$ form $CuIn_xGa_{1-x}Se_2$ alloy (CIGS) in any ratio of components. Importantly, varying the ratio of $CuInSe_2$ and $CuGaSe_2$, there is a slight change in the material parameters except the band gap. The possibility of regulating the band gap semiconductor in the range of 1.0-1.04 eV for $CuInSe_2$ to 1.68 eV for $CuGaSe_2$ are doubtless advantages of $CuIn_xGa_{1-x}Se_2$ (Birkmire, 2008).[7] The dependence of the band gap of $CuIn_xGa_{1-x}Se_2$ on x is described by the formula (Alonso, 2002):

$$E_g(x) = 1.010 + 0.626x - 0.167x(1-x).$$ (2)

For a long time, $CuInSe_2$ and $CuIn_xGa_{1-x}Se_2$ have been considered as promising materials for high-performance thin-film solar cells and fabrication of monolithically interconnected modules intended for cost-effective power generation (Shafarman & Stolt, 2003).

Parameters of $CuIn_xGa_{1-x}Se_2$ can be fitted as optimal for the photoelectric conversion. The fundamental absorption edge is well described by expression $a \sim (hv - E_g)^{1/2}/hv$ as for a typical direct band gap semiconductor. When the photon energy hv exceeds the band gap E_g, the absorption coefficient of material from any content of Ga quickly exceeds values $\sim 10^4$ cm^{-1} so that the absorptivity of the material turns out to be the largest among all thin film (Fig. 4). This ensures effective absorption of solar radiation by $CuIn_xGa_{1-x}Se_2$ layer of micron-level thick – an important factor in reducing the cost of production. Efficiency of $CuInSe_2$ solar cell is within 12-15%, and in the case of $CuIn_xGa_{1-x}Se_2$ a record value of $\sim$ 20% is reached among all types of thin-film solar cells (Repins, et al., 2008; Green et al, 2011). Widening the band gap of $CuIn_xGa_{1-x}Se_2$ leads to an increase in open circuit voltage while reducing the absorptivity of the material and hence decreasing the short circuit current. Theoretical estimation shows that the maximum efficiency of solar cells should be observed when E_g = 1.4-1.5 eV, when the atomic ratio for Ga in CIGS is $\sim$ 0.7, but according to the experimental data, this occurs when $E_g \approx 1.15$ eV that corresponds to Ga/(Ga+In) $\approx$ 0.3.

---

[6] Chalcopyrite (copper pyrite) is a mineral $CuFeS_2$, which has a tetragonal crystal structure.
[7] Sometimes part of Se atoms substitute for S.

Structural, electrical and optical properties of $CuIn_xGa_{1-x}Se_2$ are sensitive to deviations from the stoichiometric composition, native defects and grain sizes in the film. Because of the native defects (mainly In vacancies and Cu atoms on In sites), the conductivity of CIGS is p-type. It can be controlled by varying the Cu/In ratio during growth of the material. Stoichiometric and copper-enriched material has a p-type conductivity and grain sizes of 1-2 µm, while the material indium-enriched has n-type conductivity and smaller grains. $CuIn_xGa_{1-x}Se_2$ within the solar cell contains a large amount of Na (~ 0.1%), which are predominantly found at the grain boundaries rather than in the bulk of the grains and can improve solar cell performance. Depending on the pressure of selenium, the type conductivity of material as a result of annealing can be converted from p-type to n-type – or vice versa. Charge carrier density can vary widely from 10^{14} cm^{-3} to 10^{19} cm^{-3}. In general, the desirable conductivity and carrier concentration can be relatively easy to obtain without special doping, but only the manipulating technological conditions of $CuIn_xGa_{1-x}Se_2$ deposition.

Literature data on the charge carrier mobility in thin-film $CuIn_xGa_{1-x}Se_2$ are quite divergent. The highest hole mobility is fixed as 200 cm²/V·s at 10^{17} cm^{-3} hole concentration. It is likely that the conductivity across grain boundaries in this case plays a significant role. In $CuIn_xGa_{1-x}Se_2$ single crystals, mobility of holes lies within the 15-150 cm²/V·s range for holes and in the 90-900 cm²/V·s range for electrons (Neumann & Tomlinson, 1990; Schroeder & Rockett, 1997).

The first photovoltaic structures based on $CuInSe_2$ with efficiency of ~ 12% were established back in 1970's by evaporating n-CdS onto p-$CuInSe_2$ single crystal (Wagner et al., 1974; Shay et al., 1975). Shortly thin-film $CdS/CuInSe_2$ solar cells were fabricated with efficiency 4-5% (Kazmerski et al., 1976), interest to which became stable after the Boeing company had reached 9.4% efficiency in 1981 (Mickelson & Chen, 1981; Shafarman & Stolt, 2003). Such solar cells were produced by simultaneous thermal evaporation of Cu, In and Se from separate sources on heated ceramic substrates coated with thin layer of Mo (*thermal multi-source co-evaporation process*). Later the method of simultaneous deposition Cu, In, Ga and Se become widely used to create $CuIn_xGa_{1-x}Se_2$ layers. Chemical composition of material is determined by temperatures of sources: 1300-1400° C for Cu, 1000-1100°C for In, 1150-1250°C for Ga and 300-350°C for Se. The main advantage of this technology is its flexibility; the main problem is the need for careful control of flow of Cu, In, Ga and Se, without which it is impossible to have adequate reproducibility characteristics of the film. In this regard, attractive is the so-called *two-step process*, that is, the deposition of Cu, In and Ga on substrates at a low temperature with subsequent a reactive heat-treatment of Cu-In-Ga films in a hydrogen-selenium (H_2Se) atmosphere at temperatures above ~ 630°C (Chu et al., 1984). Application of Cu, In and Ga can be achieved by various methods at low temperatures, among them is ion sputtering, electrochemical deposition and other methods that are easier to implement in mass production. Selenization can be conducted at atmospheric pressure at relatively low temperatures of 400-500°C. The main problem of this technology is the complexity of controlling the chemical composition of material as well as high toxicity of H_2Se.

To date, the co-deposition of copper, indium, gallium and selenium as well as selenization remain the main methods in the manufacture of CIGS solar cells.

In the first thin-film $CuInSe_2$ solar cells, heterojunction was made by deposition of CdS on $CuInSe_2$ thin film, which also served as front transparent electrode (Mickelson & Chen, 1981). Characteristics of solar cell are improved if on $CuInSe_2$ (or $CuIn_xGa_{1-x}Se_2$) first to

deposit undoped CdS, and then low-resistive CdS doped with In or Ga (pre-inflicted undoped CdS layer is called the "buffer" layer). Due to a relatively narrow band gap (2.42 eV), CdS absorbs solar radiation with a wavelengths λ < 520 nm, without giving any contribution to the photovoltaic efficiency. Absorption losses in the CdS layer can be reduced by increasing the band gap, alloying with ZnS (CdZnS) that results in some increase in the efficiency of the device. Its further increase is achieved by thinning CdS layer to 50 nm or even 30 nm followed by deposition of conductive ZnO layer, which is much more transparent in the whole spectral region (Jordan, 1993; Nakada, T. & Mise, 2001). The best results are achieved when ZnO is deposited in two steps, first a high-resistance ZnO layer and then a doped high-conductivity ZnO layer. Often, ZnO films are deposited by magnetron sputtering from $ZnO:Al_2O_3$ targets or by reactive sputtering, which requires special precision control technology regime. For high-efficiency cells the TCO deposition temperature should be lower than 150°C in order to avoid the detrimental interdiffusion across CdS/CIGS interface (Romeo et al., 2004).

Usually, $Cu(In,Ga)Se_2$ solar cells are grown in a substrate configuration which provides favorable process conditions and material compatibility. Structure of a typical solar cell is shown in Fig. 9. To reduce the reflection losses at the front surface of ZnO, an anti-refection MgF_2 coating with thickness of ~ 100 nm is also practised. The substrate configuration of solar cell requires an additional encapsulation layer and/or glass to protect the cell surface. In modules with cover glasses, to use any anti-refection coating is not practical.
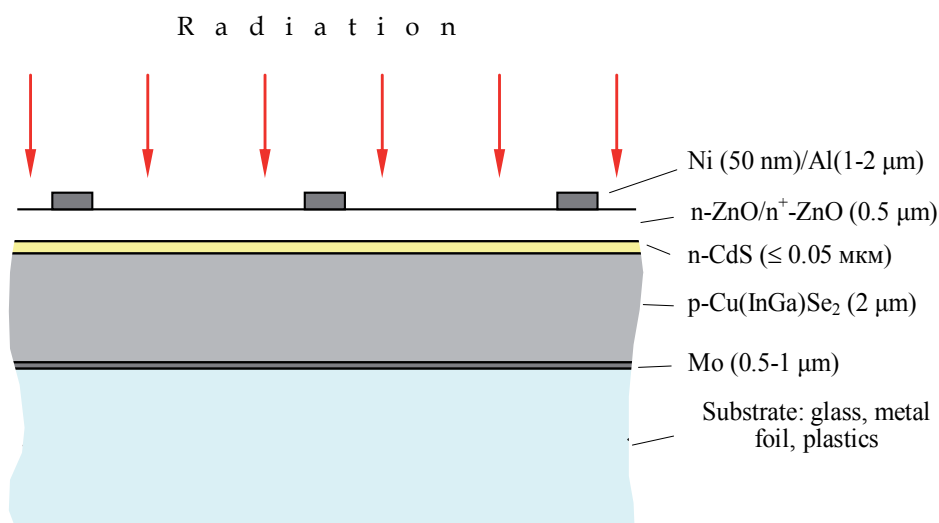
Fig. 9. Schematic cross section of a typical $Cu(In,Ga)Se_2$ solar module.

CdS layer is made by chemical precipitation from an aqueous alkali salt solution of cadmium ($CdCl_2$, $CdSO_4$, CdI2, $Cd(CH3COO)_2$), ammonia (NH_3) and thiourea ($Sc(NH_2)_2$ in molar ratio, for example, 1.4:1:0.1 (*chemical bath deposition*). Pseudo-epitaxial deposition of CdS dense films is carried out by immersing the sample in electrolyte for several minutes at temperatures from 60 to 80°C or at room temperature followed by heating electrolyte to the same temperature. The pseudo-epitaxial character of deposition is promoted, firstly, by small (~ 0.6%) difference of $CuInSe_2$ and CdS lattice spacing, which, however, increases with

increasing Ga content in CuInxGa$_{1-x}$Se$_2$ (to ~ 2% at x = Ga/(Ga+In) = 0.5), and, secondly, by the cleansing effect of electrolyte as a surface etchant of CuIn$_x$Ga$_{1-x}$Se$_2$ (ammonia removes oxides on the surface). Depending on the conditions of deposition, the film may have hexagonal, cubic or a mixed structure with crystallite sizes of several tens of nanometers. Typically, film is somewhat non-stoichiometric composition (with an excess of Cd) and contains impurities O, H, C, N that can become apparent in a noticeable narrowing of the band gap. It is believed that the Cd in Cu(InGa)Se$_2$ modules can be handled safely, both with respect to environmental concerns and hazards during manufacturing (Shafarman & Stolt, 2003).

At relatively low temperature of deposition, the mutual penetration (migration) of elements at the CdS/CuIn$_x$Ga$_{1-x}$Se$_2$ interface takes place to a depth of 10 nm (Cd replace Cu). It should be noted that vacuum deposition of CdS, used in solar cells on single crystals CuIn$_x$Ga$_{1-x}$Se$_2$, is not suitable for thin film structures and does not allow to obtain the dense film of necessary small thickness and requires too high deposition temperature (150-200ºC). Deposition of CdS by ion sputtering gives better results, but still inferior to chemical vapor deposition.

Metal contacts in the form of narrow strips to the front surface of Cu(In,Ga)Se$_2$ device is made in two steps: first a thin layer of Ni (several tens of nanometers), and then Al layer with thickness of several microns. Purpose of a thin layer is to prevent the formation of oxidation layer.

As substrate for CuIn$_x$Ga$_{1-x}$Se$_2$ solar cells, the window soda-lime-silica glass containing 13-14% Na$_2$O can be used. The coefficients of linear expansion of this glass and CuIn$_x$Ga$_{1-x}$Se$_2$ are quite close (9×10^{-6} K^{-1}) in contrast to borosilicate glass, for which the coefficient of linear expansion is about half. Glass is the most commonly used substrate, but significant efforts have been made to develop flexible solar cells on polyimide and metal foils providing less weight and flexible solar modules. Highest efficiencies of 12.8% and 17.6% have been reported on polyimide and metal foils, respectively (Tiwari etal., 1999; Tuttle et al., 2000). Cu(In,Ga)Se$_2$ modules have shown stable performance for prolonged operation in field tests.

As already mentioned, it is believed that the p-n junction is formed between p-CuIn$_x$Ga$_{1-x}$Se$_2$ and n-ZnO, "ideal" material that serves as a "window" of solar cell (ZnO has band gap of 3.2 eV, high electrical conductivity and thermal stability). However, a thin underlayer CdS (~ 0.05 nm) affect a strong influence on the characteristics of solar cell by controlling the density of states at the interface and preventing unwanted diffusion of Cu, In, Se in ZnO.

Somewhat simplified energy diagram of solar cell based on CuIn$_x$Ga$_{1-x}$Se$_2$ is shown in Fig. 10.

Band discontinuity ΔE_c = 0.3 eV at the CdS/CuIn$_x$Ga$_{1-x}$Se$_2$ interface causes considerable band bending near the CuIn$_x$Ga$_{1-x}$Se$_2$ surface, and, thus, the formation of p-n junction (Schmid et al., 1993). Diffusion of Cd in CuIn$_x$Ga$_{1-x}$Se$_2$ during chemical vapor deposition of CdS also promotes this resulting in forming p-n *homojunction near surface* of CuIn$_x$Ga$_{1-x}$Se$_2$.

Marginal impact of losses caused by recombination at the CdS/CuIn$_x$Ga$_{1-x}$Se$_2$ interface is explained by the creation of p-n junction, despite the fact that no measures are preventable to level the lattice difference and defects on the surface which is in the air before deposition of CdS.

As always, the short-circuit current of CuIn$_x$Ga$_{1-x}$Se$_2$ solar cell is the integral of the product of the external quantum efficiency and the spectral density of solar radiation power. QE_{ext}, which, in turn, is determined primarily by the processes of photoelectric conversion in the CuIn$_x$Ga$_{1-x}$Se$_2$ absorber layer, i.e. by the internal quantum yield of the device QE_{int}.

It is believed that the solar cell can neglect recombination losses at the CdS/Cu(In,Ga)Se$_2$ interface and in the space-charge region and then one can write (Fahrenbruch A. & Bube, 1983):
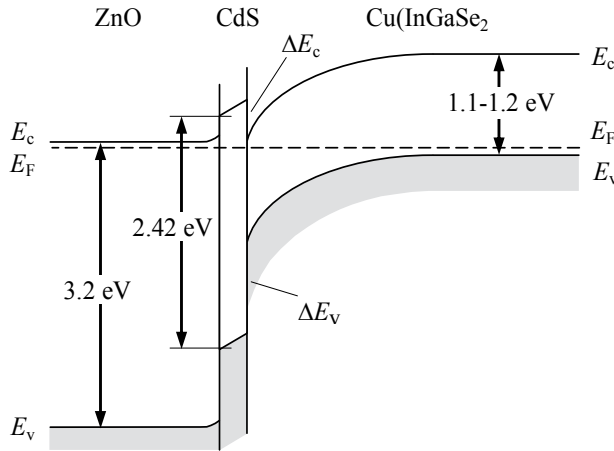
Fig. 10. Energy diagram of ZnO/CdS/CuIn$_x$Ga$_{1-x}$Se$_2$ solar cell.

$$QE_{int} = 1 - \frac{\exp(-\alpha W)}{1 + \alpha L_n}, \qquad (3)$$

where a is the light absorption coefficient, and W is the space-charge region width.

Besides QE_{int}, external quantum efficiency is also controlled by the above-mentioned reflection at the front surface of the device, reflection at all other interfaces, the band gap of CuIn$_x$Ga$_{1-x}$Se$_2$ and the transmittances of CdS and ZnO window layers.

Fig. 11 shows the measured spectral distribution of quantum efficiency of solar cells based on CuIn$_x$Ga$_{1-x}$Se$_2$ with different composition x = 0, 0.24 and 0.61, and hence with different band gap of semiconductor E_g = 1.02, 1.16 and 1.40 eV, respectively.

Another important characteristic of CuIn$_x$Ga$_{1-x}$Se$_2$ solar cell, the open-circuit voltage, is determined by the charge transport mechanism in the heterostructure. Neglecting recombination at the interface of CdS-CuIn$_x$Ga$_{1-x}$Se$_2$, the current-voltage characteristics of solar cells can be presented in the form

$$J = J_d - J_{ph} = J_o \exp\left[\frac{q}{nkT}(V - R_sJ)\right] + GV - J_{ph} \qquad (4)$$

where J_d is the dark current density, J_{ph} is the photocurrent density, n is the ideality factor, R_s is the series resistance, and G is the shunt conductivity.

The experimental curves are often described by Eq. (4) at n = 1.5 ± 0.3 that leads to the conclusion that the dominant charge transfer mechanism is recombination in the space charge region. If recombination level is located near mid-gap, $n \approx 2$, and in case of shallow level $n \approx 1$. In real CuIn$_x$Ga$_{1-x}$Se$_2$, the levels in the band gap are distributed quasi-continuously.

If the minority carrier diffusion length is short, the losses caused by recombination at the rear surface of CuIn$_x$Ga$_{1-x}$Se$_2$ is also excluded. In the best solar cells the electron lifetime is 10^{-8}-10^{-7} s (Nishitani et al., 1997; Ohnesorge et al., 1998). When describing transport properties CuIn$_x$Ga$_{1-x}$Se$_2$, it can to be acceptable that grain boundaries do not play any noticeable role since the absorber layer has a *columnar structure* and the measured current does not cross the grain boundaries. As notes, solar cells have the highest photovoltaic efficiency if x = Ga/(In + Ga) $\approx$ 0.3, i.e., $E_g \approx$ 1.15 eV. Under AM1.5 global radiation, the
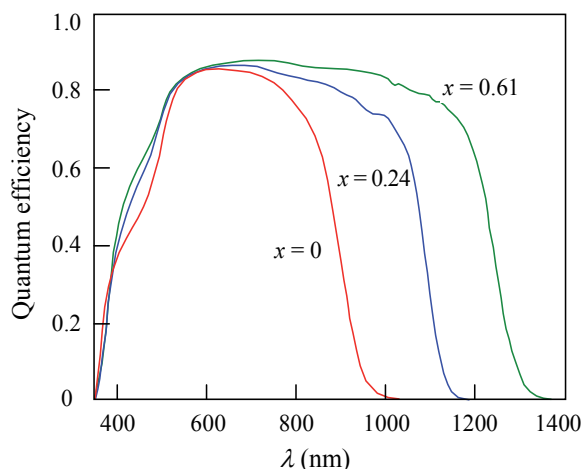
Fig. 11. Spectral distribution of quantum efficiency of $CuIn_xGa_{1-x}Se_2$ solar cells with x = 0, 0.24 and 0.61 (Shafarman & Stolt, 2003).

highest value of short-circuit current density J_{sc} = 35.2 mA/sm² is observed for solar cells with E_g = 1.12 eV (Contreras et al., 1999). If short-circuit current decreases with increasing Ga content, the open-circuit voltage V_{oc} increases. With increasing temperature V_{oc} markedly reduces. For E_g = 1.16 eV, for example, V_{oc} reduces from ~ 0.75 V at 220 K to ~ 0.55 V at 320 K. Introduction of Ga in $CuInSe_2$ compound attracts of professionals by the fact that it reduces the cost of In, which is widely used in LCD monitors, computers, TV screens and mobile phones. Therefore there is an attempt to reduce the content of In in $CuIn_xGa_{1-x}Se_2$ solar cells up to 5-10%, even slightly losing the photovoltaic conversion efficiency.

The efficiencies of laboratory $CuIn_xGa_{1-x}Se_2$ solar cells and modules of large area are significantly different. The reason is that the production of modules requires the introduction of technology different qualitatively from that used in the traditional semiconductor electronics, and a significant lack of deep scientific basis of applied materials. As a result of research, aimed to reducing the cost of $CuIn_xGa_{1-x}Se_2$ solar modules (which were originally more expensive compared to devices on amorphous silicon), Würth Solar (Germany) and Shell Solar Industries (USA) developed the first commercial $CuIn_xGa_{1-x}Se_2$ solar modules and initiated their large-scale production, which began in 2006 in Germany.

In the production of such modules are also engaged other companies in a number of countries, among them Zentrum für Sonnenenergie- und Wasserstoff-Forschung – ZSW (Germany), Energy Photovoltaics, Inc. and International Solar Electric Technology (USA), Angstrom Solar Centre (Sweden), Showa Shell and Matsushita (Japan) and others. Technology for production of solar modules on flexible substrates involving «roll-to-roll» technology was developed by Global Solar Energy (USA, Germany).

$CuIn_xGa_{1-x}Se_2$-based photovoltaics, along with other thin-film PV devices, continue to attract an interest first and foremost because of their potential to be manufactured at a lower cost than Si wafer or ribbon based modules. To reach their potential for large-scale power generation with higher throughput, yield, and performance of products, there is a need for continued improvement in the fundamental science, deposition equipment and processes based on well-developed models. Note also that the scarce supply of In may make it difficult to implement CIGS technology on a large scale.

3.3 Cadmium telluride

Cadmium telluride (CdTe) is a semiconductor with the band gap of 1.47-1.48 eV (290-300 K), optimal for solar cells. As a-Si, CIS and CIGS, CdTe is a direct-gap semiconductor, so that the thickness of only a few microns is sufficient for almost complete absorption of solar radiation (97-98%) with photon energy $h\nu > E_g$ (Fig. 4). As the temperature increases the efficiency of CdTe solar cell is reduced less than with silicon devices, which is important, given the work of solar modules in high-power irradiation. Compared to other thin-film materials, technology of CdTe solar modules is simpler and more suitable for large-scale production.

Solar cells based on CdTe have a rather long history. Back in 1956, Loferski theoretically grounded the use of InP, GaAs and CdTe in solar cells as semiconductors with a higher efficiency of photoelectric conversion compared with CdS, Se, AlSb and Si (Loferski, 1956). However, the efficiency of laboratory samples of solar cells with p-n junctions in monocrystalline CdTe, was only ~ 2% in 1959, has exceeded 7% only in 20 years and about 10% later (Minilya-Arroyo et al, 1979; Cohen-Solal et al., 1982). The reason for low efficiency of these devices were great losses caused by surface recombination and technological difficulties of p-n junction formation with a thin front layer. Therefore, further efforts were aimed at finding suitable *heterostructures*, the first of which was p-Cu_2Te/n-CdTe junction with efficiency of about 7%, that was proved too unstable through the diffusion of copper. It was investigated other materials used as heteropartners of n-type conductivity with wider band gap compared with CdTe: ITO, In_2O_3, ZnO performed the function of "window" through which light is introduced in the photovoltaic active layer of absorbing CdTe.

In 1964, the first heterojunctions obtained by spraying a thin layer of n-CdS on the surface of p-CdTe single crystal were described (Muller & Zuleeg, 1964). The first *thin-film* CdTe/CdS/SnO_2/glass structures that became the prototype of modern solar cells, was established in Physical-Technical Institute, Tashkent, Uzbekistan in 1969 (Adirovich et al., 1969). Over the years it became clear that the CdS/CdTe heterostucture has a real prospect of the introduction into mass production of solar modules, despite the relatively narrow band gap of CdS as a "window" layer. The crystal of CdTe adopts the wurtzite crystal structure, but in most deposited CdTe films, hexagonally packed alternating Cd and Te layers tend to lie in the plane of the substrate, leading to columnar growth of crystallites. At high temperature, CdTe grows stoichiometrically in thin-film form as natively p-doped semiconductor; no additional doping has to be introduced. Nevertheless, the cells are typically "activated" by using the influence of $CdCl_2$ at elevated temperatures (~ 400°C) that improves the crystallinity of the material.

In the early 21st century it has been succeeded to achieve a compromise between the two main criteria acceptable for manufacturing CdTe solar modules – sufficient photoelectric conversion efficiency and cheapness of production (Bonnet, 2003). This was possible thanks to the development of a number of relatively simple and properly controlled method of applying large area of CdTe and CdS thin layers that is easy to implement in large-scale production: close-space sublimation, vapor transport deposition, electrodeposition, chemical bath deposition, sputter deposition, screen printing. Obstruction caused by considerable differences of crystal lattice parameters of CdTe and CdS (~ 5%), largely overcome by straightforward thermal treatment of the produced CdTe/CdS structure. It is believed that this is accompanied by a mutual substitution of S and Te atoms and formation an intermediate $CdTe_{1-x}S_x$ layer with reduced density of states at the interface of CdTe and CdS, which may adversely affect the efficiency of solar cell. Simple methods of production and

formation of barrier structures, that do not require complex and expensive equipment, are an important advantage of the solar cell technology based on CdTe.

When producing solar cells, CdS and CdTe layers are usually applied on a soda-lime glass superstrate (~ 3 mm thick), covered with a transparent electrically conductive oxide layer (TCO), e.g., F-doped SnO_2 (SnO_2:F) or ITO (In_2O_3 + SnO_2) (Fig. 12) (Bonnet, 2003).[8] They are often used in combination with a thin (high-resistivity) SnO_x sublayer between the TCO and the CdS window layer, which prevents possible shunts through pinholes in the CdS and facilitates the use of a thinner CdS layer for reducing photon absorption losses for wavelengths shorter than 500 nm (Bonnet, 2002). At the final stage, after deposition of the back electrodes, solar cells are covered by another glass using the sealing material (etylenvinil acetate, EVA), which provides durability and stability of the devices within 25-35 years.

Processes of photoelectric conversion in thin-film CdS/CdTe structure are amenable to *mathematical description*. This is of practical importance because it allows to investigate the dependence of the efficiency of solar cells on the parameters of the materials and the barrier structure as well as to formulate recommendations for the technology. These parameters are, primarily, (i) the width of the space-charge region, (ii) the lifetime of minority carriers, (iii) their diffusion length, (iv) the recombination velocity at the front and back surfaces of the CdTe absorber layer, (v) its thickness.

R a d i a t i o n

Glass (~ 3 мм)
TCO (~ 0.25 μm)
CdS (≤ 0.1 μm)
CdTe (3-7 μm)
Rear contact
Sealing material
Glass (~ 3 μm)
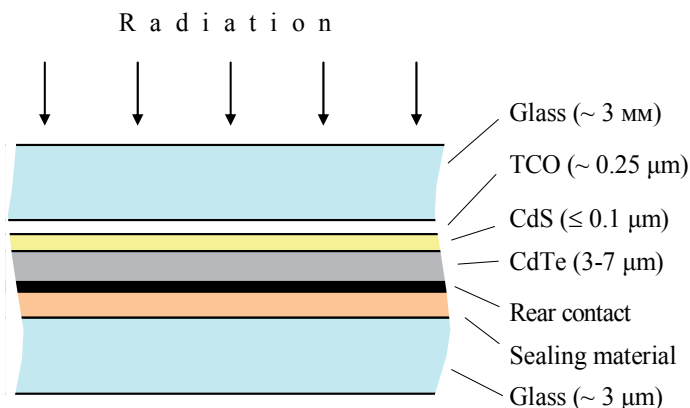
Fig. 12. Cross-section of thin film solar cell CdS/CdTe.

One of the main characteristics of a solar cell is the *spectral distribution of quantum efficiency* (spectral response), which is ultimately determined the short-circuit current density of the CdS/CdTe heterostructure.

It is known that in CdS/CdTe solar cells only the CdTe layer contributes to the light-to-electric energy conversion, while the CdS "window" layer only absorbs light in the range λ < 500-520 nm thereby reducing the photocurrent. Therefore in numerous papers a band bending (and hence a depletion layer) in CdS is not depicted on the energy diagram (see, for example, Birkmire & Eser, 1997; Fritsche et al., 2001; Goetzberger et al, 2003), i.e. the

---

[8] The CdTe solar cells can be produced in both substrate and superstrate configurations, but the latter is preferable. The substrate can be a low-cost soda-lime glass for growth process temperatures below 550°C, or alkali-free glass for high-temperature processes (550–600°C) (Romeo et al., 2004).

depletion layer of the CdS/CdTe diode structure is virtually located in the p-CdTe layer (Fig. 13). This is identical to the case of an asymmetric abrupt p-n junction or a Schottky diode, i.e. the potential energy $\varphi(x,V)$ and the space-charge region width W in the CdS/CdTe heterojunction can be expressed as (Sze, 1981):

$$\varphi(x,V) = (\varphi_o - qV)\left(1 - \frac{x}{W}\right)^2 , \qquad (5)$$

$$W = \sqrt{\frac{2\varepsilon\varepsilon_o(\varphi_o - qV)}{q^2(N_a - N_d)}} , \qquad (6)$$

where ε_o is the electric constant, ε is the relative dielectric constant of the semiconductor, $\varphi_o = qV_{bi}$ is the barrier height at the semiconductor side (V_{bi} is the built-in potential), V is the applied voltage, and $N_a - N_d$ is the uncompensated acceptor concentration in the CdTe layer. The *internal* photoelectric quantum efficiency η_{int} can be found from the continuity equation with the boundary conditions. The exact solution of this equation taking into account the *drift* and *diffusion components* as well as surface recombination at the interfaces leads to rather cumbersome and non-visual expressions (Lavagna et al., 1977). However, in view of the real CdS/CdTe thin-film structure, the expression for the *drift* component of the quantum efficiency can be significantly simplified (Kosyachenko et al., 2009):

$$\eta_{drift} = \frac{1 + \dfrac{S}{D_n}\left(\alpha + \dfrac{2}{W}\dfrac{\varphi_o - qV}{kT}\right)^{-1}}{1 + \dfrac{S}{D_n}\left(\dfrac{2}{W}\dfrac{\varphi_o - qV}{kT}\right)^{-1}} - \exp(-\alpha W) \cdot \qquad (7)$$

where S is the recombination velocity at the front surface, D_n is the electron diffusion coefficient related to the electron mobility μ_n through the Einstein relation: $qD_n/kT = \mu_n$.

For the *diffusion* component of the photoelectric quantum yield that takes into account surface recombination at the back surface of the CdTe layer, one can use the exact expression obtained for the p-layer in a p-n junction solar cell (Sze, 1981)

$$\eta_{dif} = \frac{\alpha L_n}{\alpha^2 L_n^2 - 1}\exp(-\alpha W) \times$$

$$\times \left\{\alpha L_n - \frac{\dfrac{S_b L_n}{D_n}\left[\cosh\left(\dfrac{d-W}{L_n}\right) - \exp(-\alpha(d-W))\right] + \sinh\left(\dfrac{d-W}{L_n}\right) + \alpha L_n \exp(-\alpha(d-W))}{\dfrac{S_b L_n}{D_n}\sinh\left(\dfrac{d-W}{L_n}\right) + \cosh\left(\dfrac{d-W}{L_n}\right)}\right\}, \qquad (8)$$

where d is the thickness of the CdTe absorber layer, S_b is the recombination velocity at its back surface.

The *total* quantum yield of photoelectric conversion in the CdTe absorber layer is the sum of the two components: $\eta_{int} = \eta_{drift} + \eta_{dif}$.

Fig. 14 illustrates a comparison of the calculated curve $\eta_{ext}(\lambda)$ using Eqs. (5)-(8) with the measured spectrum (Kosyachenko et al., 2009). As seen, very good agreement between the calculated curve and the experimental points has been obtained.
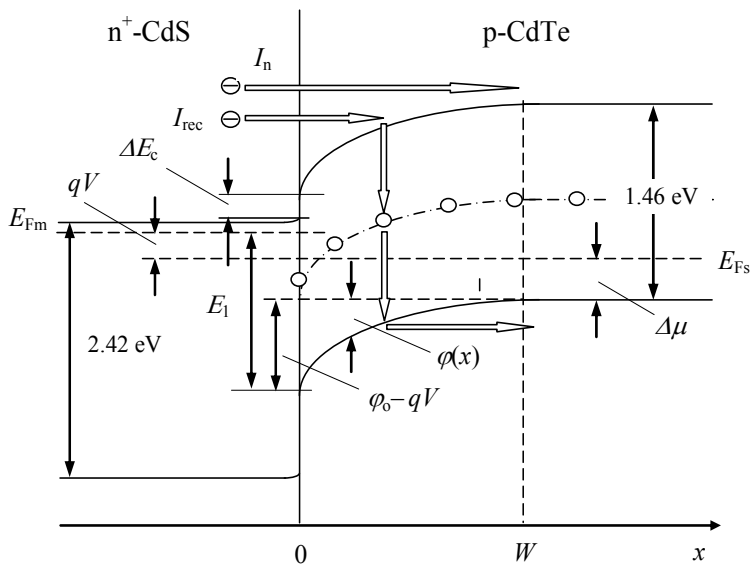
Fig. 13. The energy band diagram of CdS/CdTe thin-film heterojunction under forward bias. The electron transitions corresponding to the recombination current I_{rec} and over-barrier diffusion current I_n are shown.
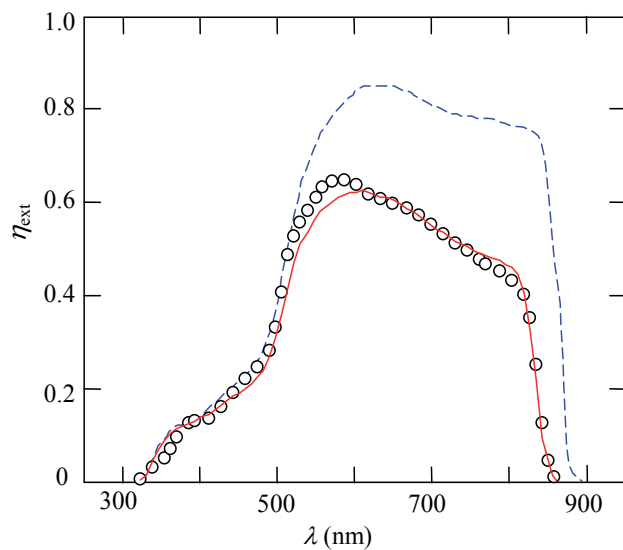
Fig. 14. Comparison of the measured (circles) and calculated (solid line) quantum efficiency spectrum η_{ext}. The dashed line shows the spectrum of 100 % *internal* efficiency.

The expressions for quantum efficiency spectra can be used to calculate the short-circuit current density J_{sc} using AM1.5 solar radiation Tables ISO 9845-1:1992 (Standard ISO, 1992). If Φ_i is the spectral radiation power density and $h\nu$ is the photon energy, the spectral density of the incident photon flux is $\Phi_i/h\nu_i$ and then

$$J_{sc} = q \sum_i \eta_{\text{int}}(\lambda) \frac{\Phi_i(\lambda)}{h v_i} \Delta \lambda_i , \qquad\qquad (9)$$

where $\Delta \lambda_i$ is the wavelength range between the neighboring values of λ_i (the photon energy $h v_i$) in the table and the summation is over the spectral range 300 nm $\leq \lambda \leq \lambda_g = hc/E_g$.

The calculation results of the *drift* component of short-circuit current density J_{drift} using Eqs. (7) and (9) lead to important practical conclusions (Kosyachenko et al., 2008).

If $S = 0$, the short-circuit current gradually increases with widening W and approaches a maximum value $J_{\text{drift}} = 28.7$ mA/cm^2 at $W > 10$ μm. Surface recombination decreases J_{drift} only in the case if the electric field in the space-charge region is not strong enough, i.e. when the uncompensated acceptor concentration $N_a - N_d$ is low. As $N_a - N_d$ increases and consequently the electric field strength becomes stronger, the influence of surface recombination becomes weaker, and at $N_a - N_d \geq 10^{16}$ cm^{-3} the effect of surface recombination is virtually eliminated. However in this case, J_{drift} decreases with increasing $N_a - N_d$ because a significant portion of radiation is absorbed outside the space-charge region. Thus, the dependence of drift component of the short-circuit current on the uncompensated acceptor concentration $N_a - N_d$ is represented by a curve with a maximum at $N_a - N_d \approx 10^{15}$ cm^{-3} ($W \approx 1$ μm).

The *diffusion* component of short-circuit current density J_{dif} is determined by the thickness of the absorber layer d, the electron lifetime τ_n and the recombination velocity at the back surface of the CdTe layer S_b. If, for example, $\tau_n = 10^{-6}$ s and $S_b = 0$, then the total charge collection in the neutral part is observed at $d = 15\text{-}20$ μm and to reach the total charge collection in the case $S_b = 10^7$ cm/s, the CdTe thickness should be 50 μm or larger (Kosyachenko et al., 2008). In this regard the question arises why for total charge collection the thickness of the CdTe absorber layer d should amount to several tens of micrometers. The matter is that, as already noted, the value of d is commonly considered to be in excess of the effective penetration depth of the radiation into the CdTe absorber layer in the intrinsic absorption region of the semiconductor, i.e. in excess of $d = 10^{-4}$ cm = 1 μm. With this reasoning, the absorber layer thickness is usually chosen at a few microns. However, one does not take into account that the carriers, arisen outside the space-charge region, *diffuse* into the neutral part of the CdTe layer penetrating deeper into the material. Having reached the back surface of the CdTe layer, carriers recombine and do not contribute to the photocurrent. Considering the spatial distribution of photogenerated electrons in the neutral region shows that at $S_b = 7 \times 10^7$ cm/s, typical values of $\tau_n = 10^{-9}$ s and $N_a - N_d = 10^{16}$ cm^{-3} and at $d = 1\text{-}2$ μm, surface recombination "kills" most of electrons photogenerated in the neutral part of the CdTe layer (Kosyachenko et al., 2009).

Fig. 15 shows the calculation results of the *total* short-circuit current density J_{sc} (the sum of the drift and diffusion components) vs. $N_a - N_d$ for different electron lifetimes τ_n. Calculations have been carried out for the CdTe film thickness $d = 5$ μm which is often used in the fabrication of CdTe-based solar cells. As can be seen, at $\tau_n \geq 10^{-8}$ s the short-circuit current density is 26-27 mA/cm^2 when $N_a - N_d > 10^{16}$ cm^{-3} and for shorter electron lifetime, J_{sc} peaks at $N_a - N_d = (1\text{-}3) \times 10^{15}$ cm^{-3}.

As $N_a - N_d$ is in excess of this concentration, the short-circuit current decreases since the drift component of the photocurrent reduces. In the range of $N_a - N_d < (1\text{-}3) \times 10^{15}$ cm^{-3}, the short-circuit current density also decreases, but due to recombination at the front surface of the CdTe layer.
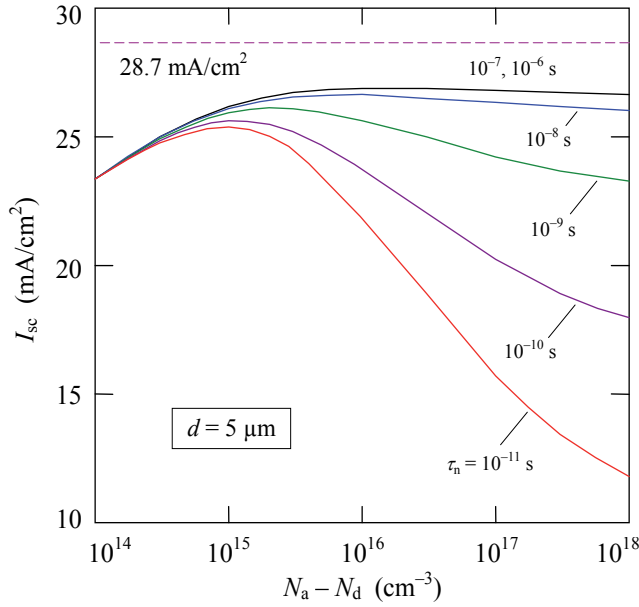
Fig. 15. *Total* short-circuit current density J_{sc} of a CdTe-based solar cell as a function of the uncompensated acceptor concentration N_a – N_d calculated at the absorber layer thickness d = 5 μm for different electron lifetime τ_n.

The *I-V* characteristic determined the open-circuit voltage and fill factor of CdS/CdTe solar cells is most commonly described by the semi-empirical formulae similar to Eq. (4), which consists the so-called "ideality" factor and is valid for some cases. Our measurements show, however, that such "generalization" of the formulae does not cover the observed variety of the CdS/CdTe solar cell *I-V* characteristics. The measured voltage dependences of the forward current are not always exponential and the saturation of the reverse current is *never* observed.

On the other hand, our measurements show that the *I-V* characteristics of CdS/CdTe heterostructures and their temperature variation are governed by the generation-recombination Sah-Noyce-Shockley theory (Sah at al., 1957). According to this theory, the dependence $I \sim \exp(qV/nkT)$ at $n \approx 2$ takes place only in the case, where the generation-recombination energy level is located near the middle of the band gap. If the level moves away from the mid-gap the coefficient n becomes close to 1 but only at low forward voltage. If the forward voltage elevates, the *I-V* characteristic modifies in the dependence where $n \approx 2$ and at higher voltages the dependence I on V becomes even weaker (Sah et al., 1957; Kosyachenko et al., 2004). Certainly, at higher forward currents, it is also necessary to take into account the voltage drop across the series resistance R_s of the bulk part of the CdTe layer by replacing the voltage V in the discussed expressions with V – $I·R_s$.

The Sah-Noyce-Shockley theory supposes that the generation-recombination rate in the space-charge region is determined by expression

$$U(x,V) = \frac{n(x,V)p(x,V) - n_i^2}{\tau_{po}\left[n(x,V) + n_1\right] + \tau_{no}\left[p(x,V) + p_1\right]} ,\qquad (10)$$

where $n(x,V)$ and $p(x,V)$ are the carrier concentrations in the conduction and valence bands, n_i is the intrinsic carrier concentration. The n_1 and p_1 values in Eq. (10) are determined by the energy spacing between the top of the valence band and the generation-recombination level E_t, i.e. $p_1 = N_v \exp(- E_t/kT)$ and $n_1 = N_c \exp[- (E_g - E_t)/kT]$, where $N_c = 2(m_n kT/2\pi\hbar^2)^{3/2}$ and $N_v = 2(m_p kT/2\pi\hbar^2)^{3/2}$ are the effective density of states in the conduction and valence bands, m_n and m_p are the effective masses of electrons and holes, and τ_{no} and τ_{po} are the lifetime of electrons and holes in the depletion region, respectively.

The recombination current under forward bias and the generation current under reverse bias are found by integration of $U(x, V)$ throughout the entire depletion layer:

$$J_{gr} = q \int_0^W U(x,V)dx \; . \tag{11}$$

In Eq. (10) the expressions for $n(x,V)$ and $p(x,V)$ in the depletion region have the forms:

$$p(x,V) = N_c \exp\left[-\frac{\Delta\mu + \varphi(x,V)}{kT} \right], \tag{12}$$

$$n(x,V) = N_v \exp\left[-\frac{E_g - \Delta\mu - \varphi(x,V) - qV}{kT} \right], \tag{13}$$

where $\Delta\mu$ is the energy spacing between the Fermi level and the top of the valence band in the bulk of the CdTe layer, $\varphi(x,V)$ is the potential energy given by Eq. (5).

Over-barrier (diffusion) carrier flow in the CdS/CdTe heterostructure is restricted by high barriers for both majority carriers (holes) and minority carriers (electrons) (Fig. 13). That is why, under low and moderate forward voltages, the dominant charge transport mechanism is caused by recombination in the space-charge region. However, as qV nears φ_o, the over-barrier currents due to much stronger dependence on V become comparable and even higher than the recombination current. Since in CdS/CdTe heterojunction the barrier for holes is considerably higher than that for electrons, the *electron* component dominates the over-barrier current, which can be written as (Sze, 1981):

$$J_n = q\frac{n_p L_n}{\tau_n}\left[\exp\left(\frac{qV}{kT} \right) - 1 \right], \tag{14}$$

where $n_p = N_c \exp[- (E_g - \Delta\mu)/kT]$ is the concentration of electrons in the neutral part of the p-CdTe layer.

Thus, the dark current density $J_d(V)$ in CdS/CdTe heterostructure is the sum of the generation-recombination and diffusion components:

$$J_d(V) = J_{gr}(V) + J_n(V) \; . \tag{15}$$

The results of comparison between theory and experiment are demonstrated in Fig. 16 on the example of *I-V* characteristic, which reflects especially pronounced features of the transport mechanism in CdS/CdTe solar cell (Kosyachenko et al., 2010). As is seen, there is an extended portion of the curve (0.1 < V < 0.8 V), where the dependence $I \sim \exp(qV/AkT)$ holds for $n = 1.92$ (rather than 2!).
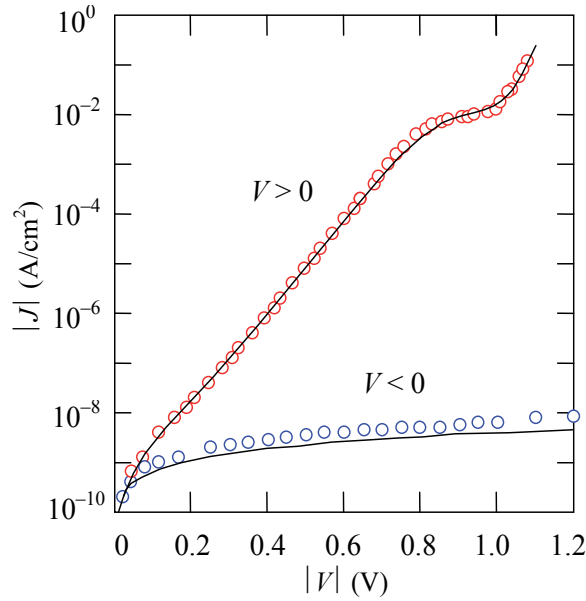
Fig. 16. Room-temperature *I-V* characteristic of thin-film CdS/CdTe heterostructure. The circles and solid lines show the experimental and calculated results, respectively.

At higher voltages, the deviation from the exponential dependence toward lower currents is observed. However, if the voltage elevates still further (> 1 V), a much steeper increase of forward current occurs. Analysis shows that all these features are explained in the frame of mechanism involving the generation-recombination in the space-charge region in a wide range of moderate voltages completed by the over-barrier diffusion current at higher voltages.

One can see in Fig. 16 that the *I-V* characteristic calculated in accordance with the above theory are in good agreement with experiment both for the forward and reverse connections of the solar cell. Note that the reverse current increases continuously with voltage rather than saturates, as requires the commonly used semi-empirical formula.

Knowing the dark *I-V* characteristic, one can find the *I-V* characteristic under illumination as

$$J(V) = J_d(V) - J_{ph} \tag{16}$$

and determine the open-circuit voltage and fill factor. In Eq.(16) $J_d(V)$ and J_{ph} are the dark current and photocurrent densities, respectively. Of course, it must be specified a definite value of the density of short circuit current J_{sc}. Keeping in view the determination of conditions to maximize the photovoltaic efficiency, we use for this the data shown in Fig. 15, i.e. set $J_{sc} \approx 26$ mA/cm^2. This is the case for $N_a - N_d = 10^{15}$-10^{16} cm^{-3} and a film thickness $d = 5$ μm, which is often used in the fabrication of CdTe-based solar cells.

Fig. 17 shows the open-circuit voltage V_{oc} and the efficiency η of CdS/CdTe heterostructure as a function of effective carrier lifetime τ calculated for various resistivities of the p-CdTe layer ρ.

As seen in Fig. 17(a), the open-circuit voltage V_{oc} considerably increases with lowering ρ and increasing τ (as ρ varies, $\Delta\mu$ also varies affecting the value of the recombination current, and especially the over-barrier current).
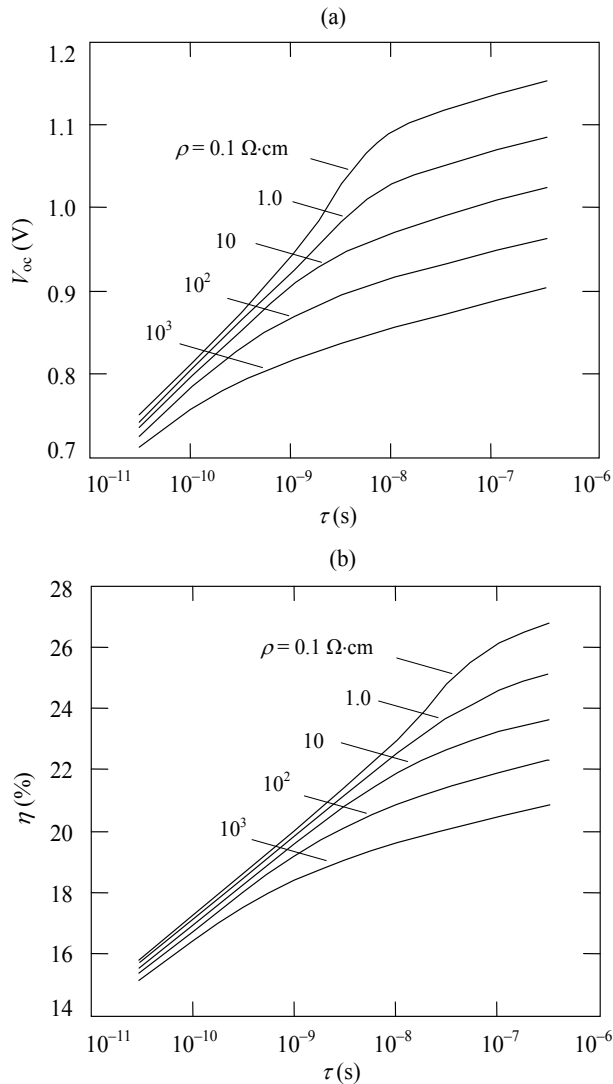
Fig. 17. Dependences of the open-circuit voltage V_{oc} (a) and efficiency η (b) of CdS/CdTe heterojunction on the carrier lifetime τ calculated by Eq. (16) using Eqs. (10)-(15) for various resistivities ρ of the CdTe layer.

In the most commonly encountered case, as $\tau = 10^{-10}$-10^{-9} s, the values of $V_{oc} = 0.8$-0.85 V (0.75-0.8 V for commercial devices) are far from the maximum possible values of 1.15-1.2 V, which are reached on the curve for $\rho = 0.1$ Ω·cm and $\tau > 10^{-8}$ s.

As seen in Fig. 17(b), the dependence of the efficiency $\eta = P_{out}/P_{irr}$ on τ remarkably increases from 15-16% to 21-27.5% when τ and ρ changes within the indicated limits (P_{irr} is the AM 1.5 solar radiation power 100 mW/cm²). For $\tau = 10^{-10}$-10^{-9} s, the efficiency lies near 17-19% and the enhancement of η by lowering ρ of the CdTe layer is 0.5-1.5%. Thus, assuming $\tau = 10^{-10}$-10^{-9} s, the calculated results turn out to be quite close to the experimental efficiencies of the best thin-film CdS/CdTe solar cells (16-17%).

The enhancement of η from 16-17% to 27-28% is possible if the carrier lifetime increases to $\tau \geq 10^{-6}$ s and the resistivity of CdTe reduces to $\rho \approx 0.1$ Ω·cm. This also requires an increase in the short-circuit current density. As follows from the foregoing, the latter is possible for the thickness of the CdTe absorber layer of 20-30 μm and even more. Evidently, this is not justified for large-scale production of solar modules.

In the early years of 21 century, the technology and manufacturing of solar modules based on CdTe, which could compete with silicon counterparts was developed. With mass production, the efficiency of CdTe modules is 10-11% with the prospect of an increase in a few percents in the coming years (Multi Year Program Plan, 2008). The cost of modules over the past five years has decreased three times and crossed the threshold $1.0 per Wp, that is much less than wafer or ribbon based modules on silicon. In 2012-2015, the cost of CdTe-based solar modules is expected to be below $ 0.7 per Wp.

It should be noted that the growth rates of CdTe module production over the last decade are the highest in the entire solar energy sector. Over the past 5 years, their annual capacity increased more than an order of magnitude, greatly surpassing the capacity of the counterparts based on a-Si and in a few times – based on CIS (CIGS). In Germany, Spain, USA and other countries, CdTe solar photovoltaic power plants with a capacity of several megawatts up to several tens of megawatts have been built. Annual production of solar modules based on CdTe by only one company First Solar, Inc. in 2009-2010 exceeded 1.2 GW). This company is the largest manufacturer of solar modules in the world, which far exceeded the capacities of perennial leaders in the manufacture of solar modules and continues to increase production, despite the economic and financial crisis. Other well known companies such as AVA Solar and Prime Star Solar (USA), Calyxo GmbH and Antec Solar Energy AG (Germany), Arendi SRL (Italy) are also involved in the production of CdTe solar modules. In May 2010 the General Electric company announced plans to introduce production of CdTe thin-film solar modules based on technology developed at the National Renewable Energy Laboratory and PrimeStar Solar. These facts remove any doubt on the prospects of solar energy based on CdTe.

One of the arguments advanced against the use of CdTe in solar energy is based on the fact that natural resources of Cd and Te are limited.

Indeed, Cd and Te are rare and scattered elements; their content in the earth's crust is $\sim 10^{-5}$% and $\sim 10^{-7}$-10^{-6}%, respectively. Currently, there are no commercial deposits of Cd and Te in the world; Cd and Te are extracted as byproducts in the production of mainly zinc and copper, respectively. The limiting raw factor for development of solar energy through the production of CdTe is Te. For the world needs, cadmium is annually produced just 150-200 tons. According to the National Renewable Energy Laboratory, the U.S. Department of Energy and other agencies, annual production of Te as a byproduct of copper production can be increased to $\sim$ 1.5 tons. For the module production with capacity of 1 GW, approximately 70 tons of Te are needed at present 10-11% efficiency of modules. Using each year, for example, 1 thousand tons one can make solar modules with power $\sim$ 15 GW. Thus, through Te only as a byproduct in the production of Cu, accelerated development of solar energy based on CdTe can last for several decades. Other currently unused stocks of tellurium, particularly in South America, China, Mexico and other places of the globe are also known. With good reason Te was not the focus of geological exploration, however, studies in recent years show that, for example, underwater crusts throughout the ocean basins is extremely rich in Te, whose content of Te $\sim 10^9$ times higher compared with ocean water and $\sim 10^4$ times higher than in the Earth's crust (Hein et al., 2003). These stocks of

tellurium in a relatively small depth of ocean (e.g. ~ 400 m) can easily meet the needs of the whole world's energy. It should also be noted that the additional costs of Cd and Te will not arise after 25-35 years, when CdTe solar panels expend their resources. The technologies for *recycling* the worked-out products, which allows majority of the components (~ 90%) to use in the production of new solar modules, have been already developed.

Another objection to the proliferation of CdTe solar cells, which opponents argue, is that the Cd, Te and their compounds are extremely harmful to humans.

Indeed, Cd and Te are toxic heavy metals; Cd is even cancer-causing element. However, the research of many independent experts of the National Renewable Energy Laboratory and Brookhaven National Laboratory show that CdTe compound is chemically stable, biologically inert and does not constitute a threat to human health and the environment both in terms of production and exploitation of solar modules (Bonnet, 2000; Fthenakis, 2008). Cd emissions to the atmosphere is possible only if the temperature exceeds ~ 1050ºC in case of fire. However, CdTe in solar module is between two glass plates in a sealed condition. With this design, glass will melt at temperatures much lower than 1050ºC, CdTe will turn in the molten mass that does not allow the allocation of Cd and Te in the atmosphere. It has been shown that the release of cadmium to the atmosphere is lower with CdTe-based solar cells than with silicon photovoltaics. Despite much discussion of the toxicity of CdTe-based solar cells, this is technology that is reliably delivered on a large scale.

4. Conclusions

Analysis of photovoltaics development leads to the negative conclusion that the desired rate of increase in the capacity of solar energy based on single-crystalline, polycrystalline and amorphous silicon can not be provided. Despite a long history, the share of PV currently amounts to a small fraction of the overall balance of the world power sector, and even according to the most optimistic forecasts, will not dominate in 2050. Resources of hydroelectric and wind energy are limited, the expansion of nuclear power is highly problematic from a security standpoint. This means that a significant fraction of the energy will be generated by natural gas, oil, coal, oil shale, biomass, which can lead to irreversible changes in climate on Earth. The main reason for the slow development of the photovoltaics based on wafer or ribbon silicon (as its main direction) is the high consumption of materials, energy and labor, and hence too low productivity and high cost of production. This is determined by the *fundamental* factor because the single-crystalline and polycrystalline silicon are indirect-gap semiconductors. The technology of solar modules based on direct-gap amorphous silicon is quite complicated, and their stabilized efficiency is too low for use in large-scale energy. In this regard, there is an urgent need to involve other areas of photovoltaics in energy production. Thin-film technologies using direct-gap semiconductors such as CIGS and CdTe hold the promise of significantly accelerating the development of photovoltaics. Intensive research and development of thin-film technologies based on other materials, for example, organic and die-sensitizes solar cells is also being conducted. The main advantages of thin-film technology are less material consumption, lower requirements to the parameters of the materials, ease of engineering methods of manufacture, and the possibility of full automation. All of this provides better throughput of manufacturing and lower production costs, i.e. just what is lacking in wafer or ribbon based silicon photovoltaics. CdTe and CIGS based modules have proved their viability. Solar power stations based on these materials with a capacity from a few megawatts to a few tens of megawatts have already

been built; several agreements for the construction of such plants with a capacity higher by one or even two orders of magnitude have been concluded. A growing number of companies are involved in the production of CdTe and CIGS based modules. Broad front of research on the possibility of increasing the efficiency of the modules, which in mass production is much lower than the theoretical predictions, are being conducted. The aforesaid, of course, does not preclude participation in the production of electrical energy of photovoltaics based on single-crystalline, polycrystalline, ribbon and amorphous silicon with different designs of solar cell structures. A large number of companies are involved in the production of the silicon modules, which are continually evolving, making a potential contribution to the energy, but they cannot solve the problem globally for the foreseeable future.

5. Acknowledgements

6. References

Adirovich, E.I., Yuabov, Yu.M., Yagudaev, G.R. (1969). Photoelectric phenomena in film diodes with heterojunction. *Sov. Phys. Semicond*. 3, 61-65

Alonso, M.I., Garriga, M., Durante Rincón, C.A., Hernández, E. and León, M. (2002). Optical functions of chalcopyrite $CuGa_xIn_{1-x}Se_2$ alloys. *Applied Physics A: Materials Science & Processing*, 74, 659-664.

Basore, P.A. (2006). CSG-2: Expanding the production of a new polycrystalline silicon PV technology. *Proc. of the 21st European Photovoltaic Solar Energy Conference*.

Birkmire, R.W. & Eser, E. (1997). Polycrystalline thin film solar cells: Present status and future potential, *Annu. Rev. Mater. Sc.* 27, 625.

Birkmire, R.W. (2008). Pathways to improved performance and processing of CdTe and $CuInSe_2$ based modules. C*onference Record of 33rd IEEE Photovoltaic Specialists Conference*. pp. 47-53.

Bonnet, D. (2001). Cadmium telluride solar cells. In: *Clean Electricity from Photovoltaics*. Ed. By M.D. Archer and R. Hill. Imperial College Press, New York. pp. 245-275.

Bonnet, D., Oelting, S., Harr, M., Will, S. (2002). Start-up and operation of an integrated 10MWp thin film PV module factory. *Proceedings of the 29th IEEE Photovoltaic Specialists Conference*, pp. 563–566.

Bonnet, D. (2003). Cadmium telluride thin-film PV modules. in: *Practical Handbook of Photovoltaics: Fundamentals and Applications*, edited by T. Markvart and L. Castaner, (Elseiver, New York,). p. 333-366.

Britt, J. & Ferekides, C. (1993). Thin Film CdS/CdTe Solar Cell with 15.8% efficiency. *Appl. Phys. Lett.* 62, 2851-2852.

Carlson, D.E. & Wronski, C.R. (1976). Amorphous silicon solar cell. *Appl. Phys. Lett.* 28, 671-672

Chamberlain, G.A. (1983). Organic solar cells: a review. *Solar Cells,* 8, 47-83.

Chiba, Y.; Islam, A.; Watanabe, Y.; Koyama, R.; Koide, N.; & Han, L. (2006). Dye-Sensitized Solar Cells with Conversion Efficiency of 11.1% *Jpn. J. Appl. Phys.* 45, L638-L640.

Chu, T.L, Chu, S., Lin, S., Yue, J. (1984). Large Grain Copper Indium Didiselenide Films. *J. Electrochemical Soc*. 131, 2182-2185.

Contreras, M.A., Egaas, B., Ramanathan, K., Hiltner, J., Swartzlander, A., Hasoon, F., Noufi, R. Progress towards 20% efficiency in Cu(In,Ga)Se$_2$ polycrystalline thin-film solar cells. (1999). *Prog. Photovolt: Res. Appl.* 7, 311-316.

Deckman, H.W., Wronski, C.R., Witzke, H. and Yablonovitch, E. (1983). Optically enhanced amorphous silicon solar cells. *Appl. Phys. Lett*. 42, 968-970.

Deng, S. & Schiff, E.A. (2003). Amorphous Silicon–based Solar Cells. In: *Handbook of Photovoltaic Science and Engineering,* Second Edition. Edited by A. Luque and S. Hegedus. John Wiley & Sons, Ltd., pp. 505-565.

EPIA Global market outlook for photovoltaics until 2015. (2011). European Photovoltaic Industry Association. www.epia.org.

EUR 24344 PV Status Report 2010. Institute for Energy. Joint Research Centre. European Commission. (2010). http://www.jrc.ec.europa.eu.

Fahrenbruch, A. & Bube, R., (1983). *Fundamentals of Solar Cells*, 231–234, Academic Press, New York.

Faraji, M., Sunil Gokhale, Choudhari, S. M., Takwale, M. G., and S. V. Ghaisas. (1992). High mobility hydrogenated and oxygenated microcrystalline silicon as a photosensitive material in photovoltaic applications. *Appl. Phys. Lett*. 60, 3289-3291.

Ferrazza, F. (2003). Silicon: manufacture and properties. In: *Practical Handbook of Photovoltaics: Fundamentals and Applications*, edited by T. Markvart and L. Castaner (Elseiver, New York), pp. 137-154.

Fritsche, J., Kraft, D., Thissen, A., Mayer, Th., Klein & A., Jaegermann W. (2001). Interface engineering of chalcogenide semiconductors in thin film solar cells: CdTe as an example, *Mat. Res. Soc. Symp.* Proc. , 668, 601-611.

Fthenakis, V.M., Kim, H.C., and Alsema, E. (2008). Emissions from Photovoltaic Life Cycles. *Environ. Sci. Technol*. 42, 2168-2174.

Goetzberger, A. , Hebling, C. & Schock, H.-W. (2003). Photovoltaic materials, history, status and outlook. *Materials Science and Engineering* R40, 1-46.

Cohen-Solal, G., Lincot, D., Barbe, M. (1982). High efficiency shallow p(+)nn(+) cadmium telluride solar cells. in: *Photovoltaic Solar Energy Conference*; Proceedings of the 4th International Conference, 621-626.

Cooke, M. (2008). CdTe PV progresses to mass production. *Semiconductors Today*, 3, 74-77.

Grätzel, M. (2003). Dye-sensitized solar cells. *J. Photochem. Photobiol. C: Photochem. Rev.* 4, 145-153.

Gratzel, M. (2004). Conversion of sunlight to electric power by nanocrystalline dye-sensitized solar cells. *J. Photoch. & Photobiology* A164, Issue: 1-3, 3-14.

Gray, J.L., Schwartz, R.J., Lee, Y.J. (1990). Development of a computer model for polycrystalline thin-film CuInSe$_2$ and CdTe solar cells. *Annual report 1 January – 31 December 1990*. National Renewable Energy Laboratory/TP-413-4835, 1-36.

Green, M.A., Emery, K., Hishikawa, K.Y. & Warta, W. (2011). Solar Cell Efficiency Tables (version 37). *Progress in Photovoltaics: Research and Applications 19*, pp. 84-92. ISSN 1099-159X.

Guter, W., Schöne, J., Philipps, S., Steiner, M., Siefer, G., Wekkeli, A., Welser, E, Oliva, E, Bett, A., and Dimroth F.(2009). Current-matched triple-junction solar cell reaching 1.1% conversion efficiency under concentrated sunlight, *Appl. Phys. Lett*. 94, 023504 (8 pages).

Han, S.-H., Hasoon, F.S., Hermann, A.M., Levi, D.H. (2007). Spectroscopic evidence for a surface layer in CuInSe$_2$:Cu deficiency. *Appl. Phys. Lett*. 91, 021904 (5 pages).

Haugeneder, A.; Neges, M.; Kallinger, C.; Spirkl, W.; Lemmer, U.; Feldmann, J.; Scherf, U.; Harth, E.; Gügel, A.; Müllen, K. (1999). Exciton diffusion and dissociation in conjugated polymer/fullerene blends and heterostructures. *Phys. Rev*. B., 59, 15346-15351.

Hegedus, S. & Luque, A. (2011). Achievements and Challenges of Solar Electricity from Photovoltaics. In: *Handbook of Photovoltaic Science and Engineering,* Second Edition. Edited by A. Luque and S. Hegedus. John Wiley & Sons, Ltd., pp. 2-38.

Hein, J.R., Koschinsky, A., and Halliday, A.N. (2003). Global occurrence of tellurium-rich ferromanganese crusts and a model for the enrichment of tellurium. *Geochimica et Cosmochimica Acta*, 67, 1117-1127.

http://refractiveindex.info/?group=CRYSTALS&material=a-Si.

http://www1.eere.energy.gov/solar/pdfs/solar_program_mypp_2008-2012.pdf. *Multi Year Program Plan 2008-2012*. U.S. Department of Energy.

Jager-Waldau, A. (2010). Research, Solar Cell Production and Market Implementation of Photovoltaics. *Luxembourg: Office for Official Publications of the European Union*. 120 pp.

Ji, J. J. & Shi, Z. (2002). Texturing of glass by SiO$_2$ film. *US patent* 6, 420, 647.

Jordan, J. (1993). *International Patent Application*. WO93/14524.

Kazmerski, L.L., White, F.R., and Morgan, G.K. (1976). Thin-film CuInSe$_2$/CdS heterojunction solar cells. *Appl. Phys. Lett*. 29, 268-270.

Keppner, H., Meier, J. Torres, P., Fischer, D., and Shah, A. (1999). Microcrystalline silicon and micromorph tandem solar cells. *Applied Physics A: Materials Science & Processing*. 69, 169-177.

King, R. (2008). Multijunction cells: record breakers, *Nature Photonics*, 2, 284– 285.

Kosyachenko, L.A., Maslyanchuk, O.L., Motushchuk, V.V., Sklyarchuk, V.M. (2004). Charge transport generation-recombination mechanism in Au/n-CdZnTe diodes. *Solar Energy Materials and Solar Cells*. 82, 65-73.

Kosyachenko, L.A., Grushko, E.V., Savchuk, A.I. (2008). Dependence of charge collection in thin-film CdTe solar cells on the absorber layer parameters. *Semicond. Sci. Technol*. 23, 025011 (7pp).

Kosyachenko, L., Lashkarev, G., Grushko, E., Ievtushenko, A., Sklyarchuk, V., Mathew X., and Paulson, P.D. (2009). Spectral Distribution of Photoelectric Efficiency of Thin-Film CdS/CdTe Heterostructure. *Acta Physica Polonica*. A 116 862-864.

Kosyachenko, L.A., Savchuk, A.I., Grushko, E.V. (2009). Dependence of the efficiency of a CdS/CdTe solar cell on the absorbing layer's thickness. *Semiconductors*, 43, 1023-1027.

Kosyachenko, L.A., Grushko, E.V. (2010). Open_Circuit Voltage, Fill Factor, and Efficiency of a CdS/CdTe Solar Cell. *Semiconductors*, 44, 1375–1382.

Kuwano, Y., Ohniishi, Nishiwaki, H., Tsuda, S., Fukatsu, T., Enomoto, K., Nakashima, Y., and Tarui, H. (1982). Multi-Gap Amorphous Si Solar Cells Prepared by the Consecutive, Separated Reaction Chamber Method. *Conference Record of the 16th IEEE Photovoltaic Specialists Conference*, (San Diego, CA, 27-30.9.1982), pp. 1338-1343.

Lavagna, M., Pique, J.P. & Marfaing, Y. (1977). Theoretical analysis of the quantum photoelectric yield in Schottky diodes, *Solid State Electronics*, 20, 235-240.

Loferski, J.J. (1956). Theoretical Considerations Governing the Choice of the Optimum Semiconductor for Photovoltaic Solar Energy Conversion. *J. Appl. Phys*. 27, 777-784.

Mauk, M., Sims, P., Rand, J., and Barnett. (2003). A. Thin silicon solar cells In: *Practical Handbook of Photovoltaics: Fundamentals and Applications*, edited by T. Markvart and L. Castaner (Elseiver, New York), p. 185-226.

Meier, J., Flückiger, R., Keppner, H., and A. Shah. (1994). Complete microcrystalline p-i-n solar cell—Crystalline or amorphous cell behavior? *Appl. Phys. Lett.* 65, 860-862.

Meier, J., Dubail, S., Fischer, D., Anna Selvan, J.A., Pellaton Vaucher, N., Platz, Hof, C., Flückiger, R., Kroll, U., Wyrsch, N., Torres, P., Keppner, H., Shah, A., Ufert, K.-D. (1995). The 'Micromorph' Solar Cells: a New Way to High Efficiency Thin Film Silicon Solar Cells. *Proceedings of the 13th EC Photovoltaic Solar Energy Conference*, Nice, pp. 1445–1450.

Meier, J., Dubail, S., Cuperus, J., Kroll, U., Platz, R., Torres, P., Anna Selvan, J.A., Pernet, P., Beck, N., Pellaton Vaucher, N., Hof, Ch., Fischer, D., Keppner, H., Shah, A. (1998). Recent progress in micromorph solar cells. *J. Non-Crystalline Solids*. 227–230, 1250–1256.

Meyers, P.V. & Albright, S.P. (2000). Technical and Economic opportunities for CdTe PV at the turn of Millennium. *Prog. Photovolt.: Res. Appl.* 8, 161-169.

Mickelsen, RA. & Chen, W.S. (1981). Development of a 9_4% efficient thin-film $CuInSe_2/CdS$ solar cell. *Proc.15th IEEE Photovoltaic Specialists Conference*, New York,; 800–804.

Muller, R.S. & Zuleeg, R. (1964). Vapor-Deposited, Thin-Film Heterojunction Diodes. *J. Appl. Phys*. 35, 1550-1558.

Multi Year Program Plan 2008-2012. U.S. Department of Energy. http://www1.eere.energy.gov/ solar/pdfs/solar_program_mypp_2008-2012.pdf

Minilya-Arroyo, J., Marfaing, Y., Cohen-Solal, G., Triboulet, R. (1979). Electric and photovoltaic properties of CdTe p-n homojunctions. *Sol. Energy Mater*. 1, 171-180.

Nakada, T. & Mise, T. (2001). High-efficiency superstrate type cigs thin film solar cells with graded bandgap absorber layers. *Proceedings of the 17th European Photovoltaic Solar Energy Conference*, Munich. 1027–1030.

Nishitani, M., Negami, T., Kohara, N., and Wada, T. (1997). Analysis of transient photocurrents in Cu(In,Ga)Se2 thin film solar cells. *J. Appl. Phys*. 82, 3572-3575.

Neumann, H., Tomlinson, R.D. (1990). Relation between electrical properties and composition in $CuInSe_2$ single crystals. *Sol. Cells*. 28, 301-313.

Ohnesorge, B., Weigand, R., Bacher, G., Forchel, A., Riedl, W., and Karg, F. H. (1998). Minority-carrier lifetime and efficiency of Cu(In,Ga)Se2 solar cells. *Appl. Phys Lett*. 73, 1224-1227.

O'Regan, B. & Grätzel, M. (1991). A Low-Cost, High-Efficientcy Solar-Cell Based on Dye-Sensitized Colloidal TiO2 Films, *Nature*, 353, No. 6346, 737-740.

Paulson, P.D. , Birkmire, R.W. and Shafarman, W.N. (2003). Optical Characterization of $CuIn_{1-x}Ga_xSe_2$ Alloy Thin Films by Spectroscopic Ellipsometry. *J. Appl. Phys*., 94, 879-888.

Repins, I., Contreras, M.A., Egaas, B., DeHart, C., Scharf, J., Perkins, C.L., To, B., and Noufi. R. (2008). 19·9%-efficient ZnO/CdS/CuInGaSe2 solar cell with 81.2% fill factor. *Progress in Photovoltaics: Research and Applications*. 16, 235–239.

Romeo, A., M. Terheggen, Abou-Ras, D., Bőtzner, D.L., Haug, F.-J., Kőlin, M., Rudmann, D., and Tiwari, A.N. (2004). Development of Thin-film Cu(In,Ga)Se2 and CdTe Solar Cells. *Prog. Photovolt: Res. Appl.*;12, 93–111.

Spear, W.E. & Le Comber, P.G. (1975). Substitutional doping of amorphous silicon. *Solid State Commun*. 17, 1193-1196.

Schmid, D., Ruckh, M., Grunvald, M., Schock. H. (1993). Chalcopyrite/defect chalcopyrite heterojunctions on the basis $CuInSe_2$. *J. Appl. Phys*. 73, 2902-2909.

Schroeder, D.J., Rockett, A.A. (1997). Electronic effects of sodium in epitaxial CuIn$_{1-x}$Ga$_x$Se$_2$. *J. Appl. Phys.* 82, 4982-4985.

Shafarman, W.N. & Stolt, L. (2003). Cu(InGa)Se2 Solar Cells. In: *Handbook of Photovoltaic Science and Engineering,* Second Edition. Edited by A. Luque and S. Hegedus. John Wiley & Sons, Ltd., pp. 567-616.

Sah C., Noyce R. & Shockley W. (1957). Carrier generalization recombination in p-n junctions and p-n junction characteristics, *Proc. IRE.* 45, 1228–1242.

Shah, J., Meier, A., Buechel, A., Kroll, U., Steinhauser, J., Meillaud, F., Schade, H. (2006). Towards very low-cost mass production of thin-film silicon photovoltaic (PV) solar modules on glass. *Thin Solid Film.* 502, 292-299.

Shay, J.L., Wagner, S., and Kasper, H.M. (1975). Efficient CuInSe$_2$/CdS solar cells. *Appl. Phys. Lett.* 27, 89-90.

Staebler, D.L. & Wronski, C.R. (1977). Reversible conductivity changes in discharge-produced amorphous Si. *Appl. Phys. Lett.* 31, 292-294.

Standard of International Organization for Standardization ISO 9845-1:1992. Reference solar spectral irradiance at the ground at different receiving conditions.

Sze, S. (1981). *Physics of Semiconductor Devices,* 2nd ed. (Wiley, New York).

Szlufcik, J., Sivoththaman, S., Nijs, J.F., Mertens, R.P., and Overstraeten, R.V. (2003). Low cost industrial manufacture of crystalline silicon solar cells. In: *Practical Handbook of Photovoltaics: Fundamentals and Applications*, edited by T. Markvart and L. Castaner (Elseiver, New York), pp. 155-184.

Tang, C.W. (1986). 2-Layer Organic Photovoltaic Cell. *Appl. Phys. Lett.*, 48, 183-185.

Tiwari, A.N., Krejci, M., Haug, F.-J., Zogg, H. (1999). 12_8% Efficiency Cu(In, Ga)Se$_2$ solar cell on a flexible polymer sheet. *Progress in Photovoltaics: Research and Applications.* 7, 393–397.

Tuttle, J.R., Szalaj, A., Keane, J.A. (2000). 15_2% AMO/1433 W/kg thin-film Cu(In,Ga)Se$_2$ solar cell for space applications. *Proceedings of the 28th IEEE Photovoltaic Specialists Conference*, pp. 1042–1045.

Von Roedern, B., Kroposki, B., Strand, T. and Mrig, L. (1995). *Proccedings of the 13th European Photovoltaic Solar Energy Conference.* p. 1672-1676.

Von Roedern, B. & del Cueto, J.A. (2000). Model for Staebler-Wronski Degradation Deduced from Long-Term, Controlled Light-Soaking Experiments. *Materials Research Society's Spring Meeting*. San Francisco, California, April 24-28, 2000. 5 pages.

Von Roedern, B. (2006). Thin-film PV module review: Changing contribution of PV module technologies for meeting volume and product needs. *Renewable Energy Focus*. 7, 34-39.

Wagner, S., Shay, J. L., Migliorato, P., and Kasper, H.M. (1974). CuInSe$_2$/CdS heterojunction photovoltaic detectors. *Appl. Phys. Lett.* 25, 434-435.

Widenborg, P.I. & Aberle, A.G. (2007). Polycrystalline Silicon Thin-Film Solar Cells on AIT-Textured Glass Superstrates. *Advances in OptoElectronics*. 24584 (7 pages).

Wu, X., Kane, J.C., Dhere, R.G., DeHart, C., Albin, D.S., Duda, A., Gessert. T.A., Asher, S., Levi. D.H., Sheldon, P. (2002). 16.5% Efficiency CdS/CdTe polycristalline thin-film solar cells. *Proceedings of the 17th European Photovoltaic Solar Energy Conference and Exhibition*, Munich, 995–1000.

www.firstsolar.com/recycling.

Yang, J, Banerjee, A, Guha, S. (1997). Triple-junction amorphous silicon alloy solar cell with 14.6% initial and 13.0% stable conversion efficiencies. *Appl. Phys. Lett.* 70, 2975-2977.

Enhanced Diffuse Reflection of Light by Using a Periodically Textured Stainless Steel Substrate

Shuo-Jen Lee and Wen-Cheng Ke
Yuan Ze University, Taiwan,
R.O.C.

1. Introduction

The flexible solar cells fabricated on a stainless steel substrate are being widely used for the building of integrated photovoltaics (BIPVs) in recent years. Because stainless steel has many advantages, such as low cost, high extension, ease of preparing etc. It was believed that the wide application of BIPVs especially rooftop applications, would be the biggest market for flexible PV technology (Kang et al. 2006, Otte et al. 2006, Chau et al. 2010, Fung et al. 2008). Until now, one of the main challenges of the BIPVs remains how to improve the conversion efficiency. Since, the path length of the photovoltaic effect is considerable shorter in a thin film solar cell resulting in reduced efficiency. Many researchers have focused on light trapping, and have adopted a different TCO technology, such as LP-CVD, PVD, to increase the path length of the incoming light, and improve the photovoltaic conversion efficiency of thin film solar cells (Selvan et al. 2006, Llopis et al. 2005, Söderström et al. 2008, Müller et al. 2004). Moreover, light trapping provides some significant advantages including, reduction of the cell thickness, reduced processing time and reduced cost, improved cell efficiency and the improved stability of amorphous Si (a-Si:H).

The idea of trapping light inside a semiconductor by total internal reflection was reported by John in 1965 (John 1965). It also indicated that the effective absorption of a textured semiconductor film could be enhanced by as much as a factor of 60 over a plane-parallel film (Yablonovitch and Cody 1982). It should be mentioned that a major limitation to thin film solar cell efficiency is the long absorption length of the long wavelength photons and the low thickness of the absorber layer. The absorption length of amorphous silicon (a-Si:H) with a bandgap of 1.6 eV, for red and infrared solar photons, exceeds 1 µm and 100 µm, respectively (Ferlanto et al. 2002, Zhou and Biswas 2008). However, for a-Si:H the hole diffusion length is ~300-400 nm, which limits the solar cell absorber layer thickness to less than the hole diffusion length (Curtin et al., 2009). This makes it exceedingly difficult to harvest these photons since the absorber thickness of a p-i-n single junction solar cell is limited to only a few hundred nanometers for efficient carrier collection. In addition, the low-cost approach of thin-film silicon solar cells is very sensitive to film thickness, since the throughput increases with the decrease in layer thickness. Thus, sophisticated light trapping is an essential requirement for the design of thin-film solar cells (Rech et al., 2002).

Enhanced light-trapping in thin film solar cells is typically achieved by a textured metal backreflector that scatters light within the absorbing layer and increases the optical path length of the solar photons. In our recent researches [Lee et al., 2009], various processing

techniques including, electro-polishing, sandblasting, photolithography, lift-off and wet-chemical etching were used to create periodically textured structures on the different types of stainless steel substrates. The relationships between the surface morphology of textured stainless steel substrate and optical properties will be carefully discussed.

2. Surface treatment of texturing stainless steel substrate

2.1 Electro-polishing process

In this study, electrochemical processing was used to achieve sub-micro texturing stainless steel substrate base on the fundamental electrochemical reaction items as (1)-(3).

Anode chemical reaction:

$$Fe^{2+}+2(OH)^{-}\rightarrow Fe(OH)_2 \text{ or } Fe(OH)_3 \tag{1}$$

$$OH^{-}\rightarrow O_2\uparrow+H_2 \text{ (Parasitic reaction)} \tag{2}$$

Cathode chemical reaction:

$$2H^{+}\rightarrow H_2\uparrow \tag{3}$$

The electro-polishing system is shown in Fig. 1. The important parameters are as follows:

1.   Substrate clean by acid-washing in H_2O_2:H_2SO_4=1:3 solution.
2.   Electrolyte solution (Na_2SO_4) with concentration of 60-100 (g/L).
3.   Current density in electro-polishing (EP) process is 0.1-1.0 (A/cm²).

The clamp was used to hold the anode and cathode plates. The anode and cathode plates were separated by Teflon with thickness of 1 cm. Fig. 2 shows the optical microscopy (OM) images of 304 SS substrate with and without EP process. The average surface roughness (Ra) of 304 SS substrate increased from 0.045 μm to 0.197 μm after the EP process with current density of 1A/cm² in 10 min.
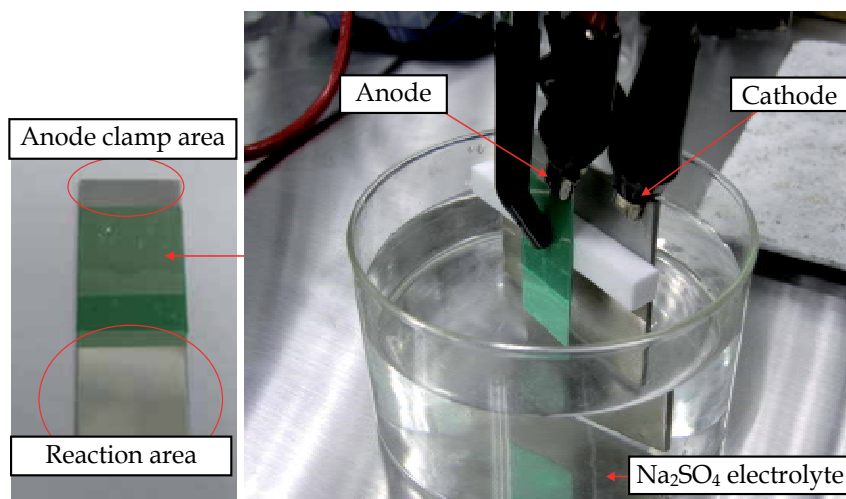
Fig. 1. Experimental set-up of the EP process.

2.2 Sand blasting process

The glass sand (#320) was used to form randomly textured surface with cave size of several µm to tens µm on the surface of stainless steel substrate. The average surface roughness (Ra) of 304 SS substrate increased from 0.277 µm to 6.535 µm after the sand blasting process. The OM images of raw 304 SS substrate and with sand blasting process were shown in Fig. 3.
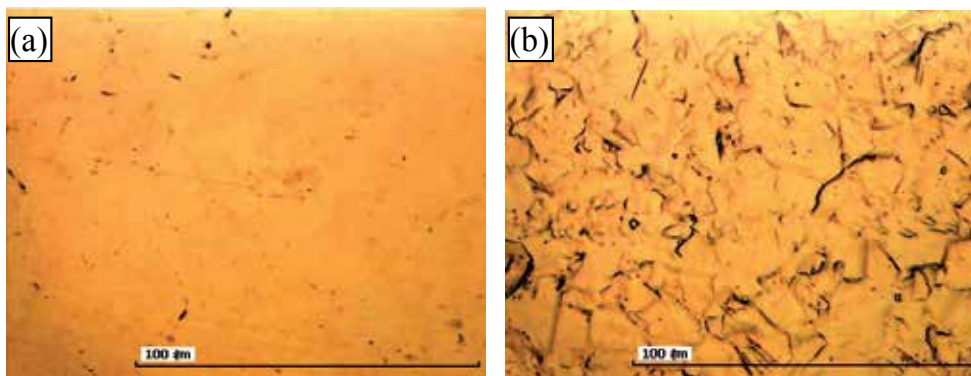
Fig. 2. The OM images (x2000) of (a) raw 304 SS substrate surface and (b) 304 SS substrate surface with EP process.
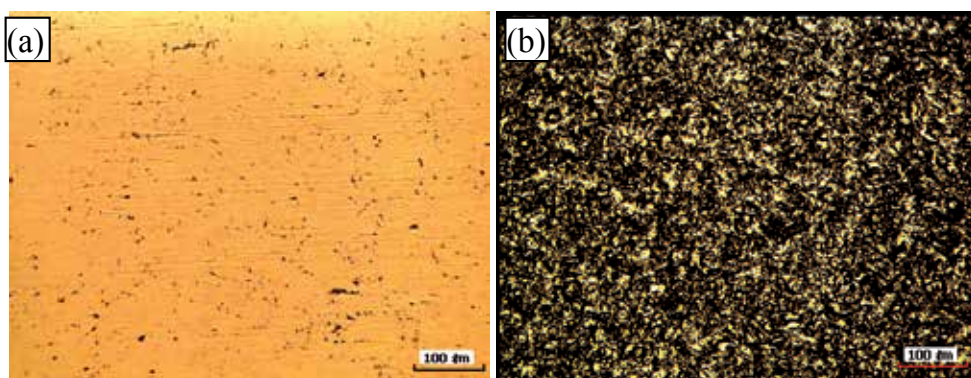
Fig. 3. The OM images (x400) of (a) raw 304 SS substrate surface and (b) 304 SS substrate surface with sand blasting process.

2.3 Photolithography process

The photo-mask patterns were designed by CAD. Photolithography is a process of using light to transfer a geometric pattern from a photo-mask to a photo-resist on a 430BA SS substrate. The steps involved in the photolithographic process are metal cleaning, barrier layer formation, photo-resist application, soft baking, mask alignment, exposure and development, and hard-baking. After the photolithographic process, the 430BA SS substrate is etched by aqua regia ($HNO_3 : HCl = 1 : 3$). There are two types of photo-mask patterns: one, different diameters but with the same interval, and two, the same diameters but with a different interval. They are both designed to study light trapping for the application of thin film solar cells. Finally, silver coating technique by e-beam evaporation was used to improve the TR and DR rates of the 430BA SS substrate.

2.4 Lift-off and etching process

In this study, lift-off and etching processes were used to fabricate the different textures of the 304BA SS substrates. The striped texture was created on the 304BA SS substrate using the lift-off process. After the hard-baking process, a silver (Ag) thin film was deposited on the substrate by e-beam evaporation. An acetone solution was used to remove the residual photo resistor (PR). The depth of the striped texture was controlled by the thickness of the Ag thin film deposited. Four different striped textures were created on the 304BA SS substrates, including period/height: 6/0.1, 6/0.3, 12/0.1 and 12/0.3 μm. Two other types of textured 304BA SS substrate, the ridged-stripe and pyramid texture with 22.5 μm width were created by the etching process. After hard-baking, the 304BA SS substrate was etched by aqua regia (HNO_3 : HCl : DI water＝1 : 3 : 4). The etching temperature was 28-35℃ with an etching time of 7-12 min. to control the etching depth of the textured 304BA SS substrate. The detail experimental flow charts of lift-off and etching processes are shown in Fig. 4 and Fig. 5, respectively.

3. Optical properties of textured stainless steel substrate

3.1 Measurements of optical properties of textured stainless steel substrate

The total reflection (TR) and diffuse reflection (DR) rates of incident light from the textured substrate were carefully studied by using a Perkin Elmer Lambda 750S spectrometer. It was known that the specula reflection takes place on a smooth surface, and the angle of reflection is the same as the angle of incidence. DR is a phenomenon where an incident beam of light strikes an uneven or granular surface and then scatters in all directions. In Fig. 6, the 6 cm
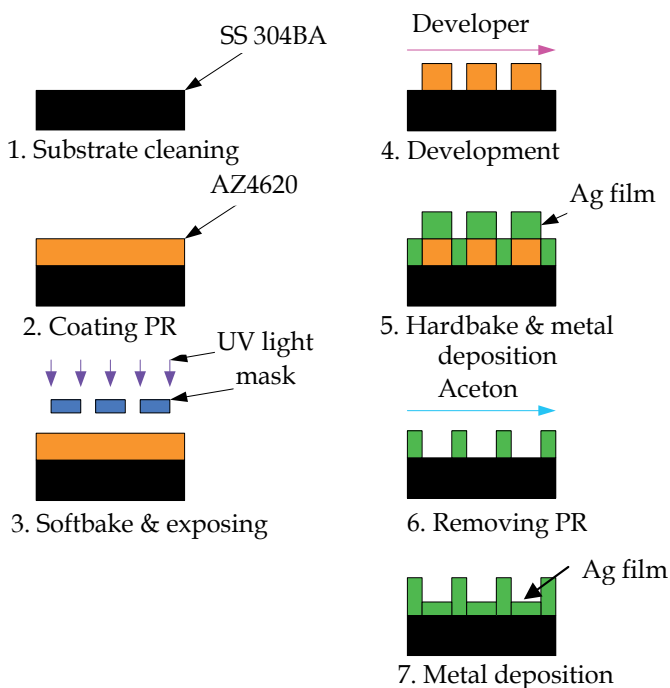
Fig. 4. The experimental flow charts of lift-off process.

Integrating Sphere is used for diffuse reflectance measurements. Reflectance measurements include total and diffuse reflectance at an incident angle of 8 degrees. Specular reflectance can be calculated from the total and diffuse reflectance measurements. The TR and DR rate of a textured substrate are important indexes when increasing the light trapping efficiency of thin-films solar cells.
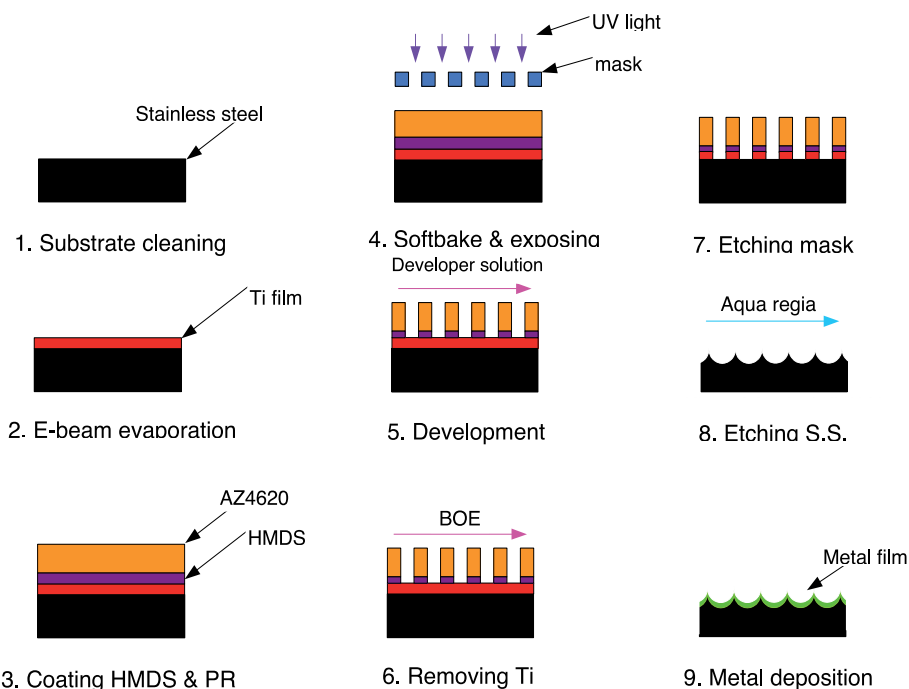
Fig. 5. The experimental flow charts of etching process.
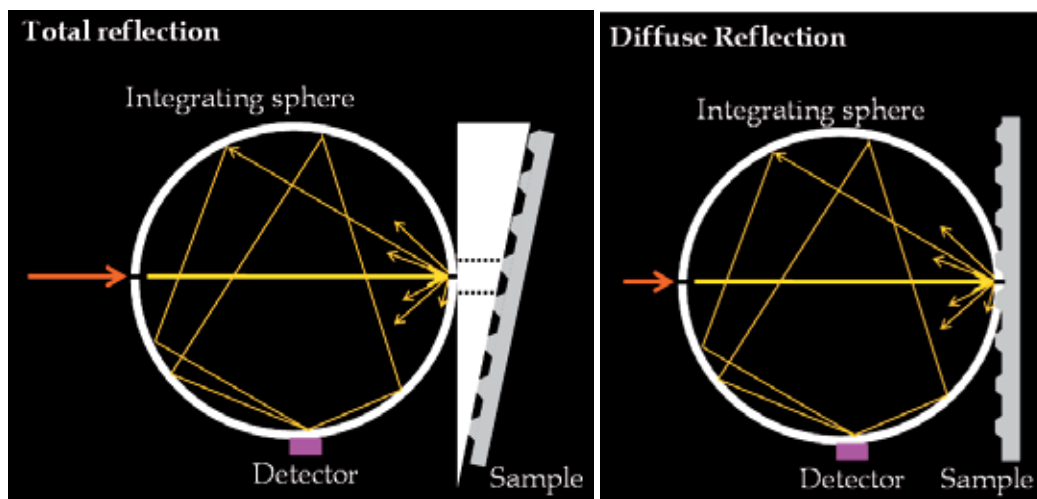
Fig. 6. The total reflection and diffuse reflection measured by integrating Sphere.

3.2 Optical properties on periodically textured 430BA stainless steel substrate

Lately the light trapping properties of textured substrates have attracted substantial interest because of their potential to reduce the thickness of solar cell material. In this study, the different kinds of textured patterns formed on 430BA SS substrate have been proposed for the purpose of trapping light in the application of thin film solar cells. Figure 7 shows the surface morphology of the 430BA SS substrate etched by using aqua regia. It should be noted that the dark and light regions of the OM images indicate the concave structure and the flat surface on the textured 430BA SS substrate, respectively.

In order to understand the optical reflection of a textured 430BA SS substrate, the Perkin Elmer Lambda 900 spectrometer was used to analyze both the TR and DR rates of incident light. The TR and DR rates versus the wavelength curves for the raw and textured 430BA SS substrates are shown in Fig. 8 and Fig. 9, respectively. The "D" and "G" indicate the diameter and the gap for these periodically textured 430BA SS substrates, respectively. It must be noted that the discontinued data line in the wavelength of 850 to 950nm was due to the change in detector, from a PMT to a PbS detector. First, we compared the textured 430BA SS substrates with different diameters of 2, 4 and 6μm and with the same interval of 3μm. In Fig. 8, it was found that the DR rate at the wavelength of 600nm increases substantially, from 4.5% of a raw 430BA SS substrate to 19.7 %, 23.1% and 31.8% for textured 430BA SS substrates with a diameter of 2, 4 and 6μm, respectively. It was evident that for the same areas of analysis, the larger the size of the concave shape, the worse the TR rate would
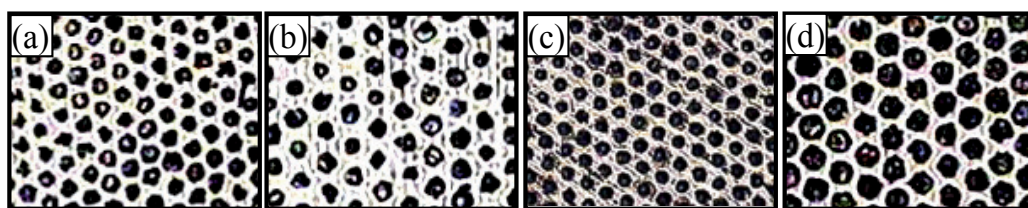
Fig. 7. The OM images of a concave periodically textured 430BA SS substrate with a diameter/gap of (a) 4/5 μm (b) 4/7 μm (c) 4/3 μm (d) 6/3 μm.

Fig. 8. The TR and DR rates versus the wavelength curves for raw 430BA SS substrate at different diameter of textured 430BA SS substrate.
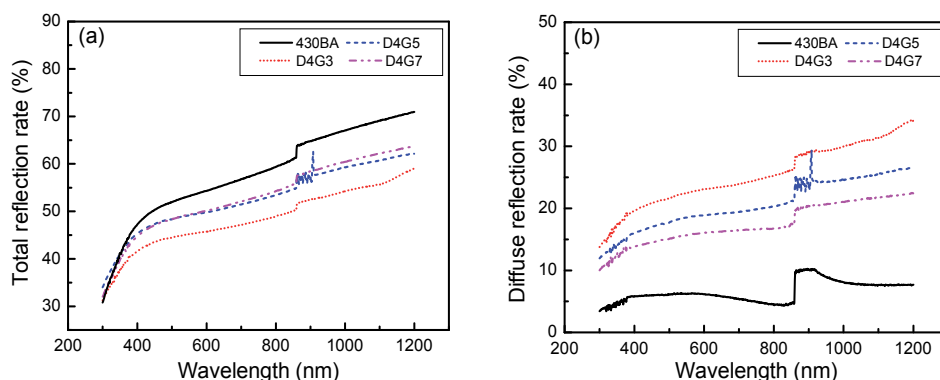
Fig. 9. The TR and DR rates versus the wavelength curves for raw 430BA SS substrate at different intervals of textured 430BA SS substrate.

be, resulting in a better diffuse reflection rate. We also investigated the TR and DR rates of the textured 430BA SS substrate with a different interval for samples with a fixed diamete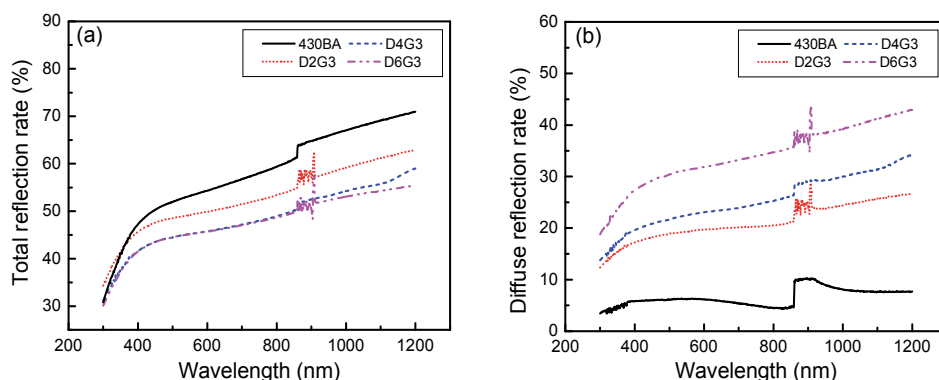r of 4µm. In Fig. 9 we found that the DR rate at the wavelength of 600 nm decreased from 23.1% for a diameter/gap of 4/3 µm textured 430BA SS substrate to 18.9% and 16.1% respectively for a diameter/gap of 4/5µm and 4/7µm textured 430BA SS substrates. The decrease of the DR rate is related to the increase in the interval of the concave substrate.

The textured surface of the 430BA SS substrate leads to a lower TR rate compared to a specular surface of raw 430BA SS substrate. The lowering of the TR rate for the textured surface of the 430BA SS substrate can be understood on the basis of (a) the multiple scattering as a result of the multiple reflections from the textured surface of the 430BA SS substrate and a concomitant reduction in light intensity at each reflection due to the finite value of reflectance for 430BA SS, (b) light trapping in the indentations of a highly textured surface. Therefore, the results show that the textured 430BA SS substrate can generate a random distribution of light by reflection from a textured surface.

It is known that the incident light is reflected back into the cell for a second pass and subsequent passes. This phenomenon results in enhanced absorption in the cell. Thus, a back reflector should possess high reflectance in the solar part of the spectrum, which makes Ag a good candidate. Thus, we also performed the Ag coating on a textured 430BA SS substrate to study the TR and DR rates of incident light. The TR and DR rates versus the wavelength of textured 430BA SS with a silver film thickness of 300 nm are shown in Fig. 10. The peak at around 325 nm can be attributed to the diffuse reflectance spectrum of the deposited Ag film on the surface of the textured 430BA SS substrate (Xiong et al. 2003). In Fig. 10, the DR rate at the 600 nm wavelength are 40.6%, 47.2% and 64.6%, respectively for a diameter/gap of 2/3, 4/3 and 6/3 µm Ag film coated/textured 430BA SS substrate. The DR rate of Ag film coated/textured 430BA SS substrate increased about 2 times in comparison with the uncoated textured 430BA SS substrate (see Fig. 8). Similar results were also observed in Fig. 11 for the Ag film coated/textured 430BA SS substrate with a different interval for samples with a fixed diameter of 4µm. In addition, the TR rate increased to more than 90% for the Ag film coated/textured 430BA SS substrate which was an 80% improvement over the uncoated textured 430BA SS substrate.

Fig. 10. The TR and DR rates versus wavelength curves for Ag film deposited at different diameter of textured 430BA SS substrate.
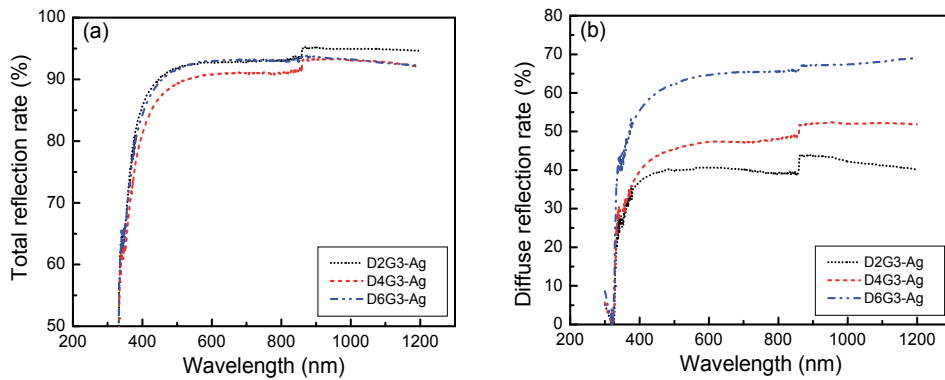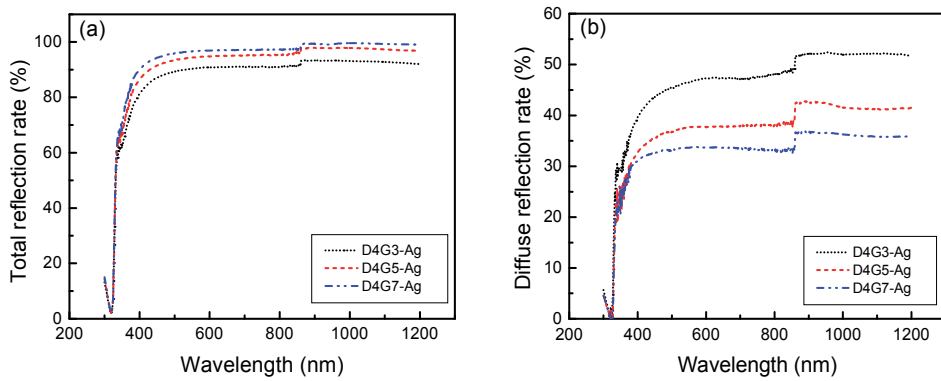

Fig. 11. The TR and DR rates versus wavelength curves for Ag film deposited at different intervals of textured 430BA SS substrate.
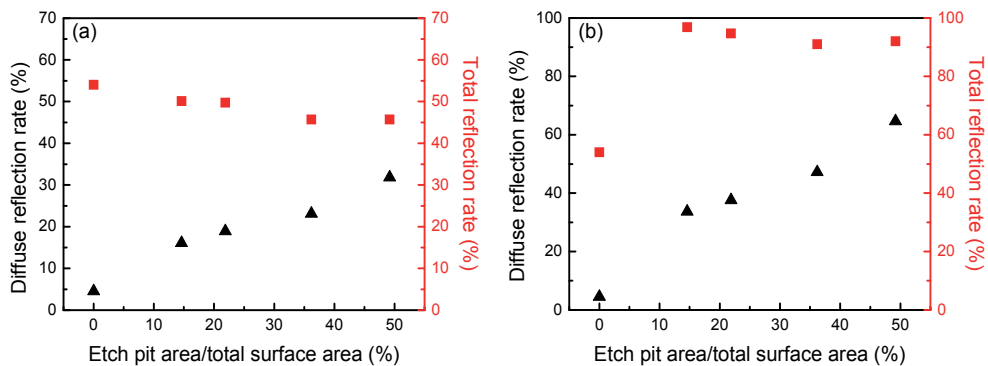
Fig. 12. The TR and DR rates as a function of the ratio of the etch pit area to the total surface area for (a) the textured 430BA SS and (b) the Ag film coated/textured 430BA SS.

From Fig. 8, it is evident that the TR and DR rates are not only dependent on the size of the concave shape but also depend on the interval of the concave substrate. Fig. 12(a) and (b) show the TR rate and DR rates as a function of the ratio of the etch pit area to the total surface area for the textured 430BA SS and the Ag film coated/textured 430BA SS, respectively. The ratio of the etch pit area to the total surface area is calculated by the number of pit in the total surface area multiplied by the single pit area divided by the total surface area. The total surface area is the analysis area in the spectrometer, measuring 1 cm². It is evident that the DR rate increased with the increase effectiveness of the pit regions compared to the smooth regions for both the textured 430BA SS and the Ag film coated/textured 430BA SS. However, the TR rate showed the opposite trend compared with the DR rate and decreased with the increase of the ratio of the etch pit area to total surface area. It is worth noting that once again the TR rate for the the Ag film coated/textured 430BA SS was more than 90% even the ratio of the etch pit area to the total surface area was 50%.

As shown in Figs. 8-11, we found that the increase in TR and DR rates as increase in light wavelength differed in the infrared range. The TR and DR rates clearly increased with the increasing light wavelength of the textured 430BA SS substrate. However, the TR and DR rates didn't increase with the increasing light wavelength of the Ag film coated/textured 430BA SS substrate. Huang et al. indicated that a metal with a lower work function can enhance the Raman signal of diamond films, which is referred to as surface-enhanced Raman scattering (SERS) (Huangbr et al. 2000). A very similar effect, surface-enhanced infrared absorption (SEIRA) was reported to occur with thin metal films (Hartstein et al. 1980, Hatta et al. 1982, Osawa 1997). Moreover, it was reported that the enhancement depends greatly on the morphology of the metal surface (Nishikawa et al. 1993). Fig. 13 shows the SEM image of an Ag film coated/textured 430BA SS substrate. It was found that the surface was covered with Ag particles ranging in size from tens to hundreds of nanometers. Thus, we believe that the difference in increase of the TR and DR rates in the infrared range for the textured 430BA SS and the Ag film coated/textured 430BA SS reflectors are due to the absorption in the infrared range by the Ag films. Further, the surface morphology was related to the thickness of the Ag film and must be carefully investigated in future study.
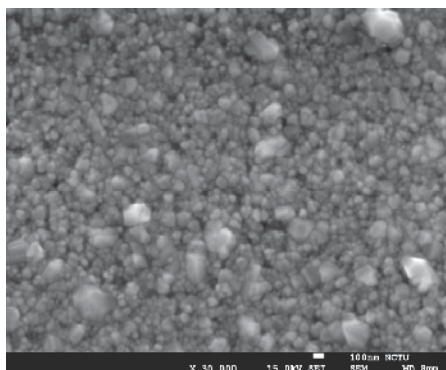
Fig. 13. The SEM image of Ag film coated/textured 430BA SS substrate.

3.3 Optical properties on periodically textured 304BA stainless steel substrate

Fig. 14 shows the OM images of the striped texture on the 304BA SS substrate. There are four patterns (i.e. the period/depth of 12/0.1, 12/0.3, 6/0.1, and 6/0.3 μm) which are designed and

used to study the TR and DR rates of the 304BA SS substrate. The stripe width and depth of the samples were measured by a surface profiler. The TR and DR rates versus the wavelength curves for untreated and the stripe-textured 304BA SS substrates are shown in Fig. 15. The "P" and "D" indicate the period and the depth for the periodically textured 304BA SS substrates, respectively. It was found that the DR rate at the wavelength of 600 nm increased substantially, from 3.5% of an untreated 304BA SS substrate to 10.5%, 21.8%, 18.2% and 39.4% for textured 304BA SS substrates with a period/depth of 12/0.1, 12/0.3, 6/0.1, and 6/0.3 µm, respectively. In addition, the TR rate of the untreated 304BA SS was 67.7% and increased to ~97% for the striped textured 304BA SS substrate due to the high reflection of the Ag film on its surface. It was evident that for the same areas of analysis, the smaller the period and the larger the depth, the better the DR rate would be, resulting in a better diffuse reflection rate.
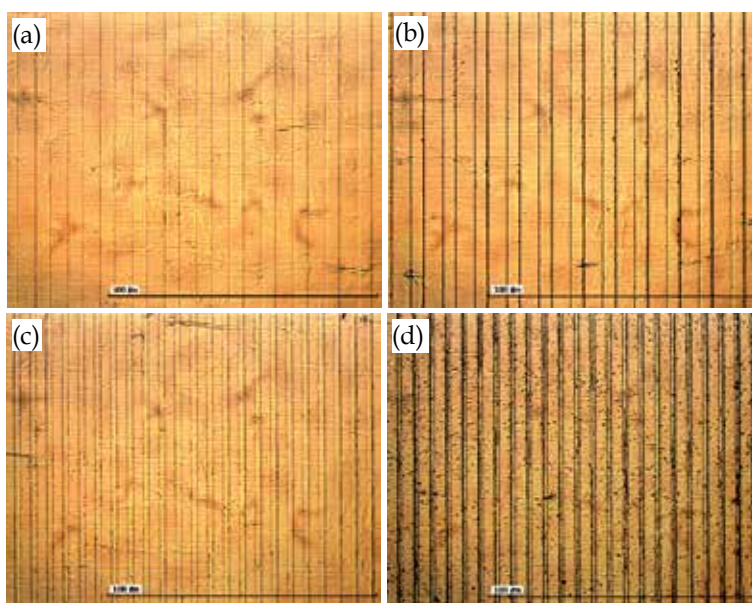
Fig. 14. The OM images of the stripe-textured 304BA SS substrate with a period/depth of (a) 12/0.1 µm (b) 12/0.3 µm (c) 6/0.1 µm (d) 6/0.3 µm.
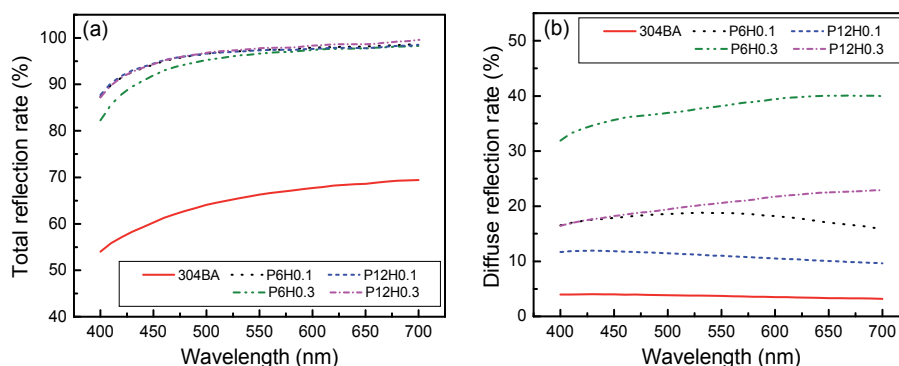
Fig. 15. The TR and DR rates versus the wavelength curves for untreated and stripe-textured 304BA SS substrates.

In our previous study (Lee et al. 2009), it was found that for a textured 430BA SS substrate the DR rate increased with the increased effectiveness of the etch-pit regions compared to that of the smooth regions. Thus, the large and deeply etched areas of the textured 304BA SS indicated that they can improve the DR rate of a textured 304BA SS substrate. In order to improve the DR rate even further, we design two other kinds of textured 304BA SS substrates, the ridged-stripe and the pyramid texture. 3D images of the ridged-stripe and pyramid texture are shown in Figs. 16(a) and (b), respectively. The etching depth and the width for both textured 304BA SS substrates were estimated to be ~6.5 µm and ~22.5 µm, respectively. The aspect ratio (i.e. depth/width) was ~1/3.5 indicating that the opening angle α of the textured surface was about ~120º. It should be noted that the etching depth is controlled by the PR thickness and the etching time. In general, a thick PR and a long etching time can create the deeper textured 304BA SS substrate.
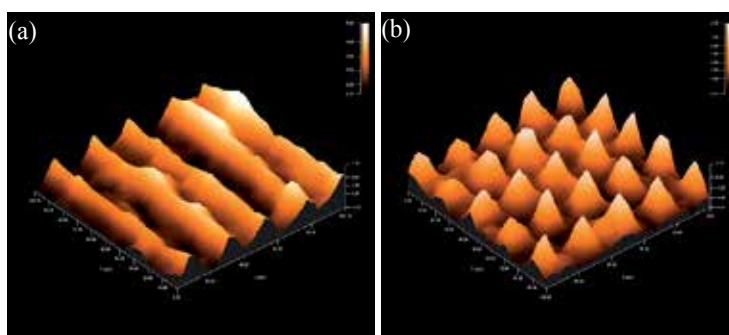
Fig. 16. The 3D images of (a) ridged-stripe and (b) pyramid 304BA SS substrate.

The TR and DR rates of the ridged-stripe and pyramid textured 304BA SS substrates are shown in Fig. 17. We found that the DR rate at the wavelength of 600 nm increased from 3.5 % for the untreated 304BA SS substrate to 60.1% for the pyramid and 63.1% for the ridged-stripe textured 304BA SS substrate. In addition, the DR rate also increased 1.5 times at the period/depth of 6/0.3 µm for the stripe-textured 304BA SS substrate. However, the textured substrates had a lower TR rate compared to the untreated 304BA SS substrate. The lowering of the TR rate for the textured surface of the 304BA SS substrate can be explained as follows (a) the multiple scattering is the result of the multiple reflections from the ridged-stripe or pyramid textured surface of the 304BA SS substrate, and the etching pit reduction in light intensity at each reflection is due to the finite value of the reflectance for the 304BA SS substrate, (b) light trapping occurs in the indentations of a highly textured surface. Therefore, the results show that the textured 304BA SS substrate can generate a random distribution of light through reflection from a textured surface.

It is well known that the incident light is reflected back into the cell for a second pass and subsequent passes. This phenomenon results in enhanced absorption in the cell. Thus, a back reflector must possess high reflectance in the solar part of the spectrum, making Ag or Al good candidates. However, Al films absorb the incident light wavelength of 800 nm and reduce the light conversion efficiency. On the other hand, the reflection of Ag film can achieve 99% from the visible to the IR wavelength (Jenkins and white 1957). Thus, we also used an Ag coating on a textured 304BA SS substrate to study the TR and DR rates of incident light. The TR and DR rates versus the wavelength of ridged-stripe and pyramid textured 304BA SS substrates with a silver film thickness of 150 nm are shown in Fig. 18. The

DR rates at the 600 nm wavelength were 95.6% and 96.8%, for the ridged-stripe and pyramid Ag film coated/texture 304BA SS substrates, respectively. The DR rate increased about 15-fold in comparison with the Ag coated untreated 304BA SS substrate. In addition, the TR rates at the 600 nm wavelength were 96.7% and 96.8%, for the ridged-stripe and pyramidal Ag film coated/texture 304BA SS substrates, respectively.
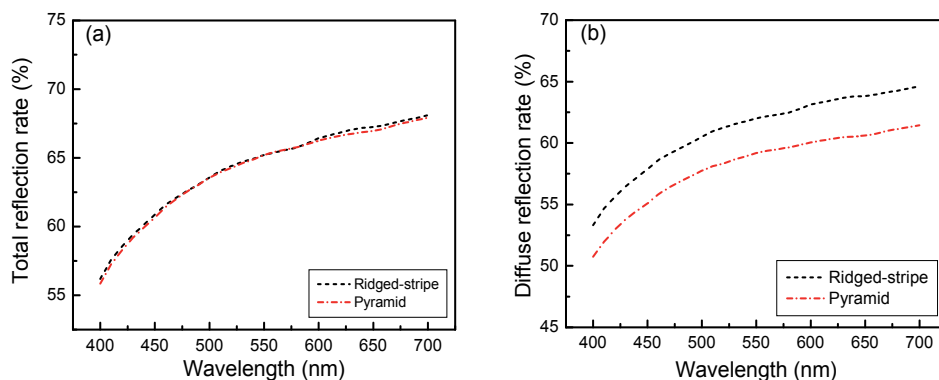
Fig. 17. The TR and DR rates versus the wavelength curves for ridged-stripe and pyramid textured 304BA SS substrates.
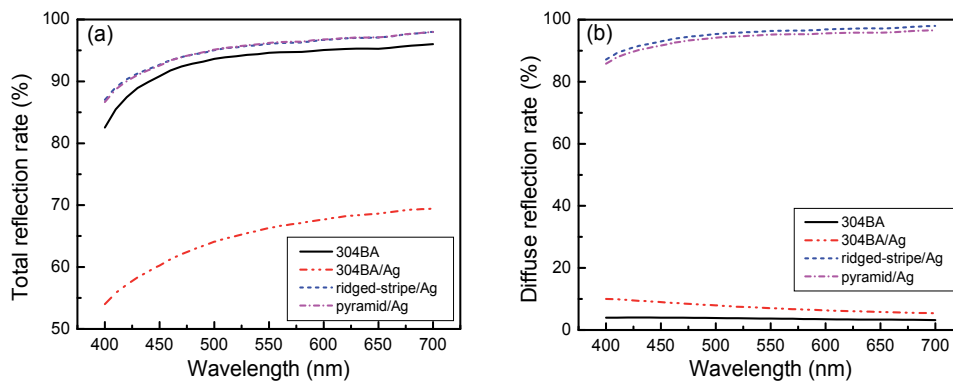
Fig. 18. The TR and DR rates versus the wavelength curves for Ag films coated/untreated 304BA SS substrate and Ag film coated/ridged-stripe and pyramid textured 304BA SS substrates.

Fig. 19 shows the relationship between the DR/TR rates and the total effective area of the Ag film coated/textured 304BA SS substrate. It should be noted that the total effective area was defined by the incident light reaching the textured 304BA SS substrate in an area of 100×100 µm². For example, the total effective area of the stripe textured 304BA SS substrate was calculated by the etched side wall area added to the untreated area of 10000 µm². For the ridged-stripe textured 304BA SS, the total effective area was calculated by summing the

nine ridged-surfaces within an area measuring 100×100 µm². For the pyramid textured 304BA SS substrate, the total effective area was calculated by adding 25 pyramid-textured surfaces to the no-pyramid-coverage areas. Since the high reflection property of Ag films, the TR rate was almost higher than 90% after Ag-film coating of the textured 304BA SS substrates. It is worth noting that the DR rate increased linearly with the increase in total effective area of the stripe-textured 304BA SS substrate. However, the increase of the DR rate with the increase in the total effective area for the ridged-stripe and pyramid textured 304BA SS substrate was much more dramatic. We believe that the dramatic increase in the DR rate was due to the fact that the textured surface generated a random distribution of light by reflection from the textured surface. The aspect ratio for the ridged-stripe and pyramidal textured 304BA SS substrate were about 1/3.5 with an opening angle of 120°. In addition, the diffuse rate was defined when the incident light angle was zero, and the reflection light of that angle was larger than 8⁰ over the incident light. Thus, the increased light diffuse due to the 120° opening angle of the texture surface caused the dramatic increase of the DR rate for the ridged-stripe and pyramid textured 304BA SS substrate. In addition, weakly absorbed light is totally reflected internally at the top surface of the cell as long as the angle of incidence inside the a-Si at the a-Si/TCO interface is greater than 16⁰ (Banerjee and Guha 1991). It was indicated that the tilt angle of the V-shaped light trapping configuration substantially increases the photocurrent generation efficiency (Rim et al. 2007). The photocurrent increased with the increase of the tilt angle of the V-shaped configuration and is believed to enhance the number of ray bounces per unit cell area over that in a planar structure at each point in the V-fold structure. Therefore, the tilted angle of the textured surface is related to the DR and TR rate, and must be carefully investigated in future study.
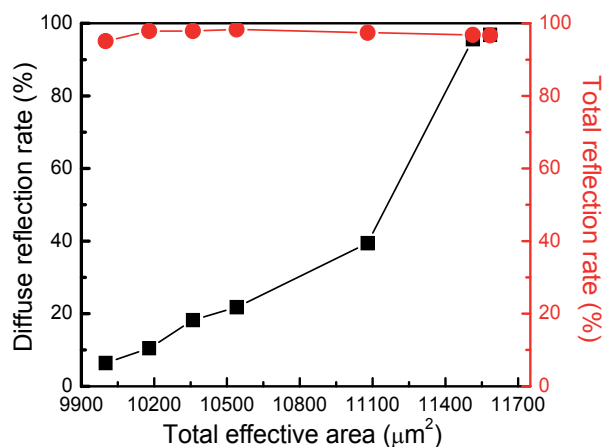
Fig. 19. The TR and DR rates as a function of the total effective area for Ag films coated on textured 304BA SS substrates.

4. Conclusions

We have demonstrated that a large diameter or a small interval of a concave shaped structure made from textured 430BA SS substrate can improve the DR rate of light.

However, the textured surface of a 430BA SS substrate led to a lower TR rate compared to a specular surface of raw 430BA SS substrate. This was due to the trapping of light in the hollows of the highly textured surface. Moreover, coating the textured 430BA SS substrate with an Ag film substantially improved not only the DR rate but also the TR rate of the incident light. The slow increase of the TR and DR rates versus the wavelength in the IR region of the Ag coated/textured 430BA SS substrates was due to the Ag absorption effect. We believe that Ag coated/textured 430BA SS substrates can generate a random distribution of light, increase the light trapping efficiency and be applied in thin films solar cells.

In addition, the DR and TR rate of the stripe, ridged-stripe and pyramid textured 304BA SS substrate were investigated to determine the optimal surface for increasing their light trapping efficiency. The DR rate increased with the increase in the total effective area of the Ag film coated/stripe textured 304BA SS substrate. It is believed that the tilt angle of the textured 304BA SS substrate increases the DR rate. The experimental results showed that the DR rate and the TR rate of the Ag film coated/ ridged-stripe textured 304BA SS substrate can achieve up to ~97% and 98% efficiency, respectively. The DR and TR rate of the Ag film coated/ridged-stripe textured 304BA SS substrates increased 28-fold and 1.4-fold, respectively, compared with the untreated 304BA SS substrate. The drastically increased DR rate is due to not only the increase in total effective area, but also to the decrease in the opening angle of the ridged textured substrate which generates a more random distribution of light by scattering.

5. Acknowledgment

6. References

Banerjee A. and S. Guha. (1991). Study of back reflectors for amorphous silicon alloy solar cell application. *J. Appl. Phys.*, Vol. 69, pp. 1030., ISSN: 1089-7550

Curtin Benjamin, Rana Biswas, and Vikram Dalal. (2009). Photonic crystal based back reflectors for light management and enhanced absorption in amorphous silicon solar cells. *Appl. Phys. Lett.* Vol. 95, pp. 231102., ISSN: 1077-3118

Chau Joseph Lik Hang, Ruei-Tang Chen, Gan-Lin Hwang, Ping-Yuan Tsai and Chien-Chu Lin. (2010). Transparent solar cell window module. *Sol. Energy Mater. Sol. Cells.*, Vol. 94, pp. 588., ISSN: 0927-0248.

Deckman H. W., C. R. Wronski, H. Wittzke, and E. Yablonovitch. (1983). Optically enhanced amorphous silicon solar cells. *Appl. Phys. Lett.*, Vol. 42, pp. 968., ISSN: 1077-3118.

Ferlanto A. S., G. M. Ferreira, J. M. Pearce, C. R. Wronski, R. W. Collins, X. Deng, and G. Ganguly. (2002). Analytical model for the optical functions of amorphous semiconductors from the near-infrared to ultraviolet: Applications in thin film photovoltaics. *J. Appl. Phys.*, Vol. 92, pp. 2424., ISSN: 1089-7550

Fung Taddy Y. Y. and H. Yang. (2008). Study on thermal performance of semi-transparent building-integrated photovoltaic glazings. *Energy and Buildings.,* Vol. 40, pp. 341-350., ISSN: 0378-7788.

Hartstein A., J. R. Kirtley, J. C. Tsang. (1980). Enhancement of the Infrared Absorption from Molecular Monolayers with Thin Metal Overlayers. *Phys. Rev. Lett.*, Vol. 45, pp. 201. , ISSN: 1079-7114

Hatta A., T. Ohshima, W. Suëtaka. (1982). Observation of the enhanced infrared absorption of p-nitrobenzoate on Ag island films with an ATR technique. *J. Appl. Phys. A.*, Vol. 29, pp. 71., ISSN: 2158-3226

Huang B. R., K. H. Chen, W. Z. Ke. (2000). Surface-enhanced Raman analysis of diamond films using different metals. *Mater. Lett.*, Vol.42, pp. 162., ISSN:0167-577X

He Chun, Ya Xiong, Jian Chen, Changhong, Xihai Zhu. (2003). Photoelectrochemical performance of Ag–TiO$_2$/ITO film and photoelectrocatalytic activity towards the oxidation of organic pollutants. *J. Photochem. Photobiol. A.*, Vol. 57, pp. 71., ISSN: 1010-6030

Jenkins F. A. and H. E. White. (McGraw Hill, New York, 1957). *Fundamentals of Optics.*, P. 522. ISBN: 0070-8534-60

John A. E. St., U. S. Patent No. 3 487 223

Llopis F. and I. Tobías. (2005). The role of rear surface in thin silicon solar cells. *Sol. Energy Mater. Sol. Cells.,* Vol. 87, pp. 481., ISSN: 0927-0248

Lee Shuo Jen, Shiow Long Chen, Cheng Wei Peng, Chih Yuan Lin, Wen Cheng Ke. (2009). Enhanced diffuse reflection of light into the air using silver coating on periodically textured 430BA stainless steel substrate. *Mater. Chem. Phys.,* Vol. 118, pp. 219-222., ISSN: 0254-0584

Müller J., B. Rech, J. Springer and M. Vanecek (2004). TCO and light trapping in silicon thin film solar cells. *Sol. Energy.* Vol. 77, pp. 917., ISSN: 0038-092X

Nishikawa Y., T. Nagasawa, K. Fujiwara, M. Osawa. (1993). Silver island films for surface-enhanced infrared absorption spectroscopy: effect of island morphology on the absorption enhancement. *Vib. Spectrosc.*, Vol. 6, pp. 43., ISSN: 0924-2031

Otte K., L. Makhova, A. Braun, I. Konovalov. (2006). Flexible Cu(In,Ga)Se$_2$ thin-film solar cells for space application. *Thin Solid Films.*, Vol. 511, pp. 613., ISSN: 0040-6090

Osawa M. (1997). Dynamic Processes in Electrochemical Reactions Studied by Surface-Enhanced Infrared Absorption Spectroscopy (SEIRAS). *Bull. Chem. Soc. Jpn.*, Vol. 70, pp. 2861., ISSN: 0009-2673

Rech B., O. Kluth, T. Repmann, T. Roschek, J. Springer, J. Müller, F. Finger, H. Stiebig, and H. Wagner. (2002). New materials and deposition techniques for highly efficient silicon thin film solar cells. *Sol. Energy Mater. Sol. Cells.,* Vol. 74, pp. 439., ISSN: 0927-0248

Rim Seung-Bum, Shanbin Zhao, Shawn R. Scully, Michael D. McGehee and Peter Peumans. (2007). An effective light trapping configuration for thin-film solar cells. *Appl. Phys. Lett.* Vol. 91, pp. 243501. ISSN: 1077-3118

Selvan J. A. Anna., A. E. Delahoy, S. Guo and Y. M. Li. (2006). A new light trapping TCO for nc-Si:H solar cells. *Sol. Energy Mater. Sol. Cells.*, Vol. 90, pp. 3371., ISSN: 0927-0248

Sőderstrőm T., F. –J. Haug, V. Terrazzoni-Daudrix, and C. Ballif, J. (2008). Optimization of
        amorphous silicon thin film solar cells for flexible photovoltaics. *J. Appl. Phys.*, Vol.
        103, pp. 114509-1., ISSN: 1089-7550

Yablonovitch E. and G. Cody. (1982). Intensity enhancement in textured optical sheets for
        solar cells. *IEEE Trans. Electron. Devices ED.*, Vol. 29, pp. 300., ISSN: 0018-9383

Zhou Dayu and Rana Biswas. (2008). Photonic crystal enhanced light-trapping in thin film
        solar cells. *J. Appl. Phys.*, Vol. 103, pp. 093102. , ISSN: 1089-7550

Low Cost Solar Cells Based on Cuprous Oxide

Verka Georgieva, Atanas Tanusevski[1] and Marina Georgieva
Faculty of Electrical Engineering and Information Technology,
[1]Institute of Physics, Faculty of Natural Sciences and Mathematics,
The "St. Cyril & Methodius"University, Skopje,
R. of Macedonia

1. Introduction

The worldwide quest for clean and renewable energy sources has encouraged large research activities and developments in the field of solar cells. In recent years, considerable attention has been devoted to the development of low cost energy converting devices. One of the most interesting products of photoelectric researches is the semiconductor cuprous oxide cell. As a solar cell material, cuprous oxide -Cu_2O, has the advantages of low cost and great availability. The potential for Cu_2O using in semiconducting devices has been recognized since, at least, 1920. Interest in Cu_2O revived during the mid seventies in the photovoltaic community (Olsen et al.,1982). Several primary characteristics of Cu_2O make it potential material for use in thin film solar cells: its non-toxic nature, a theoretical solar efficiency of about 9-11%, an abundance of copper and the simple and inexpensive process for semiconductor layer formation. Therefore, it is one of the most inexpensive and available semiconductor materials for solar cells. In addition to everything else, cuprous oxide has a band gap of 2.0 eV which is within the acceptable range for solar energy conversion, because all semiconductors with band gap between 1 eV and 2 eV are favorable material for photovoltaic cells (Rai, 1988).

A variety of techniques exist for preparing Cu_2O films on copper or other conducting substrates such as thermal, anodic and chemical oxidation and reactive sputtering. Particularly attractive, however, is the electrodeposition method because of its economy and simplicity for deposition either on metal substrates or on transparent conducting glass slides coated with highly conducting semiconductors, such as indium tin oxide (ITO), SnO_2, In_2O_3 etc. This offers the possibility of making back wall or front wall cells as well. We have to note that electrochemical preparation of cuprous oxide (Cu_2O) thin films has reached considerable attention during the last years.

Electrodeposition method of Cu_2O was first developed by Stareck (Stareck, 1937). It has been described by Rakhshani (Jayanetti & Dharmadasa, 1996, Mukhopadhyay et al.,1992, Rakhshani et al.1987, Rakhshani et al., 1996). In this work, a method of simple processes of electrolysis has been applied.

Electrochemical deposition technique is an simple, versatile and convenient method for producing large area devices. Low temperature growth and the possibility to control film thickness, morphology and composition by readily adjusting the electrical parameters, as well as the composition of the electrolytic solution, make it more attractive. At present,

electrodeposition of binary semiconductors, especially thin films of the family of wide - bend gap II-IV semiconductors (as is ZnO), from aqueous solutions is employed in the preparation of solar cells. A photovoltaic device composed of a p-type semiconducting cuprous (I) oxide (Cu_2O) and n-type zinc oxide (ZnO) has attracted increasing attention as a future thin film solar cell, due to a theoretical conversion efficiency of around 18% and an absorption coefficient higher than that of a Si single crystal (Izaki et al. 2007)

Therefore, thin films of cuprous oxide (Cu_2O) have been made using electrochemical deposition technique. Cuprous oxide was electrodeposited on copper substrates and onto conducting glass coated with tin oxide (SnO_2), indium tin oxide (ITO) and zinc oxide (ZnO). Optimal conditions for high quality of the films were requested and determined. The qualitative structure of electrodeposited thin films was studied by x-ray diffraction (XRD) analysis. Their surface morphology was analyzed with scanning electronic microscope (SEM). The optical band gap values Eg were determined. To complete the systems Cu/Cu_2O, SnO_2/Cu_2O, ITO/Cu_2O and ZnO/Cu_2O as solar cells an electrode of graphite or silver paste was painted on the rear of the Cu_2O. Also a thin layer of nickel was vacuum evaporated on the oxide layer. The parameters of the solar cells, such the open circuit voltage (V_{oc}), the short circuit current (I_{sc}), the fill factor (*FF*), the diode quality factor (*n*), serial (*Rs*) and shunt resistant (*Rsh*) and efficiency (η) were determined. The barrier height (*Vb*) was determined from capacity-voltage characteristics.

Generally is accepted that the efficiency of the cells cannot be much improved. (Minami et al.,2004). But we successed to improve the stability of the cells, using thin layer of ZnO, making heterojunctions Cu_2O based cells.

2. Structural, morphological and optical properties of electrodeposited films of cuprous oxide

2.1 Experimental
2.1.1 Preparation of the films
A very simple apparatus was used for electrodeposition. It is consisted of a thermostat, a glass with solution, two electrodes (cathode and anode) and a standard electrical circuit for electrolysis. The deposition solution contained 64 g/l anhydrous cupric sulphate ($CuSO_4$), 200 ml/l lactic acid ($C_3H_6O_3$) and about 125 g/l sodium hydroxide (NaOH), (Rakhshani et al.1987, Rakhshani & Varghese, 1987). Cupric sulphate was dissolved first in distilled water giving it a light blue color. Then lactic acid was added. Finally, a sodium hydroxide solution was added, changing the color of the solution to dark blue with pH = 9. A copper clad for printed circuit board, with dimension 50 μm, 2.5×7 cm², was used as the anode. Copper clad and conducting glass slides coated with ITO and SnO_2 were used as a cathode. Experience shows that impurities (such as dirt, finger prints, etc.) on the starting surface material have a significant impact on the quality of the cuprous oxide. Therefore, mechanical and chemical cleaning of the electrodes, prior to the cell preparation, is essential. Copper boards were polished with fine emery paper. After that, they were washed by liquid detergent and distilled water. The ITO substrates were washed by liquid detergent and rinsed with distilled water. The SnO_2 substrates were soaked in chromsulphuric acid for a few hours and rinsed with distilled water. Before using all of them were dried.

Thin films of Cu_2O were electrodeposited by cathodic reduction of an alkaline cupric lactate solution at 60^0 C . The deposition was carried out in the constant current density regime. The deposition parameters, as current density, voltage between the electrodes and deposition

time were changed. The Cu_2O films were obtained under following conditions: 1) current density j = 1,26 mA/cm^2, voltage between the electrodes V = 0,3 - 0,38 V and deposition time t = 55 min. Close to the value of current density, deposition time and Faraday's law, the Cu_2O oxide layer thickness was estimated to be about 5 μm.

The potentiostatic mode was used for deposition the Cu_2O films on glass coated with SnO_2 prepared by spray pyrolisis method of 0.1 M water solution of $SnCl_2$ complexes by NH_4F . The applied potential difference between anode and cathode was constant. It was found that suitable value is V = 0,5 to 0,6 V. The deposition current density at the beginning was dependent on the surface resistance of the cathode. For a fixed value of the potential, the current decreased with increasing film thickness. The film thickness was dependent on deposition current density j. For current density of about 1 mA/cm^2 at the beginning and deposition time of about 2 h, the film thickness was 5-6 μm approximately. The thickness of deposited film was determined using a weighting method, as $d = m/\rho\, s$, where m is the mass and s is the surface of the film. A density ρ, of 5.9 g/cm^3 was used.

The deposition of Cu_2O on a commercial glass coated with ITO was carried out under constant current density. The ITO/Cu_2O films was obtained under the following conditions: current density j = 0,57 mA/cm^2, voltage between the electrodes V = 1,1 - 1,05 V and deposition time t = 135 min. The Cu_2O oxide layer thickness was estimated to be about 5 μm. All deposited films had reddish to reddish-gray color.

2.1.2 Structural properties

The structure of the films was studied by X – ray diffraction, using CuKα radiation with a wavelength of 0.154 nm. The Bragg angle of 2θ was varied between 20^0 and 50^0. The XRD spectrums of the films samples, deposited on copper, glass coated by SnO_2 and glass coated by ITO are shown in Fig.1, Fig.2 and Fig.3 respectively. It was found that all films are polycrystalline and chemically pure Cu_2O with no traces of CuO. XRD peaks corresponded to Cu_2O and the substrate material. The XRD spectrums indicate a strong Cu_2O peak with (200) preferential orientation.

2.1.3 Morphological properties

The surface morphology of the films was studied by a scanning electron microscope JEOL model JSM 35 CF. Fig.4, Fig.5 and Fig.6 show the scanning electron micrographs of Cu_2O films deposited on copper, glass coated by SnO_2 and glass coated by ITO respectively. The photographs indicate a polycrystalline structure. The grains are very similar to each other in size and in shape. They are about 1 μm and less in size for the film deposited on copper, 1-2 μm for the film deposited on SnO_2 and about 1 μm for the film deposited on ITO.

2.1.4 Optical band-gap energy determination

The optical band-gap is an essential parameter for semiconductor material, especially in photovoltaic conversion. In this work it was determined using the transmittance spectrums of the films. The optical transmission spectrums were recording on Hewlett-Packard (model 8452 A) spectrophotometer in the spectral range 350-800 nm wavelength. Thin layers of a transparent Cu_2O were preparing for the optical transmission spectrums recording. The optical transmission spectrum of about 1,5 μm thick Cu_2O film deposited on glass coated with SnO_2 is presented in Fig.7. There are two curves, one (1) recorded before annealing and the other one (2) after annealing of the film for 3h at 130^{0}C.
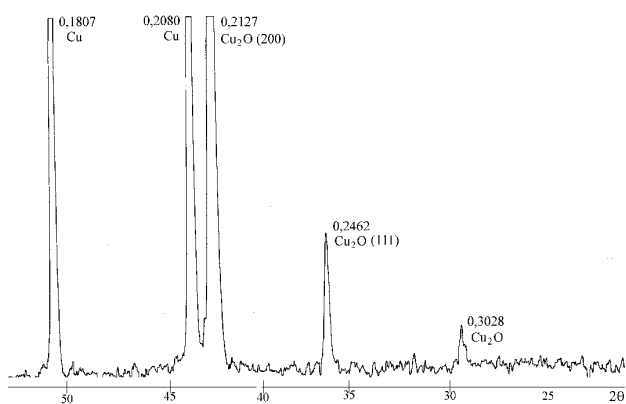
Fig. 1. X-ray diffraction spectrum of a Cu₂O film deposited on copper
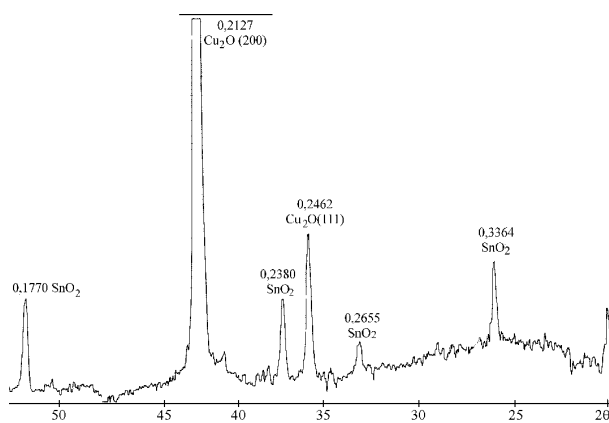
Fig. 2. X-ray diffraction spectrum of a Cu₂O film deposited on SnO₂
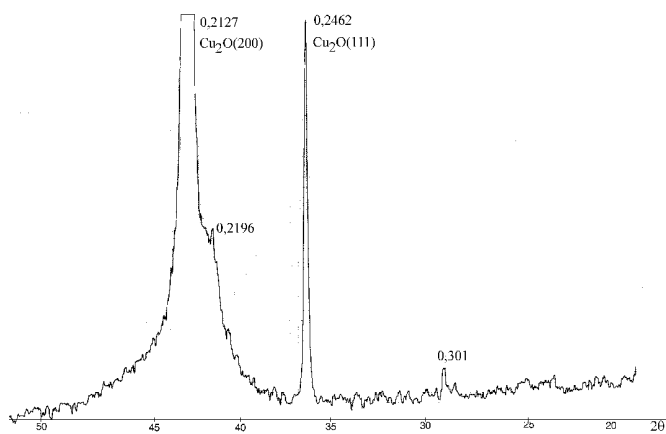
Fig. 3. X-ray diffraction spectrum of a Cu₂O film deposited on ITO
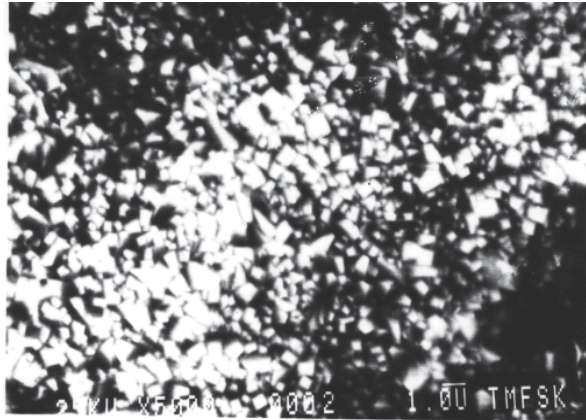
Fig. 4. Micrograph obtained from a scanning electron microscope of Cu_2O deposited on copper
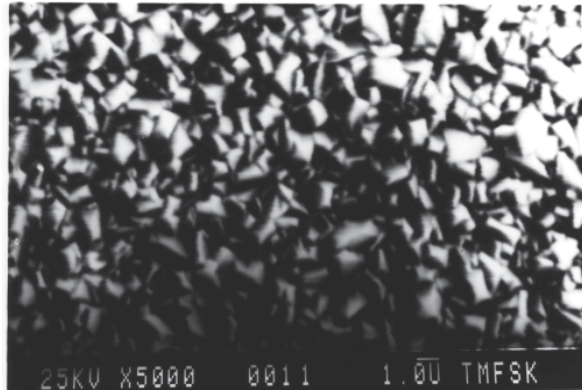
Fig. 5. Micrograph obtained from a scanning electron microscope of Cu_2O deposited on SnO
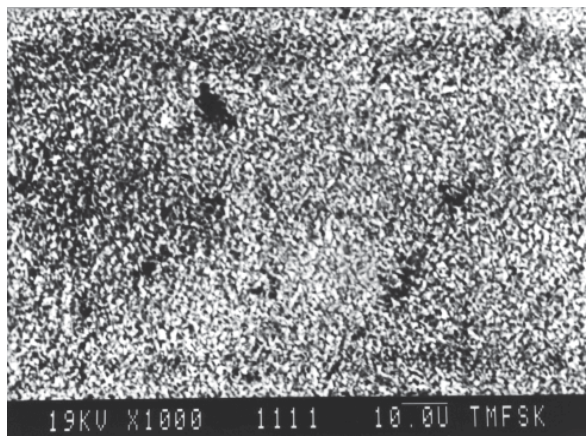
Fig. 6. Micrograph obtained from a scanning electron microscope of Cu_2O deposited on ITO
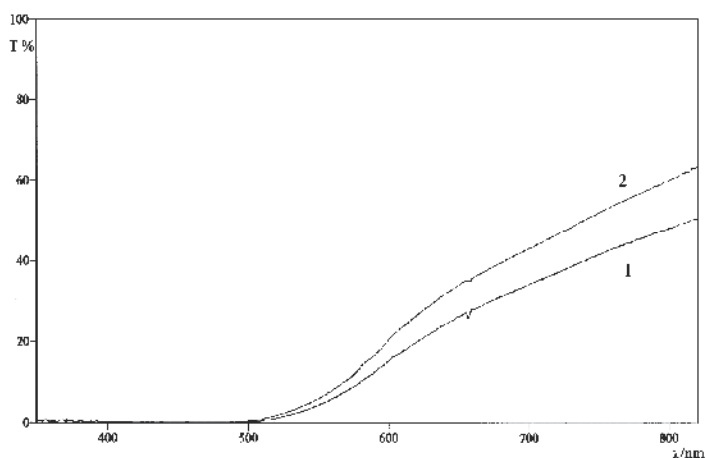
Fig. 7. Optical transmission spectrum of a 1,5 μm thick Cu_2O/SnO_2 film
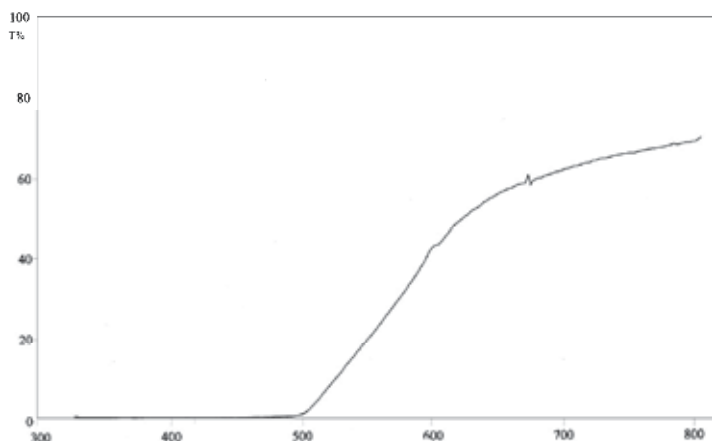
Fig. 8. Optical transmission spectrum of a 0,9 μm thick Cu_2O/ITO film

We can see that there is no difference in the spectrums. The absorption boundary is unchangeable. That means that the band gap energy is unchangeable with or without annealing. The little difference comes from different points recording, because the thickness of the film is not uniform. The transmittance spectrum of about 0,9 μm thick Cu_2O film, deposited on ITO, is presented in Fig. 8.

For determination of the optical band gap energy E_g , the method based on the relation

$$\alpha h\nu = A(h\nu - E_g)^{n/2},\tag{1}$$

has been used, where n is a number that depends on the nature of the transition. In this case its value was found to be 1 (which corresponds to direct band to band transition) because that value of n yields the best linear graph of $(\alpha h\nu)^2$ versus $h\nu$.

The values of the absorption coefficient α were calculated from the equation

$$\alpha = \frac{A}{d}, \tag{2}$$

where d is the film's thickness determined using weighing method, and A is the absorbance determined from the values of transmittance, $T(\%)$, using the equation

$$A = \ln\frac{100}{T(\%)}. \tag{3}$$

The values of the optical absorption coefficient α in dependence on wavelength are shown in Fig. 9 for Cu$_2$O/SnO$_2$ film and Fig. 10 for Cu$_2$O/ITO film
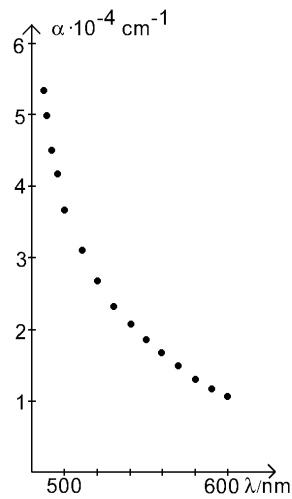
Fig. 9. Coefficient α vs wavelength λ for Cu$_2$O/SnO$_2$ film
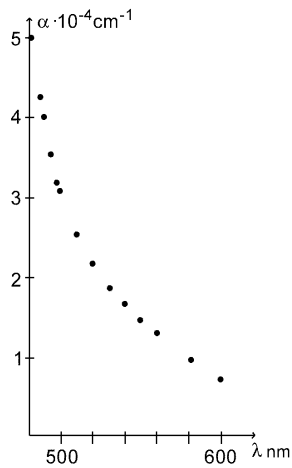
Fig. 10. Coefficient α vs wavelength λ for Cu$_2$O/ITO film

Fig.11 and Fig.12 show $(\alpha h\nu)^2$ versus $h\nu$ dependence for the Cu_2O/SnO_2 film and Cu_2O/ITO film corresponding. The intersection of the straight line with the $h\nu$ axis determines the optical band gap energy E_g. It was found to be 2,33 eV for Cu_2O/SnO_2 film and 2,38 eV for Cu_2O/ITO. They are higher than the value of 2 eV given in the literature and obtained for Cu_2O polycrystals. These values are in good agreement with band gaps
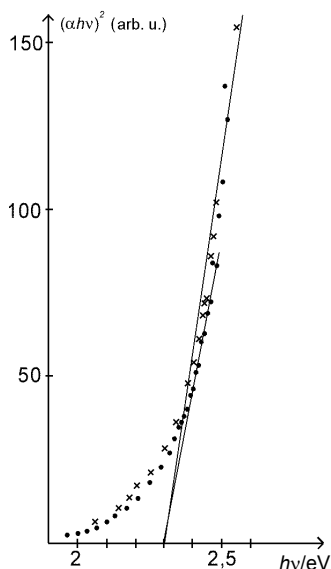
Fig. 11. Graphical determination of the optical band gap energy for Cu_2O/SnO_2 film
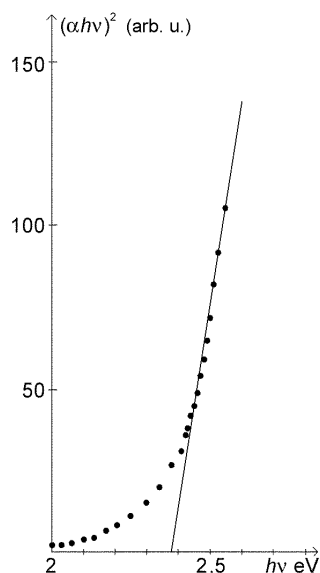
(x - before annealing; · - after annealing)

Fig. 12. Graphical determination of the optical band gap energy for Cu_2O/ITO film

determined from the spectral characteristics of the cells made with electrodeposited Cu_2O films. The value of the energy band gap of Cu_2O/ITO is little higher than the value of Cu_2O/SnO_2 film. The reason is maybe different size of the grains.

Fig.11 shows that there is no different in optical band gap energy determined from the curve plotted before annealing and from the curve plotted after annealing. Also, Fig.11 and Fig.12 show that there is no shape absorption boundary in the small energy range of the photons. Probably defects and structural irregularities are present in the films.

The optical band-gap of the films was determined using the transmitance spectrums. It was found to be 2,33 eV for Cu_2O/SnO_2 film and 2,38 eV for Cu_2O/ITO.

3. Preparation of the Cu_2O Schottky barrier solar cells

Cu_2O Schottky barrier solar cells can be fabricated in two configurations, the so called back wall and front wall structures. By vacuum evaporating a thin layer of nickel on the Cu_2O film, photovoltaic cells have been completed as back wall type cells (Fig.13), or by depositing carbon or silver paste on the rear of the Cu_2O layers, photovoltaic cells have been completed as front wall type cells (Fig.14). Nickel, carbon or silver paste are utilized to form ohmic contacts with cuprous oxide films. From the energy band diagram (Fig.15) we can see that the Cu_2O work function $\Phi_s = \chi + 1{,}7$ eV, (χ is the electron affinity of Cu_2O) (Olsen et al.,1982, Papadimitriou et al.,1990). That means that Cu_2O will make ohmic contact with metals characterized with work function higher than 4,9 eV, as are Ni, C. Gold and silver essentially form ohmic contacts. A carbon or silver back contact was chosen because of simplicity and economy of the cell preparation. The rectifying junction exists at the interface between the cooper and Cu_2O layers in the case of back wall cells. In the case of front wall cells the rectifying junction exists at the interface between the SnO_2 (ITO) and Cu_2O layers.
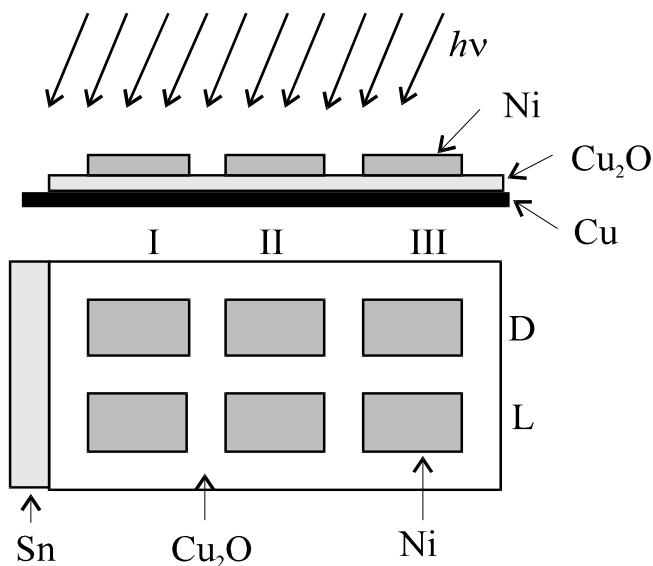
Fig. 13. Profile and face of Cu/Cu_2O back wall cell structure
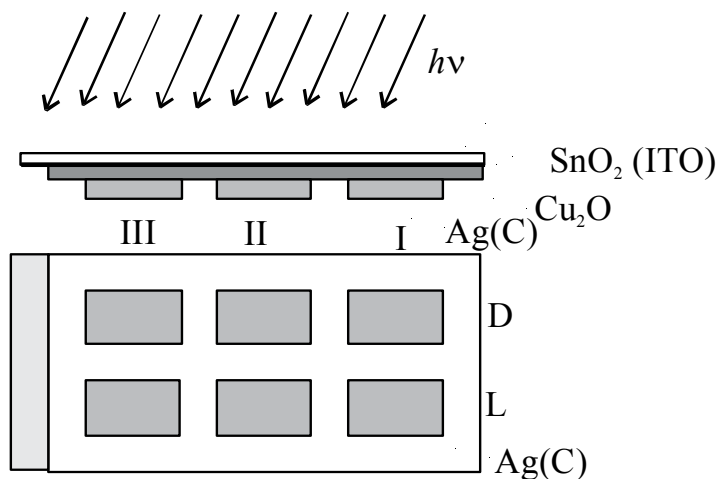
Fig. 14. Profile and rare of SnO_2 (ITO)/Cu_2O front wall cell structure

The evaporation of nickel has been made with Balzers apparatus under about $5,33 \times 10^{-3}$ Pa pressure. The optical transmission of the nickel layer was 50% for 550nm wavelength. The total cell active area is 1.0 cm². Antireflectance coating or any special collection grids have not been deposited.
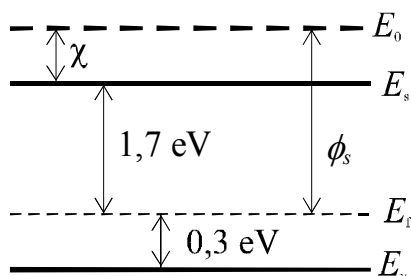
Fig. 15. Energy band diagram for Cu_2O

4. Current-voltage characteristics of the cells

The current-voltage characteristics of the best ITO/Cu_2O/C, Ni/Cu_2O/Cu and SnO_2/Cu_2O/C solar cells have been recorded in darkness and under 100 mW/cm² illumination, point by point. The light intensity was measured by Solar Meter Mod.776 of Dodge Products. The measurement was carried out using an artificial light source with additional glass filter, 10 mm thick to avoid heating of the cells. I-V characteristics, Fig.16, Fig.17 and Fig.18, were recorded first with periodically illumination of the source (curve ∘) to avoid the heating of the cell. After that I-V characteristics were recorded with continually illumination (curve ×). It is noted that the open circuit voltage V_{oc} and the short circuit current density I_{sc} decrease with increase in temperature. V_{oc} drops because of increase reverse current saturation with temperature because minority carriers increase with increase in temperature. I_{sc} decrease because of increase the recombination of the charges.

It should be stressed that this cells showed photovoltaic properties after heat treatment of the films for 3 hrs at 130 ^{0}C in a furnace. This possibly results in a decrease of sheet resistance value of the Cu_2O films, which was not measured, or in transformation the Cu_2O semiconductor from n to p type after heat treatment. Before heating V_{oc} and I_{sc} were about zero or negative. The serial resistance R_s and shunt resistance R_{sh} for all types of the cells were evaluated from I-V characteristics.

| Cell type | R_{so} | R_s | R_{sh} |
	kΩ	kΩ	kΩ
ITO/Cu$_2$O/C	10	1,02	76
Ni/Cu$_2$O/Cu	20	8,3	40
SnO$_2$/Cu$_2$O/C	14	3,3	25

Table 1. Serial and shunt resistance

The values are given in Table 1. R_{so} is evaluated from the dark characteristics (curve Δ) as dV/dI for higher values of forward applied voltage. R_{sh} is evaluated as dV/dI from the dark characteristics in reverse direction for lower values of the applied voltage (Olsen & Bohara, 1975). R_s is evaluated from the light I-V characteristics and it decreases with illumination. That means that R_s is photoresponse. The high series resistance R_s and low shunt resistance R_{sh} are one of the reasons for poor performance of the cell.

Several cell parameters were evaluated from the *I-V* characteristics. Table 2 contains the optimal current and voltage values (I_m and V_m), the open circuit voltage (V_{oc}), the short circuit current (I_{sc}) and evaluated values of the fill factor FF $\left(FF = \dfrac{I_m V_m}{I_{sc} V_{oc}} \right)$, the efficiency η

$\left(\eta = FF \dfrac{I_{sc} V_{oc}}{P_{in}} \right)$ and diode factor *n*.

| Cell type | I_m | V_m | I_{sc} | V_{oc} | FF | η | n |
	μA	mV	μA	mV	%	10^{-2} %	
ITO/Cu$_2$O/C	130	180	245	340	28	2,34	2,23
Ni/Cu$_2$O/Cu	28	120	50	270	24	0,70	2,06
SnO$_2$/Cu$_2$O/C	46	90	74	225	25	0,41	2,20

Table 2. Cell parameters

The diode factor was evaluated from the logarithmic plot of the dependence of I_{sc} versus V_{oc} which were measured for different illumination. The diode factor defined as

$$n = \frac{q}{kT} \frac{\Delta V_{oc}}{\Delta \ln I_{sc}}$$
(4)

is about 2 for all type of the cells.

The performances of the cells depend on the starting surface material, the type of the junction, post deposition treatment and the ohmic contact material. From the I-V characteristics, we can see that the cells are with poor performances, low fill factor FF and

very low efficiency. The high R_s and low R_{sh} (which is very far from ideally solar cell) are one of the reasons for poor performances. Because of high series resistance R_s, the values of the short circuit current density are very low. By depositing gold instead of nickel or graphite paste, the performance may be improved by decreasing of R_s.
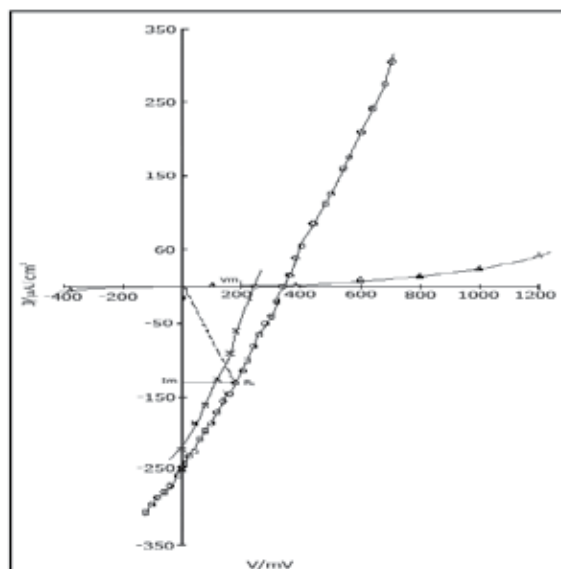
Fig. 16. I-V characteristics for ITO/Cu$_2$O/C solar cell ∘-periodically illumination (100 mW/cm^2); ×-continually illumination(100 mW/cm^2); Δ-dark characteristic
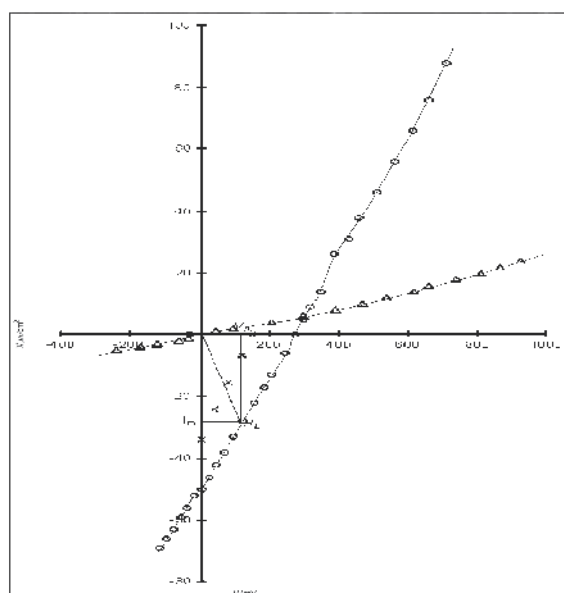
Fig. 17. I-V characteristics for Ni/Cu$_2$O/Cu solar cell o-periodically illumination (100 mW/cm^2); ×-continually illumination(100 mW/cm^2); Δ-dark characteristic
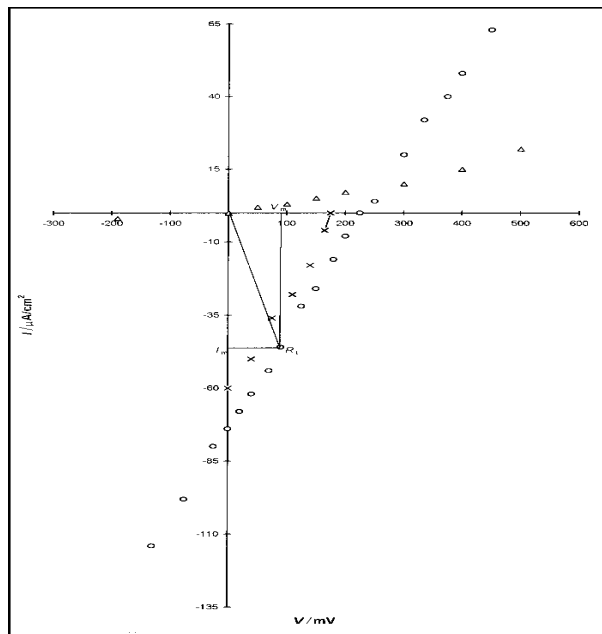
Fig. 18. I-V characteristics for SnO$_2$/Cu$_2$O/C solar cell o-periodically illumination (100 mW/cm^2); ×-continually illumination(100 mW/cm^2); Δ-dark characteristic

5. Potential barrier height determination of the cells

Capacitance as a function of reverse bias voltage at room temperature of Ni/Cu$_2$O/Cu, SnO$_2$/Cu$_2$O/graphite and ITO/Cu$_2$O/graphite solar cells was measured by RCL bridge on alternating current (HP type) with built source with 1000 Hz frequency.

Results for 1/C^2 versus reverse bias voltage for all these types of cells are shown in Fig 19, Fig 20 and Fig 21, before annealing (□), immediately after annealing (•) and after three months of annealing (×). The dependence is straight line. The intercepts of the straight line with x-axis correspond to the barrier height V_b. Cu/Cu$_2$O cell showed photovoltaic effect without post deposition heat treatment and their photovoltaic properties are almost unchangeable in time (fig.19). In contrast to this cell, the ITO/Cu$_2$O (fig.20) and SnO$_2$/Cu$_2$O (fig.21) cells no showed photovoltaic properties and no potential barrier was found to exist (Georgieva &Ristov, 2002). Before annealing, the open circuit voltage V_{oc} and the short circuit current I_{sc} were about zero.

After annealing of the films for 3 h at 130^{0}C, the devices exhibited good PV properties and the potential barrier excised. But this situation was not stationary. That is another essential factor in the properties of these cells indicating the possibility of chemical changes in ITO/Cu$_2$O and SnO$_2$/Cu$_2$O junction (Papadimitriou et al.,1981).

The values of barrier height V_b and the open circuit voltage V_{oc} upon illumination by an artificial white light source of 100 mW/cm^2 for all types of cells are presented in table 3. Also in this table are given their values after aging for 3 months (∗). Only Cu/Cu$_2$O cell has stationary values of V_b and V_{oc}. The values of barrier height V_b are great then the values of open circuit voltage V_{oc}. The great V_b gives the great $V_{oc,}$ in consent with the photovoltaic theory.
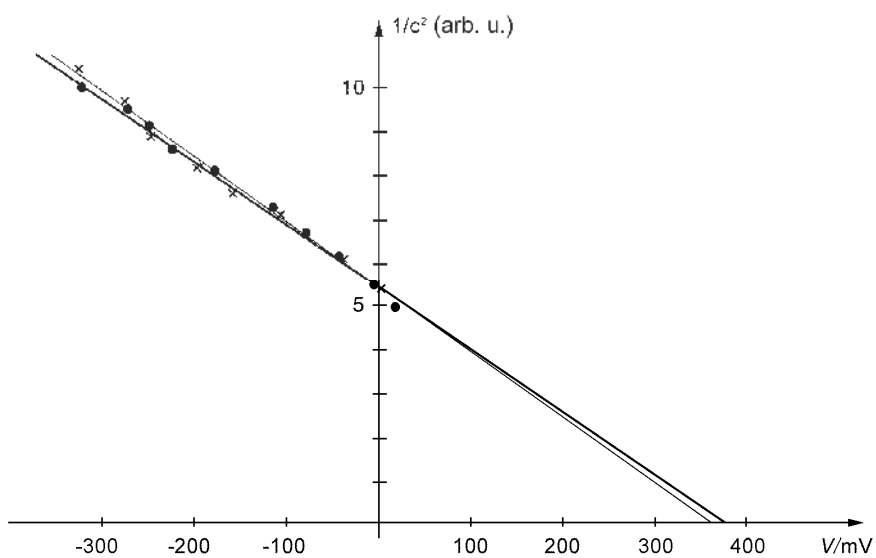
Evaluation of the barrier height, before annealing (□); after annealing (•); after 3 months of annealing (×).

Fig. 19. $1/C^2$ vs applied voltage of Cu/Cu$_2$O cell.
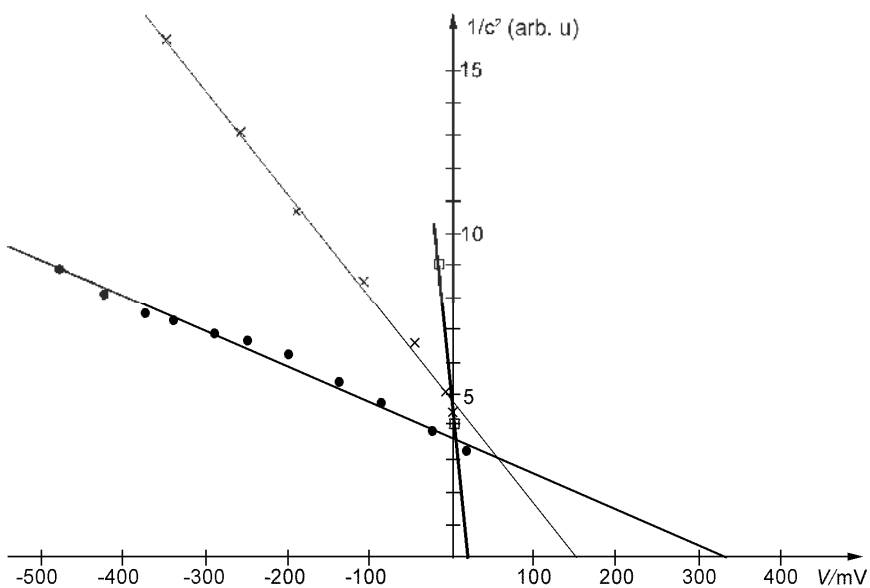
Evaluation of the barrier height, before annealing (□); after annealing (•); after 3 months of annealing (×).

Fig. 20. $1/C^2$ vs applied voltage of ITO/Cu$_2$O cell.

Cell type	Cu/Cu$_2$O	ITO/Cu$_2$O	SnO$_2$/Cu$_2$O	
V_b (mV)	(mV)	378	330	180
V_{oc} (mV)	310	249	118	
V_b^* (mV)	370	150	60	
V_{oc}^* (mV)	310	105	30	

Table 3. Values of barrier height V_b and open circuit voltage V_{oc} for all types of cells after annealing and after aging for 3 months (∗).
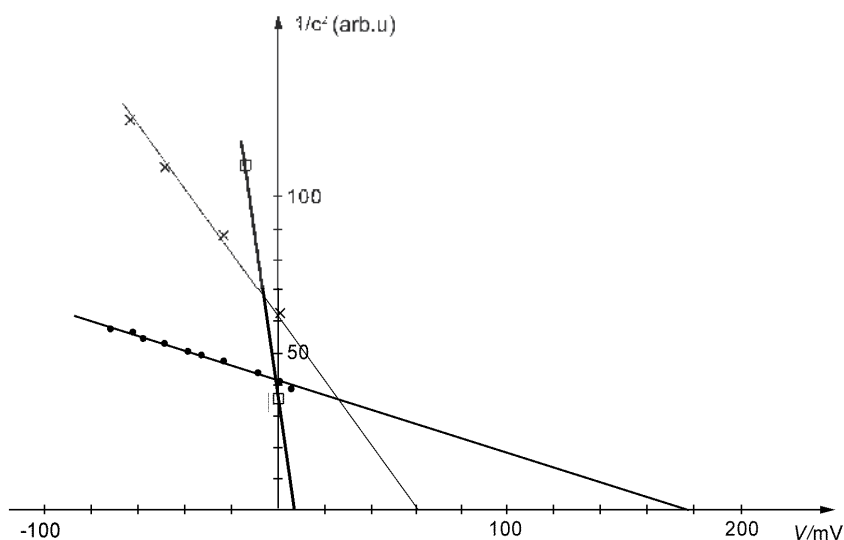
Evaluation of the barrier height, before annealing (□); after annealing (•); after 3 months of annealing (×).

Fig. 21. $1/C^2$ vs applied voltage of SnO$_2$/Cu$_2$O cell.

6. ZnO/Cu₂O heterojunction solar cells

Until now, we have made Schottky barrier solar cells. As we could not improve their efficiency and their stability, we decided to make heterojunction p-n solar cells based on a p-type Cu$_2$O thin films. We selected ZnO as an n-type semiconductor. ZnO is a transparent oxide that is widely used in many different applications, including thin film solar cells. The p-n junction was fabricated by potentiostatic deposition of the ZnO layer onto SnO$_2$ conducting glass with a sheet resistance of 14 Ω/ and potentiostatic deposition of Cu$_2$O onto ZnO, Fig.22.

6.1 Electrochemical depositing of ZnO

ZnO/Cu$_2$O heterojunction solar cells were made by consecutive cathodic electrodeposition of ZnO and Cu$_2$O onto tin oxide covered glass substrates. Zinc oxide (ZnO) was cathodically deposited on a conductive glass substrate covered with SnO$_2$ as cathode by a potentiostatic method (Dalchiele et al.,2001, Izaki et al.,1998, Ng-Cheng-Chin et al.,1998). Conducting glass slides coated with SnO$_2$ films are commercial samples. The electrolysis takes place in a
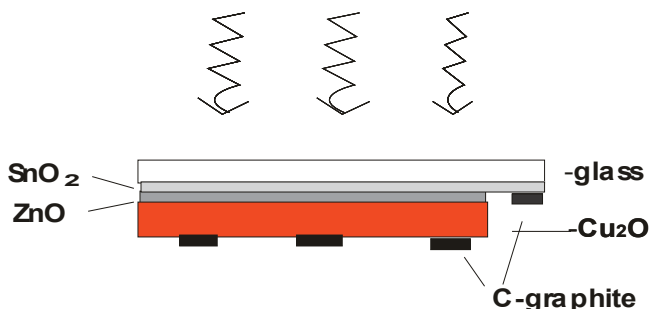
Fig. 22. Profil of ZnO/Cu$_2$O hetrojunction solar cells

simple aqueous 0,1M zinc nitrate [Zn (NO$_3$)$_2$] solution with pH about 6, maintained at 70^{0}C temperature. The cathodic process possibly can be described by the following reaction equations (Izaki & Omi, 1992):

$$Zn(NO_3)_2 \rightarrow Zn^{2+} + 2NO_3^-$$

$$NO_3^- + H_2O + 2e^- \rightarrow NO_2 + 2OH^-$$

$$Zn^{2+} + 2OH^- \rightarrow Zn(OH)_2 \rightarrow ZnO + H_2O \qquad (5)$$
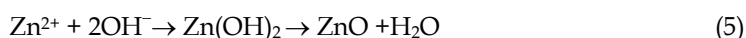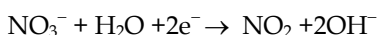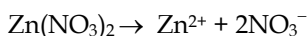
ZnO films were electrochemically grown at constant potential of 0.8 V between the anode and cathode. For a fixed value of the potential, a current density decreased with increasing the film thickness. The deposition time was varying from 10 min to 30 min. Deposited films were rinsed thoroughly in distilled water and allowed to dry in air at room temperature. The anode was zinc of 99.99% purity.

The deposition conditions of the thin films of Cu$_2$O have been described in 2.1.1. The deposition potential is pH sensitive. It suggests, also and it has already been reported that the Cu$_2$O layer was formed by the following reaction:

$$2Cu^{2+} + 2e^- + 2OH^- \rightarrow Cu_2O + H_2O, \qquad (6)$$
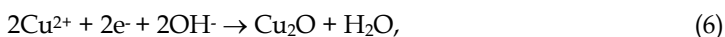
even this reaction does not explain the large pH dependence of deposition potential (Izaki et al. 2007, Wang & Tao, 2007). The present study was conducted, in a first instance, on undoped zinc oxide films and cuprous (I) oxide films. The structure of the films was studied by X-ray diffraction measurements using monochromatic Cu K$_\alpha$ radiation with a wavelength of 0,154 nm operated at 35 kV and 24 mA. Morphology and grain size was determined through micrographs on a JEOL JSM 6460 LV scanning electron microscope.

Figure 23 shows the X-ray diffraction patterns of ZnO film prepared at 0.8 V potential for 10 min. The Bragg angle of 2θ was varied between 20^0 and 70^0. It can be seen that the film has crystalline structure. XRD peaks corresponding to ZnO (signed as C) and the substrate material SnO$_2$ (signed as K) were determined with JCPDS patterns. The XRD spectrum indicates a strong ZnO peak with a (0002) or (1011) preferential orientation.

Figure 24 shows a scanning electron micrograph of undoped electrodeposited ZnO film.The photograph shows small rounded grains. It is difficult to determine the grain size from the micrograph. But using Scherrer's equation ($D = \dfrac{0,9\lambda}{\beta \cos \theta}$), the apparent crystallite size of ZnO is about 20nm, which means that it is nanostructured film
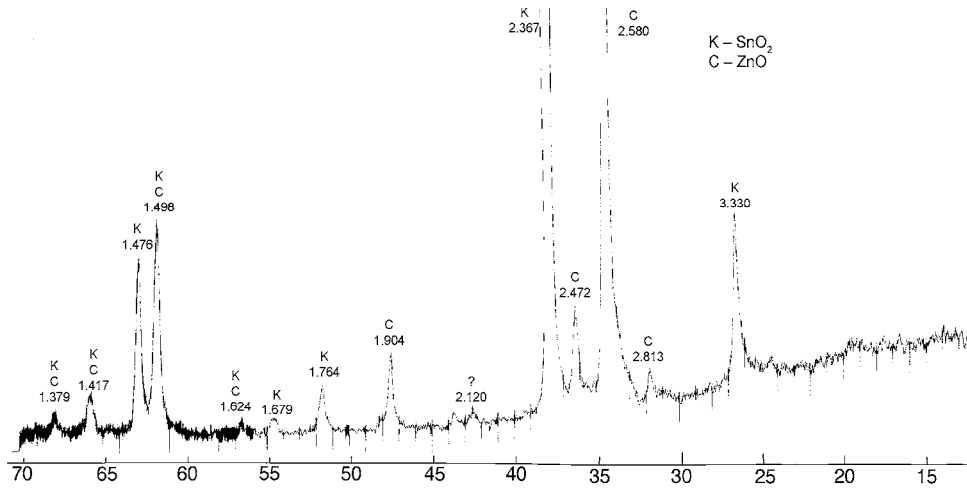
Fig. 23. X-ray diffraction spectrum of undoped electrodeposited ZnO film at 65⁰C
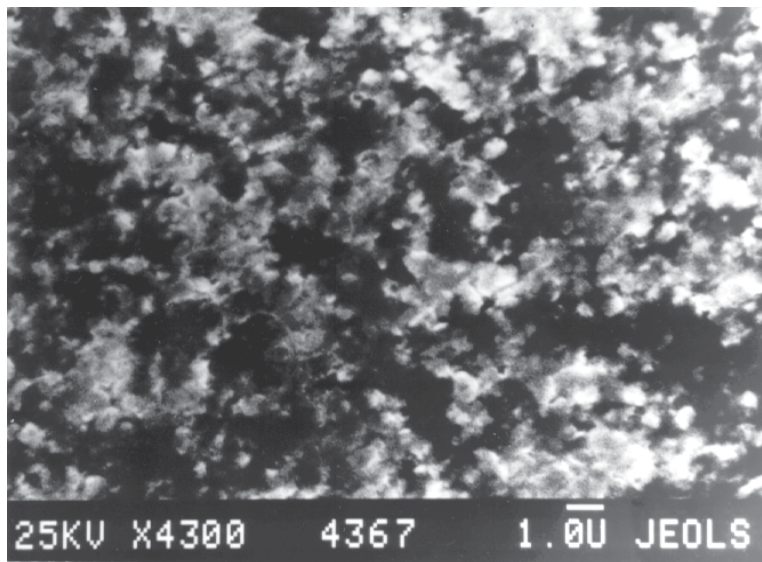
Fig. 24. SEM micrograph of undoped electrodeposited pure ZnO

Thin films of ZnO grown by electrochemical deposition technique on SnO_2/glass substrate are optically transparent in a visible spectral region, extending to 300 nm wavelength.

The transmission is relatively low ($\sim$ 50%) in the blue region (400–450 nm) Fig.25. The transmission maximum is about 60–70% through the red light region. Probably defects and structural irregularities are presented in the films, indicating low transmission.

Assuming an absorption coefficient α corresponding to a direct band to band transition and making a plot of $(\alpha h\nu)^2$ versus energy $h\nu$, the optical band gap energy Eg was determined through a linear fit. It was found to be 3.4 eV , which corresponds to the documented room temperature value of 3.2 to 3.4 eV.
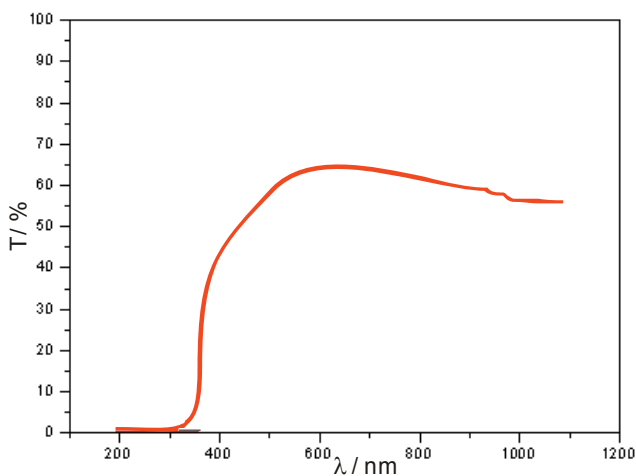
Fig. 25. Optical transmission spectrum of ZnO film

6.2 Some characteristic of the cells

To complete $Cu_2O/ZnO/SnO_2$ heterojunction as solar cell, thin layer of carbon paste or carbon spray was deposited on the rear of the Cu_2O. Front wall cells were formed. A carbon back contact was chosen because of simplicity and economy of the cell preparation and because the cells with carbon give high values of the short circuit current density despite the evaporated layer of nickel. The total cell active area was 1 cm^2. Antireflectance coating or any special collection grids have not been deposited. The best values of the open circuit voltage $V_{o\,c}$= 330 mV and the short circuit current density I_{sc} = 400 μm/cm^2 were obtained by depositing carbon paste and illumination of 100 mW/cm^2. The V_{oc} increases as logarithmic function with solar

radiation, ($Voc = \dfrac{kT}{e}\ln\left(\dfrac{I_{sc}}{I_0}+1\right)$). The *Isc* increases linear with solar radiation, (Fig.26).

Our investigations show that the ZnO layer improves the stability of the cells. That results in a device with better performances despite of the Schhotky barrier solar cells (Cu_2O/SnO_2). First, the cells show photovoltaic properties without annealing, because potential barrier was formed without annealing. The barrier fell for a few days which result in decreasing the open circuit voltage despite the values of V_{oc} for just made cells. It decreases from 330 mV to 240 mV. But after that the values of V_{oc} keep stabilized, because of stabilized barrier potential. It wasn't case with Schotkky barrier solar cells, because barrier potential height decreases with aging. In ZnO/Cu_2O cells, thermal equilibrium exists. The V_{oc} decreases and I_{sc} increases with increasing the temperature, that is characteristic for the real solar cell. It could be seen from the current-voltage (*I-V*) characteristic in incident light of 50mW/cm^2, Fig.27.

Barrier potential height was determined for one device from capacitance measurement as a function of reverse bias voltage at room temperature. Capacitance dependence of reverse bias voltage at room temperature was measured by RCL bridge on alternating current (HP type) with bilt source with 1000 Hz frequency. Results for (1/C^2) versus voltage are shown in Figure 28. The Cu_2O/SnO_2 cells without the ZnO layer show a lower V_{oc}. The improvement in V_{oc} could be due to the increase of the barrier height using ZnO layer as n-type semiconductor.
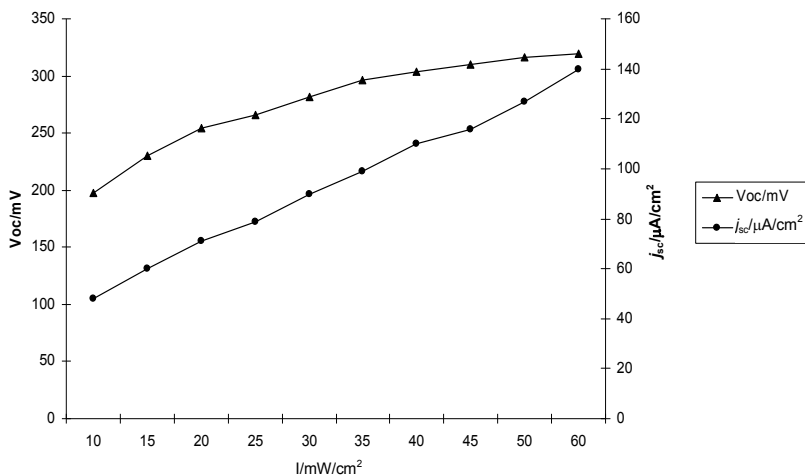
Fig. 26. Dependence of the V_{oc} and I_{sc} vs. solar irradiation

The values of barrier height V_b and the open circuit voltage V_{oc} upon illumination of 100 mW/cm^2 for just made cell and the cell after few days are presented in table 4. Also in this table are given their values after few days of depositing. The values of the barrier height are great than the values of open circuit voltage V_{oc}. The grate V_b gives the great V_{oc}, that correspondent to the photovoltaic theory.

Cu$_2$O/ZnO/SnO$_2$ cell	V_b(mV)	V_{oc}(mV)
just made	368	330
after few days	276	240

Table 4. Values of barrier height V_b and open circuit voltage V_{oc} for just made cell and after few days.
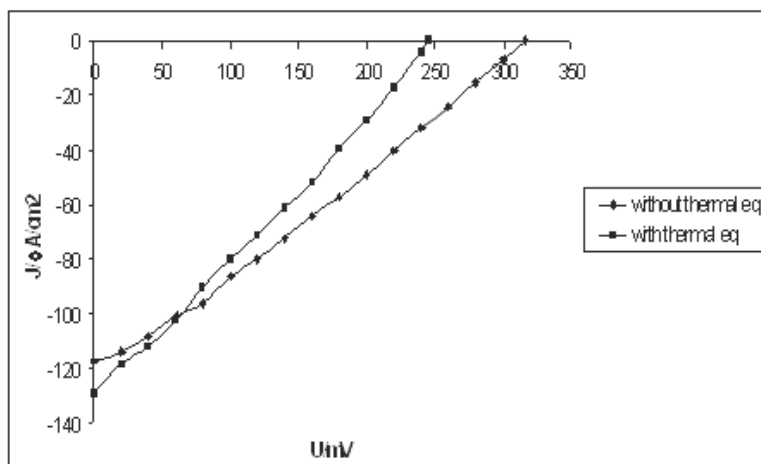
Fig. 27. Volt-current characteristics of the Cu$_2$O/ZnO/SnO$_2$ solar cell upon 50mW/cm^2 Illumination
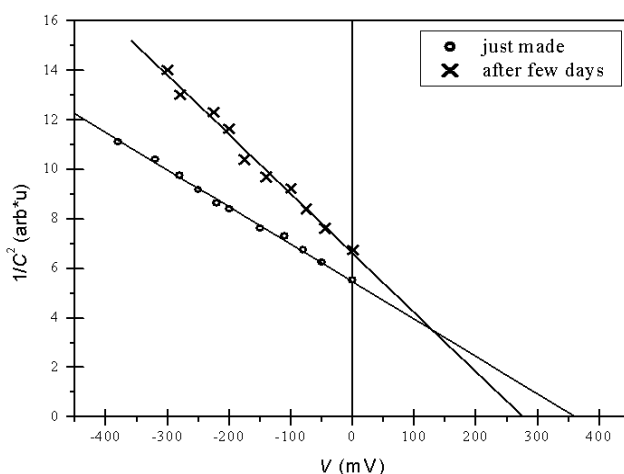
Fig. 28. $1/C^2$ vs applied voltage of $Cu_2O/ZnO/SnO_2$ cell

The values Voc=316 mV, Isc=0,117 mA/cm^2, fill factor =0,277, upon 50mW/cm^2 illumination are compared with the values: Voc=190 mV, Isc=2,08 mA/cm^2, fill factor = 0,295; upon 120mW**/cm²** illumination (Katayama et al. 2004) made with electrochemical deposition technique. Maybe doping of the ZnO films with In, Ga and Al (Machado et al., 2005, Kemell et al., 2003) will decrease the resistivity and increase the electro conductivity of the films, consequently and the short circuit current density of the cells.

7. Conclusion

The performance of the Cu_2O Schottky barrier solar cells are found to be dependent on the starting surface material, the type of the junction, post deposition treatment and the ohmic contact material. Better solar cells have been made using an heterojunction between Cu_2O and n-type TCO of ZnO. It is a suitable partner since it has a fairly low work function. Our investigation shows that the ZnO layer improves the stability of the cells. That results in a device with better performances despite of the Schhotky barrier solar cells (Cu_2O/SnO_2). First, the cells show photovoltaic properties without annealing, because potential barrier was formed without annealing. To improve the quality of the cells, consequently to improve the efficiency of the cells, it has to work on improving the quality of ZnO and Cu_2O films, because they have very high resistivity, a factor which limits the cells performances. Doping of the ZnO films with In, Ga and Al will decrease the resistivity of the deposited films and increase their electroconductivity. SEM micrographs show that same defects are present in the films which act as recombination centers. Behind the ohmic contact, maybe one of the reason for low photocurrent is just recombination of the carriers and decreasing of the hole cocentracion with the time. The transmittivity in a visible region have to increase. Also, it is necessary to improve the ohmic contact, consequently to increase the short circuit current density (*Isc*). For further improvement of the performances of the cells maybe inserting of a buffer layer at the heterojunction between Cu_2O and ZnO films will improve the performance of the cells by eliminating the mismatch defects which act as recombination centers. Also it will be protection of reduction processes that maybe exists between ZnO and Cu_2O.

Even low efficiency it may be acceptable in countries where the other alternative energy sources are much more expensive.

8. Acknowledgment

9. References

Dalchiele E.A., Giorgi P.,.Marotti R.E, at all. Electrodeposition of ZnO thin films on n-Si(100), *Solar Energy Materials &Solar Cells* 70 (2001) 245-254

GeorgievaV. Ristov M. (2002) Electrodeposited cuprous oxide on indium tin oxide for solar applications, *Solar Energy Materials & Solar Cells* 73, p 67-73

Izaki M., Omi T,J. (1992).,*Electrochem.Soc.*1392014

Izaki M, Ishizaki H., Ashida A. at all. (1998), *J.Japan Inst.Metals*, Vol. 62,No.11pp.1063-1068

Izaki M., Shinagawa T., Mizuno K., Ida Y., Inaba M., and Tasaka A., (2007) Electrochemically constructed p-Cu_2O/n-ZnO heterojunction diode for photovoltaic device *J.Phys.D:Appl.Phys.*40 3326-3329.

Jayanetti J.K.D., Dharmadasa I.M, (1996), *Solar Energ.Mat.andSolar Cells* 44 251-260

Katayama J., Ito K. Matsuoka M. and Tamaki J., (2004) Performance of Cu_2O/ZnO solar cells prepared by two-step electrodeposition *Journal of Applied Electrochemistry*, 34: 687-692,

Kemell M., Dartigues F., Ritala M., Leskela M, (2003) Electrochemical preparation of In and Al doped Zno thin films for $CuInSe_2$ solar cells, *Thin Solid Films* 434 20-23

Machado G., Guerra D.N., Leinen D., Ramos-Barrado J.R. Marotti R.E., Dalchiele E.A., (2005), Idium doped zinc oxide thin films obtained by electrodeposition ,*Thin Solid Films* 490 124-131

Minami T.,.Tanaka H, Shimakawa T., Miyata T., Sato H., (2004) High-Efficiency Oxide Heterojunction Solar cells Using Cu_2O Sheets *Jap.J.Appl.Phys.*,43, p.917-919

Mukhopadhyay A.K.,.Chakraborty A.K, Chattarjae A.P. and.Lahriri S.K, (1992), *Thin Solid Films*, 209, 92-96

Olsen L.C., Bohara R.C., Urie M.W., (1979) *Appl.Phys.Lett,* 34, p. 47

Olsen L.C., Addis F.W. and Miller W., (1982-1983), *Solar Cells*, 7 247-249

Papadimitriou L., Economu N.A and Trivich, (1981), *Solar Cells*, 3 73

Papadimitriou L., Valassiades O. and Kipridou A., (1990), *Proceeding,* 20th ICPS, Thessaloniki, 415-418

Ng-Cheng-Chin F., Roslin M.,.Gu Z.H and Fahidy T.Z., (1998) *J.Phys.D.Appl.Phys.*31 L71-L7

Rai B.P., (1988) Cu_2O Solar Cells *Sol. Cells* 25 p.265.

Rakhshani A.E (1986) Preparation, characteristics and photovoltaic properties of cuprous oxide-A review *Solid-State Electronics* Vol. 29.No.1. pp.7-17.

Rakhshani A.E., Jassar A.A.Al and.Varghese J. (1987) Electrodeposition and characterization of cuprous oxide *Thin Solid Films*, 148,pp.191-201

Rakhshani A.E.and Varghese J., (1987) Galvanostatic deposition of thin films of cuprous oxide *Solar Energy Materials*, 15,23,

Rakhshani A.E., Makdisi Y. and Mathew X., (1996), *Thin Solid Films*, 288, 69-75

Stareck, U.S. Patents 2, 081, 121 *Decorating Metals*, 1937

Wang L. and Tao M. (2007) Fabrication and Characterization of p-n Homojunctions in Cuprous Oxide by Electrochemical Deposition, *Electrochemical and Solid-State Letters*, 10 (9) H248-H250

Application of Electron Beam Treatment in Polycrystalline Silicon Films Manufacture for Solar Cell

L. Fu

College of Materials Science, Northwestern Polytechnical University, Xian,
State Key Laboratory of Solidification Processing
P. R. China

1. Introduction

Solar cell attracts more and more attentions recently since it transfers and storages energy directly from the sun light without consuming natural resources on the earth and polluting environment. In 2002, the solar industry delivered more than 500 MW per year of photovoltaic generators. More than 85% of the current production involved crystalline silicon technologies. These technologies still have a high cost reduction potential, but this will be limited by the silicon feedstock (Diehl et al., 2005; Lee et al., 2004). On the other hand the so-called second generation thin film solar cells based on a-Si, µc-Si, Cu(In,Ga)(Se,S)2, rare earth or CdTe have been explored(Shah et al.,2005; Li et al.,2004). Crystalline silicon on glass (CSG) solar cell technology was recently developed by depositing silicon film on a glass substrate with an interlayer. It can addresses the difficulty that silicon wafer-based technology has in reaching the very low costs required for large-scale photovoltaic applications as well as the perceived fundamental difficulties with other thin-film technologies (M. A. Green et al., 2004). This technology combines the advantages of standard silicon wafer-based technology, namely ruggedness, durability, good electronic properties and environmental soundness with the advantages of thin-films, specifically low material use, large monolithic construction and a desirable glass substrate configuration.

This Chapter will descript research about the polycrystalline silicon thin film absorber based on CSG technology with high efficiency. Line shaped electron beam recrystallized polycrystalline silicon films of a 20µm thickness deposited on the low cost borosilicate glass-substrate, which are the base for a solar cell absorber with high efficiency and throughput. It is known that the morphology of polycrystalline silicon film and grain boundaries have strong impact on the photoelectric transformation efficiency in the later cell system. Thus, this study concentrates on the influence of recrystallization on the silicon-contact interface and the surface morphology.

2. Experiment methods

Fig. 1 shows the schematic illustration of the silicon solar cell used in this work. The substrate of polycrystalline silicon thin film is Borosilicate glass, which is $10\times10\times0.07\text{cm}^3$ in size. A pure tungsten layer of 1.2µm was sputtered on the glass substrate at DC of 500W in

an argon atmosphere, which has almost the same thermal expansion coefficient of 4.5×10^{-6}K^{-1} as that of the silicon film (Linke et al., 2004; Goesmann et al., 1995). This tungsten interlayer was used as a thermal and mechanical supporting layer for deposition of the silicon film. Nanocrystalline silicon films were then deposited on the tungsten interlayer by the plasma enhanced chemical vapour deposition process (PECVD) within $SiHCl_3$ and H_2 atmosphere. Details of the process were described in References (Rostalsky et al., 2001; Gromball et al., 2004, 2005). The power density used was 2.5W/cm^2. The gap in the PECVD parallel plate reactor was 10mm and the substrate temperature was 550°C. The flow rate $H_2/SiHCl_3$ is 0.25 to reduce the hydrogen and chlorine content in the film. Boron trichloride (BCl_3) was added in the gas for an in-situ p-doping. The process pressure was chosen to 350 Pa for the minimized stress. At the above conditions, the deposition rate up to 200nm/min was obtained. After a silicon film of 15-20μm thickness was deposited, a SiO_2 layer of 400nm thickness was deposited on the top of the silicon from $SiHCl_3$ and N_2O within 5 min to prevent balling up.
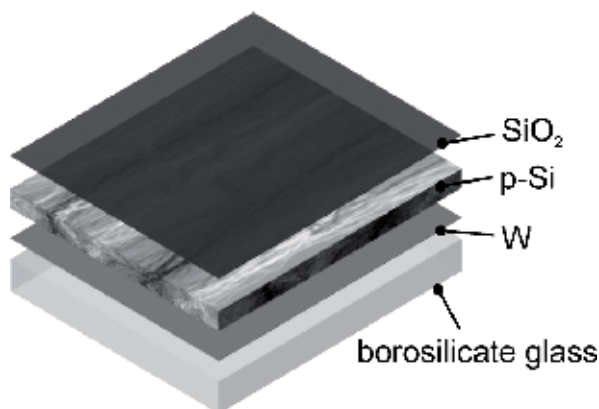
Fig. 1. Structure of thin film silicon solar cell
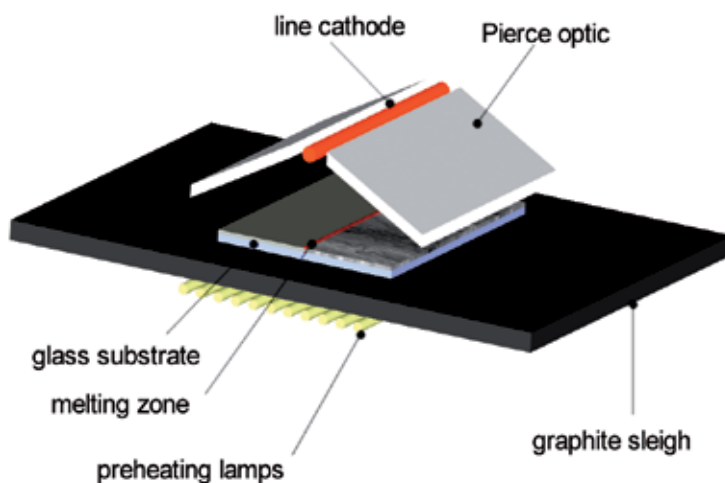
Fig. 2. Schematic of the linear electron beam recrystallization system (Gromball et al., 2005)

The P-doped polycrystalline silicon absorber of 10cm² was melted and recrystallized by a controlled line shaped electron beam (size in 1×100mm²) as described in Fig.2. The appearance of the sample after recrystallization was shown in Fig.3. The samples are preheated from the backside to 500°C within 2 min by halogen lamps. The electron beam energy density applies to the films is a function of the emission current density, the accelerating voltage and the scan speed. The scan speed is chosen to 8mm/s and the applied energy density changes between 0.34J/mm² and 0.4J/mm². To obtain the required grain size, the silicon should be melted and re-crystallized. Therefore, temperature in the electron beam radiation region should be was over the melting point of silicon of 1414°C. The surface morphology of the film, as well as distribution of WSi_2 phase under different energy densities has been investigated by means of a LEO-32 Scanning Electron Microscopy.

Fig. 3. Appearance of polycrystalline silicon absorber after recrystallization

3. Results and discussion

3.1 Microstructure of the capping layer

The applied recrystallization energy density strongly influences the surface morphology and microstructure of the recrystallized silicon film. With the energy increasing, the capping layer becomes smooth and continuous and less and small pinholes form in the silicon film. Excess of recrystallization energy density leads to larger voids in the capping layer, more WSi_2/Si eutectic crystallites, a thinner tungsten layer and a thicker tungstendisilicide layer.

Fig.4 gives the top view of the polycrystalline silicon film after the recrystallization. The EB surface treatment leads to recrystallization to obtain poly-Si films with grain sizes in the order of several 10μm in width and 100μm in the scanning direction as shown in Fig.5. The polycrystalline silicon films in Fig.4 are EB remelting with four different EB energy densities. Area A was treated with an energy density of 0.34J/mm² (the lowest of the four areas) while area D was treated with an energy density of 0.4J/mm² (highest of the four areas) on the same nanocrystalline silicon layer.

Fig. 4. Top view of the recrystallized silicon film, with increase of applied energy density from the left to the right
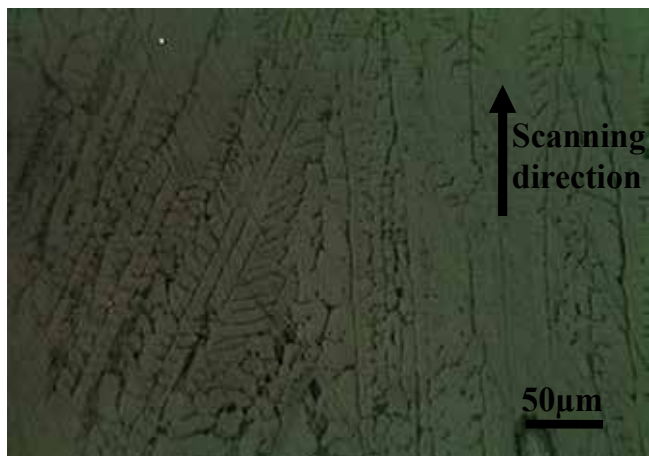
Fig. 5. Grain microstructure of Ploy-Silicon absorber after recrystallization
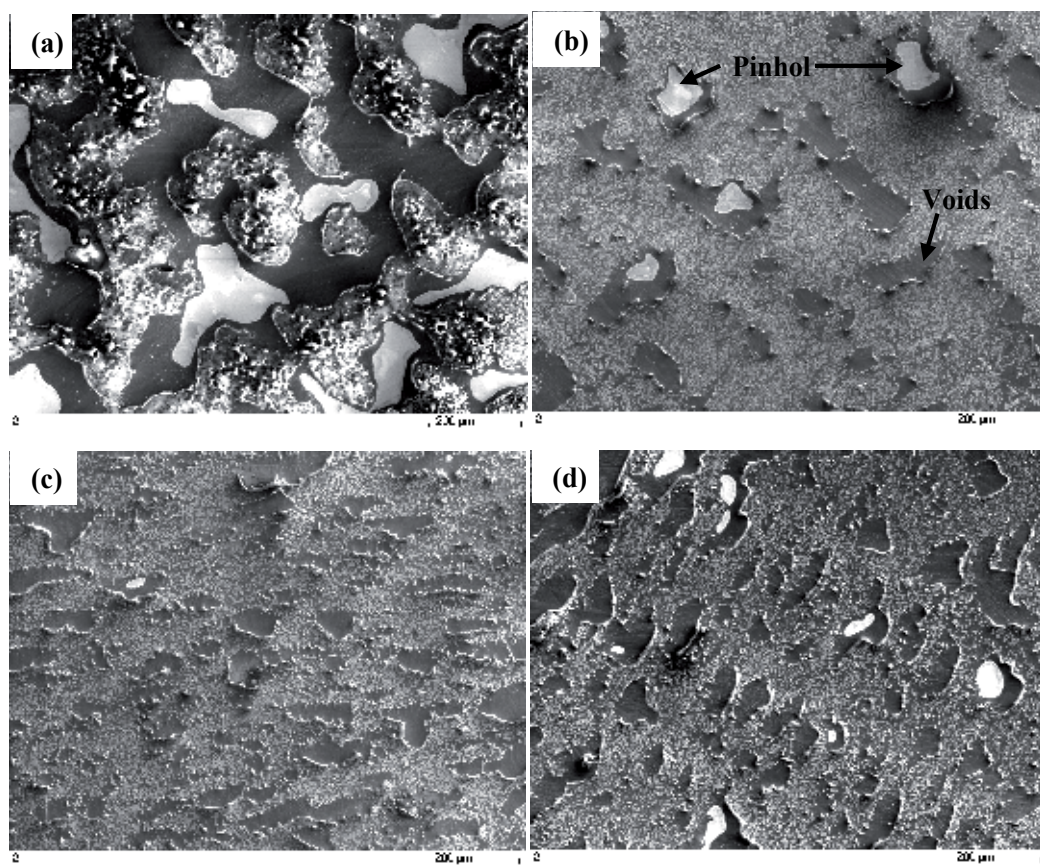
(a) ϵ=0.34J/mm2 ; (b) ϵ=0.36J/mm2 ; (c) ϵ=0.38J/mm2; (d) ϵ=0.4J/mm2

Fig. 6. Surface morphology of the recrystallized silicon layer under different energy density ϵ (Fu et al., 2007)

Fig.6 and Fig.7 show the morphology and microstructure of the EB treated layers. The nanocrystalline silicon is zone melted and recrystallized (ZMR) completely under all the energy chosen in this experiment. It can be seen that after the EB surface treatment, micro-sized silicon grains were formed in all the samples treated under different electron beam energy density ϵ.

The outmost surface was silicon dioxides with some voids and pinholes (bright spots), as shown in Fig.6. Large areas with a rough surface were where the silicon dioxide capping layer (SiO_2) existed. The voids (the dark area in Fig.6) in the silicon dioxide capping layer penetrated into the silicon layer with smooth edges. The bright areas were the bottom of the pinholes in which the WSi_2 remained.

Influences of the EB energy density on the morphology of deposited films are summarized in Table 1. The energy density influences the surface morphology of the film system strongly. The capping layer exhibited more voids when a lower EB energy density was used, as shown in Fig.6a. The SiO_2 capping layer is rougher and appeared as discontinuous droplet morphology in this condition. In addition, large tungstendisilicide pinholes formed due to the lower fluidity and less reaction between the silicon melt and the tungsten interlayer. When the EB energy density was increased, the capping layer becomes smoother and the size of voids was reduced. The number and size of pinholes also became smaller. However, when excess EB energy was applied, the solidification process became unstable and the amount of pinholes increased again. The silicon dioxide capping layer became discontinuous in this case, as shown in Fig. 6d.
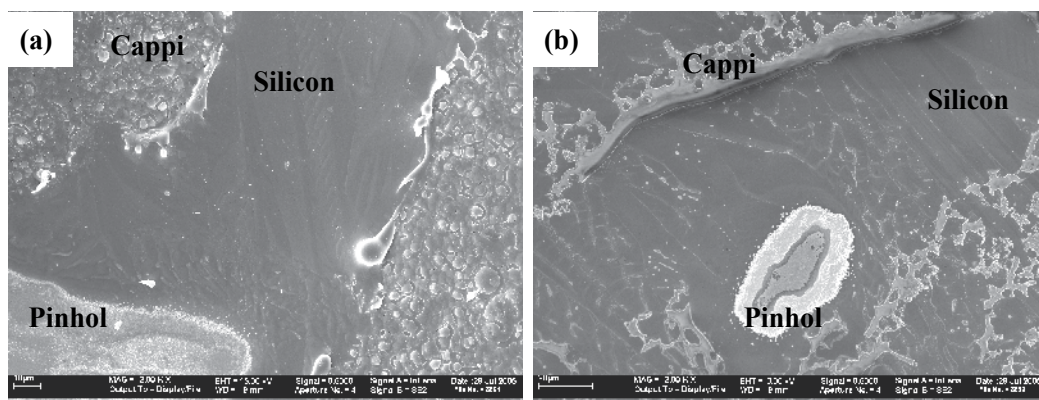
(a) ϵ=0.34J/mm² ; (b) ϵ=0.4J/mm²

Fig. 7. Microstructure of the capping layer and silicon grain under different energy density ϵ (Fu et al., 2007)

It was suggested that the voids are caused by the volume change of the capping layer and the silicon melt during the recrystallization process. Early work [6] suggested that the silicon dioxide in the capping layer could be considered as a fluid with a relatively high viscosity at the EB treatment temperature. For the same amount of silicon, the volume of the solid V_S is about 1.1 times of that of the liquid V_L. Therefore, during solidification process of the silicon melt, the volume increases will produce a curved melt surface. This will generates a tensile stress in the capping layer because of he interface enlargement between the viscous capping layer and the molten silicon. Once the critical strain of the capping layer is surpassed, voids will form in the capping layer. Due to the surface tension of the capping layer and its

adhesion to the silicon melt the capping layer also arches upwards and widens the voids. This effect is enhanced by thermal stress and outgassing during the solidification process [5]. As the size, area and viscosity of the SiO_2 layer is affected by the EB energy density, the size and the number of the voids in the capping layer are dependant on the EB energy density as well.

Energy level	SiO_2 capping/ voids	pinholes	$W_{remaining}$/ WSi_2 ratio	WSi_2/Si eutectic
Low (0.34J/mm²)	rough, droplet morphology	High density, biggest (>200µm)	21.7%	fine
Middle (0.36-0.38J/mm²)	smooth, continuous	sporadic, small size (<50µm)	13.3%	coarse
High (0.4J/mm²)	smooth, discontinuous	Low density, bigger(<100µm)	10.5%	coarser and widely spread

Table 1. Influence of the recrystallization energy on the surface morphology of the silicon film system

3.2 Formation of eutectic (WSi_2/Si)

This Chapter gives the details about the formation of Tungstendisilicide (WSi_2). The film system consists of a 20µm thick silicon layer on a 1.2µm thick tungsten film. Tungstendisilicide (WSi_2) is formed at the interface tungsten/silicon but also at the grain boundaries of the silicon. Because of the fast melting and cooling of the silicon film, the solidification process of the silicon film is a nonequilibrium solidification process.

It was claimed that tungstendisilicides were formed in their tetragonal (Hansen, 1958; Döscher et al., 1994) by the solid/solid state reaction and the solid/liquid state reaction between tungsten and silicon according to equation (1) and (2).

$$2Si_{(s)} + W_{(s)} \xrightarrow{700°C-1390°C} WSi_{2(s)} \tag{1}$$

$$2Si_{(l)} + W_{(s)} \xrightarrow{>1390°C} WSi_{2(s)} \tag{2}$$
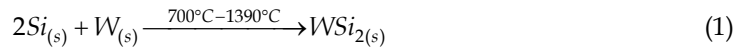
Formation of the eutectics can be explained using the phase diagram of the Si-W alloy system, as shown in Fig.8. The reactions should start at temperatures above 700°C. The eutectic crystallites (WSi_2/Si) are precipitated from the silicon melt at a eutectic concentration of 0.8 at% W at the eutectic temperature 1390°C in thermal equilibrium. With the temperature increased to above the eutectic temperature (1390°C) for tungsten enriched silicon melt, the WSi_2 layer mainly formed through a solid-liquid reaction and the thickness of the silicide layer increased rapidly. Because 100ms (the FWHM of the electron beam related to the scan speed) were sufficient to generate the tungstendisilicide layer. However, in this experiment, the solidification process of the nanocrystalline silicon was completed within 12.5 seconds for a sample of 10cm² area. Therefore, the solidification process was completed in a nonequilibrium state and the liquid-solid transformation line will divert from equilibrium line shown in Fig.8. At the beginning of the silicon solidification, the formation of tungstendisilicide crystallites will be suppressed by the rapid freezing and followed by the formation of solid silicon. These crystallites start to form just below the

liquid-solid transformation temperature, and their growth will be not immediately accompanied by the tungstendisilicide crystallite formation. Therefore, the silicon phase forms dendrites, which grow over a range of temperature like ordinary primary crystallites. Below the eutectic reaction temperature, the remaining melt solidifies eutectically as soon as the melt is undercooled to a critical temperature to allow silicon crystallite growth.
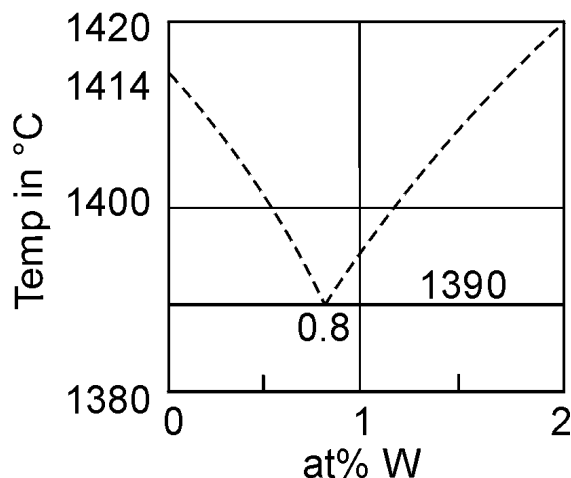
Fig. 8. Phase diagram of the Si-W alloy system in equilibrium (Hansen, 1958)

3.3 Microstructure and distribution of the eutectic crystallites (WSi2/Si) under different recrystallization energy

Tungstendisilicide (WSi$_2$) was formed at the tungsten/silicon interface but also at the grain boundaries of the silicon throughout all the EB energy density range. A top view scanning electron spectroscopy (SEM) and EDX analysis of the surface region showed that eutectic structure (tungstendisilicide precipitates / silicon) were mainly localized at the recrystallized silicon grain boundaries, as is shown in Fig.9. A typical hypoeutectic structure was found in the exposed silicon layer, which consisted of cored primary silicon dendrites (dendritic characteristic was not very evident) surrounded by the eutectic of the silicon and the tungstendisilicide precipitates. In this eutectic, tungstendisilicide (white areas in the lamellar shape) grew until the surrounding silicon melt had fully crystallized. The eutectic statistically distributed at the primary silicon grain boundaries. The formation and distribution of the eutectic depended on the crystallization and the growth dynamic of the tungsten enriched silicon melt. This is a nonequilibrium solidification process.

The size and the amount of the tungstendisilicide/silicon eutectic depended on the course of the process: when the higher the energy was used in the recrystallization process of the silicon layer, more and large tungstendisilicide crystals grew in the silicon melt. In addition, the WSi2/Si eutectic became coarser at the primary silicon grain boundaries and spread more widely. This was due to the prolonged solidification period for the tungsten enriched silicon melt in the remaining liquid, primarily at the grain boundary. At these sites, the tungstendisilicide crystallites precipitated in the final solidification areas at lower temperature than in case of equilibrium, due to the high tungsten concentration in the
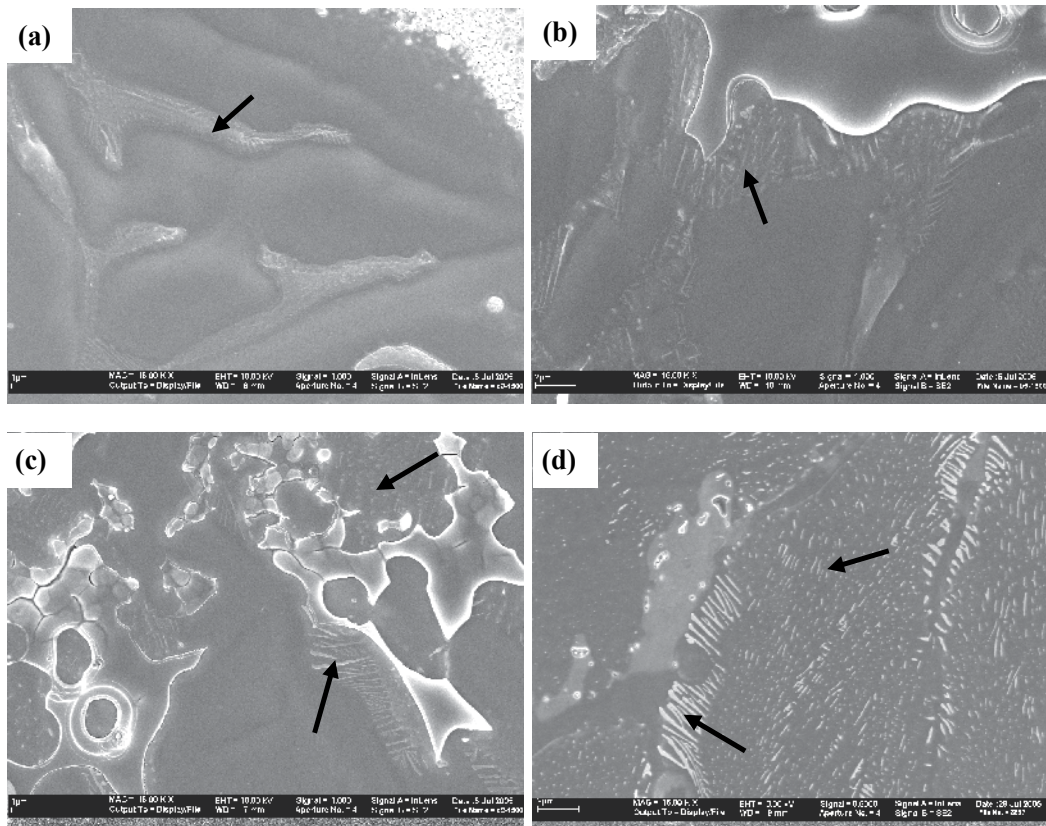
(a) ε=0.34J/mm²; (b) ε=0.36J/mm²; (c) ε=0.38J/mm²; (d) ε=0.4J/mm²

Fig. 9. SEM results of the eutectic structure under different recrystallization energy density ε (Fu et al., 2007)
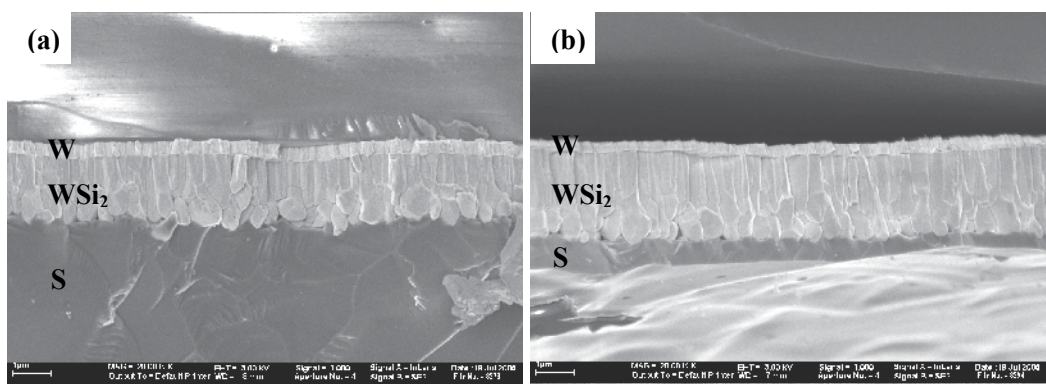
(a) ε=0.34J/mm² ; (b) ε=0.40J/mm²

Fig. 10. Cross section of typical silicon film system under different energy density ε (Fu et al., 2007)

volume. For high EB energy density there was more time for the precipitation and growth of tungstendisilicide and thus more tungstendisilicide crystallites were precipitated at the silicon grain boundaries. The strong tendency of formation of tungstendisilicide at the primary grain boundaries would reduce the efficiency of the solar absorber. Thus a high energy density is not favorable for the recrystallization process.

Fig.10 shows the cross section of a typical resolidified silicon film remelted with different EB energy densities. Tungstendisilicides (WSi_2) were formed in the region between the tungsten layer and the silicon layer without relationship to the EB energy density range applied in this research. A thick tungstendisilicide of 2.0-2.86µm exhibited in this experiment. The higher the applied EB energy density, the thicker the tungstendisilicide layer between the tungsten and the silicon layer, the thinner the remaining tungsten layer will be.
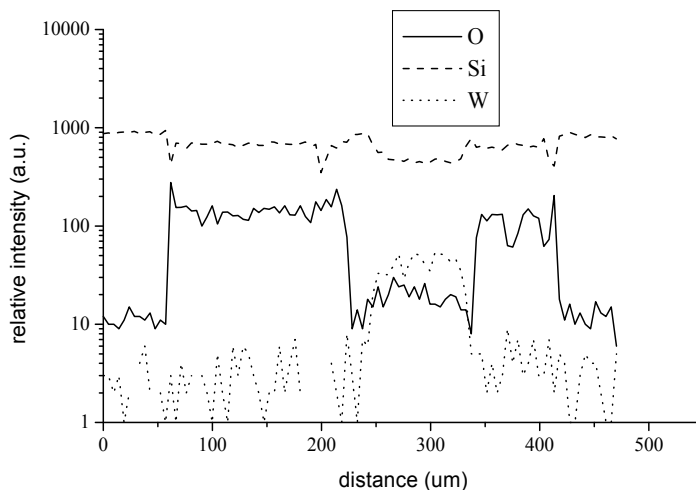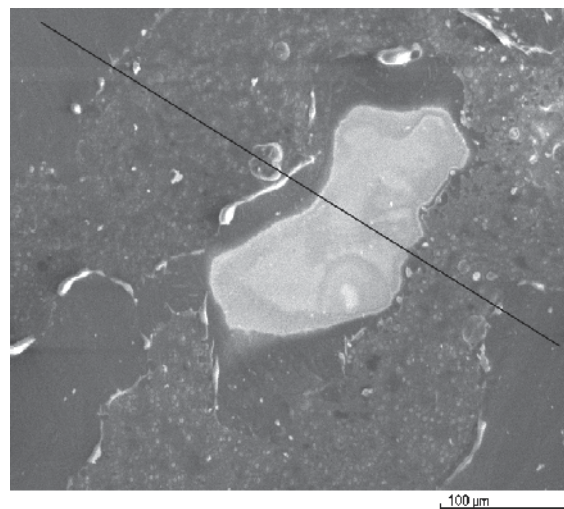
Fig. 11. SEM top view of the recrystallized silicon film in the pinhole area and its EDX line profile mapping results

3.4 Impurities in the recrystallized silicon film

The relatively high chlorine and hydrogen concentrations in the order of 0.5at% lead to outgassing during the recrystallization in completely melting regimes. This effect makes the capping layer arch upwards and widens the voids. Isolated pinholes in the silicon film can be observed. A weak hydrogen chloride peak is detected by mass spectrometry in the base gas atmosphere of the recrystallization chamber. Fig.11 shows an area surrounding a pinhole taken with SEM and the relative element concentrations measured by energy dispersive x-ray analysis (EDX) along the black line. There are no chlorine and hydrogen in the area surrounding a pinhole in the recrystallized film.

4. Summary

This Chapter descried the influence of the applied EB energy density used for the recrystallization process on the surface morphology of the ploy-silicon film system. At a low EB energy density, the voids were formed in the capping layer and the SiO_2 capping layer exhibited a rougher and droplet morphology. With the increase of EB energy density, the capping layer became smooth and the size of the voids decreased. The size and amount of pinholes increased again if the EB energy density was too high. This also led to the formation of larger voids in the capping layer as well as coarser and wider spreading of a WSi_2/Si eutectic crystallite at the grain boundaries.

This Chapter also gave the details about the formation of Tungstendisilicide (WSi_2). The tungstendisilicide precipitates/silicon eutectic structures were mainly localized in at the tungsten/silicon interface but also at the grain boundaries of the silicon throughout all the EB energy density range, as well as the relationship between energy density and microstructure of WSi_2/W areas. Tungstendisilicide forms in its tetragonal by the reaction of tungsten with silicon. WSi_2 improves the wetting and adhesion of the silicon melt but the tungsten layer may degrade the electrical properties of the solar absorber. The formation and distribution of the eutectic depended on the crystallization and the growth dynamic of the tungsten enriched silicon melt. This is a nonequilibrium solidification process.

A tungstendisilicide layer was formed between the tungsten layer and the silicon layer for all EB energy densities used. The higher the applied EB energy density, the thicker the tungstendisilicide layer grows and the thinner the tungsten layer left. It is important to perform the recrystallization process at a moderate energy density to suppress the formation of both WSi_2/Si eutectic and pinholes. In addition, there are no chlorine and hydrogen in the area surrounding a pinhole after recrystallization because of outgassing during the solidification.

5. Acknowledgements

6. References

Diehl W., Sittinger V. & Szyszka B. (2005). Thin film solar cell technology in Germany. *Surface and Coatings Technology*, Vol.193, No. 1-3, (April 2005), pp.329-334, ISSN: 0257-8972

Döscher M., Pauli M. and Müller J. (1994). A study on WSi_2 thin films, formed by the reaction of tungsten with solid or liquid silicon by rapid thermal annealing. *Thin Solid Films*, Vol.239, No. 2, (March 1994), pp.251-258, ISSN: 0040-6090

Dutartre D. (1989). Mechanics of the silica cap during zone melting of Si films. *Journal of Apply Physics*, Vol.66, No. 3, (August 1989), pp.1388-1391, ISSN: 0021-8979

Fu L., Gromball F., Groth C., Ong K., Linke N. & Müller J. (2007). Influence of the energy density on the structure and morphology of polycrystalline silicon films treated with electron beam. *Materials Science and Engineering B*, Vol.136, No. 1, (January 2007), pp.87–91, ISSN: 0921-5107

Green M. A., Basore P. A., Chang N., Clugston D., Egan R., Evans R. Hogg D., Jarnason S., Keevers M., Lasswell P., O'Sullivan J., Schubert U., Turner A., Wenham S. R. & Young T. (2004). Crystalline silicon on glass (CSG) thin-film solar cell modules. *Solar Energy*. Vol.77, No. 6, (December 2004), pp.857-863, ISSN: 0038-092X

Goesmann F. & Schmid-Fetzer R. (1995). Stability of W as electrical contact on 6H-SiC: phase relations and interface reactions in the ternary system W-Si-C. *Materials Science and Engineering B*, Vol. 34, No. 2-3, (November 1995), pp.224-231, ISSN: 0921-5107

Gromball F., Heemeier J., Linke N., Burchert M. & Müller J. (2004). High rate deposition and in situ doping of silicon films for solar cells on glass. *Solar Energy Materials & Solar Cells*, Vol.84, No. 1-4, (October 2004), pp.71-82, ISSN: 0927-0248

Gromball F., Ong K., Groth C., Fu L., Müller J., Strub E., Bohne W. & Röhrich J. (2005). Impurities in electron beam recryatallised silicon absorbers on glass, *Proceedings of 20th European Photovoltaic Solar Energy Conference and Exhibition*, Barcelona, Span, July, 2005.

Hansen M. (1958). Constitution of binary alloys, In: *Metallurgy and Metallurgical Engineering Series*, Kurt Anderko, pp.100-1324, McGraw-Hill Book Company, ISBN-13: 978-0931690181, ISBN-10: 0931690188, London

Lee G. H., Rhee C. K. & Lim K. S. (2006). A study on the fabrication of polycrystalline Si wafer by direct casting for solar cell substrate. *Solar Energy*, Vol.80, No. 2, (February 2006), pp.220-225, ISSN: 0038-092X

Li B. J., Zhang C. H. & Yang T. (2005). *Journal of Rare Earths*. Vol.23, No. 2, (April 2005), pp.228-230, ISSN: 1002-0721

Linke N., Gromball F., Heemeier J. & Mueller J. (2004). Tungsten silicide as supporting layer for electron beam recryatallised silicon solar cells on glass, *Proceedings of 19th European Photovoltaic Solar Energy Conference and Exhibition*, Paris, France, July, 2004.

Rostalsky M. & Mueller J. (2001). High rate deposition and electron beam recrystallization of silicon films for solar cells. *Thin Solid Films*, Vol.401, No. 1-2, (December 2001), pp.84-87, ISSN: 0040-6090

Shah A. V., Schade H., Vanecek M., Meier J., Vallat-Sauvain E., Wyrsch N., Kroll U., Droz C. & Bailat J. (2004). Thin-film silicon solar cell technology. *Progress in Photovoltaics: Research and Applications*. Vol.12, No. 2-3, (March 2004), pp.113-142, ISSN: 1099-159X

Electrodeposited Cu$_2$O Thin Films for Fabrication of CuO/Cu$_2$O Heterojunction

Ruwan Palitha Wijesundera
Department of Physics, University of Kelaniya, Kelaniya
Sri Lanka

1. Introduction

Solar energy is considered as the most promising alternative energy source to replace environmentally distractive fossil fuel. However, it is a challenging task to develop solar energy converting devices using low cost techniques and environmentally friendly materials. Environmentally friendly cuprous oxide (Cu$_2$O) is being studied as a possible candidate for photovoltaic applications because of highly acceptable electrical and optical properties. Cu$_2$O has a direct band gap of 2 eV (Rakhshani, 1986; Siripala et al., 1996), which lies in the acceptable range of window material for photovoltaic applications. It is a stoichiometry defect type semiconductor having a cubic crystal structure with lattice constant of 4.27 Å (Ghijsen et al., 1988; Wijesundera et al., 2006). The theoretical conversion efficiency limit for Cu$_2$O based solar cells is about 20% [5].

Thermal oxidation was a most widely used method for the preparation of Cu$_2$O in the early stage. It gives a low resistive, p-type polycrystalline material with large grains for photovoltaic applications. It was found that Cu$_2$O grown at high temperature has high leakage-current due to the shorting paths created during the formation of the material, and it causes low conversion efficiencies. Therefore it was focused to prepare Cu$_2$O at low temperature, which may provide better characteristics in this regard. Among the various Cu$_2$O deposition techniques (Olsen et al., 1981; Aveline & Bonilla, 1981; Fortin & Masson, 1981; Roos et al., 1983; Sears & Fortin, 1984; Rakhshani, 1986; Rai, 1988; Santra et al., 1992; Musa et al., 1998; Maruyama, 1998; Ivill et al., 2003; Hames & San, 2004; Ogwa et al., 2005), electrodeposition (Siripala & Jayakody, 1986, Siripala et al., 1996; Rakhshani & Varghese, 1987a, 1988b; Mahalingam et al., 2004; Tang et al., 2005; Wijesundera et al., 2006) is an attractive one because of its simplicity, low cost and low-temperature process and on the other hand the composition of the material can be easily adjusted leading to changes in physical properties. Most of the techniques produce p-type conducting thin films. Many theoretical and experimental studies (Guy, 1972; Pollack & Trivich, 1975; Kaufman & Hawkins, 1984; Harukawa et al., 2000; Wright & Nelson, 2002; Paul et al., 2006) have been revealed that the Cu vacancies originate the p-type conductivity. However, electrodeposition (Siripala & Jayakody, 1986, Siripala et al., 1996; Wijesundera et al., 2000; Wijesundera et al., 2006) of Cu$_2$O thin films in a slightly acidic aqueous baths produce n-type conductivity. Further it has been reported that the origin of this n-type behavior is due to oxygen vacancies and/or additional copper atoms. Recently, Garutara *et al.* (2006) carried out the photoluminescence (PL) characterisation for the electrodeposited n-type

polycrystalline Cu_2O, and confirmed that the n-type conductivity is due to the oxygen vacancies created in the lattice. This n-type conductivity of Cu_2O is very important in developing low cost thin film solar cells because the electron affinity of Cu_2O is comparatively high. This will enable to explore the possibility of making heterojunction with suitable low band gap p-type semiconductors for application in low cost solar cells.

Most of the properties of the electrodeposited Cu_2O were reported to be similar to those of the thermally grown film (Rai, 1988). The electrodeposition of Cu_2O is carried out potentiostatically or galvanostatically (Rakhshani & Varghese, 1987a, 1988b; Mahalingam et al., 2000; Mahalingam et al., 2002). Dependency of parameters (concentrations, pH, temperature of the bath, deposition potential with deposits) had been investigated by several research groups (Zhou & Switzer, 1998; Mahalingam et al., 2002; Tang et al., 2005; Wijesundera et al., 2006). The results showed that electrodeposition is very good tool to manipulate the deposits (structure, properties, grain shape and size, etc) by changing the parameters. Various electrolytes such as cupric sulphate + ethylene glycol alkaline solution, cupric sulphate aqueous solution, cupric sulphate + lactic acid alkaline aqueous solution, cupric nitrate aqueous solution and sodium acetate+ cupric acetate aqueous solution, have been reported in the electrodeposition of Cu_2O.

Cu_2O-based heterojunctions of ZnO/Cu_2O (Herion et al., 1980; Akimoto et al., 2006), CdO/Cu_2O (Papadimitriou et al., 1981; Hames & San, 2004), ITO/Cu_2O (Sears et al., 1983), TCO/Cu_2O (Tanaka et al., 2004), and Cu_2O/Cu_xS (Wijesundera et al., 2000) were studied in the literature, and the reported best values of V_{oc} and J_{sc} were 300 mV and 2.0 mA cm^{-2}, 400 mV and 2.0 mA cm^{-2}, 270 mV and 2.18 mA cm^{-2}, 400 mV and 7.1 mA cm^{-2}, and 240 mV and 1.6 mA cm^{-2}, respectively.

Cupric oxide (CuO) is one of promising materials as an absorber layer for Cu_2O based solar cells because it is a direct band gap of about 1.2 eV (Rakhshani, 1986) which is well matched as an absorber for photovoltaic applications. It is also stoichiometry defect type semiconductor having a monoclinic crystal structure with lattice constants a of 4.6837 Å, b of 3.4226 Å, c of 5.1288 Å and β of 99.54^o (Ghijsen et al., 1988). CuO had been wildly used for the photocatalysis applications. However, CuO as photovoltaic applications are very limited in the literature. The photoactive CuO based dye-sensitised photovoltaic device was recently reported by the Anandan *et al*. (2005) and we reported the possibility of fabricating the p-CuO/n-Cu_2O heterojunction (Wijesundera, 2010).

2. Growth and characterisation of electrodeposited Cu₂O

Electrodeposition is a simple technique to deposit Cu_2O on the large area conducting substrate in a very low cost. Electrodeposition of Cu_2O from an alkaline bath was first developed by Starek in 1937 (Stareck, 1937) and electrical and optical properties of electrodeposited Cu_2O were studied by Economon (Rakhshani, 1986). Rakshani and co-workers studied the electrodeposition process under the galvanostatic and potentiostatic conditions using aqueous alkaline $CuSO_4$ solution, to investigate the deposition parameters and properties of the material. Properties of the electrodeposited Cu_2O were reported to be similar to those of the thermally grown films (Rai, 1988) except high resistivity. Siripala *et al*. (Siripala & Jayakody, 1986) reported, for the first time, the observation of n-type photoconductivity in the Cu_2O film electrodes prepared by the electrodeposition on various metal substrates in slightly basic aqueous $CuSO_4$ solution in 1986. However, we have reported that electrodeposited Cu_2O thin films in a slightly acidic acetate bath attributed n-type conductivity.

Potentiostatic electrodeposition of Cu$_2$O thin films on Ti substrates can be investigated using a three electrode electrochemical cell containing an aqueous solution of sodium acetate and cupric acetate. Cupric acetate are used as Cu^{2+} source while sodium acetate are added to the solution making complexes releasing copper ions slowly into the medium allowing a uniform growth of Cu$_2$O thin films. The counter electrode is a platinum plate and reference electrode is saturated calomel electrode (SCE). Growth parameters (ionic concentrations, temperature, pH of the bath, and deposition potential domain) involved in the potentiostatic electrodeposition of the Cu$_2$O thin films can be determined by the method of voltommograms.

voltammetric curves were obtained in a solution containing 0.1 M sodium acetate with the various cupric acetate concentrations, while temperature, pH and stirring speed of the baths were maintained at values of 55 ^{o}C, 6.6 (normal pH of the bath) and 300 rev./min respectively. Curve a) in Fig. 1 is without cupric acetate and curves b), c) and d) are cupric acetate concentrations of 0.25 mM, 1 mM and 10 mM respectively. Significant current increase can not be observed in absence with cupric acetate and cathodic peaks begin to form with the introduction of Cu^{2+} ions into the electrolyte. Two well defined cathodic peaks are resulted at –175 mV and –700 mV Vs SCE due to the presence of cupric ions in the electrolyte and these peaks shifted slightly to the anodic side at higher cupric acetate concentrations. First cathodic peak at –175 mV Vs SCE attributes to the formation of Cu$_2$O on the substrate according to the following reaction.

$$2Cu^{2+} + H_2O + 2e^- \Rightarrow Cu_2O + 2H^+$$
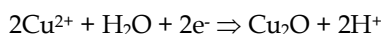
Second cathodic peak at –700 mV Vs SCE attributes to the formation of Cu on the substrate according to the following reaction.

$$Cu^{2+} + 2e^- \Rightarrow Cu$$

By examining the working electrode, it can be observed that the electrodeposition of deposits on the substrate is possible in the entire potential range. However, as revealed by the curves in Fig. 1, at higher concentrations the peaks are getting broader and therefore the formation of Cu and Cu$_2$O simultaneously is possible at intermediate potentials (curve d of Fig. 1). The deposition current slightly increases and the peaks are slightly shifted to the positive potential side as increasing the bath temperature range of 25 ˚C to 65 ˚C.

Fig. 2 shows the dependence of the voltammetric curves on the pH of the deposition bath. It is seen that cathodic peak corresponding to the Cu deposition is shifted anodically by about 500 mV and cathodic peak corresponding to the Cu$_2$O deposition is shifted anodically by about 100 mV. This clearly indicates that acidic bath condition favours the deposition of copper over the Cu$_2$O deposition and the possibility of simultaneous deposition of Cu and Cu$_2$O even at lower cathodic potentials. This is further investigated in the following sections.

The potential domain of the first cathodic peak gives the possible potentials for the electrodeposition of Cu$_2$O films while second cathodic peak evidence the possible potential domain for the electrodeposition of Cu films. It is evidence that Cu$_2$O can be electrodeposited in the range of 0 to -300 mV Vs SCE and Cu can be electrodeposited in the range of -700 to -900 mV Vs SCE. The potential domains of the electrodepostion of Cu$_2$O and Cu are independent of the Cu^{2+} ion concentration and the temperature of the bath. However, the deposition rate is increased with the increase in the concentration or the temperature of the bath.
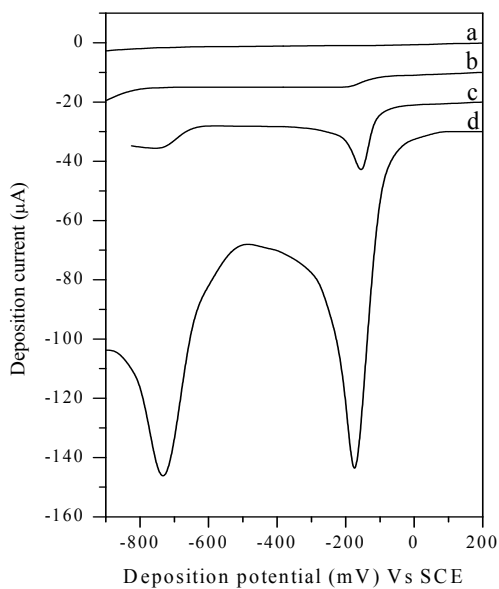
Fig. 1. Voltammetric curves of the Ti electrode (4 mm²) obtained in a solution containing 0.1 M sodium acetate and cupric acetate concentrations of a) 0 mM, b) 0.25 mM, c) 1 mM and d) 10 mM
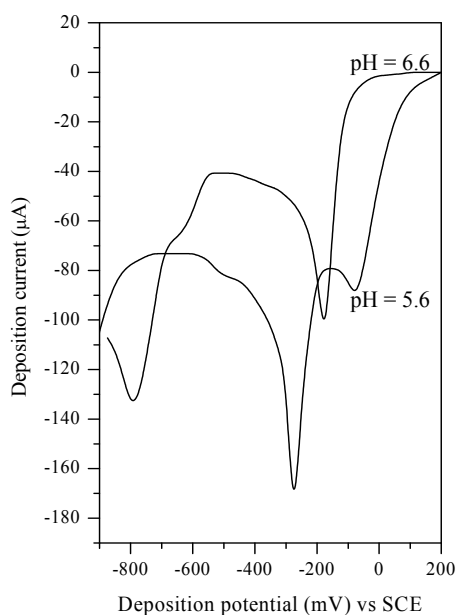
Fig. 2. Voltammetric curves of the Ti electrode (4 mm²) in an electrochemical cell containing 0.1 M sodium acetate and 0.01 M cupric acetate solutions at two different pH values (pH was adjusted by adding diluted HCI).

Cu$_2$O film deposition potential domain can be further verified by the X-ray diffraction (XRD) spectra obtained for the films electrodeposited at various potentials (-100 to -900 mV Vs SCE). Fig. 3 shows the XRD spectra of the films deposited at a) -200 mV Vs SCE, b) -600 mV Vs SCE and c) -800 mV Vs SCE on Ti substrates in a bath containing 0.1 M sodium acetate and 0.01 M cupric acetate aqueous solution. Fig. 3(a) shows five peaks at 2θ values of 29.58°, 36.43°, 42.32°, 61.39° and 73.54° corresponding to the reflections from (110), (111), (200), (220) and (311) atomic plans of Cu$_2$O in addition to the Ti peaks. Fig. 3(b) exhibits three additional peaks at 2θ values of 43.40°, 50.55° and 74.28° corresponding to the reflection from (111), (200) and (220) atomic plans of Cu in addition to the peaks corresponding to the Cu$_2$O and Ti substrate. It is evident that the intensity of Cu peaks increases with increase of the deposition potential with respect to the SCE while decreasing the intensities of Cu$_2$O peaks. Peaks corresponding to the Cu$_2$O disappeared with further increase in deposition potential. XRD of Fig. 3(d) exhibits peaks corresponding to Cu and Ti only. Thus, in the acetate bath single phase polycrystalline Cu$_2$O thin films with a cubic structure having lattice constant 4.27 Å are possible only with narrow potential domain of 0 to -300 mV Vs SCE while Cu thin films having lattice constant 3.61 Å are possible at potential –700 mV and above Vs SCE.
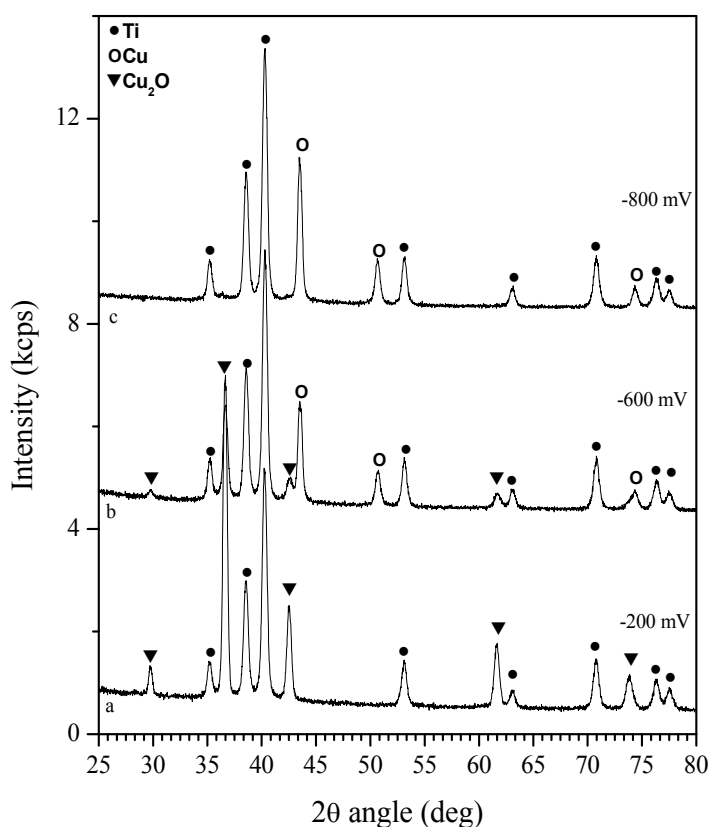
Fig. 3. XRD spectra obtained for the films deposited on Ti substrate at the potentials (a) -200 mV Vs SCE, (b) -600 mV Vs SCE and (c) -800 mV Vs SCE

Fig. 4 shows the scanning electron micrographs (SEMs) of the above set of samples. It is evident that the surface morphology depends on the deposition potential and the films grown on Ti substrate are uniform and polycrystalline. Grain size of Cu_2O is in the range of ~1-2 μm. It is observed that the Cu_2O thin film deposited at –200 mV Vs SCE exhibit cubic structure (Fig. 4(a)) and deviation from the cubic structure can be observed when deposition potential deviate from the -200 mV Vs SCE. Thus, polycrystalline Cu_2O thin films with cubic grains are possible only within a very narrow potential domain of around –200 mV Vs SCE. Fig. 4(b) shows the existence of spherical shaped Cu on top of Cu_2O when film deposited at –400 mV Vs SCE. The co-deposition of Cu with Cu_2O is evident in the XRD spectra, too. This small grains of Cu distributed over the Cu_2O surface will be useful in some other applications. It is clear from XRD and SEM results that Cu_2O, Cu_2O + Cu, and Cu microcrystalline thin films can be separately electrodeposited on Ti substrate by changing the deposition potential from –100 mV to –900 mV Vs SCE using the same electrolyte.
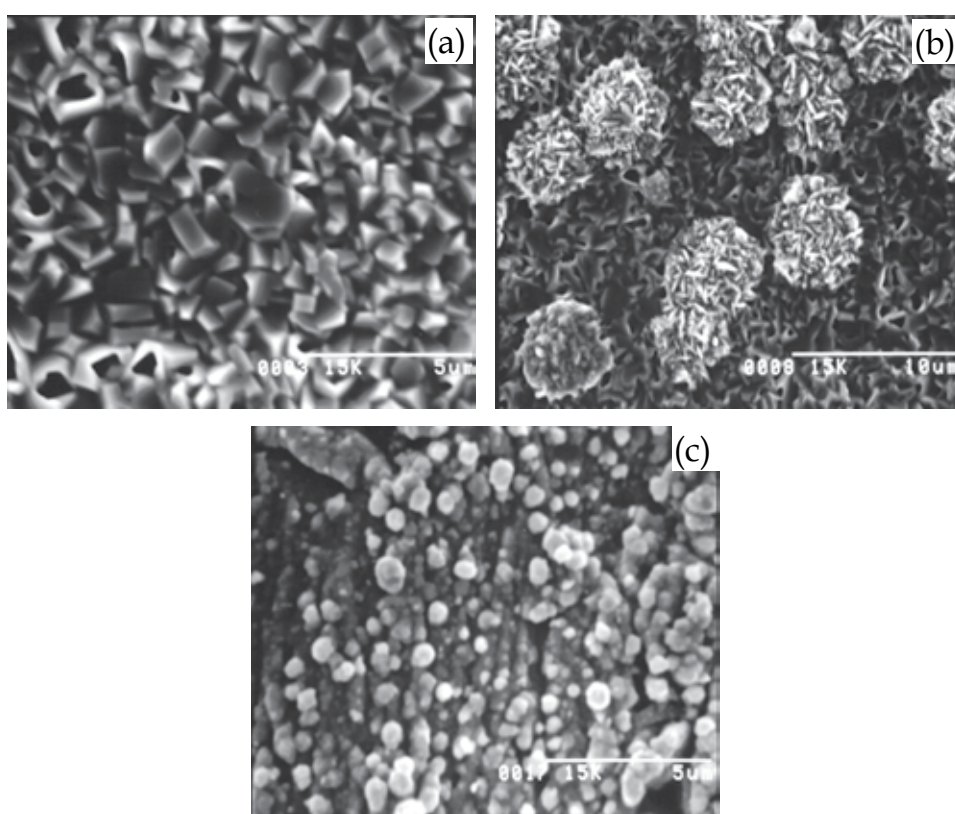
Fig. 4. Scanning electron micrographs of thin films electrodeposited at (a) -200 mV Vs SCE, (b) -400 mV Vs SCE and (c) -800 mV Vs SCE

Cu_2O thin films produce negative photovoltages in a photelectrochemical cell (PEC) containing 0.1 M sodium acetate under the white light illumination of 90 W/m². Active area of the film in a PEC was ~1 mm². The magnitudes of the photovoltage and the photocurrent of Cu_2O films deposited at –100 mV to –500 mV Vs SCE were 125 mV and 5 μA, 168 mV and 6.5 μA, 172 mV and 8 μA, 210 mV and 15 μA and 68 mV and 1 μA respectively. Also Cu_2O

film deposited at –600 mV Vs SCE shows the photoactivity but magnitudes of the photovoltage and photocurrent were very small. The best photoresponse we have obtained for the Cu_2O thin film deposited at –400 mV Vs SCE. This may be due to the better charge transfer process between Cu_2O and electrolyte due to the randomly distributed Cu spheres on top of Cu_2O thin films as shown in Fig. 4.

The optical absorption measurements of the Cu_2O thin films on indium doped tin oxide (ITO) substrate deposited at -100 mV to -600 mV Vs SCE indicate that the electrodeposited Cu_2O has a direct band gap of 2.0 eV, and the band gap of the material is independent of the deposition potential.

Photoactivity of the films was further studied by the dark and light current-voltage measurements. Fig. 5 shows the dark and light current-voltage characteristics in a PEC of the films deposited at (a) –200 mV and (b) –400 mV Vs SCE. Current-voltage measurements were obtained in three electrode electrochemical cell. The change of the sign of the photocurrent with the applied voltage shows the evidence for the existence of two junctions within the Ti/Cu_2O/electrolyte system. Particularly with the positive applied bias voltage, the Cu_2O/electrolyte junction become dominant and thereby the n-type photosignal is produced, when negative bias voltage is applied the Ti/Cu_2O junction become dominant and therefore a p-type signal is produced. Similar results have been reported earlier on the ITO/Cu_2O/electrolyte system (Siripala et al., 1996) and ITO/Cu_2O/Cu_xS system (Wijesundera et al., 2000). It has been reported earlier that both n- and p-type photosignals can be obtained in the currant–voltage scans due to the existence of Ti/Cu_2O and Cu_2O/electrolyte Schottky type junctions. The enhancement of n-type signal could be due to the enhancement of Cu_2O/electrolyte junction as compared with the Ti/Cu_2O junction.
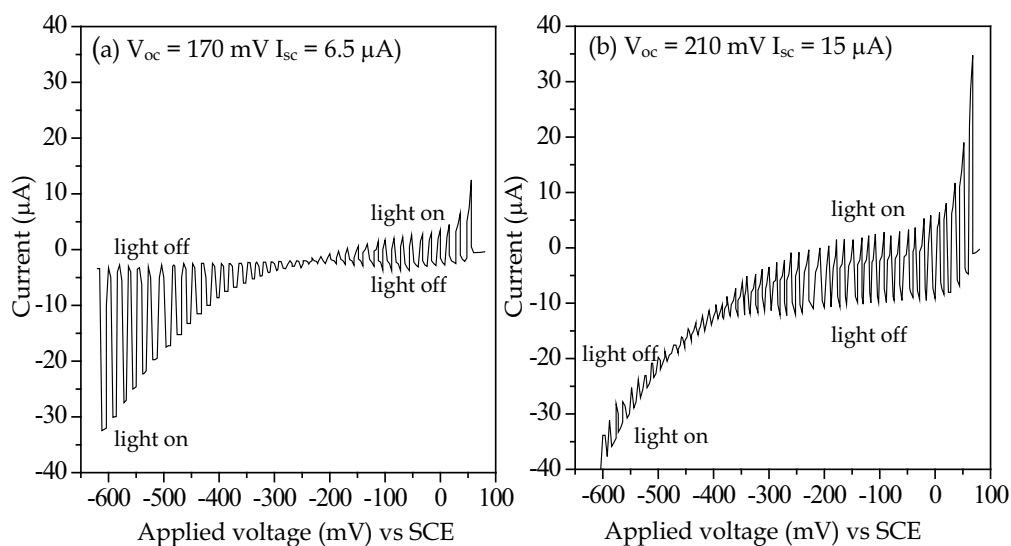
Fig. 5. Dark and light current-voltage characteristics for the films deposited at (a) -200 mV and (b) -400 mV Vs SCE in a PEC containing 0.1 M sodium acetate under the white light illumination of 90 W/m² (effective area of the film is ~1 mm²).

Single phase polycrystalline n-type Cu_2O thin films can be potentiostatically electrodeposited on conducting substrates selecting proper deposition parameters and these

films are uniform and well adhered to substrate. Garutara *et al.* (Garuthara & Siripala, 2006) carried out the photoluminescence (PL) characterisation for the electrodeposited n-type polycrystalline Cu_2O. They showed the existence of the donor energy level of 0.38 eV below the bottom of the conduction band due to the oxygen vacancies and confirmed that the n-type conductivity is due to the oxygen vacancies created in the lattice. Previously reported electrodeposited Cu_2O in a various deposition bath, except slightly acidic acetate bath, attribute p-type conductivity due to the Cu vacancies created in the lattice as thermally grown films.

3. Growth and characterisation of CuO thin films

It is expected that Cu_2O thin films can be oxidized by the annealing in air and thus converted into CuO. Therefore, annealing effects of the electrodeposited Cu_2O thin films in air were investigated in order to obtain a single phase CuO thin films on Ti substrate. Cu_2O thin films on Ti substrates were prepared under the potentiostatic condition of -200 mV Vs SCE for 60 min. in the three electrode electrochemical cell containing 0.1 M sodium acetate and 0.01 M cupric acetate aqueous solution. Temperature of the bath was maintained to 55 ˚C and the electrolyte was continuously stirred using a magnetic stirrer. All the thin films are uniform and having a thickness of about 1 μm which was calculated by monitoring the total charge passed during the film deposition through the working electrode (WE).

The bulk structure of the films, which were annealed at different temparatures and durations, can be determined by XRD measurements and Fig. 6 shows the XRD spectra of the films annealed at 150 to 500 ˚C in air, in addition to the as grown Cu_2O. Results show that Cu_2O structure remains stable even though films are annealed at 300 ˚C, as reported by Siripala *et al.* (1996). Formation of CuO structure can be observed when films are aneealed at
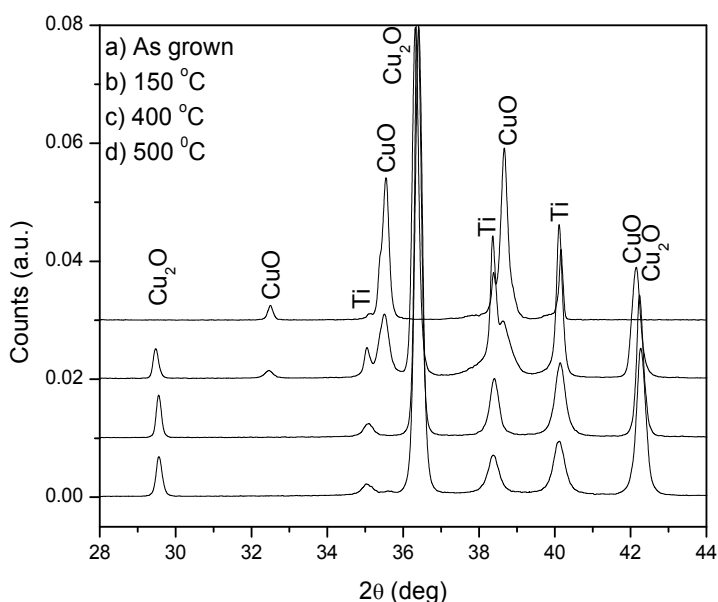
Fig. 6. X-ray diffraction patterns of electrodeposited Cu_2O thin films a) as grown and annealed at b) 150 ºC, c) 400 ºC and d) 500 ºC

400 ᵒC for 15 min. Fig. 6 shows that the intensities of the peaks correspondent to the CuO structure increases while intensities of the peaks correspondent to the Cu_2O structure decreases with the increasing of annealing temperature and duration. The reflections from the Cu_2O structure disappear when the film is annealed at 500 ˚C for 30 min. in air. It is reveled that the single phase CuO thin films on Ti substrate can be prepared by annealing Cu_2O in air.

The surface morphology of the annealing Cu_2O thin films is studied with SEMs. Fig. 7 shows SEMs of (a) as grown, and annealed in air at (b) 175 ˚C, (c) 400 ˚C and (d) 500 ˚C. Results reveal that, by increasing the annealing temperature, the size of the cubic shape polycrystalline grain gradually increase up to 200 ˚C, change to the different shape at 400 ᵒC and converted to the monoclinic like shape polycrystalline grain at 500 ᵒC. Cu_2O thin films have the cubic-like polycrystalline grains. SEMs clearly show that structural phase transition take place from Cu_2O, Cu_2O-CuO, CuO as reveal by the XRD patterns. CuO crystallites are in the order of 250 nm.
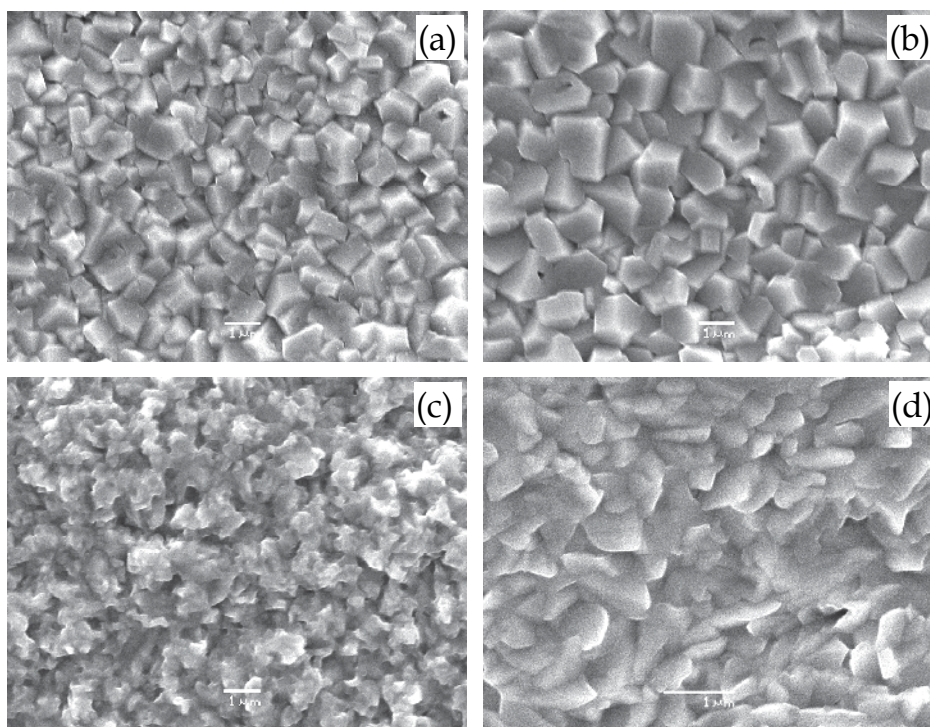
Fig. 7. Scanning electron micrographs of the electrodeposited semiconductor Cu_2O thin films a) as grown and annealed in air at (b) 175 ˚C, (c) 400 ˚C and (d) 500 ˚C

Photosensitivity (V_{oc} and I_{sc}) of the annealed electrodeposited Cu_2O thin films in a two electrode PEC cell containing 0.1 M sodium acetate aqueous solution, under white light illumination of 90 W/m², shows that initial n-type photoconductivity changes to the p-type after annealing 300 ᵒC. Type of the photoconductivity of the Cu_2O thin films can be converted from n- to p-type with annealing because of Cu_2O structure remain same even if films annealed at 300 ᵒC as revealed by XRD patterns.
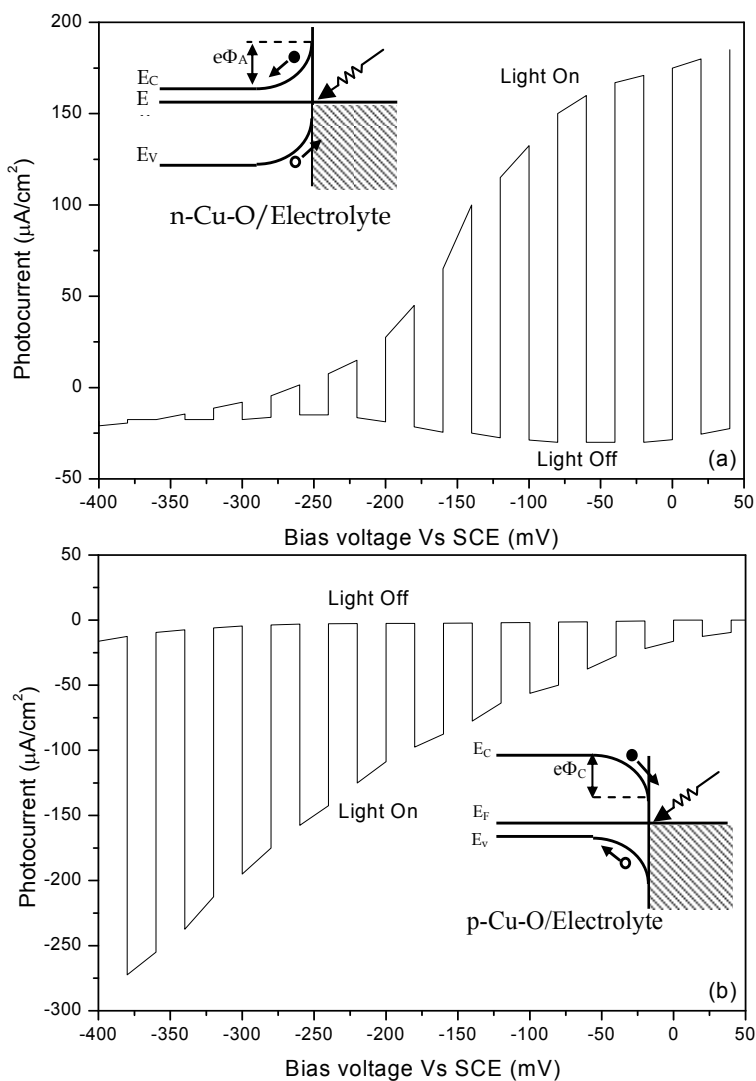
Fig. 8. Dark and light current voltage characteristics of electrodeposited Cu_2O thin film electrodes annealed at (a) 250 ˚C and (b) 300 ˚C. Energy level diagrams for n-type and p-type Cu_2O films in the electrolyte are shown in the insets, where the electron, hole, anodic and cathodic potential are denoted by solid and open circles, $e\Phi_A$ and $e\Phi_C$ respectively.

The photoactivity of the thin films has been further studied by the dark and light current voltage characteristics in a three electrode electrochemical cell. The counter and the reference electrodes are Pt plate and SCE, respectively. The bias voltage has been applied to the working electrode (Ti/Cu_2O) with respect to the SCE. Fig. 8 shows the dark and light

current-voltage characteristics of the thin films annealed at (a) 250 ˚C and (b) 300 ˚C. The similar behaviour is observed for the thin films annealed at less than 250 ˚C and annealed at grater than 300 ˚C, respectively, and is reproducible for each film. In Fig. 8(a), the anodic photocurrent increases with increasing the anodic potential. This suggests that the n-type photoconductivity is due to an anodic potential behaviour, and is reproducibly observed for the thin films annealed at < 250 ˚C. This suggests that the n-type photoconductivity is due to the anodic potential barrier formed at the semiconductor/electrolyte interface, as the inset of Fig. 8(a). However, the photocurrent-potential behaviour is completely changed for the film annealed at ≥ 300 ˚C. In Fig. 8(b), the cathodic photocurrent results from the cathodic potential barrier formed at the interface, as shown in the inset. This cathodic photoresponse assures that the electrical conductivity of the electrodeposited Cu₂O films can be changed from the n-type to p-type property by annealing in air. Fig. 9 shows the dark and light current-voltage characteristics of the CuO thin film in a PEC cell containing 0.1 M sodium acetate aqueous solution. The cathodic photocurrent is produced in the range from the anodic to cathodic bias potentials, and the cathodic photocurrent increases with increasing the cathodic potential. This suggests that the p-type photoconductivity is due to the cathodic potential barrier forms at the semiconductor/electrolyte interface. It reveals that the electrodeposited CuO thin films are p-type semiconductors.

Structural phase transition from Cu₂O to CuO with annealing and the quality of thin films can be further investigated using Extended X-ray Absorption Fine Structure (EXAFS) which gives local structure around Cu ions. Fig. 10 shows the X-ray absorption spectra (XAS) in the region of 8800 to 9430 eV near the Cu-K edge for the thin films, annealed at 150, 400, and 500 ˚C by using the florescence detection (FD) method. XAS suggest that the local structures around Cu ions in the annealed Cu₂O thin films are remain same when films annealed at less than 300 ˚C and significantly different when films annealed at grater than 300 ˚C.

Refinements of a Fourier transformation spectrum |F(R)| obtained from the oscillating EXAFS spectra can be used to study the quality of Cu₂O and CuO thin films. Fig. 11, solid circles show the observed |F(R)| of the thin film annealed at 150 ˚C, where the abscissa is a radial distance (R(Å)) from a X-ray absorbing Cu ion to its surrounding cations and anions. Fig. 11, a solid line shows a theoretical |F(R)|. The refinement produces a good fit between the observed and theoretical |F(R)| indicating the local structure around Cu ions of the film is verymuch similar to the ideal Cu₂O structure. Fig. 12 is similar refinement for CuO thin film. These results convince that the thin films are high quality single phase Cu₂O and CuO structures (free of amorphous phases and impurities). Detail investigation has been reported (Wijesundera et al., 2007).

It is characterised that single phase Cu₂O thin films are converted to two phase Cu₂O and CuO composit films with increasing the annealing temperature. Single phase CuO thin films can be obtained by annealing at 500 ˚C for 30 min in air. Extended X-ray absorption fine structure (EXAFS) near the Cu K edge of the Cu₂O thin films (annealed at 150 ˚C for 15 min.) and CuO thin films (annealed at 500 ˚C for 30 min.) are confirmed that the films are high quality single phase Cu₂O and CuO (free of amophous phases) respectively. Conductivity type of the films strongly depends on the annealing treatment. n-type conductivity of the Cu₂O thin films are changed to p-type when the films are annealed at 300 ˚C. CuO thin films are photoactive and p-type in a PEC containing 0.1 M sodium acetate.
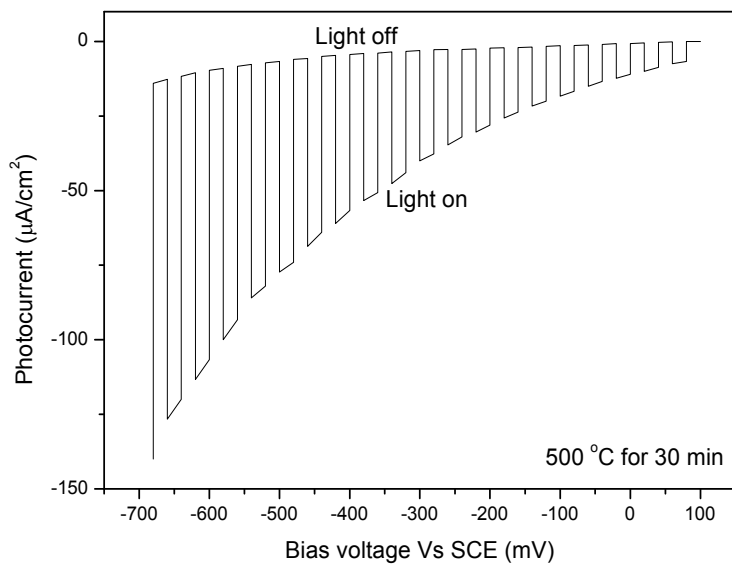
Fig. 9. Dark and light current voltage characterisation of CuO thin film in a PEC cell containing 0.1 M sodium acetate aqueous solution.
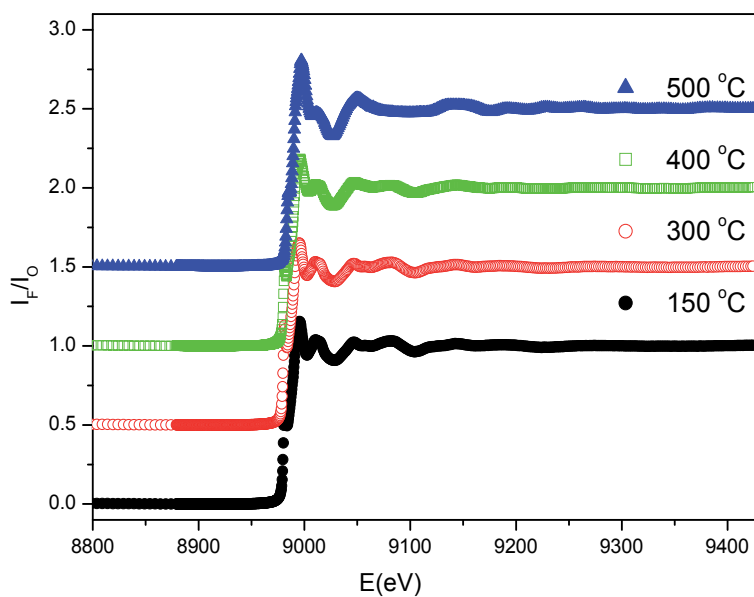
Fig. 10. X–ray absorption spectra of annealed Cu_2O thin at 150, 300, 400 and 500°C in air
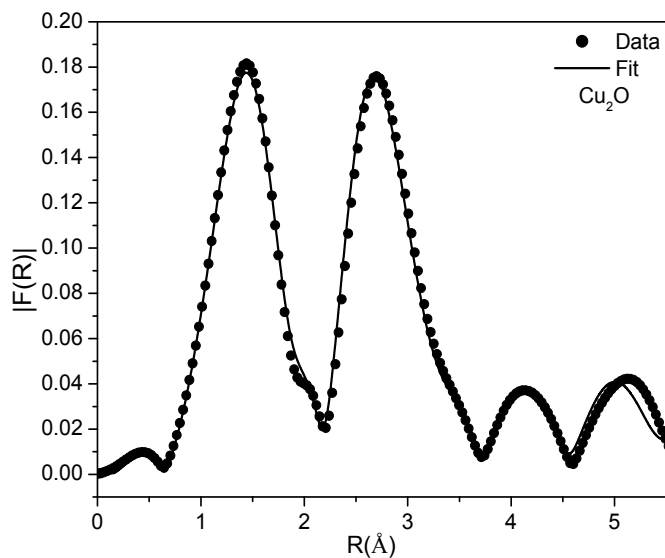
Fig. 11. Theoretical |F(R)| of the EXAFS spectrum at Cu K-edge obtained by the least squares refinement compared to the observed |F(R)| for the Cu₂O thin film annealed at 150˚C
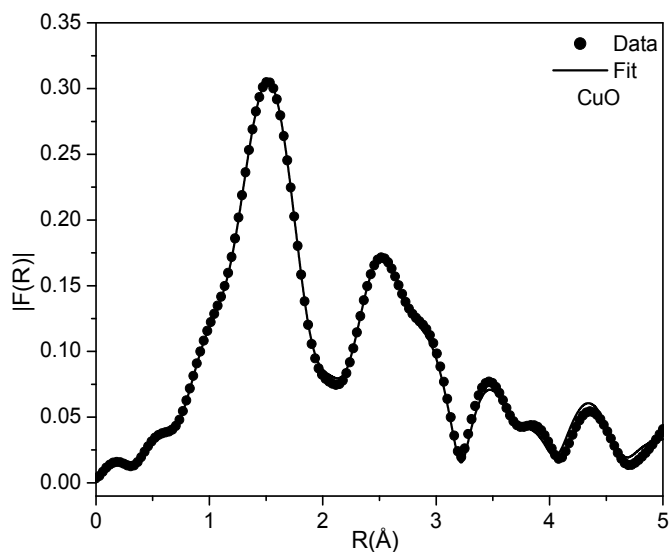
Fig. 12. Theoretical |F(R)| of the EXAFS spectrum at Cu K-edge obtained by the least squares refinement compared to the observed |F(R)| for the Cu₂O thin film annealed at 500˚C

4. Fabrication and characterisation of CuO/Cu$_2$O heterojunction

In order to fabricate CuO/Cu$_2$O thin film hetorojunction, thin films of n-type Cu$_2$O are potentiostatically electrodeposited on a Ti substrate in an acetate bath and are annealed at 500 °C for 30 min. in air for the growth of p-type CuO thin films. Thin films of Cu$_2$O are potentiostatically electrodeposited on Ti/CuO electrodes at different deposition potentials Vs SCE while maintaining the same electrolytic conditions, which used to deposit Cu$_2$O on the Ti substrate. Deposition period is varied form 240 min to 120 min in order to obtain sufficient thickness of the films. Film thickness was calculated by monitoring the total charge passed during the film deposition and it was ~1 μm.

Bulk structures of the electrodeposited films on Ti/CuO were studied by the XRD patterns. Fig. 13 shows the XRD patterns of the films deposited on Ti/CuO electrodes at the deposition potentials of -250, -400, -550 and -700 mV Vs SCE. XRD patterns evidence the formation of Cu$_2$O for all deposition potentials on Ti/CuO electrodes while Cu deposition starts in addition to the Cu$_2$O when the film deposited at -700 mV Vs SCE. Single phase Cu$_2$O are possible at the deposition potentials less than -700 mV Vs SCE. XRD patterns further show that peak intensities corresponding atomic reflection of Cu$_2$O increase with deposition potential. It indicates that amount of Cu$_2$O deposit is increased by increasing deposition potential. This is further studied by using SEM.
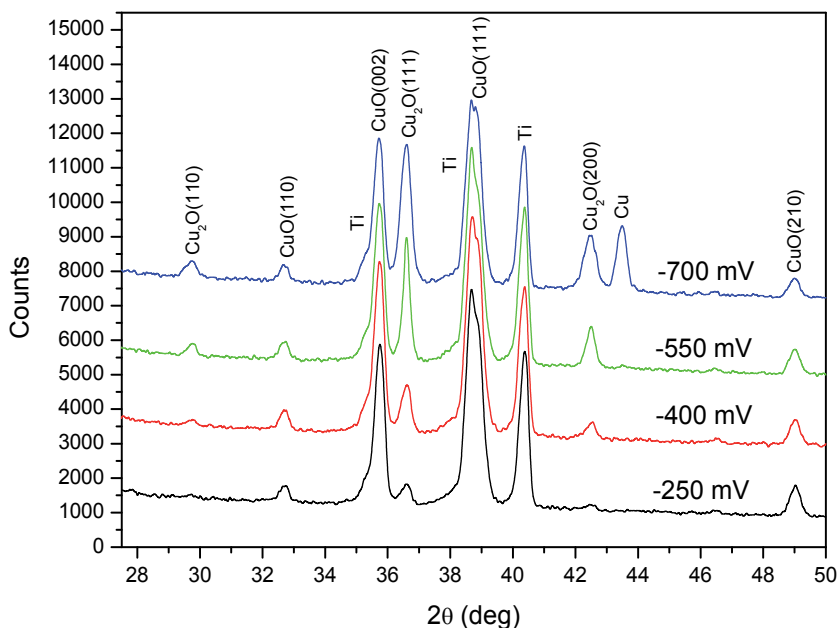
Fig. 13. XRD pattern of thin films electrodeposited on Ti/CuO electrode at the potentials -250, -400, -550 and -700 mV Vs SCE

The surface morphology of the films prepared on the Ti/CuO electrode at the different deposition potentials was studied using the SEMs in order to identify the Cu$_2$O thin film deposition conditions on Ti/CuO electrode. Figs. 14(a) to (c) show the SEMs of Cu$_2$O films deposited on the Ti/CuO at -250 to -550 mV Vs SCE. Fig. 14(a) shows the cubic shape Cu$_2$O

grains on the CuO film and Figs. 14(a) to (c) show that the amount of Cu_2O increases with increasing the deposition potential. The SEMs reveal that the well covered Cu_2O layer can be deposited on Ti/CuO electrode under the potentiostatical condition of -550 mV Vs SCE and above. Grain size of the Cu_2O deposited on Ti substrate is in the range of ~ 1-2 μm as shown in Fig. 14(a) while it is lower to 1 μm when Cu_2O deposited on CuO at the deposition potential of -550 mV Vs SCE. The SEM with low magnification of Cu_2O deposited at -700 mV Vs SCE clearly shows the existence of Cu on the surface of Cu_2O as shown in the XRD pattern of the film deposited at -700 mV Vs SCE.
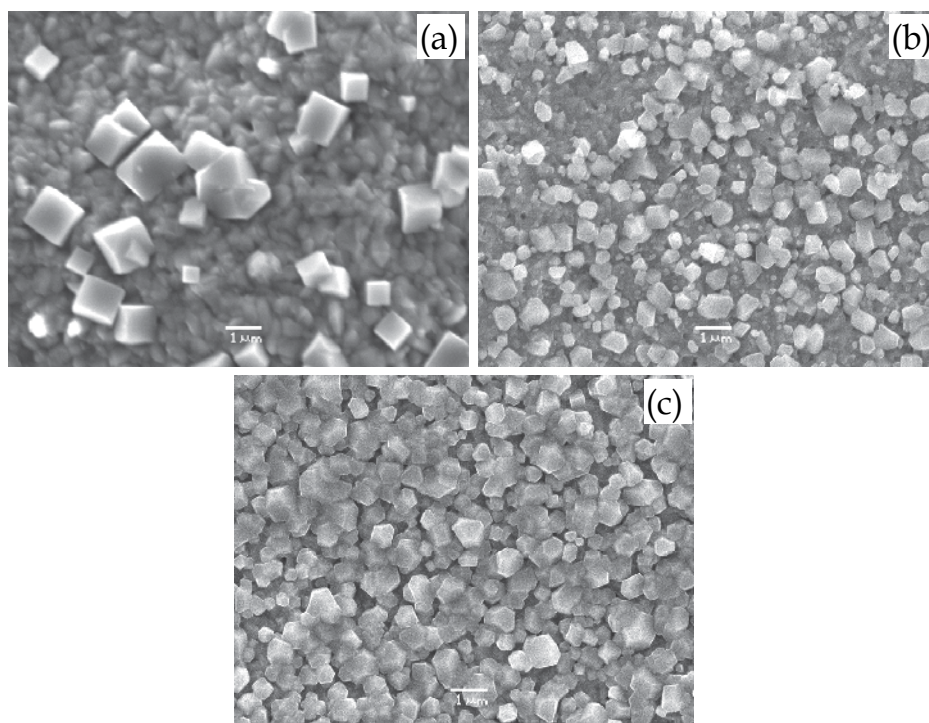
Fig. 14. Scanning electron micrograph of Cu_2O thin films electrodeposited on Ti/CuO electrode at (a) -250 mV, (b) -400 mV and (c) -550 mV Vs SCE

XRD and SEM reveal that well-covered single phase polycrystalline Cu_2O thin film on the Ti/CuO electrode can be possible at the deposition potential of −550 mV Vs SCE in an acetate bath. Structural matching of two semiconductors is very essential for fabricating a heterojunction. In general, the cubic-like Cu_2O grains and the monoclinic-like CuO grains are not match with each other to make the CuO/Cu_2O heterojunction. However, the electrodeposition technique produces the good matching of the Cu_2O grains to the monoclinic-like CuO grains. The shape of the grains can be easily changed when the electrodeposition technique is used to grow a semiconductor. The electrodeposition is a very good tool to fabricate the heterojunctions as it does not depend on the grain shape of the material. Further, the SEMs of the Cu_2O/CuO heterojunction suggested that the Cu_2O polycrystalline grains are grown from the surfaces of the CuO polycrystalline grains and make the good contacts between two thin film layers. For the completion of the device, very

thin (few angstroms) Au grid consists of 1×8 mm² rectangular areas are deposited on Cu_2O using a vacuum sputtering technique. The electrical contacts to the Cu_2O surface (front contacts) is made using mechanically pressed transparent ITO plate to the Au grid, where the Ti substrate serves as back electrical contact to the CuO surface. The Ti/CuO/Cu_2O/Au heterojunction gave the open circuit voltage (V_{oc}) of 210 mV, short circuit current (J_{sc}) of 310 μA cm², fill factor (FF) of 0.26 and efficiency (η) of 0.02% under the white light illumination of 90 mWcm⁻². At the initial stage of fabrication the junction, the shape of the I–V characteristic as shown in Fig. 15 and values of V_{oc} and J_{sc} are encouraging despite the low photoactive performance of the heterojunction.
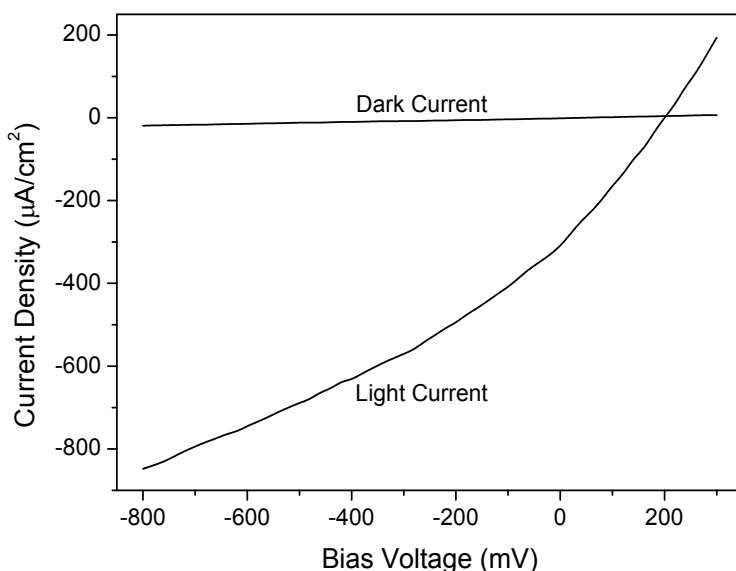
Fig. 15. Dark and light current-voltage characteristics of Ti/CuO/Cu_2O/Au heterojunction under the white light illumination of 90 mW/cm²

For the better performance, very thin Cu_2O films should be used due to the high resistance of electrodeposited Cu_2O and should be find out better ohmic contact to the Cu_2O. Best omic contact to the n-type Cu_2O may be Al but not the Au. Au is very good omic contact to p-type Cu_2O. n-type electrodeposted Cu_2O has high resistivity is due to low doping density. Growth of the n-type Cu_2O with suitable dopent hasn't been achieved in the litterateur and it will be very important in developing Cu_2O based solar cells.

CuO/Cu_2O heterojunction was further investigated by means of X-ray diffractions and X-ray absorption spectra (XAS) at the Cu-K edge with grazing angle measurements. Layer by layer structural information of the CuO/Cu_2O heterojunction can be studied with grazing angle measurements. Fig. 16 shows the grazing angle (φ) dependency of the X-ray diffraction patterns of the CuO/Cu_2O heterojunction. The Ti peak of highest intensity at $2\theta = 40 \cdot 23$ degree is indexed by (0,1,1) and (1,1,1) reflections of hexagonal structure and are not observed below φ ~ 2·0 degree. On the other hand, the reflections of Cu_2O and CuO structures are observed in all the grazing angles, though the reflections of Cu_2O structure shows the different grazing angle dependence to those of the CuO ones. Fig. 17 shows grazing angle dependency of (1,1,1) reflection of Cu_2O, (1,1,-1) reflection of CuO, (1,1,1) reflection of Ti, and intensity ratio of

$Cu_2O(1,1,1)$ and $CuO(1,1,-1)$ reflections. The results suggest that Cu_2O grain layer can only be observed below $\varphi = 0.1$ degree. With increasing the grazing angle, CuO grain layer can be observed gradually, as Ti-reflections. The bulk structural information of Cu_2O layer can be obtain for the grazing angles around 2.5 degree since it produces highest intensity of (1,1,1) reflection of Cu_2O. It reveals that it is possible to obtain optimum structural information within the Cu_2O/CuO junction region in addition to the Cu_2O, CuO, and Ti for the grazing angles slightly grater than 2.5 degree. Further it is found that the intensity ratio of the (1,1,1) reflection and (1,1,-1) reflection is approximately constant above $\varphi = 5.0$ degree, in contrast to the intensity of the Ti-reflection. It shows that the bulk structural information of bi-layer (Cu_2O and CuO) can be studied at the grazing angle 5 degree or greater
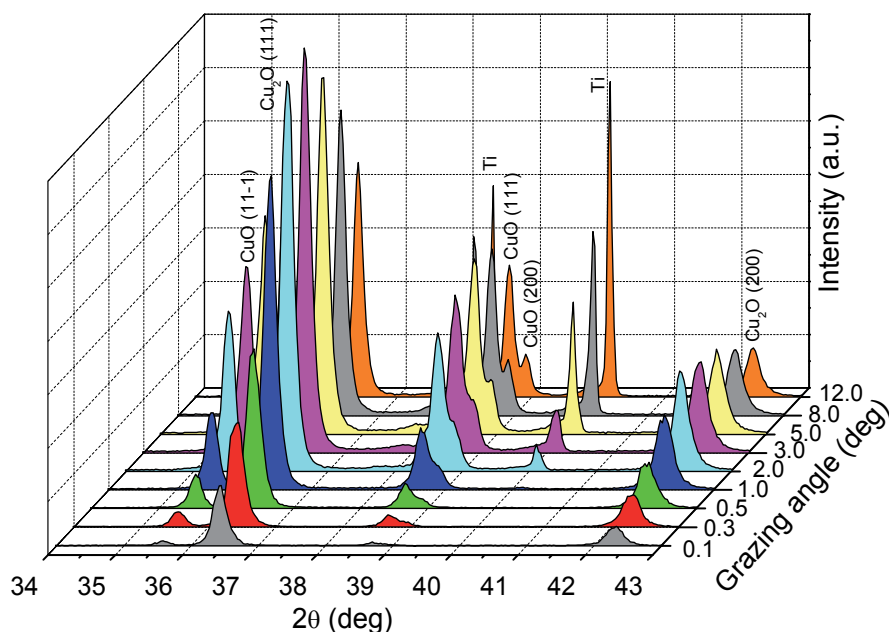
Fig. 16. Grazing angle dependency of the X-ray diffraction patterns for the electrodeposited Ti/CuO/Cu₂O heterojunction

The structural deformation localized around Cu ions of the CuO/Cu₂O heterojunction can be investigated from EXAFS. Fig. 18 shows the expanded partial XAS at Cu-K edge of Ti/CuO/Cu₂O heterojunction at $\varphi = 0.3$ to 10.0 deg. The electrodeposited CuO/Cu₂O thin film heterojunction include Cu ions sited at different structures of Cu₂O and CuO. The spectra result from a convoluted XAS induced by interference between the X-ray photoelectron waves emitted by X-ray absorbing Cu ions and the backscattering waves of its surrounding ions for both structures. The grazing angle dependency of the XAS suggests that the incident X-ray beam penetrate the thin films of Cu₂O and CuO grains by the different path distance. It can be considered that the XAS measurements obtained at low grazing angles (0.3 and 0.5 deg) should be mainly the XAS of Cu₂O thin film, which is the front layer of the heterojunction. Therefore, the XAS at $\varphi = 0.5$ and 3.0 deg are compared with the observed XAS of the electrodeposited thin films of Cu₂O and CuO. Fig. 19 shows the comparsion of the expanded partial XAS at grazing angles of 0.5 and 3.0 deg and of the
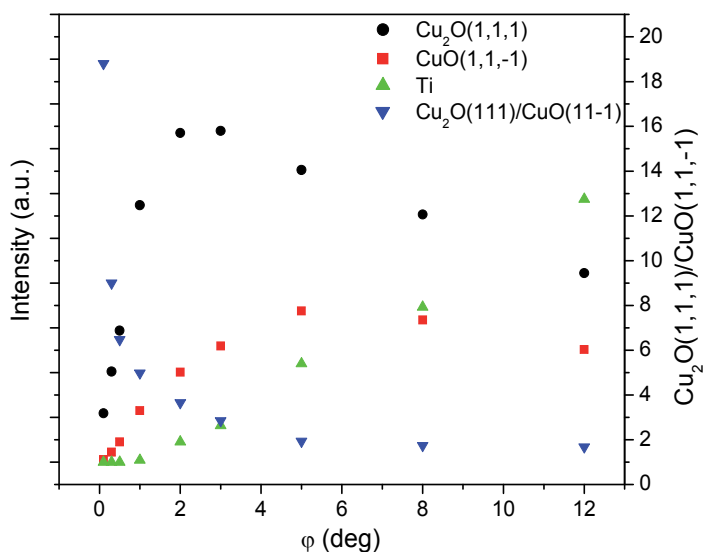
Fig. 17. Grazing angle dependency of the (1,1,1) reflection of the Cu_2O, (1,1,-1) reflection of the CuO structure, the (1,1,1) reflection of Ti and intensity ratio of Cu_2O (1,1,1) and CuO (1,1,-1) reflections

electrodeposited Cu_2O and CuO thin films, in addition to the calculated one of (0·5Cu_2O + 0·5CuO). However, XAS (local structure around Cu ions) at low grazing angles are not similar with Cu_2O. It shows that the XAS obtained at even low grazing angles are the convoluted spectra induced by the Cu_2O and CuO structures. The convolution effect of the XAS can be studied by fitting the observed XAS at φ = 0.5 deg from a simple mathematical convolution of Cu_2O-XAS and CuO-XAS. Fig. 19 shows that the observed XAS at φ = 0.5 deg is very similar to the calculated one of 0.5(Cu_2O-XAS) + 0.5(CuO-XAS). However, XAS at low grazing angles can be analyzed by a simple mathematical convolution of Cu_2O and CuO structures but not for the grazing angles higher than 0.5 deg. This reveals that the complex XAS results from the convoluted spectra induced from unknown structure in addition to the Cu_2O and CuO structures. The XAS modulation due to the unknown structure depends on the grazing angles, and the maximum XAS modulation appears at the grazing angle of 3.0 deg. This suggests that the junction region has very complex structure.

XAS of CuO/Cu_2O hetrojunction with different grazing angles can be further compared by studying corresponding Fourier transformations of the oscillating EXAFS spectra. Fig. 20 shows the observed $|F(R)|$ for the bi-layer thin film of Ti/CuO/Cu_2O heterojunction at φ = 0·5 and 3·0 degrees and for the electrodeposited Cu_2O and CuO thin films with calculated one of (0·5Cu_2O + 0·5CuO). It is further confirmed that the $|F(R)|$ obtained at φ = 0·5 and 3·0 degrees are not similar with that of Cu_2O structure and CuO one, but more complex. Comparison between the $|F(R)|$ of the bi-layer thin film obtained at φ = 0·5 degree and the calculated one of (0·5Cu_2O + 0·5CuO) suggests that the $|F(R)|$ of the bi-layer thin film is also convoluted by those of the Cu_2O and CuO structures. As in Fig. 20 peak amplitudes are very small for the $|F(R)|$ at φ = 3.0 deg compared to the others. It implies that structure in the junction region is diluted one (the surrounding ions around the Cu absorbing ion do not well arranged). Results reveal that the formation of amorphous structure in the interface of CuO/Cu_2O heterojunction. It can be expected that amorphous
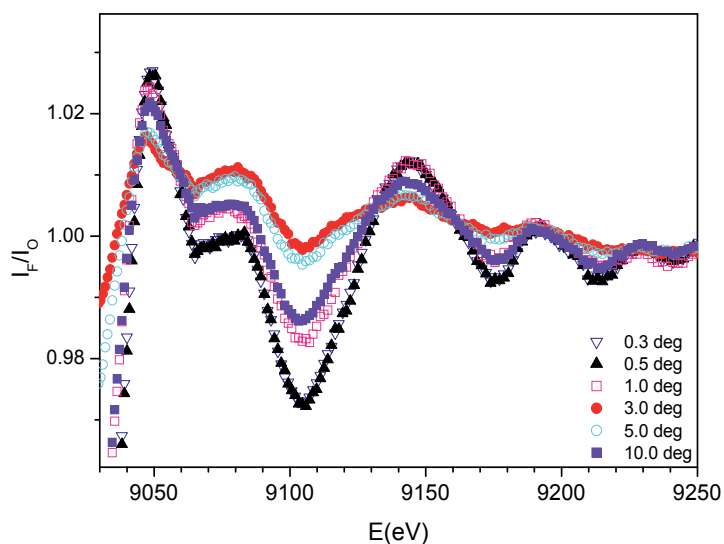
Fig. 18. Oscillating amplitudes I$_F$/I$_o$ of the X–ray absorption spectra of the Ti/CuO/Cu$_2$O heterojunction at φ = 0·3 to 10·0 degrees
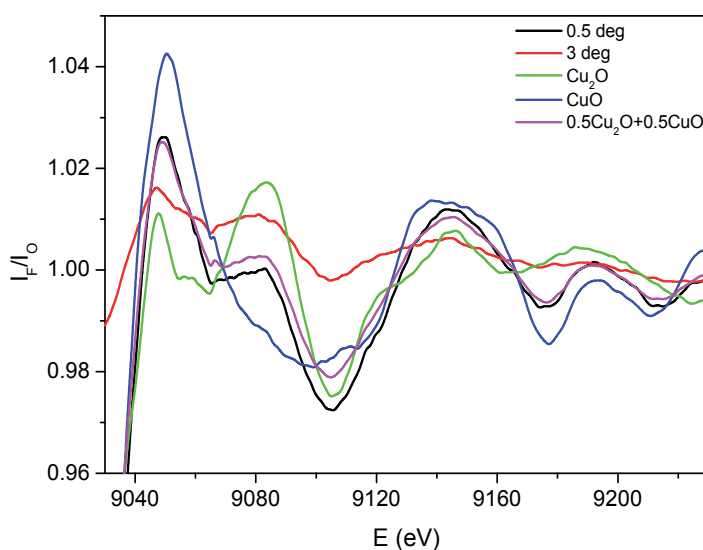
Fig. 19. Oscillating amplitudes I$_F$/I$_o$ of the X–ray absorption spectra of the Ti/CuO/Cu$_2$O heterojunction at grazing angles of 0.5 and 3.0 degrees and of the electrodeposited Cu$_2$O and CuO thin films, in addition to the calculated one of (0·5Cu$_2$O + 0·5CuO)

structure formed in the middle of the CuO/Cu$_2$O heterojunction attributes better lattice matching between CuO and Cu$_2$O interface. Further, it can be considered that formation of the smooth energy band lineup at the interface of CuO/Cu$_2$O heterojunction without spikes at the conduction and valance bands (ΔE$_c$ and ΔE$_v$). Band lineup between two semiconductors is a crucial parameter leading to better photoactive properties.
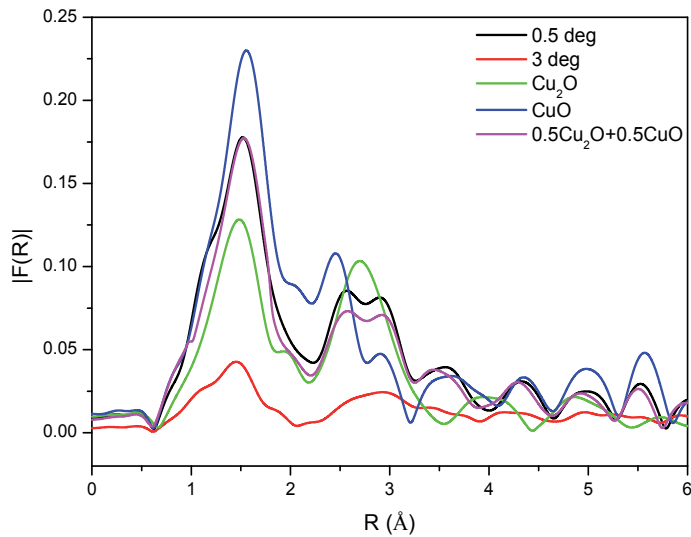
Fig. 20. Amplitudes |F(R)| obtained from the Fourier transformation of the EXAFS spectra of the Ti/CuO/Cu$_2$O heterojunction at φ = 0·5 and 3·0 degrees and of the electrodeposited Cu$_2$O and CuO thin films and the calculated one of (0·5Cu$_2$O + 0·5CuO)

5. Conclusion

Single phase polycrystalline Cu$_2$O thin films on Ti substrate can be electrodeposited using an acetate bath in a potential range of 0 to -300 mV Vs SCE. Thin films are well adherent to the Ti substrate and uniform having grain size of ~1-2 μm. Cu$_2$O deposited in an acetate bath at the pH of 6.6 produces n-type photoconductivity in a PV applications. The n-type photoconductivity of the as-grown Cu$_2$O thin film can be converted to p-type by annealing the films at 300 ℃ in air. Therefore, it is reasonable to believe that the origin of the n-type Cu$_2$O is the oxygen ion vacancies created in the crystal lattice, and the conductivity-type conversion is due to the increment of the oxygen content in the lattice with annealing in air. Single phase polycrystalline CuO thin films can be prepared by annealing the electrodeposited Cu$_2$O at 500 ℃ for 30 min in air. Films produce p-type photoresponse in a PEC. Well covered n-type Cu$_2$O thin film can be electrodeposied on Ti/CuO electrode at -550 mV Vs the SCE in an acetate bath. Films consist of microcrystallites of about 1 μm and are well adherent to the CuO. By depositing a suitable mettle grid on the Cu$_2$O thin film, p-CuO/n-Cu$_2$O heterojunction solar cell can be fabricated. The Ti/CuO/Cu$_2$O/Au heterojunction solar cell results in V$_{oc}$ of 210 mV and J$_{sc}$ of 310 μA. This initial stage performance can be enhanced by depositing very thin Cu$_2$O films leading to minimize the resistance of the Cu$_2$O and choosing better ohmic contact to the Cu$_2$O. Best ohmic contact to the n-type Cu$_2$O may be Al but not the Au. X-ray diffractions and the X-ray absorption spectra, using the synchrotron radiation, reveal that Cu$_2$O and CuO are high quality semiconducting thin films (free of amorphous phases) but amorphous structure is formed between CuO and Cu$_2$O while Cu$_2$O deposition on CuO.

6. Acknowledgment

7. References

Akimoto, K., Ishizuka, S., Yanagita, M., Nawa, Y., Goutam K. P. & Sakurai, T. (2006). Thin film deposition of Cu₂O and application for solar cells. *Sol. Energy*, Vol. 80, 715-722

Anandan, S., Wen, X. & Yang, S. (2005). Room temperature growth of CuO nanorod arrays on copper and their application as a cathode in dye-sensitized solar cells. *Mater. Chem. Phys.*, Vol. 93, 35-40

Aveline, A. & Bonilla, I. R. (1981). Spectrally selective surfaces of cuprous oxide (Cu₂O). *Sol. Energy Mater.*, Vol. 5, 2, 211-220

Fortin, E. & Masson, D. (1981). Photovoltaci effects in Cu₂O-Cu cells growing by anodic oxidation. *Solid-St. Electron.*, Vol. 25, 4, 281-283

Garuthara, R. & Siripala, W. (2006). Photoluminescence characterization of polycrystalline n-type Cu₂O films. *J. Luminescence*, Vol. 121, 173-178

Ghijsen, J., Tjeng, L.H., Elp, J. V., H. Eskes, Westerink, J., & Sawatzky, G.A. (1988). Electronic structure of Cu₂O and CuO. *Phys. Rev.*, Vol. 38, 11322-11330

Guy, A. C. (1972). *Introduction to Material Science (International Student Edition)*, McGraw-Hill, Tokyo

Hames,Y. & San, S. E. (2004).CdO/Cu₂O solar cells by chemica deposition. *Sol. Energy*, Vol. 77, 291-294

Harukawa, N., Murakami, S., Tamon, S., Ijuin, S., Ohmori, A., Abe, K. & Shigenari, T. (2000). Temperature dependence of luminescence lifetime in Cu₂O. *J. Luminescence*, Vol. 87-89, 1231-1233

Herion, J., Niekisch E. A. & Scharl, G. (1980). Investigation of metal oxide/cuprous oxide heterojunction solar cell. *Sol. Energy Mater.*, Vol. 4, 101-112

Ivill, M., Overberg, M. E., Abernathy, C. R., Norton, D. P., Hebard, A. F., Theoropoulou, N. & Budai, J. D. (2003). Properties of Mn-doped Cu₂O semiconducting thin films grown by pulsed-laser deposition. *Solid-St. Electronics*, Vol. 47, 2215-2220

Kaufman, R. G. & Hawkins, R. T. (1984). Defect luminescence of thin films of Cu₂O on copper. *J. Electrochem. Soc.*, Vol. 131, 385-388

Mahalingam, T., Chitra, J. S. P., Chu, J. P. & Sebastian, P. J. (2004). Preparation and microstructural studies of electrodeposited Cu₂O thin films. *Mater. Lett.*, Vol. 58, 1802-1807

Mahalingam, T., Chitra, J. S. P., Rajendran, S. & Sebastian, P. J. (2002). Potentiostatic deposition and characterisation of Cu₂O thin films. *Semicond. Sci. Technol.*, Vol. 17, 565- 570

Mahalingam, T., Chitra, J. S. P., Rajendran, S., Jayachandran, M. & Chockalingam, M. J. (2000). Galvanostatic deposition and characterization of cuprous oxide thin films. *J. Crys. Growth*, Vol. 216, 304-310

Maruyama, T. (1998). Copper oxide thin films prepared by chemical vapor deposition from copper dipivaloylmethanate. *Sol. Energy Mater. Sol. Cells*, Vol. 56, 85-92

Musa, A. O., Akomolafe, T. & Carter, M. J. (1998). Production of cuprous oxide, a solar cell material, by thermal oxidation and a study of its physical and electrical properties. *Sol. Energy Mater. Sol. Cells*, Vol. 51, 305-316

Ogwa, A. A., Bouquerel, E., Ademosu, O., Moh, S., Crossan, E. & Placido, F. (2005). An investigation of the surface energy and optical transmittance of copper oxide thin films prepared by reactive magnetron sputtering. *Acta Materialia*, Vol. 53, 5151-5159

Olsen, L. C., Addis, F. W. & Miller, W. (1981-1983). Experimental and theoretical studies of Cu_2O solar cells. *Sol. Cells*, Vol. 7, 247-279

Papadimitriou, L., Economou N. A. & Trivich, D. (1981). Heterojunction solar cells on cuprous oxide. *Sol. Cells*, Vol. 3, 73-80

Paul, G. K., Nawa, Y., Sato, H., Sakurai, T. & Akimoto, K. (2006). Defects in Cu_2O studied by deep level transient spectroscopy. *Appl. Phys. Lette.*, Vol. 88, 141900

Pollack, G. P. & Trivich, D. (1975). Photoelectric properties of cuprous oxide. *J. Appl. Phys.*, Vol. 46, 163-173

Rai, B. P. (1988). Cu_2O solar cells: a review. *Sol. Cells*, Vol. 25, 265-272

Rakhshani, A.E. (1986). Preparation, charaterestics and photovoltaic proporties of cuprus oxide – a review. *Soild State Electronics*, Vol. 29, No. 1, 7-17

Rakhshani, A. E. & Varghese, J. (1988). Potentiostatatic electrodeposition of cuprous oxide. *Thin Solid Films*, Vol. 157, 87-95

Rakhshani, A. E. & Varghese, J. (1987). Galvanostatic deposition of thin films of cuprous oxide. *Sol. Energy Mater.*, Vol. 15, 237-248

Roos, A., Chibuye, T. & Karlsson, B. (1983). Proporties of oxide copper sufaces for solar cell applications II. *Sol. Energy Mater.*, Vol. 7, 453 467-480

Santra, K., Chitra, C. K., Mukherjee, M. K. & Ghosh, B. (1992). Copper oxide thin films grown by plasma evaporation method. *Thin Solid Films*, Vol. 213, 226-229

Sears, W. M., Fortin, E. & Webb, J. B. (1983). Indium tin oxide/Cu_2O photovoltaic cells. *Thin Solid Film*, Vol. 103, 303–309

Sears,W. M. & Fortin, E. (1984). Preparation and properties of Cu_2O/Cu photovoltaic cells. *Sol. Energy Mater.*, Vol. 10, 93-103

Siripala, W., Perera, L. D. R. D., De Silva, K. T. L., Jayanetti, J. K. D. S., & Dharmadasa, I. M. (1996). Study of annealing effects of cuprous oxide grown by electrodeposition technique. *Sol. Energy Mater. Sol. Cells*, Vol. 44, 251-260

Siripala, W. & Jayakody, J. R. P. (1986). Observation of n-type photoconductivity in electrodeposited copper oxide film electrodes in a photoelectrochemical cell. *Sol. Energy Mater.*, Vol. 14, 23-27

Stareck, J. E. (1937). US Patent #2,081,121

Tanaka, H., Shimakawa, T., Miyata, T., Sato H. & Minami, T. (2004). Electrical and optical properties of TCO–Cu_2O heterojunction devices. *Thin Solid Films*, Vol. 469, 80-85

Tang, Y., Chen, Z., Jia, Z., Zhang, L. & Li, J. (2005). Electrodeposition and characterization of nanocrystalline cuprous oxide thin films on TiO_2 films. *Mater. Lett.*, Vol. 59, 434-438

Tiwari, A.N., Pandya, D.K. & Chopra, K.L. (1987). Fabrication and analysis of all-sprayed $CuInS_2$/ZnO solar cells. *Solar Cells*, Vol. 22, 263-173

Wijesundera, R.P., Hidaka, M., Koga, K., Sakai, M., & Siripala,W. (2006). Growth and characterisation of potentiostatically electrodeposited Cu_2O and Cu thin films. *Thin Solid Films*, Vol. 500, 241-246

Wijesundera, R. P., Perera, L. D. R. D., Jayasuriya, K. D., Siripala, W., De Silva, K. T. L., Samantilleka A. P. & Darmadasa, I. M. (2000). Sulphidation of electrodeposited cuprous oxide thin films for photovoltaic applications. *Sol. Energy Mater. Sol. Cells,*Vol. 61, 277-286

Wijesundera, R. P. (2010). Fabrication of the CuO/Cu_2O heterojunction using an electrodeposition technique for solar cell applications. *Semicond. Sci. Technol.*, Vol. 25, 1-5

Wijesundera, R.P., Hidaka, M., Koga, K., Sakai, M., Siripala, W., Choi, J.Y. & Sung, N. E. (2007). Effects of annealing on the properties and structure of electrodeposited semiconducting Cu-O thin films, *Physica Status of Solidi (b)*, Vol. **244,** 4629-4642

TCO-Si Based Heterojunction Photovoltaic Devices

Z.Q. Ma[1] and B. He[2]

[1]SHU-Solar E PV Laboratory, Department of Physics, Shanghai University, Shanghai
[2]Department of Applied Physics, Donghua University, Shanghai
P. R. China

1. Introduction

It is a common viewpoint that the adscription of the PV research and industry in future has to be the lower cost and higher efficiency. However, those monocrystal as well as multi-crystalline silicon wafer require very expensive processing techniques to produce low defect concentrations, and they are made by complicated wet chemical treatment, high-temperature furnace steps, and time-cost metallization. Thus, a high PV module cost exists for the first-generation technology. Recently, a strong motivation in R&D roadmap of PV cells has been put forward in thin film materials and heterojunction device fields. A large variety of possible and viable methods to manufacture low-cost solar cells are being investigated. Among these strategies, transparent conductive oxides (TCOs) and polycrystalline silicon thin films are promising for application of PV and challenging to develop cheap TCOs and TCO/c-Si heterojunction cells.

Converting solar energy into electricity provides a much-needed solution to the energy crisis in the world is facing today. Solar cells (SC) fabricated on the basis of semiconductor–insulator– semiconductor (SIS) structures are very promising because it is not necessary to obtain a p–n junction and the separation of the charge carriers generated by the solar radiation is realized by the electrical field at the insulator–semiconductor interface. Such SIS structures are obtained by the deposition of thin films of TCO on the oxidized semiconductor surface. One of the main advantages of SIS based SC is the elimination of high temperature diffusion process from the technological chain, the maximum temperature at the SIS structure fabrication by PVD/CVD being not higher than 450 °C. Besides that, the superficial layer of silicon wafer, where the electrical field is localized, is not affected by the impurity diffusion. The TCO films with the band gap in the order of 2.5–4.5 eV are transparent in the whole region of solar spectrum, especially in the blue and ultraviolet regions, which increase the photo response in comparison with the traditional SC. The TCO layer assists the collection of charge carriers and at the same time is an antireflection coating. The most utilized TCO layers are SnO_2, In_2O_3 and their mixture ITO, as well as zinc oxide (ZnO). The efficiency of these kinds of devices can reach the value of more than 10% (Koida et al., 2009).

Transparent conducting oxides (TCOs), such as ZnO, Al-doped ZnO or ITO ($SnO_2:In_2O_3$), are an increasingly significant component in photovoltaic (PV) devices, where they act as electrodes, structural templates, and diffusion barriers, and their work function are

dominant to the open-circuit voltage. The desirable characteristics of TCO materials that are common to all PV technologies are similar to the requirements for TCOs for flat-panel display applications and include high optical transmission across a wide spectrum and low resistivity. Additionally, TCOs for terrestrial PV applications must be used as low-cost materials, and some may be required in the device-technology specific properties. The fundamentals of TCOs and the matrix of TCO properties and processing as they apply to current and future PV technologies were discussed.

As an example, the In_2O_3:SnO_2(ITO) transparent conducting oxides thin film was successfully used for the novel ultraviolet response enhanced PV cell with silicon-based SINP configuration. The realization of ultraviolet response enhancement in PV cells through the structure of ITO/SiO_2/np-Silicon frame (named as SINP), which was fabricated by the state of the art processing, have been elucidated in the chapter. The fabrication process consists of thermal diffusion of phosphorus element into p-type texturized crystal Si wafer, thermal deposition of an ultra-thin silicon dioxide layer (15-20Å) at low temperature, and subsequent deposition of thick In_2O_3:SnO_2 (ITO) layer by RF sputtering. The structure, morphology, optical and electric properties of the ITO film were characterized by XRD, SEM, UV-VIS spectrophotometer and Hall effects measurement, respectively.

The results showed that ITO film possesses high quality in terms of antireflection and electrode functions. The device parameters derived from current-voltage (I-V) relationship under different conditions, spectral response and responsivity of the ultraviolet photoelectric cell with SINP configuration were analyzed in detail. We found that the main feature of our PV cell is the enhanced ultraviolet response and optoelectronic conversion. The improved short-circuit current, open-circuit voltage, and filled factor indicate that the device is promising to be developed into an ultraviolet and blue enhanced photovoltaic device in the future.

On the other hand, the novel ITO/AZO/SiO_2/p-Si SIS heterojunction has been fabricated by low temperature thermally grown an ultrathin silicon dioxide and RF sputtering deposition ITO/AZO double films on p-Si texturized substrate. The crystalline structural, optical and electrical properties of the ITO/AZO antireflection films were characterized by XRD, UV-VIS spectrophotometer, four point probes, respectively. The results show that ITO/AZO films have good quality. The electrical junction properties were investigated by I-V measurement, which reveals that the heterojunction shows strong rectifying behavior under a dark condition. The ideality factor and the saturation current of this diode is 2.3 and 1.075×10^{-5}A, respectively. In addition, the values of I_F/I_R (I_F and I_R stand for forward and reverse current, respectively) at 2V is found to be as high as 16.55. It shows fairly good rectifying behavior indicating formation of a diode between AZO and p-Si. High photocurrent is obtained under a reverse bias when the crystalline quality of ITO/AZO double films is good enough to transmit the light into p-Si.

In device physics, the tunneling effect of SIS solar cell has been investigated in our current work, depending on the thickness of the ultra-thin insulator layer, which is potential for the understanding of quantum mechanics in the photovoltaic devices.

2. Review of TCO thin films

2.1 Development of TCOs
2.1.1 Feature of TCO
Most optically transparent and electrically conducting oxides (TCOs) are binary or ternary compounds, containing one or two metallic elements. Their resistivity could be as low as

10^{-5} Ω cm, and their extinction coefficient k in the visible range (VIS) could be lower than 0.0001, owing to their wide optical band gap (Eg) that could be greater than 3 eV. This remarkable combination of conductivity and transparency is usually impossible in intrinsic stoichiometric oxides; however, it is achieved by producing them with a non-stoichiometric composition or by introducing appropriate dopants. Badeker (1907) discovered that thin CdO films possess such characteristics. Later, it was recognized that thin films of ZnO, SnO_2, In_2O_3 and their alloys were also TCOs. Doping these oxides resulted in improved electrical conductivity without degrading their optical transmission. Al doped ZnO (AZO), tin doped In_2O_3, (ITO) and antimony or fluorine doped SnO_2 (ATO and FTO), are among the most utilized TCO thin films in modern technology. In particular, ITO is used extensively in acoustic wave device, electro-optic modulators, flat panel displays, organic light emitting diodes and photovoltaic devices.

The actual and potential applications of TCO thin films include: (1) transparent electrodes for flat panel displays (2) transparent electrodes for photovoltaic cells, (3) low emissivity windows, (4) window defrosters, (5) transparent thin films transistors, (6) light emitting diodes, and (7) semiconductor lasers. As the usefulness of TCO thin films depends on both their optical and electrical properties, both parameters should be considered together with environmental stability, abrasion resistance, electron work function, and compatibility with substrate and other components of a given device, as appropriate for the application. The availability of the raw materials and the economics of the deposition method are also significant factors in choosing the most appropriate TCO material. The selection decision is generally made by maximizing the functioning of the TCO thin film by considering all relevant parameters, and minimizing the expenses. TCO material selection only based on maximizing the conductivity and the transparency can be faulty.

Recently, the scarcity and high price of Indium needed for ITO materials, the most popular TCO, as spurred R&D aimed at finding a substitute. Its electrical resistivity (ρ) should be $\sim 10^{-4}$ Ω cm or less, with an absorption coefficient (α) smaller than 10^4 cm^{-1} in the near-UV and VIS range, and with an optical band gap >3eV. A 100 nm thick film TCO film with these values for and will have optical transmission (T) 90% and a sheet resistance (R_S) of < 10 Ω/□. At present, AZO and ZnO:Ga (GZO) semiconductors are promising alternatives to ITO for thin-film transparent electrode applications. The best candidates is AZO, which can have a low resistivity, e.g. on the order of 10^{-4} Ω cm, and its source materials are inexpensive and non-toxic. However, the development of large area, high rate deposition techniques is needed.

Another objective of the recent effort to develop novel TCO materials is to deposit p-type TCO films. Most of the TCO materials are n-type semiconductors, but p-type TCO materials are required for the development of solid lasers, as well as TFT or PV cells. Such p-type TCOs include: ZnO:Mg, ZnO:N, ZnO:In, NiO, NiO:Li, $CuAlO_2$, Cu_2SrO_2, and $CuGaO_2$ thin films. These materials have not yet found a place in actual applications owing to the stability.

Published reviews on TCOs reported exhaustively on the deposition and diagnostic techniques, on film characteristics, and expected applications. The present paper has three objectives: (1) to review the theoretical and experimental efforts to explore novel TCO materials intended to improve the TCO performance, (2) to explain the intrinsic physical limitations that affect the development of an alternative TCO with properties equivalent to those of ITO, and (3) to review the practical and industrial applications of existing TCO thin films.

2.1.2 Multiformity of TCOs

The first realization of a TCO material (CdO, Badeker 1907)) occurred slightly more than a century ago when a thin film of sputter deposited cadmium (Cd) metal underwent incomplete thermal oxidation upon postdeposition heating in air. Later, CdO thin films were achieved by a variety of deposition techniques such as reactive sputtering, spray pyrolysis, activated reactive evaporation, and metal organic vapor phase epitaxy (MOVPE). CdO has a face centered cubic (FCC) crystal structure with a relatively low intrinsic band gap of 2.28 eV. Note that without doping, CdO is an n-type semiconductor. The relatively narrow band gap of CdO and the toxicity of Cd make CdO less desirable and account for receiving somewhat dismal attention in its standard form. However, its low effective carrier mass allows efficiently increasing the band gap of heavily doped samples to as high as 3.35 eV (the high carrier concentration results in a partial filling of a conduction band and consequently, in a blue-shift of the UV absorption edge, known as the Burstein–Moss effect) and gives rise to mobility as high as 607 cm^2/V s in epitaxial CdO films doped with Sn. The high mobility exhibited by doped CdO films is a definite advantage in device applications. Cd-based TCOs such as CdO doped with either indium (In), tin (Sn), fluorine (F), or yttrium (Y), and its ternary compounds such as $CdSnO_3$, Cd_2SnO_4, $CdIn_2O_4$ as well as its other relevant compounds all have good electrical and optical properties. The lowest reported resistivity of Cd-based TCOs is 1.4×10^{-4} Ω cm, which is very good and competitive with other leading candidates. The typical transmittance of Cd-based TCOs in the visible range is 85%–90%. Although the Cd-based TCOs have the desired electrical and optical properties, in addition to low surface recombination velocity, which is very desirable, they face tremendous obstacles in penetrating the market except for some special applications such as CdTe/CdS thin film solar cells due to the high toxicity of Cd. It should be noted that the aforementioned solar cells are regulated and cannot be sold. To circumvent this barrier, the manufacturers lease them for solar power generation instead. Consequently, our attention in this chapter is turned away for discussing this otherwise desirable conducting oxide.

Revelations dating back to about 1960s that indium tin oxide (ITO), a compound of indium oxide (In_2O_3) and tin oxide (SnO_2), exhibits both excellent electrical and optical properties paved the way for extensive studies on this material family. In_2O_3 has a bixbyite-type cubic crystal structure, while SnO_2 has a rutile crystal structure. Both of them are weak n-type semiconductors. Their charge carrier concentration and thus, the electrical conductivity can be strongly increased by extrinsic dopants which is desirable. In_2O_3 is a semiconductor with a band gap of 2.9 eV, a figure which was originally thought to be 3.7 eV. The reported dopants for In_2O_3-based binary TCOs are Sn, Ge, Mo, Ti, Zr, Hf, Nb, Ta, W, Te, and F as well as Zn. The In_2O_3-based TCOs doped with the aforementioned impurities were found to possess very good electrical and optical properties. The smallest laboratory resistivities of Sn-doped In_2O_3 (ITO) are just below 10^{-4} Ω cm, with typical resistivities being about 1×10^{-4} Ω cm. As noted above, despite the nomenclature of Sn-doped In_2O_3 (ITO), this material is really an In_2O_3-rich compound of In_2O_3 and SnO_2. SnO_2 is a semiconductor with a band gap of 3.62 eV at 298 K and is particularly interesting because of its low electrical resistance coupled with its high transparency in the UV–visible region. SnO_2 grown by molecular beam epitaxy (MBE) was found to be unintentionally doped with an electron concentration for different samples in the range of $(0.3–3) \times 10^{17}$ cm^{-3} and a corresponding electron mobility in the range of 20–100 cm^2/V s. Fluorine (F), antimony (Sb), niobium (Nb), and tantalum (Ta) are most commonly used to achieve high n-type conductivity while maintaining high optical transparency.

Much as ITO is the most widely used In_2O_3-based binary TCO, fluorine-doped tin oxide (FTO) is the dominant in SnO_2-based binary TCOs. In comparison to ITO, FTO is less expensive and shows better thermal stability of its electrical properties as well chemical stability in dye-sensitized solar cell (DSSC). FTO is the second widely used TCO material, mainly in solar cells due to its better stability in hydrogen-containing environment and at high temperatures required for device fabrication. The typical value of FTO's average transmittance is about 80%. However, electrical conductivity of FTO is relatively low and it is more difficult to pattern via wet etching as compared to ITO. In short, more efforts are beginning to be expended for TCOs by researchers owing to their above-mentioned uses spurred by their excellent electrical and optical properties in recently popularized devices. Germanium-doped indium oxide, IGO (In_2O_3:Ge), and fluorine-doped indium oxide, IFO (In_2O_3:F), reported by Romeo et al., for example, have resistivities of about $2 \times 10^{-4}\,\Omega$ cm and optical transmittance of $\geq$ 85% in the wavelength range of 400–800 nm, which are comparable to their benchmark ITO. Molybdenum-doped indium oxide, IMO (In_2O_3:Mo), was first reported by Meng et al.. Later on, Yamada et al. reported a low resistivity of $1.5 \times 10^{-4}\,\Omega$ cm and a mobility of 94 cm^2/V s, and Parthiban et al. reported a resistivity of 4×10^{-4} Ω cm, an average transmittance of >83% and a mobility of 149 cm^2/V s for IMO. Zn-doped indium oxide, IZO (In_2O_3:Zn), deposited on plastic substrates showed resistivity of 2.9×10^{-4} Ω cm and optical transmittance of $\geq$ 85%. Suffice it to say that In_2O_3 doped with other impurities have comparable electrical and optical properties to the above-mentioned data as enumerated in many articles.

The small variations existing among these reports could be attributed to the particulars of the deposition techniques and deposition conditions. To improve the electrical and optical properties of In_2O_3 and ITO, their doped varieties such as ITO:Ta and In_2O_3:Cd–Te have been explored as well. For example, compared with ITO, the films of ITO:Ta have improved the electrical and optical properties due to the improved crystallinity, larger grain size, and the lower surface roughness, as well as a larger band gap, which are more pronounced for ITO:Ta achieved at low substrate temperatures. The carrier concentration, mobility, and maximum optical transmittance for ITO:Ta achieved at substrate temperature 400°C are 9.16×10^{20} cm^{-3}, 28.07 cm^2/V s and 91.9% respectively, while the corresponding values for ITO are 9.12×10^{20} cm^{-3}, 26.46 cm^2/V s and 87.9%, respectively. Due to historical reasons, propelled by the above discussed attributes, ITO is the predominant TCO used in optoelectronic devices. Another reason why ITO enjoys such predominance is the ease of its processing. ITO-based transparent electrodes used in LCDs consume the largest amount of indium, about 80% of the total. As reported by Minami and Miyata (January, 2008), about 800 tons of indium was used in Japan in 2007. Because approximately 80%–90% of the indium can be recycled, the real consumption of indium in Japan in 2007 is in the range of 80–160 tons. The total amount of indium reserves in the world is estimated to be only approximately 6000 tons according to the 2007 United States Geological Survey. It is widely believed that indium shortage may occur in the very near future and indium will soon become a strategic resource in every country.

Consequently, search for alternative TCO films comparable to or better than ITO is underway. The report published by NanoMarkets in April 2009 (Indium Tin Oxide and Alternative Transparent Conductor Markets) pointed out that up until 2009 the ITO market was not challenged since the predicted boom in demand for ITO did not happen, partially due to the financial meltdown. The price of indium slightly varied from about US700$/kg in 2005 to US1000$/kg in 2007 and then to US700$/kg in 2009 which is still too expensive for

mass production. On the other hand, the market research firm iSupply forecasted in 2008 that the worldwide market for all touch screens employing ITO layers would nearly double, from \$3.4 billion to \$6.4 billion by 2013. Therefore, ITO as the industrial standard TCO is expected to lose its share of the applicable markets rather slowly even when alternatives become available. The report by NanoMarkets is a good guide for both users and manufacturers of TCOs.

In addition to ZnO-based TCOs, it also remarks on other possible solutions such as conductive polymers and/or the so-called and overused concept of nano-engineered materials such as poly (3, 4-ethylenedioxythiophene) well known as PEDOT by both H.C. Starck and Agfa, and carbon nanotube (CNT) coatings, which have the potentials to replace ITO at least in some applications since they can overcome the limitations of TCOs. Turning our attention now to the up and coming alternatives to ITO, ZnO with an electron affinity of 4.35 eV and a direct band gap energy of 3.30 eV is typically an n-type semiconductor material with the residual electron concentration of~10^{17} cm^{-3}. However, the doped ZnO films have been realized with very attractive electrical and optical properties for electrode applications. The dopants that have been used for the ZnO-based binary TCOs are Ga, Al, B, In, Y, Sc, V, Si, Ge, Ti, Zr, Hf, and F. Among the advantages of the ZnO-based TCOs are low cost, abundant material resources, and non-toxicity. At present, ZnO heavily doped with Ga and Al (dubbed GZO and AZO) has been demonstrated to have low resistivity and high transparency in the visible spectral range and, in some cases, even outperform ITO and FTO. The dopant concentration in GZO or AZO is more often in the range of 10^{20}–10^{21} cm^{-3} and although we obtained mobilities near 95 cm^2/V s in our laboratory in GZO typical reported mobility is near or slightly below 50 cm^2/V s. Ionization energies of Al and Ga donors (in the dilute limit which decreases with increased doping) are 53 and 55 meV, respectively, which are slightly lower than that of In (63 meV). Our report of a very low resistivity of~8.5×10^{-5} Ω cm for AZO, and Park et al. reported a resistivity of ~8.1×10^{-5} Ω cm for GZO, both of which are similar to the lowest reported resistivity of~7.7×10^{-5} Ω cm for ITO. The typical transmittance of AZO and GZO is easily 90% or higher, which is comparable to the best value reported for ITO when optimized for transparency alone and far exceeds that of the traditional semi-transparent and thin Ni/Au metal electrodes with transmittance below 70% in the visible range. The high transparency of AZO and GZO originates from the wide band gap nature of ZnO. Low growth temperature of AZO or GZO also intrigued researchers with respect to transparent electrode applications in solar cells. As compared to ITO, ZnO-based TCOs show better thermal stability of resistivity and better chemical stability at higher temperatures, both of which bode well for the optoelectronic devices in which this material would be used. In short, AZO and GZO are the TCOs attracting more attention, if not the most, for replacing ITO. From the cost and availability and environmental points of view, AZO appears to be the best candidate. This conclusion is also bolstered by batch process availability for large-area and large-scale production of AZO.

To a lesser extent, other ZnO-based binary TCOs have also been explored. For readers'convenience, some references are discussed at a glance below. B-doped ZnO has been reported to exhibit a lateral laser-induced photovoltage (LPV), which is expected to make it a candidate for position sensitive photo-detectors. In-doped ZnO prepared by pulsed laser deposition and spray pyrolysis is discussed, respectively. Y-doped ZnO deposited by sol–gel method on silica glass has been reported. The structural, optical and electrical properties of F-doped ZnO formed by the sol–gel process and also listed almost all the relevant activities in the field. For drawing the contrast, we should reiterate that among

all the dopants for ZnO-based binary TCOs, Ga and Al are thought to be the best candidates so far. It is also worth nothing that $Zn_{1-x}Mg_xO$ alloy films doped with a donor impurity can also serve as transparent conducting layers in optoelectronic devices. As well known the band gap of wurtzite phase of $Zn_{1-x}Mg_xO$ alloy films could be tuned from 3.37 to 4.05 eV, making conducting $Zn_{1-x}Mg_xO$ films more suitable for ultraviolet (UV) devices. The larger band gap of these conducting layers with high carrier concentration is also desired in the modulation-doped heterostructures designed to increase electron mobility. In this vein, $Zn_{1-x}Mg_xO$ doped with Al has been reported in Refs. The above-mentioned ZnO-based TCOs have relatively large refractive indices as well, in the range of 1.9–2.2, which are comparable to those of ITO and FTO. For comparison, the refractive indices of commercial ITO/glass decrease from 1.9 at wavelength of 400 nm to 1.5 at a wavelength of 800 nm, respectively. The high refractive indices reduce internal reflections and allow employment of textured structures in LEDs to enhance light extraction beyond that made feasible by enhanced transparency alone. The dispersion in published values of the refractive index is attributed to variations in properties of the films prepared by different deposition techniques. For example, amorphous ITO has lower refractive index than textured ITO. It is interesting to note that nanostructures such as nanorods and nanotips as well as controllable surface roughness could enhance light extraction/absorption in LEDs and solar cells, thus improving device performance. Fortunately, such nanostructures can be easily achieved in ZnO by choosing and controlling the growth conditions. One disadvantage of ZnO-based TCOs is that they degrade much faster than ITO and FTO when exposed to damp and hot (DH) environment. The stability of AZO used in thin film $CuInGaSe_2$ (CIGS) solar cells, along with Al-doped $Zn_{1-x}Mg_xO$ alloy, ITO and FTO, by direct exposure to damp heat (DH) at 85°C and 85% relative humidity. The results showed that the DH-induced degradation rates followed the order of AZO and $Zn_{1-x}Mg_xO \gg$ ITO > FTO. The degradation rates of AZO were slower for films of larger thickness which were deposited at higher substrate temperatures during sputter deposition, and underwent dry-out intervals. From the point of view of the initiation and propagation of degrading patterns and regions, the degradation behavior appears similar for all TCOs despite the obvious differences in the degradation rates. The degradation is explained by both hydrolysis of the oxides at some sporadic weak spots followed by swelling and popping of the hydrolyzed spots which are followed by segregation of hydrolyzed regions, and hydrolysis of the oxide–glass interfaces.

In addition to those above-mentioned binary TCOs based on In_2O_3, SnO_2 and ZnO, ternary compounds such as Zn_2SnO_4, $ZnSnO_3$, $Zn_2In_2O_5$, $Zn_3In_2O_6$, $In_4Sn_3O_{12}$, and multicomponent oxides including $(ZnO)_{1-x}(In_2O_3)x$, $(In_2O_3)_x(SnO_2)_{1-x}$, $(ZnO)_{1-x}(SnO_2)_x$ are also the subject of investigation. However, it is relatively difficult to deposit those TCOs with desirable optical and electrical properties due to the complexity of their compositions. Nowadays ITO, FTO and GZO/AZO described in more details above are preferred in practical applications due to the relative ease by which they can be formed. Although it is not within the scope of this article, it has to be pointed out for the sake of completeness that CdO along with In_2O_3 and SnO_2 forms an analogous In_2O_3–SnO_2–CdO alloy system. The averaged resistivity of ITO by different techniques is ~$1 \times 10^{-4}\Omega \bullet cm$, which is much higher than that of FTO. For FTO, the typically employed technique is spray pyrolysis which can produce the lowest resistivity of ~3.8×10^{-4} $\Omega \bullet cm$. For AZO/GZO, the resistivities listed here are comparable to or slightly higher than ITO but their transmittance is slightly higher than that of ITO. Obviously, AZO and GZO as well as other ZnO-based TCOs are promising to replace ITO for transparent electrode applications in terms of their electrical and optical properties. There are also few

reports for some other promising n-type TCOs, which could find some practical applications in the future. They are titanium oxide doped with Ta or Nb, Ga_2O_3 doped with Sn and $12CaO \cdot 7Al_2O_3$ (often denoted $C_{12}A_7$). These new TCOs are currently not capable of competing with ITO/FTO/GZO/AZO in terms of electrical or optical properties. We should also point out that n-type transparent oxides under discussion are used on top of the p-type semiconductors and the vertical conduction between the two relies on tunneling and leakage. The ideal option would be to develop p-type TCOs which are indeed substantially difficult to attain.

3. Crystal chemistry of ITO

Crystalline indium oxide has the bixbyite structure consisting of an 80-atom unit cell with the Ia3 space group and a 1-nm lattice parameter in an arrangement that is based on the stacking of InO_6 coordination groups. The structure is closely related to fluorite, which is a face-centered cubic array of cations with all the tetrahedral interstitial positions occupied with anions. The bixbyite structure is similar to fluorite except that the MO_8 coordination units (oxygen position on the corners of a cube and M located near the center of the cube) of fluorite are replaced with units that have oxygen missing from either the body or the face diagonal. The removal of two oxygen ions from the metal-centered cube to form the InO_6 coordination units of bixbyite forces the displacement of the cation from the center of the cube. In this way, indium is distributed in two nonequivalent sites with one-fourth of the indium atoms positioned at the center of a trigonally distorted oxygen octahedron (diagonally missing O). The remaining three-fourths of the indium atoms are positioned at the center of a more distorted octahedron that forms with the removal of two oxygen atoms from the face of the octahedron. These MO_6 coordination units are stacked such that one-fourth of the oxygen ions are missing from each {100} plane to form the complete bixbyite structure. A minimum in the thin-film resistivity is found in the ITO system when the oxygen partial pressure during deposition is optimized. This is because doping arises from two sources, four-valent tin substituting for three-valent indium in the crystal and the creation of doubly charged oxygen vacancies. This is due to an oxygen-dependent competition between substitutional Sn and Sn in the form of neutral oxide complexes that do not contribute carriers. Amorphous ITO that has been optimized with respect to oxygen content during deposition has a characteristic carrier mobility (40 cm²/V s) that is only slightly less than that of crystalline films of the same composition. This is in sharp contrast to amorphous covalent semiconductors such as Si, where carrier transport is severely limited by the disorder of the amorphous phase. In semiconducting oxides formed from heavy-metal cations with $(n-1)d^{10}ns^0$ ($n \leq 4$) electronic configurations, it appears that the degenerate band conduction is not band-tail limited.

4. ZnO thin films

Another important oxide used in PV window and display technology applications is doped ZnO, which has been learned to have a thin-film resistivity as low as 2.4×10^{-4} $\Omega \bullet cm$. Although the resistivity of ZnO thin films is not yet as small as the ITO standard, it does offer the significant benefits of low cost relative to In-based systems and high chemical and thermal stability. In the undoped state, zinc oxide is highly resistive because, unlike In-based systems, ZnO native point defects are not efficient donors. However, reasonable

impurity doping efficiencies can be achieved through substitutional doping with Al, In, or Ga. Most work to date has focused on Al - doped ZnO, but this dopant requires a high degree of control over the oxygen potential in the sputter gas because of the high reactivity of Al with oxygen. Gallium, however, is less reactive and has a higher equilibrium oxidation potential, which makes it a better choice for ZnO doping applications. Furthermore, the slightly smaller bond length of Ga–O (1.92Å) compared with Zn–O (1.97 Å) also offers the advantage of minimizing the deformation of the ZnO lattice at high substitutional gallium concentrations. The variety of ZnO thin films has been expatiated elsewhere.

5. Electrical conductivity of TCO

TCOs are wide band gap (E_g) semiconducting oxides, with conductivity in the range of 10^2 – 1.2×10^6 (S). The conductivity is due to doping either by oxygen vacancies or by extrinsic dopants. In the absence of doping, these oxides become very good insulators, with the resistivity of $> 10^{10}$ Ω cm. Most of the TCOs are n-type semiconductors. The electrical conductivity of n-type TCO thin films depends on the electron density in the conduction band and on their mobility: $\sigma = \mu\, n\, e$, where μ is the electron mobility, n is its density, and e is the electron charge. The mobility is given by:

$$\mu = e\,\tau\,/\,m^* \tag{1}$$

where τ is the mean time between collisions, and m* is the effective electron mass. However, as n and τ are negatively correlated, the magnitude of μ is limited. Due to the large energy gap ($E_g > 3$ eV) separating the valence band from the conducting band, the conduction band can not be thermally populated at room temperature (kT~0.03 eV, where k is Boltzmann's constant), hence, stoichiometric crystalline TCOs are good insulators. To explain the TCO characteristics, the various popular mechanisms and several models describing the electron mobility were proposed.

In the case of intrinsic materials, the density of conducting electrons has often been attributed to the presence of unintentionally introduced donor centers, usually identified as metallic interstitials or oxygen vacancies that produced shallow donor or impurity states located close to the conduction band. The excess donor electrons are thermally ionized at room temperature, and move into the host conduction band. However, experiments have been inconclusive as to which of the possible dopants was the predominant donor. Extrinsic dopants have an important role in populating the conduction band, and some of them have been unintentionally introduce. Thus, it has been conjectured in the case of ZnO that interstitial hydrogen, in the H^+ donor state, could be responsible for the presence of carrier electrons. In the case of SnO_2, the important role of interstitial Sn in populating the conducting band, in addition to that of oxygen vacancies, was conclusively supported by first-principle calculations. They showed that Sn interstitials and O vacancies, which dominated the defect structure of SnO_2 due to the multivalence of Sn, explained the natural nonstoichiometry of this material and produced shallow donor levels, turning the material into an intrinsic n-type semiconductor. The electrons released by these defects were not compensated because acceptor-like intrinsic defects consisting of Sn voids and O interstitials did not form spontaneously. Furthermore, the released electrons did not make direct optical transitions in the visible range due to the large gap between the Fermi level and the energy level of the first unoccupied states. Thus, SnO_2 could have a carrier density with minor effects on its transparency.

The conductivity σ is intrinsically limited for two reasons. First, n and τ cannot be independently increased for practical TCOs with relatively high carrier concentrations. At high conducting electron density, carrier transport is limited primarily by ionized impurity scattering, i.e., the Coulomb interactions between electrons and the dopants. Higher doping concentration reduces carrier mobility to a degree that the conductivity is not increased, and it decreases the optical transmission at the near-infrared edge. With increasing dopant concentration, the resistivity reaches a lower limit, and does not decrease beyond it, whereas the optical window becomes narrower. Bellingham were the first to report that the mobility and hence the resistivity of transparent conductive oxides (ITO, SnO_2, ZnO) are limited by ionized impurity scattering for carrier concentrations above 10^{20} cm^{-3}. Ellmer also showed that in ZnO films deposited by various methods, the resistivity and mobility were nearly independent of the deposition method and limited to about 2×10^{-4} Ω cm and 50 cm^2/Vs, respectively. In ITO films, the maximum carrier concentration was about 1.5×10^{21} cm^{-3}, and the same conductivity and mobility limits also held. This phenomenon is a universal property of other semiconductors. Scattering by the ionized dopant atoms that are homogeneously distributed in the semiconductor is only one of the possible effects that reduce the mobility. The all recently developed TCO materials, including doped and undoped binary, ternary, and quaternary compounds, also suffer from the same limitations. Only some exceptional samples had a resistivity of $\leq 1\times10^{-4}$ Ω cm.

In addition to the above mentioned effects that limit the conductivity, high dopant concentration could lead to clustering of the dopant ions, which increases significantly the scattering rate, and it could also produce nonparabolicity of the conduction band, which has to be taken into account for degenerately doped semiconductors with filled conduction bands.

6. Optical properties of TCO

The transmission window of TCOs is defined by two imposed boundaries. One is in the near-UV region determined by the effective band gap Eg, which is blue shifted due to the Burstein–Moss effect. Owing to high electron concentrations involved the absorption edge is shifted to higher photon energies. The sharp absorption edge near the band edge typically corresponds to the direct transition of electrons from the valence band to the conduction band. The other is at the near infrared (NIR) region due to the increase in reflectance caused by the plasma resonance of electron gas in the conduction band. The absorption coefficient (α) is very small within the defined window and consequently transparency is very high. The positions of the two boundaries defining the transmission window are closely related to the carrier concentration. For TCOs, both boundaries defining the transmission window shift to shorter wavelength with the increase of carrier concentration. The blue-shift of the near-UV and near-IR boundaries of the transmission window of GZO as the carrier concentration increased from 2.3×10^{20} cm^{-3} to 10×10^{20} cm^{-3}. The blue-shift of the onset of absorption in the near-UV region is associated with the increase in the carrier concentration blocking the lowest states (filled states) in the conduction band from absorbing the photons. The Burstein–Moss effect owing to high electron concentrations has been widely observed in transmittance spectra of GZO and AZO. A comparable or even larger blue-shift in the transmittance spectra of GZO has been reported with absorption edge at about 300 nm wavelength corresponding to a bang gap of about 4.0 eV. The plasma frequency at which the free carriers are absorbed has a negative correlation with the free carrier concentration.

Consequently, the boundary in the near-IR region also shifts to the shorter wavelength with increase of the free carrier concentration. The shift in the near-IR region is more pronounced than that in the near-UV region. Therefore, the transmission window becomes narrower as the carrier concentration increases. This means that both the conductivity and the transmittance window are interconnected since the conductivity is also related to the carrier concentration as discussed above. Thus, a compromise between material conductivity and transmittance window must be struck, the specifics of which being application dependent. While for LED applications the transparency is needed only in a narrow range around the emission wavelengths, solar cells require high transparency in the whole solar spectral range. Therefore, for photovoltaics, the carrier concentration should be as low as possible for reducing the unwanted free carrier absorption in the IR spectral range, while the carrier mobility should be as high as possible to retain a sufficiently high conductivity. Optical measurements are also commonly employed to gain insight into the film quality. For example, interference fringes found in transmittance curves indicate the highly reflective nature of surfaces and interfaces in addition to the low scattering and absorption losses in the films. The particulars of interferences are related to both the film thickness and the incident wavelength, which can be used to achieve higher transmittance for TCOs. In the case of a low quality TCO, deep level emissions occurring in photoluminescence (PL) spectra along with relatively low transmittance are attributed to the lattice defects such as oxygen vacancies, zinc vacancies, interstitial metal ions, and interstitial oxygen. High-doping concentration-induced defects in crystal lattices causing the creation of electronic defect states in band gap similarly have an adverse effect on transparency. In GZO, as an example, at very high Ga concentrations (10^{20}–10^{21} cm^{-3}), the impurity band merges with the conduction band causing a tail-like state below the conduction band edge of intrinsic ZnO. These tail states are responsible for the low-energy part of PL emission. Therefore, the defects, mainly the oxygen-related ones, in TCOs have to be substantially reduced, if not fully eliminated, through the optimal growth conditions to attain higher transmittance.

7. Application of TCO in solar cells

Solar cells exploit the photovoltaic effect that is the direct conversion of incident light into electricity. Electron–hole pairs generated by solar photons are separated at a space charge region of the two materials with different conduction polarities. Solar cells represent a very promising renewable energy technology because they provide clean energy source (beyond manufacturing) which will reduce our dependence on fossil oil. The principles of operation of solar cells have been widely discussed in detail in the literature and as such will not be repeated here. Rather, the various solar cell technologies will be discussed in the context of conduction oxides. Solar cells can be categorized into bulk devices (mainly single-crystal or large-grain polycrystalline Si), thin film single- and multiple-junction devices, and newly emerged technology which include dye-sensitized cells, organic/polymer cells, high-efficiency multi-junction cells based on III–V semiconductors among others. Crystalline silicon modules based on bulk wafers have been dubbed as the "first-generation" photovoltaic technology. The cost of energy generated by PV modules based on bulk-Si wafers is currently around $3–$4/Wp and cost reduction potential seems limited by the price of Si wafers. This cost of energy is still too high for a significant influence on energy production markets. Much of the industry is focused on the most cost efficient technologies in terms of cost per generated power. The two main strategies to bring down the cost of

photovoltaic electricity are increasing the efficiency of the cells and decreasing their cost per unit area. Thin film devices (also referred to as second generation of solar cells) consume less material than the bulk-Si cells and, as a result, are less expensive. The market share of the thin film solar cells is continuously growing and has reached some 15% in year 2010, while the other 85% is silicon modules based on bulk wafers. Alternative approaches also focused on reducing energy price are devices based on polymers and dyes as the absorber materials, which include a wide variety of novel concepts. These cells are currently less efficient than the semiconductor-based devices, but are attractive due to simplicity and low cost of fabrication.

TCO are utilized as transparent electrodes in many types of thin film solar cells, such as a-Si thin film solar cells, CdTe thin film solar cells, and CIGS thin film solar cells. It should be mentioned that, for photovoltaic applications, a trade-off between the sheet resistance of a TCO layer and its optical transparency should be made. As mentioned above, to reduce unwanted free carrier absorption in the IR range, the carrier concentration in TCO should be as low as possible, while the carrier mobility should be as high as possible to obtain sufficiently high conductivity. Therefore, achieving TCO films with high carrier mobility is crucial for solar cell applications.

7.1 Si thin film solar cells

In addition to the well-established Si technology and non-toxic nature and abundance of Si, the advantage of thin film silicon solar cells is that they require lower amount of Si as compared to the devices based on bulk wafers and therefore are less expensive. Several different photovoltaic technologies based on Si thin films have been proposed and implemented: hydrogenated amorphous Si (a-Si:H) with quasi-direct band gap of 1.8 eV, hydrogenated microcrystalline Si (μc-Si:H) with indirect band gap of 1.1 eV, their combination (micromorph Si), and polycrystalline Si on glass (PSG) solar cells. The first three technologies rely on TCOs as front/back electrodes. This thin film p–i–n solar cell is fabricated in a so-called superstrate configuration, in which the light enters the active region through a glass substrate. In this case, the fabrication commences from the front of the cell and proceeds to its back.

First, a TCO front contact layer is deposited on a transparent glass substrate, followed by deposition of amorphous/microcrystalline Si, and a TCO/metal back contact layer. Therefore, the TCO front contact must be sufficiently robust to survive all subsequent deposition steps and post-deposition treatments. To obtain high efficiency increasing the path length of incoming light is crucial, which is achieved by light scattering at the interface between Si and TCO layers with different refractive indices, so that light is "trapped" within the Si absorber layer. The light trapping allows reduction of the thickness of the Si absorber layer which paves the way for increased device stability. Therefore, TCO layers used as transparent electrodes in the Si solar cells have a crucial impact on device performance. In addition to high transparency and high electrical conductivity, a TCO layer used as front electrode should ensure efficient scattering of the incoming light into the absorber layer and be chemically stable in hydrogen-containing plasma used for Si deposition, and act as a good nucleation layer for the growth of microcrystalline Si. The bottom TCO layer between Si and a metal contact works as an efficient back reflector as well as a diffusion barrier.

To increase light scattering, surface texturing of the front and back TCO contact layers is commonly used. As discussed above, the TCOs for practical applications are ITO, FTO and

GZO/AZO. For reasons mentioned in the text dealing with the discussion of various TCO materials, FTO films have been widely used in solar cells to replace ITO. Alternatively, FTO coated ITO/glass substrate have been proposed to overcome the shortcomings of pure ITO. FTO is the one typically used but cost-effective SnO_2-coated glass substrates on large areas (~1 m^2) are still not being used as a standard substrate. On the other hand, AZO has emerged as a promising TCO material for solar cells. The AZO/glass combination has better transparency and higher conductivity than those of commercial FTO/glass substrates. Another benefit is that AZO is more resistant to hydrogen-rich plasmas used for chemical vapor deposition of thin film silicon layers as compared to FTO and ITO. The AZO films on glass for thin film silicon solar cells have a sheet resistance of about 3Ω/sq for a film thickness of ~1000 nm, a figure which degrades for thinner films. They also reported a transmittance of ~90% in the visible region of the optical spectrum for a film thickness of ~700 nm, which enhances for thinner films. These thin film silicon solar cells all have high external quantum efficiencies in the blue and green wavelength regions due to the good transmittance of the AZO films and good index matching as well as a rough interface for avoiding reflections. The highest external quantum efficiency is about 85% at a wavelength of 500 nm. However, as mentioned earlier, AZO degrades much faster than ITO and FTO in dampheat environment.

7.2 CdTe thin film solar cells

CdTe has a direct optical band gap of about 1.5 eV and high absorption coefficient of >10^5 cm^{-1} in the visible region of the optical spectrum, which ensures the absorption of over 99% of the incident photons with energies greater than the band gap by a CdTe layer of few micrometers in thickness. CdTe solar cells are usually fabricated in the superstrate configuration, i.e., starting at the front of the cell and proceeding to the back, as described above for the Si solar cells. CdTe is of naturally p-type conductivity due to Cd vacancies. Separation of the photo-generated carriers is performed via a CdTe/CdS p-n heterojunction. CdS is an n-type material because of native defects, and has a band gap Eg~2.4 eV, which causes light absorption in the blue wavelength range which is undesirable. For this reason, the CdS layer is made very thin and is commonly referred to as a "window layer", emphasizing that photons should pass through it to be absorbed in the CdTe "absorber layer". The basic traditional module of CdTe solar cell is composed of a stack of 'Metal/CdTe/CdS/TCO/glass'. The fabrication begins with the deposition of a TCO layer onto the planar soda lime glass sheet followed by the deposition of the CdS window layer and the CdTe light absorber layer, ~ 5 μm in thickness. Efficiencies of up to 16.5% have been achieved with small-area laboratory cells, while the best commercial modules are presently 10%–11% efficient. The thin CdS window layer poses a problem shared by both CdTe and CIS-based thin film modules, which will be discussed in the next section. Since this layer should be very thin (50–80 nm in thickness), pinholes in CdS provide a direct contact between TCO and the CdS absorber layer, creating short circuits and reducing dramatically the efficiency. This problem is especially severe for CdTe cells, because sulfur readily diffuses into the CdTe layer during post-growth annealing further decreasing the CdS layer thickness.

To mitigate this issue, thin buffer layers made of highly resistive transparent oxides are incorporated between the TCO contact and the CdS window. SnO_2 layers are commonly used as such buffers, although $ZnSnO_x$ films also have been proposed. The exact role of the

buffer layers is not fully understood, whether it simply prevents short circuits by introducing resistance or also changes the interfacial energetics by introducing additional barriers, and optimization of this interface is a critical need. TCO materials typically used in CdTe solar cells are ITO and FTO. Reports for AZO in CdTe cells are very few. The use of ZnO-based TCOs in CdTe solar sells of superstrate configuration is hampered by its thermal instability and chemical reaction with CdS at high temperatures (550–650°C) typically used for CdTe solar cells fabrication. To resolve this problem, Gupta and Compaan applied low temperature (250°C) deposition by magnetron sputtering to fabricate superstrate configuration CdS/CdTe solar sells with AZO front contacts. These cells yielded efficiency as high as 14.0%. Bifacial CdTe solar cells make it possible to increase the device NIR transmission as the parasitic absorption and reflection losses are minimized. The highest efficiency of 14% was achieved from a CdTe cell with an FTO contact layer. The device performance depends strongly on the interaction between the TCO and CdS films. Later, the same group has noted a substantial In diffusion from ITO to the CdS/CdTe photodiode, which can be prevented by the use of undoped SnO_2 or ZnO buffers. Application of TCO as the back contact also allows fabrication of bifacial CdTe cells or tandem cells, which opens a variety of new applications of CdTe solar cells.

7.3 CIGS thin film solar cells

Copper indium diselenide ($CuInSe_2$ or CIS) is a direct-bandgap semiconductor with a chalcopyrite structure and belongs to a group of miscible ternary I–III–VI_2 compounds with direct optical bandgaps ranging from 1 to 3.5 eV. The miscibility of ternary compounds, that is the ability to mix in all proportions, enables quaternary alloys to be deposited with any bandgap in this range. A large light absorption coefficient of $>10^5$ cm^{-1} at photon energies greater than a bandgap allows a relatively thin (few μm in thickness) layer to be used as the light absorber. The alloy systems with optical bandgaps appropriate for solar cells include $Cu(InGa)Se_2$, $CuIn(SeS)_2$, $Cu(InAl)Se_2$, and $Cu(InGa)S_2$. Copper indium–gallium diselenide $Cu(InGa)Se_2$ (or CIGS) has been found to be the most successful absorber layer among chalcopyrite compounds investigated to date. The bandgap is ~1.0 eV for $CuInSe_2$ and increases towards the optimum value for photovoltaic solar energy conversion when gallium is added to produce $Cu(In, Ga)Se_2$. An energy bandgap of 1.25–1.3 eV corresponds to the maximum gap achievable without loss of efficiency. Further increase in the Ga fraction reduces the formation energies of point defects, primary, copper vacancies which makes them more likely to form. Also, a further increase in gallium content makes the absorber layers too highly resistive to be used in solar cells. Therefore, most CIGS devices are produced with an energy bandgap below 1.3 eV, which limits their V_{OC} at ~700 meV. Note that both CIS- and CIGS-based devices are usually dubbed as the CIS technology in the literature. The CIS technology provides the highest performance in the laboratory among all thin-film solar cells, with confirmed power conversion efficiencies of up to 20.1% for small (0.5 cm^2) cells fabricated by the Zentrum fuer Sonnenenrgie-und-Wasserstoff–Forschung and measured at the Fraunhofer Institute for Solar Energy Systems, and many companies around the world are developing a variety of manufacturing approaches aimed at low-cost, high-yield, large-area devices which would maintain laboratory-level efficiencies.

Similarly, TCO layers are generally used for the front contact, whereas a reflective contact material (Ag, frequently in combination with a TCO interlayer, is the most popular one) is needed on the back surface to enhance the light trapping in absorber layers. The optical

quality of these materials substantially affects the required thickness of the absorber layers in terms of providing the absorption of an optimal amount of irradiation. Depending on the application, devices are fabricated in either a ''substrate'' or a ''superstrate'' configuration. The superstrate configuration is based on TCO-coated transparent glass substrates, and the layers are deposited in a reversed sequence, from the top (front) to the bottom (back). The deposition starts with a contact window layer of a photodiode and ends with a back reflector. Light enters the cell through the glass substrate.

In the superstrate configuration, it is important for the TCO as substrate material to be not only electrically conductive and optically transparent, but also be chemically stable during solar-cell material deposition. The superstrate design is particularly suited for building integrated solar cells in which a glass substrate can be used as an architectural element. In the case of the substrate configuration, solar cells are fabricated from the back to the front, and the deposition starts from the back reflector and is finished with a TCO layer. For some specific applications, the use of lightweight, unbreakable substrates, such as stainless steel, polyimide or PET (polyethylene terephtalate) is advantageous.

8. A novel violet and blue enhanced SINP silicon photovoltaic device

8.1 Introduction

Violet and blue enhanced semiconductor photovoltaic devices are required for various applications such as optoelectronic devices for communication, solar cell, aerospace, spectroscopic, and radiometric measurements. Silicon photodetector are sensitive from infrared to visible light but have poor responsivity in the short wavelength region. Since the absorption coefficient of crystal Si is very high for shorter wavelengths in the violet region and is small for longer wavelengths. The heavily doped emitter may contain a dead layer near the surface resulting in poor quantum efficiency of the photoelectric device under short wavelength region.

In order to improve the responsivity of silicon photodiode at the 400-600nm, a novel ITO/SiO_2/np Si SINP violet and blue enhanced photovoltaic device (SINP is the abbreviation of semiconductor/insulator/np structure) was successfully fabricated using thermal diffusion of phosphorus for shallow junction, a very thin silicon dioxide and ITO film as an antireflection/passivation layer. The schematic and bandgap structure of the novel SINP photovoltaic device are whown here (Fig.1 and Fig.2). The very thin SiO_2 film
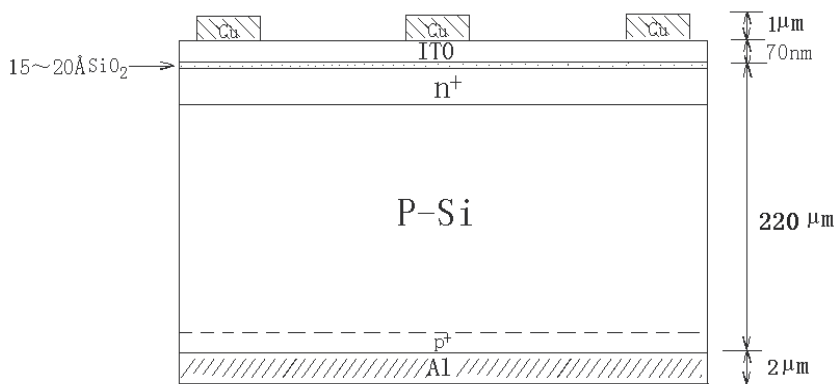
Fig. 1. Schematic of the novel SINP photovoltaic device.

$3.1eV$

$1.12eV$

$3.6eV$

$2.4eV$

$3.8eV$

n^+-ITO $\begin{smallmatrix}15\sim20Å\\ SiO_2\end{smallmatrix}$ n–Si   p–Si p^+–Si
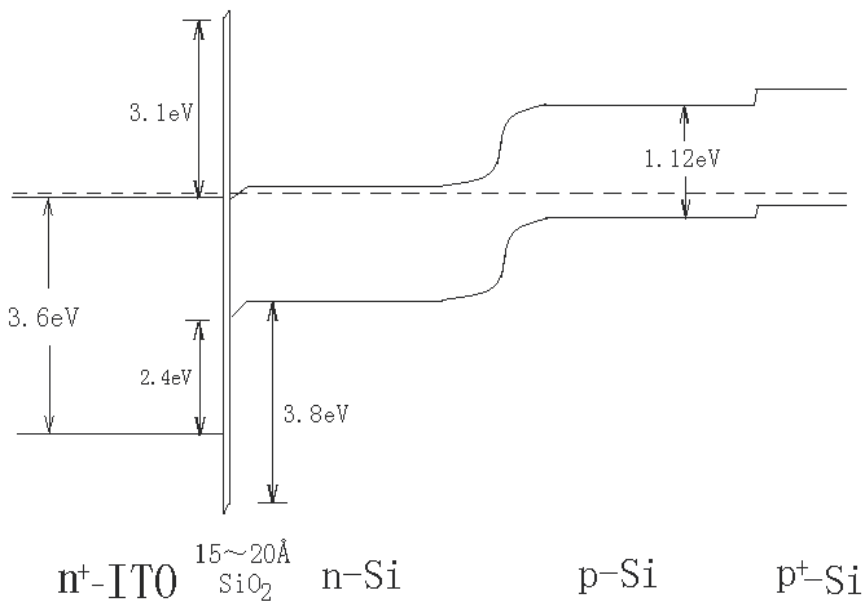
Fig. 2. Bandgap structure of the novel SINP photovoltaic device.

not only effectively passivated the surface of Si, but also reduced the mismatch of ITO and Si. Since a low surface recombination is imperative for good quantum efficiency of the device at short wavelength. The ITO film is high conducting, good antireflective (especially for violet and blue light) and stable. In addition, a wide gap semiconductor as the top film can serve as a low-resistance window, as well as the collector layer of the junction. Therefore, it can eliminate the disadvantage of high sheet resistance, which results from shallow junction. Because the penetration depth of short wavelength light is thin, the shallow junction is in favor of improving sensitivity.

8.2 Experimental in detail

The starting material was 2.0 Ωcm p-type CZ silicon. In the present, two types of shallow and deep junction n-emitters for violet and near-infrared SINP photovoltaic devices were made in an open quartz tube using liquid $POCl_3$ as the doping source. The sheet resistance is 37Ω/□ and 10Ω/□, while the junction depth is 0.35μm and 1μm, respectively. After phosphorus-silicon glass removing, a 2 μm Al metal electrode was deposited on the p-silicon as the bottom electrode by vacuum evaporation. The 15~20Å thin silicon oxide film was successfully grown by low temperature thermally (500°C for 20 min in N_2:O_2=4:1 condition) grown oxidation technology. The 70 nm ITO antireflection film was deposited on the substrate in a RF magnetron sputtering system. Sputtering was carried out at a working gas (pure Ar) pressure of 1.0Pa.

The Ar flow ratio was 30 sccm. The RF power and the substrate temperature were 100W and 300°C, respectively. The sputtering was processed for 0.5h.The ITO films were also prepared on glass to investigate the optical and electrical properties. Finally, by sputtering, a 1μm Cu metal film was deposited with a shadow mask on the ITO surface for the top grids electrode. The area of the device is 4.0 cm².

8.3 Results and discussion
8.3.1 Optical and electric properties of ITO films

In order to learn the optical absorption and energy band structure of ITO film, the transmission spectrum of the ITO film deposited on the glass substrate was measured (Fig.3). The thickness of ITO film is about 700 Å. The average transmittance of the film is about 95% in the visible region and the band-edge at 325nm.While the optical band gap of ITO film is about 3.8 eV by calculation. The reflection loss for ITO film on a texturized Si surface was indicated (Fig.4) from UV to the visible regime, which is much lower than that of Si_3N_4 film that are widely made by PECVD technology. This shows that ITO film effectively reduced reflection loss in short-wavelength, which is suitable for antireflection
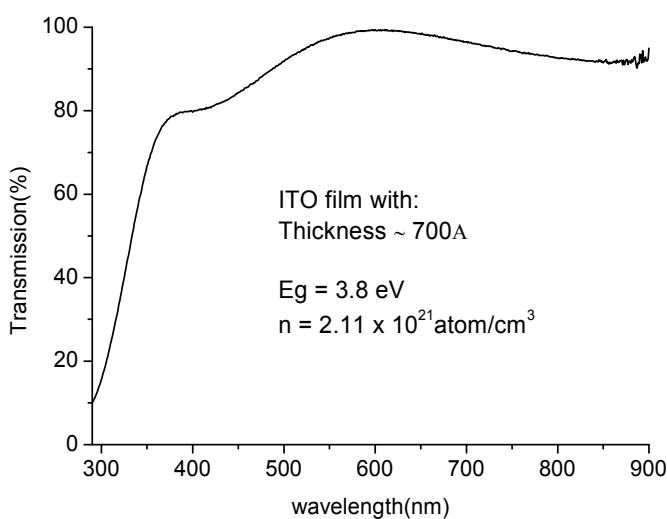
Fig. 3. Transmission spectrum of the ITO film.
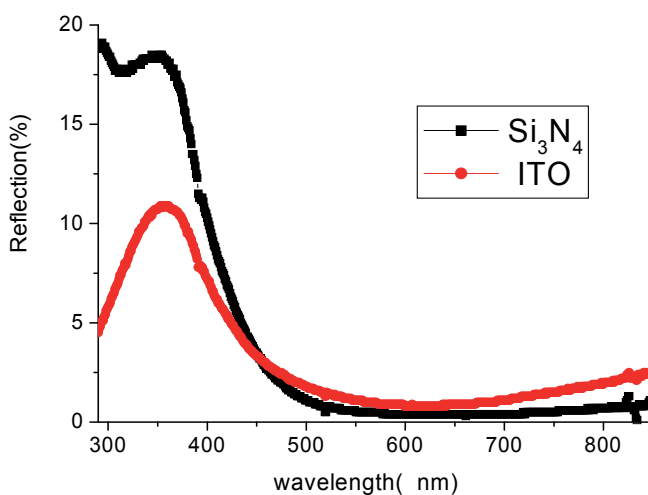
Fig. 4. Comparison of the reflections for ITO and Si_3N_4 films on a texturized Si surface.

coating in violet and blue photovoltaic device. Electrical properties of the ITO film were measured by four-point probe and Hall effect measurement. The square resistance and the resistivity are low to 17Ω/ ▢ and 1.19×10^{-4} Ω·cm, respectively, while carrier concentration is high to 2.11×10^{21} atom/cm^3.
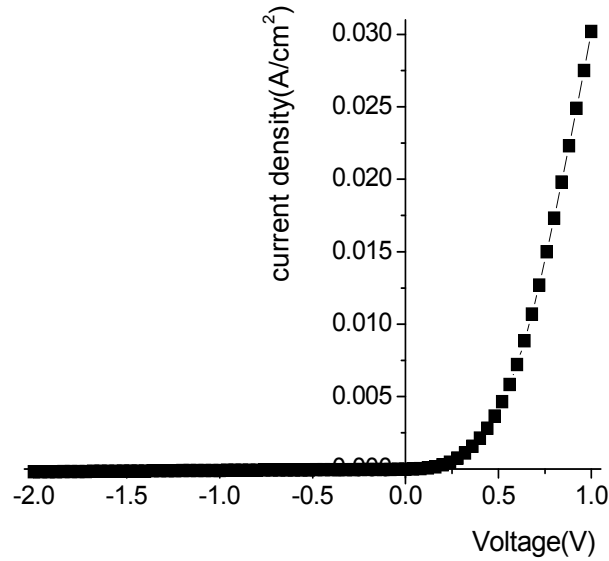
Fig. 5. I-V curve of the violet and blue enhanced (shallow junction) SINP photovoltaic device in dark.
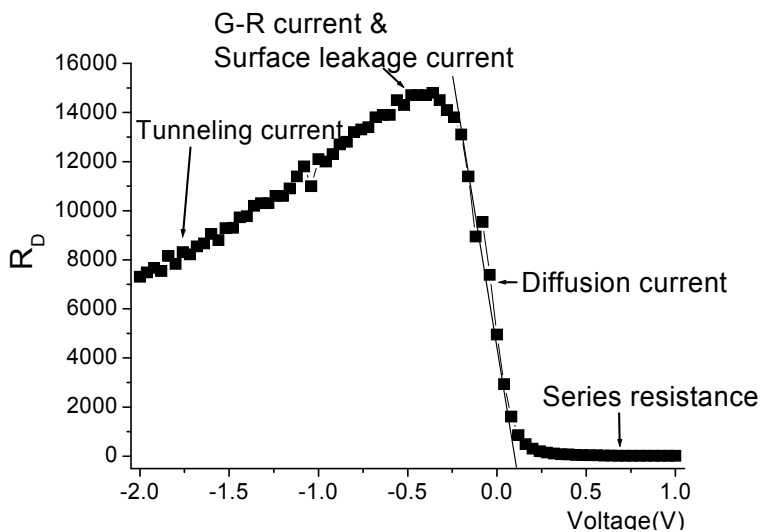
Fig. 6. The variation of resistance for SINP violet device via voltage (R_D-V curve).
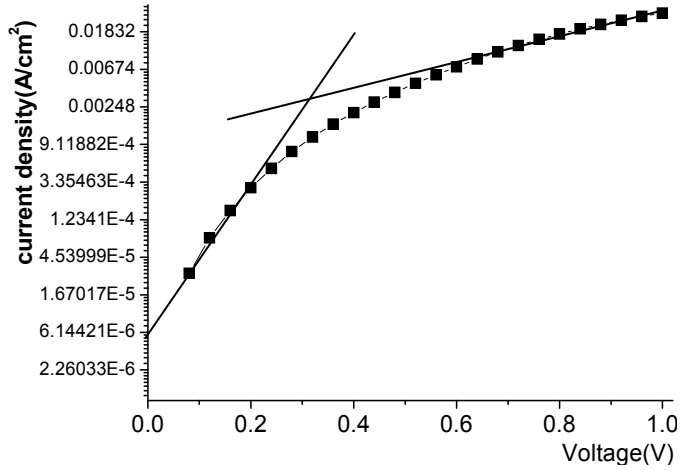
Fig. 7. The corresponding logarithmic scale in current with forward bias condition.

8.3.2 I-V characteristics

In our study, the current-voltage characteristic of the violet SINP device was measured in dark at room temperature (in Fig.5). I-V curves of the devices show fairly good rectifying behaviors. Basing on the dark current as a function of the applied bias, the corresponding diode resistance defined as $R_D = (\frac{dI}{dV})^{-1}$ is derived and shown (in Fig.6). The series resistance arose from ohmic depletion plays a dominant role when the forward bias is larger than 0.25 V. When the voltage varies within 0.2 V and - 0.2 V, the resistance slightly increases as the diffusion current in the base region. When the inversion voltage increases from - 0.2 to - 0.5 V, the leakage current and the recombination current in the surface layers restrain the increase of the dynamic resistance, which keeps the R_D – V curve in an invariation state. In the high inversion voltage region, the tunneling current plays a dominant role.

The plot of ln(J) against V, is shown (in Fig.7), which indicates that the current at low voltage (V < 0.3 V) varies exponentially with voltage. The characteristics can be described by the standard diode equation: $J = J_0(e^{\frac{qV}{nk_BT}} - 1)$ where q is the electronic charge, V is the applied voltage, k_B is the Boltzmann constant, n is the ideality factor and J_0 is the saturation current density. Calculation of J_0 and n from is obtained the measurements (in Fig.7). The value of the ideality factor of the violet SINP device is determined from the slop of the straight line region of the forward bias log(I)-V characteristics. At low forward bias (V< 0.2 V), the typical values of the ideality factors and the reverse saturation current density are 1.84 and 5.58×10-6A/cm2, respectively.

Using the standard diode equation $J = J_0(e^{\frac{qV}{nk_BT}} - 1)$, where n = 1.84 and J_0 = 5.58×10-6 A/cm2. The result of calculation is similar to that of the measurement (in I-V curve). By the same calculation method, the ideality factor and the reverse saturation current density of deep junction SINP photovoltaic device are 2.21 and 4.2 × 10-6 A/cm2, respectively. This result indicates that the recombination current $J_r \approx \exp(qV/2kT)$ dominates in the forward current. The rectifying behaviors and the composition of dark current for violet SINP photovoltaic device is better than deep junction SINP device, because the ideality factor of the violet SINP
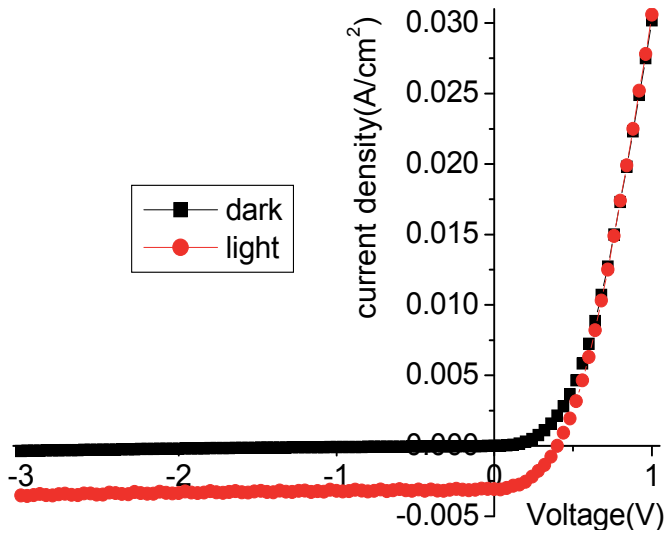
Fig. 8. I-V characteristic of the violet and blue enhanced SINP photovoltaic devices in dark and light (6.3 mW/cm² - white light), respectively.
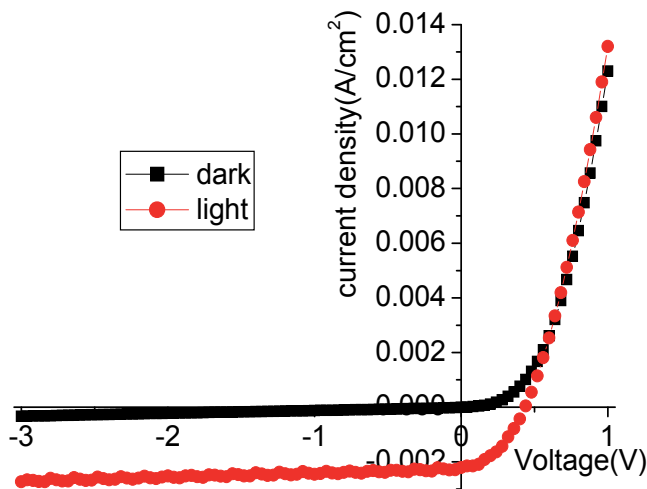
Fig. 9. I-V characteristic of the deep junction SINP devices in dark and light (6.3 mW/cm² - white light), respectively.

photovoltaic device (n=1.84) is lower than that of the deep junction SINP device (n=2.21). Furthermore, the values of I_F/I_R (I_F and I_R stand for forward and reverse current, respectively) at 1V for violet SINP device and deep junction SINP device are found to be as high as 324.7 and 98.4, respectively.

The weak light-injection I-V characteristics of the novel SINP devices with low power white light (6.3mW/cm²) illuminating were measured at 23°C. It is observed that the novel SINP device exhibits a good photovoltaic effect and rectifying behavior in the photon – induced carrieres transportation. On the other side, another essential physical parameter is internal

quantum efficiency (IQE) or external quantum efficiency (EQE) for the evaluation of the spectra response of the light (Fig.8 and Fig.9). The photocurrent density ($\sim 3.08 \times 10^{-3}$ A/cm^2) of violet and blue enhanced SINP photovoltaic device is much higher than that of deep junction SINP device ($\sim 2.23 \times 10^{-3}$A/cm^2), at V = 0.

8.3.3 Spectral response and responsivity

The comparison of IQE, EQE and the responsivity for the violet and blue SINP photovoltaic device and the deep junction SINP photovoltaic device has been illustrated (in Fig.10 ~ Fig.12). In visible light region, the internal and external quantum efficiencies (IQE and EQE) of the devices are in the range of 75% to 85%. In the violet and blue region, the IQE and EQE of shallow junction violet SINP device is much higher than that of the deep junction SINP device. For example, the EQE and the responsivity of the violet SINP device are 70% and 285mA/W at 500nm, respectively, while the EQE and the responsivity of the deep junction SINP device are 42% and 167mA/W at 500nm, respectively. The spectral responsivity peak of violet and blue SINP photovoltaic device is 487mA/W at about 800nm. While the spectral responsivity peak of deep junction SINP photovoltaic device is 471mA/W at about 860nm. The high quantum efficiency and the responsivity of violet and blue enhanced photovoltaic cell attribute to the shallow junction and the good conductive, and the violet and blue antireflection of ITO film.
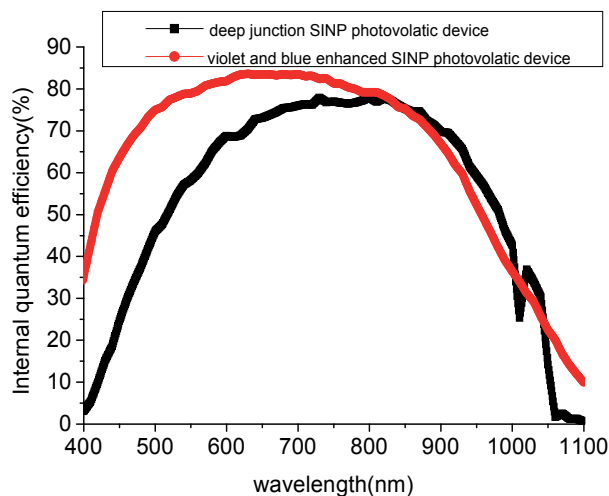
Fig. 10. Comparison of IQE for violet and blue SINP photovoltaic device and the deep junction SINP photovoltaic device.
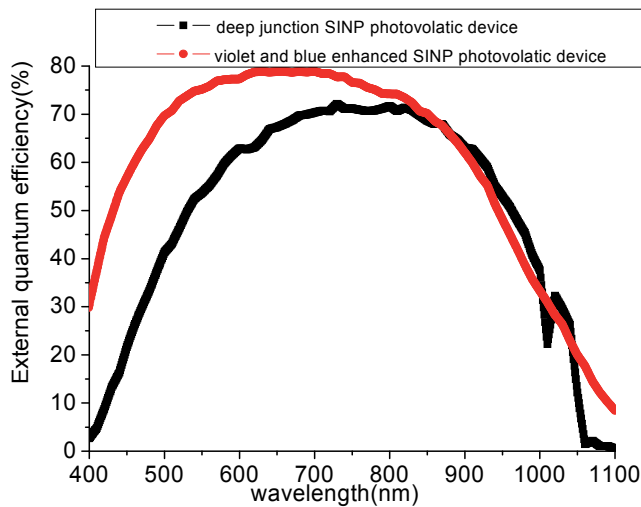
Fig. 11. Comparison of EQE for violet and the blue SINP photovoltaic device and the deep junction SINP photovoltaic device.
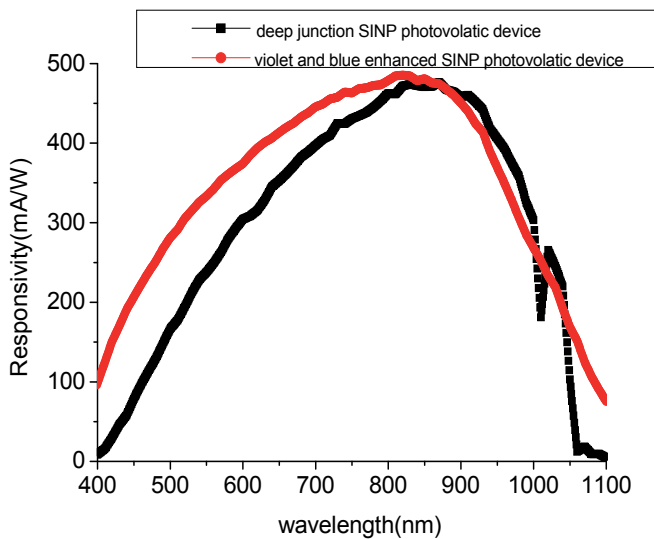
Fig. 12. Comparison of the responsivity for the violet and blue SINP photovoltaic device and the deep junction SINP photovoltaic device.

8.3.4 Conclusions

The novel ITO/SiO_2/np Silicon SINP violet and blue enhanced photovoltaic device has been fabricated by thermal diffusion of phosphorus for shallow junction to enhance the spectral responsivity within the wavelength range of 400-600nm, the low temperature thermally grown a very thin silicon dioxide and RF sputtering ITO antireflection coating to reduce the reflected light and enhance the sensitivity. The ITO film was evinced to a high quality by UV-VIS spectrophotometer, four point probe and Hall-effect measurement. Fairly good

rectifying and obvious photovoltaic behaviors are obtained and analyzed by I-V measurements. The spectral response and the responsivity with a higher quantum efficiency of the violet SINP photovoltaic device and the deep junction SINP photovoltaic device were analyzed in detail. The results indicated that the novel violet and blue enhanced photovoltaic device could be not only used for high quantum efficiency of violet and blue enhanced silicon photodetector for various applications, but also could be used for the high efficiency solar cell.

9. Fabrication and photoelectric properties of AZO/SiO$_2$/p-Si heterojunction device

9.1 Introduction

As shown in the previous work, semiconductor-insulator-semiconductor (SIS) diodes have certain features, which make them more attractive for the solar energy conversion than conventional Shottky, MIS, or other heterojunction structures (Mridha et al., 2007). For example, efficient SIS solar cells such as indium tin oxide (ITO) on silicon have been reported, where the crystal structures and the lattice parameters of Si (diamond, a = 0.5431 nm), SnO$_2$ (tetragonal, a = 0.4737 nm, c = 0.3185 nm), In$_2$O$_3$ (cubic, a = 1.0118 nm) show that they are not particularly compatible and thus not likely to form good devices. However, the SIS structure is potentially more stable and theoretically more efficient than either a Schottky or a MIS structure. The origins of this potential superiority are the suppression of majority-carrier tunneling in the high potential barrier region of SIS structure, and the existence of thin interface layer which minimizes the amount and the impact of the interface states. This results in an extensive choice of the p-n junction partner with a matching band gap in the front layer. In addition, the top semiconductor film can serve as an antireflection coating (Dengyuan et al., 2002), a low-resistance window, and the collector of the p-n junction as well.

Furthermore, the semiconductor with a wide band gap as the top layer of SIS structure can eliminate the surface dead layer which often occurs within the homojunction devices, such as the normal bulk silicon based solar cells. On the other side, this absence of the light absorption of visible region in a surface layer can improve the ultraviolet response of the internal quantum efficiency. Among many transparent conductive oxides (TCO) of the transition metals, ZnO:Al is one the best n-type semiconductor layer. It has high conductivity, high transmittance, optimized surface texture for light trapping, and large band gap of $E_g \approx$ 3.3 eV. Thus, in this description, we show a photovoltaic device with AZO/SiO$_2$/p-Si frame, as an attempt to study its opto-electronic conversion property and the I-V features as well. The schematic and the bandgap structure of the novel AZO/SiO$_2$/p-Si SIS heterojunction device was show here (Fig.13).

9.2 Experimental in details

For the purpose of fabricating SIS structure, p-type Si (100) wafers were used as the substrates of the heterojunction device. The wafers were firstly prepared by a stand cleaning procedure, then, they were dipped in 10% HF solution for one minute to remove native oxide layer. Finally, the wafers were dried in a flow gas of nitrogen.

By thermal evaporation, 1 µm-thick Al electrode was deposited on the back side. Then the samples were annealed at 500°C for 20 min in N$_2$:O$_2$=4:1 condition to form good ohmic contact and a very thin oxide layer (about 15～20Å) was grown on the p-Si surface.

The Al doped ZnO films were deposited on the oxidized silicon substrates in a RF magnetron sputtering system. The target was a sintered ceramic disk of ZnO doped with 2 wt% Al_2O_3 (purity 99.99%). The base pressure inside the chamber was pumped down to less than 5×10^{-4} Pa. Sputtering was carried out at a working gas (pure Ar) pressure of 1Pa. The Ar flow ratio was 30 sccm. The RF power and the temperature on substrates were kept at 100W and 300°C, respectively. The sputtering was proceeded for 2.5 hours. The area is 2×2 cm^2.

The thickness of AZO film was measured by step profiler. The optical transmission of the films was measured by UV-VIS spectrophotometer. The electrical properties of Al doped ZnO films were characterized by four point probe. The current-voltage characteristics of the device was measured by Agilent 4155C semiconductor parameter analyzer (with probe station, the point diameter of a probe is 5 µm).
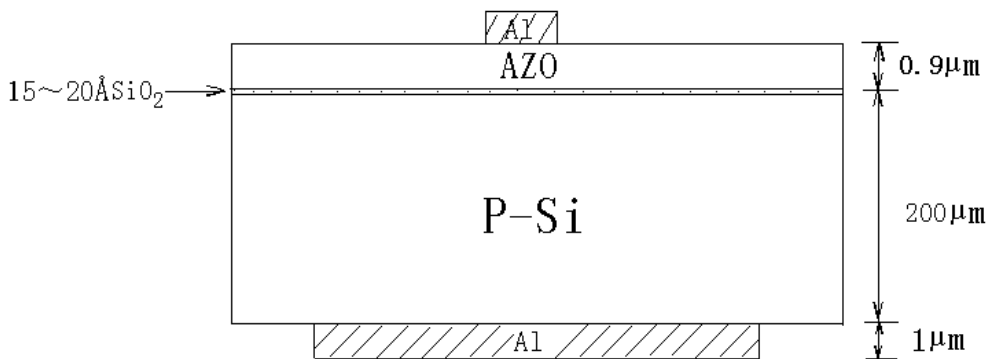
Fig. 13. The structure of AZO/SiO$_2$/p-Si heterojunction PV device.
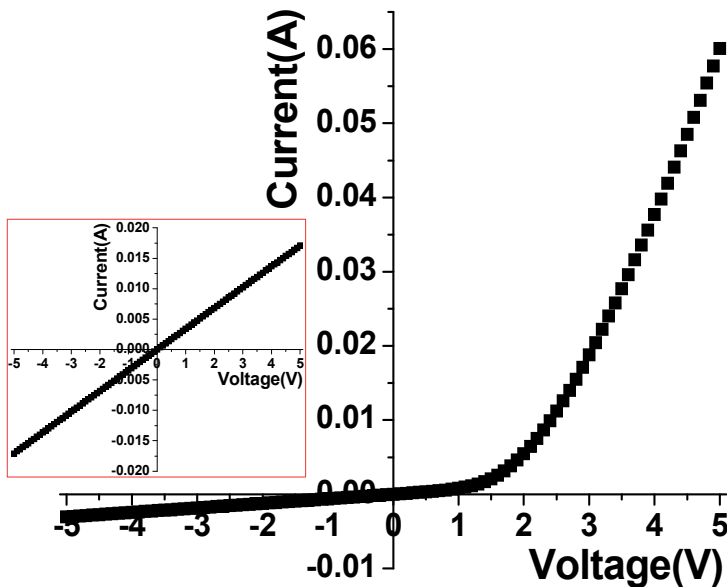
Fig. 14. I-V curve of the Al/AZO/SiO$_2$/p-Si/Al heterojunction device in dark.
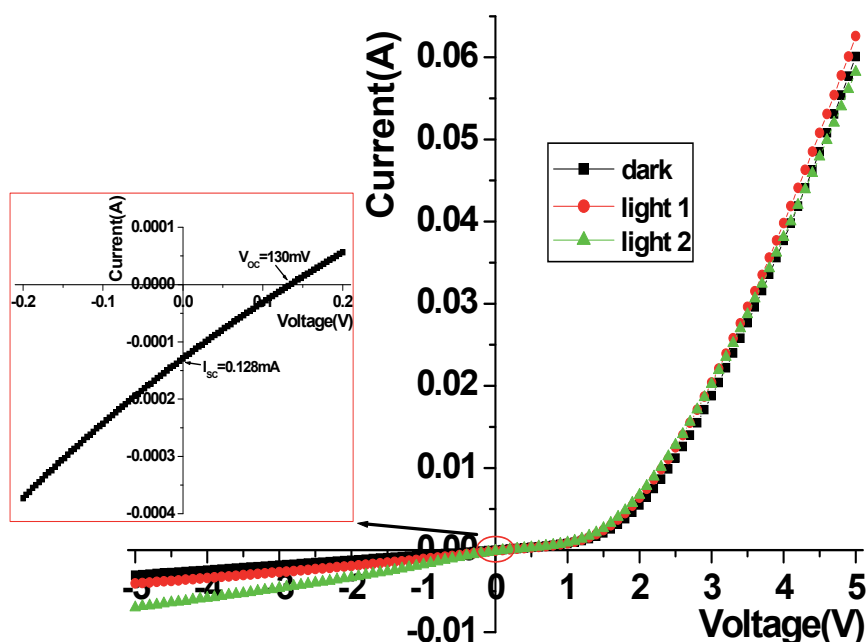
Fig. 15. I-V characteristic of the $AZO/SiO_2/p$-Si/Al heterojunction device in dark and light (light-1: 6.3mW/cm^2 white light; Light-2: 20W halogen lamp)

9.3 I-V characteristics

A linear I-V behavior between the two electrodes on the surface of ZnO:Al film indicates a good ohmic contact. The current-voltage characteristic of the $AZO/SiO_2/p$-Si/Al heterojunction device was measured at room temperature in the dark (Fig.14). Typical rectifying is observed for this heterojunction with polar to covalent semiconductors structure. The weak photon irradiation I-V characteristics were measured under two kinds of illumination by low power white light (6.3mW/cm^2) lamp and 20W halogen lamp (in Fig.15). The good rectifying with the increase of photoelectric current was observed for the typical interface mismatching device. Under reverse bias conditions the photocurrent caused by the ZnO surfaces exposing in the low power white light lamp and 20W halogen lamp was obviously much larger than the dark current. For example, when the reverse bias is -5V, the dark current is only 3.05×10^{-3}A.While the photocurrent reach to 4.06×10^{-3}A and 6.99×10^{-3}A under low power white light and halogen lamp illumination, respectively.

9.4 Conclusions

The novel $AZO/SiO_2/p$-Si/ heterojunction has been fabricated by magnetron sputtering deposition AZO film on p-Si substrate. Fairly good rectifying and photoelectric behaviors are observed and analyzed by I-V measurements in detail. The ideality factor and the saturation current of this diode is 20.1 and 1.19×10^{-4}A, respectively. The results indicated that the novel $AZO/SiO_2/p$-Si/ heterojunction device could be not only used for low cost solar cell, but also could be used for the high quantum efficiency enhanced photodiode in UV and visible lights, and also for other applications.

10. References

Ashok, S.; Sharma, P.P.; Fonash, S.J. (1980) IEEE Transactions on Electron Devices 27, (1980) pp. 725-730

Bruk, L.; Fedorov, V.; Sherban, D.; Simashkevich, A.; Usatii, I.; Bobeico, E.; Morvillo, P. (2009) "Isotype bifacial silicon solar cells obtained by ITO spray pyrolysis", Materials Science and Engineering B 159–160 (2009) pp.282–285

Baik, D.G.; Cho, S.M. (1999). "Application of sol-gel derived films for ZnO/n-Si junction solar cells, Thin Solid Films 354 (1999) pp.227-231

Chaabouni, F.; Abaab, M. Rezig, B. (2006). "Characterization of n-ZnO/p-Si films grown by magnetron sputtering", Superlattices and Microstructures, vol 39, (2006) pp.171-178

Cheknane, Ali (2009) "Analytical modelling and experimental studies of SIS tunnel solar cells", J. Phys. D: Appl. Phys. 42 (2009) pp.115302-115307

Chen, X. D.; Ling, C. C.; Fung, S.; Beling, C. D. (2006). "Current transport studies of ZnO/p-Si heterostructures grown by plasma immersion ion implantation and deposition", Applied Physics Letters, vol 88, (2006) pp.132104-132107

Canfield, L.R.; Kerner, J.; Korde, R. (1990). "Silicon photodiodes optimized for the EUV and soft xray regions", EUV.X-Ray.andGamma-Ray Instrumentation for Astronomy. SPIE vol 1344 , (1990) pp. 372−377

Granqvist, C.G. (2007) "Transparent conductors as solar energy materials: A panoramic review", Sol. Ener. Mater. Sol. Cells 91, (2007) pp.1529-1598

Granqvist, Claes G. (2007) "Transparent conductors as solar energy materials: A panoramic review", Solar Energy Materials & Solar Cells 91 (2007) pp.1529–1598

He, B.; Ma, Z.Q. et al., (2009). "Realization and Characterization of ITO/AZO/SiO$_2$/p-Si SIS Heterojunction", Superlattices and Microstructures 46, (2009) pp.664-671

He, B.; Ma, Z.Q. et al., (2010). "Investigation of ultraviolet response enhanced PV cell with silicon-based SINP configuration", SCIENCE CHINA Technological Sciences 53, (2010) pp.1028-1037

Koida, T.; Fujiwara, H.; Kondo, M. (2009) "High-mobility hydrogen-doped In$_2$O$_3$ transparent conductive oxide for a-Si:H/c-Si heterojunction solar cells", Solar Energy Materials & Solar Cells 93 (2009) pp.851–854

Kittidachachan, P.; Markvart, T.; Ensell, G.J.; Greef, R.; Bagnall, D.M. (2005). "An analysis of a "dead layer" in the emitter of n+pp+ solar cells", Photovoltaic Specialists Conference, Conference Record of the Thirty-first IEEE, vol 3-7, (Jan., 2005) pp. 1103-1106

Mridha, S.; Basak, Durga. (2007). "Ultraviolet and visible photoresponse properties of n-ZnO/p-Si heterojunction", Journal of Applied Physics, Vol 101, (2007) pp.083102

Ramamoorthy, K.; Kumar, K.; Chandramohan, R.; Sankaranarayanan, K. (2006) "Review on material properties of IZO thin films useful as epi-n-TCOs in opto-electronic (SIS solar cells, polymeric LEDs) devices", Materials Science and Engineering B 126 (2006) pp.1–15

Song, Dengyuan; Aberle, Armin G.; Xia, James (2002). "Optimisation of ZnO:Al films by change of sputter gas pressure for solar cell application", Applied Surface Science 195, (2002) pp.291-296

Singh, R.; Rajkanan, K.; Brodie, D.E.; Morgan, J.H. (1980) IEEE Transactions on Electron Devices 27, (1980) pp. 656-662

Wenas, Wilson W.; Riyadi, S. (2006). "Carrier transport in high-efficiency ZnO/SiO$_2$/Si solar cells", Solar Energy Materials and Solar Cells 90，(2006) pp.3261-3267

Crystalline Silicon Thin Film Solar Cells

Fritz Falk and Gudrun Andrä
Institute of Photonic Technology
Germany

1. Introduction

In the last few years the marked share of thin film solar cells increased appreciably to 16.8% (in 2009). The main part of that increase refers to CdTe modules (9.1%) followed by silicon thin film cells, that is amorphous silicon (a-Si) cells or tandem cells consisting of a-Si and nanocrystalline silicon (μc-Si). For a review on thin film solar cells in general see (Green, 2007) and on a-Si/μc-Si cells see (Beaucarne, 2007). The a-Si cells suffer from a low efficiency. In the lab the highest efficiency up to now is 10.1% on 1 cm² (Green et al., 2011), whereas in the industrial production modules reach about 7%. In order to achieve the required electronic quality of hydrogenated amorphous silicon (a-Si:H), low deposition rate (max. 50 nm/min) PECVD (plasma enhanced chemical vapour deposition) is used for deposition which makes production more expensive as compared to CdTe modules. This is even worse for the layer system in a-Si/μc-Si tandem cells for which the more than 1 μm thick nanocrystalline μc-Si layer is deposited by PECVD, too, however with much lower deposition rates in the 10 nm/min range. Cells consisting just of μc-Si reached 10.1% efficiency (Green et al., 2011), just as a-Si-cells, whereas tandem cells arrived at 11.9%, both for lab cells, whereas in production the results are below 10%. The low deposition rate combined with the limited efficiency, make these cells not too competitive compared to CdTe cells, which, at lower cost, reach 11% in industrial production, or to CIGS (Copper-indium-gallium-diselenide) cells with similar efficiencies.

As an alternative, polycrystalline (grains in the μm range) or multicrystalline (grains >10 μm) silicon thin film solar cells receive growing interest (Beaucarne et al., 2006). The present paper reviews the status of these cells, and on the other hand gives details of laser based preparation methods, on which the authors have been working for many years.

Both types, poly- and multicrystalline silicon thin film cells, are prepared by depositing amorphous silicon followed by some crystallization process. One main advantage of the crystallization process is that the electronic quality of the virgin a-Si is not important. Therefore high rate deposition processes such as electron beam evaporation or sputtering can be used which are much less expensive as compared to low rate PECVD. In case of sputtering doped thin films can be deposited by using doped sputtering targets, whereas in electron beam evaporation the dopands are coevaporated from additional sources. So, in these deposition processes the use of toxic or hazardous gases such as silane, phosphine or diborane is avoided, reducing the abatement cost.

Polycrystalline silicon layers for solar cells can be prepared in a single crystallization step. The layer system containing the doping profile is deposited in the amorphous state and is

crystallized in a furnace to result in grains about 1 μm in size. This process had been industrialized by the company CSG and is described in Sect. 2. In the lab CSG reached 10.4% efficiency on 90 cm² minimodules (Keevers et al., 2007). Alternatively pulsed excimer laser melting and solidification can been used, which is a standard process in flat panel display production (Sect. 2).

Preparation of multicrystalline silicon thin film solar cells with grains exceeding 10 μm in size is under investigation. This topic is extensively dealt with in Sect. 3. Usually a two-step preparation scheme is used. In a first step a multicrystalline thin seed layer with the desired crystal structure is prepared (Sect. 3.3), which in a second step is epitaxially thickened (Sect. 3.4). For both, seed layer preparation and epitaxial thickening, different processes have been tested. There are, however, attempts to crystallize the complete layer stack of a thin film solar cell in one electron beam melting step (sect. 3.2). The idea for the multicrystalline cells is that in the large grains recombination is reduced, if the crystal quality is high enough, so that the efficiency should exceed that of cells with μm sized grains. Particularly, if the ratio of grain size to layer thickness is large (e.g. 50), such as in multicrystalline wafer cells, a similar efficiency potential is expected. This would require 100 μm large grains for 2 μm thick silicon layers. The preparation methods for large grained multicrystalline silicon layers divide in low and high temperature processes. The high temperature processes are rather straight forward for producing large grains (Beaucarne et al., 2004). However, temperature resistant substrates are required which are expensive. Much more demanding are preparation methods working at temperatures endured by low cost substrates such as glass. One such method is diode laser crystallization. The epitaxial thickening processes, as well, divide in high and low temperature processes with the same drawbacks and advantages. Several methods are presented in Sect. 3. The result of seed layer preparation as well as epitaxial thickening, via melt or in the solid state, depends on temperature history and is explained by the kinetics of phase transformation. The basic notions of this theory as far as they are important for silicon thin film solar cell preparation, are summarized in Sect. 5. Post-crystallization treatments such as rapid thermal annealing and hydrogen passivation are explained in Sect. 4.

Even single crystalline silicon thin film cells have been prepared by a transfer process starting from a silicon wafer from which a layer is detached and epitaxially thickened to several 10 μm thickness (Reuter et al., 2009; Brendel, 2001; Brendel et al., 2003; Werner et al., 2009) to reach an efficiency of 17%. This type of cells, which are much thicker than the poly- and multicrystalline silicon thin film cells, and which cannot be prepared in the typical sizes of thin film technology such as > 1 m², is not the topic of this paper.

2. Polycrystalline silicon thin film solar cells: 1 μm grains

Polycrystalline silicon thin film solar cells in superstrate configuration have been fabricated industrially for some years by the company CSG in Thalheim, Germany. These are the only cells with grains above 1 μm ever fabricated industrially. The preparation steps are as follows (Green et al., 2004). On a borosilicate glass substrate spherical glass beads are deposited, which finally are responsible for light trapping. Then an about 70 nm thick SiN antireflection and barrier layer is deposited by PECVD. On top about 1.5 μm amorphous silicon (a-Si:H) is deposited again be PECVD including the final doping profile n⁺pp⁺. The silicon layer is crystallized in the solid state in an 18 h furnace annealing step at about 600°C during which grains of about 1 μm in size form. To activate the dopants a rapid (2 min)

thermal annealing step at 900°C follows. The silicon layers are passivated by a hydrogen plasma treatment. Finally rather demanding structuring and contacting processes follow. In production, modules 1x1.4 m² in size reached about 7% efficiency. In the lab 10.4% efficiency were achieved on 92 cm² minimodules (Keevers et al., 2007). The production was stopped, probably because of the high cost PECVD deposition, which was used because the method was the only one available for silicon deposition in the m² range. In the lab, high rate electron beam evaporation was tested as an alternative which delivered minimodules with the efficiency of 6.7%, similar to that of the industrially produced modules (Egan et al., 2009; Sontheimer et al., 2009).

The grain size originating in the furnace anneal is dictated by the interplay of crystal nucleation within the amorphous matrix and growth of the nuclei (see Sect. 5). One can influence both processes by the temperature of the annealing step. Practically, however, there is not much choice. At lower temperature the annealing time required for complete crystallization would reach unrealistic high values so that this is not possible in production. Higher temperatures are not endured by the glass substrate for the time span needed for crystallization. Even at 600°C 18 h are required for crystallization and high temperature resistant borosilicate glass has to be used instead of a much cheaper soda lime glass.

As an alternative for the furnace crystallization pulsed excimer laser crystallization via the melt is a process industrially used in flat panel display production. For this application, however, rather thin films (<100 nm) are required and the resulting grain size is rather small, typically below 1 µm. In the context of solar cell preparation requiring films thicker than 1 µm this method has been mentioned only rarely (Kuo, 2009).

3. Multicrystalline silicon thin film solar cells: grains > 10 µm

3.1 Basic considerations

As mentioned in the last paragraph, grains larger than about 1 µm cannot be prepared by direct deposition of crystalline silicon, nor by solid phase crystallization of a-Si nor via melting a-Si by short laser pulses. Large grains can be produced from the melt only if the melt is cooled below the equilibrium melting point slowly so that the melt stays long enough in a region of low nucleation rate and there is time enough for the few nucleating crystallites to grow to large size. Low cooling rate means low heat flow into the substrate following from a low temperature gradient in the substrate. This can be achieved if the melting time of the silicon layer is larger than in excimer laser crystallization, i.e. much larger than 100 ns. To reach longer melting times the energy for melting has to be delivered on a longer time scale. For energy delivery scanned electron beams or scanned laser beams have been used. However, the longer melting time has the consequence, that dopand profiles, introduced into the virgin a-Si for emitter, absorber, and back surface field, get intermixed due to diffusion. Typical diffusion constants in liquid silicon are in the 10^{-4} to 10^{-3} cm²/s range (Kodera, 1963) so that dopands will intermix over a distance of 1 µm within 10 to 100 µs. Nevertheless a one-step crystallization procedure for a solar cell layer system has been done by electron beam melting, discussed in Sect. 3.2. Alternatively a two-step procedure has been used. In a first step a thin seed layer is crystallized to large grains from a-Si by laser irradiation. In a second step the seed is thickened epitaxially. Seed and epitaxial layer can be differently doped so that the seed can act as the emitter and the epitaxial layer as the absorber of the solar cell. Alternatively, the seed may act as a highly doped back surface field layer with the epitaxial layer acting as a moderately doped absorber. The emitter is generated on top in a third preparation step.

An important issue in any of the mentioned preparation steps is the choice of the substrate. This choice depends on the thermal load the substrate experiences during the silicon crystallization process. Plastic substrates are not useful for any of the processes described in Sect. 3 since the substrate temperature well exceeds 200°C. One usually divides the crystallization methods into low temperature processes for which glass can be used as a substrate and high temperature processes for which glass is not sufficient. Instead, ceramics (e.g. alumina) or graphite has been used. These substrate materials, however, are much more expensive than glass so that the economic consequences for the high temperature routes are not so pleasant.

Typically, in high as in low temperature processes some barrier layer is used to prevent the diffusion of foreign atoms from the substrate material into the silicon layer during the processing steps. The barrier layer has to fulfil different requirements except of its main purpose. First of all it has to withstand liquid silicon, i.e. it should not decompose or react with the silicon melt. Moreover, it should not release gases which would blow off the silicon layer. Then it should be well wetted by liquid silicon. Otherwise the silicon film during melting could dewet to form droplets. This latter requirement is the reason that SiO_2 is not useful as a barrier layer. Silicon nitride or silicon carbide are better suited. However, if deposited by PECVD the layers contain too much hydrogen which is released during silicon melting so that the silicon films are destroyed. According to our experience sputtered silicon nitride is well suited if prepared correctly.

3.2 Single step layer preparation - electron beam crystallization

As mentioned in Sect. 3.1 silicon solar cell absorbers in substrate configuration have been prepared by electron beam crystallization in a one step process (Gromball et al., 2004; Amkreuz et al., 2009). On a glass substrate with a barrier layer (e.g. SiC) 7 to 15 µm of p-doped (10^{17} cm^{-3} B) nanocrystalline silicon was deposited by high rate (up to 300 nm/min) PECVD from trichlorosilane. This layer was crystallized by scanning a line shaped electron beam (15 cm x 1 mm). At a scanning rate of 1 cm/s a beam energy density of 500mJ/cm² has been used so that any position is treated for about 0.1 s. The resulting grain size is in the mm range. To get a solar cell a 30 nm thick n-doped a-Si heteroemitter was deposited onto the crystalline absorber by PECVD. The maximum solar cell parameters achieved so far were j_{sc} = 12.4 mA/cm², V_{oc} = 487 mV, and an efficiency of 3.5% (Amkreuz et al., 2009). Obviously the absorber doping is too high and a back surface field is missing. Work is ongoing to improve these cells.

3.3 Two-step process - seed preparation

In the two-step preparation method first a thin seed layer with the desired crystal structure is prepared which can be used as a back surface field layer or as emitter in the final solar cell. The absorber is then prepared by epitaxial thickening of the seed. In case of a cell in superstrate configuration (illumination through the glass), the seed layer should be rather thin. This is to reduce light absorption in the seed which is highly doped (as emitter or as back surface field layer) and shows only low photovoltaic activity. Two seed preparation methods have been investigated: aluminium induced crystallization (Fuhs et al., 2004) as well as laser crystallization.

3.3.1 Aluminum induced crystallization for seed preparation

Aluminum induced crystallization (AIC) works as follows: On to the substrate an aluminum layer is deposited by sputtering or evaporation. On top follows an amorphous silicon layer.

When the Al/a-Si layer system is heated (350°C…550°C below the eutectic temperature of the Al-Si system at 577°C) a layer exchange process takes place combined with silicon crystallization, which is completed, at 500°C, in about 30 min. (Pihan et al., 2007). Finally, a crystalline silicon layer rests on the glass and is covered by an aluminium layer, which may contain silicon islands. The silicon layer is highly p-doped typically by 10^{19} cm^{-3} Al (Antesberger et al., 2007). It has been reported that the details of the process and the properties of the final silicon layer depend on the thickness of an aluminum oxide layer which was present between Al and a-Si before the tempering step. Typical resulting silicon grain sizes are in the range of 10 µm. The preferred grain orientation is (100) but other orientations occur as well (Schneider et al., 2006a). Typical layer thicknesses are 300 nm for Al and 375 nm for Si (Fuhs et al., 2004), which is a bit high for seed layers. However, even silicon films thinner than 100 nm have been crystallized by AIC (Antesberger, 2007). Some work has been done to understand the thermodynamics and the kinetics of the process (Wang et al., 2008; Sarikov et al., 2006; Schneider et al., 2006b). It seems that silicon diffuses through the thin alumina layer into the aluminum where it preferably further diffuses towards the glass along the aluminum grain boundaries. When aluminum gets supersaturated by silicon, nucleation of silicon crystallites starts preferably at the interface to the glass substrate. The driving force for the process is the free energy difference between metastable amorphous and absolutely stable crystalline silicon. Finally, the a-Si completely has diffused through the aluminum which then rests on top. Before the crystalline silicon layer can be used as a seed, the aluminum layer has to be removed, e.g. by wet chemical etching using HCl. Challenging is the removal of the silicon islands included in the aluminum layer and of the aluminum oxide film. The removal of both is crucial for good epitaxy (Rau et al., 2004). The inverse process with the starting sequence glass/a-Si/Al and the final sequence glass/Al/c-Si works as well (Gall et al., 2006). It has some advantages for cells in substrate configuration, e.g. that a Al back contact is formed automatically. However, the Al/Si contact has the consequence that any further processing steps, e.g. epitaxy, cannot be performed above the eutectic temperature of the Al-Si system of 577°C. For this reason the inverse process was abandoned.

There has been done a lot of work on silicon crystallization by other metals, e.g. Au, Ni, but these methods did not find application in solar cell preparation.

3.3.2 Laser crystallization for seed preparation

To get large silicon crystals by laser crystallization the beam of a cw laser is scanned so that the irradiation time at each position is in the ms range, much larger than during pulse laser irradiation mentioned in Sect. 2. Under these conditions the temperature gradient and therefore the heat flow in the substrate is low so that the melt undercools only slowly, nucleation rates are low, and nucleated crystals have time enough to grow to large sizes (see Sect. 5). First results on this method date back to the late 1970ies (Gat et al., 1978; Colinge et al., 1982). At these times laser crystallization was performed for applications in microelectronics. Therefore amorphous silicon on wafers covered by oxide was used as starting material. The only available well suited lasers were argon ion lasers emitting green light at 514 nm wavelength with a total power of up to 15 W. Typically a circular Gaussian beam with diameter in the 40 µm range was scanned across the sample. At a scanning rate of 12.5 cm/s already in 1978 grains 2x25 µm in size were produced (Gat et al., 1978). Due to the high thermal conductivity of the wafer substrate a rather high power density is needed for melting and crystallization in this case. Only later glass was discovered as a useful substrate

for thin film transistor applications (Michaud et al., 2006) as well as for solar cells (Andrä et al., 1998; Andrä et al. 2000). On glass with low thermal conductivity power densities of about 20 kW/cm² are needed at scanning speeds of several cm/s. Due to the limited laser power the spot diameter was limited to about 100 μm.
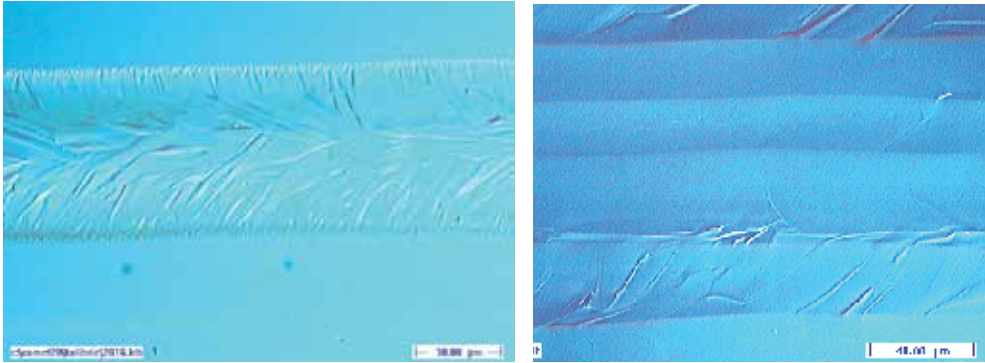
Fig. 1. Optical micrograph of a silicon layer crystallized by scanning the circular beam of an argon ion laser. Left: single scan; right: overlapping scans

Fig. 1 (left) shows an optical micrograph of a single trace produced by scanning a circular Ar ion laser beam. At the rim very fine crystals were produced. There the laser power just was able to generate a temperature a bit above the melting point of a-Si, which is well below the melting point of crystalline silicon (see Sect. 5.1). In the rim region a strongly undercooled melt is generated which immediately (that is must faster than the irradiation time) crystallizes to fine grained (about 100 nm) silicon. Towards the center of the trace the power density increases so that the temperature gets higher, the undercooling gets lower, and a bit larger grains solidify. In the central part the laser power is high enough to produce a silicon melt above the equilibrium melting point of crystalline silicon (1412°C). There solidification occurs only when the laser beam already has passed. The slowly undercooling liquid silicon is in contact with the small crystallites of the rim region which crystallized earlier. From these, lateral epitaxial growth takes place. The crystallization direction coincides with the temperature profile following the scanned laser beam. Those of the many nuclei are successful in epitaxy for which the fastest crystallographic growth direction coincides with the temperature gradient. Therefore, a selection mechanism is active and only few of the potential nuclei grow. As a consequence large grains form several 10 μm wide and over 100 μm long. To get not just one crystalline trace but a completely crystallized area, one just has to scan the laser beam in overlapping rows (Fig. 1, right). In the second row the laser beam remelts part of the previous row with the consequence that now the melt is in contact with the large grains produced in the previous row. Therefore large crystals are already present for lateral epitaxy to occur. In this way large areas covered by large grains can be produced. Defect population in films generated in this way has been investigated (Christiansen et al., 2000). The dislocation density was rather low. Grain boundaries are mostly $\Sigma 3$ and $\Sigma 9$ twin boundaries which are expected to be not active electrically. The grain orientation is at random with no preferential texture.

Later on, for crystallization the argon ion laser was replaced by a solid state cw Nd:YAG laser, emitting green light of 532 nm wavelength after frequency doubling. Similar results were obtained with this laser type (Andrä et al., 2005a). Both, argon ion as well as Nd:YAG lasers,

have rather limited power so that it is impossible to crystallize seed layers for large area solar cells in an industrial environment. For example, a 1 m² module would require many hours laser treatment. Therefore, when looking for high power lasers we ended up with diode lasers, emitting in the near infrared. However, the absorption coefficient of a-Si for 806 nm radiation, the shortest wavelength available for high power diode lasers, at room temperature is only about 0.3 µm⁻¹, as compared to 25 µm⁻¹ for green light. Fig. 2 shows the absorption of 806 nm radiation in amorphous silicon (electron beam deposited, hydrogen free) as calculated from optical properties (*n* and *k*) measured from room temperature up to 600°C and extrapolated up to 1000°C. The maxima and minima are due to interference effects in the silicon layer.

Obviously there exists a problem for thin films, particularly at room temperature. In thin films, only a small amount of the incoming radiation is absorbed at room temperature. Therefore, to heat the silicon film, a rather high power density is needed. When heating started successfully then the absorption increases and a run-off sets in which is only limited after melting, when the reflectivity jumps up. So the process has some inherent instability, which can be handled only when one preheats the substrate to about 600°C so that laser heating starts at a higher absorption already. The substrate heating has another positive effect, namely to reduce the cracking tendency of the glass substrate, for which we use a borosilicate glass (Schott boro 33) with a thermal expansion coefficient very near to that of silicon. Work using diode lasers for crystallization started 2006 (Andrä et al., 2006).

For our seed layer crystallization we use LIMO line focus lasers (806 nm wavelength, 13 mm x 0.1 mm focus and 30 mm x 0.1 mm focus) with maximum power density of up to 25 kW/cm² (Andrä et al., 2006), allowing for scanning speeds up to several cm/s. Fig. 3 shows an EBSD map of a crystallized region demonstrating large grains in the 100 µm range in 450 nm thick films. With the diode laser we can go down to 100 nm thin films. In these the grains size is in the 30 µm range. A further problem with thin films is dewetting. This means that holes form when the silicon film is liquid. It even happens that the holes grow to large sizes and only a part of the substrate is covered by silicon. Dewetting can be reduced if the wetting angle of liquid silicon on the substrate is low. This can be influenced by the barrier layer on the glass substrate.
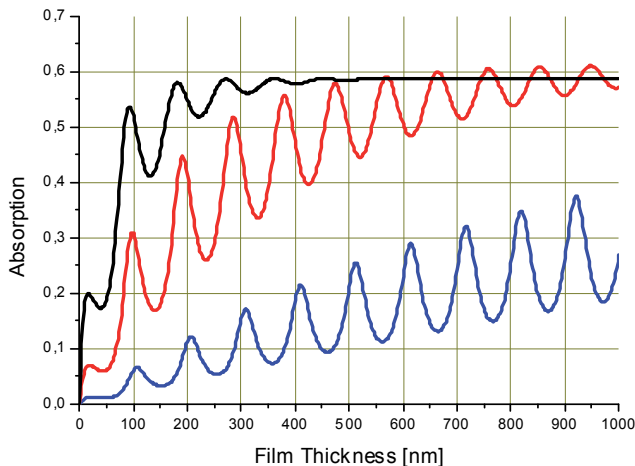
Fig. 2. Absorption of 806 nm diode laser radiation in an amorphous silicon thin film on glass as depending on film thickness. Film temperature 20°C (blue), 600°C (red), and 1000°C (black).
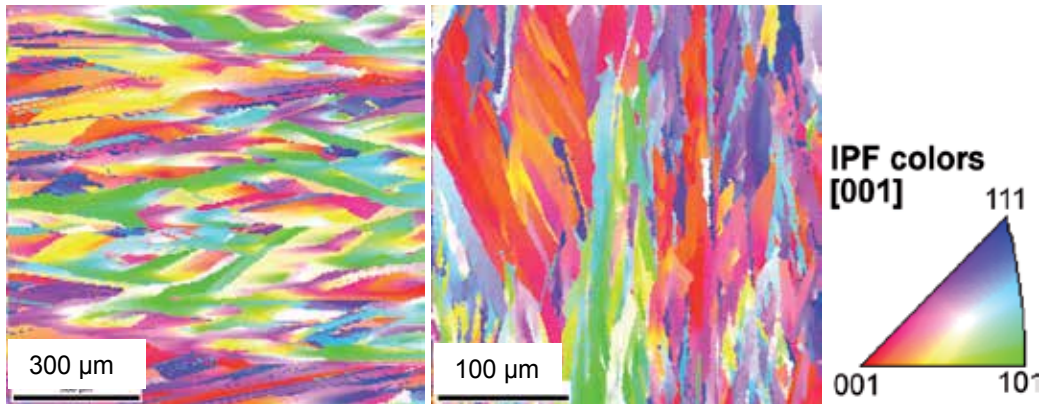
Fig. 3. EBSD map (inverse pole figure) of diode laser crystallized seed layers 450 nm (left) and 110 nm (middle) thick. Color code for grain orientation is shown on the right.

Concerning the throughput, laser companies are just developing line focus diode lasers with long lines (Lichtenstein 2010) which would allow crystallization of a 1 m² module within minutes.

If seed layers thinner than 100 nm are to be crystallized diode lasers cannot be used due to too low absorption even when preheated. We tested a pulsed green laser (JenLas ASAMA) emitting 515 nm wavelength radiation (Andrä et al., 2010). This laser has a line focus up to 100 mm long and 5 to 10 µm wide and it delivers 600 ns pulses at a repetition rate of up to 80 kHz. At a fluence of about 1.2 J/cm² the sample was shifted 1.5 µm between subsequent pulses. In this way 60 nm thin seed layers were crystallized without any preheating with resulting grains several µm wide and several 10 µm long (Fig. 4). Obviously, the melt generated during each laser pulse solidifies by lateral epitaxy so the grains generated by the previous pulse grow stepwise. Finally long grains form, which continue over many pulses. Since the width of the melt is 5 µm in our case and the melt exists for a time interval in the several µs range, the solidification speed is in the m/s range. This value is near the maximum following from solidification kinetics (see Sect. 5).
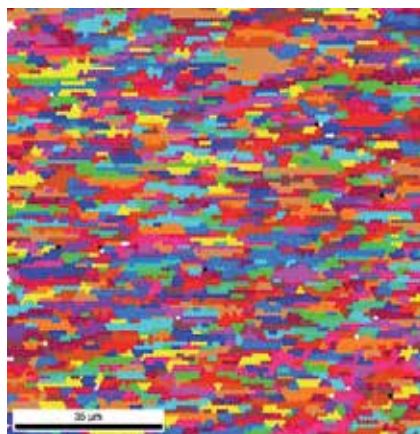
Fig. 4. EBSD map (inverse pole figure) of pulse laser crystallized seed layers 60 nm thick.

3.4 Two step process - epitaxial thickening

In the two step preparation method on top of the multicrystalline seed layer the absorber of the solar cell is prepared by epitaxial growth. Several methods have been used which can be classified into direct epitaxial deposition and deposition as amorphous silicon followed by epitaxial crystallization, either in the solid state by furnace or by laser annealing or via laser melting. Particularly in the cases without melting the cleanliness of the interface between crystalline seed and amorphous silicon to be epitaxially crystallized is an issue. Any contaminants present, even small amounts of a monolayer, will jeopardize epitaxial crystallization or at least increase the amount of extended defects in the epitaxial layer appreciably. First of all, any silicon oxide has to be removed from the seed surface. This can be achieved by HF. A 2% to 5 % solution in water is most useful. Success can be observed by the naked eye. When HF has removed the oxide the silicon surface gets hydrogenated which makes the surface hydrophobic and the etching solution dewets, i.e. forms droplets. Then the HF solution can be blown off by nitrogen. The hydrogenated surface state remains stable in ambient air at room temperature for about 1 h so that there is time enough to introduce the sample into a deposition chamber for a-Si deposition. However, other possible contaminants are not so easily removed. It turned out as useful to start with an RCA cleaning step before HF treatment. The RCA step removes e.g. organic contaminants.

3.4.1 Direct epitaxial deposition

The simplest epitaxial thickening procedure is direct epitaxial deposition of silicon on top of the seed layer. Several processes have been investigated in the past, high temperature CVD and, at intermediate temperature, electron beam evaporation, ECRCVD, and hot wire CVD.

The high temperature route has been reviewed recently (Beaucarne et al., 2004). The highest efficiency reached so far with this method is 8% (Gordon et al., 2007). On an alumina substrate seed layers were prepared by aluminium induced crystallization. Epitaxial thickening for the p-doped absorber with rates up to 1.4 µm/min was done by thermal CVD at 1130°C from trichlorosilane. The final emitter was prepared by phosphorus diffusion, or an a-Si heteroemitter was deposited by PECVD. Corresponding to the seed layer the grain size in the absorber is several 10 µm. It is expected that the efficiency is not so much limited by the grain size but by intragrain defects, which have been thoroughly investigated (van Gestel et al., 2009).

Even higher efficiencies of 11.1% were reached on seed layers crystallized by lamp heater zone melting on graphite and high temperature epitaxy for absorber growth (Kunz et al., 2008). The high temperature process has the advantage that it works on any grain orientation of the seed. However, high temperature resistant substrates such as alumina, silica, glass ceramics, or graphite are needed, which are not very feasible for large scale production.

At intermediate temperature both, electron beam evaporation, partly modified by ion assisted deposition, or ECR-CVD (electron cyclotron resonance CVD) has been tested for epitaxy on AIC seed layers. ECR-CVD was successfully applied at 585°C substrate temperature (Rau et al., 2004). However, epitaxy worked well only on (100)-oriented grains, which is the most common orientation following from AIC, but not the only one. At 670°C epitaxy by hot wire CVD worked on any grain orientation with a rate of 100 nm/min. Ion assisted deposition, that is electron beam evaporation plus some ionization of the silicon atoms, was tested for epitaxy as well. For the deposition a temperature ramp was carefully optimized with maximum temperature below 700°C. The deposition rate was 300 nm/min. The highest achieved open circuit voltage of solar cells was 453 mV (Straub et al., 2005). Direct epitaxy during electron

beam evaporation at 550°C substrate temperature has successfully been demonstrated (Dogan et al., 2008). Solar cells prepared with this process reached 346 mV open circuit voltage and 2.3% efficiency, which is a bit low as compared to the values achieved by other methods.

3.4.2 Solid phase epitaxy in furnace

Technically the most simple way to achieve epitaxial growth is to deposit first an amorphous layer on top of the cleaned seed layer, and then to epitaxially crystallize the layer by furnace annealing in the solid state. The layer to be crystallized can already contain the desired doping profile which remains during the annealing step. The main critical point with this simple procedure is that not only an epitaxial crystallization front moves into a-Si, but also spontaneous nucleation will occur within a-Si followed by growth of crystallites. So there exists a competing process to the desired epitaxy. The question arises, which of the two succeeds. The speed of the epitaxial front of course depends on temperature (described by Jackson-Chalmers equation, see Sect. 5.1) and so does nucleation, described by classical nucleation theory (Sect. 5.2), and growth of nuclei, the latter phenomena described together by Avrami-Mehl equation (Sect. 5.4). An important point, which makes SPE possible, is that, if no nuclei pre-exist in the amorphous matrix, nucleation does not start immediately. Instead it needs some time, called time lag of nucleation, until a stationary population of nuclei evolves (Sect. 5.3). Only after that time lag the stationary nucleation rate applies at fixed temperature, described by classical nucleation theory, and crystal nuclei appear. So any successful epitaxy relies on the time lag of nucleation. The thickness of an epitaxially crystallized layer is just given by the time lag of nucleation times the speed of the epitaxial crystallization front. After the time lag, in the virgin amorphous silicon crystalline nuclei of random orientation appear resulting in fine grained material, such as is generated by direct furnace crystallization (see Sect. 2) without seed. For successful epitaxy one has to make sure that within the amorphous phase there are no nuclei present which could form during deposition already.

In the last few years we developed the technique of SPE on diode laser crystallized seed layers on borosilicate glass substrates (Andrä et al., 2008a; Schneider et al., 2010). The virgin a-Si layers including a doping profile were deposited at high rate (typically 300 nm/min) by electron beam evaporation at a substrate temperature in the 300°C range. At that temperature no nuclei form within a-Si. The layer system was then annealed in a furnace under ambient air. To control the progress of crystallization, an in situ measurement technique was installed. For this purpose, the beam of a low power test laser was sent through the sample. The transmitted intensity was monitored by a photocell. Since a-Si has a different optical absorption from c-Si, the progress of crystallization can be monitored easily. In particular, the crystallization process is complete when the transmission does not change any more. Fig. 5 shows a transmission electron micrograph of a cross section of an epitaxially thickened silicon film.
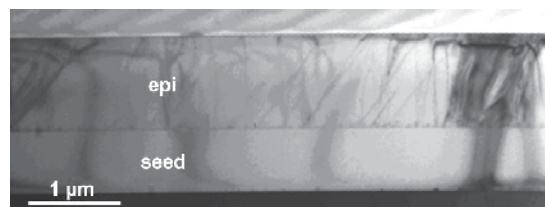
Fig. 5. Transmission electron microscopic cross section image of a film epitaxially thickened by furnace annealing.

In summary we could epitaxially crystallize up to 1.6 μm of a-Si at a temperature of 630°C within 3 h. The epitaxial quality as determined by EBIC was best in (100) oriented grains and worst in (111) grains. Moreover, the epitaxial crystallization speed depends on orientation and on the doping level. Higher doped layers crystallize faster. Solar cells prepared on these layers reached an efficiency of 4.9% after hydrogen passivation (Schneider et al., 2010). By TEM cross section investigations it was shown that the seed layers contain only very few extended defects such as dislocations, whereas the epitaxial layer contains much more. It seems that the cleaning procedure of the seed surface prior to a-Si deposition is crucial for good epitaxial quality. At least the dislocation density in the epitaxial layer could be reduced by an additional RCA cleaning step before removal of oxide by HF. However, this did not reflect in the achieved solar cell efficiencies.

3.4.3 Layered laser crystallization

The epitaxy method of layered laser crystallization has been developed in our group years ago (Andrä et al. 2005b, Andrä et al., 2008a). The principle is simple. During deposition of a-Si on top of the seed layer excimer laser pulses are applied repeatedly, which melt the newly deposited a-Si and a bit of the crystalline silicon beneath so that after each pulse epitaxial solidification occurs. Again, the layer thickness to be crystallized by one laser shot is limited by a competing nucleation process in the undercooling melt after the laser pulse. According to our experience about 200 nm of a-Si can be epitaxially crystallized by one laser pulse. The typical laser fluence needed is 550 mJ/cm². However, when during the whole thickening process the thickness of the crystalline layer beneath the newly deposited a-Si increases from the initial seed layer (say 200 nm) to the final absorber thickness (say 2 μm) the laser parameters or the thickness of the newly deposited a-Si have to be adjusted so that the laser pulse just melts the a-Si and bit of c-Si beneath. This adjustment is necessary because the thermal properties of glass, c-Si, and a-Si differ so that the temperature profiles change during the process if the laser energy would be kept constant. In the layered laser crystallization process epitaxy works independently of the grain orientation, which is an advantage since crystal orientation in the seed is at random. For the process, the laser pulse has to be fed through a window in the deposition chamber onto the growing layer. In this way the pulses can be applied without stopping deposition. For a-Si deposition we use electron beam evaporation which has first the advantage of high deposition rate, at least an order of magnitude higher than for PECVD, and secondly the advantage that deposition is directed so that no deposition occurs at the laser window. Doping is achieved by co-deposition of boron or phosphorus. In our device we can deposit and laser irradiate substrates of up to 10x10 cm². The single laser spot has a size of 6x6 mm² with top hat profile. To cover the whole substrate area the laser spot is scanned over the substrate by a scanning mirror placed outside the deposition chamber. In order to avoid cracks in the glass substrate heating to about 600°C helps. Upscaling the system to m² surely is a challenge but not outside the technical possibilities. If properly optimized, about 10 laser pulses are needed at each position during absorber deposition to prepare a 2 μm thick epitaxial film. This makes sense only if the laser is fed into the deposition chamber and is applied without braking deposition, as we do it in our lab scale equipment.

In the epitaxial layer prepared by layered laser crystallization the number of extended defects like dislocations is much lower as compared to solid state epitaxy. This is because the mobility of crystallizing atoms is much higher in the melt than in a-Si so that correct placement is easier. The highest efficiencies achieved in solar cells prepared using the

method were 4.8% at an open circuit voltage of 517 mV (Andrä et al., 2005b; Andrä et al., 2007). These values were measured on cells without any light trapping.

3.4.4 Liquid or solid phase epitaxy by diode laser irradiation

The layered laser crystallization method described in the last section has the drawback that up-scaling into the industrial scale is not so easy. This is due to the fact, that the laser beam has to be fed into the deposition chamber and several pulses have to be applied at each position. That was the motivation for us to look for a method in which the complete absorber thickness is deposited in the amorphous state on top of the seed and to apply a single laser treatment to epitaxially crystallize the whole system in one run after deposition outside the deposition chamber.

The most obvious way to achieve epitaxy is via the liquid phase similar to layered laser crystallization. The main difference is that the whole amorphous absorber precursor layer is melted in one step down to the seed, so that epitaxial solidification is to occur after irradiation. It is a challenge to melt about 1 µm of a-Si without completely melt the about 200 nm thin c-Si seed beneath which would hamper any epitaxy. To crystallize a layer system more than 1 µm thick, a short pulse laser is useless. To get the required energy into the system the pulse fluence would have to be so large that ablation would occur at the surface. Moreover, the cooling rate of the melt after a short laser pulse would be so high, that nucleation is expected to occur in a surface near region before the epitaxial solidification front reaches the surface. Therefore we decided to use a scanned cw diode laser for this purpose with irradiation times in the ms range. In this case the cooling rate is low enough so that the melt stays long enough in a slightly undercooled state with low nucleation rate until the epitaxial solidification front reaches the surface. We succeeded in epitaxially crystallizing 500 nm in one run. However, forming of cracks is an issue. Moreover, due to the strong diffusion in the melt which intermixes any pre-existing doping profile, absorber and emitter cannot be crystallized in one step.

An alternative is solid phase epitaxy in which the amorphous layer is heated by the laser to a temperature of about 1100°C, below the melting point of a-Si. At such high temperature the solid phase epitaxial speed was determined to several 100 nm/s high so that epitaxy of 1 µm should be complete within several seconds.

4. Post-crystallization treatment

4.1 Emitter preparation

The emitter of the final solar cell can be prepared in different ways. One is to include emitter doping into the deposition sequence of the layer system so that no additional emitter preparation step is needed. This way has been chosen in the CSG process and in layered laser crystallization. It cannot be applied in case of liquid phase epitaxy of the whole layer stack (Sect. 3.4.4) since during melting for several ms, diffusion in the liquid state would intermix any dopand profile introduced during deposition. In this case, phosphorus doping of a boron doped absorber as in conventional wafer cells can be performed. The only difference is that the doping profile has to be much shallower. Another variant is to use amorphous heteroemitters. IMEC has found that this is the best emitter for their thin film solar cells prepared by the high temperature route (Gordon et al., 2007).

4.2 RTA and hydrogen passivation

To improve the solar cell performance some post-crystallization treatment is required. One point is dopand activation, the other defect passivation.

In order that dopand atoms like boron or phosphorus really lead to a free carrier concentration higher than the intrinsic one, it is necessary that the dopand atoms are included substitutionally in the lattice, i.e. that they rest on regular lattice positions replacing a silicon atom. If they are included interstitially, resting not on regular lattice positions, they are useless. If the silicon lattice forms from the melt the mobility of atoms is high enough so that the dopand atoms can occupy lattice positions. In this case no additional means are needed to make them active. This is not so in case of solid state crystallization. There most of the dopand atoms are included interstitially so that they are inactive. To let them replace silicon atoms substitutionally an additional heat treatment is needed, which is realized by a rapid thermal annealing (RTA) step. In the CSG process, for example, the whole system is heated to about 900°C for 2 min to achieve dopand activation (Keevers et al., 2007). It has been a lot of speculation if this RTA step also improves the grain structure by reducing the number of extended defects. This seems not to be the case (Brazil & Green, 2010).

In any case a hydrogen passivation step has to follow, in which different types of defects e.g. dislocations and grain boundaries, are passivated. Usually, a remote hydrogen plasma is applied to the layer system for 10 to 30 min at about 500°C. Crucial is that during cooling down at the end of the process the plasma has to be applied for some time. A lot of optimization work has been devoted to this passivation step (Rau et al., 2006), which easily can improve the open circuit voltage of the cell by 200 mV.

5. Kinetics of phase transformation

In Sect. 5 the basics of phase transformation relevant for silicon thin film crystallization, both from the melt and in the solid state are summarized (Falk & Andrä, 2006). The Section divides in the propagation of already present phase boundaries and in nucleation, including non-stationary nucleation. Kinetics of aluminum induced crystallization has already been reviewed (Pihan et al., 2007) and is not treated in the following. The facts presented in this section are the background for any successful crystallization of amorphous silicon, in the furnace or by laser irradiation. Quantitative values following from the equations depend on the material parameters of the system involved. These are rather well known for crystalline and for liquid silicon, mostly in the whole range of temperature involved in the processes. This is not the case for amorphous silicon, the properties of which strongly depend on the preparation conditions. They may appreciably differ for hydrogenated a-Si prepared by PECVD and hydrogen free a-Si deposited by electron beam evaporation. Therefore, quantitative predictions have to be taken with some care.

5.1 Propagation of phase boundaries

The propagation speed of already present phase boundaries into a metastable phase, i.e. the growth of a crystal into the undercooled melt or into amorphous silicon, can quantitatively be described by the Jackson-Chalmers-Frenkel-Wilson equation

$$v = v_0 e^{-g^*/kT} \left(1 - e^{\Delta\mu/kT} \right) \tag{1}$$

The prefactor $v_0 = a_0\gamma\nu$ depends on the atomic vibration frequency (Debye frequency) ν, the jump distance a_0 of the order of the lattice parameter of silicon and on a geometry factor γ of the order of 1. $\Delta\mu > 0$ is the difference in chemical potential of the phases involved. For the transition from liquid to crystalline $\Delta\mu$ may be approximated by

$$\Delta\mu = \Delta h_c (1 - \frac{T}{T_{mc}}) \tag{2}$$

where Δh_c is the latent heat per mole for melting and T_{mc} is the equilibrium melting temperature of 1685 K. For the crystallization of amorphous silicon $\Delta\mu$ is given in the literature (Donovan et al., 1983). g* is an activation energy for the jump of an atom from the parent to the final phase and is related to the self-diffusion coefficient D according to

$$D = \frac{a_0^2}{\gamma} \nu \, e^{-g^*/kT} \tag{3}$$

Results for crystallization from the melt and in the solid state are given in Figs. 6 and 7. In the melt the crystallization speed vanishes at the equilibrium melting point T_{mc} to increase to a maximum of about 16 m/s at 200 K undercooling. At even lower temperature the solidification front gets slower due to the increasing influence of the activation energy. At temperatures above the melting point the phase front runs into the crystal, i.e. the crystal melts and the speed changes sign. In Fig. 6. also the melting speed of amorphous silicon is shown (with opposite sign as compared to c-Si). Melting of a-Si starts at T_{ma}, which, depending on the deposition conditions of a-Si, is 200 to 300 K lower than the melting point of c-Si.

The crystallization speed in amorphous silicon shown in Fig. 7 increases with temperature, and reaches about 1 mm/s near the melting point of a-Si. At 600°C the speed is only about 0.2 nm/s which well correlates with the results obtained in furnace solid phase epitaxy (Sect. 3.4.2).
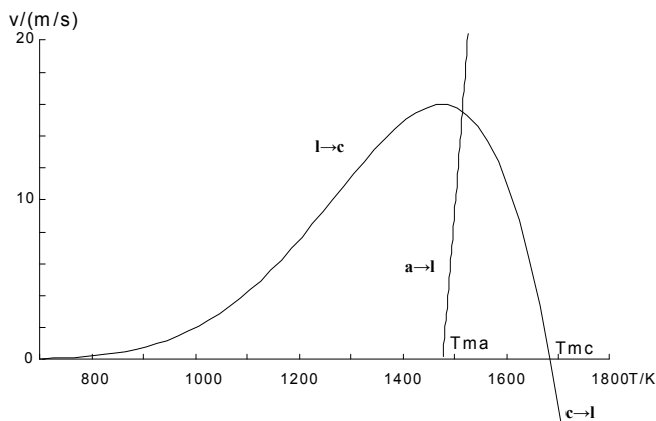
Fig. 6. Speed of the phase boundaries liquid-crystalline (lc) and amorphous liquid (al) for crystalline solidification form the melt and melting of a-Si, respectively.
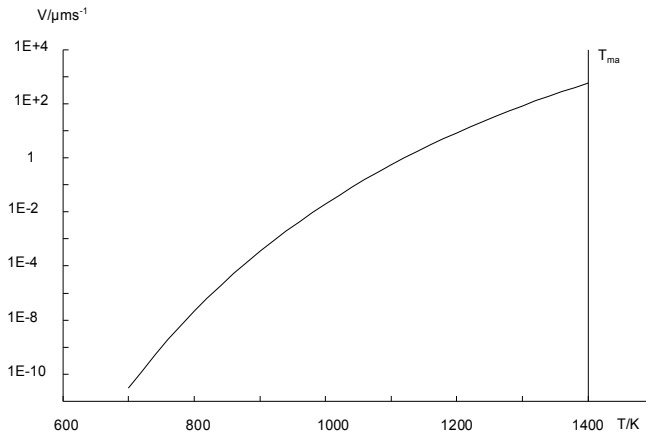
Fig. 7. Speed of a crystallization front in amorphous silicon as depending on temperature

5.2 Stationary nucleation rate

Classical nucleation theory gives the nucleation rate J, i.e. the number of nuclei appearing in a metastable phase per volume and time interval at given temperature. The value applies after some induction time (Sect. 5.3) and as long as not too much of the parent phase is consumed.

$$J = (36\pi)^{1/2} \gamma \nu \frac{j_c^{2/3}}{V_m} \sqrt{\frac{\Delta G_c}{3 j_c^2 \pi kT}} \; e^{\frac{\Delta G_c + g^*}{kT}} \tag{4}$$

In this formula V_m is the atomic volume and j_c and ΔG_c are the number of atoms in and the free energy of a critical nucleus of the new phase in the matrix of the parent phase, respectively. These are given by

$$j_c = \frac{32\pi}{3} V_m^2 \frac{\sigma^2}{\Delta\mu^2} \tag{5}$$

$$\Delta G_c = \frac{16\pi}{9} V_m^2 \frac{\sigma^3}{\Delta\mu^2} = \frac{1}{2} j_c \Delta\mu \tag{6}$$

σ is the interface energy between both the phases, which, however, is hard to determine independently of nucleation phenomena, and, in addition, may depend on temperature. Moreover, σ strongly influences the nucleation rate since via Eqs. 5&6 it enters Eq. 4 in the third power within the exponential. For crystallization in an undercooled silicon melt the stationary nucleation rate is plotted in Fig. 8 for a temperature dependent interfacial energy according to σ = (43,4+0.249 T/K) mJ/m^2 (Ujihara et al., 2001). Down to about 300 K below the equilibrium melting point the nucleation rate is very low to change within 100 K of further cooling by 35 orders of magnitude. Below 1200 K the nucleation rate gets rather flat at a value of 10^{35} m^{-3}s^{-1} = 0.1 nm^{-3}ns^{-1}. The stationary nucleation rate of crystallization in amorphous silicon is plotted in Fig. 9. There the values increase by 16 orders of magnitude when temperature is increased from 600 K to 1200 K. The nucleation rate then flattens off at 10^{17} m^{-3}s^{-1} = 0.1 μm^{-3}s^{-1} up to the melting point of a-Si of 1400 K.
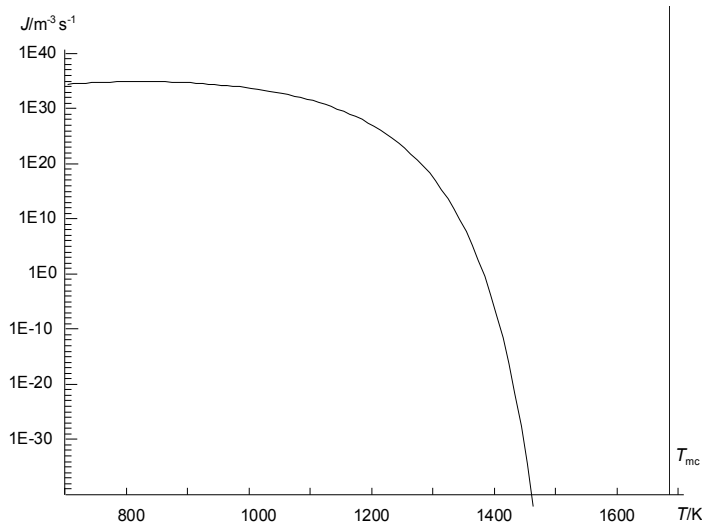
Fig. 8. Stationary nucleation rate for crystallization in an undercooled silicon melt
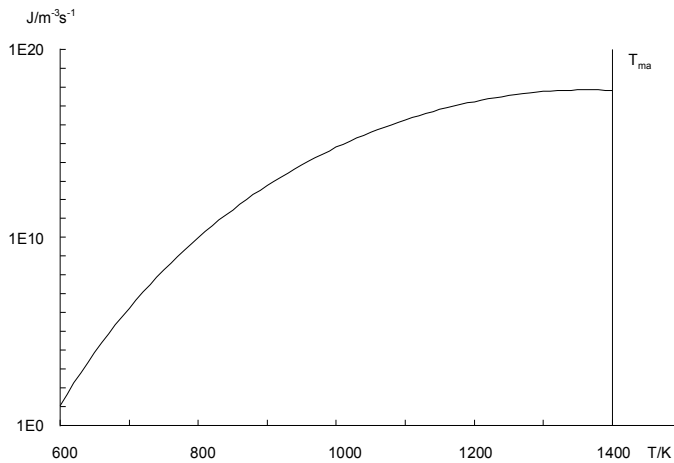
Fig. 9. Stationary nucleation rate for crystallization of amorphous silicon

5.3 Non-stationary nucleation

When the temperature of a system is changed abruptly from a value where the parent phase is absolutely stable and there are no nuclei present to another temperature where it gets metastable, then a population of nuclei evolves. Finally, a stationary distribution of nuclei emerges which leads to the stationary nucleation rate of Eq. 4. The master equation for the population of nuclei can be solved numerically. By some approximations a closed form for non-stationary nucleation rate has been derived (Kashchiev, 1969), which leads to the stationary value after some time lag of nucleation, which is given by

$$\tau = \frac{12}{\pi^2} \frac{kT}{\Delta G_c} \frac{j_c^2}{\beta_c} \tag{7}$$

β_c is the attachment rate of atoms to the critical nucleus given by

$$\beta_c = \gamma g v j_c^{2/3} e^{-g^*/kT} \tag{8}$$

Here g is an accommodation coefficient of the order of 1. The result for nucleation of c-Si from the melt is shown in Fig. 10. The time lag diverges at the equilibrium melting point and has a minimum of 30 ps around 1350 K. At all relevant temperatures the time lag is so small that it does not play any role in laser crystallization with pulses longer than 1 ns.

This is different for solid phase crystallization of amorphous silicon as shown in Fig. 11. The time lag goes down from 10^{13} s (or 300.000 years) at 600 K to 0.01 s at the melting point of a-Si (1400 K). That means that below 300°C crystallization never occurs whereas in the CSG process of furnace crystallization at 600°C the time lag is in the range of 2 h which does not play a major role when complete crystallization takes 18 h. However, it gives an upper limit for epitaxial growth by furnace annealing as described in Sect. 3.4.2.
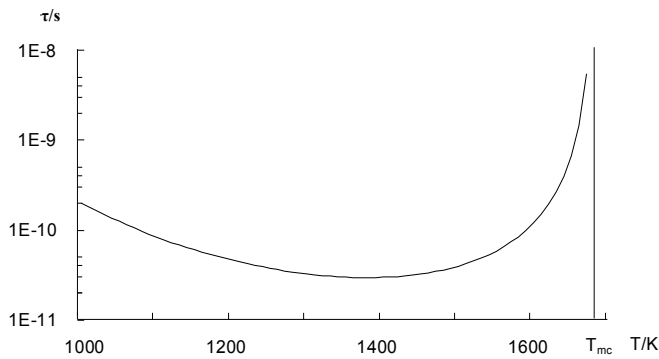
Fig. 10. Time lag of nucleation for crystallization from the melt for a fixed value of interfacial energy σ of 400 mJ/m²
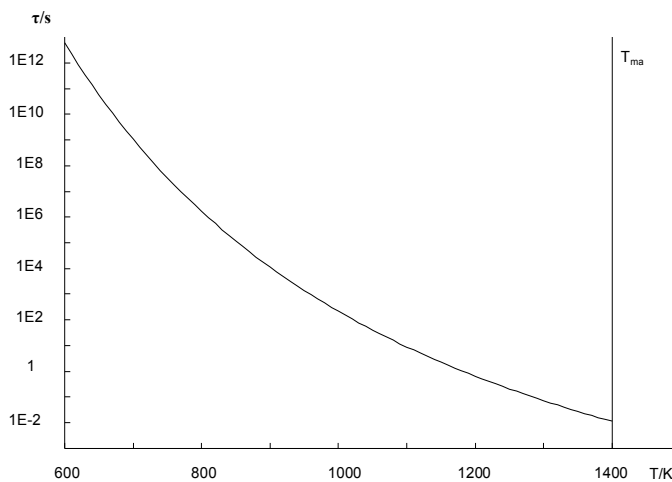
Fig. 11. Time lag of nucleation for crystallization of amorphous silicon

5.4 Complete kinetics of transformation

Stationary nucleation together with the growth of supercritical nuclei according to the Jackson-Chalmers equation leads to a continuous increase of the amount of the new phase on account of the parent phase. When one takes account that during the progress of phase transformation more and more parent phase is consumed and less volume is available for actual transformation, one ends up with the Avrami-Mehl equation (Avrami, 1940) for the volumetric amount of the new phase α

$$\alpha = 1 - e^{t^4/t_c^4} \tag{9}$$

with the characteristic time

$$t_c = \sqrt[4]{\frac{3}{\pi J v^3}} \tag{10}$$

J is the stationary nucleation rate of Eq. 4 and v is the speed of propagation of a phase front according to Jackson-Chalmers Eq. 1. In deriving Eq. 9 the time lag of nucleation τ has been neglected. To include this effect, one simply replaces t by $(t-\tau)$ in Eq. 9 for $t>\tau$. The resulting average grain size when the parent phase has been consumed completely is given by

$$D = 1.037 \sqrt[4]{\frac{v}{J}} \tag{11}$$

So the grains are the larger the higher the Jackson-Chalmers speed and the lower the nucleation rate is, which sounds reasonable. To get large grains from an undercooled melt one should keep the temperature in a range of not too high undercooling, where nucleation rate is low and growth rate is high (Figs. 6 and 8). Fig. 12 shows the expected final grain size in solid phase crystallization of amorphous silicon. It shows that in the CSG process at about 600°C (see Sect. 3.) grains of several μm are to be expected, which is in accordance with experiments. By increasing the crystallization temperature one cannot change the grain size appreciably. Lowering the temperature would lead to a rather high time needed for crystallization due to higher time lag of nucleation (Fig. 11), lower nucleation rate (Fig. 9), and lower growth rate (Fig. 7).
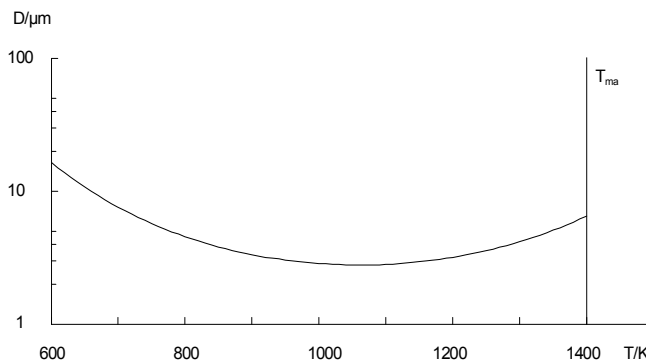
Fig. 12. Average grain size after solid phase crystallization of amorphous silicon as depending on temperature

6. Conclusion

Multi- and polycrystalline silicon thin film solar cells receive growing interest worldwide. Presently, the maximum efficiency reached by these types of cells is 10.4%. Different cell concepts and preparation methods are under investigation and no clear favourite way is identified up to now. The concepts differ in the resulting grain structure, i.e. size and quality, but also in the preparation technologies used and the processing time needed. Today it is not clear which of the methods will succeed in industrial production. In all the methods, pin holes in the films are an issue since they lead to shunting of the final cells. Another issue is dopand deployment, particularly along grain boundaries. This also may lead to shunting, which today limits the open circuit voltage to slightly above 500 mV. A further point is that TCO cannot easily be used as a front contact in superstrate cells since it hardly withstands the temperatures needed for crystallization. Usually a highly doped silicon layer is used instead, which, however, has somewhat low transparency.

Very important for thin film crystalline solar cell is a perfect light management so that about 2 μm of silicon is enough to absorb the solar spectrum. This can be achieved either by structured substrates or by texturing the surface. In the first case, the irregular substrate surface should not influence the crystallization behaviour. In the second case, the rough surface should not increase surface recombination. Generally, passivation of defects and of the surface is a crucial preparation step.

Concerning the theoretical description of the processes involved in crystallization, the basic equations are well understood. However, there are some issues with the material parameters involved, which, particularly for amorphous silicon, strongly depend on deposition conditions and therefore need to be determined individually. But even if numerical predictions may not completely coincide with experiments due to inadequate numerical values of the materials parameters, general trends can reliably be predicted.

All the mentioned issues need further investigation. Careful study of these topics is expected to lead to full exploitation the potential of the material. Multicrystalline thin film cells with a ratio of grain size over film thickness similar to multicrystalline wafer cells should deliver, if prepared correctly, comparable efficiencies. Therefore we expect the poly- and multicrystalline silicon thin film solar cells to gain increasing significance and may replace microcrystalline silicon cells. Multicrystalline silicon also can act as one partner in tandem cells which would further increase the efficiency.

7. Acknowledgment

8. References

Amkreutz, M.; Müller, J.; Schmidt, M.; Haschke, J.; Hänel, T. & Schulze, T.F. (2009). Optical and electrical properties of electron beam crystallized thin film silicon

solar cells on glass substrates. *Proc. 24th Europ. Photovoltaic Solar Energy Conf.*, pp. 2506-2509

Andrä, G.; Bergmann, J.; Falk, F.; Ose, E. & Stafast, H. (1998). Laser Induced Crystallization of Amorphous Silicon Films on Glass for Thin Film Solar Cells. *Physica status solidi (a),* Vol. 166, pp. 629-634

Andrä, G.; Bergmann, J.; Falk, F. & Ose, E. (2000). Preparation of single crystalline regions in amorphous silicon layers on glass by Ar+ laser irradiation. *Applied Surface Science,* Vol. 154-155, pp. 123-129

Andrä, G.; Bergmann, J. & Falk, F. (2005a). Laser crystallized multicrystalline silicon thin films on glass. *Thin Solid Films,* Vol. 487, pp. 77-80

Andrä, G.; Bergmann, J.; Bochmann, A.; Falk, F.; Dauwe, S. & Kieliba, T. (2005b). Characterization and simulation of multicrystalline LLC-Si thin film solar cells. *Proc. 20th Europ. Photovoltaic Solar Energy Conf.*, pp. 1171-1174

Andrä, G.; Bochmann, A.; Falk, F.; Gawlik, A.; Ose, E. & Plentz J. (2006). Diode laser crystallized multicrystalline silicon thin film solar cells on glass. *Proc. 21st Europ. Photovoltaic Solar Energy Conf.*, pp. 972-975

Andrä, G.; Plentz, J.; Gawlik, A.; Ose, E.; Falk, F. & Lauer, K. (2007). Advances in multi-crystalline LLC-Si thin film solar cells. *Proc. 22nd Europ. Photovoltaic Solar Energy Conf.*, pp. 1967-1970

Andrä, G.; Gimpel, T.; Gawlik, A.; Ose, E.; Bochmann, A.; Christiansen, S.; Sáfrán, G.; Lábár, J.L. & Falk, F. (2008a). Epitaxial Growth of Silicon Thin Films for Solar Cells. *Proc. 23rd Europ. Photovoltaic Solar Energy Conf.* 2008, pp. 2194-2198

Andrä, G.; Lehmann, C.; Plentz, J.; Gawlik, A.; Ose, E. & Falk, F. (2008b). Varying the Layer Structure in Multicrystalline LLC-Silicon Thin-Film Solar Cells. *Proc. 33rd IEEE Photovoltaic Specialists Conf.,* pp. 457-462

Andrä, G.; Bergmann, J.; Gawlik, A.; Höger, I.; Schmidt, T.; Falk, F.; Burghardt, B. & Eberhardt, G. (2010). Laser Induced Crystallization Processes for Multicrystalline Silicon Thin Film Solar Cells. *Proc. 25th Europ. Photovoltaic Solar Energy Conf.* 2010, pp. 3538-3542

Antesberger, T.; Jaeger, C.; Scholz, M. & Stutzmann, M. (2007). Structural and electronic properties of ultrathin polycrystalline Si layers on glass prepared by aluminum-induced layer exchange. *Applied Physics Lett.,* Vol. 91, pp. 201909

Avrami, M. (1940), Kinetics of Phase Change. II Transformation-Time Relations for Random Distribution of Nuclei, *J. Chemical Physics,* Vol. 8, pp. 212-224

Beaucarne, G.; Bourdais, S. ; Slaoui, A. & Poortmans, J. (2004). Thin-film polycrystalline Si solar cells on foreign substrates : film formation at intermediate temperatures (700-1300°C). *Applied Physics A,* Vol. 79, pp. 469-480

Beaucarne, G.; Gordon, I.; van Gestel, D.; Carnel, L. & Poortmans, J. (2006). Thin-film poly-crystalline silicon solar cells: An emerging photovoltaic technology. *Proc. 21st European Photovoltaic Solar Energy Conference,* pp. 721-725

Beaucarne, G. (2007). Silicon thin-film solar cells. *Advances in OptoElectronics*, Vol. 2007, Article ID 36970

Brazil, I. & Green, M.A. (2010). Investigating polysilicon thin film structural changes during rapid thermal annealing of a thin film crystalline silicon on glass solar cell. *J. Materials Sci.: Materials in Electronics,* Vol. 21, pp. 994-999

Brendel, R. (2001). Review of layer transfer process for crystalline thin-film silicon solar cells. *Japanese J. Applied Physics*, Vol. 40, pp. 4431-4439

Brendel, R.; Feldrapp, K.; Horbelt, R. & Auer, R. (2003). 15.4%-efficient and 25 µm-thin crystalline Si solar cell from layer transfer using porous silicon. *Physica status solidi (a)*, Vol. 197, pp. 497-501

Christiansen, S.; Nerding, M.; Eder, C.; Andrae, G.; Falk, F.; Bergmann, J.; Ose, E. & Strunk H.P. (2000). Defect population and electrical properties of Ar$^+$-laser crystallized polycrystalline silicon thin films. *Materials Res. Soc. Symp. Proc.,* Vol. 621, art. Q7.5.1

Colinge, J.P.; Demoulin, E.; Bensahel, D. & Auvert, G. (1982). Use of selective annealing for growing very large grain silicon on insulator films. *Applied Physics Lett.*, Vol. 41, pp. 346-347

Dogan, P.; Rudigier, E.; Fenske, F.; Lee, K.Y.; Gorka, B.; Rau, B.; Conrad, E. & Gall, S. (2008). Structural and electrical properties of epitaxial Si layers prepared by e-beam evaporation. *Thin Solid Films,* Vol. 516, pp. 6989-6993

Donovan, E.P.; Spaepen, F.; Turnbull, D.; Poate, J.M. & Jacobson, D.C. (1983). Heat of crystallization and melting point of amorphous silicon. *Applied Physics Lett.,* Vol. 42, pp. 698-700

Egan, R.; Keevers, M.; Schubert, U.; Young, T.; Evans, R.; Partlin, S.; Wolf, M.; Schneider, J.; Hogg, D.; Eggleston, B.; Green, M.; Falk, F.; Gawlik, A.; Andrä, G.; Werner, M.; Hagendorf, C.; Dogan, P.; Sontheimer, T. & Gall, S. (2009). CSG minimodules using electron-beam evaporated silicon. *Proc. 24th Europ. Photovoltaic Solar Energy Conf. 2009*, pp. 2279-2285

Falk, F. & Andrä, G. (2006), Laser crystallization – a way to produce crystalline silicon films on glass or polymer substrates. *J. Crystal Growth,* Vol. 287, pp. 397-401

Fogarassy, E; de Unamuno, S.; Legagneux, P.; Plais, F.; Pribat, D.; Godard, B. & Stehle, M. (1999). Surface melt dynamics and super lateral growth regime in long pulse duration excimer laser crystallization of amorphous Si films. *Thin Solid Films,* Vol. 337 pp. 143-147

Fuhs, W.; Gall, S.; Rau, B.; Schmidt, M. & Schneider, J. (2004). A novel route to a poly-crystalline silicon thin-film solar cell. *Solar Energy,* Vol. 77, pp. 961-968

Gall, S.; Schneider, J.; Klein, J.; Hübener, K.; Muske, M.; Rau, B.; Conrad, E.; Sieber, J.; Petter, K.; Lips, K.; Stöger-Pollach, M.; Schattschneider, P. & Fuhs, W. (2006). Large-grained polycrystalline silicon on glass for thin-film solar cells. *Thin Solid Films,* Vol. 511, pp. 7-14

Gat, A.; Gerzberg, L.; Gibbons, J.F.; Magee, T.J.; Peng, J. & Hong, J.D. (1978). cw laser anneal of polycrystalline silicon: Crystalline structure, electrical properties. *Applied Physics Lett.*, Vol. 33, pp. 775-778

Gordon, I.; Carnel, L.; Van Gestel, D.; Beaucarne, G. & Poortmans, J. (2007). 8% efficient thin-film polycrystalline-silicon solar cells based on aluminum-induced crystallization and thermal CVD. *Progress in Photovoltaics,* Vol. 15, pp. 575-586

Green, M.A.; Basore, P.A.; Chang, N.; Clugsto, D.; Egan, R.; Evans, R.; Hogg, D.; Jarnason, S.; Keevers, M.; Lasswell, P.; O'Sullivan, J.; Schubert, U., Turner, A.; Wenham, S.R.; & Young, T. (2004). Crystalline silicon on glass (CSG) thin-film solar cell modules. *Solar energy,* Vol. 77, pp. 857-863

Green, M.A. (2007). Thin-film solar cells: review of materials, technologies and commercial status. *J. Materials Science: Materials in Electronics,* Vol. 18, pp. S15-S19

Green, M.A.; Eemery, K.; Hishikawa, Y. & Warta, W. (2011). Solar cell efficiency tables (version 37). *Progress in Photovoltaics*, Vol. 19, pp. 84-92

Gromball, F.; Heemier, J.; Linke, N.; Burchert, M. & Müller, J. (2004). High rate deposition and in situ doping of silicon films for solar cells on glass. *Solar Energy Materials and Solar Cells*, Vol. 84, pp. 71-82

Hatano, M.; Moon, S; Lee, M.; Grigoropoulos, C.P. & Suzuki, K. (2001). Excimer laser-induced melting and resolidification dynamics of silicon thin films. *J. Korean Physical Society,* Vol. 39, pp. S419-S424

Jackson, K.A. & Chalmers, B. (1956), Kinetics of Solidification. *Canadian J. Physics,* Vol. 34, pp. 473-490

Kunz, T.; Burkert, I.; Gawehns, N. & Auer, R. (2008). Crystalline silicon thin-film solar cells on graphite or SiC-ceramic substrates. *Proc. 23rd Europ. Photovoltaic Solar Energy Conf.* (2008), pp. 2202-2204

Kashchiev, D. (1969). Solution of the non-steady state problem in nucleation kinetics. *Surface Science,* Vol. 14, pp. 209-220

Keevers, M.J.; Young, T.L.; Schubert, U. & Green, M.A. (2007). 10% efficient CSG mini-modules, *Proc. 22nd Europ. Photovoltaic Solar Energy Conference,* pp. 1783-1790

Kodera, H. (1963). Diffusion coefficients of impurities in silicon melt. *Japanese J. Applied Physics*, Vol. 2, pp. 212-219

Kuo, C.-C. (2009) Fabrication of large-grain polycrystalline silicon for solar cells. *Laser Physics,* Vol. 19, pp. 143-147

Lichtenstein, N.; Baettig, R.; Brunner, R.; Müller, J.; Valk, B.; Gawlik, A.; Bergmann, J. & Falk, F. (2010). Scalable, High Power Line Focus Diode Laser for Crystallizing of Silicon Thin Films. *Physics Procedia,* Vol. 5, pp. 109-117

Mariucci, L; Pecora, A; Fortunato, G.; Spinella, C. & Bongiorno, C. (2003). Crystallization mechanisms in laser irradiated thin amorphous silicon films. *Thin Solid Films,* Vol. 427, pp. 91-95

Michaud, J.F.; Rogel, R.; Mohammed-Brahim, T. & Sarret, M. (2006). Cw argon ion laser crystallization of silicon films: Structural properties. *J. Non-Crystalline Solids*, Vol. 352, pp. 998-1002

Pihan, E.; Slaoui, A. & Maurice, C. (2007). Growth kinetics and crystallographic properties of polysilicon thin films formed by aluminium-induced crystallization, *J. Crystal Growth,* Vol. 305, pp. 88-98

Rau, B.; Sieber, J.; Schneider, J.; Muske, M.; Stöger-Pollach, M.; Schattschneider, P.; Gall, S. & Fuhs, W. (2004). Low-temperature Si epitaxy on large-grained polycrystalline seed layers by electron-cyclotron resonance chemical vapor deposition. *J. Crystal Growth,* Vol. 270, pp. 396-401

Rau, B.; Conrad, E. & Gall, S. (2006). Influence of post-deposition treatment of absorber layers on poly-Si thin-film solar cells on glass grown by ECRCVD. *Proc. 21st Europ. Photovoltaic Solar Energy Conf.,* pp. 1418-1421

Reuter, M.; Brendle, W.; Tobail, O. & Werner, J.H. (2009). 50 µm thin solar cells with 17.0% efficiency. *Solar Energy Materials and Solar Cells,* Vol. 93, pp. 704-706

Sarikov, A.; Schneider, J.; Klein, J.; Muske, M. & Gall, S. (2006). Theoretical study of the initial stage of the aluminium-induced layer-exchange process. *J. Crystal Growth,* Vol. 287, pp. 442-445

Schneider, J.; Sarikov, A.; Klein, J.; Muske, M.; Sieber, J.; Quinn, T.; Reehal, H.S.; Gall, S. & Fuhs, W. (2006a). A simple model explaining the preferential (100) orientation of silicon thin films made by aluminum-induced layer exchange. *J. Crystal Growth,* Vol. 287, pp. 423-427

Schneider, J.; Schneider, A.; Sarikov, A.; Klein, J.; Muske, M.; Gall, S. & Fuhs, W. (2006b). Aluminum-induced crystallization: Nucleation and growth process. *J. Non-Crystalline Solids,* Vol. 352, pp. 972-97

Schneider, J.; Dore, J.; Christiansen, S.; Falk, F.; Lichtenstein, N.; Valk, B.; Lewandowska, R.; Slaoui, A.; Maeder, X.; Lábár, J.; Sáfrán, G.; Werner, M.; Naumann, V. & Hagendorf, C. (2010). Solar Cells from Crystalline Silicon on Glass Made by Laser Crystallised Seed Layers and Subsequent Solid Phase Epitaxy. *Proc. 25th Europ. Photovoltaic Solar Energy Conf. 2010*, pp. 3573-3676

Sontheimer, T.; Dogan, P.; Becker, C.; Gall, S.; Rech, B.; Schubert, U.; Young, T.; Partlin, S.; Keevers, M. & Egan, R.J. (2009). 6.7% efficient poly-Si thin film mini-modules by high-rate electron-beam evaporation. *Proc. 24th Europ. Photovoltaic Solar Energy Conf. 2009*, pp. 2478-2481

Straub, A.; Inns, D.; Terry, M.L.; Huang, Y.; Widenborg, P.I. & Aberle A.G. (2005). Optimisation of low-temperature silicon epitaxy on seeded glass substrates by ion-assisted deposition. *J. Crystal Growth,* Vol. 280, pp. 385-400

Teplin, C.W.; Branz, H.M.; Jones, K.M.; Romero, M.J.; Stradins, P. & Gall, S. (2007). Hot-wire chemical vapor deposition epitaxy on polycrystalline silicon seeds on glass. *Materials Research Society Symposium Proc.,* Vol. 989-A06-16: Amorphous and Poly-crystalline Thin-Film Silicon Science and Technology 2007, pp. 133-137

Ujihara, T.; Sazaki, G., Fujiwara, K.; Usami, N. & Nakajima, K. (2001). Physical model for the evaluation of solid-liquid interfacial tension in silicon. *J. Applied Physics,* Vol. 90 (2001), pp. 750-755

Van Gestel, D.; Gordon, I.; Bender, H.; Saurel, D.; Vanacken, J.; Beaucarne, G. & Poortmans, J. (2009). Intragrain defects in polycrystalline silicon layers grown by aluminum-induced crystallization and epitaxy for thin-film solar cells. *J. Applied Physics,* Vol. 105, p. 114507

Wang, Z.M. ; Wang, J.Y.; Jeurgens, L.P.H. & Mittemeijer, E.J. (2008). Thermodynamics and mechanism of metal-induced crystallization in immiscible alloy systems: Experiments and calculations on Al/a-Ge and Al/a-Si bilayers. *Physical Review B,* Vol. 77, pp. 045424

Werner, J.H.; Dassow, R.; Rinke, T.J.; Köhler, J.R. & Bergmann, R.B. (2001). From poly-crystalline to single crystalline silicon on glass. *Thin Solid Films*, Vol. 383, pp. 95-101

8

Architectural Design Criteria for Spacecraft Solar Arrays

Antonio De Luca
VEGA Space GmbH
Germany

1. Introduction

Scope of this chapter is to provide design criteria for spacecraft solar arrays at system level.

The design a satellite solar array is usually influenced by several constraints; mission profile, chosen attitude, overall spacecraft configuration, mass and sizing requirements, etc.

Moreover, its design has to be harmonised with the chosen solar array power conditioning, in order to optimize mass, dimensions, and also particular constraints coming from EMC and thermal environments.

The chapter is basically composed of the following sections;

1. General description of the current solar cell technologies currently used in space, with particular attention to the triple junction solar cells.
2. Mathematical model of an equivalent solar cell circuit, to be used for performance calculations in a numerical simulation environment.
3. Mathematical description of a simplified thermal model of a solar array in order to analyse solar array performances in orbit.
4. Short definition of cosmic radiation effects.
5. The satellite power budget, starting point for the solar array sizing
6. The impact of the power conditioning architecture on the solar array (electrical operative point, EMC considerations).
7. The configuration of the solar array with respect to the spacecraft.
8. Some design examples for different missions and satellite configurations.
9. Numerical simulations of solar array performances as function of the mission profile (orbit propagation, slew manoeuvres, attitudes of particular interest).

2. Solar cells for space applications

Since the beginning of the astronautic era, photovoltaic devices have been considered for the generation of electrical power on board spacecrafts because of their high power output per unit mass, associated with the fundamental advantage of not having moving parts, present, instead, in all the most used electrical power generators for both terrestrial and aeronautical applications (turbines, motors, alternators, etc.). Therefore the PV array is static, does not produce vibrations or noise, and does not need an active cooling. The Russians were the first, in 1958, to launch a satellite powered with silicon solar cells.

Solar cells for space applications have to be highly efficient, capable to stand thousands of thermal cycles in orbit where the temperature, according to the mission profile may vary from -150 °C to more than 120 °C. They have to show a limited degradation during time due to cosmic radiations and Ultraviolet, and they have to resist to the mechanical solicitations mainly linear accelerations and vibrations during launch and orbital manoeuvres, because of these constraints the cells for space are smaller than those for terrestrial applications.

In order to have the highest conversion efficiency, solar cells for space application are developed from mono-crystalline materials. In the past silicon was the most used and the reachable bulk efficiency was not higher than 14%. The advent of GaAs based solar cells in the last decade of the 20th century took the efficiency up to 19%, and nowadays triple junction solar cells show more than 30%.

Figure 1 shows a very simplified structure of triple junction cell.
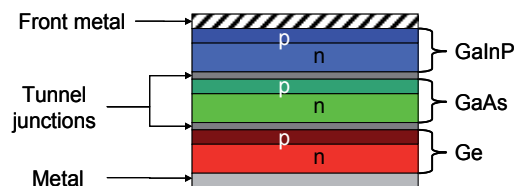
Fig. 1. Triple junction solar cell structure

While figure 2 reports the quantum efficiency for each junction, it can be clearly seen that the increased efficiency is due to wider wavelength coverage of the absorbed radiation.
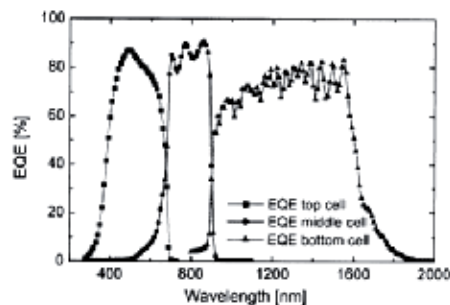
Fig. 2. Equivalent quantum efficiency as function of wavelength

Triple junction GaAs solar cells are populating more and more solar generators worldwide, while manufacturers are actively working on four to six junction cells as a way forward always increasing conversion efficiency. Consequently, there is a need to improve the understanding of the electrical dynamic behaviour of multi-junction based solar array considering that the proper design of solar array regulators requires, among others, a good mastering of the solar section/regulator interface. In order to better understand EMC aspects connected to the chosen regulation philosophy, which will be discussed further, it is worth to have a quick look at the equivalent capacitance present at the output of a triple junction cell. The figure 3 reports the capacitance measured across strings composed of 15 cells. The cells used are produced by AZUR SPACE Solar Power GmbH. It can be observed that at high voltages the capacitance is considerably increased. Such behaviour has to be

taken into account when the power conditioning architecture is chosen, and the relevant devices designed.
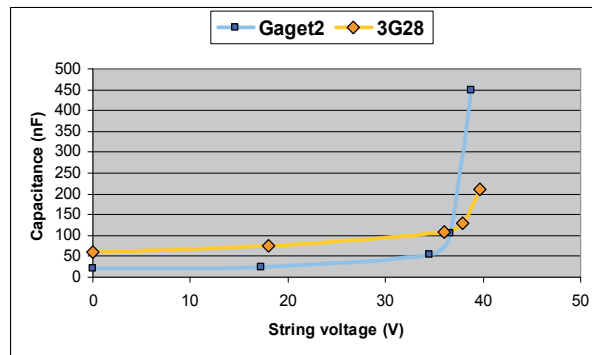
Fig. 3. Capacitance identified for the 15 cells string, Gaget2 and 3G28 (AZUR SPACE products)

3. Solar cell equivalent circuit

The mathematical model of a photovoltaic cell has to take into account the following factors capable to influence the solar cell behaviour.
1. Intensity of the incident light.
2. Operative absolute temperature.
3. Degradation by cosmic radiation.

The solar cell model, derived from the Mottet-Sombrin's one, is basically a current generator driven by the value of the voltage applied at its terminal according to the equivalent circuit reported below. Generally speaking a solar cell is a particular p-n junction where the diffusion process (diode D1) co-exists with the generation and recombination effect of the charge carrier (diode D2) induced by the presence of crystalline defects. This model was tested using data relevant to the AZUR SPACE 28% solar cell, as reported in the datasheet provided by the Manufacturer, and available on company web-site.
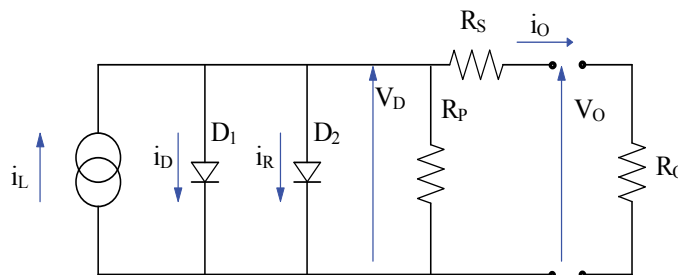
Fig. 4. Equivalent Circuit of solar cell

The relevant Kirchhoff equations are:

$$i_o = i_L - i_D \cdot \left[\exp\left(\frac{q \cdot V_D}{k \cdot T} \right) - 1 \right] - i_R \cdot \left[\exp\left(\frac{q \cdot V_D}{2k \cdot T} \right) - 1 \right] - \frac{V_D}{R_p} \tag{1a}$$

$$V_o = V_D - R_S \cdot i_o \tag{1b}$$

Where:

$K = 1.381 \times 10^{-23}$ (J/°K) is the Boltzmann constant;

$q = 1.602 \times 10^{-19}$ (C) is the electron charge;

i_L, i_D e i_R are respectively the current due to illumination, and the reverse currents of the diodes D_1 e D_2; they are function of the temperature.

The equations (1) give the output voltage V_o, and current I_o as function of the voltage drop V_d over the diodes D_1 and D_2. The second and third term of (1_a) represent the typical voltage-current laws of the diodes, and the currents i_D and i_R are the reverse currents of the diodes dependent from the physics of the solar cell.

In general, the solar cell is characterised by the following data provided in the manufacturer's data sheet, the table below gives the values relevant to the one used for testing the model:

$\mathbf{I_{sc}}$	506.0 mA	Short circuit current;
$\mathbf{I_{mp}}$	487.0 mA	Maximum power current;
$\mathbf{V_{mp}}$	2371.0 mV	Maximum power voltage;
$\mathbf{V_{oc}}$	2667.0 mV	Open circuit voltage;
$\mathbf{dI_{sc}/dT}$	0.32 mA/°K	Short circuit current temperature coefficient
$\mathbf{dI_{mp}/dT}$	0.28 mA/°K	Max. power current temperature coefficient
$\mathbf{dV_{mp}/dT}$	-6.1 mV/°K	Max. power voltage temperature coefficient;
$\mathbf{dV_{oc}/dT}$	-6.0 mV/°K	Open circuit voltage temperature coefficient.

Such data are given in AM0 (1367.0 W/m²) conditions at T_{ref}=28 °C (301.15 °K) reference temperature.

Usually the series resistance is around 300mΩ for a triple junction cell, while for the shunt one 500Ω maybe assumed. Such resistances may be considered in a first approximation as constant in the operating temperature range of the cell.

The values of i_L, i_D and i_R at the reference temperature can be calculated with the (1) in the three main point of the V-I curve; short circuit, maximum power and open circuit, by the least square method.

The next step is to define how these currents change with temperature.

Concerning $\mathbf{i_D}$ e $\mathbf{i_R}$ it is possible to write:

$$i_D = C_D \cdot T^{5/2} \cdot \exp\left(\frac{E_g}{n_1 \cdot T} \right) \tag{2a}$$

$$i_R = C_R \cdot \exp\left(\frac{E_g}{n_2 \cdot k \cdot T} \right) \tag{2b}$$

Where $\mathbf{C_D}$ and $\mathbf{C_R}$ are constants independent from temperature, and E_g is the Energy of the prohibited band gap:

$$E_g = E_{g0} - \frac{\left(\alpha_e \cdot T^2 \right)}{\left(T + \beta_e \right)} \quad \text{(mA/cm²)} \tag{3}$$

With E_{g0} = 1.41 eV, α_e=-6.6×10^{-4} eV/°K, and β_e=552 °K.
The current **i_L** due to illumination is given instead by

$$i_L(T) = K(T) \cdot \eta(T) \cdot J_{tot} \quad (\text{mA/cm}^2) \tag{4}$$

Where J_{tot} is light intensity (W/ m^2), $\eta(T)$ is the efficiency of the cell, $K(T)$ is a coefficient to be determined as function of the temperature.

n_1 e n_2 are two coefficients depending on the adopted solar cell technology:

At this point all the terms of the equations (1) can be defined at any temperature and by setting as input the operating voltage V_o and solving the system by the Newton-Raphson numerical scheme is possible to calculate the output current i_o.

Figure 5 shows the V-I curves relevant to Triple Junction AZUR SPACE solar cell starting from the datasheet available on the web site, as function of temperature at Begin Of Life (BOL); the black asterisks are the maximum power points calculated according to the datasheet. In figure 6 V-I curves for different illumination levels are reported.
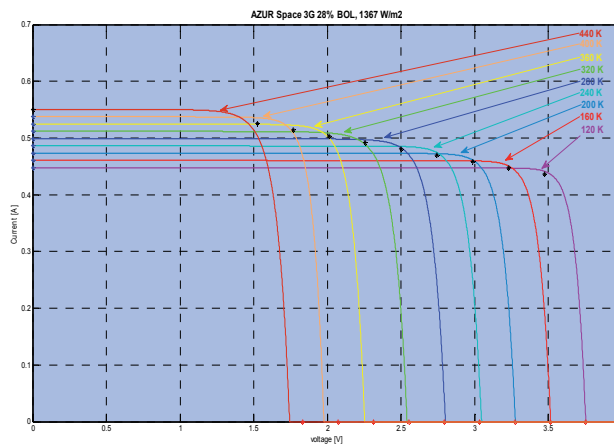
Fig. 5. Computed V-I curves as function of temperature using AZUR SPACE 3G 28% data
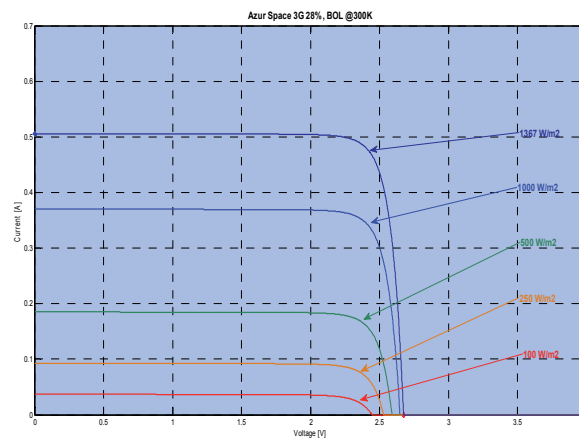
Fig. 6. Computed V-I curves as function of illumination using AZUR SPACE 3G 28% data

4. Solar panel thermal model

What said above clearly highlights the need of a thermal model of the solar panel taking into consideration the heat exchange on both sides of it in case of a deployable one; or usually considering the rear side as adiabatic in case of the panel is body mounted. The panel is considered as rigid, with honeycomb structure on which the solar cells are applied; the following table reports the components recognizable in solar panel cross-section:

Components from front to rear side	Thickness, μm
Coverglass	150 - 500
Coverglass adhesive	50 - 100
Solar cell	100 - 200
Cell adhesive	100
Kapton insulation	50
Face skin (Carbon fibre)	-
Adhesive	100
Honeycomb (Aluminium)	Up to 4 cm
Adhesive	100
Face skin (Carbon fibre)	-
Black paint	50

Table 1. Solar panel composition

The panel temperature is computed taking into account the direct sun radiation, the albedo radiation, the irradiation to deep space, and irradiation between the earth surface and the panel itself. The sun illumination is variable during the year and considering only missions around the earth it may range between 1315.0 (summer solstice) and 1426 W/m2 (winter solstice), while the albedo of the earth surface is about 30% of the incident sun illumination. The panel exchanges heat with the deep space and this is seen as a black body at 3°K, as well as the earth irradiates as a black body at 250°K. The following simplifying assumptions can been made; a deployed solar panel does not exchange heat with the outer surfaces of the satellite body, a body mounted solar panel is adiabatically isolated from the rest of the satellite body and finally the panel surface temperature is considered as uniform. The conduction across the panel also plays an important role, and it has to be taken into account in case of a deployed solar panel. At a first glance, the in-plane conductivity may be neglected, this because under the hypothesis of uniform temperature over the panel, the heat exchange between adjacent cells is basically zero.

The thermal equilibrium is computed by solving the differential equation which takes into account the different heat exchange modalities.

$$C \cdot \frac{dT}{dt} = Q_{Rad} + Q_{Alb} + Q_{Earth} + Q_{Space} + Q_{cond} \tag{5}$$

Where:

$$Q_{Rad} = \alpha (1 - \eta) \cos \vartheta \cdot J \tag{6}$$

It is the contribution of the direct sun radiation J that is not converted into electrical power by the photovoltaic cell;

$$Q_{alb} = \alpha \left(1 - \eta\right) \cdot F \cdot Al \cdot F_{1-2} \cdot J \tag{7}$$

It is the contribution of the albedo radiation;

$$Q_{Earth} = \sigma \cdot \varepsilon \cdot F_{12} \cdot (T_E^4 - T^4) \tag{8}$$

It is the heat exchanged with the Earth surface.

$$Q_{Space} = \sigma \cdot \varepsilon \cdot (1 - F_{12}) \cdot T^4 \tag{9}$$

It is the heat released to the deep space.

$$Q_{cond} = \frac{\left(T_{front} - T_{rear}\right)}{\Delta x} \cdot k \tag{10}$$

Is the heat transmitted by conduction between the front and rear faces of the panel at T_{front} and T_{rear} temperature respectively.

The parameters appearing in these equations have the following meanings:

C = thermal capacitance of the panel per unit area, main contribution is provided the honeycomb structure;

α = solar cell absorptivity;

ε = solar cell emissivity;

Al = albedo coefficient, about 0.3 for earth;

F = albedo visibility factor;

F_{12} = View factor between radiating surface and planet

σ = Stephan-Boltzmann, constant: 5.672×10^{-8} W/(m²×°K⁴);

T_E = Black body equivalent temperature of the earth;

ϑ = incidence angle of the sunlight on the panel;

k = panel transverse thermal conductivity;

Δx =panel thickness;

The radiating view factor of a flat surface with respect to the Earth surface is function of the altitude h, earth radium R⊕ and the angle λ between the nadir and the normal to the panel. The albedo view factor is computed according to the following formulas:

$$F_{alb} = \left[1 - \cos\left(\beta_{app}\right)\right] \cdot \cos\left(\beta\right) \tag{11}$$

Where β is the angle between the nadir and the earth-sun direction:

$$\beta_{app} = \arcsin\left(\frac{R_\oplus}{h + R_\oplus}\right) \tag{12}$$

The integration in the time domain of the equation (5) gives the actual temperature of the panel along the propagation of the orbit in eclipse and sunlight, taking into account the orientation of the panel itself with respect to the earth and the sun. The thermal model

exposed so far is sufficient for the design of a solar array for space application at system level.
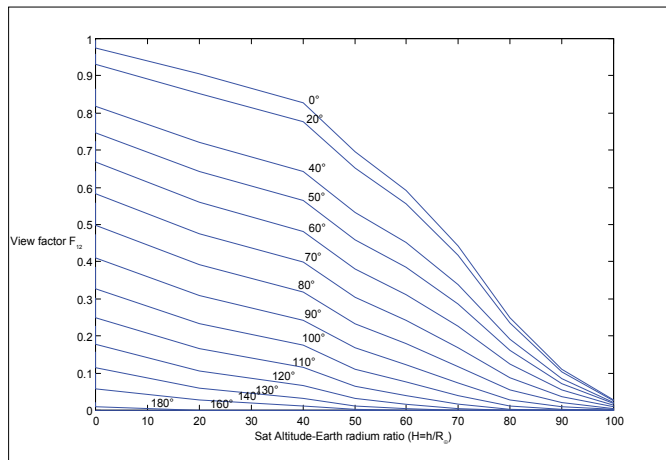
Fig. 7. View Factors F_{12} as function of $H=h/R_{\oplus}$, parameter:λ
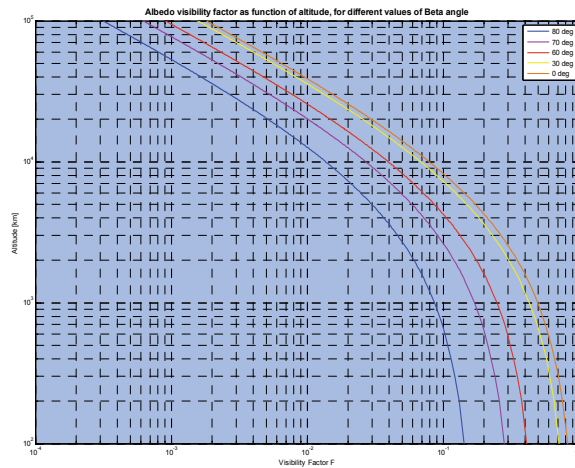
Fig. 8. Albedo Visibility factor F as function of h for different β value

5. Degradation due to space environment

Space is a hostile environment for the electronic components in general and solar cells in particular. The sun radiates energy in almost the whole electromagnetic spectrum, from radio waves to gamma rays, and abundant charged particles impinging on a surface cause damages which cumulate over the mission lifetime (fluence Φ). The behaviour of solar cells in a radiation environment can be described in terms of the changes in the engineering output parameters of the devices. The radiation usually of interest in the study of degradation of materials and devices consists of energetic or fast massive particles (i.e. electrons, protons, neutrons or ions). The major types of radiation damage phenomena in

solids which are of interest to the solar array designer are ionisation and atomic displacement.

Ionisation occurs when orbital electrons are removed from an atom or molecule in gases, liquids, or solids. The measure of the intensity of ionising radiation is the roentgen. The measure of the absorbed dose in any material of interest is usually defined in terms of absorbed energy per unit mass. The accepted unit of absorbed dose is the rad (100 erg/g or 0.01 J/kg). For electrons, the absorbed dose may be computed from the incident fluence Φ (in cm^{-2}) as: Dose (rad) = 1.6×10^{-8} dE/dx Φ, where dE/dx (in MeV cm^2 g^{-1}) is the electron stopping power in the material of interest. In this manner, the effects of an exposure to fluxes of trapped electrons of various energies in space can be reduced to an absorbed dose. By the concept of absorbed dose, various radiation exposures can be reduced to absorbed dose units which reflect the degree of ionisation damage in the material of interest. This concept can be applied to electron, gamma, and X-ray radiation of all energies. Several ionisation related effects may degrade the solar cell assemblies. The reduction of transmittance in solar cell cover glasses is an important effect of ionising radiation.

The basis for solar cells damage is the displacement of semiconductor atoms from their lattice sites by fast particles in the crystalline absorber. The displaced atoms and their associated vacancies after various processes form stable defects producing changes in the equilibrium of carrier concentrations and in the minority carrier lifetime. Such displacements require a certain minimum energy similar to that of other atomic movements. Seitz and Koehler [1956] estimated the displacement energy is roughly four times the sublimation energy. Electron threshold energies up to 145 keV have been reported. Particles below this threshold energy cannot produce displacement damage, therefore the space environment energy spectra are cut off below this value. The basic solar cell equations (1) may be used to describe the changes which occur during irradiation. This method would require data regarding the changes in the light generated current, series resistance, shunt resistance, but most investigations have not reported enough data to determine the variations in the above parameters. The usual practice is then to reduce the experimental data in terms of changes in the cell short circuit current (I_{sc}), open circuit voltage (V_{oc}), and maximum power (P_{max}). The variation of common solar cell output parameters during irradiation can be described as shown for I_{sc} in the following case:

$$I_{sc} = I_{sc0} - C \log (1 + \Phi / \Phi_x) \tag{13}$$

Where Φ_x represents the radiation fluence at which I_{sc} starts to change to a linear function of the logarithm of the fluence. The constant C represents the decrease in I_{sc} per decade in radiation fluence in the logarithmic region. In a similar way, for the V_{oc} it can be written;

$$V_{oc} = V_{oc0} - C' \log (1 + \Phi / \Phi_x). \tag{14}$$

And for the maximum power;

$$P_{max} = P_{max0} - C'' \log (1 + \Phi/\Phi_x). \tag{15}$$

In the space environment a wide range of electron and proton energies is present; therefore some method for describing the effects of various types of radiation is needed in order to get a radiation environment which can be reproduced in laboratory. It is possible to determine an equivalent damage due to irradiation based upon the changes in solar cell parameters which are in some way related to the minority carrier diffusion length.

The I_{sc} variation in each environment is described by the equation for I_{sc}. In this case, two constants, C and Φ_x, are required to describe the changes in I_{sc}. It has been shown that the constant C, under solar illumination, does not greatly vary for different radiation environments. For electron irradiations in the 1 MeV and greater range, C is about 4.5 to 5.5 mA cm^{-2}/decade. In case of proton and neutron, C approaches 6 to 7 mA cm^{-2} /decade.

For solar cells with the same initial I_{sc}, the constant Φ_x is a measure of the damage effectiveness of different radiation environments. The constant Φ_x for a particular radiation can be determined graphically on a semi-log plot at the intersection of the starting I_{sc} and the extrapolation of the linear degradation region.
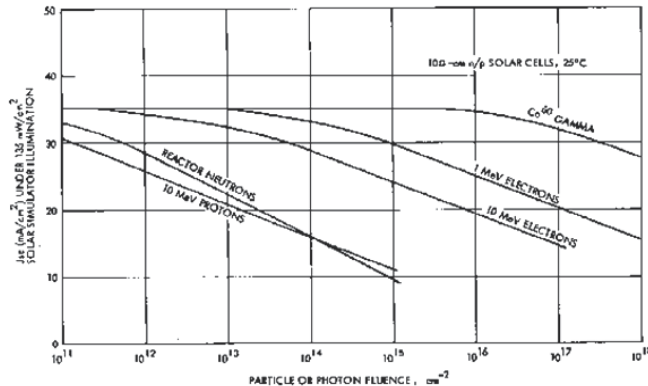
Fig. 9. Variation of solar cell short circuit current with fluence for various radiations

It is the practice to define an arbitrary constant referred to as the critical fluence Φ_c. One method of defining this value is that fluence which degrades a solar cell parameter 25% below its BOL state. But such a parameter is valid only when comparing cells with similar initial parameters. To eliminate this problem, critical fluence may be alternatively defined as that fluence which will degrade a cell parameter to a certain value. By use of the critical fluence or the diffusion length damage coefficient, it is possible to construct a model in which the various components of a combined radiation environment can be described in terms of a damage equivalent fluence of a selected mono-energetic particle. 1 MeV Electrons are a common and significant component of space radiation and can be produced conveniently in a test environment. For this reason, 1 MeV electron fluence has been used as a basis of the damage equivalent fluences which describe solar cell degradation.

The degradation due to radiation effects on solar cell cover-glass material in space is difficult to assess. The different radiation components of the environment act both individually and synergistically on the elements of the shielding material and also cause changes in the interaction of shielding elements. However, the most significant radiation effects in cover materials involve changes in the transmission of light in the visible and near infrared region.

The methods for estimating solar cell degradation in space are based on the techniques described by *Brown et al.* [1963] and *Tada* [1973ab]. In summary, the omni-directional space radiation is converted to a damage equivalent unidirectional fluence at a normalised energy and in terms of a specific radiation particle. This equivalent fluence will produce the same damage as that produced by omni directional space radiation considered if the relative damage coefficient (RDC) is properly defined to allow the conversion. When the equivalent

fluence is determined for a given space environment, the parameter degradation can be evaluated in the laboratory by irradiating the solar cell with the calculated fluence level of unidirectional normally incident flux. The equivalent fluence is normally expressed in terms of 1 MeV electrons or 10 MeV protons. The three basic input elements necessary to perform degradation calculations are:

1. degradation data for solar cells under normal incidence 1 MeV electron irradiation;
2. effective relative damage coefficients for omni-directional space electrons and protons of various energies for solar cells with various cover-glass thicknesses;
3. Space radiation environment data for the orbit of interest.

The equivalent 10 MeV proton fluence can be converted to equivalent 1 MeV electron fluence as follows: $\Phi_{1MeV\,e} = 3000\ \Phi_{i10MeV\,p}$.

In cases when the cell degradation is entirely dominated by proton damage, the cell degradation could be estimated more accurately by calculating the equivalent 10 MeV proton fluence and using 10 MeV proton cell damage data, than by using the equivalent 1 MeV electron fluence and electron data.

To use cover-glass darkening data, a procedure is necessary to evaluate the absorbed dose produced by the various radiation components of the space environment. The procedure is similar to that used for equivalent fluence, with the exception that the absorbed dose varies with depth in the cover material.

6. The power and energy budget

The starting point for the solar array sizing is the correct identification of the power demand throughout the whole mission of the spacecraft.

Such power demand may change during the satellite lifetime either because of different operational modes foreseen during the mission or, more simply, because of degradation of the electrical performances of the electrical loads (in majority electronic units).

Taking into consideration what just said, an analysis of power demand is performed, including peak power, of all the loads installed either in the platform or as payload for each identified phase of the mission. Because of presence of sun eclipses, and possible depointings along the orbit, an analysis of the energy demand is also performed, this because in case of insufficient illumination the on board battery will supply the electrical power, and the solar array has to be sized in order to provide also the necessary power for its recharge. The power budget is based on peak power demands of the loads, while the energy budget is based on average consumptions.

It is good practice consider power margins both at unit and electrical system level.

The consumption of each unit is calculated considering the following criteria:

• 20% margin with respect to expected power demand if the unit design is new.
• 10% margin if the unit design has a heritage from a previous similar one.
• 5% margin if the unit is recurrent.

Several electronic units work in cold or hot redundancy; this has to be taken into account when summing the power demands.

Once the power demand is defined including the margins above, it is advisable to add 20% extra margin at system level and defined at the beginning of the project. Such margin is particularly useful during the satellite development in order to manage eventual power excesses of some units beyond the margins defined at unit level. In this way eventual Request For Deviation (RFD) issued by the subcontractors can be successfully processed

without endangering the whole spacecraft design. This is particularly true for scientific missions, where many times the development of the instruments may reveal so challenging that an excess of power demand cannot be excluded a priori.

At this point harness distribution losses are introduced, 2% of the power demand defined with all margins at unit and system level may be a good compromise between losses containment and harness mass.

The Power Control and Distribution Unit (PCDU) is the electronic unit devoted for the solar array and battery power conditioning and regulation, power distribution and protection, execution of received telecommands (i.e. switch on/off of the loads) and telemetry generation. Its power consumption without considering the efficiencies of primary bus power converters depends on the management of the digital interfaces with the on-board computers, the control loop and protection electronics, the value of such consumption is not immediate to calculate but it can be said that a PCDU capable to manage 1kW can consume about 30W. However it consumption strongly depend on the number of implemented distribution lines, and relevant electronic protections.

Now its time to add the power needed for the recharge of the battery, this power strongly depend on the mission profile, and many times the maximum discharge of the battery occurs at launch, from lift-off up to the successful sun acquisition by the satellite with optimal sun pointing of the solar panels. Some times due to the complexity of the satellite design and mission profile it is not possible to have a full recharge of the battery in one orbit before the next eclipse, then the power allocated for such incumbency has to assure a positive battery recharge trend throughout a limited number of orbits.

The power delivered by the solar array is conditioned by suitable power converters in order to provide it to the loads with a regulated voltage, or at list with the voltage varying between a maximum and minimum value. These converters may have an efficiency between 98.5% and 95% and the choice of their topology is made according to several criteria and constraint dictated by the overall satellite system design. Such efficiencies are taken into account adding up to an additional 5% to the budget defined so far.

The harness losses between solar array and PCDU may be calculated having as objective 1V voltage drop at the maximum required power; again, considerations about the harness mass can provoke the change of such objective.

Finally, in case of the European ECSS standard (ECSS-E-ST-20C) is considered as applicable, an additional 5% margin on power availability shall be assured at the satellite acceptance review End of Life (EOL) conditions and one solar array string failed.

7. Solar array sizing; impact of the power conditioning and electromagnetic constraints

The definition of the solar array, conceived as a set of solar cells connected in series to form a string and strings connected in parallel cannot be made without considering the power conditioning device placed at its output in order to have the electrical power delivered within a certain voltage range. This is not the suitable seat for a complete examination of all the possible power conditioning and power architecture solutions, what can be said is that there are two main concepts: the Direct Energy Transfer (DET) and the Maximum Peak Power Tracking (MPPT). These two methods of regulation have an important impact on the solar array design not only from the sizing point of view, but also from the electromagnetic compatibility (EMC) one. The following section will detail the impact of the adopted power

conditioning concept, and some sizing constraints mainly raised by the space environment such as electrostatic discharges and earth magnetic field.

7.1 Regulation based on Sequential Switching Shunt Regulator (S³R)

The first concept is based on the use of a shunt regulator; the figure below shows the electric schematic of a cell of a Sequential Switching Shunt Regulator (S³R), several solar array strings can be connected in parallel to the input of the regulator's cell; the voltage at the terminals of the output capacitor (Main Bus capacitor) is regulated by the switching of the MOSFET contained in the blue oval.
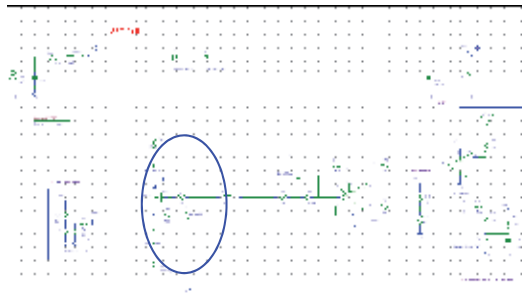
Fig. 10. Electrical Section of a Sequential Switching Shunt Regulator (S³R)
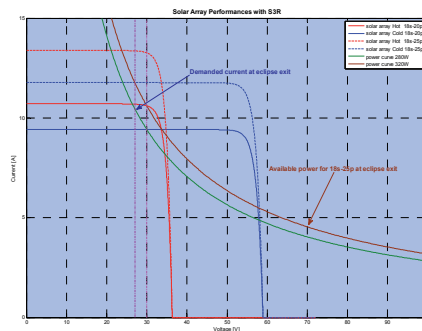
Fig. 11. Solar array working points as function of required power

The operating voltage of the solar array is constant and equal to main bus nominal voltage plus the voltage drops due the two diodes in series along the line, the solar array harness, and the blocking diode placed at the string positive output. In case of a fully regulated power bus, this operating voltage remains fixed during both sunlight and eclipse periods throughout the orbit; if the power bus is instead a battery regulated one it implies that the bus voltage decreases during eclipse periods, when the battery discharges, provoking a migration of the operating point of the solar array towards the short circuit one.

Supposing a power need of 280W, Figure 11 shows that a solar array composed of 20 strings of 18 cells (18s – 20p), at the eclipse exit (V_{array}= 27V) cannot provide the required power. In this condition the battery keeps discharging, lowering further down the operating voltage. This power bus lock-up has to be avoided increasing the number of strings in parallel. Adding 5 more strings (i.e. 25% more) the solar array can deliver 320W at 27V when cold;

therefore 40W become available to assure the battery charge. However, this increase might not be enough for assuring a full recharge of the battery in one orbit, or a positive recharge trend through several orbits; and an assessment of the energy budget by numerical simulation becomes necessary, taking into account orbital and attitude constraints.

7.2 Regulation based on Maximum Peak Power Point Tracker (MPPT)

The MPPT concept is based on the use of a switching dc-dc converter; usually it has a buck topology, where the primary voltage at solar array side is always higher of the secondary one on the distribution bus. Figure 12 shows an example of this type of converter. There are three control loops; a conductance control of the output current, an output voltage controller, and the Maximum Peak Power Tracker which regulates the output voltage of the solar array around the maximum power point in case of maximum power demand. In all the cases the required power is lower than the maximum available one the operating voltage of the solar array is kept between the maximum power voltage and the open circuit one.
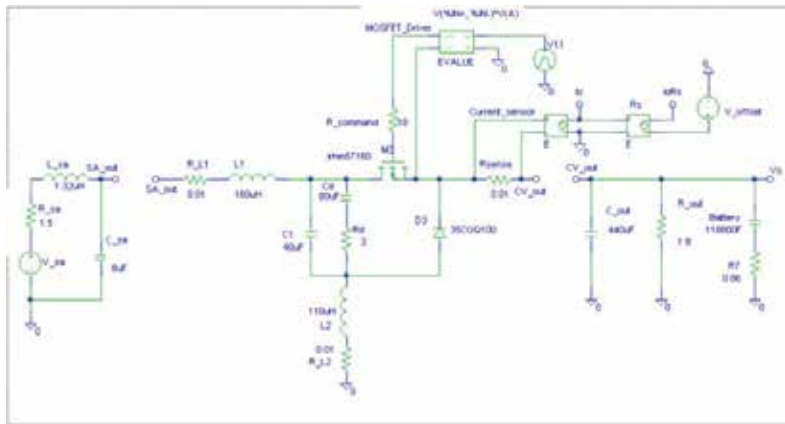
Fig. 12. Low ripple Buck converter topology

When this power conditioning concept is applied the solar array operating voltage is always independent from the bus one. Hence the phenomenon of the lock-up mentioned for the S3R is not present and the solar array does not need to be sized in order to cope with such issue.
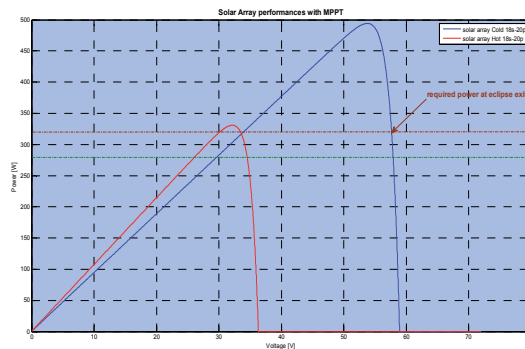
Fig. 13. Solar array P-V curves and required power, MPPT power conditioning

Figure 13 clearly shows that the original array composed of 20 strings is now capable to deliver the needed power in both hot and cold conditions, providing power to the loads (280W) and the additional 40W for the recharge of the battery.

Clearly from the sizing point of view of the array, the MPPT provides unquestionable benefits, but the price to be paid consist in additional mass (inductances and capacitances, as it can be seen in figure 12), and higher complexity because of the presence of three control loops.

7.3 Electromagnetic Compatibility (EMC)

The design of a spacecraft solar array and its power conditioner has to satisfy several requirements, not only in terms of mass, dimensions and power output, but also in terms of electromagnetic compatibility. This is particularly true for scientific mission, when instruments highly sensitive to electromagnetic fields may be boarded. In these cases it becomes crucial for the success of the mission to know which electromagnetic fields are generated at solar array level due to the circulating current and its frequency content, once this is connected to the power conditioning unit. The wires connecting the solar array to the PCDU, via the Solar Array Driving Mechanism (SADM) when necessary, are always twisted pairs (positive and return), but the return connections of the strings are routed on the rear side of the panel, they are not twisted of course, hence the solar array can behave as a transmitting antenna at frequencies which may result incompatible with some of the equipments on board.
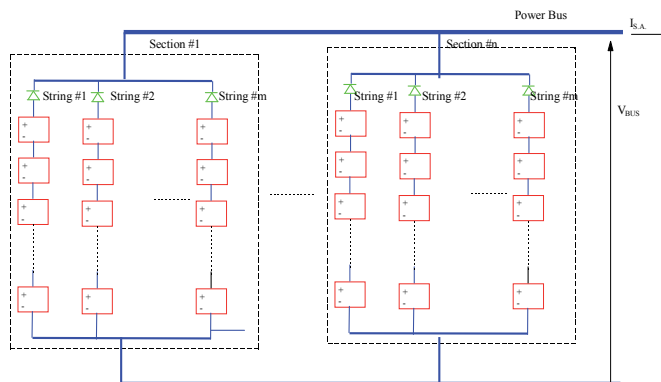
Fig. 14. Solar array electrical scheme

These issues are strongly dependent on the power conditioning approach adopted.

In the case of the S3R, with reference to figure 10, it can be seen that within the blue oval there is the shunt switch (MOSFET) together with a linear regulator in order to limit the current spikes at the regulator input when the MOSFET switches ON/OFF. Such spikes are strongly dependent on the total output capacitance of the strings connected in parallel and hence from the capacitance of the single triple junction solar cell. Fewer cells are in a string, or more strings in parallel, higher is this capacitance. The linear regulator can reduce the amplitude of the spikes by a suitable sizing of the dump resistor. For sake of completeness, the inductances present in the circuit diagram are the parasitic ones. Figure 15 shows the frequency spectrum of the current circulating in the harness between solar array and power regulator for different values of the dump resistor. The next figure 16 instead shows the

frequency spectrum of the current for the same solar array section when the power conditioning is made by a buck converter with a MPPT control loop. It can be immediately seen that in case of MPPT power conditioning the current ripple on the solar array harness is much lower at low frequencies, not higher than 8 mA; and therefore such solution may be interesting when the power subsystem has to cope to very stringent requirements from EMC point of view.
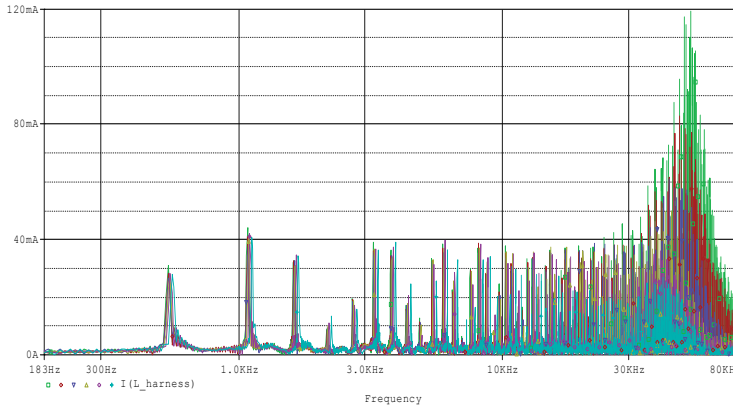
Fig. 15. Frequency spectrum of Solar Array output current for S³R power conditioning
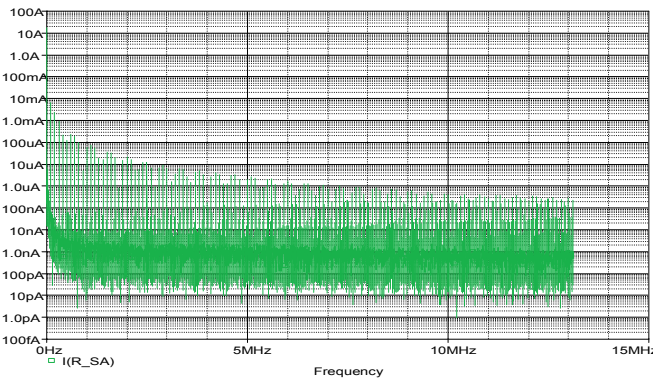
Fig. 16. Frequency Spectrum of Solar Array output current for MPPT power conditioning

7.4 Effect of the Earth magnetic field

The interaction between the Earth magnetic field **B** and the currents circulating in each string generate a torque disturbing the desired attitude of the whole spacecraft. The magnetic moment **M** due to the current is given by

$$M = I \cdot A \tag{16}$$

Where **I** is the current and **A** is the area of the current loop; in the case of the solar array this area corresponds in a first approximation to cross section of the panel substrate; on the front face of it the cells are mounted, on the rear face the return harness is implemented.
The resulting torque is

$$T = M \times B = M \cdot B \cdot \sin \vartheta \tag{17}$$

The direction of the torque is such that the dipole tends to orient itself parallel to lines of force of **B**, minimizing the potential energy and achieving a stable position.

This torque has to be in principle neutralised by the Attitude and Orbit Control System of the satellite, which implies the usage of thrusters (i.e. fuel consumption) or increased authority of magneto-torques and/or reaction wheels (electrical power and mass impact).

Clearly there are two ways for the minimisation of this torque; the first one is the minimisation of the areas of the current loops; the second one concern the layout of the solar array strings; adjacent strings can be disposed on the panels in opposite directions, such that the individual torques generated are balanced. With this solution, solar cells having the positive terminal at the string open circuit voltage will lay very close to cells having the negative terminal at 0V. And this opens the door to another issue to be faced.

7.5 Electrostatic Discharges (ESD)

The space plasma is the cause of the accumulation of electrostatic charges on the spacecraft surfaces. The energy of the plasma changes with the altitude; it is around 10,000 eV at about 36,000 km (Geostationary Orbits, GEO) decreasing to 0.1 eV for below 1,000 km (Low Earth Orbits, LEO), within the Van Allen Belts. For what concern the solar arrays it can be said that the interconnections between solar cells and the cell edges are exposed to plasma, and the output voltage resulting at the terminals of a string plays an important role. The worst scenario occurs at BOL, at the minimum operative temperature (eclipse exit). In these conditions the open circuit voltage is at the maximum value, if triple junction solar cells are used and a string is for instance composed of 34 cells, this voltage can be above 90V; this is the maximum voltage between two adjacent cells.

The value of the maximum current that can flow through a conductive part of the array (usually the current of a single string if each is protected by a diode) is also important; indeed it has been proofed that in order to have a self sustained secondary arc, minimum value of the current for a particular voltage is needed. In case of ECSS standard applies, in particular "Spacecraft Charging – Environment Induced Effects on the Electrostatic Behaviour of Space Systems (**ECSS-E-20-06**)", then it can be said that no tests are required to prove the safety of the solar array to secondary arcing when the maximum voltage-current couple available between two adjacent cells on the panel, separated with 0.9mm as nominal value, is below the threshold in the following table:

VOLTAGE	CURRENT	COMMENTS
70 V	0.6 A	No self sustained secondary arcing possible
50 V	1.5 A	No self sustained secondary arcing possible
30 V	2 A	No self sustained secondary arcing possible
10 V	-	Voltage is too low to allow any arcing

Table 2. ESD limit conditions

An inter-cell gap between strings of adjacent sections may be defined at 2 mm, cell to cell, that means 1.85 mm between cover-glasses. Finally, taking into account tolerances of the tools used during manufacturing of the solar array, it results that the distance between adjacent strings is always higher than 1.6 mm

8. Solar array configurations

The solar arrays mounted on a satellite can have very different shapes, accommodations and dimensions. The configuration of a solar panel is the result of several design iterations made at satellite level, considering the mission requirements, the needed power, the dimensions, mass, and the spacecraft attitude to be kept during the whole lifetime and in all the possible satellite working modes. However three or four main configurations of the solar array can be identified.

8.1 Spinning satellite
The first configuration is the one characterising a spinning satellite. The satellite usually has cylindrical shape with the symmetry axis as the rotation one. This configuration was the first one to be adopted; the available power is not elevated with respect to the panel surface, indeed the equivalent active area results from the division of the actual area of panel by π. The satellite Meteosat is a good example; this configuration is nowadays rarely used, but in some cases is still interesting for scientific satellites like those of the Cluster mission.

Fig. 17. Solar Array for spinning Satellite, Meteosat Second Generation (Credits: ESA - MSG Team)

8.2 Body mounted panels
The second configuration foresees the panels body mounted to the spacecraft walls. The panels are rigidly fixed to the structure and their orientation towards to the sun is never optimal.

Fig. 18. Body mounted solar array, GOCE (Credits: ESA - AOES Medialab)

This solution has been recently adopted for earth observation and scientific satellites with a reduced power need, no more than 1 kW. In case of earth observation satellites the nadir-

pointing attitude of the instruments results in highly variable illumination of the panel, therefore the computation energy budget can be quite challenging because the power subsystem may have power coming from both solar array and battery pack at the same time along the orbit. This behaviour may significantly reduce the useful time for the recharge of the battery in sunlight, and an oversized solar panel may be needed. The ESA spacecraft GOCE is a good example of such body mounted panels; two of them are installed on the fixed "wings" of the satellite, the other two are on the "fuselage". It is worth to note that the temperatures on the solar panels are very different between one another, this because of the different illumination levels and different thermal exchange of the wings (remaining colder) with respect to the fuselage (hotter panels). Such configuration, dictated by many other requirements at satellite level, can have a huge impact in the complexity of the power conditioning concept to be adopted.

8.3 Deployable wings

The third one is the classical double deployable wing. This solution is classical for telecommunication geostationary satellites. Each wing is moved by a Solar Array Driving Mechanism having the rotation axis perpendicular to the orbital plane. The illumination is optimized by the automatic orientation of the panels. This kind of configuration is the best solution when several kilowatts are needed, as in the case of recent telecom satellites. Each wing is then composed of several panels kept folded at launch, and then progressively deployed by suitable mechanisms at early phase of the mission. The satellite Hylas-1 gives a good example for such solution.
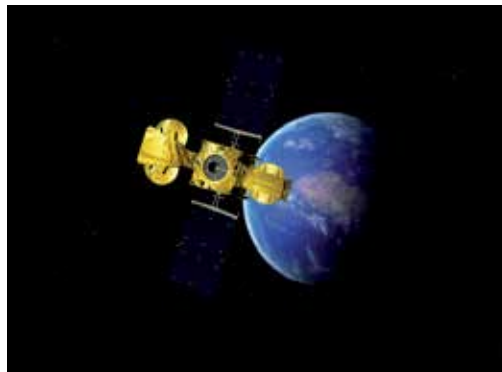
Fig. 19. Deployable Solar panels, Hylas-1 (Credits: ESA - J. Huart.)

9. Design and simulation examples

The following two examples will show how a spacecraft solar array, composed of one or more panels having different orientations, provide the needed power during the mission. The examples reported consider body mounted panels, having a fixed orientation with respect to the satellite body axes. This kind of panels is typically used for small and medium satellites, with a power demand less than 1 kW. If on one hand they are relatively cheap and easy to realise, on the other they may require additional efforts for the proper assessment of the energy budget throughout the orbits. This is particularly true in case of the power bus is an unregulated one, having wide voltage variations because of the battery

charge and discharge cycling. In conclusion their design may be particularly challenging because of their typical small size, many times conditioned by the allowed dimensions and mass of the satellite, and the irregular illumination along the orbit.

The first example concerns an Earth observation satellite made as a cube. Three lateral sides are covered by solar cells; the fourth one accommodates the instruments and is Nadir pointing. The last two sides of the cube are parallel to the orbital plane. This configuration of the satellite is such that the illumination of each panel results to be almost sinusoidal, when the sun-light is incident on the panel itself. The temperatures will follow the same type of law, and the available electrical power as well. The orbit is sun-synchronous, and the transmitters are working when the ground stations are visible. The satellite is small; its required power is about 160W, and 60W are consumed by two different transmitters at different transmission frequencies. Each panel accommodates 8 strings of 18 cells each; the power conditioning is based on the S3R regulator with a battery power bus (battery directly connected to the distribution bus. This architecture is the one which can be prone to the lock-up of the power bus previously described, due to over-discharge of the battery after eclipse periods. The problem is however mitigated by the possibility to have a sun-bathing mode when the satellite passes over the oceans and in any case in the southern hemisphere. In this operative mode two of the three panels will have the common edge oriented towards the Sun, the sunlight incidence will be 45 deg. Figure 20 shows when these sun-bathing phases can occur (red ground-track).
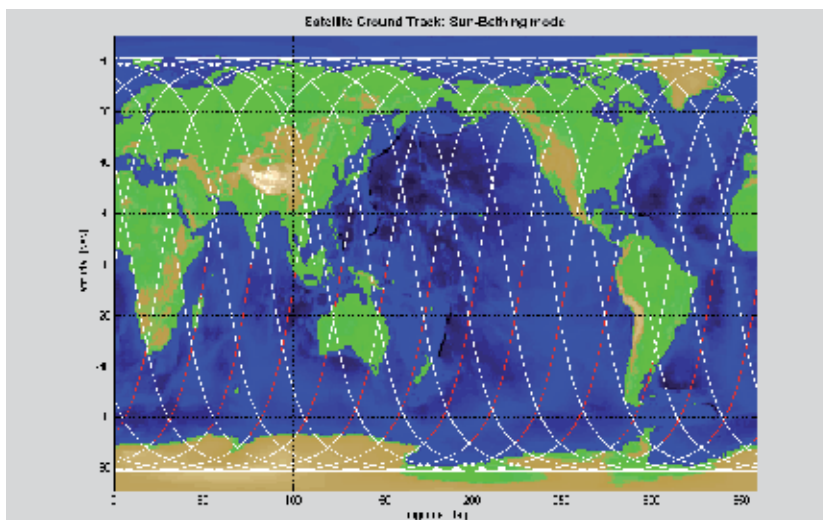
Fig. 20. Satellite ground track

As said, the required power is mainly function of the duty cycle of the transmitters when the ground stations are visible. In this example the three ground stations, typically used for earth observation missions are Kiruna (light blue), Fairbanks (magenta), and Redu (yellow). Figure 21 shows when these stations are visible, together with the eclipse periods (blue ground track). The illuminations of the panels for 24 hours (14 orbits) simulation are reported in figure 22. It can be clearly seen when the sun bathing occurs: panel #3 shows a constant illumination of about 950 W, while the panel #2 (magenta) has a slight increase due to the albedo effect; the panel #1 results to be not illuminated.
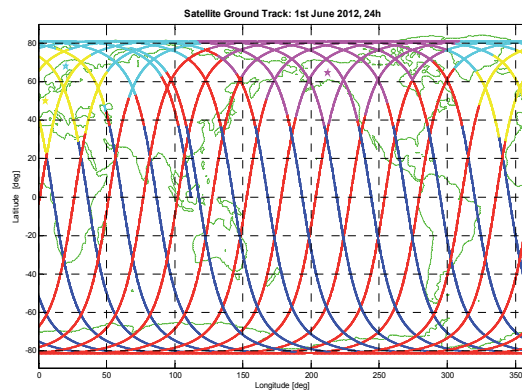
Fig. 21. Ground station visibility and eclipses

Figure 23 shows the calculated temperatures for the three panels. Finally, figure 24 reports the available power from the array, the power exchanged by the battery, and the power required by the loads; from this plot it can be clearly seen the power delivered by the battery is adequately balanced by the power used for recharging them.
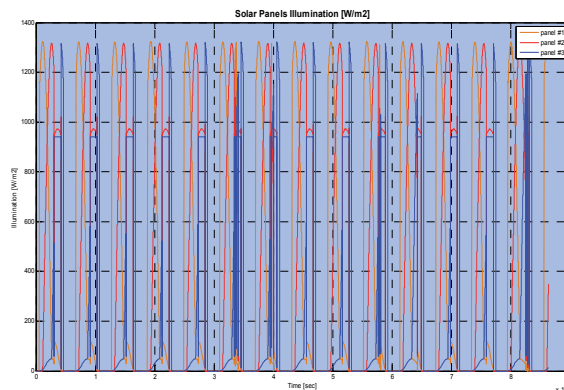
Fig. 22. Illumination of solar panels over 24 hours period
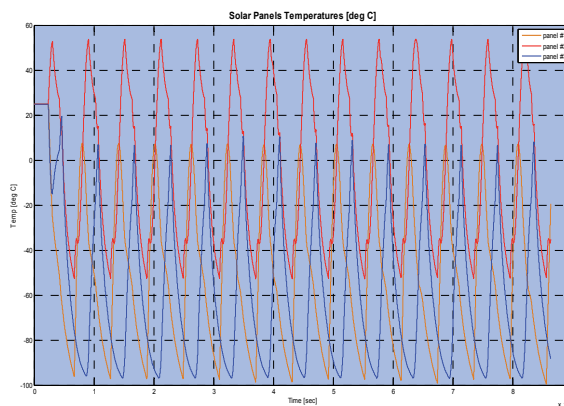
Fig. 23. Temperature of solar panels over 24 hours period
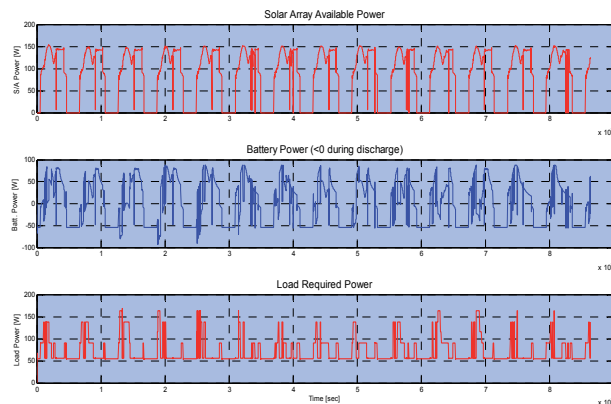
Fig. 24. Power Balance

The second example concern the design of a body mounted solar array which output power is conditioned by a MPPT control system. This is the case of LISA Pathfinder, which solar array is composed of 39 strings of 24 cells each, for 650W required power in EOL conditions. The nominal attitude during the mission is sun pointing, and the limited surface available for the solar array is due to mission and spacecraft configuration constraints. At a certain stage of the project it was decided to separate the solar panel from the rest of the structure by dedicated supports. This solution introduced the possibility to have different working temperatures between the strings and cells belonging to the same string, because of different thermal exchange modalities among centre and periphery of the panel.

Fig. 25. LISA Pathfinder artistic impression

Therefore it was worth to analyse whether a temperature gradient of 30 °C between centre and periphery may originate knees in the I-V curve that may be recognised as false maximum power points by the MPPT control loop, leading to a block of the working point of the array in a non optimal position. Figure 26 shows the layout of the solar cells within their strings, adjacent rows of cells of the same colour belong to the same string. The resulting I-V curve (green) of the whole array is showed in figure 27, as term of comparison the two V-I curves calculated considering constant temperature are also reported as term of comparison. To be observed that the cell with the lowest temperature in a string rules the maximum current flowing trough the string itself. From the plot it can be concluded there are no knees between the open circuit voltage and the maximum power knee such to provoke the lock of the MPPT tracker around a false maximum power working condition.
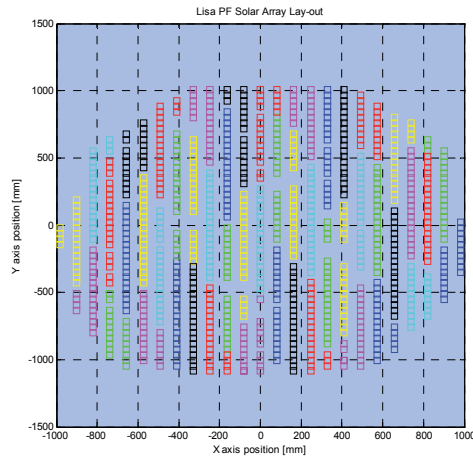
Fig. 26. Solar array layout

Figure 28 shows the illumination and the temperature reached by the solar panel in the first orbits after launch, the temperature over the panel is now considered as constant. It can be observed that the illumination takes into account also the contribution of the albedo just before and after an eclipse (no illumination), as expected from a solar panel always pointing towards to the sun throughout the orbit.

The figure 29 shows now the extended temperature profile over a period of 24 hours, together with output voltage and current; to be observed that from the fourth orbit onwards the temperature shows an slight increase after 70% of sunlight period has elapsed; this happens because when the battery is fully charged; the maximum power is not required anymore, the operating voltage of the array shifts toward the open circuit value. At the same time it can be seen that the output current decreases. This temperature increase is due to the difference between the maximum available power and the required one; the unused power warms up the array.
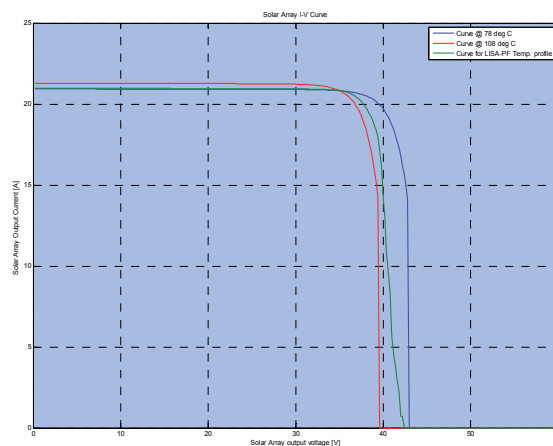
Fig. 27. LISA Pathfinder Solar array, V-I curve
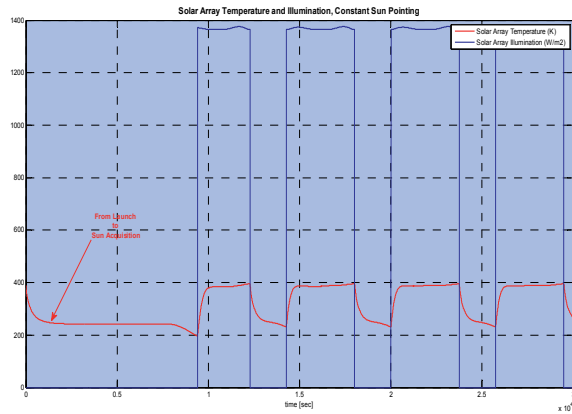
Fig. 28. Solar Array Illumination and temperature, launch phase and first 3 orbits
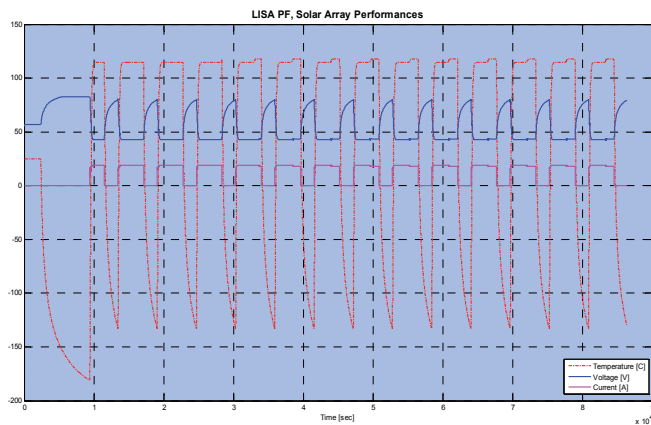
Fig. 29. Solar array temperature, output voltage and current

Finally, figure 30 shows the Depth Of Discharge (DOD %) of the battery from launch. The DOD is progressively recovered the first four orbits. After the fourth one, a stable charge–discharge cycling is reached.
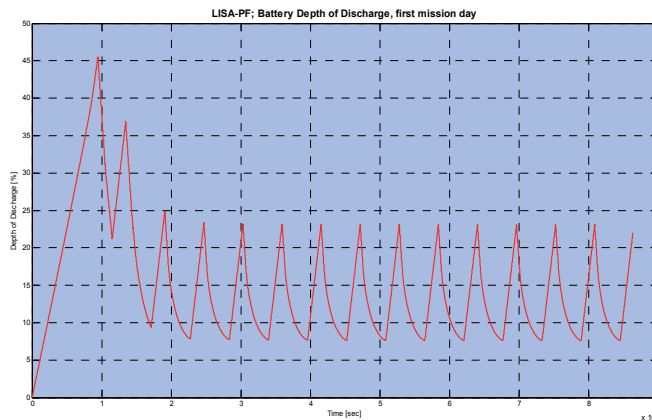
Fig. 30. Battery Depth of Discharge (DOD %) for launch phase and first mission day.

10. Conclusions

Objective of this chapter was to provide guidelines for the design at system level of a solar array for satellites. Such kind of application has to be compliant with severe requirements mainly dictated by the harsh space environment mainly in terms of temperature levels, cosmic radiations which provoke wide variations of the performances together with their continuous degradation. Mass and size of the panels are main constraints with respect to the required power as well as optimal orientation towards to the sun, several times limited by other requirements at spacecraft and mission level. The actual state of the art is represented by triple junction solar cells capable to have a bulk efficiency of more than 30%.

Typical accommodations of these arrays have been illustrated and a few design examples provided. These examples have been chosen among those may be considered as particularly challenging with respect to the required power and energy budgets coupled with mission constraints.

11. References

AZUR SPACE Solar Power GmbH, 3G-28% Solar Cell Data-sheet
        http://azurspace.de/index.php?mm=89

Strobl, G. et al.; (2002). Advanced GaInP/Ga(In)As/Ge Triple junction Space Solar Cells, *Proceedings of ESPC 2002 6th European Space Power Conference*, ESA-SP 502, Oporto, Portugal, May 2002.

Neugnot, N. et al.; (2008). Advanced Dynamic Modelling of Multi-junction Gallium Arsenide Solar Arrays, *Proceedings of ESPC 2008 8th European Space Power Conference*, Konstanz, Germany, Sept. 2008.

Tada, H. and Carter, J., Solar Cell Radiation Handbook, *JPL Report* 77-56, Caltech, Pasadena, 1977

Mottet, S., Solar Cells Modelisation for Generator Computer Aided Design and Irradiation Degradation, *ESA Symposium on Photovoltaic Generators in Space*, pagg. 1-10, Heidelberg, 1980.

Ferrante, J., Cornett, J. & Leblanc, P., Power System Simulation for Low Orbit Space craft: the EBLOS Computer Program, *ESA Journal* Vol 6, 319-337, 1982.

Diffuse Surfaces, *ESA PSS-03-108* Issue 1, 1989

O'Sullivan, A. Weinberg: The Sequential Switching Shunt Regulator (S³R)*; Proceedings Spacecraft Power Conditioning Seminar,* ESA SP-126, 1977

Colombo, G., Grasselli, U., De Luca, A., Spizzichino, A., Falzini, S.; Satellite Power System Simulation, *Acta Astronautica*, Vol. 40, No. 1, pp 41-49, 1997.

De Luca, A. et al.; The LISA Pathfinder Power System, *Proceedings of ESPC 2008 8th European Space Power Conference*, Konstanz, Germany, Sept. 2008.

De Luca, A., Chirulli, G.; Solar Array power Conditioning for a spinning satellite, *Proceedings of ESPC 2008 8th European Space Power Conference*, Konstanz, Germany, Sept. 2008.

De Luca. A.; Simulation of the Power System of a Satellite, graduation thesis, *ESA EAD (European Aerospace Database)*,Quest Accession Number 96U03072, 1996. or *Database NASA*, Quest Accession Number 96N48163, 1996.

Power Output Characteristics
of Transparent a-Si BiPV Window Module

Jongho Yoon
Hanbat National University
Republic of Korea

1. Introduction

Energy-related concerns about traditional resources include the depletion of fossil fuel, a dramatic increase in oil prices, the global warming effect caused by pollutant emissions from conventional energy resources, and the increase in the energy demand. These concerns have resulted in the recent remarkable growth of renewable energy industries [1-3]. Furthermore, renewable energy has become a significantly important research area for many researchers as well as for governments of many countries as they attempt to ensure the safety, long-term capability, and sustainability of the use of global alternative energy resources [2]. Renewable energy resources include solar, geothermal, wind, biomass, ocean, and hydroelectric energy. [4] In particular, both solar (i.e. photovoltaics) and wind energy are considered to be leading technologies with respect to electrical power generation.

The study of photovoltaics (PV) has been carried out since the 1980s' and is currently the most significant renewable energy resources available. According to the Renewable Energy Policy Network for the 21st Century (REN21), there has been a strong growth in the use of PV of 55 % and the worldwide solar PV electric capacity is expected to increase from 1,000 MW in 2000 to 140,000 MW by 2030 [5]. Moreover, it is forecast by the European Renewable Energy Council that this renewable electric energy could become sufficient to cover the base load and half of the global electricity energy demand by 2040 [6]. Generally in the PV industry, crystalline silicon has generally occupied about 95 % of the market share of materials, while only 5 % of all solar cells use amorphous silicon [7]. However, in order to improve the cost efficiency of solar cells by using less material, the thin-film PV module with amorphous silicon has become an active research and development (R&D) area [8]. In particular, solar cells that use amorphous silicon have the advantage of being able to generate a higher energy output under high temperatures than crystalline silicon solar cells, which are less affected by the temperature increase with respect to performance of electricity output than are the crystalline silicon solar cells. Moreover, installed at the rooftop and on the exterior wall of the building, a thin-film solar cell can be conveniently used as a façade that generates power for the entire building. This system is known as a building integrated photovoltaic system (BIPV). The thin-film solar cell can also provide the advantage of heat insulation and shading when incorporated into a harmonious building design. Therefore, the thin-film solar cell is expected to be a very bright prospect as a new engine for economical growth in the near future. Currently in Korea, many researchers are conducting

vigorous research on PV with respect to the application of crystalline silicon solar cells. An example of such research includes the evaluation of the power output of PV modules with respect to the ventilation of the rear side of the module. However, research on the transparent thin-film solar cell as a building façade application including windows and doors is only in its early stages.

Therefore, the objective of this study is to establish building application data for the replacement of conventional building materials with thin-film solar cells. In this study, an evaluation is carried out on the performance of the thin-film solar cell through long-term monitoring of the power output according to the inclined slope (the incidence angle). This is conducted by using a full-scale mock-up model of the thin-film solar cell applied to a double glazed system. In addition, the aim of the application data of the thin-film solar cell is to analyze the effect of both the inclined slope and the azimuth angle on the power output performance by comparing this data with the simulation data for PV modules[9].

2. Methodology

In this study, a full-scale mock-up model was constructed in order to evaluate the power output performance of a PV module laminated with a transparent thin-film solar cell. A mock-up model was designed for a PV module that had a range of inclined slopes, and was used to measure the power output according to the slope (incidence angle) and the azimuth angle. The collected experimental data was then compared with the simulated data for a power performance analysis.

A commercialized single plate transparent thin-film solar cell with amorphous silicon was used in this study (KANEKA, Japan). This was modified into a double glazed PV module in order to install the mock-up model for this study.

Using the full-scale mock-up model, the system output was monitored for 9 months. A computer simulation (TRNSYS, University of Wisconsin, USA) of the PV module was also performed at the same time, and empirical application data was calibrated for the statistical analysis of power performance based on the inclined slope and the azimuth angle. In particular, the annual power output of the PV module was obtained by analyzing the data obtained from the remaining 3 months on the basis of the 30 years' standard weather data in Korea.

3. Double-glazed PV module

In Korea, it is an obligatory requirement that building materials such as windows and doors for a residence should be double glazed in order to ensure adequate heat insulation. Moreover, as the demand for energy efficiency buildings increases, the efficiency of double glazed window systems is improving with respect to heat insulation, as is the efficiency of exterior wall systems of buildings. Therefore, the photovoltaic characteristic of thin-film solar cells was measured in terms of the transmittance of the cell prior to evaluation of the PV module (Figure 1). The results of this measurement showed an average transmittance of 10 % at the range of visible radiation between 390 nm and 750 nm.

Using this thin-film solar cell, a single plate PV module was manufactured to a thickness of 10 mm, and the PV module was then modified as a double glazed module of 27 mm thick, consisting of a 12 mm air space and a 5 mm thick layer of common transparent glass, as shown in Figure 2.
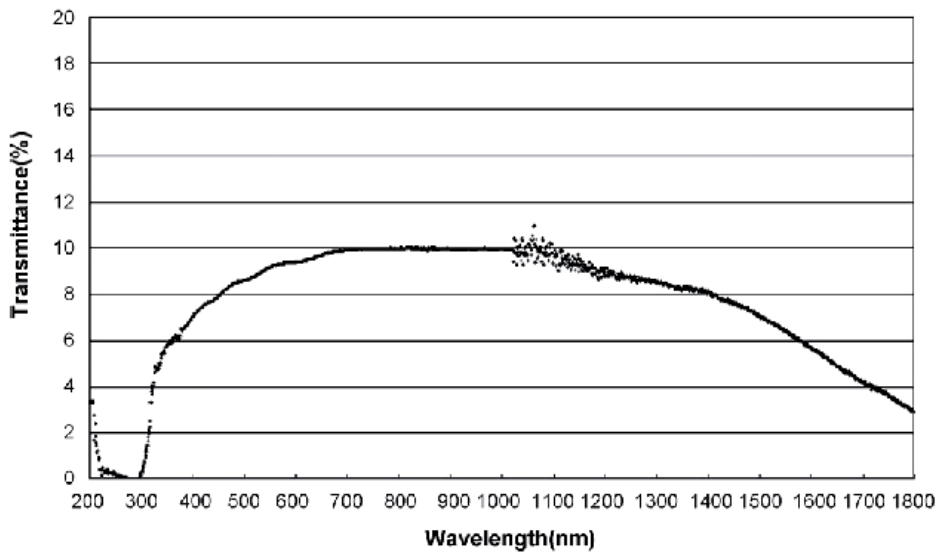
Fig. 1. Transmittance of PV module depending on the wavelength
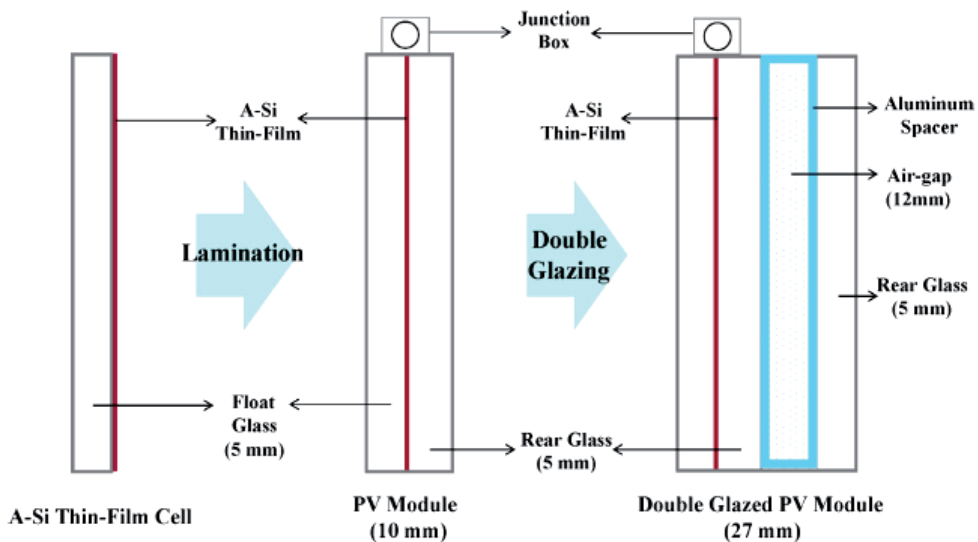
Fig. 2. Preparation for single plate of double-glazed PV module using transparent amorphous silicon (A-Si) thin-film cell.

From the performance evaluation of the heat insulation, the prepared PV module exhibited a 2.64 W/m²·℃ thermal transmittance, as shown in Figure 3. However, it showed an 18 % solar heat gain coefficient (SHGC), which was much lower than that measured for the common double glazed window. WINDOW 6.0 and THERM5.0 (LBNL, USA) were used to analyze the heat insulation of the standard type of double glazed PV module widely used

for the heat insulation of building windows and doors. This analysis allowed for the evaluation of heat transfer under a two dimensional steady state for the user defined fitting system at a given circumstance.
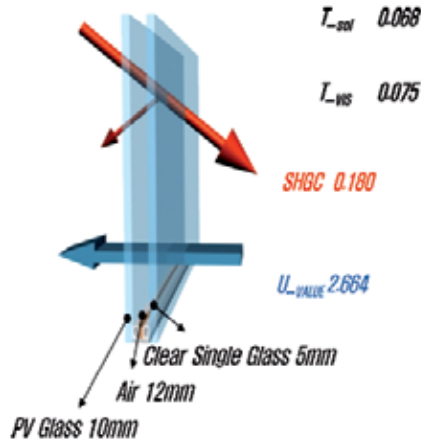
Fig. 3. Optical and thermal characteristics of double-glazed PV module (T_sol is the solar transmittance, T_vis is the transmittance of visible radiation, SHGC is the solar heat gain coefficient, and U_value is the thermal transmittance of PV module).module

Figure 4 shows a plane figure of a 10 mm thick and 980 × 950 mm single plate PV module, and a PV module consists of 108 cells in series. The electrical characteristics of the prepared PV module are listed in Table 1.
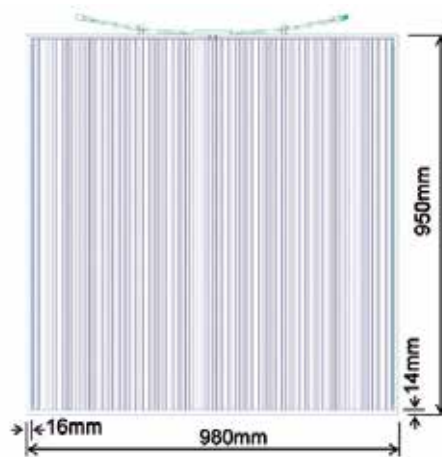
Fig. 4. Plane figure of a single plate PV module.

4. Full-scale mock-up model

A full-scale mock-up model was constructed with the dimensions of 8 m long, 5 m wide, and 3.5 m high, as shown in Figure 5. In order to demonstrate the impact of the inclined

Item	Specification
Module thickness (mm)	10
Module efficiency (%)	7
Maximum power output (W)	44.0
Maximum voltage (V)	59.6
Maximum electric current (A)	0.74
Open circuit voltage (V)	91.8
Short circuit current (A)	0.972

Table 1. Specification of the tested thin-film PV module

slope (incidence angle) on the power output, the inclined angles were varied on the mock-up by installing both a tilted roof at 30° and a common roof without any slope. The mock-up faced south in order to maintain a compatible solar irradiance with the location of Yongin, Gyeonggi, Korea. Two separated spaces were prepared in order to test the thin-film PV module (Test room A in Figure 5(a)) and the common double glazed window (Test room B in Figure 5(a)) as a reference. The spaces were 2 m long, 3 m wide, and 2.7 m high. The double glazed PV module and the common double-glazed window were installed in each separated test room at different inclined angles (0 ^{o}, 30 ^{o}, and 90 ^{o}).

A mock-up model was also constructed in order to monitor the electric current, voltage, power, temperature, and solar irradiation depending on the inclined angle of the PV module. The double glazed thin-film PV module revealed only a 10 % transmittance (See Figure 1), but this was as sufficient as the common double glazed window for observing the outside.

5. Power performance of PV module

5.1 PV module performance measured in mock-up model

The total solar irradiance and power output of the PV module, depending on the inclined angle of double glazing, were monitored through the mock-up model for 9 months from November 2006 to August 2007. Data obtained from the mock-up was collected based on minute-averaged data, and the final data of 12,254,312 was statistically analyzed based on 56 variables. Firstly, daily data was rearranged into monthly data. Secondly, minute-based data was averaged and combined into an hourly data. Finally, each group was analyzed in terms of an arithmetic mean, standard deviation, minimum, and maximum value. The empirical data in this study was limited in DC output, which was obtained from the load using resistance without an inverter. Thus, it is assumed that there may be a number of differences between the data measured in this study and the empirical data controlled by maximum power peak tracking (MPPT) using an inverter.

Figure 6 shows the hourly data, which was yearly-averaged, of the intensity of solar irradiance and DC output depending on the inclined angle of the double glazed PV module. Based on the data measured at noon, the inclined slope of 30 ^{o} (SLOPE _30) revealed an insolation of 528.4 W/m², which shows a greater solar irradiation than that for the slopes of 0 ^{o} (SLOPE_0, 459.6 W/m²) and 90 ^{o} (SLOPE_90, 385.0 W/m²), as shown in Figure 6(a). Consequently, the average power output at noon also exhibited 19.9 W for SLOPE_30, which was higher than that shown in the data for SLOPE_0 (15.76 W) and SLOPE_90 (8.6 W) (See Figure 6(b)).
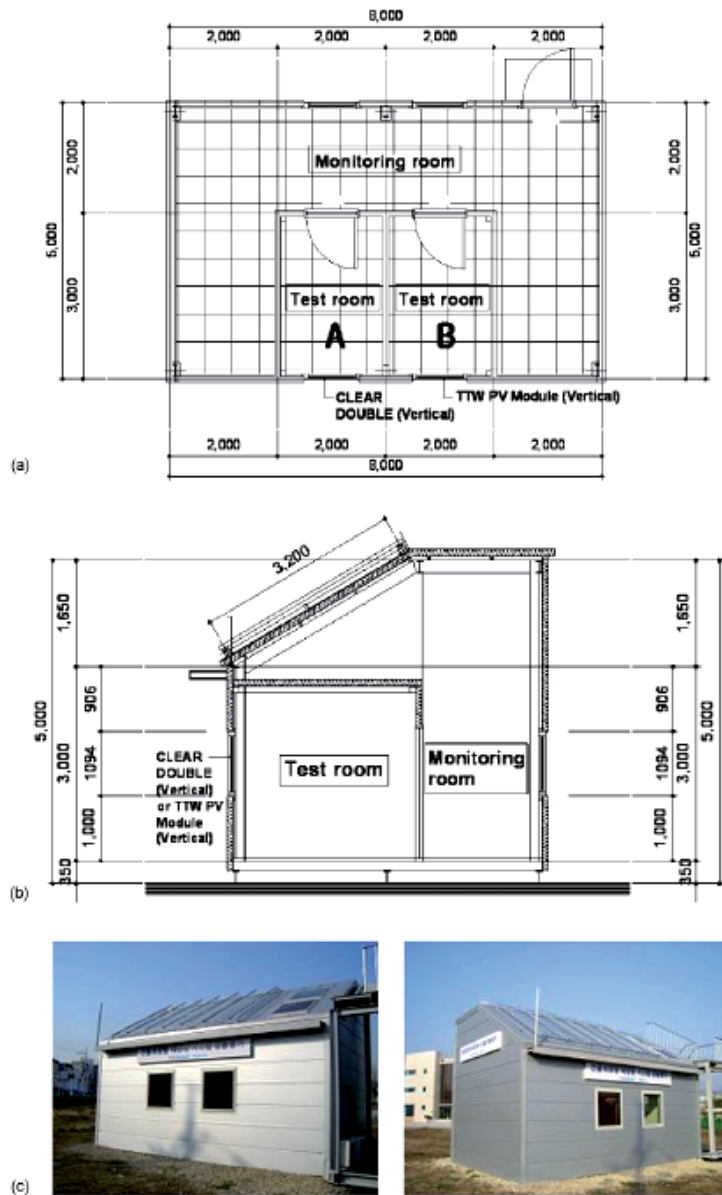
Fig. 5. Full-scale mock-up model: (a) a floor plan view, (b) a cross-sectional view, and (c) photographs of mock-up model.

5.2 Effect of intensity of solar irradiance

Figure 7 depicts the relationship between the solar irradiance taken from the PV module and the DC power output depending on the inclined angle of the module. For all PV modules, the power output increased with an increase in solar irradiance. While the increase rate of power output was particularly retarded under the lower solar irradiance, there was a very steep increase of power output under the higher solar irradiance (See Figure 7).
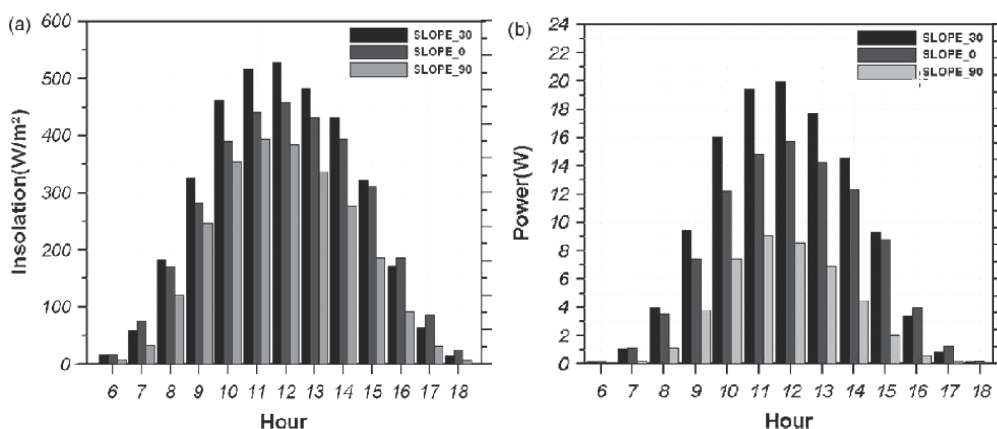
Fig. 6. Monitoring data of PV module depending on the slope through the mock-up model: hourly data averaged yearly: (a) solar irradiance and (b) power output.

By observing the degree of scattering for each inclined PV module as shown in Figure 7, there was a higher density of power output distribution for SLOPE_30 under the higher solar irradiance. On the other hand, the lowest distribution of power output was revealed for SLOPE_90, even under the higher solar irradiance. The monthly-based analysis revealed that a double glazed PV module inclined at 30 ° (SLOPE_30) produced the greatest power output due to the acquisition of a higher solar irradiation. This result can also be achieved from a PV module with an incidence angle of 40.2 °, implying that it is more efficient to acquire solar irradiation than any other factor (See Figure 7(b)).

In the case of SLOPE_0, there were significant differences in power output with respect to solar irradiance depending on monthly variation (See Figure 7(a)). Specifically, the maximum solar irradiance in December is only 500 W/m² resulting in a power output of 10 W. On the other hand, the maximum solar irradiance of 1,000 W/m² with over 50 W power output was recorded for June. This high efficiency of power performance for SLOPE_0 during the summer could be due to the incidence angle of 36.1 °, which was low enough to absorb solar irradiation.

The reverse tendency of power output for SLOPE_0 was shown for SLOPE_90, which was installed at the horizontal plane. Specifically, a maximum power output of above 30 W was observed. This was due to a quiet efficient solar irradiance with the maximum solar irradiation gain of over 900 W/m² occurring in December. However, a lower solar irradiance of around 500 W/m² with less than 10 W power output was observed during the summer months from June to August. This can be explained by the difference in the incidence angle of the PV module depending on the inclined slope, i.e., the lower incidence angle of 36.6 ° for SLOPE_90 was observed during the winter, particularly in January, while the higher value of 84.6 ° was observed during the summer, especially in June. This implies that solar irradiation capable of producing a much higher power output can be easier to be achieved with a lower incidence angle of solar radiation to the PV module.

5.3 Monthly based analysis of power performance

Figure 8 shows the amount of solar irradiation and power output accumulated for each month depending on the inclined angle of the PV module. A fairly effective solar irradiance
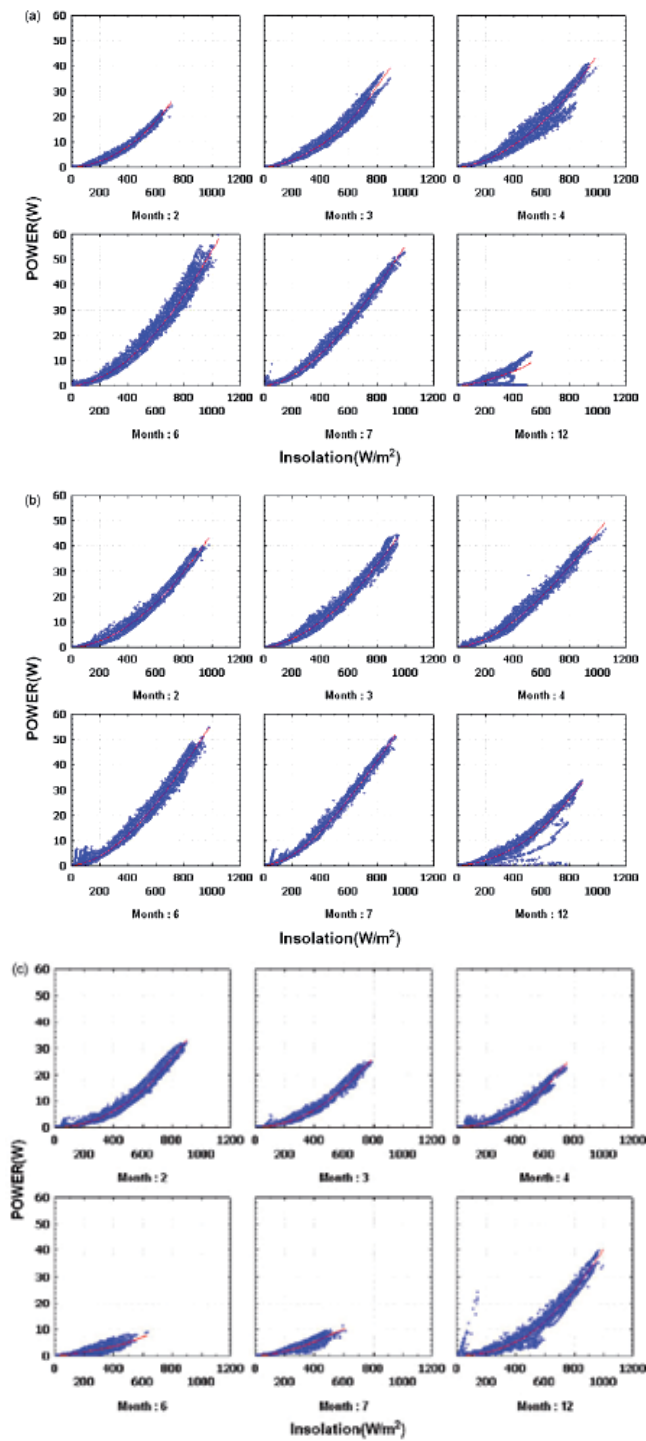
Fig. 7. Power output data of PV modules based on monthly variation of solar irradiance measured in the mock-up model: (a) slope 0, (b) slope 30, and (c) slope 90, respectively.

of 147.7 kWh/m² was obtained from SLOPE_30 during May, and the lowest value of 75.3 kWh/m² was obtained in December (See Figure 8(a)). The horizontal module of SLOPE_0 resulted in the highest solar irradiance in June and the lowest value in January. On the other hand, the PV module installed at the vertical window exhibited the highest solar irradiance (115 kWh/m²) in January and the lowest (50.2 kWh/m²) in August. This can be explained by the highly effective solar irradiance of both of the PV modules that were installed horizontally (SLOPE_0) and tilted at a slope of 30 °. This was due to the smaller incidence angle, defined as the angle between the incident solar ray and the normal line, close to the horizontal plane during the summer and related to the height of the sun, while the PV module installed vertically (SLOPE_90) obtained an effective solar irradiance due to the smaller incidence angle during the winter.

An analysis was also carried out on the monthly power performance depending on the inclined angle of the PV module, as shown in Figure 8(b). From the monthly data in Figure 8(b), it can be seen that the most effective power output during the summer, particularly for June, was obtained at SLOPE_30 and SLOPE_0. However, the highest power output was obtained at SLOPE_90 for January. This could be due to the variation of solar irradiance from each PV module from the different incidence angles based on the height of the sun.

In this study, the best power performance among all the tested PV modules was that obtained by the PV module tilted at an angle of 30 ° (SLOPE_30), comparing with those installed horizontally (SLOPE_0) and vertically (SLOPE_90).
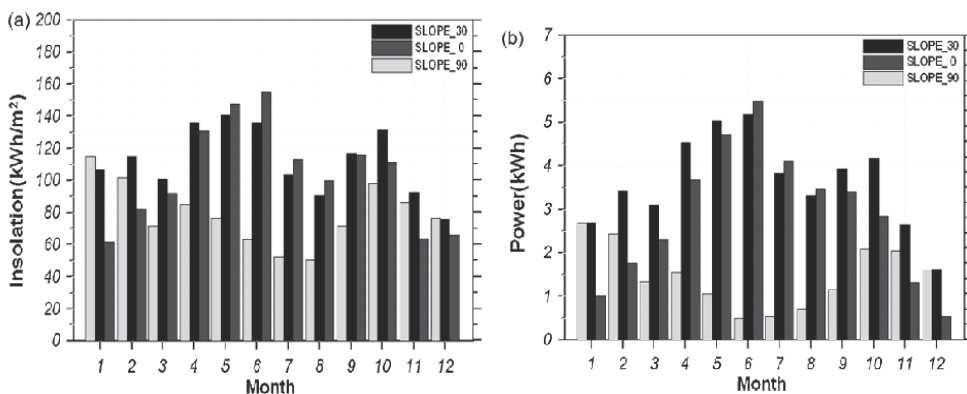
Fig. 8. Monitoring data of PV module depending upon the slope through the mockup model: monthly accumulated data of (a) solar irradiance and (b) power output.

5.4 Hourly based analysis of power performance

Figures 10~12 show the statistically analyzed monthly power generation data of PV module depending the inclined slope. The name of each part is provided for the better understanding in Figure 9. ■ sign in each box indicates Mean value, □ and ⊠ signs indicate the range of Mean±S.D (Standard Deviation), Whisker Ⅰ sign indicates the range between maximum and minimum values. For example, in the first graph of Figure 10, the mean value at 12pm in January is approximately 20W, S.D. (Standard Deviation) is 5~30W, maximum value is 40W and the minimum value is 0W. The statistical data on how much power is generated in each hour can be easily understood with these graphs. Furthermore, the maximum and minimum ranges can also be easily analyzed, enabling the comparison of characteristic behaviors depending on the inclined angle.
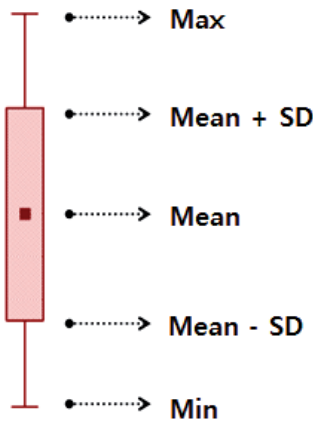
Fig. 9. Explanation of Box-Whisker graph
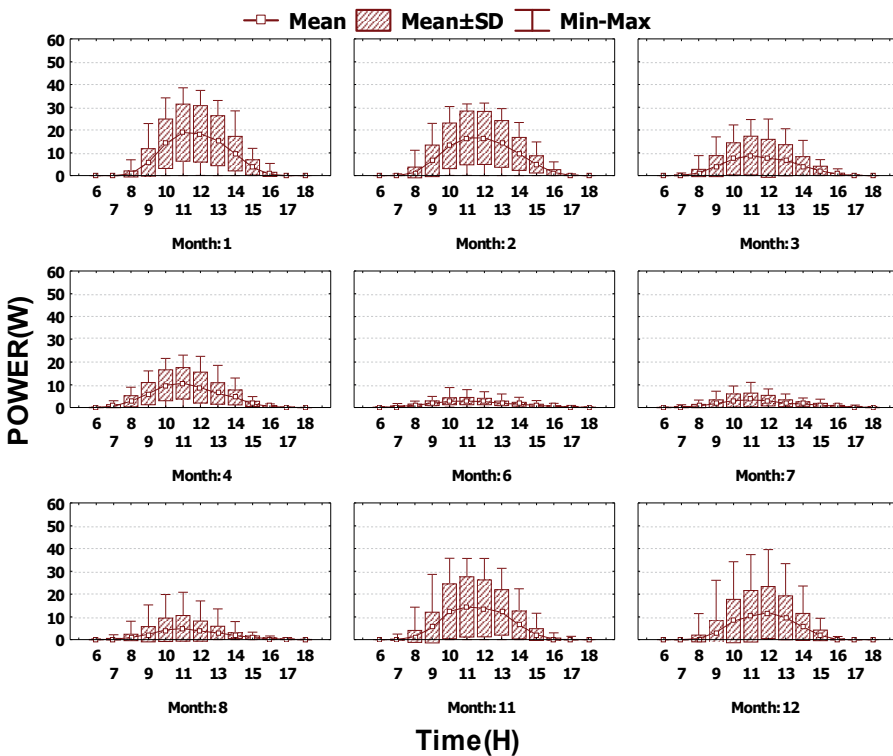
Fig. 10. Power generation of SLOPE._90° in each timestep

In case of vertical PV module, the power generation turns out be significant in Janurary due to a farily effective solar irradiance. It showed the power generation of 20W on average at noon. On the other hand, in June when there is no high solar irradiance due to high incidence angle, the power generation was less then 10W on average at noon. The inclined slope of 30 ° showed the best power generation during the measurement period. Especially the power generation was the greatest in June with 30W on average at noon.
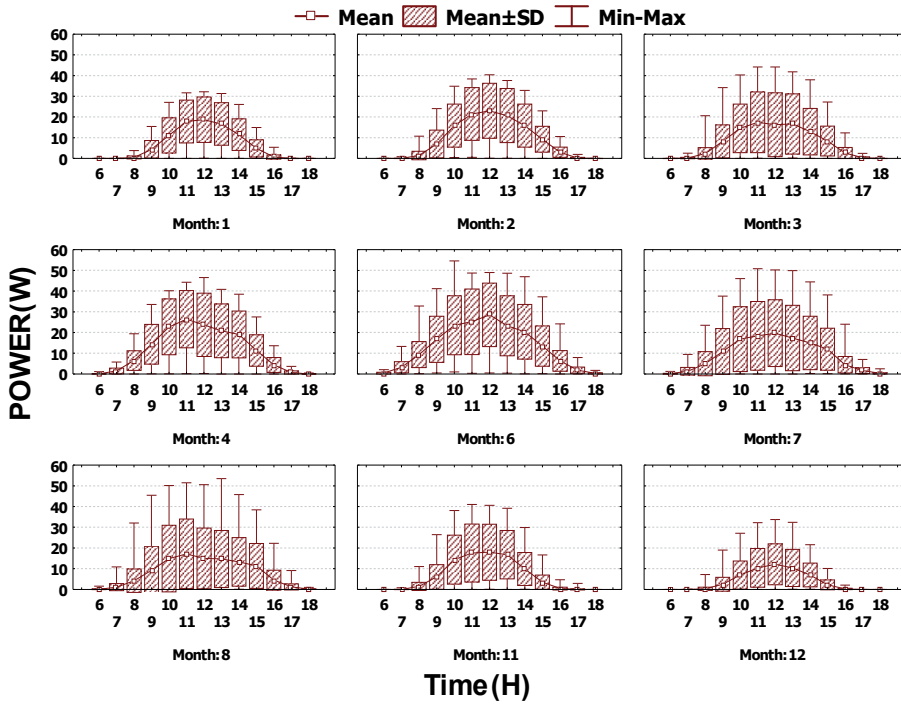
Fig. 11. Power generation of SLOPE._30° in each timestep
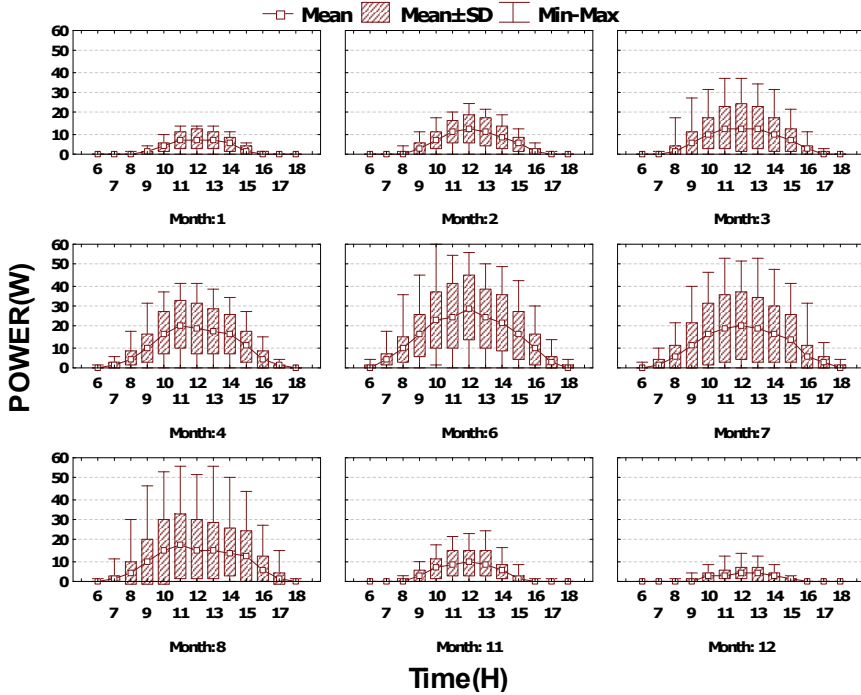
Fig. 12. Power generation of SLOPE._0° in each timestep

In case of horizontal PV module, it showed effective power generation performance in the summer similar to the case of the inclined slope of 30 °, showing more than 30W generation on average at noon. However, the generation barely exceeded 10W in December due to high incidence angle and low solar irradiance. The hourly average power generation depending on each inclined angle is illustrated in Figure 13. In case of inclined angle (SLOPE_30), it showed power generation of 20W on average at noon, while the horizontal PV module showed 15W on average. Vertical PV (SLOPE_90) showed the low generation performance of 8W on average. Table 5.5 summarizes the hourly average power generation, voltage and electric current.
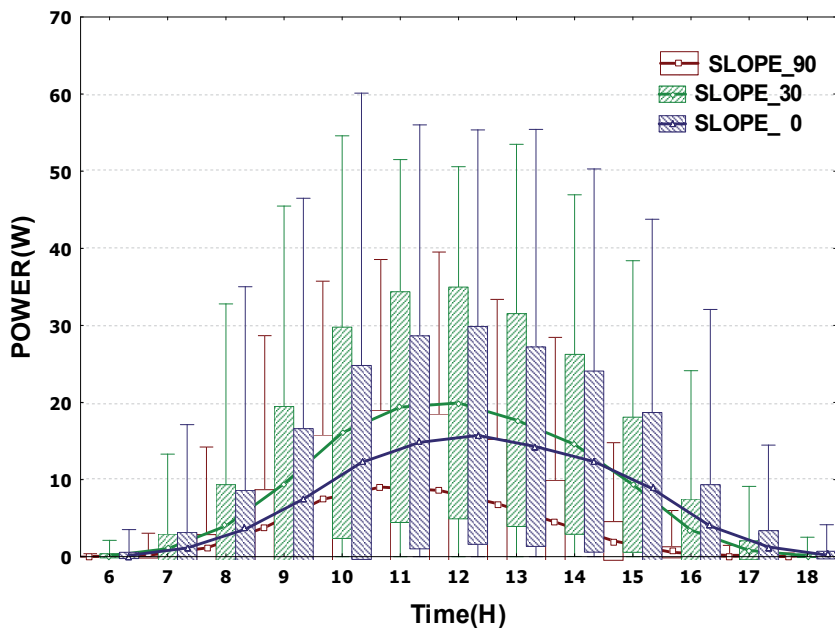
Fig. 13. Annual hourly averaged power generation

5.5 Analysis of power performance through simulation

In this study, TRNSYS (Ver. 14.2, Solar Energy Laboratory, Univ. of Wisconsin, USA) was used as a simulation program to analyze the performance of power output for a double glazed PV module. Generally, TRNSYS has been widely used to compute the hourly data for power output, solar irradiance, temperature, and wind speed for both PV systems and solar heat energy systems [10]. From the simulation program, the relative error was verified, and a comparison was then made of the power output from the experimental and the computed data, as shown in Figure 14. In addition, the experimental data from the PV module with an inclined angle of 30 ° (SLOPE_30) was compared with the simulated data in terms of the annual power output: 1,060 kWh/kWp was obtained from the experiment and 977 kWh/kWp was estimated from the computational simulation. This computed data showed a relative error of 8.5 %, which is considered to be a reliable result within the error tolerance. Thus, the computational simulation was conducted to demonstrate the power output performance of a PV module installed at various inclined angles.
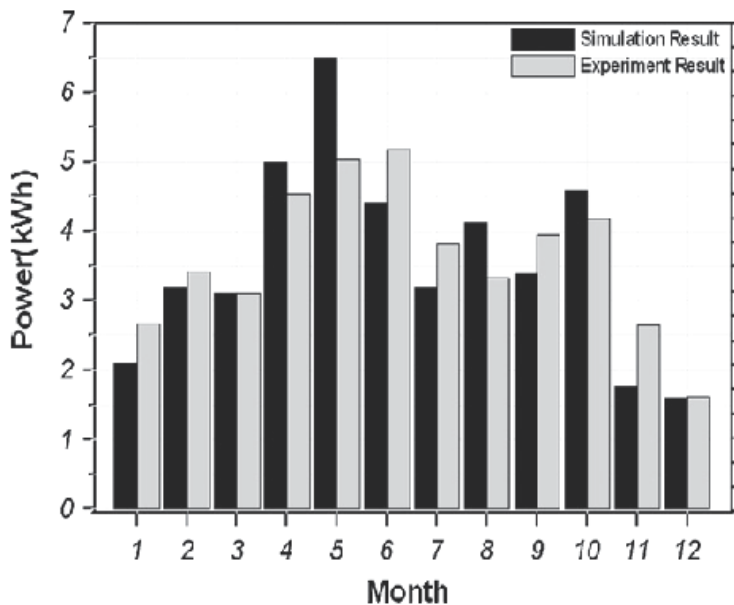
Fig. 14. Power output data calibration by comparing the experimental data to the computed data obtained from the simulation program (TRNSYS).

Power performance analyses were performed of PV modules facing south (azimuth = 0 º) depending on the different inclined angles of 0 º, 10 º, 30 º, 50 º, 70 º, and 90 º. The data set consisted of the experimental data for 0 º, 30 º, and 90 º and the computed data for 10 º, 50 º, and 70 º. Figure 15 illustrates the monthly power output depending on the inclined angle ranging from 0 º to 90 º south (azimuth = 0 º). PV modules that were tilted at an angle below 30 º showed a relatively good power performance of over 6 kWh in the summer, while those with an inclined angle above 50 º demonstrated a power performance of less than 6 kWh. The most effective annual power output data of 977 kWh/kWp was obtained at an inclined angle of 30 º (SLOPE_30), as shown in Figure 16. On the other hand, the lowest annual power output of 357 kWh/kWp was obtained from the PV module with a slope of 90 º (SLOPE_90), which was 37 % of the annual power output of SLOPE_30. From Figure 16, it can be seen that the annual power output performance was effective in the order of SLOPE_10 (954 kWh/kWp), SLOPE_0 (890 kWh/kWp), SLOPE_50 (860 kWh/kWp), and SLOPE_70 (633 kWh/kWp).

The power generation performance depending on the angle of the azimuth was also estimated for PV modules with different inclined slopes, as shown in Figure 17. Similarly, a PV module inclined at an angle of 30 º showed the most effective power output data for all directions in terms of azimuth angles, and the lowest data was obtained from that with an inclined angle of 90 º. For the PV module inclined at an angle of 30 º, the best power performance among the analyzed PV modules facing various directions was obtained for the PV module that was installed to the south (azimuth = 0 º). It can be seen from Figure 17 that different azimuth angles affected the power performance of PV modules: that is, the power performance decreased as the direction of the PV module was changed from the south to the east and west, in comparison to the PV modules that were inclined at the slope of 30 º, as listed in Table 2.
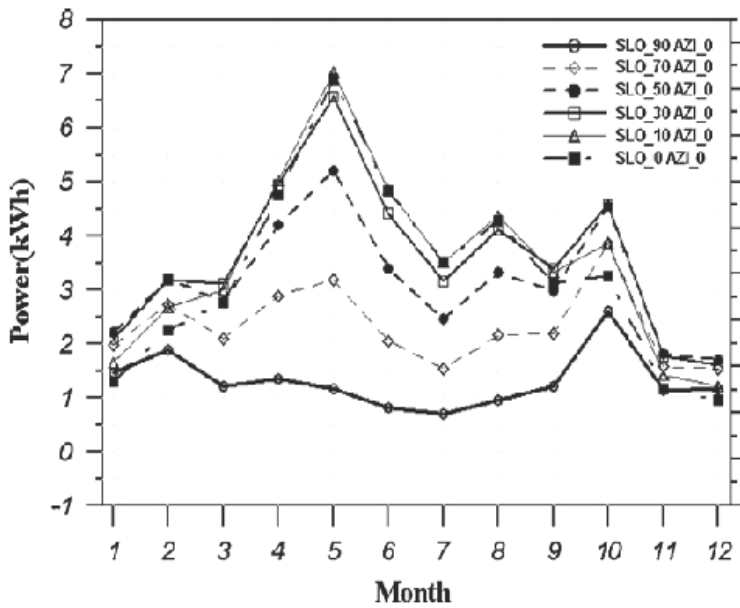
Fig. 15. Monthly power output data of PV module depending on the slope,
and facing south (azimuth = 0).
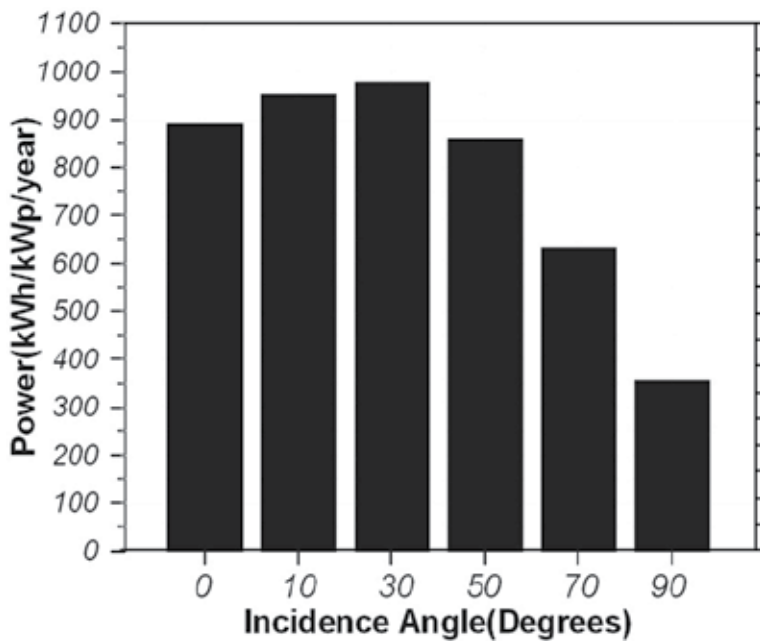
Fig. 16. Annual power production of PV module depending on the slope, and facing south
(azimuth = 0).
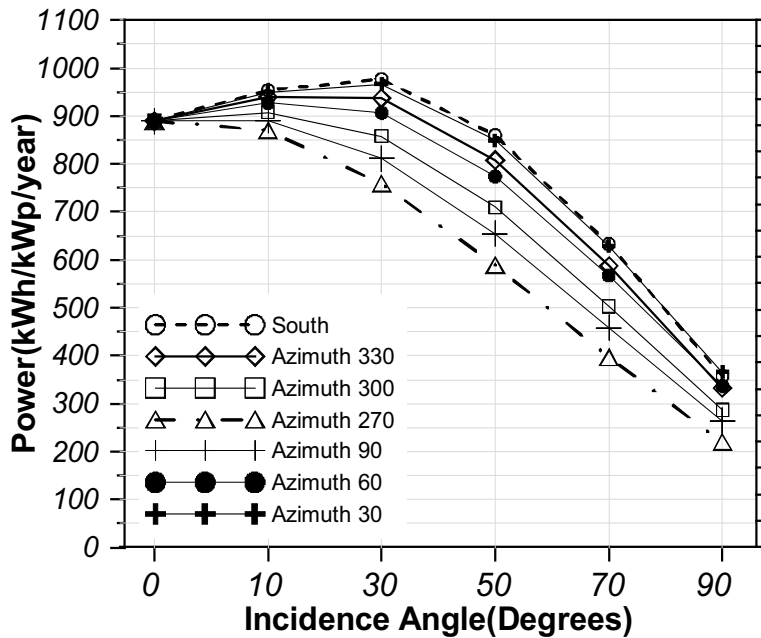
Fig. 17. Annual power production of PV modules with various slopes depending on the angle of azimuth ranging from 0 to 90

Angle of azimuth (º)	Direction	Power performance efficiency[a] (%)
0	South	100
30	Southwest 30 º	99
60	Southwest 60 º	93
90	West	83
270	East	78
300	Southeast 60 º	88
330	Southeast 30 º	96

a. Power performance efficiency was calculated from the percent of power output at each azimuth angle on the basis of the power output data of PV module to the south.

Table 2. Power performance efficiency of PV module with a slope of 308 depending on azimuth angle

It can be seen from Figure 17 that for the annual power performance of several PV modules, the power output increased with an increase of the inclined angle below 30 º, and decreased with an increase of the inclined angle above 30 º. In particular, at inclined slopes above 60 º there was a steep decline of power performance with the increase of the inclined slope, as shown in Figure 17. This could be due to the incidence angle modifier correlation (IAM) of glass attached to the PV module, which showed a similar tendency in IAM depending on the inclined angle [11], as can be seen in Figure 18. Actually, IAM should be computed as a function of incidence angle (θ) when estimating the power output of the PV module, by using the following Equation (1) [11]:

$$IAM = 1 - (1.098 \times 10^{-4})\theta - (6.267 \times 10^{-6})\theta^2 + (6.583 \times 10^{-7})\theta^3 - (1.4272 \times 10^{-8})\theta^4 \qquad (1)$$
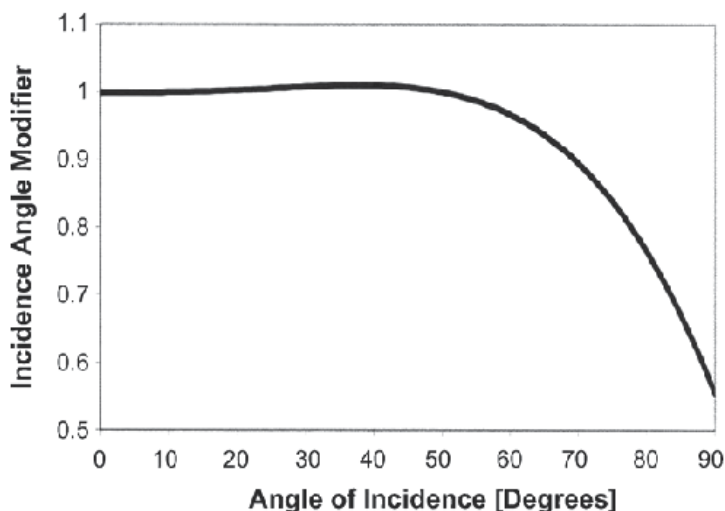
Fig. 18. Correlation of incidence angle modifier given by King et al. (1994).

Accordingly, a characteristic of the glass attached to the PV module is considerably influential so that the solar transmittance (Tsol) remarkably decreases with an increase in the inclined slope of the PV module from the higher incidence angle. Therefore, the solar transmittance efficiency can significantly affect the power output of the PV module.

6. Power efficiency of PV module

6.1 Hourly based analysis of the power efficiency
The power efficiency can be calculated by multiplying total irradiation by the PV window area. Annual averaged power efficiency is illustrated in Fig. 19.

$$\eta_{S,\tau} = \frac{E_{use,\tau}}{A_a \times H_\tau}$$

$\eta_{S,\tau}$; Power Efficiency
$E_{use,\tau}$; Power Output(Wh)
A_a ; PV windows area (m²)
H_τ ; Total irradiation on the PV windows

Annual average power efficiencies of the inclined slope of 30 º (SLOPE_30), horizontal PV module (SLOPE_0) and vertical PV module (SLOPE_90) turned out to be 3.19%, 2.61% and 1.77%, respectively, indicating that the inclined slope of 30 º showed the greatest efficiency. On the other hand, the horizontal PV showed the highest instantaneous peak power efficiency of 6.0% followed by those of the inclined slope of 30 º (5.6%) and vertical PV (4.0%) angles. In terms of the monthly average power efficiency depending on each inclination angle, the inclined slope of 30 º (SLOPE_30) showed 3.82% in June and the horizontal PV (SLOPE_0) showed 3.63% in July. The inclined slope of 30 º showed 2.15 % of efficiency and the horizontal PV showed 0.81% in December. On the other hand, the vertical

PV (SLOPE_90) showed the peak efficiency of 2.38% in February and lowest efficiency of 0.80% in June. The inclined slope of 30 º (SLOPE_30) showed the greatest annual average power efficiency of 3.19%, followed by horizontal and vertical PV modules showing efficiencies of 2.61% and 1.77%, respectively.
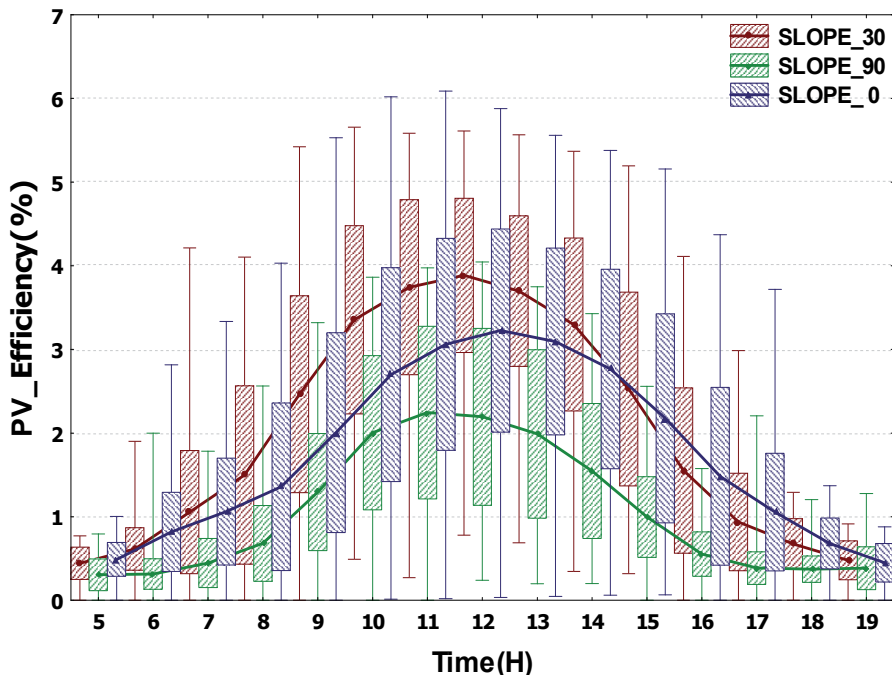
Fig. 19. Annual hourly averaged power efficiency

6.2 Effect of power efficiency by the intensity of solar irradiance
Assuming the solar irradiance of 900 W/m², the power efficiencies of the inclined slope of 30º and horizontal PV reached 5%, while the vertical PV partially exceeded 3%. The inclined slope of 30 º and horizontal PV showed relatively high power efficiency even under high solar irradiance conditions, while the efficiency of vertical PV significantly dropped after reaching 500W/m². The inclined slope of 30 º and horizontal PV can obtain relatively uniform solar irradiance throughout the year and thus the high power efficiency can be achieved over the large range of solar irradiance, while the vertical PV absorb the low solar irradiance during the winter period and thus the power efficiency is reduced in those low irradiance conditions.

6.3 Power efficiency by the temperature variation
The correlation between the power efficiency and the PV surface temperature variation is illustrated. Under the low solar irradiance, the data is scattered and thus did not show the clear correlation. However, it showed the clear correlation between PV efficiency and the surface temperature under the solar irradiance higher than 600W/m², i.e., the PV efficiency is improved at higher surface temperature. This is due to the fact that the higher surface temperature enhances the power efficiency in case of amorphous PV as opposed to crystalline silicon solar cell (c-Si solar cell).
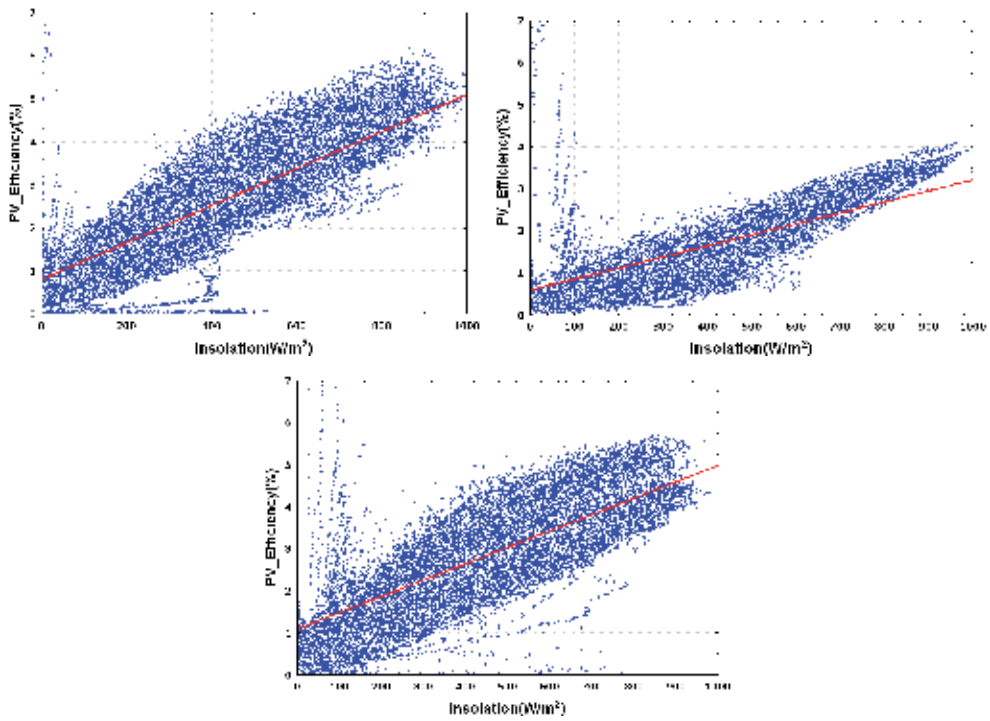
Fig. 20. Correlation between solar insolation and power efficiency (SLOPE_90°, SLOPE_30°, SLOPE_0°)
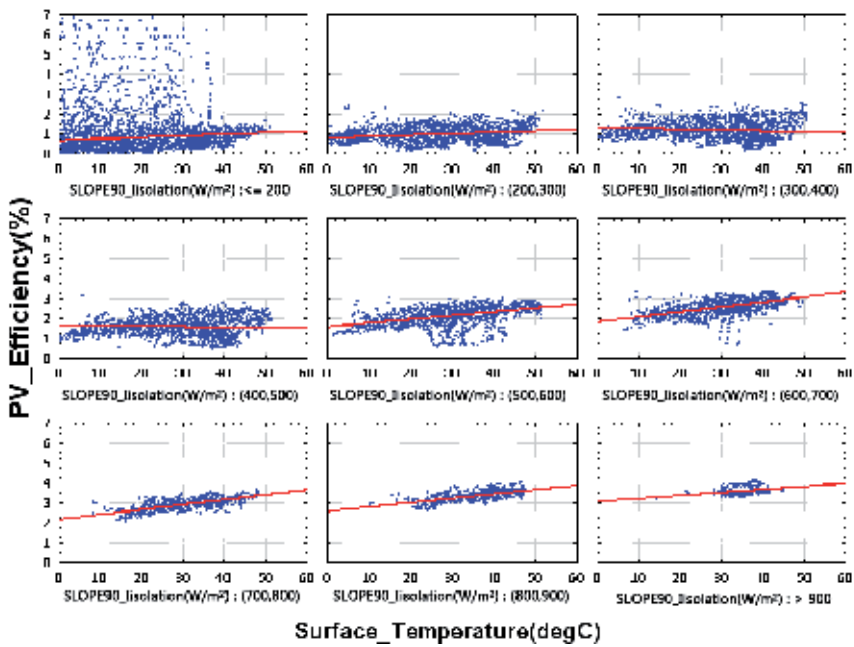
Fig. 21. Correlation between the surface temperature and power efficiency (SLOPE_90°)
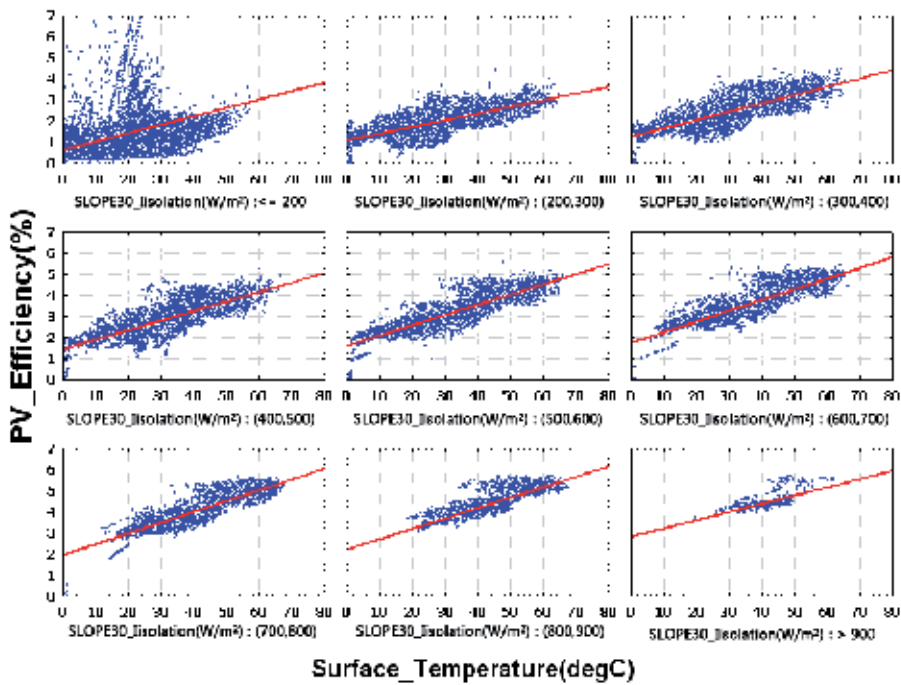
Fig. 22. Correlation between the surface temperature and power efficiency (SLOPE_30°)
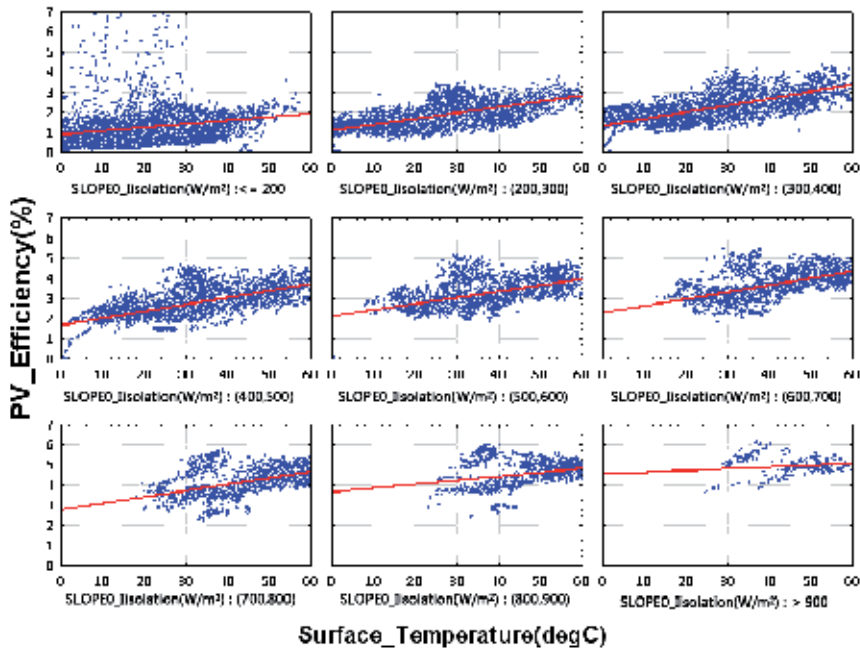
Fig. 23. Correlation between the surface temperature and power efficiency (SLOPE_0°)

6.4 Power efficiency by the solar incidence angle

The PV efficiencies of each inclination angle under different solar incidence angle and solar irradiance are illustrated in the figures below. In case of vertical PV module (SLOPE_90), the power efficiency showed constant value until the solar incidence angle of 65° and it started to rapidly drop after 65°. These characteristics are considered to be the effect of absorbed solar insolation (incident angle modifier) depending on the solar incidence angle reaching the PV module glass wall. This phenomenon did not take place in case of the inclined slope of 30 º (SLOPE_30) due to the low PV efficiency at the solar incidence angle higher than 65°. Likewise, the horizontal PV module was not affected by incident angle modifier as well in most of the solar radiation conditions except for the high solar incidence angle of greater than 65° and the low solar insolation of less than 400W/m² where the efficiency was rather decreased.

It turns out that the power efficiency of PV module is largely affected by the solar incidence angle, solar azimuth and altitude. Furthermore, the rapid decrease in the PV efficiency during the summer period is due to the reduced solar transmittance through the window system at the solar incidence angle higher than 70°, showing the impact of the front glass of PV module on the power efficiency.
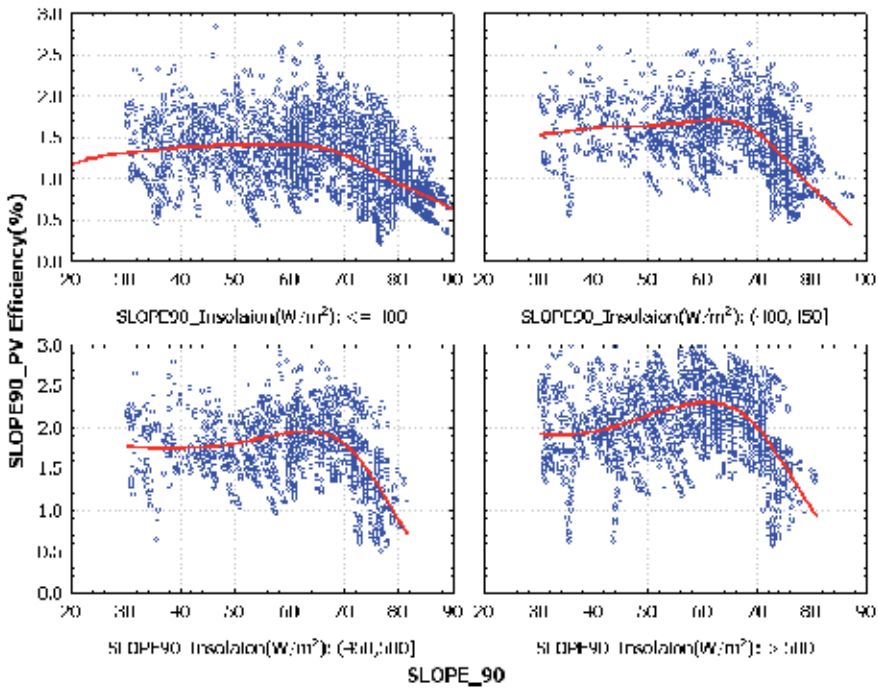
Fig. 24. PV module power efficiency vs. solar incidence angle (SLOPE_90°)
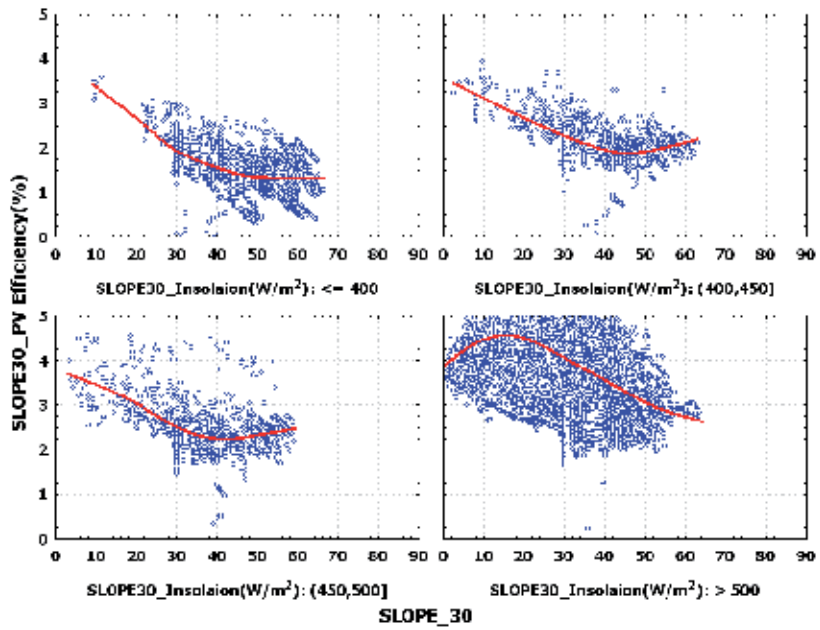
Fig. 25. PV module power efficiency vs. solar incidence angle (SLOPE_30°)
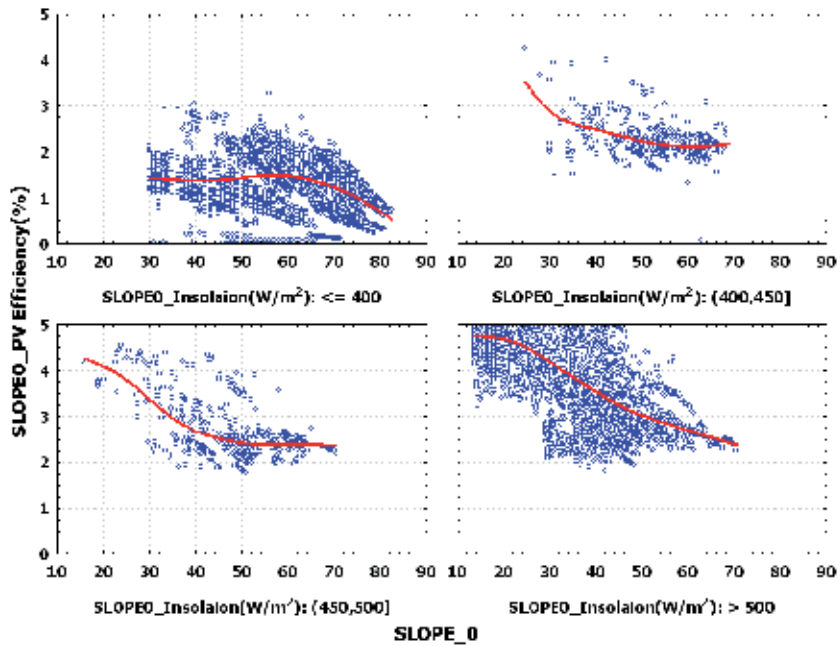
Fig. 26. PV module power efficiency vs. solar incidence angle (SLOPE_0°)

7. Conclusion

This study evaluated a transparent PV module in terms of power generation performance depending on installation conditions such as the inclined slope (incidence angle) and the azimuth angle. The objective of this evaluation was to provide useful data for the replacement of traditional building windows by BIPV system, through the experimental results measured in the full-scale mock-up system.

1. The annual power output of the PV module was measured through the mock-up model. The PV module that was installed at a slope of 30 ° exhibited a better performance of 844.4 kWh/kWp annual power output than the vertical PV module with a slope of 90 °.
2. The experimental data was compared with the computed data obtained from the simulation program. The computed data is considered to be reliable with a relative error of 8.5 %. The best performance of annual power output was obtained from the PV module with a slope of 30 ° facing south, at an azimuth angle of 0 °. The inclined angle was one of the factors that significantly influenced the power generation performance of the PV module, which varied within a range of 24 % on average and provided a maximum difference of 63% in the power output at the same azimuth angle.
3. In terms of the computed power output from a slope of 30 ° depending on the azimuth angle, the PV module facing south exhibited the most effective performance compared to other azimuth angles. The direction in which the PV module faces can also be a very important factor that can affect the power performance efficiency by 11 % on average and by a maximum of 22 %, depending on the azimuth angle.

8. References

[1] Y. Kuwano, Progress of photovoltaic system for houses and buildings in Japan, Renewable Energy 15 (1998) 535–540.
[2] A. Ja¨ger-Waldau, Photovoltaics and renewable energies in Europe, Renewable and Sustainable Energy Reviews 11 (2007) 1414–1437.
[3] A. Stoppato, Life cycle assessment of photovoltaic electricity generation, Energy 33 (2008) 224–232.
[4] A. Hepbasli, A key review on exergetic analysis and assessment of renewable energy resources for a sustainable future, Renewable and Sustainable Energy Reviews 12 (2008) 593–661.
[5] A. Zahedi, Solar photovoltaic (PV) energy; latest developments in the building integrated and hybrid PV systems, Renewable Energy 31 (2006) 711–718.
[6] S. Teske, A. Zervos, O. Schafer, Energy revolution, Greenpeace International, European Renewable Energy Council (EREC) (2007).
[7] R.W. Miles, G. Zoppi, I. Forbes, Inorganic photovoltaic cells, Materials Today 10 (2007) 20–27.
[8] S. Guha, Amorphous silicon alloy photovoltaic technology and applications, Renewable Energy 15 (1998) 189–194.
[9] J.H. Song, Y.S. An, S.G. Kim, S.J. Lee, Jong-Ho Yoon, Y.K. Choung, Power output analysis of transparent thin-film module in building integrated photovoltaic system(BIPV), Energy and Building, Volume 40, Issue 11, (2008) 2067-2075
[10] TRNSYS, A transient system simulation program version 14.2 Manual. Solar Energy Laboratory: University of Wisconsin, Madison, USA, 2000.
[11] D.L. King, et al., Measuring the solar spectral and angle of incidence effects on photovoltaic modules and irradiance sensors, in: Proceedings of the IEEE Photovoltaic Specialists Conference, 1994, pp. 1113–1116.

Influence of Post-Deposition Thermal Treatment on the Opto-Electronic Properties of Materials for CdTe/CdS Solar Cells

Nicola Armani[1], Samantha Mazzamuto[2] and Lidice Vaillant-Roca[3]
[1]IMEM-CNR, Parma
[2]Thifilab, University of Parma, Parma
[3]Lab. of Semicond. and Solar Cells, Inst. of Sci. and Tech. of Mat.,
Univ. of Havana, La Habana
[1,2]Italy
[3]Cuba

1. Introduction

Thin film solar cells based on polycrystalline Cadmium Telluride (CdTe) reached a record efficiencies of 16.5% (Wu et al. 2001a) for laboratory scale device and of 10.9% for terrestrial module (Cunningham, 2000) about ten years ago. CdTe-based modules production companies have already made the transition from pilot scale development to large manufacturing facilities. This success is attributable to the peculiar physical properties of CdTe which make it ideal for converting solar energy into useful electricity at an efficiency level comparable to silicon, but by consuming only about 1% of the semiconductor material required by Si solar cells. Because of the easy up-scaling to an industrial production as well as the low cost achieved in the recent years by the manufacturers, the CdTe technology has carved out a remarkable part of the photovoltaic market. Up to now two companies (Antec Solar and First Solar) have a noticeable production of CdTe based modules, which are assessed as the best efficiency/cost ratio among all the photovoltaic technologies.

Since the record efficiency of such type solar cells is considerably lower than the theoretical limit of 28-30% (Sze, 1981), the performance of the modules, through new advances in fundamental material science and engineering, and device processing can be improved. Further studies are required to reveal the physical processes determining the photoelectric characteristics and the factors limiting the efficiency of the devices.

The turning point for obtaining the aforementioned high efficiency values was the application of a Cl-based thermal treatment to the structures after depositing the CdTe layer (Birkmire & Meyers, 1994; McCandless & Birkmire, 1991). The device performance improvement is due to a combined beneficial effect on the materials properties and on the p-n junction characteristics. CdTe grain size increase (Enriquez & Mathew, 2004; Luschitz et al., 2009), texture properties variations (Moutinho et al., 1998), grain boundary passivation, as well as strain reduction due to S diffusion from CdS to the CdTe layer and recrystallization mechanism (McCandless et al., 1997) are the common observed effects.

In the conventional treatment, based on a solution method, the as-deposited CdTe is coated by a CdCl$_2$ layer and then annealed in air or inert gas atmosphere at high temperature. Afterwards, an etching is usually made to remove some CdCl$_2$ residuals and oxides and to leave a Te-rich CdTe surface ready for the back contact deposition. This etching is usually carried out with a Br-methanol solution or by using a mixture of HNO$_3$ and HPO$_3$. Alternative methodologies avoiding the use of solutions have been developed: the CdTe films are heated in presence of CdCl$_2$ vapor or a mixture made by CdCl$_2$ and Cl$_2$ vapor, or HCl (Paulson & Dutta 2000). Vapor based treatments reduce processing time since combining the exposure to CdCl$_2$ and annealing into one step.

All these post-deposition treatments have been demonstrated to strongly affect the morphological, structural and opto-electronic properties of the structures. The changes induced by the chlorine based treatments depend on how the CdTe and CdS were deposited. For example, in CdTe films having an initial sub micrometer grain size, it promotes a recrystallization mechanism, followed by an increase of the grains. This recrystallization process takes place in all CdTe films having specific initial physical properties, and does not depend on the deposition method used to grow the films. Recrystallization together to grain size increase has been observed in CdTe films deposited by Closed Space Sublimation (CSS), Physical Vapor Deposition (PVD) or Radio Frequency Sputtering. The chlorine based treatment may or may not induce recrystallization of the CdTe films, depending on the initial stress state of the material, and the type and conditions of the treatment. For this reason, the recrystallization process wasn't observed in CSS samples which are deposited at higher temperatures and have an initial large grain size, while, for example CdTe films deposited by Sputtering that are characterized by small grains lower than 1μm in size, an increase up to one order of magnitude was obtained (Moutinho et al., 1998, 1999). The driving force for the recrystallization process is the lattice-strain energy at the times and temperatures used in the treatment.

Changes in structural properties and preferred orientation are also observed. The untreated CdTe material usually grows in the cubic zincblende structure, with a preferential orientation along the (111) direction. Depending on the deposition method, these texture properties can be lost, in place of a completely disoriented material. The Cl-based annealing induces a lost of the preferential orientation as demonstrated by literature X-Ray Diffraction (XRD) works explaining in terms of σ value calculation (Moutinho et al. 1998, 1999). However, this treatment is important even in films that do not recrystallize because it decreases the density of deep levels inside the bandgap and changes the defect structure, resulting in better devices.

Maybe the crucial effect of the treatment is related to the p-n junction characteristics. This treatment promotes interdiffusion between CdTe and CdS, resulting in the formation of CdTeS alloys at the CdTe–CdS interface. The CdTe$_{1-x}$S$_x$ and CdS$_{1-y}$Te$_y$ alloys form via diffusion across the interface during CdTe deposition and post-deposition treatments and affect photocurrent and junction behavior (McCandless & Sites, 2003).

Formation of the CdS$_{1-y}$Te$_y$ alloy on the S-rich side of the junction reduces the band gap and increases absorption which reduces photocurrent in the 500–600 nm range. Formation of the CdTe$_{1-x}$S$_x$ alloy on the Te-rich side of the junction reduces the absorber layer bandgap, due to the relatively large optical bowing parameter of the CdTe–CdS alloy system.

Despite the promising results, the transfer to an industrial production of the commonly adopted CdCl$_2$ based annealing may increase the number of process steps and consequently the device final cost (Ferekides et al., 2000). Since CdCl$_2$ has a quite low evaporation

temperature (about 500°C in air), it cannot be stored in a large quantity, since it is dangerous because it can release Cd in the environment in case of fire. Secondly, $CdCl_2$ is soluble in water and, as a consequence, severe security measures must be taken to preserve environmental pollution and health damage. Another drawback is related to the use of chemical etchings, such as HNO_3 and HPO_3 or Br-Methanol solution, implying that a proper disposal of the used reagents has to be adopted since the workers safety in the factory must be guaranteed. In order to overcome the aforementioned drawbacks, we substituted the $CdCl_2$ based process with an alternative, completely dry CdTe post-deposition thermal treatment, based on the use of a mixture of Ar and a gas belonging to the Freon family and containing chlorine, such as difluorochloromethane (HCF_2Cl)(Bosio et al., 2006, Romeo N. et al., 2005). This gas is stable and inert at room temperature and it has not any toxic action. Moreover, the post-treatment chemical etching procedures have been eliminated by substituting them with a simple vacuum annealing.

The only drawback in using a Freon gas could be that it is an ozone depleting agent, but, in an industrial production, it can be completely recovered and reused in a closed loop. In this paper, it will be demonstrated how the CdTe treatment in a Freon atmosphere works as well as the treatment carried out in presence of $CdCl_2$.

This method was successfully applied to Closed Space Sublimation (CSS) CdS/CdTe solar cells, by obtaining high-efficiency up to 15% devices (Romeo N. et al., 2007). This original approach may produce modifications on the material properties, different than the usual $CdCl_2$-based annealing. For this reason, in this work, the efforts are focused on the investigation of the peculiar effects of the treatment conditions on the morphology, structural and luminescence properties of CdTe thin films deposited by CSS on Soda-Lime glass/TCO/CdS. All the samples were deposited by keeping unmodified the growth parameters (temperatures and layer thicknesses), in order to submit as identical as possible materials to the annealing. Only the HCF_2Cl partial pressure and the Ar total pressure in the annealing chamber have been varied.

The aim of the present work is to correlate the effect of this new, all dry post-deposition treatment, on the sub-micrometric electro-optical properties of the CSS deposited CdTe films, with the effect on the device performances. Large area SEM-cathodoluminescence (CL) analyses have allowed us to observe an increase of the overall luminescence efficiency and in particular a clear correlation between the defects related CL band and the HCF_2Cl partial pressure in the annealing atmosphere. By the high spatial (lateral as well as in-depth) resolution of CL, a sub-micrometric investigation of the single grain radiative recombination activity and of the segregation of the atomic species, coming from the Freon gas, into grain boundary has been performed.

The HCF_2Cl partial pressure has been changed from 20 to 50 mbar, in order to discriminate the Freon gas effect from the others annealing parameters. A clear correlation between the CL band intensities and the HCF_2Cl partial pressure has been found and a dependence on the lateral luminescence distribution has been observed.

The results obtained from the material analyses have been correlated to the performances of the solar cells processed starting from the glass/ITO/ZnO/CdS/CdTe structures studied. Electrical measurements in dark and under illumination were carried out, in order to determine the characteristic photovoltaic parameters of the cell and to investigate the transport processes that take place at the junction. In particular the device short circuit current density (J_{SC}), open circuit voltage (V_{OC}) fill factor (ff) and efficiency (η) have been measured as a function of the HCF_2Cl partial pressure. The most efficient device obtained by

this procedure, corresponding to 40 mbar HCF_2Cl partial pressure in the 400mbar Ar total pressure, has η=14.8%, J_{SC}=26.2mA/cm², V_{OC} = 820mV and ff=0.69.

The solar cells were then submitted to an etching procedure in a Br–methanol mixture at 10% to eliminate the back contacts and part of the CdTe material in some portion of the specimens. On the beveled surface, CL analyses have been performed again in order to extract information as close as possible to the CdTe/CdS interface and to compare the results to the depth-dependent CL analyses.

Finally, a model of the electronic levels present in the CdTe bandgap before and after the HCF_2Cl treatment has been proposed as well as a model of the interface region modifications due to the annealing.

2. Materials growth and devices preparation

CdTe is a II-VI semiconductor with a direct energy-gap of 1.45eV at room temperature that, combined with the very high absorption coefficient, 10^4-10^5 cm^{-1} in the visible light range, makes it one of the ideal materials for photovoltaic conversion, because a layer thickness of a few micrometers is sufficient to absorb 90% of incident photons. For thin film solar cells is required a p-type material, which is part of the p-CdTe/n-CdS heterojunction. The electrical properties control was easily developed for single-crystal CdTe, grown from the melt or vapor, at high temperature (above 1000°C), by introducing doping elements during growth. On the contrary, in polycrystalline CdTe, where grain boundaries are present, all metallic dopants tend to diffuse along the grain boundaries, making the doping unable to modify the electrical properties and producing shunts in the device.

CdTe solar cell is composed by four parts (Fig. 1) deposited on a substrate like Soda-Lime Glass (SLG):

1. The *Front Contact* is composed by a Transparent Conducting Oxide (TCO) that is a doped metallic oxide like In_2O_3:Sn (ITO)(Romeo N. et al., 2010) , ZnO:Al (AZO)(Perrenoud et al., 2011), $CdSnO_4$ (CTO)(Wu, 2004), SnO_2:F (FTO) (Ferekides et al., 2000), etc.; and a very thin layer of a resistive metal oxide like SnO_2 (Ferekides et al., 2000), ZnO (Perrenoud et al., 2011; Romeo N. et al. 2010), Zn_2SnO_4 (Wu et al. 2001b). The role of the latter film is to hinder the diffusion of contaminant species from TCO and SLG toward the upper layers of the cell such as the window layer (CdS) or the absorber one (CdTe). Moreover it separates TCO and CdS in order to limit the effects of pinholes that could be present in CdS film.

   In our work, TCO is made by 400nm thick ITO film and 300nm thick ZnO both of them deposited by sputtering. ITO showed a sheet resistance of about 5Ω/cm², while the resistivity of ZnO was on the order of 10^3 Ω cm.

2. The *Window Layer* is usually an n-type semiconductor; Cadmium Sulphide (CdS) is the most suitable material for CdTe-based solar cells, thanks to its large bandgap (2.4eV at room temperature) and because it grows with n-type conductivity without the introduction of any dopants. Here, CdS film was deposited by reactive RF sputtering in presence of Ar+10%CHF_3 flux. Its nominal thickness was 80nm.

3. The *Absorber Layer* is a 6-10μm thick film. The deposition techniques and the treatment on CdTe will be explained deeply later.

4. The *Back Contact* is composed by a buffer layer and a Mo or W film. The utility of the buffer layer is to form a low resistive and ohmic contact on CdTe.

Influence of Post-Deposition Thermal Treatment on the
Opto-Electronic Properties of Materials for CdTe/CdS Solar Cells
213

The cell is completed by a scribing made on the edge of all the cells in order to electrically separate the front contact from the back one.
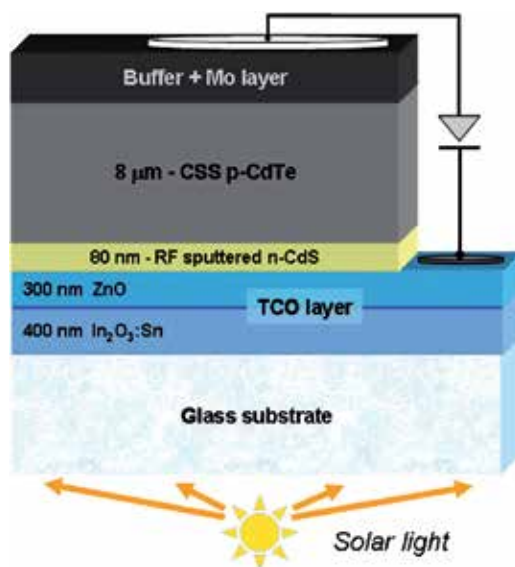
Fig. 1. Schematic representation of the CdS/CdTe solar cell heterostructure. The layers succession and thicknesses are the ones used in the present work.

2.1 CSS Growth of CdTe layers

CdTe thin films have been deposited by several deposition techniques such as High Vacuum Evaporation (HVE)(Romeo A. et al., 2000), Electro-Deposition (ED)(Josell et al., 2009; Kosyachenko et al., 2006; Levy-Clement, 2008; Lincot, 2005), Chemical Vapour Deposition (CVD)(Yi & Liou, 1995), Metal-Organic Chemical Vapor Deposition (MOCVD)(Barrioz, 2010; Hartley, 2001; Zoppi, 2006), Spray Pyrolysis (Schultz et al., 1997), Screen Printing (Yoshida, 1992 & 1995) Sputtering (Compaan et al., 1993; Hernández-Contreras et al., 2002; Plotnikov et al., 2011) and Close Spaced Sublimation (CSS)(Chu et al., 1991; Romeo N. et al., 2004; Wu, 2004).

Among these techniques, CdTe deposited by CSS allowed to obtain best results for solar cells (world record photovoltaic solar energy conversion ~16.5%; Wu, 2004).

CSS is a physical technique based on a high temperature process. The apparatus is showed in Fig. 2 and it is composed by a vacuum chamber inside which the substrate and the source are placed at a distance of few millimeters (2-7mm). The difference in temperature between the substrate and the source is kept around 50-150°C. Deposition takes place in presence of an inert gas (Ar) or a reactive one (O_2, etc.) with a total pressure of about 1-100mbar. The gas creates a counter-pressure which reduces re-evaporation from the substrate and forces the atoms from the source to be scattered many times by the gas atoms before arriving to the substrate, so that the material to be deposited acts like it has a higher dissociation temperature and higher temperature respect to sublimation under vacuum are necessary.

CSS allows to obtain CdTe film with a very high crystalline quality and grains of about one order of magnitude larger (~10μm) than films deposited by other deposition techniques (Sputtering, HVE, etc.) and, for this reason, with a low lattice defect density (Romeo A. et al., 2009).
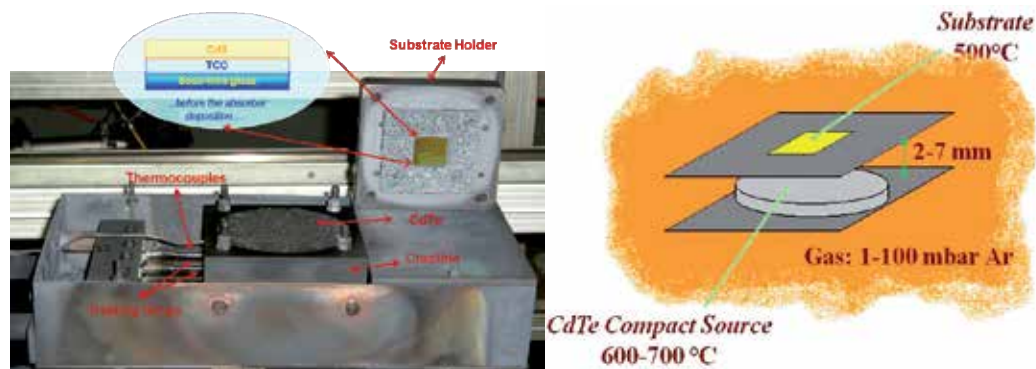
Fig. 2. Picture of the CSS setup used for growing the CdTe films studied (left); Detail of the growth region of the CSS chamber (right).

In our work, CdTe was deposited in 1mbar Ar atmosphere, keeping the substrate and source temperatures at 500°C and 600°C respectively. The CdTe thickness was 6-8 μm.

The high substrate temperature (~500°C) favors the formation of a mixed compound CdS_xTe_{1-x} at the interface between CdS and CdTe directly during CdTe deposition, as shown in the phase diagram (Lane et al., 2000). The mixed compound formation, by means of S diffusion toward CdTe and Te diffusion toward CdS, is advantageous in order to get high efficiency CdS/CdTe solar cells. In fact, its formation is required in order to minimize defect density at the interface acting as traps for majority carriers crossing the junction, caused by the lattice mismatch between CdS and CdTe that is about 10%.

2.2 HCF$_2$Cl post-deposition thermal treatment

The Cl-treatment on CdTe surface is a key point in order to rise the photocurrent and so the efficiency of the solar cell.

During Cl-treatment CdTe goes in vapor phase as explained by the following reaction (McCandless, 2001):

$$CdTe(s)+CdCl_2(s) \rightarrow 2Cd(g)+\tfrac{1}{2}Te_2(g)+Cl_2(g) \rightarrow CdCl_2(s)+CdTe(s), \qquad (1)$$
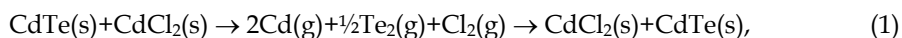
where s is the solid phase and g is the vapor phase.

After the treatment small grains disappear from CdTe surface and at the same time an increase in grain dimensions and an improvement in crystal organization can be observed. Also an improvement, in the crystal organization of the mixed compound CdS_xTe_{1-x}, at the junction, formed during CdTe deposition, can be observed.

Usually Cl-treatment is carried out by depositing on CdTe surface a CdCl$_2$ (thickness more than 100nm) film by evaporation (Potter et al., 2000; Romeo A. et al. 2000; Romeo N. et al. 1999) or by dipping CdTe in a CdCl$_2$-methanol solution (Cruz et al., 1999), then an annealing at ~380-420°C in an Ar atmosphere or in air is required and finally, an etching in Br-methanol or an annealing in vacuum is carried out in order to remove CdCl$_2$ residuals on CdTe surface. The main drawback of this treatment is that CdCl$_2$, being very hygroscopic, could be dangerous either for people and for the environment since it can release free Cd.

We have proposed a new treatment by substituting CdCl$_2$, or CdCl$_2$-methanol solution, and the following etching with a treatment at 400°C in a controlled atmosphere containing a gas belonging to the Freon® family which can free Cl at high temperature. This gas is very

stable and inert at the room temperature; moreover, in the case of an industrial production, it can be re-used in a closed loop without releasing it in atmosphere.

We suppose that the following reaction happens at 400°C during the treatment (Romeo N. et al., 2006):

$$CdTe(s) + 2Cl_2(g) \rightarrow CdCl_2(g) + TeCl_2(g) \rightarrow CdTe(s) + 2Cl_2(g). \qquad (2)$$
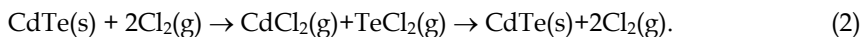
After that, an annealing is carried out at the same temperature of the treatment for few minutes in vacuum (10^{-5}mbar) in order to let $CdCl_2$ residuals re-evaporate and to obtain a clean CdTe surface ready for the back contact deposition.

In this work, the TCO/CdS/CdTe system is placed in an evacuable quartz ampoule. Before each run, the ampoule is evacuated with a turbo-molecular pump up to 10^{-6}mbar. As a source of Cl_2, a mixture of Ar+HCF_2Cl is used. The samples were prepared by changing the HCF_2Cl partial pressure. The first one was an untreated sample, while the other four ones were made by choosing four values of HCF_2Cl partial pressure that are 20, 30, 40, and 50 mbar and keeping the total pressure (Ar+HCF_2Cl) at 400 mbar. An additional specimen, annealed at 30mbar HCF_2Cl partial pressure, but with a larger total Ar+HCF_2Cl pressure of 800mbar, has been prepared, in order to study the effect of the total pressure on the recrystallization mechanisms. The Ar and the HCF_2Cl partial pressures were independently measured by two different capacitance vacuum gauges and monitored by a Varian Multi-Gauge. The quartz tube is put into an oven where a thermocouple is installed in order to control the furnace temperature, which is set at 400°C. The annealing time is 10min for all samples studied in this work. After the treatment, a vacuum for about 10min, keeping the temperature at 400°C, was made in order to remove some $CdCl_2$ residuals from the CdTe surface.

2.3 Back contact deposition and device processing

The cell is completed by back contact deposition. The formation of a ohmic and stable back contact with CdTe has always been one the most critical points in order to obtain high efficiency CdS/CdTe solar cells. Normally, CdTe is etched in order to get a Tellurium rich surface. After that, a Cu film (~2nm thick) is deposited in order to form a Cu_xTe compound that is a good non-rectifying contact for CdTe. This procedure has two disadvantages: chemical etching is not convenient because it is not scalable to an industrial level and it is polluting and the Cu thickness is too small to be controlled. In fact, if a thicker Cu film is deposited it could happen that Cu is free from the Cu_xTe formation and it could cause short circuits in the cell because it can segregate in grain boundaries.

In our work, back contact is composed by the deposition in sequence of three films. A 150-200nm thick As_2Te_3 film and a 10-20nm thick Cu film are deposited in sequence on CdTe surface by RF sputtering in Ar flux. When the deposition temperature of Cu is about 150-200°C, a substitution reaction occurs between Cu and As_2Te_3 whose final product material is Cu_xTe, mainly $Cu_{1.4}Te$ is the most stable compound (Romeo N. et al, 2006; Wu et al. 2006; Zhou, 2007). Finally, a Mo layer is deposited on top of the cell by sputtering.

2.4 Etching procedures by a Br – methanol mixture

The possibility to perform depth-dependent CL analyses, by increasing the energy of the incident electrons of the SEM, allows us to correlate the results obtained on the isolated CdTe to an analysis of the electro-optical properties close to the CdTe/CdS interface region of a complete solar cell. To do this, it is necessary to overcome the problem that summing

the back contact to the CdTe thickness, the main junction is situated around 10μm below the specimen surface. This thickness is 2 times higher than the maximum distance that the most energetic electrons in our SEM (40keV) penetrate in CdTe. In addition, it has to take into account that the back contact completely absorbs the light coming from the CdTe film, impeding any CL analyses.

In this work, a solution to this experimental difficulty has been proposed by etching the material to completely eliminate the back contact and the excess CdTe in some portion of the cells. In order to prevent the introduction of superficial defects that would affect the CL reliability, polishing methods were avoided. On the other hand, standard nitric–phosphoric acid chemical etching widely performed before metallization to improve contact formation, shows a strong preferential chemical reaction over the grain boundaries (Bätzner et al. 2001; Xiaonan et al. 1999). For these reasons, a Br–methanol mixture at 10% has been used, expecting to obtain a less selective interaction of the etching solution between the grains and its boundaries.

3. Experimental and set-up description

The methodological approach used in this work was based on the correlation between the study of HCF_2Cl treatment effect on CdTe material properties and the characterization of the photovoltaic cells parameters. There are not many works in literature that correlate the effects of CdTe post-deposition treatment and the relative changes in the electro-optical properties of CdTe with the performance of the photovoltaic device. Only recent studies (Consonni et al. 2006) on the behavior of Cl inside polycrystalline CdTe gave major results about the compensation mechanisms and the formation of complexes between native point defects (NPD) and impurities, already well established in the case of high quality single crystal CdTe (Stadler et al., 1995). The influence of post-deposition treatment on the CdTe/CdS interface region was crucial in the improvement of the device performances. The in-depth CdTe thin film properties, obtained by CL analyses, are then compared to results obtained on etched CdTe samples, treated in the same HCF_2Cl conditions. This allows us to verify the reliability of CL depth-resolution studies on polycrystalline materials and the effect of HCF_2Cl thermal treatment on the bulk CdTe properties approaching the CdTe/CdS interface.

3.1 Cathodoluminescence spectroscopy and mapping

CL is a powerful technique for studying the optical properties of semiconductors. It is based on the detection of the light emitted from a material excited by a highly energetic electron beam. The high-energy electron beam (acceleration voltage between 1-40kV), impinging on the sample surface, creates a large number of electron hole (e-h) pairs. After a thermalization process, the carriers reach the edges of the respective bands, conduction band (CB) in the case of electrons, valence band (VB) in the case of holes, and then diffuse. From the band edges, the electrons and holes can recombine, in the case of radiative recombination, the photons produce the CL signal. A more detailed description of the principles of the CL theory, in particular the fundamental of the generation and recombination mechanisms of the carriers can be found in the works of B. Yacobi and D. Holt (Yacobi & Holt, 1990) and references therein included.

CL is contemporary a microscopic and spectroscopic methodology with high spatial, lateral as well as in-depth, resolution and good spectral resolution when luminescence is detected

at low temperature. These advantages are due to the use of a focused electron beam of a SEM as excitation source. In addition, this technique allows the contemporary acquisition of spectra of the intensity of the light collected as a function of wavelength and images (mono- and pan-chromatic) of the distribution of the light. The results can be acquired from regions of different area, from 1 to several hundreds of μm^2, depending on the magnification of the SEM and on the dimensions of the parabolic mirror used as light collector.

The lateral resolution in CL imaging can be roughly defined as the minimum detectable distance between two regions presenting different CL intensity. In the SEM-CL, the spatial imaging resolution depends mainly on the size of the recombination volume (generation volume broadened for the diffusion length) of e-h pairs inside the material, entailing also a dependence on the diffusion length (L) of generated carriers. A typical value of the lateral resolution of about 200nm can be reached as a lower limit in suitable working conditions for instance on III-V semiconducting quantum confined heterostructures (Merano et al., 2006).

The in-depth analysis is a CL peculiarity which allows us to investigate the samples at different depths by changing the energy of the primary electrons. The generation, as well as the recombination volume, increases in all the three dimensions by increasing the acceleration voltage. The depth, at which the maximum CL signal is created, increases also by increasing the beam energy (E_b). By this method, it is possible to investigate crystals or thick layers inhomogeneities along the growth direction. The large grain size of the CSS deposited CdTe, higher than 1 μm, allowed us to directly investigate the grain and the grain boundary recombination properties. This possibility is very useful to study a possible gettering mechanism or a passivation effect of the grain boundaries due to the annealing.

The post-deposition thermal treatment has an effect on the CdTe surface as well as on the bulk material, reasonably as far as the CdTe/CdS interface. For this reason, a complete characterization of the CdTe electro-optical properties and of the p-n junction recombination mechanisms, by using a bulk sensitive experimental technique, is necessary. The penetration depth of 200-300nm of the laser radiation used for PL analyses is a disadvantage that could be overcome by using the high energy electrons of an SEM for exciting CL. In addition, the possibility of increasing the CL generation/recombination volume by increasing the electron beam energy allows us a depth-dependent analysis. The CL analysis of 6-8μm thick CdTe thin films, as the active layers used in the fabrication of solar cells, has particular advantages: the maximum penetration depth of the exciting electrons of the SEM beam can reach 4.8μm by using 36 keV energy. This depth is higher than the few hundreds of nanometers probed by the commonly used Ar laser (514 nm) to excite PL. It is actually possible to perform an investigation of the CdTe bulk properties by CL in place of a near-surface PL analyses. The in-depth information, that is not available with other micro- and nano-scale optical techniques, is particularly useful for example in the characterization of heterostructures, doping profile, study of extended defects along the growth direction.

However, it is important to remark that the fundamental differences between CL and PL are the amount of e-h pairs generated and the dimensions and shape of the generation volumes. In the case of laser generation, each photon creates a single e-h pair whereas a high energetic electron can generate thousands of e-h pairs. With such a large number of e-h pairs generated, the excitation of all the radiative recombination channels inside the materials is possible.

The instrument used to collect the experimental data reviewed in this work is a Cambridge 360 Stereoscan SEM with a tungsten filament (resulting beam size on the sample surface

typically ranging between a few microns and a few tens of nanometers), equipped with a Gatan MonoCL2 system (Fig. 3). The spectra, as well the panchromatic and monochromatic images, have been acquired using a dispersion system equipped with three diffraction gratings and a system of a Hamamatsu multi-alkali photomultiplier and a couple of liquid nitrogen cooled (Ge and InGaAs) solid state detectors. This experimental set up provides a spectral resolution of 2Å and a detectable 250-2200nm (0.6–4.9eV) wavelength range. By this configuration it is possible to cover a large part of the luminescence emissions of the III-V and II-VI compound semiconductors. In particular, all the possible transitions in CdTe can be detected: from the excitonic lines (around 1.59eV) down to the emissions involving mid-gap levels (0.8-0.9eV). Additionally, it is possible to change the temperature of the samples in the range 5-300K by a temperature controller interlocked with the sample-holder, thanks to a refrigerating system operating with liquid Nitrogen and liquid Helium.
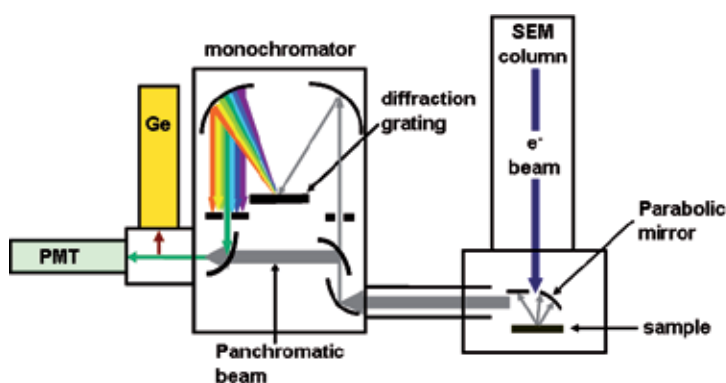
Fig. 3. Schematic representation, not in scale, of the CL experimental setup used in this work.

3.2 X-Ray diffraction

The setup used for acquiring XRD profiles was an X-Ray Diffractometer Thermo arl X'tra, vertical goniometer, theta-theta, operating in an angular range between -8° and 160°, equipped with an X-ray tube, Cu K-alpha and a solid state Si:Li detector. The angular range chosen, between 15° and 80°, assured the detection of all the contributions from the main Bragg diffractions of CdTe: (111), (220), (311), (400), (331), (422), (511).

3.3 Electrical characterization

Light J-V measurements were performed by an Oriel Corporation Solar Cells Test System model 81160, in order to measure the photovoltaic parameters such as the short-circuit current density (J_{SC}), open circuit voltage (V_{OC}), fill factor (ff) and conversion efficiency (η) of the solar cells.

Dark measurements were carried out by a Keithley 236 source system in order to measure the diode quality factor (A) of the cells as a function of the HCF_2Cl partial pressure during the CdTe treatment. A can be calculated from the diode equation in the dark:

$$A = \frac{qV}{kT} \cdot \frac{1}{\ln(\frac{J}{J_0}+1)}$$

(3)

The measure of A gave some information about the transport mechanism at the junction. If the predominant transport mechanism at the junction is the diffusion then A≈1, while if the predominant mechanism is the recombination, the value of A increased and approached to 2. The dark conductivity as a function of the temperature (84-300K) and the activation energy were performed by using a Keithley 236 source measure unit. The temperature was set by a system DL4600 Bio-Rad Microscience Division. The samples, used for this measurement, were composed by 300nm thick ZnO, 7μm thick CdTe and the back contact. The first sample was a not treated one, while the other two samples were made by treating CdTe with respectively 30 and 40mbar HCF$_2$Cl partial pressure at 400°C for 10 minutes. The total pressure (Ar+Freon®) was set at 400mbar for all the two samples.

4. Results and discussion

All the CdTe thin films were deposited on SLG/ZnO substrate by CSS; the layer thickness was about 8μm. Complete solar cells have been realized by depositing ZnO, CdS and CdTe in the identical conditions and by adding the back contact, as described in paragraphs 2.1 and 2.3. The CdTe films as well as the complete devices were annealed in Ar+HCF$_2$Cl atmosphere (see for details paragraph 2.2), by increasing the HCF$_2$Cl partial pressure from 20mbar to 50mbar and keeping the temperature at 400°C for all samples. The annealing conditions used have been summarized in table 1.

Sample	HCF$_2$Cl partial pressure (mbar)	Ar+HCF$_2$Cl total pressure (mbar)	Annealing time (mins)
UT	-	-	-
F20	20	400	10
F30L	30	400	10
F30H	30	800	5
F40	40	400	10
F50	50	400	10

Table 1. Summary of the annealing conditions used to treat the samples studied in this work

4.1 Influence of annealing on the CdTe material properties

The XRD profiles of all the CdTe films were acquired in the angular range 5°<2q<80°, from this analysis can be deduced that the films have a zinc-blend structure with a preferential orientation along the (111) direction. In all the XRD patterns the peaks related to (220), (311), (400), (331), (422) and (511) reflections are also visible. In addition a peak at 22.77° attributed to the Te$_2$O$_5$ oxide and a peak at 34.34° related to the ZnO (002) reflection are detected. In Fig. 4, only the most representative XRD profiles of the untreated CdTe and of the samples annealed with 40 mbar HCF$_2$Cl partial pressure were shown.

The preferential orientation of each film is analyzed by using the texture coefficient C$_{hkl}$, calculated by means of the following formula (Barret & Massalski 1980):

$$C_{hkl} = \frac{I_{hkl}/I^0_{hkl}}{\frac{1}{N}\sum_N I_{hkl}/I^0_{hkl}} , \qquad (4)$$

where I_{hkl} is the detected intensity of a generic peak in the XRD spectra, I^0_{hkl} is the intensity of the corresponding peak for a completely randomly oriented CdTe powder (values taken from the JCPDS) and N the number of reflections considered in the calculation. C_{hkl} values above the unity represented a preferential orientation along the crystallographic direction indicated by the hkl indices. The texture coefficients C_{111}, calculated by the formula Nr 4 for all the samples, are summarized in table 2, together with the CL intensity ratios. A better comprehension of the orientation of each thin film as a whole can be obtained by the standard deviation σ of the C_{hkl} coefficients. Each value has been calculated by the following formula:

$$\sigma = \sqrt{\frac{\sum_N (C_{hkl} - 1)^2}{N}} \qquad (5)$$

A complete randomly oriented film is expected to have a σ value as close as possible to 0.

The untreated CdTe thin film shows the highest preferential orientation along the (111) direction with a texture coefficient C_{111}=2.02. The effect of HCF_2Cl treatment is highlighted by a decrease of the (111) related intensity and by an increase of the relative intensities of the additional reflections (220), (311), (400), (331), (422) and (511), detected. The calculated σ value for the untreated CdTe is also the highest one (σ=0.52) demonstrating the oriented status of that film. This behavior is evidenced in Fig. 5, in which the calculated peak intensity ratios between each (220), (311), (400), (331), (422) and (511) additional reflection and the (111) one are plotted.

The combined effect of HCF_2Cl partial pressure and the total gas pressure, in the annealing chamber, could be also evidenced by comparing the C_{111} and σ values of the CdTe films treated by 30mbar HCF_2Cl, but higher total pressure (800mbar), sample F30H in table 2. Its values were higher than the CdTe treated with the same partial pressure and lower total pressure (sample F30L in table 1), but similar to the untreated CdTe.
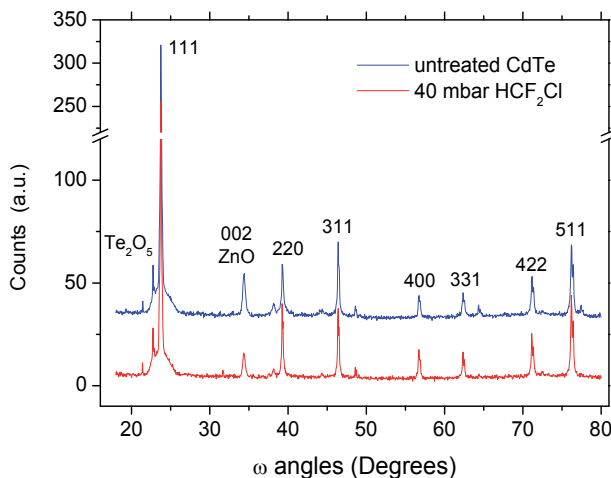
Fig. 4. XRD profiles of the untreated CdTe thin film compared to the sample annealed with 400 mbar Ar+Freon total pressure in the annealing chamber and 40mbar HCF_2Cl partial pressure.

Sample	XRD results		Morphology	1.4 eV/NBE CL intensity	
	C_{111} texture coefficient	σ	Average grain size (μm)	12 keV	25 keV
UT	2,02	0,52	11.7	0.9	0.72
F30L	1,12	0,29		2.3	3.39
F30H	1,7	0,42	10.8		10.75
F40	1,15	0,31	11.2	14.48	15.47
F50	0,56	0,36		14.74	19.97

Table 2. Summary of the results obtained by processing the XRD profiles, CL spectra and SEM images.
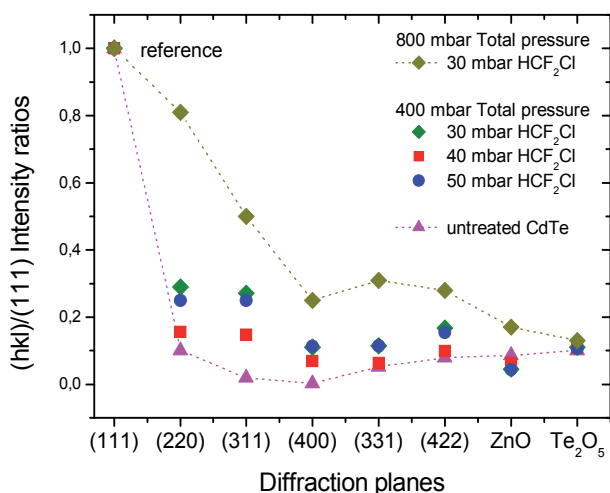
Fig. 5. Plot of intensity ratios among each diffraction (220), (311), (400), (331), (422) and (511) and the (111) one for all the studied CdTe thin films

The loss of preferential orientation due to HCF_2Cl annealing results in a slight modification of the CdTe morphology after the thermal treatment. The untreated CdTe films showed already large grains, as visible in the SEM image of Fig. 6 a. The average grain size obtained by processing the images was 11.7μm and the largest grains reached 20.4μm. The material treated with 40mbar HCF_2Cl partial pressure showed grains with dimensions similar (avg = 11.2μm) to those of the untreated one (Fig. 6 b). The observed average size confirmed that CSS grown CdTe did not show grain size increase after annealing in presence of chlorine as already described in the literature by several authors (Moutinho et al. 1998). Grain dimensions distribution extracted from the SEM images has been represented in histograms showed in Fig. 7 a and b. It could be observed that the small grains density in the HCF_2Cl treated material was reduced, producing a thinner distribution of the histogram columns.

On the contrary, all the Freon treated CdTe showed a remarkable grain shape variation with respect to the untreated sample where most of the grains appeared as tetragonal pyramids with the vertex aligned on the growth direction (Fig. 8 a). This shape justified their high preferential orientation along the (111) direction. This grain shape appeared clearly modified in the HCF_2Cl annealed films. They were more rounded and the pyramids seem to

be made up by a superposition of "terraces" (Fig. 6 b). This morphology change could be correlated to the C_{111} texture coefficient decrease. Two possible mechanisms related to the HCF_2Cl annealing could be invoked: a re-crystallization effect or an "etching-like" erosion of the grain surface. The unmodified grain size and the appearance of the terraces seem to indicate that the latter phenomenon occurred during the Freon treatment.
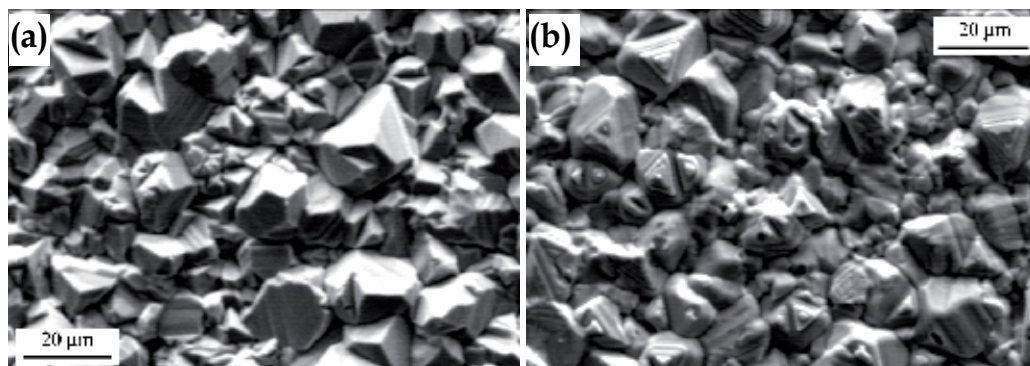
Fig. 6. SEM image of the polycrystalline CdTe surface morphology: a) untreated film; b) annealed with 40mbar HCF_2Cl
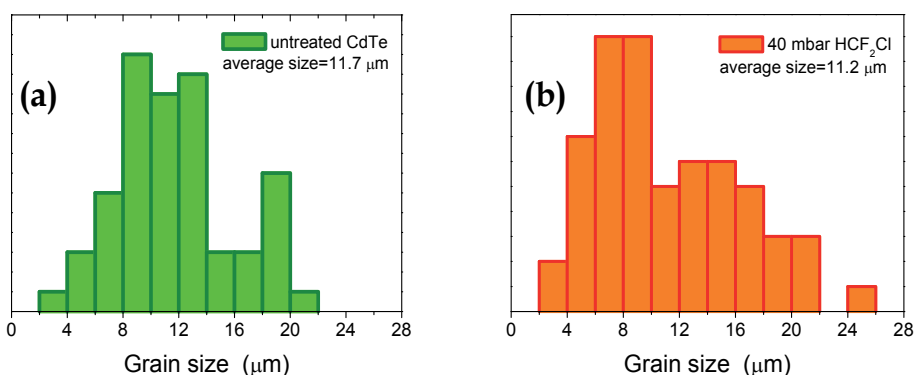
Fig. 7. Histograms of the grain size as obtained from the SEM images: a) untreated CdTe; b) CdTe annealed by 40mbar HCF_2Cl partial pressure.

The effect of thermal treatment on the CdTe bulk electro-optical properties has been studied by acquiring CL spectra at electron beam energy (E_B) of 25keV, corresponding to a maximum penetration depth of about 2.5μm. The CL generation volume dimensions were calculated by means of a numerical approach based on random walk Monte Carlo simulation developed in our laboratory (Grillo et al. 2003). The low temperature (77 K) spectrum of a 240x180 μm² region of the untreated CdTe showed the clear near bend edge (NBE) emission centered at 1.57eV. The temperature is too high to discriminate the acceptor from the donor bound excitonic line, we supposed they were superimposed underneath the NBE band. In addition to the NBE emission, two weak bands, centered at 1.47eV and 1.35eV respectively, were also detected. The 1.35eV and 1.47eV CL peaks were visible only in the untreated CdTe and their origin was not related to the HCF_2Cl treatment. The 1.35eV
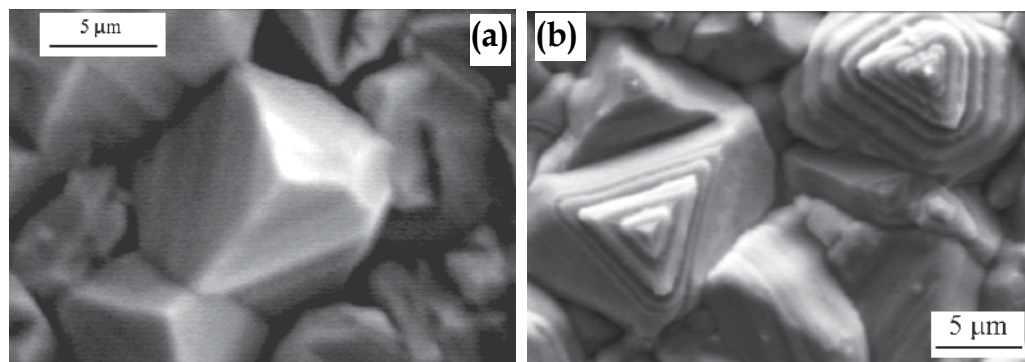
Fig. 8. a) SEM image of a typical pyramidal grain oriented along the (111) growth direction of the untreated film; b) SEM image showing pyramidal grains with terraces of the CdTe annealed by 40mbar HCF_2Cl partial pressure.

emission could be attributed to radiative recombination levels induced by impurities, like Cu, unintentionally incorporated during the CdTe deposition, or diffused from the front contact and buffer layers during the high temperature growth. The 1.47eV peak has been previously observed in polycrystalline CdTe (Cárdenas-García et al. 2005) and ascribed to the dislocation related Y-emission. In our untreated material, a clear dependence of this emission on the dislocations has not been demonstrated, but the disappearance of this peak in the annealed, high crystalline quality CdTe supports this attribution (Armani et al. 2007).

The HCF_2Cl annealing effect on the CdTe recombination mechanisms was studied by both CL spectroscopy and monochromatic (monoCL) mapping. CL spectra showed a drastic difference between untreated and HCF_2Cl annealed samples, as visible in Fig. 9. All the HCF_2Cl treated samples showed, in addition to the NBE emission, a broad CL band centered at 1.4eV which intensity increased by increasing the HCF_2Cl partial pressure, suggesting a strong dependence of this emission on the annealing. The literature studies on both single–crystal and polycrystalline CdTe (Consonni et al. 2006; Krustok et al. 1997) showed photoluminescence (PL) and CL bands centered at energies close to 1.4eV; their origin was attributed to a radiative recombination center like the well known A-center, due to a complex between a Cd vacancy (V_{Cd}) and a Cl impurity, in Cl-doped CdTe (Meyer et al. 1992; Stadler et al. 1995). The clear correlation between the 1.4eV band and the HCF_2Cl treatment supported the attribution of the 1.4eV band observed in our CdTe films to a complex like the A-centre. Either Cl or F impurities could be the origin of the level responsible for this transition. Several impurities, among which Cl and F, created acceptor levels with very similar energy values above the valence band edge as reported by Stadler et al. (Stadler W. et al. 1995). In particular the levels due to Cl and F differ solely by 9meV. The CL spectral resolution, lower than the PL one, did not allow determining the exact energy position of the 1.4 eV band with a precision better than 0.01eV. On this basis a clear attribution, to Cl or F, of the impurity creating the complex together to the V_{Cd} was impossible. The 1.4eV/NBE CL intensity ratios represented a tool to study the concentration of the V_{Cd}-Cl(F) complex responsible for the 1.4eV band; the comparison among the untreated and the annealed CdTe results obtained at 25keV have been summarized in Fig. 10.
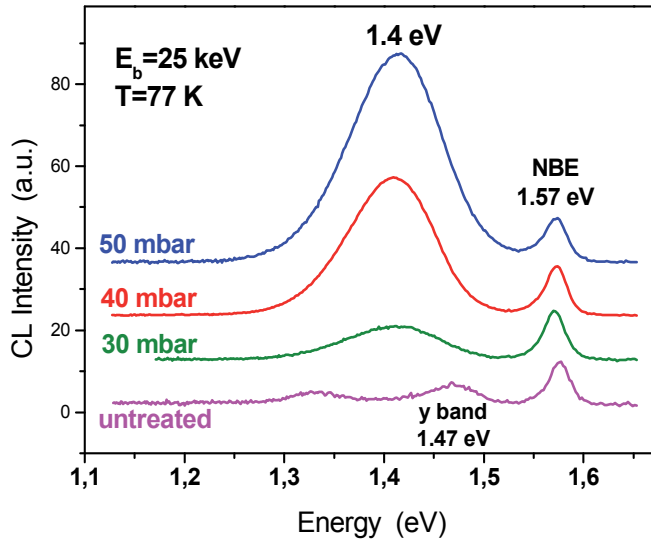
Fig. 9. Comparison among the low temperature (77 K) CL spectra (E_b=25keV) of untreated CdTe and samples annealed at a HCF_2Cl partial pressure of 30, 40 and 50 mbar.
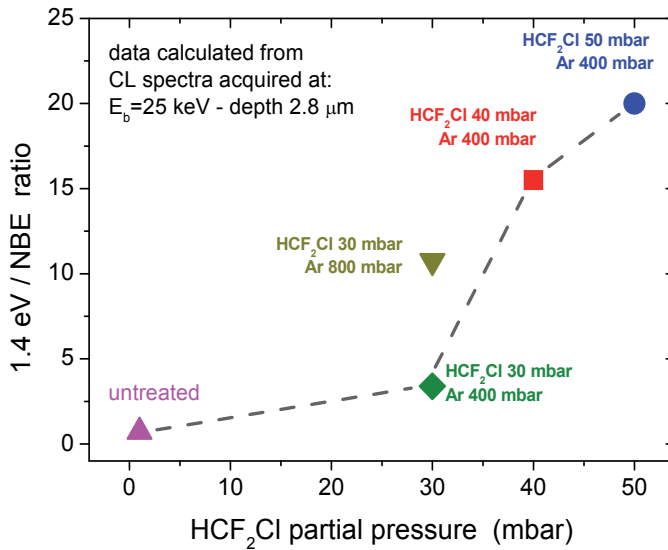
Fig. 10. Plot of the 1.4eV/NBE integrated intensity ratios. The experimental points have been calculated from spectra acquired in various regions of each CdTe film at E_b= 25keV.

One of the peculiarities of the CL technique is the possibility to increase the probing depth within the studied materials, by increasing E_B, by keeping the injection density in the generation volume constant. The effect of annealing on the CdTe luminescence behavior was expected to be more effective close to the CdTe surface. For this reason, CL spectra at lower beam energy (E_B=12keV), corresponding to a maximum penetration depth of 900nm below the CdTe surface, were collected. The comparison among untreated and annealed

samples showed a dependence of the 1.4eV emission intensity on the HCF_2Cl partial pressure similar to the highly depth 25 keV analysis. A more detailed depth-resolved study of the V_{Cd}-Cl(F) complex distribution is performed by acquiring CL spectra at different E_B from 8 to 36 keV, corresponding to a probing depth between 0,36 and 4,6 μm. Fig. 11 showed the CL spectra, normalized to the NBE intensity, in order to better highlight the 1.4eV band intensity variations. The 1.4eV emission intensity decreased till the generation volume of the CL signal extended to about 2μm, then kept almost constant for the following 2μm. This behavior could be more clearly appreciated in the inset of the figure where the 1.4eV/NBE integrated intensity ratio has been shown. Possible influence of material quality inhomogeneities along the deposition axis could be neglected because the NBE peak position did not change in the studied depth range as well as its intensity showed very small and random variations. The V_{Cd}-Cl(F) complex density was the highest close to the CdTe surface, due to the maximum effectiveness of the HCF_2Cl treatment however it decreased in depth, but not disappeared in the first 4μm of the film.
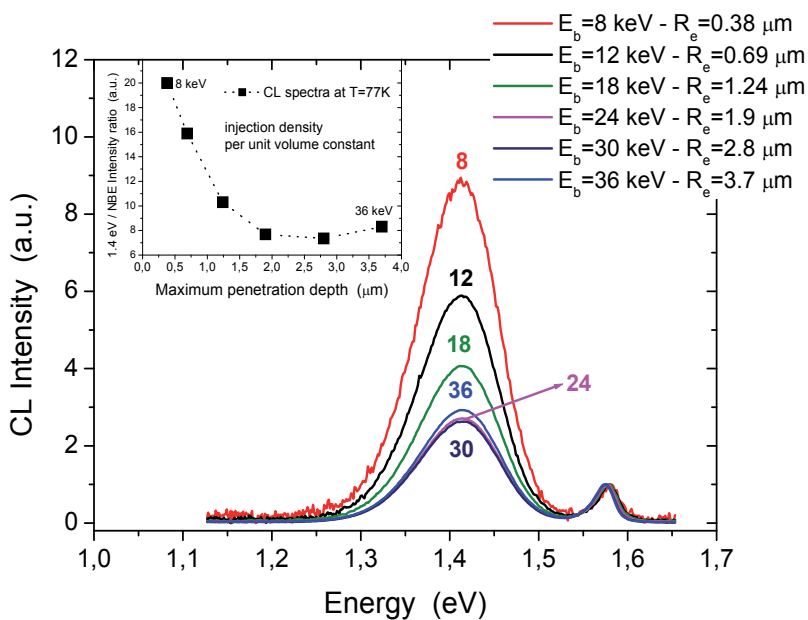
Fig. 11. Depth-dependent CL spectra acquired on the 40 mbar HCF_2Cl partial pressure annealed CdTe, by increasing E_b from 8 to 36 keV; in the inset the plot of the 1.4 eV/NBE integrated intensity ratios as a function of E_B has been shown.

The maximum E_B suitable for the SEM used for this work (36keV) was not high enough to investigate the whole CdTe film, limiting the results to about a half of the material thickness. For this reason the samples were etched in order to eliminate a portion of CdTe, leaving the material near the CdTe/CdS interface free. After the etching procedure the decreasing thickness of CdTe film edge showed a slightly sloped surface extending from the upper surface of the front contact, down to about 1μm above the CdTe/CdS interface. The SEM

image of the etched region has been shown in Fig. 13 a. CL analyses have been performed on the beveled CdTe surface, in the region closer to the interface, indicated as the "maximum etched surface" in Fig. 13 a. The comparison among the untreated CdTe and the annealed specimens was shown in Fig. 12. In the untreated and 30mbar treated samples, in addition to the NBE emission only the CL band centered at 1.47 eV has been observed. The 1.4eV band appeared only in cells treated with more than 30 mbar HCF_2Cl. By increasing the HCF_2Cl partial pressure, the 1.4eV CL intensity also increases confirming the behavior observed on the not-etched CdTe surface. On the other hand, when present, the 1.4eV CL intensities were lower than those observed on the not-etched surfaces and did not exceed the NBE intensity. This behavior was clear in Fig. 13 b, where the comparison among CL spectra acquired on the 40mbar HCF_2Cl etched surface at different depths approaching the CdTe/CdS interface was shown. The spectra were acquired from a small area (10μm wide) in order to investigate regions at the same depth. The analyzed regions have been indicated by the colored squares in Fig. 13 a. The 1.4eV CL intensity decreased remarkably from the blue to the black curve, which corresponded to regions approaching the "maximum etched region". Only in the spectrum acquired 3μm far from this region the 1.4eV band was back the dominant one. The depth-dependent decrease of the 1.4eV CL intensity could be attributed to a not-uniform distribution of the V_{Cd}-Cl(F) complex responsible for that transition because of a low diffusion of the Cl (or F) atoms within the CdTe.
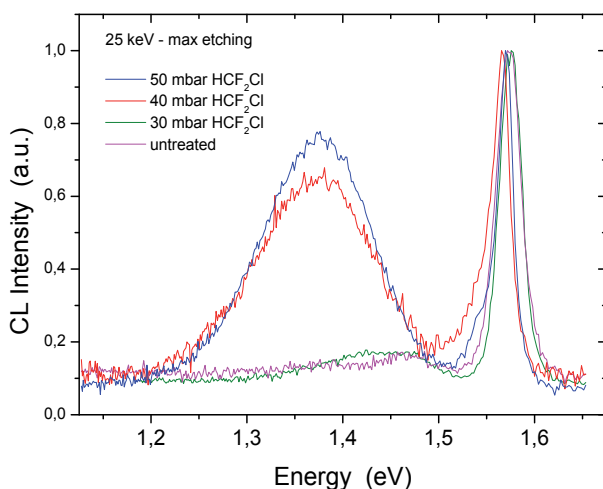
Fig. 12. Comparison among the low temperature (77 K) CL spectra (E_B=25 keV) of untreated CdTe and samples annealed at a HCF_2Cl partial pressure of 30, 40 and 50 mbar.

The spatial distribution of luminescence properties of CdTe was studied by acquiring monoCL images at the emission energies of the bands observed in the CL spectra, 1.57eV and 1.4eV respectively. The monoCL image collected at the NBE emission energy (E=1.57eV) showed the maximum intensity contribution from the central part of the grains (Fig. 14 b). The excitonic transitions came mainly from the CdTe grains, meaning that they were of good crystalline quality. On the other hand, in the same image the boundary regions between adjacent grains (*grain boundaries*) showed a dark contrast which corresponded to a very low radiative recombination efficiency. By acquiring the monoCL image at E=1.4eV

Influence of Post-Deposition Thermal Treatment on the
Opto-Electronic Properties of Materials for CdTe/CdS Solar Cells
227
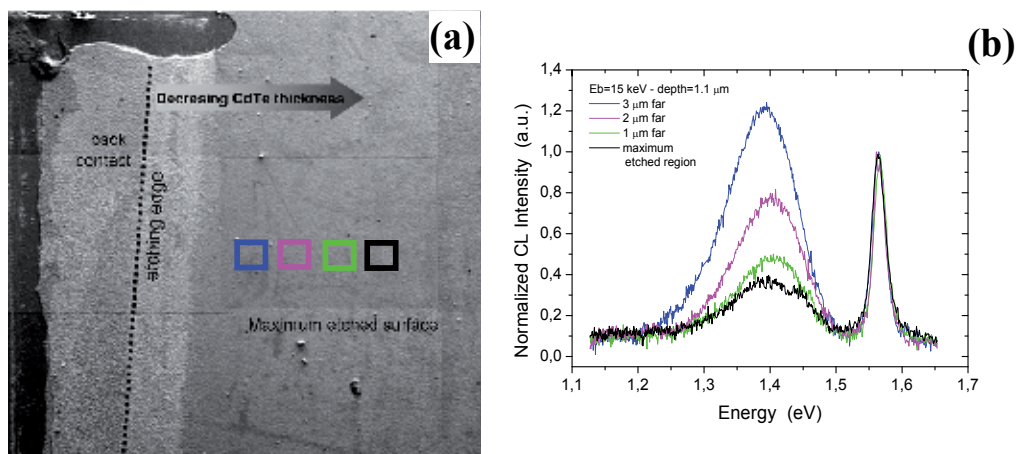
Fig. 13. a) SEM image of the etched surface of the solar cell annealed with 40 mbar HCF$_2$Cl partial pressure; b) comparison among the low temperature (77K) CL spectra (E$_b$=15keV) of the 40 mbar HCF$_2$Cl partial pressure etched solar cell.
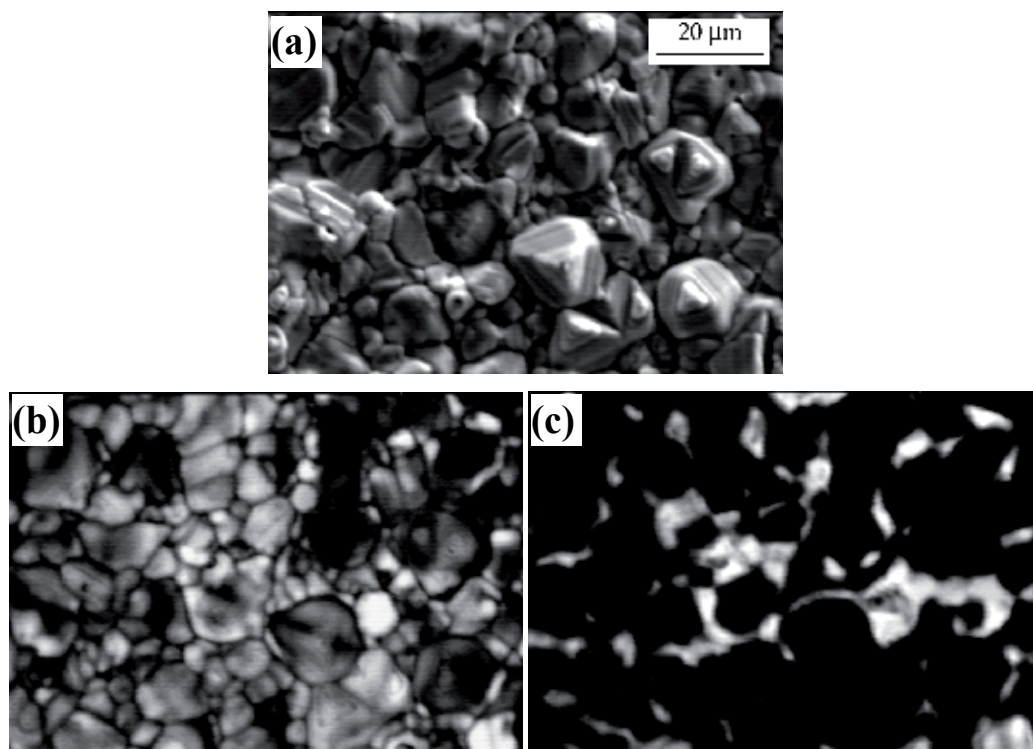
Fig. 14. 40 mbar HCF$_2$Cl partial pressure CdTe CL mapping; a) SEM image of the surface morphology; b) monoCL image at the NBE emission energy (E=1.57eV); c) monoCL at E=1.4eV emission energy.

(Fig.14 c) a complementary CL intensity distribution has been observed. The bright contrast was concentrated in the grain boundaries. For a more clear representation of the correlation between surface morphology and CdTe radiative recombination properties the corresponding SEM image has been shown (Fig. 14 a).

Taking advantage on the possibility of focusing the SEM electron beam in suitable small regions, the spectroscopic behavior of the CL in a single grain has been studied. The adopted investigation conditions were in this case "fixed beam" at E_B=12keV, which corresponded to a sub-micrometric generation volume. The CL spectra acquired in the points marked by numbered colored circles on Fig. 15 a have been shown in Fig. 15 b. The curves were normalized to the NBE emission intensity. The spectra collected inside the CdTe grain numbered 2–5 showed a high-intensity NBE emission dominating the spectra. The 1.4eV band intensity, on the contrary, exceeded the NBE one in the spectra 1 and 6, collected close to the grain edges (*grain boundary*). The spatial distribution of the 1.4eV emission intensity could be directly correlated to the non homogenous density of the V_{Cd}-Cl(F) complex responsible for that emission. A gettering of the native point defects (V_{Cd}), as well as of the incorporated impurities (Cl or F) could be suggested as the origin of this inhomogeneity. A preferential diffusion through the grain boundaries, of those impurities, during the high temperature annealing, has been supposed. The correlation between polycrystalline Cl doped CdTe structural properties and electronic levels created by the dopants in the CdTe gap has been discussed in the literature (Consonni et al. 2006, 2007) and the published results were in good agreement to those presented in this work.
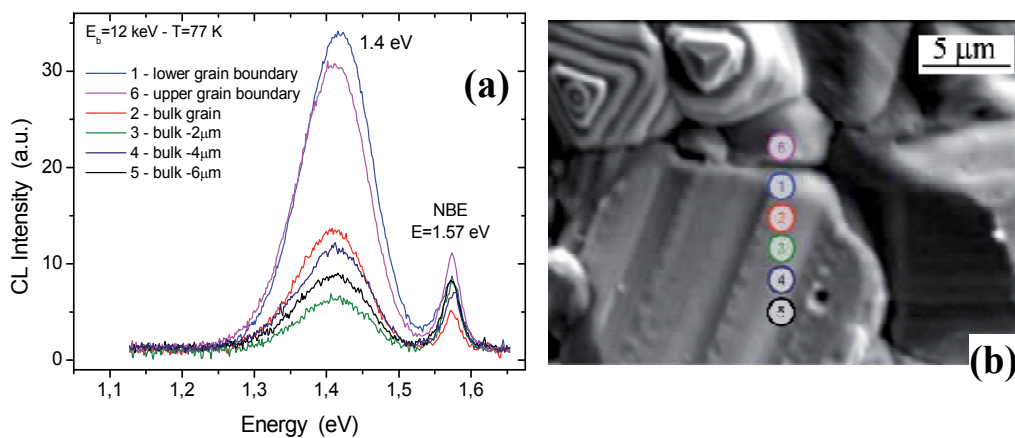
Fig. 15. a) Spatial variation of CL emissions, by acquiring the spectra in spot mode, in different points of a single CdTe grain; b) SEM image of the region where the CL spots are collected.

4.2 Comparison between the material properties and device performances

The behavior of the electro-optical properties of CdTe as a function of HCF_2Cl partial pressure, shown in the previous paragraph, did not allow to obtain information about the role of HCF_2Cl on the cell photovoltaics parameters and to investigate the transport processes taking place at the junction. The electrical properties of the annealed solar cells were compared to those of an untreated device. Dark reverse I-V curves were shown in Fig. 16 a, where the evolution of the reverse current (I_0) as a function of the HCF_2Cl partial pressure can be observed.

The diode ideality factor (A) has been calculated from those curves and its behavior as function of HCF_2Cl was also reported in Fig. 16 b. Specific processes occurring at the junction determined the reverse current and diode factor. In our case, it was observed a decrease of the reverse current when the HCF_2Cl partial pressure was increased. This behavior reached a minimum in the most efficient device obtained for this series, corresponding to 40mbar HCF_2Cl partial pressure (J_{sc}=26.2mA/cm^2, V_{oc}=820mV, ff=0.69, η=14.8%, see Fig. 17). An increase of 10mbar more reactive gas in the annealing chamber yields to a degradation of the reverse current that was increased of various orders of magnitude, showing the high reactivity of the treatment and the impact of an excess annealing on the device electrical performance. At the same time, from the behavior of A, a variation of transport mechanism depending on the treatment conditions could be suggested (Fig. 16 b). For the untreated sample, A=1.8 indicated that recombination current dominated the junction transport mechanism or that high injection conditions were present. An increase of the HCF_2Cl partial pressure gave rise to a situation in which diffusion and recombination currents take place together until the case of 40mbar HCF_2Cl partial pressure was reached, where the minimum value of A=1.2, appointed to a predominant diffusion current. The cell treated with 50mbar of reactive gas partial pressure showed a sharp modification, by increasing again the diode factor n up to 1.8. The increase of the diode reverse saturation current was responsible for a drastic reduction of ff (Fig16 b), despite the J_{SC} and V_{OC} did not change appreciably from the others HCF_2Cl annealed devices.
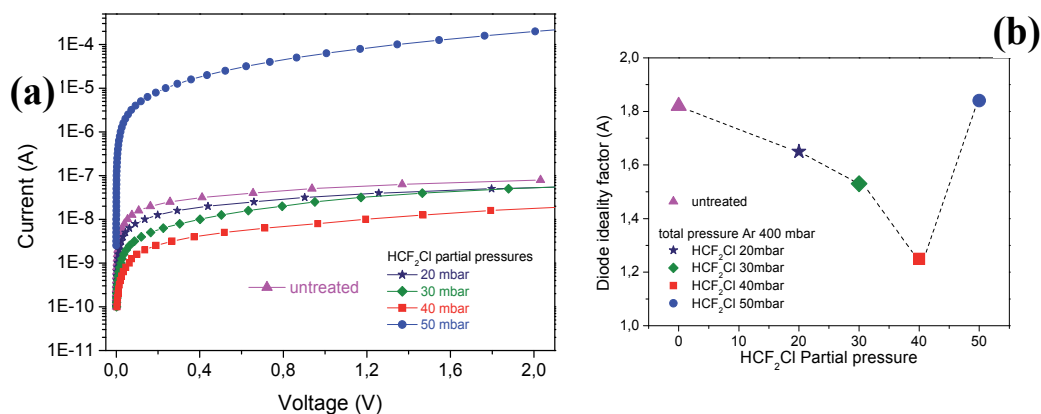
Fig. 16. a) Comparison among the dark reverse I-V curves for untreated and, 20, 30, 40 and 50 mbar of HCF_2Cl partial pressure treated solar cells; b) Diode ideality factor A as a function of the HCF_2Cl partial pressure.

The evolution of the J-V light curves (Fig. 17) of all samples showed an increase of the photovoltaic parameters by increasing the Freon partial pressure until 40mbar, while the J-V characteristic of the sample F50 showed a decrease of the fill factor to 0.25. The latter behavior could be related to a very strong intermixing between CdS and CdTe, due to the treatment, so that a very large p-n junction region was present.
A clear roll-over behavior of all the J-V curves was observed in the Fig. 17; mainly for the untreated sample and F20 and F50. This behavior was attributed to an n-p parasitic junction, opposite to the main p-n junction created by the back contact. We assume that this behavior was also strongly related to the incorporation of Cl impurities into CdTe. In our belief, the increment of the photocurrent collection should be essentially due to an increment of the

photogenerated minority carriers lifetime in the CdTe layer which suggested that the passivation of defects in absence of Cl contributed as non radiative recombination centers (Consonni et al. 2006). We considered the 50mbar HCF_2Cl cell an overtreated sample where the intermixing process was so strong that all the available CdS was consumed. The presence of shunt paths through the junction can explain the high reverse current and low fill factor values.

The luminescence properties observed on the CdTe material showed a continuous increase of the 1.4eV band intensity as a function of HCF_2Cl partial pressure; the device electrical characterization showed, on the contrary, a threshold at 40mbar partial pressure. Above this value the solar cell performances collapsed dramatically suggesting a critical correlation between HCF_2Cl annealing and junction properties.
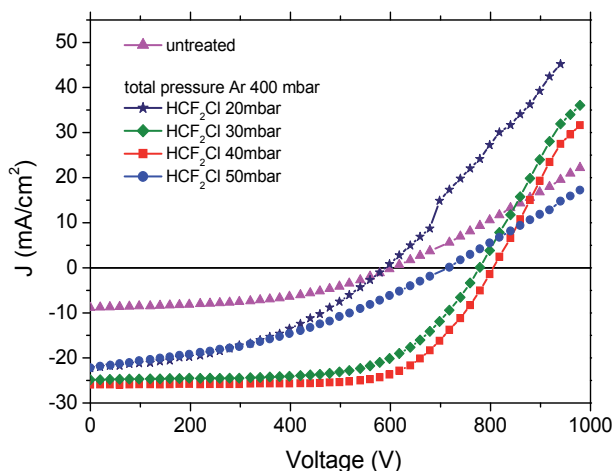
Fig. 17. Room temperature I-V characteristics under AM 1.5, 100mW/cm² illumination conditions of untreated solar cells compared to the 20, 30, 40 and 50 mbar HCF_2Cl partial pressures respectively.

The comparison between the diode factor A and the 1.4eV intensity behaviors suggested that the V_{Cd}-Cl(F) complex was beneficial for the device performances, but did not explain alone the maximum efficiency value measured for the 40 mbar annealed solar cells. A combined CdTe material doping and grain boundaries passivation effect had to be invoked. The absence of the 1.4eV band in the untreated and low HCF_2Cl partial pressure annealed CdTe after etching demonstrated that a non-radiative recombination centre was responsible for the low A values. This centre was then passivated by the Cl (or F) incorporation till the excess, for HCF_2Cl partial pressures above 40 mbar, deteriorated the p-n junction.

The complex V_{Cd}-Cl(F) formation could also be supported by the temperature dependent I-V analyses carried out on the CdTe thin film. The Arrhenius plot extracted from the CdTe dark conductivity as a function of the inverse of the temperature has been shown in Fig.18. The plot showed that, in the case of untreated CdTe the high calculated activation energy (324meV) has been related to a level due to the presence of occasional impurities like Cu, Ag or Au; the activation energy decreases by increasing the HCF_2Cl partial pressure, down to E_a=142meV for the material treated by 40mbar HCF_2Cl partial pressure. This value was in good agreement with those obtained in Cl (or F) doped CdTe single-crystals and attributed to the A-centre, due to the complex V_{Cd}-Cl(F) acceptor-like (Meyer et al. 1992).

A model of the effect of annealing as a function of HCF_2Cl partial pressure, on the bulk CdTe and its grain boundaries as well as on the CdTe-CdS intermixing mechanisms occurring at the interface has been showed in Fig. 19. The Cl (or F) impurities contained in the annealing gas penetrate into the material partially doping the CdTe. The major part was gettered to the grain boundaries, as observed in the monoCL image (Fig. 14 c), passivating them and improving conductivity. Contemporary the interdiffusion of S in the CdTe and of Te in CdS has been promoted by creating an intermixing region, which thickness increased by increasing the HCF_2Cl partial pressure, pictured by the orange region between CdTe and CdS. The poor solar cell performances of the 50mbar HCF_2Cl partial pressure annealed device have been explained by a complete consumption of the CdS layer and by destruction of the main p-n junction.
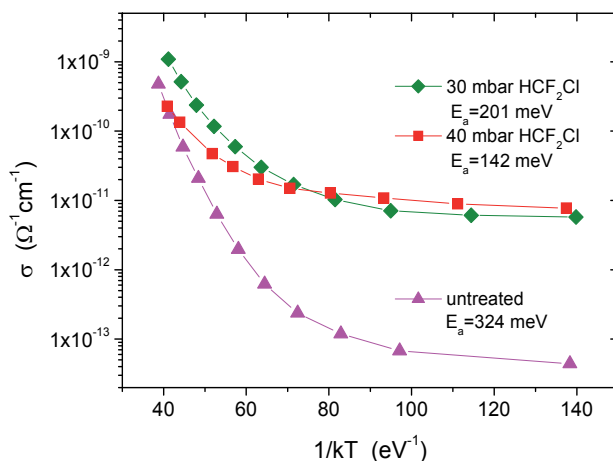
Fig. 18. Temperature dependent I-V curves collected from the untreated, 30mbar and 40mbar HCF_2Cl partial pressures respectively.
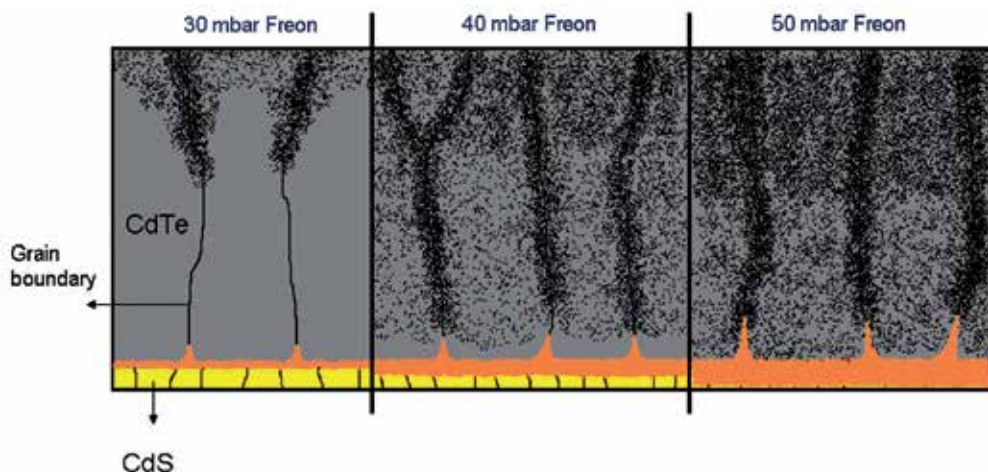
Fig. 19. Schematic representation of the effect of the HCF_2Cl treatment on defects distribution and intermixing junction formation

5. Conclusions

Thin films CdTe deposited by CSS have been submitted to a novel, full dry, post-deposition treatment based on HCF_2Cl gas. The annealing demonstrated to affect the structural properties of the materials through the loss of preferential orientation. Texture coefficient of the (111) Bragg reflection decreased from 2, for the untreated CdTe, down to 0.56 for the film treated with the highest HCF_2Cl partial pressure. On the contrary, the grain size did not show any change after annealing maintaining an average dimension of about 12μm. These results were common for high temperature CSS deposited CdTe films, while a clear dependence on the HCF_2Cl partial pressure of the electro-optical properties of the films have been observed through the presence of a 1.4 eV CL band in the annealed specimens. The transition responsible for this emission involved an electronic level in the gap with an energy of about 0.15 eV above the valence band edge, which could be attributed to a complex between cadmium vacancy and an impurity probably identified in Cl or F (V_{Cd}-Cl/F) from the annealing gas.

The combined CL mapping and spectroscopy on single CdTe grains showed that the lateral distribution of this complex was not homogeneous in the grain, but it was concentrated close to the grain boundaries. The bulk grain, on the contrary, showed a high optical quality, evidenced by the predominance of the NBE emission. The in-depth effectiveness of the HCF_2Cl annealing has been demonstrated by correlating depth-dependent CL analyses to the study of the beveled CdTe surface due to the Br-methanol etching. High density of the V_{Cd}-Cl/F complex responsible for the 1.4 eV band has been observed close to the CdTe surface; it decreased by increasing depth in the bulk region of the film about 5μm below the surface. By removing several microns of CdTe material and by approaching the CdTe/CdS interface, in the etched specimens, an HCF_2Cl partial pressure higher than 30 mbar was necessary to detect the 1.4 eV emission, this means to create the V_{Cd}-Cl/F complex. On the other hand electrical characterization determined a threshold in the beneficial role of the HCF_2Cl annealing, showing the best solar cell performances for the 40 mbar partial pressure treated device. Temperature dependent I-V analyses showed a remarkable decrease of the electronic level activation energy, from 348meV to 142meV. The last value resulted in good agreement with the energy values of the A-center found in the literature.

The comparison between the diode factor A and the 1.4 eV CL band intensity behaviors evidenced that the V_{Cd}-Cl/F complex was beneficial for the device performance, but does not explain alone the maximum efficiency value measured for the 40 mbar annealed solar cells. A tentative schematic model of the mechanisms occurring during post-deposition treatment, in the bulk CdTe and close to the CdTe/CdS interface have been also proposed. A combined CdTe-CdS intermixing and grain boundaries passivation effect has to be invoked.

6. References

Armani N., Salviati G., Nasi L., Bosio A., Mazzamuto S. and Romeo N., "Role of thermal treatment on the luminescence properties of CdTe thin films for photovoltaic applications", (2007) *Thin Solid Films*, vol. 515, pp. 6184-7, ISSN 00406090

Barret C. and Massalski T.B. Structure of Metals, edited by Pergamon, Oxford, p. 204 (1980)

Barrioz, V.; Lamb, D.A.; Jones; E.W. & Irvine, S.J.C. (2010). Suitability of atmospheric-pressure MOCVD CdTe solar cells for inline production scale. *Materials Research Society Symposium Proceedings;* ISBN: 978-160511138-4; San Francisco, CA; April 2009

Bätzner, D.L.; Romeo, A.; Zogg, H.; Wendt, R. & Tiwari, A.N. (2001) Development of efficient and stable back contacts on CdTe/CdS solar cells. *Thin Solid Films,* Vol.387, No.1-2, May 2001, pp. 151-154. ISSN: 00406090.

Birkmire, R.W.; Meyers, P.V. (1994) Processing issues for thin-film CdTe cells and modules, *Proceedings of the 24th IEEE Photovoltaic Specialists Conference*, ISSN: 01608371, Waikoloa, HI, USA, December 1994.

Bosio, A.; Romeo, N.; Mazzamuto, S. and Canevari V. (2006), Polycrystalline CdTe thin films for photovoltaic applications. *Progress in Crystal Growth and Characterization of Materials*, Vol.52, No.4, December 2006, pp. 247-279, ISSN: 09608974.

Aguilar-Hernandez J, Sastre-Hernandez J, Mendoza-Perez R, Cardenas-Garcia M and Contreras-Puente G (2005), "Influence of the CdCl2 thermal annealing on the luminescent properties of CdS-CSVT thin films", *Physica Status Solidi C - Conference and Critical Reviews*, vol. 2, No 10, p.p. 3710-3713, ISSN: 1610-1634

Chu, T.L.; Chu, S.S.; Ferekides, C.; Wu, C.Q.; Britt, J. & Wang, C. (1991). 13.4% efficient thin-film CdS/CdTe solar cells. *Journal of Applied Physics,* Vol.70, No.12, 1991, pp. 7608-7612. ISSN: 00218979

Compaan, A.D.; Tabory, C.N.; Li, Y.; Feng, Z. & Fischer, A. (1993). CdS/CdTe Solar cells by RF sputtering and by laser physical vapor deposition. *Proceedings of the 23rd IEEE Photovoltaic Specialists Conference,* pp. 394-399, ISBN: 0780312201, Louisville, KY, USA; May 10-14, 1993

Consonni V., Feuillet G. and Renet S., (2006), "Spectroscopic analysis of defects in chlorine doped polycrystalline CdTe" *J. Appl. Phys.*, vol. 99, p.p. 053502-1/7, ISSN: 0021-8979

Consonni V., Feuillet G., Bleuse j. and Donatini F., (2007) "Effects of island coalescence on the compensation mechanisms in chlorine doped polycrystalline CdTe", *J. Appl. Phys.*, vol. 101, p.p- 063522-1/6, ISSN: 0021-8979

Cruz, L.R.; Kazmerski, L.L.; Moutinho, H.R.; Hasoon, F.; Dhere, R.G. & De Avillez, R. (1999). Influence of post-deposition treatment on the physical properties of CdTe films deposited by stacked elemental layer processing. *Thin Solid Films*, Vol.350, No. 1, August 1999, pp. 44-48. ISSN: 00406090

Cunningham, D.; Davies, K.; Grammond, L.; Mopas, E.; O'Connor, M.; Rubcich, M; Sadeghi, M.; Skinner, D. and Trumbly, T. (2000). Large area Apollo module performance and reliability. *Proceedings of the 28th IEEE Photovoltaic Specialists Conference.*

Enriquez, J.P. and Mathew, X. (2004). XRD study of the grain growth in CdTe films annealed at different temperatures. *Solar Energy Materials and Solar Cells.* Vol. 81, No. 3, February 2004, pp. 363-369, ISSN: 09270248

Ferekides, C.S.; Marinskiy, D.; Viswanathan, V.; Tetali, B.; Palekis, V.; Selvaraj, P. & Morel, D.L. (2000). High efficiency CSS CdTe solar cells. *Thin Solid Films.* Vol.361, (February 2000), pp. 520-526, ISSN: 00406090

Grillo V., Armani N., Rossi F., Salviati G. and Yamamoto N., (2003), "Al.L.E.S.: A random walk simulation approach to cathodoluminescence processes in semiconductors" Inst. Phys. Conf. Ser. No 180, p.p. 559-562, ISSN 0951-3248

Hartley, A.; Irvine, S.J.C.; Halliday, D.P. & Potter, M.D.G. (2001). The influence of CdTe growth ambient on MOCVD grown CdS/CdTe photovoltaic cells. *Thin Solid Films.* Vol.387, No.1-2, May 2001, pp. 89-91. ISSN: 00406090

Hernández-Contreras, H.; Contreras-Puente, G. , Aguilar-Hernández, J. , Morales-Acevedo, A. , Vidal-Larramendi, J. & Vigil-Galán, O. (2002). CdS and CdTe large area thin films processed by radio-frequency planar-magnetron sputtering. *Thin Solid Films.* Vol.403-404, February 2002, Pages 148-152. ISSN: 00406090

Josell, D.; Beauchamp, C. R.; Jung, S.; Hamadani. B. H.; Motayed, A.; Richter, L. J.; Williams, M.; Bonevich, J. E.; Shapiro, A. ; Zhitenev, N. & Moffat, T. P. (2009). Three Dimensionally Structured CdTe Thin-Film Photovoltaic Devices with Self-Aligned Back-Contacts: Electrodeposition on Interdigitated Electrodes. *Journal of Electrochemical Society*. Vol.156, No.8, (June 2009). pp. H654-H660, ISSN: 0013-4651

Kosyachenko, L.A.; Mathew, X.; Motushchuk, V.V. & Sklyarchuk, V.M. (2006). Electrical properties of electrodeposited CdTe photovoltaic devices on metallic substrates: study using small area Au–CdTe contacts. *Solar Energy.* Vol.80, No.2, (February 2006), pp. 148-155, ISSN: 0038092X

Krustok, J; Madasson, J; Hjelt, K, and Collan H (1997) "1.4 eV photoluminescence in chlorine-doped polycrystalline CdTe with a high density of defects" *Journal of Materials Science*, vol. 32 No: 6 p.p. 1545-1550, ISSN 00222461

Lane, D.W.; Rogers, K.D.; Painter, J.D.; Wood, D.A. & Ozsan, M.E. (2000). Structural dynamics in CdS-CdTe thin films. *Thin Solid Films,* Vol.361, February 2000, pp. 1-8. ISSN: 00406090

Levy-Clement, C. (2008). Thin film electrochemical deposition at temperatures up to 180 °C for photovoltaic applications. *Proceedings of Interfacial Electrochemistry and Chemistry in High Temperature Media - 212th ECS Meeting;* ISBN: 978-160560312-4; Washington, DC; October 2007

Lincot, D. (2005). Electrodeposition of chalcogenide semiconductors. *Proceedings of 207th Electrochemical Society Meeting,* Quebec, May 2005.

Luschitz, J.; Siepchen, B.; Schaffner, J.; Lakus-Wollny, K.; Haindl, G.; Klein, A. and Jaegermann, W. (2009) CdTe thin film solar cells: Interrelation of nucleation, structure, and performance. *Thin Solid Films*, Vol. 517, No.7, February 2009, pp. 2125-2131, ISSN: 00406090.

McCandless, B.E. & Birkmire, R.W. (1991) Analysis of post deposition processing for CdTe/CdS thin film solar cells. *Solar Cells,* vol. 31, No. 6, December 1991, pp. 527-535, ISSN: 03796787.

McCandless, B.E.; Moulton, L.V. and Birkmire, R.W. (1997). Recrystallization and sulfur diffusion in $CdCl_2$-treated CdTe/CdS thin films. *Progress in Photovoltaics: Research and Applications*, Vol. 5, No.4, July 1997, pp. 249-260, ISSN: 10627995.

McCandless, B.E. (2001). Thermochemical and kinetic aspects of cadmium telluride solar cell processing. *MRS Proceedings*, Vol.668, H1.6, ISSN: 02729172, San Francisco, CA, USA; April 16-20, 2001

McCandless, B.E. & Sites, J.R. (2003) Cadmium telluride solar cells in: *Handbook of Photovoltaic Science and Engineering* Luque, A. and Hegedus, S.S., pp. 617–662, John Wiley & Sons Ltd, ISBN: 9780471491965, Chichester, UK.

McCandless, B.E. and Dobson, K.D. (2004). Processing options for CdTe thin film solar cells. *Solar Energy*, Vol. 77, No.6, December 2004, pp. 839-856, ISSN: 0038092X.

Merano, M.; Sonderegger, S.; Crottini, A.; Collin, S.; Pelucchi, E.; Renucci, P.; Malko, A.; Baier, M.H.; Kapon, E.; Ganiere, J.D. and Deveaud, B. (2006) Time-resolved cathodoluminescence of InGaAs/AlGaAs tetrahedral pyramidal quantum structures. *Applied Physics B: Lasers and Optics,* Vol. 84, No.1-2, July 2006, pp. 343-350, ISSN: 09462171.

Meyer BK, Stadler W, Hofmann DM, Ömling P, Sinerius D and Benz KW (1992), On the Nature of the Deep 1.4 eV Emission Bands in CdTe - a Study with Photoluminescence and ODMR Spectroscopy, *Journal of Crystal Growth*, vol. 117, No 1-4, p.p. 656-659 ISSN: 0022-0248

Moutinho, H.R.; Al-Jassim, M.M.; Levi, D.H.; Dippo, P.C. and Kazmerski, L.L. (1998). Effects of CdCl$_2$ treatment on the recrystallization and electro-optical properties of CdTe thin films. *Journal of Vacuum Science and Technology A: Vacuum, Surfaces and Films.* Vol.16, No.3, May 1998, pp. 1251-1257, ISSN: 07342101.

Moutinho, H.R.; Dhere, R.G.; Al-Jassim, M.M.; Levi D.H. and Kazmerski L.L. (1999). Investigation of induced recrystallization and stress in close-spaced sublimated and radio-frequency magnetron sputtered CdTe thin films. *Journal of Vacuum Science and Technology A: Vacuum, Surfaces and Films.* Vol.17, No.4, 1999, pp. 1793-1798, ISSN: 07342101.

Paulson P.D. and Dutta V (2000). Study of in situ CdCl2 treatment on CSS deposited CdTe films and CdS/CdTe solar cells, *Thin Solid Films,* vol. 370, p.p. 299-306, ISSN 00406090

Perrenaud, J, Kranz, L; Buecheler S.; Pianezzi, F. and Tiwari, A.N. (2011). The use of aluminium doped ZnO as trasparent conductive oxide for CdS/CdTe solar cells. *Thin Solid Films.* Aricle in Press. ISSN: 00406090

Plotnikov, V., Liu, X., Paudel, N., Kwon, D., Wieland & K.A., Compaan, A.D. (2011). Thin-film CdTe cells: Reducing the CdTe. *Thin Solid Films.* Article in Press. ISSN: 00406090

Potlog, T.; Khrypunov, G.; Kaelin, M.; Zogg, H. & Tiwari, A.N. (2007). Characterization of CdS/CdTe solar cells fabricated by different processes. *Materials Research Society Symposium Proceedings,* ISBN: 978-155899972-5, San Francisco, CA; April 2007

Potter, M.D.G.; Halliday, D.P.; Cousins, M. & Durose, K. (2000). Study of the effects of varying cadmium chloride treatment on the luminescent properties of CdTe/CdS thin film solar cells. *Thin Solid Films*, Vol.361, February 2000, pp. 248-252. ISSN: 00406090

Romeo, A.; Bätzner, D.L.; Zogg, H. & Tiwari, A.N. (2000). Recrystallization in CdTe/CdS. *Thin Solid Films.* Vol.361 (February 2000), pp. 420-425, ISSN: 00406090

Romeo, A.; Buecheler, S.; Giarola, M.; Mariotto, G.; Tiwari, A.N.; Romeo, N.; Bosio, A. & Mazzamuto, S. (2009). Study of CSS- and HVE-CdTe by different recrystallization processes. *Thin Solid Films*, Vol.517, No.7, February 2009, pp. 2132-2135. ISSN: 00406090

Romeo, N.; Bosio, A.; Tedeschi, R.; Romeo, A. & Canevari, V. (1999). Highly efficient and stable CdTe/CdS thin film solar cell. *Solar Energy Materials and Solar Cells*, Vol.58, No.2, June 1999, pp.209-218. ISSN: 09270248

Romeo, N.; Bosio, A.; Canevari, V. & Podestà, A. (2004). Recent progress on CdTe/CdS thin film solar cells. *Solar Energy,* Vol.77, No.6, December 2004, pp. 795-801. ISSN: 0038092X

Romeo, N.; Bosio, A.; Mazzamuto, S.; Podestà, A. and Canevari, V. (2005). The Role of Single Layers in the Performance of CdTe/CdS thin film solar cells. *Proceedings of 25th Photovoltaic Energy Conference and Exhibition,* Barcelona, Spain, June 2005.

Romeo, N.; Bosio, A.; Romeo, A.; Mazzamuto, S. & Canevari, V. (2006). High Efficiency CdTe/CdS Thin Film Solar Cells Prepared by Treating CdTe Films with a Freon Gas in Substitution of CdCl$_2$. *Proceedings of the 21st European Photovoltaic Solar Energy Conference and Exhibition,* pp.1857-1860, ISBN 3-936338-20-5, Dresden, Germany, September 4-8, 2006.

Romeo, N.; Bosio, A.; Mazzamuto, S.; Romeo, A. & Vaillant-Roca, L. (2007). "High efficiency cdte/cds thin film solar cells with a novel back-contact", *Proceedings of the 22nd European Photovoltaic Solar Energy Conference and Exhibition,* pp. 1919-1921, Milan; Italy.

Romeo, N.; Bosio, A.; Romeo, A. & Mazzamuto, S. (2010). A CdTe thin film module factory with a novel process. *Proceedings of 2009 MRS Spring Meeting;* Vol.1165, pp. 263-273, ISBN: 978-160511138-4, San Francisco, CA, USA; April 13-17, 2009

Schulz, D.L.; Pehnt, M.; Rose, D.H.; Urgiles, E.; Cahill, A.F.; Niles, D.W.; Jones, K.M.; Ellingson, R.J.; Curtis, C.J.; Ginley, D.S. (1997). CdTe Thin Films from Nanoparticle Precursors by Spray Deposition. *Chemistry of Materials.* Vol.9. No.4, April 1997, pp. 889-900. ISSN: 08974756

Stadler, W.; Hoffmann, D.M.; Alt, H.C.; Muschik, T.; Meyer, B.K.; Weigel, E.; Müller-Vogt, G.; Salk, M.; Rupp, E. and Benz, K.W. (1995) Optical investigations of defects in $Cd_{1-x}Zn_xTe$, *Physical Review B,* vol.51, No.16 1995, pp. 10619-10630, ISSN: 01631829.

Sze, S. (1981). *Physics of Semiconductor Devices* (2nd ed.), Wiley, ISBN:9780471143239, New York.

Yacobi, B.G. & Holt, D.B. (1990) *Cathodoluminescence microscopy of inorganic solids,* Plenum Press, ISBN: 0306433141, New York and London.

Yi, X. & Liou, J.J. (1995). Surface oxidation of polycrystalline cadmium telluride thin films for Schottky barrier junction solar cells. *Solid-State Electronics.* Vol.38, No.6, (1995), pp.1151-1154, ISSN: 00381101.

Yoshida, T. (1992). Analysis of photocurrent in screen-printed CdS/CdTe solar cells. *Journal of the Electrochemical Society.* Vol.139, No.8, August 1992, pp. 2353-2357. ISSN: 00134651

Yoshida, T. (1995). Photovoltaic properties of screen-printed CdTe/CdS solar cells on indium-tin-oxide coated glass substrates. *Journal of the Electrochemical Society.* Vol.142, No.9, September 1995, pp. 3232-3237. ISSN: 00134651

Wu, X.; Keane, J.C.; Dhere, R.G.; DeHart, C.; Duda, A.; Gessert, T.A.; Asher, S.; Levi, D.H. and Sheldon, P. (2001 a). 16.5% efficient CdS/CdTe polycrystalline thin-film solar cell, *Proceedings of the 17th E-PVSEC,* München, Germany; October 2001.

Wu, X.; Asher, S.; Levi, D.H.; King, D.E.; Yan, Y.; Gessert, T.A. & Sheldon, P. (2001 b). Interdiffusion of CdS and Zn_2SnO_4 layers and its application in CdS/CdTe polycrystalline thin-film solar cells. *Journal of Applied Physics*, Vol.89, No.8, April 2001, pp. 4564-4569. ISSN: 00218979

Wu, X. (2004). High-efficiency polycrystalline CdTe thin-film solar cells. *Solar Energy.* Vol.77, No6, (December 2004), pp. 803-814, ISSN: 0038092X

Wu, X.; Zhou, J.; Duda, A.; Yan, Y.; Teeter, G.; Asher, S.; Metzger, W.K.; Demtsu, S.; Wei, S.-Huai. & Noufi, R. (2007). Phase control of Cu_xTe film and its effects on CdS/CdTe solar cell. *Thin Solid Films,* Vol.515, No.15 SPEC. ISS., May 2007, pp. 5798-5803, ISSN: 00406090

Xiaonan Li,. Niles D. W,. Hasoon F. S,. Matson R. J, and Sheldon P. (1999). Effect of nitric-phosphoric acid etches on material properties and back-contact formation of CdTe-based solar cells. *J. Vac. Sci. Technol. A*, vol. 17, No 3, p.p. 805-809 ISSN: 07342101.

Zanio, K.; Willardson R.K. & Beer, A.C. (1978). *Cadmium telluride. Volume 13 of Semiconductors and semimetals. Cadmium telluride*, Academic Press, ISBN 0127521135, 9780127521138, London, UK

Zhou, J.; Wu, X.; Duda, A.; Teeter, G. & Demtsu, S.H. (2007). The formation of different phases of CuxTe and their effects on CdTe/CdS solar cells. *Thin Solid Films,* Vol. 515, No.18, June 2007, pp. 7364-7369, ISSN: 00406090

Zoppi, G.; Durose, K.; Irvine, S.J.C. & Barrioz, V. (2006). Grain and crystal texture properties of absorber layers in MOCVD-grown CdTe/CdS solar cells. *Semiconductor Science and Technology.* Vol.21, No.6, June 2006, pp. 763-770. ISSN: 02681242

Chemical Bath Deposited CdS for CdTe and Cu(In,Ga)Se₂ Thin Film Solar Cells Processing

M. Estela Calixto[1], M. L. Albor-Aguilera[2], M. Tufiño-Velázquez[2],
G. Contreras-Puente[2] and A. Morales-Acevedo[3]
[1]Instituto de Física, Benemérita Universidad Autónoma de Puebla, Puebla,
[2]Escuela Superior de Física y Matemáticas, Instituto Politécnico Nacional, México,
[3]CINVESTAV-IPN, Departamento de Ingeniería Eléctrica, México,
México

1. Introduction

Extensive research has been done during the last two decades on cadmium sulfide (CdS) thin films, mainly due to their application to large area electronic devices such as thin film field-effect transistors (Schon et al., 2001) and solar cells (Romeo et al., 2004). For the latter case, chemical bath deposited (CBD) CdS thin films have been used extensively in the processing of CdTe and Cu(In,Ga)Se₂ solar cells, because it is a very simple and inexpensive technique to scale up to deposit CdS thin films for mass production processes and because among other n-type semiconductor materials, it has been found that CdS is the most promising heterojunction partner for these well-known polycrystalline photovoltaic materials. Semiconducting n-type CdS thin films have been widely used as a window layer in solar cells; the quality of the CdS-partner plays an important role into the PV device performance. Usually the deposition of the CdS thin films by CBD is carried out using an alkaline aqueous solution (high pH) composed mainly of some sort of Cd compounds (chloride, nitrate, sulfate salts, etc), thiourea as the sulfide source and ammonia as the complexing agent, which helps to prevent the undesirable homogeneous precipitation by forming complexes with Cd ions, slowing down thus the surface reaction on the substrate. CdS films have to fulfill some important criteria to be used for solar cell applications; they have to be adherent to the substrate and free of pinholes or other physical imperfections. Moreover, due to the requirements imposed to the thickness of the CdS films for the solar cells, it seems to be a function of the relative physical perfection of the film. The better structured CdS films and the fewer flaws present, the thinner the film can be, requirement very important for the processing of Cu(In,Ga)Se₂ based thin film solar cells, thickness ~ 30 - 50 nm. In such case, the growth of the thin CdS film is known to occur via ion by ion reaction, resulting thus into the growth of dense and homogeneous films with mixed cubic/hexagonal lattice structure (Shafarman and Stolt, 2003).

The reason to choose the CBD method to prepare the CdS layers was due to the fact that CBD forms a very compact film that covers the TCO layer, in the case of the CdTe devices and the Cu(In,Ga)Se₂ layer without pinholes. Moreover, the CdS layer in a hetero-junction solar cell must also be highly transparent and form a chemical stable interface with the

Cu(In,Ga)Se$_2$ and CdTe absorbing layers. The micro-crystalline quality of the film may also be related to the formation of the CdZnS ternary layer in the case of the Cu(In,Ga)Se$_2$ and CdS$_{1-x}$Te$_x$ ternary layer for the case of CdTe, at the interface helping to reduce the effects associated to the carrier traps in it. Hence, the deposition conditions and characteristics of the CdS layer may affect strongly the efficiency of the solar cells. We have worked with this assumption in mind for making several experiments that will be described in the following paragraphs. As it will be shown, we have been able to prepare optimum CdS layers by CBD in order to be used in solar cells, and have found that the best performance of CdS/CdTe solar cells is related to the CdS layer with better micro-crystalline quality as revealed by photoluminescence measurements performed to the CdS films.

2. CdS thin films by chemical bath deposition technique (CBD)

Chemical bath deposition technique (CBD) has been widely used to deposit films of many different semiconductors. It has proven over the years to be the simplest method available for this purpose, the typical components of a CBD system are a container for the solution bath, the solution itself made up of common chemical reactive salts, the substrate where the deposition of the film is going to take place, a device to control the stirring process and temperature, sometimes a water bath is included to ensure an homogeneous temperature, an schematic diagram of the CBD system is shown in figure 1. The concentrations of the components of the solution bath for CdS can be varied over a working range and each group use its own specific recipe, so there are as many recipes to deposit CdS as research groups working in the subject. The chemical reactive salts are generally of low cost and in general it is necessary to use small quantities. The most important deposition parameters in this technique are the molar concentration, the pH, the deposition temperature, the deposition time, the stirring rate, the complexing agents added to the bath to slowing down the chemical reactions, etc. However, once they have been established these are easy to control. The CdS thin film deposition can be performed over several substrates at a time, and the reproducibility is guaranteed if the deposition parameters are kept the same every time a deposition is done. Substrates can have any area and any configuration, besides they can be of any kind, electrical conductivity is not required.
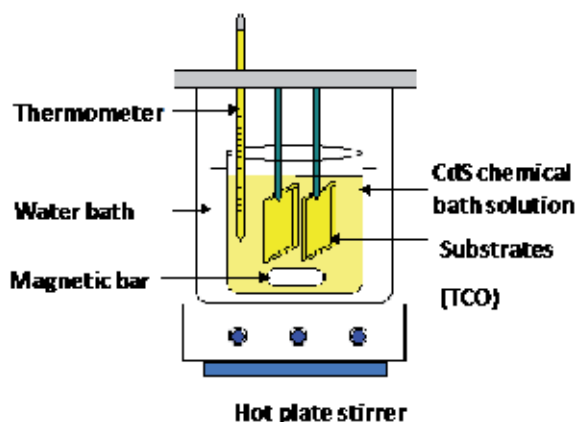
Fig. 1. Schematic diagram of a CdS chemical bath deposition system

Previously we have reported the preparation of monolayers and bi-layers of CdS deposited by chemical bath deposition technique using a solution bath based on CdCl$_2$ (0.1 M), NH$_4$Cl (0.2 M), NH$_3$ (2 M) and thiourea (0.3 M), maintaining fixed deposition time and temperature conditions and varying the order of application of the CdCl$_2$ treatment (Contreras-Puente et al., 2006). Initially, the solution is preheated during 5 min prior to add the thiourea, after that the deposition was carried out during 10 min at 75 C, then the second layer (the bilayer) was deposited at a lower deposition temperature, thus allowing us to control the growth rate of the CdS layer. This was aimed to obtain films with sub-micron and nanometric particle size that could help to solve problems such as partial grain coverage, inter-granular caverns and pinholes. In this way, CdS thin films have been deposited onto SnO$_2$: F substrates of 4 cm^2 and 40 cm^2, respectively.

Figure 2 shows the typical X-ray diffraction pattern obtained with a glancing incidence X-ray diffractometer, for CdS samples prepared in small and large area, respectively. CdS films grow with preferential orientation in the (002), (112) y (004) directions, which correspond to the CdS hexagonal structure (JCPDS 41-049). Small traces of SnO$_2$:F are observed (*) in the X-ray patterns. Figure 3 shows the morphology for both mono and bilayers of CdS films, respectively. It can be observed that bi-layer films present lower pinhole density and caverns. This is a critical parameter because it gives us the possibility to improve the efficiency of solar cell devices. Several sets of CdTe devices were made and their photovoltaic parameters analyzed, giving conversion efficiencies of ~ 6.5 % for both small and large area devices.
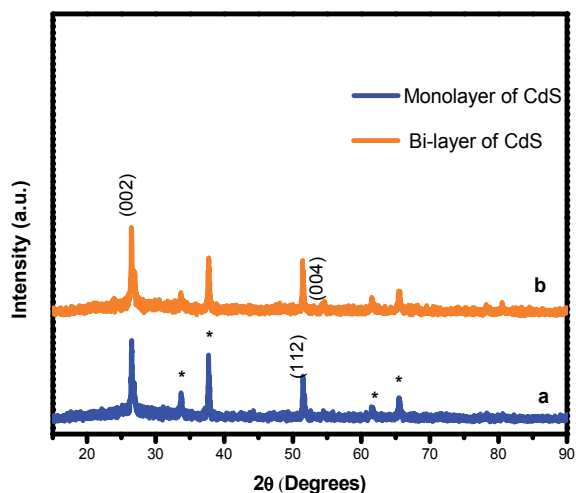
Fig. 2. X-ray diffraction patterns of mono and bi-layers of CdS

Also, we have found that the position of the substrate inside the reactor is an important factor because the kinetics of the growth changes. Figure 4 shows how the transmission response changes with substrate position inside the reactor. The deposition time for all samples was 10 min. According to figure 4a when the substrates are placed horizontally at the bottom of the reactor the CdS film grows a thickness of 150 nm, but the transmission response is poor, when the substrates are placed vertically and suspended with a pair of tweezers inside the reactor the CdS film grows a thickness of 110 nm and the transmission response is ~ 83% (see figure 4b), however in this configuration handling the substrate is

complicated. Because of this, to design a better substrate holder/support was imperative. So, a new support was designed and built to facilitate the access and handling of the samples inside the reactor. Figures 4c and 4d shown the transmission response for mono and bi-layers of CdS deposited using the new substrate support, placed in a vertical configuration inside the reactor, for both cases the values were between 85 – 95 %, being the monolayers the ones that exhibit the best response; however its morphology shows a larger surface defect density. The thickness of these samples is in the order of 100 – 120 nm.
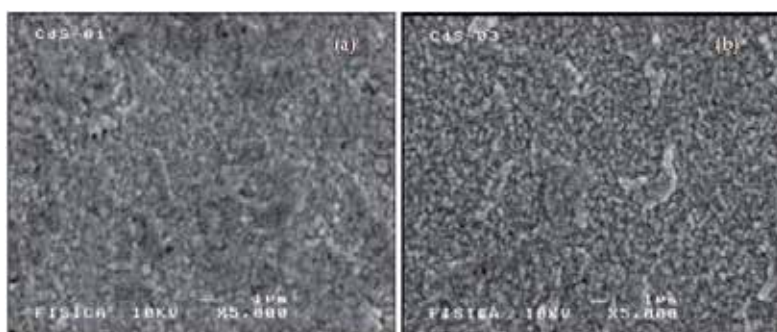
Fig. 3. SEM images of a monolayer and a bi-layer of CdS
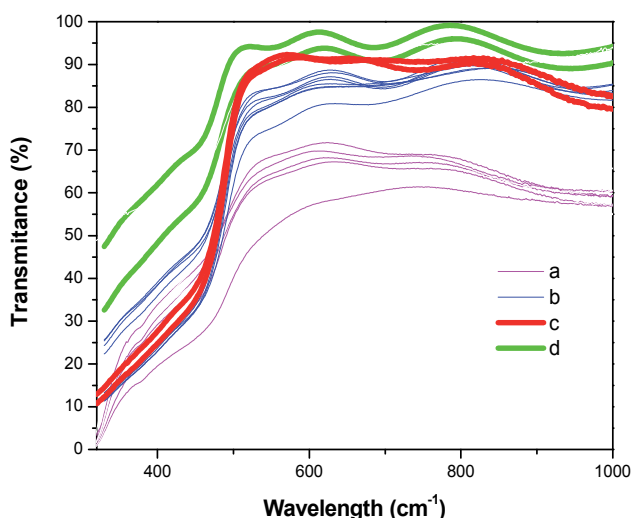
Fig. 4. Transmission response of CdS films as a function of the position inside the reactor

2.1 CdS by CBD with a modified configuration

Figure 5 shows the implementation of the new substrate support for the CBD system, from this figure it can be seen that the CBD system is the same as the one shown in figure 1 but with the addition of the substrate holder. It basically holds the substrates vertically and steady, while keeping it free to rotate along with the substrates, in such case the magnetic stirrer is no longer needed. This substrate support can be set to rotate at different speed rates, allowing the growth and kinetics of the reaction of CdS to change and in the best case to improve, improving thus the physical properties of CdS films. The design includes a

direct current motor that has the option to vary the speed rate from 0 to 50 rpm. The motor can move the substrate support made of a Teflon structure that holds up to 4 large area substrates (45 cm² each). The principal advantage of using this modified structure is the ability to handle 4 substrates at a time, placing them, inside the reactor containing the solution bath and at the same time starting the rotation, by doing this all the CdS films are expected to have a uniform growth and thickness ~ 120 nm. When the substrate holder is set to rotate inside the reactor, the kinetics of the CdS films growth was clearly affected as shown in figure 6, it can be seen that when the rotating speed goes up, the transmission
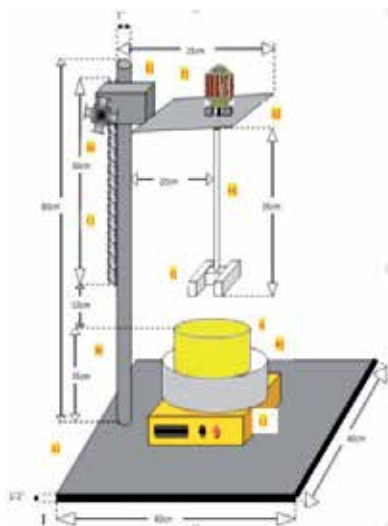
Fig. 5. Schematic diagram of the new substrate holder for the CBD system
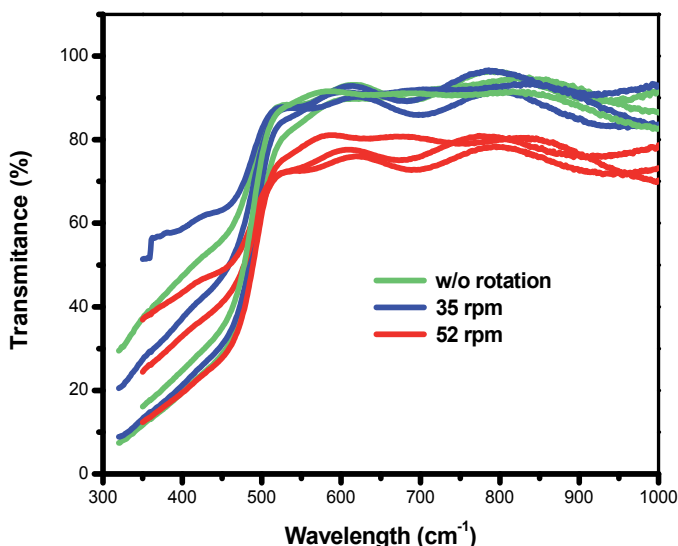
Fig. 6. Transmission response as a function of the rotation rate for CdS films prepared with the new substrate holder.

response decreases to ~ 65% compared to the samples prepared without rotation. The deposition time was set to 10 min in all cases, giving thus the growth of CdS films with 120 – 130 nm.
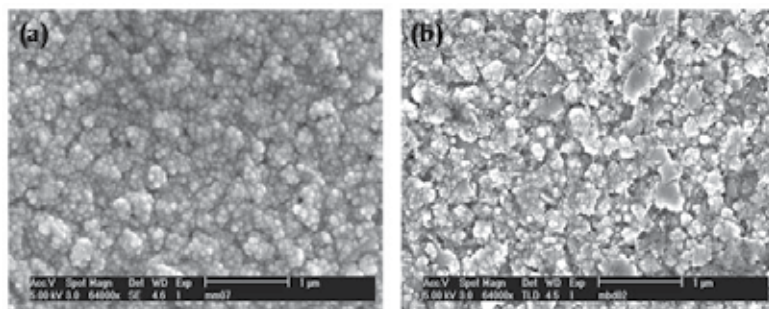
Fig. 7. SEM images of (a) mono and (b) bi-layer of CdS deposited at 35 rpm

Figure 7 shows the SEM images of CdS films prepared using the new substrate holder, according to these images, the morphology of the mono and bi-layers of CdS changes as a function of the rotating speed. Also we can clearly see an increase in the particle size for each case, for the monolayer of CdS the particle size ball- like shape of ~ 0.5 – 1 μm, but more uniform and compact compared to the particle size that the bi-layers of CdS exhibit with rotation speed set to 35 rpm, flakes-like shape with size of ~1 – 4 μm. No devices have been made so far using CdS films grown with this improved CBD system, studies are being performed and research on the subject is ongoing in order to optimize the deposition conditions, for this case.

3. Cu(In,Ga)Se$_2$ based thin films by co-evaporation technique (PVD)

Semiconducting CuInSe$_2$ is one of the most promising materials for solar cells applications because of its favorable electronic and optical properties including its direct band gap with high absorption coefficient (~10^5 cm^{-1}) thus layers of only ~2 μm thickness are required to absorb most of the usable solar radiation and inherent *p*-type conductivity. Besides, the band gap of CuInSe$_2$ can be modified continuously over a wide range from 1.02 to 2.5 eV by substituting Ga for In or S for Se, which means that this material can be prepared with a different chemical composition. Cu(In,Ga)Se$_2$ is a very forgiving material so high efficiency devices can be made with a wide tolerance to variations in Cu(In,Ga)Se$_2$ composition (Rocheleau et al., 1987 and Mitchell K. et al., 1990), grain boundaries are inherently passive so even films with grain sizes less than 1 μm can be used, and device behavior is insensitive to defects at the junction caused by a lattice mismatch or impurities between the Cu(In,Ga)Se$_2$ and CdS. The latter enables high-efficiency devices to be processed despite exposure of the Cu(In,Ga)Se$_2$ to air prior to junction formation. For Cu(In,Ga)Se$_2$ thin film solar cells processing the substrate structure is preferred over the superstrate structure. The substrate structure is composed of a soda lime glass substrate, coated with a Mo layer used as the back contact where the Cu(In,Ga)Se$_2$ film is deposited. The soda lime glass, which is used in conventional windows, is the most common substrate material used to deposit Cu(In,Ga)Se$_2$ since it is available in large quantities at low cost. Besides, it has a thermal expansion coefficient of 9×10^{-6} K^{-1} (Boyd et al., 1980) which provides a good match to the Cu(In,Ga)Se$_2$ films. The most important effect of the soda lime glass substrate on

Cu(In,Ga)Se$_2$ film growth is that it is a natural source of sodium for the growing material. So that, the sodium diffuses through the sputtered Mo back contact, which means that is very important to control the properties of the Mo layer. The presence of sodium promotes the growth of larger grains of the Cu(In,Ga)Se$_2$ and with a higher degree of preferred orientation in the (112) direction. After Cu(In,Ga)Se$_2$ deposition, the junction is formed by depositing a CdS layer. Then a high-resistance (HR) ZnO and a doped high-conductivity ZnO:Al layers are subsequently deposited. The ZnO layer reacts with the CdS forming the Cd$_x$Zn$_{1-x}$S ternary compound, which is known to have a wider band gap than CdS alone, increasing thus the cell current by increasing the short wavelength (blue) response and at the same time setting the conditions to make a better electric contact. Finally, the deposition of a current-collecting Ni/Al grid completes the device. The highest conversion efficiency for Cu(In,Ga)Se$_2$ thin film solar cells of ~ 20 % has been achieved by (Repins et al., 2008) using a three stages co-evaporation process. The processing of photovoltaic (PV) quality films is generally carried out via high vacuum techniques, like thermal co-evaporation. This was mainly the reason, we have carried out the implementation and characterization of a thermal co-evaporation system with individual Knudsen cells MBE type, to deposit the Cu(In,Ga)Se$_2$ thin films (see figure 8). The deposition conditions for each metal source were established previously by doing a deposition profile of temperature data vs. growth rate. The thermal co-evaporation of Cu(In,Ga)Se$_2$ thin films was carried out using Cu shots 99.999%, Ga ingots 99.9999%, Se shots 99.999% from Alfa Aeser and In wire 99.999% from Kurt J. Lesker, used as received. The depositions were performed on soda lime glass substrates with sputtered Mo with ~ 0.7 μm of thickness. The substrate temperature was > 500 °C, temperature of source materials was set to ensure a growth rate of 1.4, 2.2 and 0.9 Å/s for Cu, In and Ga, respectively for the metals, while keeping a selenium overpressure into the vacuum chamber during film growth.

Fig. 8. Thermal co-evaporation system with Knudsen effusion cells to deposit Cu(In,Ga)Se$_2$ thin films

Cu(In,Ga)Se$_2$ thin films were grown with different Ga and Cu ratios (Ga/(In+Ga) = 0.28, 0.34 and 0.35 respectively and Cu/(In+Ga) = 0.85, 0.83 and 0.94). The deposition time was set to 30 min for all cases. All the Cu(In,Ga)Se$_2$ samples were grown to have 2 - 3 μm thickness and aiming to obtain a relative low content of gallium ∼ 0.30 % (CuIn$_{0.7}$Ga$_{0.3}$Se$_2$), while keeping the copper ratio to III < 1 (where III = In+Ga), very important criteria to use them directly for solar cell applications, as shown in table 1. For solar cell devices, samples JS17 and JS18 were used, with a chemical composition similar to that of sample JS13.

Chemical composition (at %) by EDS						
Sample	Cu	In	Ga	Se	Ga/III	Cu/III
Reference	22.09	18.84	7.27	51.80	0.28	0.85
CIGS_5	21.27	16.73	8.88	53.69	0.35	0.83
CIGS_8	23.04	16.20	8.24	53.47	0.34	0.94
JS13	24.46	16.87	9.74	48.93	0.37	0.92

Table 1. Results of the chemical composition analysis of the co-evaporated Cu(In,Ga)Se$_2$ thin films

The morphology of the Cu(In,Ga)Se$_2$ samples is very uniform, compact and textured, composed of small particles (see figures 9a - 9c). Figure 9d shows the cross-section SEM image and a film thickness ∼ 3.5 μm, also notice the details of the textured surface of the film, due to the high temperature processing.
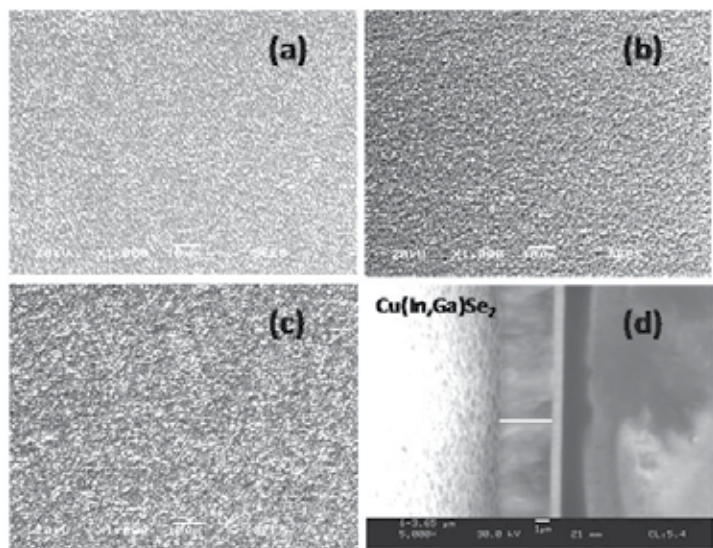
Fig. 9. SEM micrographs of co-evaporated Cu(In,Ga)Se$_2$ thin films (a - c) and (d) cross section image

The XRD patterns of the films show sharp and well defined peaks, indicating a very good crystallization, the films appear to grow with a strong (112) orientation (see figure 10) and with grain sizes ∼ 1 μm. The expected shift of the (112) reflection compared to that of the CuInSe$_2$ is also observed, which is consistent with a film stoichiometry of CuIn$_{0.7}$Ga$_{0.3}$Se$_2$ (JCPDS 35-1102).
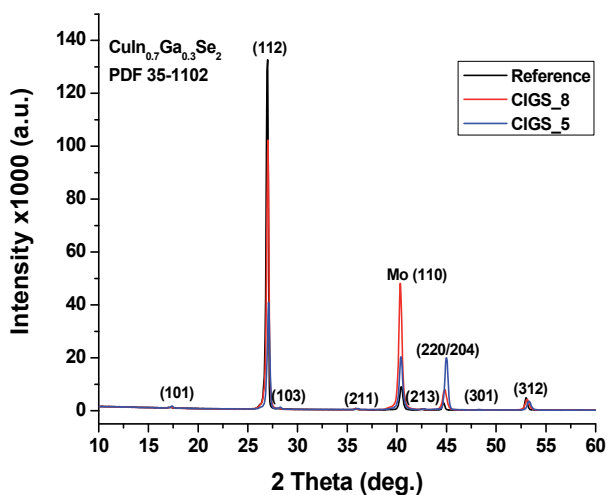
Fig. 10. XRD pattern for Cu(In,Ga)Se₂ thin films thermal co-evaporated

4. CdTe thin films by Close Spaced Vapor Transport (CSVT)

CdTe is a compound semiconductor of II-VI type that has a cubic zincblende (sphalerite) structure with a lattice constant of 6.481 A°. CdTe at room temperature has a direct band gap of 1.5 eV with a temperature coefficient of 2.3–5.4 x10^{-4} eV/K. This band gap is an ideal match to the solar spectrum for a photovoltaic absorber. Similarly to the Cu(In,Ga)Se₂, the absorption coefficient is large (around 5x10^4 cm^{-1}) at photon energies of 1.8 eV or higher (Birkmire R. and Eser E., 1997). Up to date the highest conversion efficiency achieved for CdTe solar cells is 16.5% (Wu X. et al., 2001). CdTe solar cells are p-n heterojunction devices in which a thin film of CdS forms the n-type window layer. As in the case of Cu(In,Ga)Se₂-based devices the depletion field is mostly in the CdTe. There are several deposition techniques to grow the CdTe like, physical vapor deposition, vapor transport deposition, close spaced sublimation, sputter deposition and electrodeposition (McCandless Brian E. and Sites James R., 2003). In this case, the close spaced sublimation has been selected to prepare the CdTe films for solar cell applications.

The sublimation technique for the deposition of semiconducting thin films of the II-VI group, particularly CdTe, has proven to be effective to obtain polycrystalline materials with very good optical and electrical properties. There are several steps that involve the formation of the deposited materials, these are listed as follows: 1) synthesis of the material to be deposited through the phase transition from solid or liquid to the vapor phase 2) vapor transport between the evaporation source and the substrate, where the material will be deposited in the form of thin film, and 3) vapor and gas condensation on the substrate, followed by the nucleation and grow of the films. In general, and particularly in our CdTe - case, the vapor transport is regulated by a diffusion gas model. This technique has several advantages over others because is inexpensive, has high growth rates, and it can be scaled up to large areas for mass production. The Close Spaced Vapor Transport technique, named as "CSVT", is a variant of the sublimation technique, it uses two graphite blocks, where independent high electrical currents flow and due to the dissipation effect of the electrical energy by Joule's heat makes the temperature in each graphite block to rise. One of the graphite blocks is named the source

block and the other is the substrate block. Figure 11 shows the block diagram of the CSVT system used to prepare the CdTe thin films. Between the source graphite block "A" and the substrate graphite block "B" is located the graphite boat that contains the material to be sublimated, and on top of this boat the substrate is located, in a very close proximity or close spaced. The material growth is carried out under the presence of an inert atmosphere like argon, nitrogen, etc. The growth rate of the material to be deposited can be controlled by controlling the pressure and gas flow rate. Also this inert gas can be mixed with a reactive gas like oxygen, which benefits the growth of CdTe with the characteristic p-type conductivity. The deposition parameters for this technique are: a) T_s: temperature of the source, b) T_{sub}: substrate temperature, it has to be lower than the T_s in order to avoid the re-sublimation of the material, c) d_{s-sub}: distance between the material to be deposited and the substrate and d) P_g: pressure of the inert gas inside the chamber.
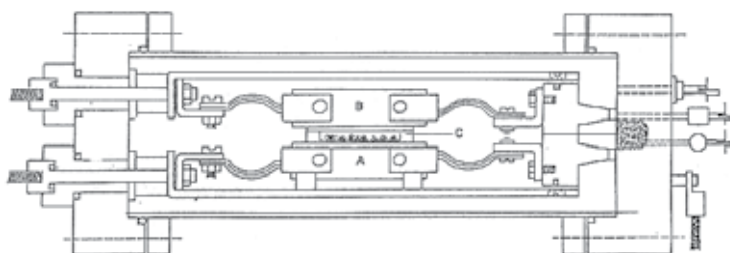
Fig. 11. Schematic diagram of a CSVT system

For the processing of CdTe thin film solar cells, it is necessary to use a *superstrate* structure, so that the CdS is deposited on SnO_2:F, in such a way that the growth process allows the film to be deposited over the whole surface, becoming a surface free of holes and caverns without empty spaces among the grains, and with a uniform grain size distribution. It is also required that the CdS layer matches well with the CdTe host, thus favoring a good growing kinetics for CdTe, as well as the formation of the CdS_xTe_{1-x} ternary compound in the interface due to the diffusion of S from CdS to CdTe. The high-efficiency CdTe solar cells to date have essentially the same *superstrate* structure. The superstrate structure is composed of a sodalime glass substrate, coated with a SnO_2:F; a transparent conductor oxide as the front contact, then a CdS layer is chemically bath deposited, followed by the deposition of a CdTe layer and finally the deposition of two layers of Cu and Au to form the back contact to complete the CdS/CdTe device. In order to achieve solar cells with high conversion efficiencies, the physical and chemical properties of each layer must be optimized (Morales-Acevedo A., 2006). The deposition of CdTe was performed by using CdTe powder 99.999% purity. The deposition atmosphere was a mixture of Ar and O_2, with equal partial pressures of O_2 and Ar. In all cases the total pressure was 0.1 Torr. Prior to all depositions the system was pumped to 8×10^{-6} Torr as the base pressure. In the CSVT-HW (hot wall) deposition, the separation between source and substrate was about 1 mm. The deposition time was 3 min for all the samples deposited with substrate and source temperatures of 550 °C and 650 °C, respectively. Under these conditions, CdTe layers of 2 – 4 μm were obtained. The CdTe thin films were also thermally treated with $CdCl_2$. As discussed before, a very important treatment independently of the deposition technique for both CdS and CdTe layers is a thermal annealing after the deposition of $CdCl_2$ on top of the CdTe layer. If the $CdCl_2$

treatment is not performed, the short circuit current density and the efficiency of the solar cell are very low. This treatment consists in depositing 300–400 nm of CdCl$_2$ on top of CdTe with a subsequent annealing at 400 °C during 15–20 min in air, or in an inert gas atmosphere like Ar. During this process the small CdTe grains are put in vapor phase and re-crystallize, giving a better-organized CdTe matrix. The presence of Cl$_2$ could favor the CdTe grain growth by means of a local vapor phase transport. In this way the small grains disappear and the CdS/CdTe interface is reorganized.

5. Processing of Cu(In,Ga)Se$_2$ and CdTe thin films into solar cells

Cu(In,Ga)Se$_2$ and CdTe PV devices are obtained by forming p-n heterojunctions with thin films of CdS. In this type of structure, n-type CdS, which has a band gap of 2.4 eV, not only forms the p-n junction with p-type CuInSe$_2$ or p-type CdTe but also serves as a window layer that lets light through with relatively small absorption. Also, because the carrier density in CdS is much larger than in CuInSe$_2$ or CdTe, the depletion field is entirely in the absorber film where electron-hole pairs are generated (Birkmire and Eser, 1997). After solar cell completion the photovoltaic parameters like I$_{sc}$, V$_{oc}$, FF and conversion efficiency were tested by doing the I-V characterization for the two structures; CdTe and Cu(In,Ga)Se$_2$. All the parameters were measured under AM1.5 illumination.

5.1 Cu(In,Ga)Se$_2$/CdS thin film solar cells

The substrate structure of a Cu(In,Ga)Se$_2$ thin film based solar cell is composed of a soda lime glass substrate, coated with a sputtered ~ 0.7 – 1 µm Mo layer as the back contact. After the thermal co-evaporation of Cu(InGa)Se$_2$ deposition, the junction is formed by chemically bath depositing the CdS with thickness ~ 30 - 50 nm. Then a high-resistance (HR) ZnO layer and a doped high-conductivity ZnO:Al layer are subsequently deposited, usually using the sputtering technique. Finally, the deposition of a current-collecting grid of Ni/Al completes the device as shown in figure 12. The total cell area is defined by removing the layers on top of the Mo outside the cell area by mechanical scribing.
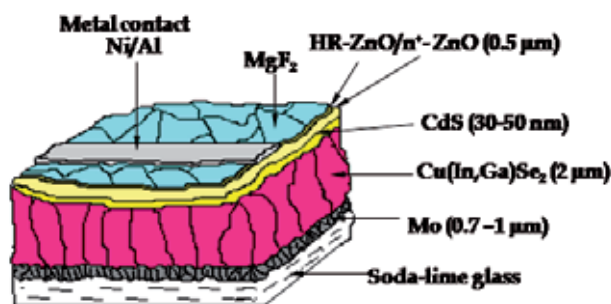
Fig. 12. Schematic configuration of a typical Cu(In,Ga)Se$_2$ thin film solar cell

5.1.1 Discussion on the Cu(In,Ga)Se$_2$ thin film based solar cells results

Two Cu(In,Ga)Se$_2$ samples were used to be processed into solar cell devices: sample JS17 had a CdS layer prepared with a recipe based on CdCl$_2$ and sample JS18 with a recipe based on CdSO$_4$ as the Cd source. The J-V parameters for devices JS17 are: area = 0.47 cm^2, V$_{oc}$ = 536 mV, J$_{sc}$ = 31.70 mA/cm^2, fill factor = 64.0 %, and η = 10.9 % (see figure 13) and for JS18 are: area

= 0.47 cm², V_{oc} = 558 mV, J_{sc} = 29.90 mA/cm², fill factor = 63.1 %, and η = 10.5 % (see figure 14). From these results, we can see that sample JS17 shows a conversion efficiency a little bit higher than JS18, this is due to the different recipe used to prepare the CdS layer as it was mentioned before. This was the only difference between the two devices, everything else was the same. From these figures, a low V_{oc} is observed, but we should expect to have a higher V_{oc} value, compared to the Ga content. The roll-over in forward bias could be indicative of a low sodium content in the Cu(In,Ga)Se₂ films. Also, the low current collection, observed for the Cu(In,Ga)Se₂ thin film devices, may be due to incomplete processing of the absorber layer. Improvements in device performance are expected with optimization of absorber processing.
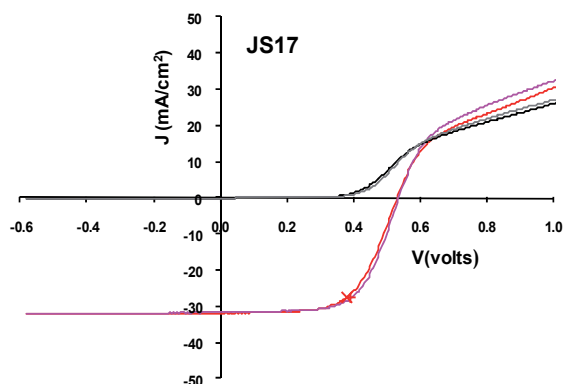
Fig. 13. J-V curves for the best Cu(In,Ga)Se₂ thin film device prepared with a CdS bath solution based on CdCl₂
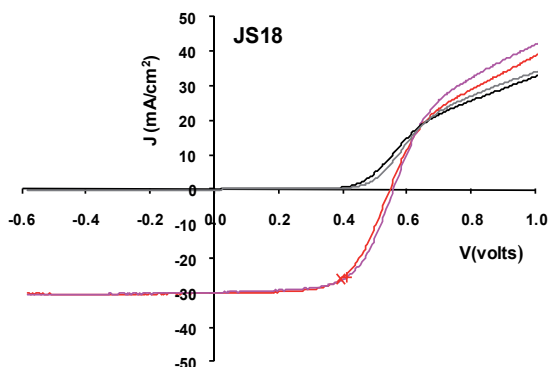
Fig. 14. J-V curves for the best Cu(In,Ga)Se₂ thin film device prepared with a CdS bath solution based on CdSO₄

5.2 CdTe/CdS thin film solar cells

The typical superstrate structure of a hetero-junction CdTe/CdS solar cell is composed of a soda lime glass substrate, coated with a sputtered transparent conducting oxide (TCO) to the visible radiation, which acts as the front contact, then a CdS layer with a thickness ~ 120 nm is chemically bath deposited, followed by the deposition of the absorber CdTe layer by close spaced vapor transport technique and finally the CdS/CdTe device is completed by depositing the ohmic back contact on top of the CdTe layer, see figure 15. For the back contact,

two layers of Cu and Au (2nm and 350 nm, respectively) were evaporated, with an area of 0.08 cm², onto the CdTe and annealed at 180 °C in Ar. The front contact was taken from the conducting glass substrate (0.5 µm thick SnO_2:F/ glass with sheet resistivity of 10 Ω/).
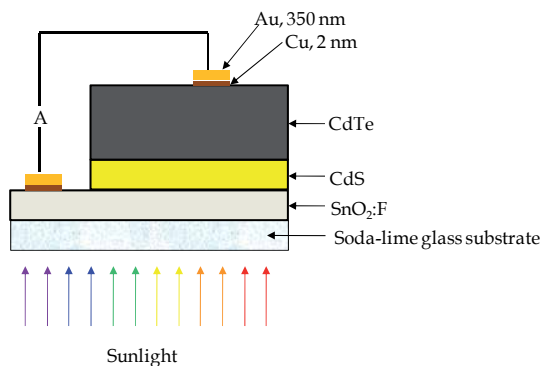
Fig. 15. Schematic configuration of a typical CdTe based solar cell

5.2.1 Variation of the S/Cd ratio in the solution for deposition of CdS by chemical bath and its effect on the efficiency of CdS/CdTe solar cells

The variation of the S/Cd ratio in the solution used in the preparation of the CdS films modifies the morphology, the deposition rate, the crystal grain size, the resistivity and the optical transmittance of these films and have an influence upon the structural and electrical properties of the CdTe layer itself, in addition to modifications of the CdS–CdTe interface. Hence, our study shows the influence of the S/Cd ratio in the solution for CdS thin films prepared by chemical bath upon the characteristics of CdS/CdTe solar cells with a superstrate structure (Vigil-Galán, et al., 2005).

The concentrations of NH_3, NH_4Cl and $CdCl_2$ were kept constant in every experiment, but the thiourea [$CS(NH_2)_2$] concentration was varied in order to obtain different S/Cd relations (R_{tc}) in the solution. All the films were grown on SnO_2:F conducting glasses (10 ohm-cm) at 75 °C. Deposition times were also varied, according to our previous knowledge of the growth kinetics (Vigil O. et al., 2001), with the purpose of obtaining films with similar thickness in all cases. The selected thiourea concentrations and deposition times for each S/Cd relation are shown in table 2.

S/Cd ratio R_{tc}	Thiourea concentration in the bath (mol/l)	Deposition time (min)
1	2.4×10^{-3}	120
2.5	6×10^{-2}	100
5	1.2×10^{-2}	120
10	2.4×10^{-2}	120

Table 2. Thiourea concentration and deposition time for each S/Cd relation

Solar cells were prepared by depositing CdTe thin films on the SnO_2:F/CBD-CdS substrates by CSVT-HW. The atmosphere used during the CdTe was a mixture of Ar and O_2, with an O_2 partial pressure of 50%. In all cases, the total pressure was 0.1 Torr. Prior to deposition the system was pumped to 8×10^{-6} Torr as the base pressure. CSVT-HW deposition of CdTe

was done by placing a CdTe graphite source block in close proximity (1 mm) to the substrate block. The deposition time was 3 min for all the samples deposited with substrate and source temperatures of 550 °C and 650 °C, respectively. Under these conditions, CdTe layers of approximately 3.5 μm were obtained. The CdTe thin films were coated with a 200 nm $CdCl_2$ layer and then annealed at 400 °C for 30 min in air. For the back contact, two layers of Cu and Au (2 nm and 350 nm, respectively) were evaporated, with an area of 0.08 cm^2, on the CdTe film and annealed at 180 °C in Ar. The growth conditions of CdTe were maintained constant for all solar cells.

5.2.2 Discussion on CdTe thin film solar cells results

Figure 16 shows the set of I–V characteristics for CdS/CdTe solar cells made with the same R_{tc} (S/Cd ratio = 5). According to our experimental conditions, the solar cells made with the same technological process have similar characteristics.
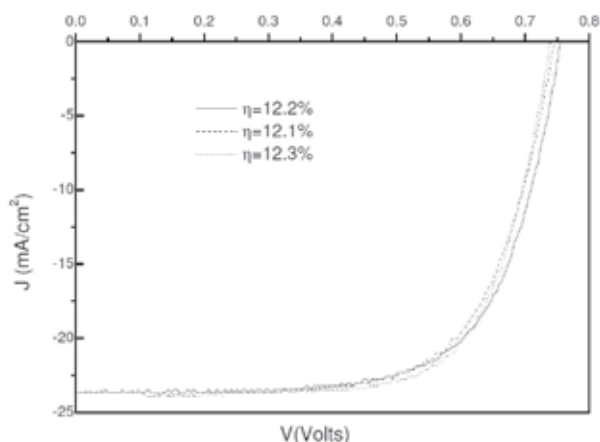
Fig. 16. J –V characteristics of three CdS/CdTe solar cells made with CdS layers grown with R_{tc} = 5 during the CBD-CdS growth process

The I–V characteristics of CdS/CdTe solar cells under AM1.5 illumination (normalized to 100 mW cm^{-2}) as a function of R_{tc} are shown in figure 17. In table 3, the average shunt (R_p) and series (R_s) resistances, the short circuit current density (J_{sc}), the open circuit voltage (V_{oc}), the fill factor (FF) and the efficiency (η) of solar cells prepared with different R_{tc} are reported. The averages were taken from four samples for each R_{tc}. As can be seen in table 3, η increases with R_{tc} up to R_{tc} = 5 and drops for R_{tc} = 10.

S/Cd ratio R_{tc}	R_s (ohm-cm²)	R_p (ohm-cm²)	J_{sc} (mA/cm²)	V_{oc} (mV)	FF (%)	η (%)
1	6.8	318	20.8	617	55.2	7.1
2.5	5.4	800	21.8	690	55.5	8.3
5	2.9	787	23.8	740	70.5	12.3
10	5.9	135	22.7	435	52	5.4

Table 3. Photovoltaic parameter results for CdS/CdTe solar cells with different S/Cd ratio (R_{tc}) in the CdS bath
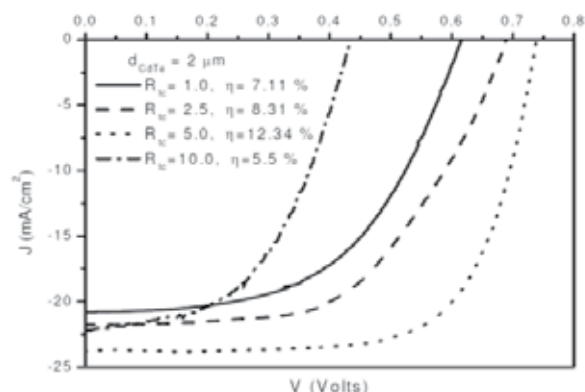
Fig. 17. Typical J–V characteristics of CdS/CdTe solar cells under illumination at 100 mW cm^{-2}, with R_{tc} as a parameter

There are several factors directly or indirectly influencing the cell behaviour, in particular the amount of S in the CBD CdS layers may influence the formation of the CdS$_{1-x}$Te$_x$ ternary compound at the CdS–CdTe interface. CdTe films grown at high temperatures, such as those produced by CSVT, produce a sulfur enriched region due to S diffusion. The amount of S penetrating the bulk of CdTe from the grain boundary must be dictated by the bulk diffusion coefficient of S in CdTe and of course by the amount of S available in the CdS films. The re-crystallization of CdTe could be affected by the morphological properties of the CdS layers grown with different S/Cd ratios. These facts have been studied by Lane (Lane D. W. et al., 2003) and Cousins (Cousins M. A. et al. 2003). From this point of view the formation of CdS$_{1-x}$Te$_x$ may be favored when the R_{tc} is increased in the bath solution. This ternary compound at the interface may cause a lower lattice mismatch between CdS and CdTe, and therefore a lower density of states at the CdTe interface region will be obtained, causing a lower value for the dark saturation current density J_0. The resistivity of the CdS and CdTe layers and their variation under illumination also change the characteristics of the cell under dark and illumination conditions. In other words, a better photoconductivity implies smaller resistivity values under illumination, with the possible improvement of the solar cell properties. In addition, optical transmittance, thickness and morphological measurements of the CBD-CdS films showed the following characteristics when increasing R_{tc}: i) band gap values are observed to increase (from 2.45 eV to 2.52 eV when changing R_{tc} from 1 to 10), ii) grain sizes become smaller (from 55.4 nm to 47.2 nm when S/Cd = 1 and 10, respectively) and iii) the average optical transmission above threshold increases from 68% to 72% when R_{tc} is increased from 1 to 10. Higher band-gap values of the window material improve the short circuit current density of the solar cells. Thin films with smaller grain sizes show fewer pinholes with a positive effect on the open circuit voltage and fill factor. In this regard, the properties of the CdS layers are correlated with the kinetic of the deposition process when the concentration of thiourea is changed. For instance, for high thiourea concentration, the reaction rate becomes large enough to promote a quick CdS precipitation which leads to the formation of agglomerates in the solution rather than nucleation on the substrate surface, while for low thiourea concentration a very slow growth process can be expected, leading to a thinner but more homogeneous layer.

6. Conclusions

We have found that CBD-CdS thin films grown under different conditions, like monolayers or bi-layers, using a standard bath configuration or a modified configuration, the principle for the deposition process is the same: a common precipitation reaction. Depending of the regime we decide to choose, we must perform an optimization of the deposition parameters in order to get the CdS film with the best physical and chemical properties. The quality of the CdS window partner and the absorber material like CdTe and Cu(In,Ga)Se$_2$ will have a great impact on the conversion efficiencies when applied into thin film solar cells.

7. Acknowledgements

8. References

Birkmire R. and Eser E. (1997), Annu. Rev. Mater. Sci., 27:625–53.

Boyd D, Thompson D, Kirk-Othmer, (1980), Encyclopaedia of Chemical Technology, Vol. 11, 3rd Edition, 807–880, John Wiley.

Contreras-Puente G., Tufino-Velazquez M., Calixto M. Estela, Jimenez-Escamilla M., Vigil-Galan O., Arias-Carbajal A., Morales-Acevedo A., Aguilar-Hernandez J., Sastre-Hernandez J., Arellano-Guerrero F.N. (2006), Photovoltaic Energy Conversion, Conference Record of the 2006 IEEE 4th World Conference.

Cousins M. A., Lane D. W., and Rogers K. D. (2003). *Thin Solid Films* 431–432, 78.

Lane D. W., Painter J. D., Cousins M. A., Conibeer G. L., and Rogers K. D. (2003). Thin Solid Films 431–432, 73.

McCandless Brian E. and Sites James R., (2003), Cadmium Telluride Solar Cells, in: Handbook of Photovoltaic Science and Engineering, Luque A. and Hegedus S., pp. 567 – 616, John Wiley & Sons, Ltd ISBN: 0-471-49196-9, West Sussex, England.

Mitchell K. et al., (1990), IEEE Trans. Electron. Devices 37, 410–417.

Morales-Acevedo A. (2006). Solar Energy 80, 675.

Repins I. et al., (2008), Prog. in Photov: Research and Applications 16, 235.

Rocheleau R, Meakin J, Birkmire R, (1987), Proc. 19th IEEE Photovoltaic Specialist Conf., 972–976.

Romeo N., Bosio A., Canevari V. and Podestà A. (2004), Solar Energy, Volume 77, Issue 6, Pages 795-801.

Shafarman W. N. and Stolt L. (2003), Cu(InGa)Se2 Solar Cells, in: Handbook of Photovoltaic Science and Engineering, Luque A. and Hegedus S., pp. 567 – 616, John Wiley & Sons, Ltd ISBN: 0-471-49196-9, West Sussex, England.

Schon, J. H., Schenker, O. and Batlogg, B. (2001), Thin Solid Films 385, p.271.

Vigil-Galan O., Arias-Carbajal A., Mendoza-Perez R., Santana-Rodríguez G., Sastre-Hernandez J., Alonso J. C., Moreno-Garcia E., Contreras-Puente G. and Morales-Acevedo A. (2005), Semiconductor Science and Technology 20, 819.

Vigil O., Arias-Carbajal A., Cruz F., Contreras-Puente G., and Zelaya-Angel O. (2001). Mats. Res. Bull. 36, 521.

Wu X. et al., (2001), Proc. 17th European Photovoltaic Solar Energy Conf. 995.

Innovative Elastic Thin-Film Solar Cell Structures

Maciej Sibiński and Katarzyna Znajdek
Technical University of Łódź, Department of
Semiconductor and Optoelectronic Devices,
Poland

1. Introduction

The idea of thin films dates back to the inception of photovoltaics in the early sixties. It is an idea based on achieving truly low-cost photovoltaics appropriate for mass production, where usage of inexpensive active materials is essential. Since the photovoltaic (PV) modules deliver relatively little electric power in comparison with combustion-based energy sources, solar cells must be cheap to produce energy that can be competitive. Thin films are considered to be the answer to that low-cost requirement [1].

Replacement of single crystalline silicon with poly and amorphous films, caused the decline of material requirements, which has led to lower final prices [2]. Furthermore, the thickness of cell layers was reduced several times throughout the usage of materials with higher optical absorption coefficients. Unique, thin film and lightweight, devices of low manufacturing costs and high flexibility, were obtained by applying special materials and production techniques, e.g. CIS, CIGS or CdTe/CdS technologies and organic elements. Taking advantage of those properties, there is a great potential of new, useful applications, such as building integrated photovoltaics (BIPV), portable elastic systems or clothing and smart textiles as well [3].

Low material utilization, mass production and integrated module fabrication are basic advantages of thin film solar cells over their monocrystalline counterparts [4]. Figure 1 (by NREL) shows the development of thin film photovoltaic cells since 1975.

The development of cadmium telluride (CdTe) based thin film solar cells started in 1972 with 6% efficient CdS/CdTe [5] to reach the present peak efficiency of 16.5% obtained by NREL researchers in 2002 [6]. Chalcopyrite based laboratory cells (CIS, CIGS) have recently achieved a record efficiency of 20% [7], which is the highest among thin film PV cells (see Table 1). Solar modules based on chalcopyrites, uniquely combines advantages of thin film technology with the efficiency and stability of conventional crystalline silicon cells [4].

Thin film solar cell type	**CIGS**	**CdTe/CdS**	**a-Si**
Cell area [cm^2]	0.5	1.0	0.25
Highest efficiency [%]	20.0	16.5	13.3
Typical efficiency range [%]	12.0 – 20.0	10.0 – 16.5	8.0 – 13.3

Table 1. Efficiencies of CIGS, CdTe and a-Si thin film solar cells [8].
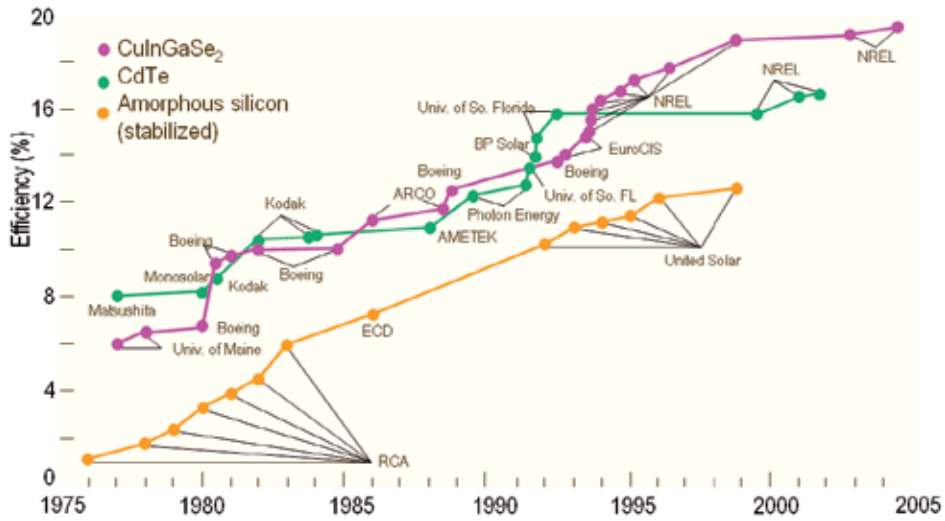
Fig. 1. Best laboratory PV cell efficiencies for thin films [source: www.nrel.gov]

To comprehend the developmental issues of thin films, it is important to examine each individually. Each has a unique set of advantages and shortcomings in terms of their potential to reach the needed performance, reliability and cost goals [1].

1.1 CdTe cells and modules

Cadmium telluride based solar cells are one of the most promising in thin film photovoltaics. With a bandgap of 1.45 eV the material well suited to match the AM 1.5 solar spectrum. Furthermore, its high absorption coefficient causes that only a few microns absorber film is required for solar cell operation. The typical thin film CdTe/CdS structure is shown on Figure 2. Figure 3 presents the total life-cycle Cd emissions to prove that CdTe based PV cell are environment friendly and health safe.
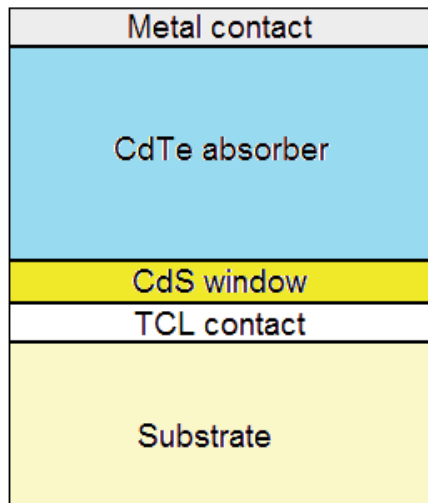
Fig. 2. Typical structure of CdTe thin film solar cell.
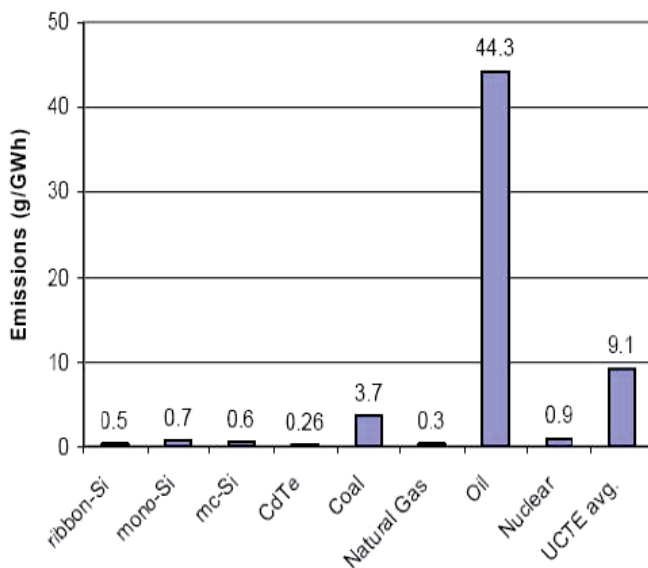
Fig. 3. Total life-cycle Cd emissions by Brookhaven National Laboratory [9].

Low-cost soda-lime glass, foil or polymer film can be used as the substrate of CdTe/CdS solar cell. The best results of 16.5% efficiency are achieved with glass substrate (Table 1). However, Laboratory for Thin Films and Photovoltaics at EMPA, Switzerland obtained 12.7% efficiency of single CdTe solar cell on polymer foil and 7.5% of monolithically interconnected flexible CdTe solar module of 32 cm² total area [10]. Transparent conductive layers (TCL) are usually thin conductive metal oxides, such as ITO (*Indium Tin Oxide*), Zn_2O_4, Cd_2SnO_4, ZnO:Al, CdO, ZnO, In_2O_3, SnO_2 or $RuSiO_4$. However, lastly in flexible solar cells, transparent conductive oxides (TCO) are being replaced by carbon nanotube (CNT) composites [11] or graphene. The CdS film is grown either by chemical bath deposition (CBD), close space sublimation (CSS), chemical vapor deposition (CVD), sputtering or vapor transport deposition (VTD). For the growth of CdTe, three leading methods are used for module fabrication: CSS, electro-deposition (ED) and VTD. Wide variety of metals can be used as back contact for thin film CdTe solar cells, e.g. Cu, Au, Cu/Au, Ni, Ni/Al, Sb/Al, Sb/Au [12].

Several thin-film PV companies are actively involved in commercializing thin-film PV technologies. In the area of CdTe technology major players are or were in the past: First Solar (USA), Primestar Solar (USA), BP Solar (USA), Antec Solar (Germany), Calyxo (Germany), CTF Solar (Germany), Arendi (Italy), Abound Solar (USA), Matsushita Battery (Japan) [8, 12, 13]. This effort lead to 18% share of CdTe cells in global PV marked in 2009 [14].

1.2 CIS/ CIGS/ CIGSS structures

Other promising material for thin film solar cell absorber layer is copper indium diselenide $CuInSe_2$. CIS has a direct bandgap of 0.95 eV which can be increased by the addition of gallium to the absorber film. About 30% of Ga added to CIS layer (CIGS cell), changes the bandgap from 0.95 eV to almost 1.2 eV, which improves its match with the AM 1.5 solar spectrum. Higher gallium content (of 40%) has a detrimental effect on the device performance, because of its negative impact on the charge transport properties. The best

gallium to indium ratio is 3:7 for high efficiency PV devices. The role of sulfur in CIGSS is to increase the bandgap of the absorber film [12], which can boost the AM 1.5 spectrum fitting even more. The typical thin film CIGS solar cell structure is shown on Figure 4. Figure 5 presents an example CIGS cell structure manufactured in the Laboratory for Thin Films and Photovoltaics at EMPA, Switzerland.
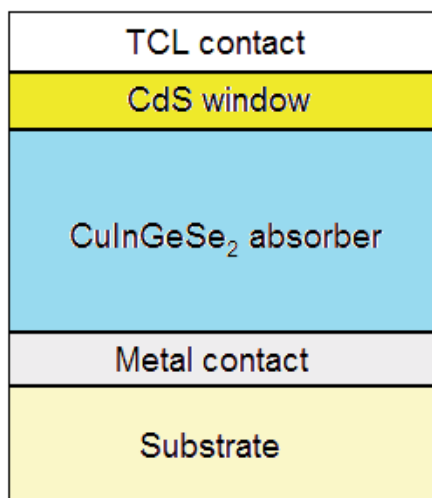
Fig. 4. Typical structure of CIGS thin film solar cell.
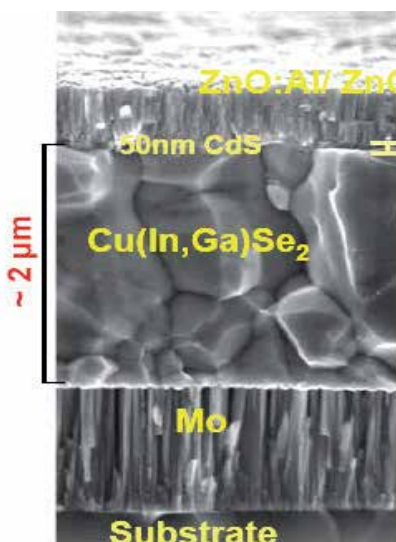
Fig. 5. CIGS cell structure manufactured at EMPA, Switzerland [8].

Worldwide, several companies are presently offering commercial thin-film PV CIGS products: Würth Solar, (Germany), Global Solar, (USA), Honda, (Japan), Showa Shell, (Japan), Sulfurcell, (Germany), Solibro (Germany), Avancis (Germany), Solyndra (USA), Centrotherm (Germany). Also, worldwide, about 34 companies are actively developing thin-

film CIGS PV technologies. These companies are using different deposition methods for growing the thin CIGS absorber layers, as is shown in Table 2 [13].

Company	Substrate	Back contact	Process	Front contact
Shell Solar	Glass	Mo	Sputter/ Selenization	ZnO
Global Solar	Steel	Mo	Co-evaporation	ITO
Miasole	Glass	Mo	Sputter	ZnO
Wurt Solar	Glass	Mo	Co-evaporation	ZnO
Avancis	Glass	Mo	Sputter/ RTP	ZnO
Daystar Tech.	Glass	Mo	Sputter	ZnO
EPV	Glass	Mo	Sputter/ Evaporation	ZnO
Ascent Solar	Polymer	Mo	Co-evaporation	ZnO
ISET	Glass/Flexible	Mo	Ink/ Selenization	ZnO
Nanosolar	Flexible	Mo	Print/ RTP	ZnO
Solo Power	Steel	Mo	ED/ RTP	ZnO

Table 2. Thin film CIGS technology.

The absorber layer for commercial products uses either co-evaporation or the two-stage process such as the deposition of the precursors (Cu, Ga, In) by sputtering followed by selenization. Absorber layer can be made out of three chalcopyrite chemical compounds: $Cu(In,Ga)Se_2$, $Cu(In,Ga)(S,Se)_2$, $CuInS_2$ which are respectively CIGS, CIGSS and CIS.

As a back, metal contact Mo deposited by sputtering is most commonly used. Majority of companies (Table 2) use ZnO as the front transparent conductive layer. Zinc oxide is deposited either by sputtering or chemical vapor deposition [13]. Window layer of CdS (or alternatives, such as ZnS [8]) can be grown by analogous methods as in CdTe solar structure (CBD, CSS, CVD etc.).

As a substrate of thin film CIGS solar cell, either glass, metal (steel) sheet or polymer might be chosen. Highest efficiencies, as noted in Table 1, were achieved for modules on glass substrate. However, such solution have several inconveniences, which are for example: bulkiness, fragility and heaviness. Flexible substrates, on the other hand, offer both manufacturing and application related advantages, such as: large active area, roll-to-roll high speed (throughput) deposition, high material utilization, low thermal budget, monolithic interconnection, lower costs, light-weight and flexibility. Table 3 presents the comparison of thin film CIGS solar cell on steel and polymer substrate.

To conclude this subsection, we should ask a question: "why thin film CIGS and CdTe solar cells are worth attention?". The answer was given and it can be summarized in several points:

1. they are highly efficient,
2. active layers can be deposited on various substrates including flexible ones,
3. they have extremely stable performance,
4. they cause no environmental or health hazards,
5. they are low cost,
6. these cells are attractive for both terrestrial and space applications [8].
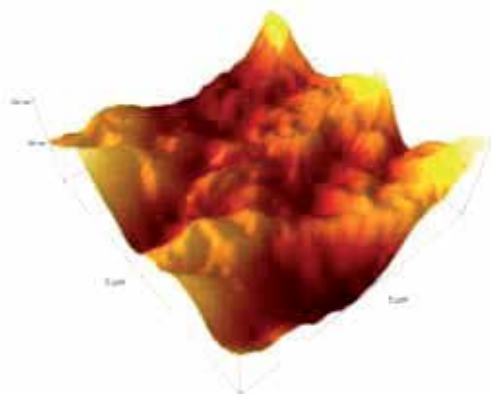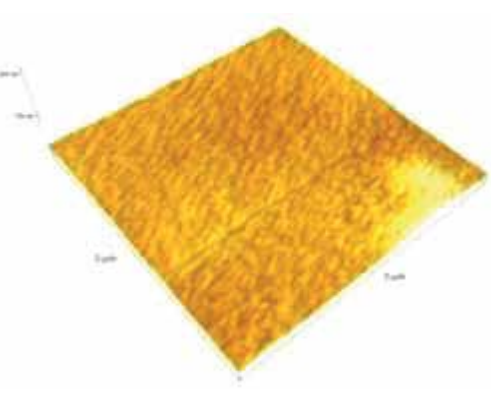
Metal (steel)	Polymer
Rough surface, kinks	Smooth surface
Conducting surface	Insulating surface
Metal impurities	No metal impurities
Barrier coatings needed for monolithic interconnection	No need of barrier coatings for monolithic interconnection
High temperature: 550- 650 °C	Low temperature: 450 °C
Highest efficiency: 18% on Ti foil	Highest efficiency: 16%

Table 3. Substrates for flexible CIGS solar modules [8].

Thin-film photovoltaic cells and modules are already widely popularized, mainly because of their small production costs and relatively high efficiency [15]. Moreover, some other, significant advantages, such as small weight and flexibility may be offered. That is the reason why large number of applications is being pursued using thin-film PV technologies, including building-integrated photovoltaics (BIPV), roof-top applications and utility-scale applications [13].

2. Manufacturing technologies of elastic thin – film CdS/CdTe solar cells

Cadmium telluride solar cells are placed among thin-film polycrystalline structures of high optical absorption and relatively low material consumption, with long development history [16]. Numerous virtues of each semiconductor compound as well as good cooperation within p-n heterojunction give the opportunity of efficient and cheap monolithic solar modules construction. Additionally, elastic structure of polycrystalline layers enables the flexibility of the manufactured modules and gives possibility of new implementations. The experiments leading to this goal were undertaken by various manufacturing technologies, however to maintain high optoelectronic parameters of the manufactured cells, independently on employed technology, proper polycrystalline structure must be preserved.

Standard technology of CdTe solar cells manufacturing is based of column grain structure. This specific material organization occurs owing to vertical growth of hexagonal CdTe and CdS grains and gives the opportunity of high optical generation, smooth vertical charge carrier transport and thus high conversion efficiency. Both semiconductors are predestined
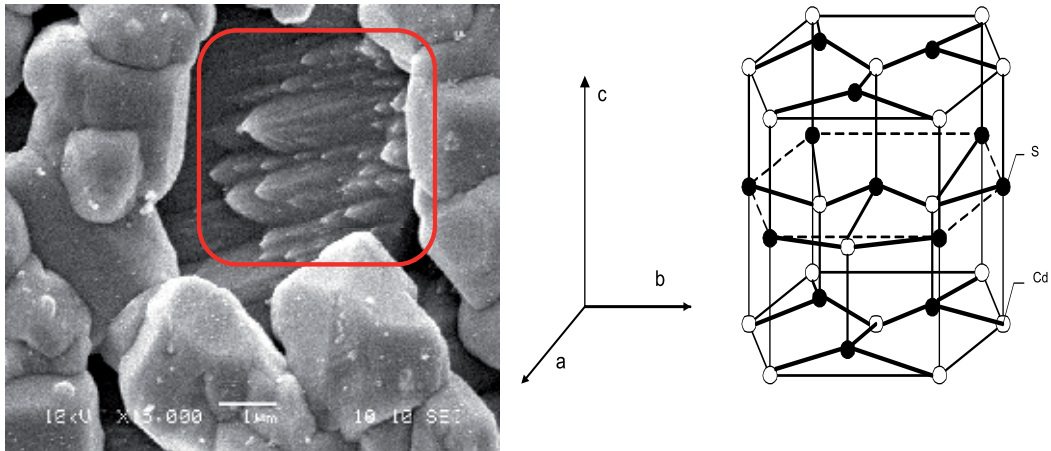
Fig. 6. SEM picture and the diagram of CdS wurtzite grains with vertical growth orientation and CdS hexagonal grain model.

to achieving of this structure under some technology circumstances [17] and may be matched with crystal constant differences not higher than 9,7% [18]. Structure of model CdS layer, obtained by authors, organized in wurtzite phase is presented in Figure 6.

The most popular manufacturing technologies of CdS/CdTe solar cells are nowadays CVD *(Chemical Vapour Deposition)* and the variants like PECVD (*ang: Plasma Enhanced CVD, or* MOCVD (*Metall Organic Chemical Vapour Deposition*) [19],CBD (*Chemical Bath Deposition) and physical methods like* PVD (*Physical Vapour Deposition*), CSS (*Close Space Sublimation*) [20], and variants of CSVT (*Close Space Vapour Transport*) [21, 22]. Alternatively screen-printing technology was also successfully employed for production of relatively thick CdTe base [23]. Morphology of the last mentioned layers was verified by authors with the help of SEM analysis indicating dense compact structure of hexagonal grains (Figure 7).
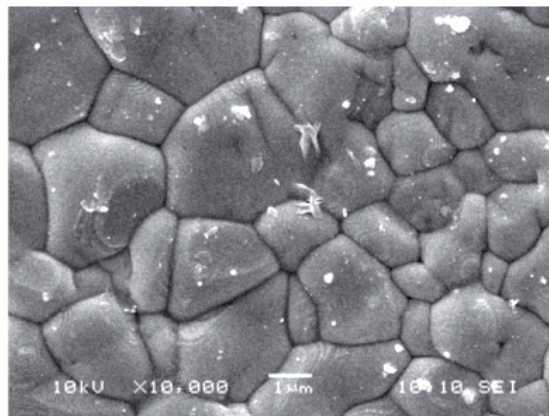
Fig. 7. SEM picture of dense, compact CdTe grain layer up to 8µm, manufactured by ICSVT technology on glass substrate.

As the additional experiments AFM profile of this layer, presented in Figure 8 was prepared.
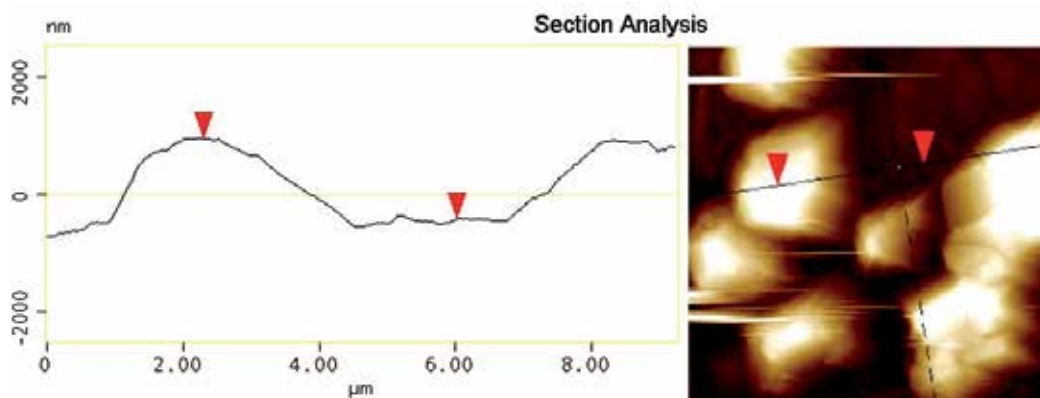
Fig. 8. AFM profiling of CdTe polycrystalline layer, made by ICSVT technology.

This measurement gives some important information about grains structure and inter-crystal surfaces. By means of polycrystalline CdS/CdTe layers profiling one may easily detect the diameter and grain shape but also the inter-grain valleys depth and possible structure fluctuations and layer discontinuities. These structure disorders may result in serious parameter losses by producing of shunt interconnections or other charge flow parasitic effects. Taking into account cadmium dichloride dissolvent presence, frequently caused by recrystallization demands morphology defects may cause a real and serious threat for CdS/CdTe structure functioning. No such phenomenon was confirmed by presented results.

All new production techniques of thin –film polycrystalline solar cells and particularly CdS/CdTe structure, designed for new application field, should be verified according to obtained layers profile to eliminate structure disorder. Since AFM spectroscopy gives the profiling results for some strictly limited area for wider statistical examination mechanical profiling of high accuracy may be applied. These experiments were also conducted for test CdS/CdTe structure. The experiment for each sample was conducted by the help of mechanical profilometer Dektak 3 VEECO Instruments. The measurements were performed for representative 100 μm scan range with 50nm resolution.

As the first analysis ICSVT CdTe layer morphology was checked (Figure 9). By this investigation the average grain diameter of 6-8μm was confirmed and the typical roughness of 1200 A. Series of measurements confirmed dense, compact structure of absorber grains with no interlayer shunts. Obtained average roughness and the CdTe grain surface profile suggests that inter-grain trenches are insufficient for significant degradation of shunt resistance value. The total layer level fluctuations are smaller than 4 μm, which taking into consideration typical glass thickness accuracy confirms homogenous thickness of the whole base layer.

Alternative technology, used for CdS/CdTe cell layers deposition is a standard PVD method. Under some circumstances it offers a possibility of semiconductor material deposition even on profiled, elastic and untypical substrates. Evaporation of examined materials caused serious technology problems connected with proper thickness of obtained layers and homogeneous structure of deposited material. Some serious parasitic effect like boiling, splitting and granulation of the material were solved by proper temperature profile and optimized one-directional tantalum evaporation source adopted by authors [24].
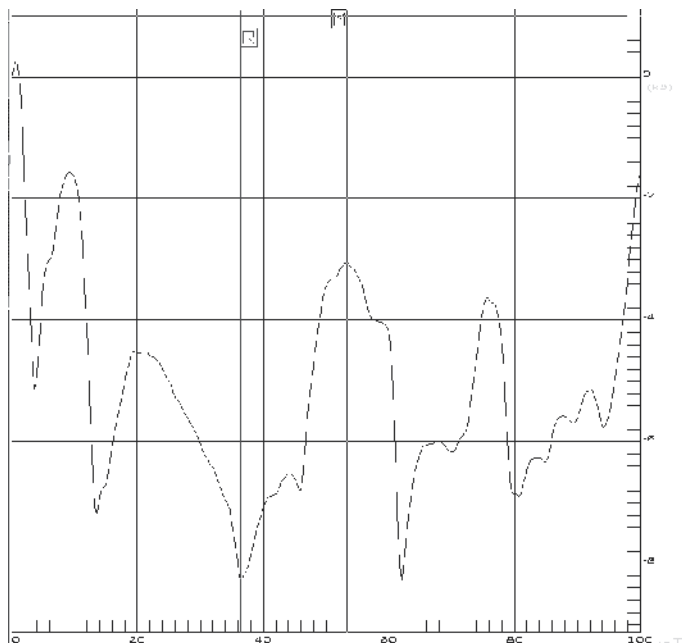
Fig. 9. Morphology of CdTe solar cell base absorber manufactured by ICSVT technology on glass substrate.

The investigation of CdTe base manufactured by evaporation and subsequent recrystallization is presented in Figure 10.
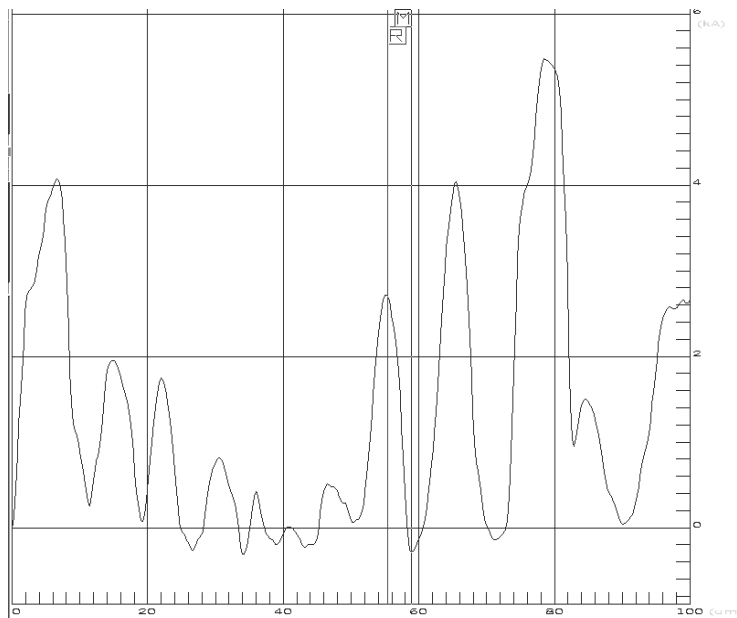
Fig. 10. Morphology of CdTe solar cell base absorber manufactured by evaporation and subsequent high-temp. recrystallization.

The measurements indicated homogenous grains of the average dimension 2-4μm. Typical roughness of 1230 μm is similar layers obtained by ICSVT, however one may observe higher peak values of grain top-trench profile. This may result in some interlayer parasitic connections. Additionally in this case, total layer thickness fluctuation is similar to the layer thickness (±2 μm), what may cause some absorber discontinuities.

Third investigated technology (Figure 11) is based on adaptation of screen-printing technique for semiconductor layers manufacturing. Printing paste is produced by milling of cadmium and tellurium in stochiometric proportion and mixing with special binder. After printing, leveling and drying process CdTe layer is recrystallized in high-temperature process similarly to the previously described way.
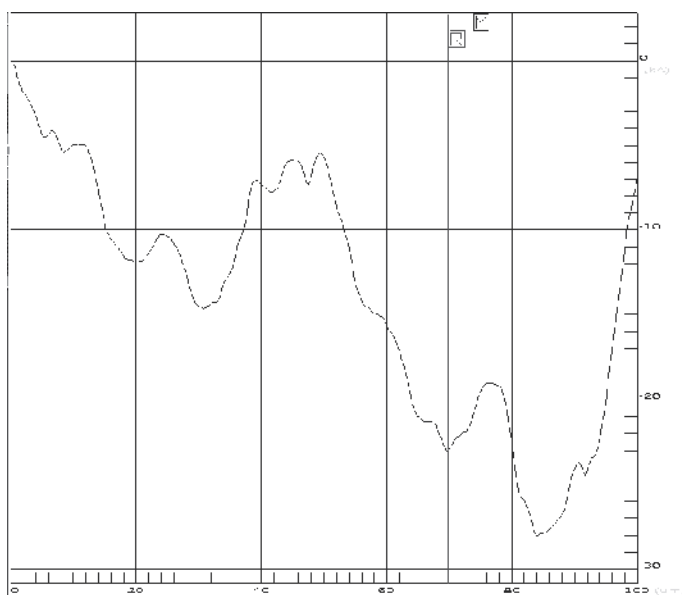
Fig. 11. Morphology of CdTe solar cell base absorber manufactured by screen-printing and subsequent high-temp. recrystalization.

Profilometry of screen-printed base (Figure 11) indicated very high thickness of investigated layer (even up to 20 μm), but also serious morphology defects. Typical roughness of obtained layers is beyond 3000μm, which exceeds 240% of average value for ICSVT and PVD techniques. Moreover obtained grains present different diameters from 1-2 μm up to 10 μm. Total layer thickness also varies strongly (locally up to 50%), which results in various optoelectronic parameters. Layers produced by screen-printing technology presents additionally high porosity, which prevents cadmium dichloride from volatilization and causes fast base oxidation and thus cell parameters degradation.

Considering the results obtained for three technologies aimed at manufacturing of CdS/CdTe solar structure on novel substrate material conclusion of their applicability and further development may be drawn.

ICSVT being the most complicated and so-far not commercialized method appeared to be the most efficient in creation of the proper polycrystalline base structure. The morphology of obtained layers confirms proper column grain structure of hexagonal CdTe crystals and thus high electrical parameters of final solar cell. Taking this into consideration further

development of this technique is desired in terms of non-flat architectonic elements as the solar cell substrate. First steps towards this goal have been undertaken.

Evaporation and post annealing of CdTe material in order to formation of proper base structure appeared to be less efficient. However simple and effective for various substrates technique leads to thin film base production only. Moreover the diameters of single grains obtained by the author are significantly lower than by ICSVT technology.

Screen – printing and sintering as the last investigated method appeared to be insufficient for the stabile cell-base production. The advantage of high layer thickness is seriously diminished by poor homogeneity, thickness instability and high surface porosity. Nevertheless screen printed layers can be effectively used as the in-production material for ICSVT or similar processes.

3. Innovative polycrystalline elastic structures, based on polymer substrates

Although CdS/CdTe cells have now entered the mass - production phase, but still there are many possibilities of their new applications fields. Basing on this idea, authors proposed the implementation of modified CdS/CdTe cell structure in universal, attractive application called BIPV (Building Integrated Photovoltaics) and also elaborated elastic cell structure [25]. The CdTe cell construction gives the opportunity of achieving these goals, under the conditions of the proper technology modifications, as well as proper substrate and contacts implementation. Due to successful application of CSS variants of CdS/CdTe manufacturing technology for effective solar cells production, further experiments towards new cell structure and properties became possible. Considering cell composition, two opposite configuration of CdTe cell became possible. Historically first one is a classical substrate configuration (Figure 12 a), whereas based on glass + ITO, emitter-based configuration is called superstrate (Figure 12 b).
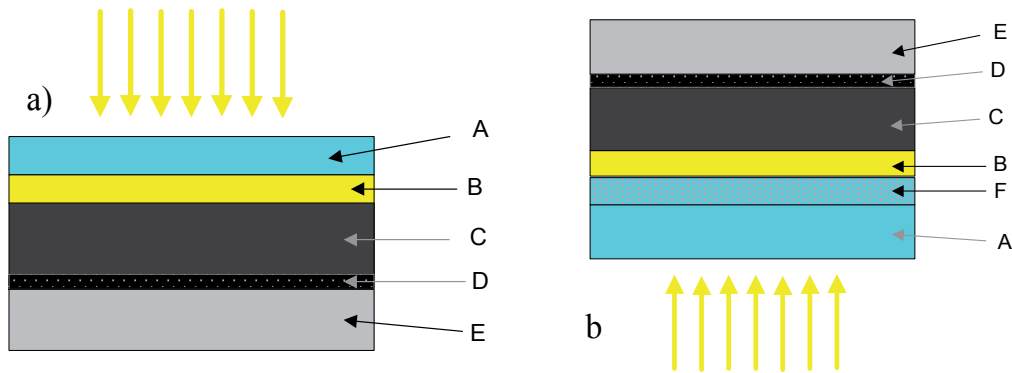
Fig. 12. Substrate a) and superstrate b) configuration of CdS/CdTe solar cell. A- glass cover, B- CdS emitter, C-CdTe base, D – base P+ sub layer, E-back contact, F-TCO layer, emitter metal contacts not visible.

Both of them possess some important advantages and technology drawbacks. Substrate configuration offers more mature manufacturing technology and lower substrate demands, while superstrate configuration ensures higher efficiencies (smaller surface shadowing) and better encapsulation. Adaptation of the described technology for new application and cell construction, demands deep consideration of all possible solutions.

Every introduced concept posses some value according to different aspects of BIPV applications and each is subsequently investigated by Technical University of Łódz research group. Ceramic substrates could be recognized as the best platform for the complete integration of the photovoltaic element with the architectonic component. One may find the reports on practical investigation of this construction for other thin –film solar cells e.g. CIS devices [26]. However, for CdS/CdTe construction, there is still research and technology adaptation needed. Additionally this kind of application is strictly connected with one particular architectonic element type such as roof-tile or brick. Moreover it has to provide the complete modular interconnection and regulation system, since the whole installation is made of hundreds of elements, working in different conditions. Furthermore, different interconnection systems (series, parallel and series-parallel) are necessary for optimum power and load polarization. Finally, standard ICSVT/CSS technology needs some fundamental modifications, in case of implementation in profiled architectonic elements (roof tiles or ornaments), since the material transport occurs only between very closely positioned source and target.

Taking into account cadmium telluride solar cells, possessing flexible construction two base materials may be considered. One is thin metal foil, while the second is the polymer material. Implementation of metal foils, for example Mo substrates, for CdTe construction has been already investigated and reported [27]. In this work we focus on polymer foil implementation as the elastic solar cell substrate. Flexibility of this material, combined with policrystalline thin-film structure properties, gives a promise that manufacturing of elastic solar panel, ready for integration with any shape architectonic substrate is possible. Moreover, it offers the opportunity of constructing both substrate and superstrate configuration of CdS/CdTe cell. Additionally, polymer foils are lightweight, high-durable materials, which enhances the possible application field of cells. Depending on the configuration, production technology and desired application different properties of the substrate foils will be demanded. Finding proper foil material and appropriate technology adaptation are the key to obtain efficient elastic PV cells.

To define the properties of polymer base foils, one may consider the specific of each configuration. So far, in the superstrate configuration highest conversion efficiencies were obtained However, in this case, polymer substrates must meet several conditions. One can mention as the most important: high optical transparency in the full conversion range of CdS/CdTe cell, ability of TCO surface electrode covering, high thermal durability, high chemical and water resistance. Apart from these specific demands, substrate foil of any configuration is expected to be light-weight, have high elongation coefficient, thermal expansion similar to semiconductor polycrystalline layers (CdS and CdTe) and be low cost. In both cases elastic cells can be easily attached to different shape architectonic elements.

Taking this into account, also substrate configuration of elastic cadmium telluride cell was investigated. As the preliminary step possible polymer material options were verified. Polymers, as the materials, are constructed on a base of multi-modular chains of single, repetitive units called monomers. In the manmade polymers, even the number of a few thousand monomer types is being achieved. The properties of manufactured polymer material depend strongly, not only on its chemical content and even monomer construction, but also on the monomers interconnecting system. Due to complexity of the typical polymer construction, it is impossible to evaluate the physical properties of these materials using theoretical analysis. This gave the prompt to the series of experiments, aimed at

comprehensive evaluation of polymer foils physical parameters, potentially efficient as the CdS/CdTe cell substrate materials.

As the test group of polymer foils wide set of materials, including standard commercial solutions as well as high – temperature polyester and polyamide, was accepted. Among polyamide foils of high thermal durability, two materials - KAPTON® and UPILEX® foils were chosen. Both of them are commercially available high-technology materials implemented in specific applications (eg: space shuttles wings and nose cover, high power loudspeakers membranes). They are characterized by high mechanical and thermal durability, high dielectric constant and UV durability. Among the polyester materials high – temperature MYLAR® material was adopted. As the reference material, popular PET foil in standard and high - temperature production version was applied. First evaluation step of material properties is a verification of their mechanical parameters. Comparison of these results is presented in Table 2.

Parameter\Foil	PET/High temp PET	UPILEX®	MYLAR®	KAPTON® HN 100
Thickness [μm]	25.0	30.0	30.0	25.4
Weight [g/m²]	30.0	44.1	41.7	35.0
Surface mass coefficient [m²/kg]	31.2	22.7	23.98	27.9
Thermal expansion [%/ 1°C]	0.025	0.018	0.007	0.005
Standard elongation (25 °C) [%]	600.0	54.0	103.5	40.0

Table 2. Main mechanical parameters of tested polymer foils.

Obtained parameters suggest similar properties of all investigated materials. However, some important differences are evident. The most important is the value of the thermal expansion coefficient (TEC). In general, one may say that in the case of high-temperature materials the value of thermal expansion is lower. Exceptionally, in the case of UPILEX® the value of this parameter is close to standard PET foil. According to considered configuration, thermal expansion coefficient of substrate foil should be adjusted to the value of the semiconductor base or emitter and contact layer. In both cases of semiconductor materials (CdS, CdTe), the value of TEC is very low (at the level of $5 \cdot 10^{-4}$ [% / °C]), but the most typical metal contacts present TEC value higher by the order of magnitude.

The critical parameter in the standard re-crystallization process, as well as in the ICSVT, is a thermal durability of layer material. The maximum values of declared operational temperature for each investigated foil are: 130°C for Standard PET, 185°C for High-temp PET, 254°C for Polyester MYLAR®, 380°C and 430°C for Polyamide KAPTON® foil. Basing on the declared temperatures and considering the ICSVT temperature demands, two most durable foils were accepted for further investigations. As the subsequent step the weight loss of KAPTON® and UPILEX® in higher temperatures was measured. The measurements of thermal durability were performed in the temperature range of a standard re-

crystallization process (450ºC - 650ºC). During the experiment, the percentage loss of the foil weight was measured. Additionally, plastic properties were tested as the indicator of usefulness for the elastic substrate application. For higher accuracy of obtained outcomes, as the additional test, the plastic properties of the materials for each temperature were estimated. Complete results of this test are presented in Table 3. Grey color of the table cell marks a permanent deformation or loss of elastic properties.

Weight in temperature:	UPILEX®		KAPTON®	
	12.5μm	25.0μm	12.5μm	25.0μm
480ºC	91.82%	95.16%	96.70%	95.30%
500ºC	91.36%	94.84%	96.00%	94.60%
550ºC	89.55%	92.26%	74.70%	81.12%
600ºC	70.00%	78.38%	Burnt	Burnt

Table 3. Temperature durability of examined foils. Dark-grey color indicates the loss of elastic properties or permanent deformation.

Analyzing obtained results, one may state that in the opposite to the manufacturer suggestions, the biggest weight loss in temperatures above 500ºC, is observed in polyamide KAPTON®. Additionally, the loss of its elastic parameters occurs very rapidly. Contrary, UPILEX®, which melting point is declared below 400ºC proved to be fairly resistant to temperatures until 550ºC. In both cases thicker foils reacted slower for the temperature rise, which was expected due to their relatively high thermal resistance. It is worth mentioning that the experiment was conducted in conditions (time, equipment) similar to the manufacturing process. However, identified maximal allowable temperature is relatively lower than standard demanded temperature for ICSVT process. There were reasonable presumptions suggesting the possibility of re-crystallization temperature decreasing, in favor of longer process duration. Thus, examined foils were conditionally positively evaluated. Taking this into account, UPILEX® foil was accepted for further experiments, leading to manufacturing of the CdS/CdTe elastic layers. Considering possible configuration of designed cell, the light transparency characteristic of investigated foil was measured. The light transmission in the conversion range of CdS/CdTe cell both of KAPTON® and UPILEX® foils is presented in Figure 13.

Due to low transmission (below 60%) in the range 400 nm – 700 nm, which would decrease largely the total cell efficiency, for UPILEX®, substrate cell configuration was chosen. Basing on presented results, experimental sample of CdTe absorber, manufactured on 25 μm UPILEX® foil was prepared. Obtained semiconductor layer is based on Cu contact of 2 μm thick, made by PVD in pressure 5·105 Torr. The total area of the sample is 30 cm² and elastic properties of all manufactured layers are preserved (Figure 14). After the investigation, the average thickness of 2 μm and good uniformity of manufactured layer was confirmed. This makes proper base for CdS layer manufacturing and completing of the elastic CdS/CdTe construction.

Obtained results confirm the assumption that flexibility of polycrystalline cadmium compound layers may be employed in alternative applications, such as elastic cell structure. Finding the proper material for substrate of these devices is a key to manufacturing of efficient cell, however it demands considering of many technological aspects. Thermal and
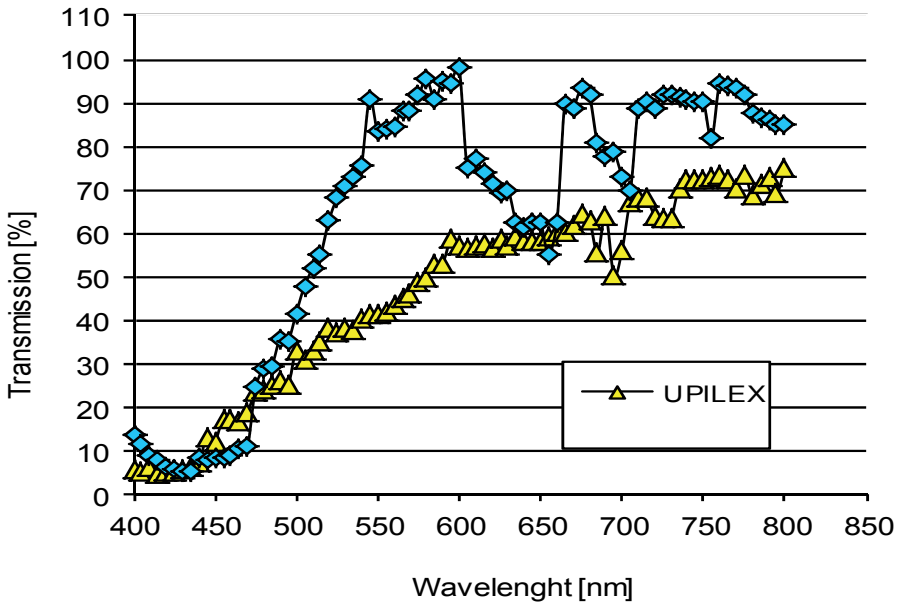
Fig. 13. Optical transparency of KAPTON® and UPILEX® foils in the wavelength range of CdS/CdTe cell effective photoconversion.

Fig. 14. Test structure of elastic CdTe layer based on UPILEX® foil and contacted by 2 μm Cu layer.

mechanical properties of some high-temperature polymer foils give the possibility to construct complete solar cell with some technological modifications (particularly during the re-crystallization process). Another important factor is a proper, flexible and durable contacting system of such cell.

4. Novel carbon nanotube contacts for proposed devices

An essential challenge in the development of flexible photovoltaic structures, excepting the elaboration of an appropriate semiconductor junction and optical properties of active layers, is providing suitable contacts. PV electrodes are required to be reliable, efficient, low cost and compatible with solar cell structure. An extremely frequently used solution is applying flexible transparent conductive oxides (TCO) as PV cell front (generally emitter) layer electrodes. As it was mentioned before emitter contacts are usually realized by using conductive transparent metal oxides, such as: SnO_2, ITO, Zn_2O_4, $CdSnO_4$, In_2O_3, ZnO:Al, as well as CdO, ZnO and $RuSiO_4$. In order to integrate solar cells into PV modules or for more convenient measurements execution, additional metal contacts attached to TCO are applied. The most popular among listed TCO compounds is indium tin oxide (ITO).

ITO is a mixture of tin (IV) oxide: SnO_2 and indium (III) oxide: In_2O_3 so called ITO. This material is characterized by high optical transmission of above 90% in visual range and relatively low electrical resistivity of $10\,\Omega/square \div 100\,\Omega/square$ for thickness of $150\,nm \div 200\,nm$. Unfortunately, applying ITO and other TCO layers in flexible photovoltaics encountered a significant barrier. Those metal oxides indicate a lack mechanical stress resistance which leads to breaking and crushing of the contact. This disadvantageous characteristic was observed and reported also during the research on flexible diode display electrodes. Furthermore, thin ITO layers are predominantly manufactured by cost-consuming magnetron sputtering method [28], which increases the final cost of new PV cell and module. Moreover, the indium resources are strictly limited and expected to be exhausted within next fifteen years of exploitation.

A novel method of creating flexible transparent contacts for solar cells is to use carbon nanotubes (CNT). Due to the broad range of potential manufacturing techniques and diversified properties of obtained layers, carbon nanotubes are becoming increasingly popular in electronic applications. Especially CNT layers obtained using low-cost technologies such as screen printing or sputtering are potentially useful in flexible electronic devices [30] and smart textiles. This subsection presents the summary of experiments which were conducted up to now and led to adaptation of carbon nanotubes as thin transparent contacts of selected flexible photovoltaic structures.

To create CNT based transparent conductive layer (TCL), preparation of particular composite is necessary. Since there is a requirement of low cost material, multilayer carbon nanotubes, synthesized in catalytic chemical vapor deposition (CCVD), were used in tested compounds. CCVD process has a drawback which causes that not perfectly pure CNT material is obtained. Although, the material contains significant amount of non CNT carbon structures and metal catalyst, either purification or alternative fabrication methods, can increase costs up to a few orders of magnitude. The average dimensions of nanotubes in the material (determined by Scanning Electron Microscopy - SEM) are $10 \div 40\,nm$ in diameter and $0.5 \div 5\,\mu m$ length, however longer structures have also been observed. Figure 15 presents HRSEM image of applied CNTs.

Carbon nanotube composites are printed on given substrates using, low cost screen printing technique. To specify a relationship between the content of CNT in the composition and the value of sheet resistance, electrical properties of printed layers was measured. Table 4 presents achieved results. All samples showed electrical conductivity and were much above the percolation threshold [11].
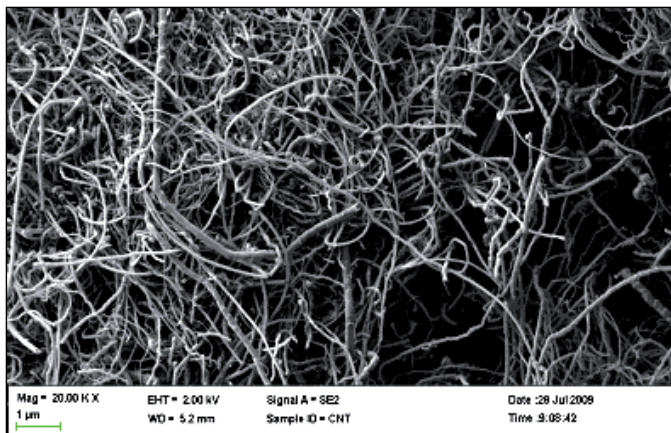
Fig. 15. HRSEM image of applied carbon nanotubes

Paste No	CNT content in the composition [%]	Sheet resistance [Ω/square]
CNT.0.1	0.10	613 k
CNT.0.25	0.25	28 k
CNT.0.5	0.50	3.3 k
CNT.1.0	1.00	870

Table 4. Sheet resistance values for samples with different CNT amount [11].

Transparent conductive layers were prepared using four composites with various CNT content (Table 1). As a substrate borosilicate glass was used. In order to compare CNT and ITO layer parameters, an identical Bo Si glass sample, covered by 160 nm sputtered ITO, was taken. As a first step of carbon nanotubes TCL application in solar cell structure, transmittance of printed layers have been measured (Figure 16).
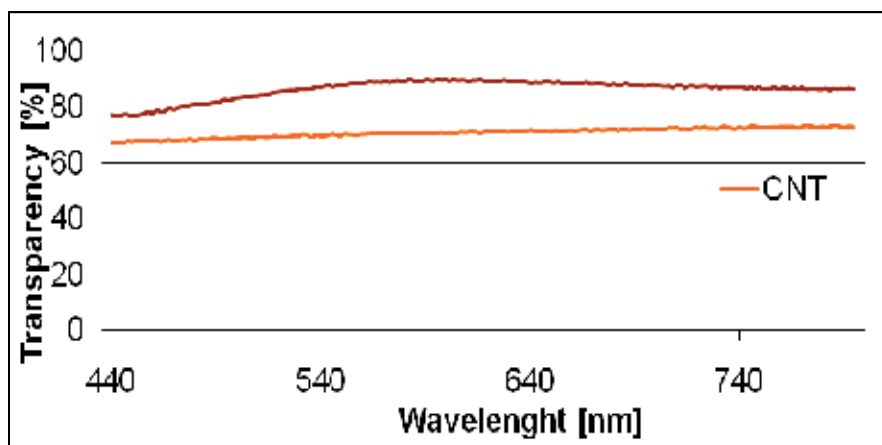
Fig. 16. Transmittance comparison of 0,25%, 1,5 µm CNT layer and 160 nm ITO on borosilicate glass, for standard solar cell absorption spectrum

A very important characteristic for printed CNT layers, is stability of the resistance while applying multiple mechanical stress. To verify this parameter for manufactured CNT layers, additional experiment was undertaken. TCL of 1.5 µm thick was screen printed on polyamide Kapton® and tested by rapid mechanical bending in 80 cycles. The results of resistivity change (Figure 17a) was compared with literature outcomes, obtained for optical ITO layer (Figure 17b).
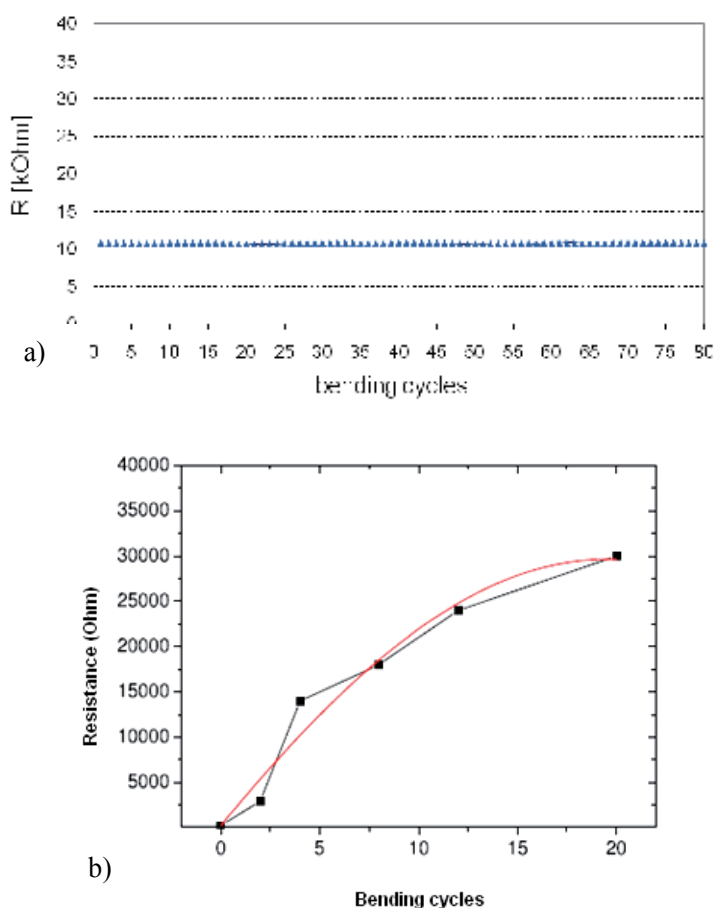
Fig. 17. Resistance changes of: a) CNT and b) ITO layers while bending [31]

After a positive estimation of CNT layers optical and electrical parameters, the possibility of implementation as a solar cell transparent conductive coating was verified. For creating models of screen printed CNT layer, as TCO replacement, in different PV cell structures, SCAPS simulator was used. Simulation models are generated by digital description of physical parameters of each structure layer, including contacts. Solar Cell Capacitance Simulator (SCAPS) is available free of charge for scientific research. Figure 18 shows I-V curves simulations, for CdTe/CdS solar cell structure with ITO and CNT contact layer. Operating parameters of simulated cells are presented in Table 4.
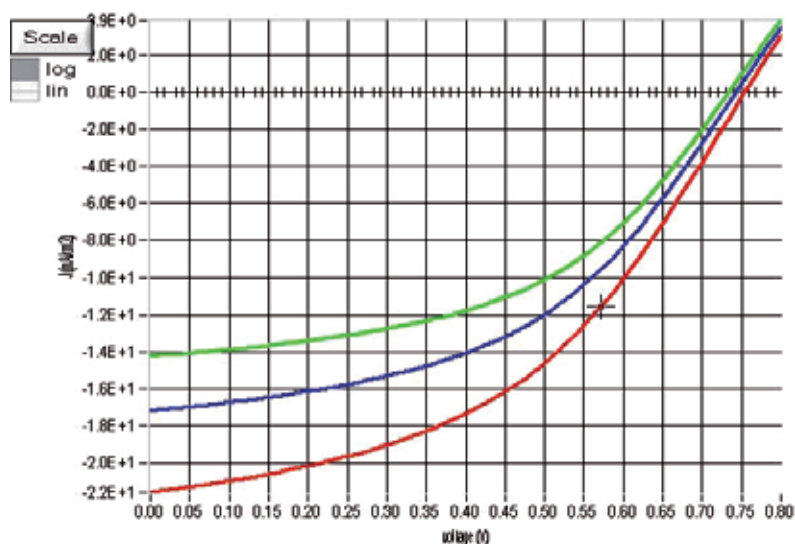
Fig. 18. SCAPS simulations of I-V characteristics of CdTe/CdS solar cell with filters: red-none, blue-ITO, green-CNT.

Filter	Open circuit voltage V_{OC} [V]	Short circuit current J_{SC} [mA/cm²]	Fill Factor FF [%]	Efficiency η [%]
none	0.754	21.602	44.99	7.33
ITO	0.743	17.194	47.00	6.00
CNT	0.733	14.236	48.50	5.06

Table 5. Electrical parameters of CdTe/CdS solar cell

5. Conclusions

Carbon nanotube layers with relatively high optical transmittance were fabricated by inexpensive screen printing technique on glass and on elastic polymer substrates as well. The average difference of 10% in transmittance within standard CdTe cell photoconversion range between 160 nm ITO and 1.5 µm 0.25% CNT layer was observed. Sheet resistance of obtained layers are at relatively high level and should be diminished for efficient photovoltaic applications. To achieve this goal special technology and material compositions (including various CNT content) are tested. The resistance of CNT layers, in opposite to standard ITO, turned out completely independent on bending, which is critical in terms of flexible solar cells construction. According to SCAPS simulations the lowest P_m drop, caused by CNT layer implementation, was observed in case of thin-film cells, which is consistent with postulate of new construction flexibility. Preliminary practical experiments confirmed the presence of photovoltaic effect in solar cell equipped exclusively with CNT emitter electrode.

Presently, due to weaker optical and electrical parameters those layers cannot be a competitive alternative to the existing transparent conductive layers. Nevertheless, they

have much better elastic properties and high prospects for improving the optical and electrical parameters, and therefore they can be potential   solar cells layers. Further experiments are planned for development of manufactured structure (including incorporation of main metal contacts) and manufacturing of thin-film cells with carbon nanotube emitter contacts. However, CNT composites obtain higher optical permeability at a lower carbon nanotubes content, which in turn, increases the resistivity of these materials. Thus, the simultaneous increasing of the permeability and reducing the resistivity is a difficult issue.

Flexible solar cells, based on thin film heterostructure are expected to be a natural development of currently produced devices. For elaboration of fully functional photovoltaic structure, ready for industrial production, many technological problems must be solved. Presented work is a small part of impact put in this process. It is highly probable that some of presented concepts will soon find the implementation in the commercially available elastic cells, based on II-VI compounds.

6. References

[1] K. Zweibel "Thin Films: Past, Present, Future" Progress in Photovoltaics, Special Issue on Thin Films, NREL 1995.

[2] O. Mah "Fundamentals of photovoltaic materials" National Solar Power Research Institute 1998 pp 1-10.

[3] A. Hepp et al. "Ultra-Lightweight Hybrid Thin-Film Solar cells: A survey of Enabling Technologies for Space Power Applications" Proc. 5th International Energy Conversion Engineering Conference and Exhibit (IECEC) St Louis 2007 p 4721.

[4] V. Bemudez, A. Moreau, N. Laurent, L. Jastrzebski "Roadmap of characterization techniques for the development of thin film photovoltaic technology" Proc. Photovoltaic Technical Conference – Thin Film 2010, Aix-en-Provence, France 2010.

[5] D. Bonnet, H. Rabenhorst "New results on the development of a thin film p-CdTe/n-CdS heterojunction solar cell" Proc. 9th IEEE Photovoltaic Specialist Conference, New York 1972 pp 129-131.

[6] X. Wu, J. Keane, R Dhere, C. DeHart, A. Duda, T. Gessert, S. Asher, D. Levi, P. Sheldon „16.5% efficiency CdS/CdTe polycrystalline thin film solar cell" Proc. 17th European Photovoltaic Solar Energy Conference, Munich 2002 pp 995-1000.

[7] ZSW Press Release 05/2010, Stuttgart, Germany 2010.

[8] A. Tiwari "Flexible solar cells for cost effective electricity. High efficiency flexible solar cells based on CIGS and CdTe" Proc. Photovoltaic Technical Conference – Thin Film 2010, Aix-en-Provence, France 2010.

[9] V. Fthenakis, EMRS-2006 Spring meeting

[10] J. Perrenoud, B. Schaffner, L. Kranz, S. Buecheler, A. Tiwari „Flexible CdTe thin film solar modules" Proc. Photovoltaic Technical Conference – Thin Film 2010, Aix-en-Provence, France 2010.

[11] M. Sibiński, M. Jakubowska, K. Znajdek, M. Słoma, B. Guzowski „Carbon nanotube transparent conductive layers for solar cells applications", Proc. 10th Electron

Technology Conf. ELTE 2010 and 34th International Microelectronics and Packaging IMAPS-CPMT Conf., 22-25.09, 2010, 81-82.

[12] H. S. Ullal, K. Zweibel, B. G. Roedem "Polycrystalline thin-film photovoltaic technologies: from the laboratory to commercialization" NREL 0-7803-5772-8/00 IEEE 2000.

[13] H.S. Ullal, B. Roedern "Thin Film CIGS and CdTe Photovoltaic Technologies: Commercialization, Critical Issues, and Applications" Proc. 22nd European Photovoltaic Solar Energy Conference (PVSEC) and Exhibition, Milan, Italy 2007

[14] P. Mints „Principal Analyst Navigant Consulting" PV Services Program 2010

[15] T. Markvart, L. Castaner "Solar Cells: Materials, Manufacture and Operation" Elsevier Amsterdam 2006.

[16] T. Nisho Thin film CdS/CdTe solar cell with 15,05% efficiency 25 th Photovoltaic Specialists Conference 1996 ss. 953 -956

[17] L. Kazmierski, W. Berry, C. Allen „Role of defects in determining the electrical properties of CdS thin films". J. Appl Phys Vol43 No8 1972 pp 3515-3527

[18] R. Bube „Photovoltaic materials" Imperial college press Londyn 1998 pp 135-136.

[19] S. Bernardi "MOCVD of CdTe on foreign substrates". Materials Science Forum Vol 203 1996 ss115-122.

[20] C. Ferekides, D Marinski, V. Viswanathan i in." High efficiency CSS solar cells". Thin Solid Films 2000 ss 520-526

[21] Mendoza-Pérez, R.b , Aguilar-Hernández, J.R.a , Sastré-Hernández, J.a , Tufiño-Velázquez, M.a, Vigil-Galán, O.a , Contreras-Puente, G.S.a , Morales Acevedo, A.c , Escamilla-Esquivel, A.a , Ortega-Nájera, B.a , Mathew, X.d , Jean-Marc-Zisae "Photovoltaic modules processing of CdS/CdTe by CSVT in 40 cm2" 2009 34th IEEE Photovoltaic Specialists Conference, PVSC 2009; Philadelphia

[22] M. Sibiński, M. Burgelman „Development of the thin-film solar cells technology". Microtherm '2000 Łódź-Zakopane 2000 ss. 53-60.

[23] B. Depuydt, I Clemminck, M. Burgelman, M. Casteleyn, . "Solar Cells with screen-printed and sintered CdTe layers on CdS/TCO substrates". Proc. of the 12th EPSEC Stephens & Associates. 1994. ss. 1554-1556

[24] M. Sibiński, Z. Lisik "Polycrystalline CdTe solar cells on elastic substrates", Bulletin of the Polish Academy of Sciences, Technical Sciences Vol. 55, No. 3, 2007, 2007, str. 287-292

[25] M. Sibiński "Thin film CdTe Solar Cells in Building Integrated Photovoltaics", 1st SWH International Conference, 13-15 (2003).

[26] I. Lauremann, I. Luck, K. Wojczykowski „CuInS2 based thin film solar cells on roof tile substrates" 17th EPSEC 1256-1259 (2001)

[27] D. Batzner, A. Romeo, D. Rudman, M. Kalin, H. Zogg, A. Tiwari . " CdTe/CdS and CIGS thin Film Solar Cells." 1st SWH International Conference 56-60 (2003),

[28] A. Hepp et al. "Ultra-Lightweight Hybrid Thin-Film Solar cells: A survey of Enabling Technologies for Space Power Applications" 5th International Energy Conversion Engineering Conference and Exhibit (IECEC) St Louis 2007 p 4721

[29] H. Sirringhaus, T. Kawase, R. H. Friend, T. Shimoda, M. Inbasekaran, W. Wu, E. P. Woo, "High-Resolution Inkjet Printing of All-Polymer Transistor Circuits", Science 15, vol. 290, no. 5499, 2000, pp. 2123 – 2126.

[30] Y. Seunghyup, Y. Changhun, H. Seung-Chan and C. Hyunsoo "*Flexible/ ITO-free organic optoelectronic devices based on versatile multilayer electrodes*" – Raport Integrated Organic Electronics Lab (IOEL)Dept. of Electrical EngineeringKorea Advanced Institute of Science and Technology (KAIST), Daejeon, Korea 2009.

Computer Modeling of Heterojunction with Intrinsic Thin Layer "HIT" Solar Cells: Sensitivity Issues and Insights Gained

Antara Datta and Parsathi Chatterjee
Energy Research Unit, Indian Association for the Cultivation of Science,
Jadavpur, Kolkata,
India

1. Introduction

Despite significant progress in research, the energy provided by photovoltaic cells is still a small fraction of the world energy needs. This fraction could be considerably increased by lowering solar cell costs. To achieve this aim, we need to economize on the material and thermal budgets, as well as increase cell efficiency. The silicon "**H**eterojunction with **I**intrinsic **T**hin layer (HIT)" solar cell is one of the promising options for a cost effective, high efficiency photovoltaic system. This is because in "HIT" cells the P/N junction and the back surface field (BSF) layer formation steps take place at a relatively low temperature (~200°C) using hydrogenated amorphous silicon (a-Si:H) deposition technology, whereas in normal crystalline silicon (c-Si) cells the wafer has to be raised to ~800°C for junction and BSF layer formation by diffusion. This means not only a lower thermal budget, but also cost reduction from thinner wafers, since the danger of the latter becoming brittle is strongly reduced at lower (~200°C) temperatures. Thin intrinsic layers on either face of the c-Si substrate, effectively passivate c-Si surface defects, which would otherwise degrade cell performance. Moreover it has been demonstrated that carriers can pass through the passivating layers without significant loss.

In this chapter, we use detailed electrical-optical modeling to understand carrier transport in these structures and the sensitivity of the solar cell output to various material and device parameters. The global electrical - optical model "Amorphous Semiconductor Device Modeling Program (ASDMP)", originally conceived to simulate the characteristics of solar cells based on disordered thin films, and later extended to model also mono-crystalline silicon and "HIT" solar cells (Nath et al, 2008), has been used for all simulations in this chapter. The model takes account of specular interference effects, when polished c-Si wafers are used, as well as of light-trapping when HIT cells are depositd on textured c-Si.

2. Historical development of HIT solar cells

One of the successful applications of hydrogenated amorphous silicon (a-Si:H) is in crystalline silicon heterojunction (HJ) solar cells. Fuhs et al (1974) first fabricated heterojunction silicon solar cells, where the absorber is P (N) type c-Si, while the emitter N

(P) a-Si:H layer is deposited by the standard plasma-enhanced chemical vapor deposition (PECVD) technique at ~200ºC. However the efficiency achieved was much lower than in c-Si solar cells. In the early 80's Prof. Y. Hamakawa and his co-workers [Osuda et al, 1983] predicted the relevance of a-Si:H /c-Si stacked solar cells in silicon applications. Following the study of Prof. Hamakawa, many research groups world wide became interested in the technological development of a-Si:H/c-Si heterojuction solar cells as an alternative to traditional diffused emitter solar cells. It was almost a decade later that Sanyo began work in 1990 on the growth of low temperature junctions on c-Si and developed a new type of heterojunction solar cells called ACJ-HIT (Artificially Constructed Junction- Heterojunction with Intrinsic Thin layer), now shortened to "HIT", with a conversion efficiency of 18.1% (Tanaka et al, 1992) that has thereafter been continuously improved to yield an outstanding 22% efficiency in 100 cm² solar cells (Taguchi et al, 2005). Moreover Sanyo also achieved 19.5% efficiency in mass production (Tanaka et al, 2003). The innovation that made this possible was the introduction of thin films of intrinsic a-Si:H on either side of the c-Si wafer, to passivate the defects on its surface, that were responsible for the low efficiency of the earlier heterojunction cells [Fuhs et al, 1974]. A low recombination surface velocity of 15 cm/s has been demonstrated for passivation by intrinsic a-Si:H by Wang et al (2005). This is as good as the best dielectric surface passivation, such as by SiO_2 and amorphous silicon nitride (SiN_x) (Meier et al, 2007). More importantly, the a-Si:H I-layer can be inserted between the c-Si and a doped layer without significant restriction to carrier transport. The device structure of HIT cells that has been developed by Sanyo is shown in Fig. 1. This cell is fabricated with CZ N-type wafer of thickness ~250 µm. The emitter (doped) layer, passivating intrinsic layers and the doped BSF layer of the cell are all thin films (a-Si:H) and deposited by the PECVD technique at ~200ºC. The device terminates with a TCO anti reflection coating followed by metallic electrodes.
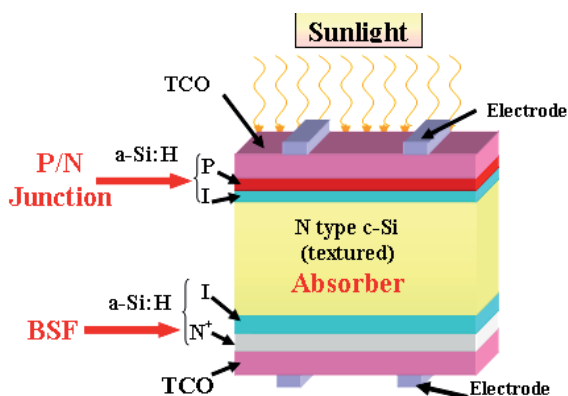
Fig. 1. Schematic diagram of HIT cell proposed by SANYO

HIT cells have (1) potential for high efficiency, (2) very good surface passivation: low surface recombination velocity, (3) low processing temperature - all processes occur at ~ 200°C resulting in low thermal budget, (4) reduced material cost (low temperature processing permits the use of thinner wafers), leading to overall cost reduction and (5) excellent stability- since the base material of the structure continues to be c-Si. With nearly 19 years of steady progress, in 2009, the best HIT solar cells have recorded a efficiency of 23% over a 100.4 cm² cell area (press release SANYO, 2009). Another advantage of HIT solar

cells is that it has excellent temperature dependence characteristics and its efficiency does not deteriorate as much as that of diffused junction c-Si cells at higher temperatures (Sakata et al, 2000). The efficiency of HIT cells deteriorates by 0.33%/° C with increase of temperature while it is 0.45%/° C for conventional c-Si solar cells. This means HIT cells would generate more output power in summer time than its diffused junction counterpart.

References	Wafer		Solar cell output parameters				Emitter & BSF deposition technique
	Type	Surface	J_{sc} mA cm^{-2}	V_{oc} mV	Fill factor	η %	
SANYO press release	N	Textured	39.50	729	0.800	23	PECVD
Schmidt et al, 2007	N	Textured	39.3	639	0.789	19.8	RF-PECVD
	P		34.3	629	0.79	17.4	
Wang et al, 2010,2008	P	Textured	36.20	678	0.786	19.3	HWCVD
	N		35.30	664	0.745	17.2	
Olibet et al, 2010, 2007	N	Flat	34.0	680	0.82	19.1	VHF-PECVD
	P		32	690	0.74	16.3	
Das et al, 2008	N	Textured	35.68	694	0.741	18.4	PECVD
Sritharathikhun et al 2008	N	Textured	35.20	671	0.76	17.9	VHF-PECVD
Damon-Lacoste, 2008	P	Flat	33.0	664	0.778	17.1	PECVD
Fujiwara & Kondo, 2009	N	Flat	32.79	631	0.764	17.5	PECVD

Table 1. Summary of best perfoemances of HIT solar cells on P- and N-type c-Si wafer.

Inspired by the outstanding performance of Sanyo HIT cells, many research groups throughout the world have been working with these cells and a-Si:H layers have been deposited by PECVD, hot-wire CVD (HWCVD) and very-high-frequency PECVD (VHF-PECVD). A summary of the best HIT solar cells reported till date is given in Table 1. We find that currently, no group has been able to duplicate what Sanyo has achieved in terms of cell efficiency. Very few groups have reached beyond 19% efficiency: Helmholtz Zentrum Berlin on N-type textured wafers (Schimdt et al, 2007) and the National Renewable Energy Laboratory (NREL) on P-type textured wafers (Wang et al, 2008, 2010) have achieved this feat. Good results have also been obtained by the group of EPFL, IMT, Neuchâtel, Switzrland with high open-circuit voltsge (V_{oc}) on flat wafers. The P-type HIT cell of Damon Lacoste et al (2008) from LPICM-Ecole Polytechnique, France also deserves mention. Here the efficiency is limited by the lower short-circuit current density (J_{sc}) characteristic of flat wafers. The difficulty in attaining the Sanyo HIT cell efficiency illustrates that the a-Si:H/c-Si HJ is indeed a very challenging structure to understand. Therefore, over the last decade scientists are using detailed computer modeling to fully understand the structure. In the next section we will briefly review the computer modeling of HIT solar cells. Recently a few groups have started fabricating HIT cells with intrinsic hydrogenated amorphous silicon oxide (I-a-SiO:H) as the buffer layer between crystalline and doped amorphous silicon. Sritharathikhun et al (2008) have achieved 17.9% cell efficiency with P-μc-SiO:H /N-c-Si cell structure and I-a-SiO:H as the buffer layer. A group from AIST (Fujiwara et al, 2009) has reported 17.5% cell efficiency with a similar cell structure.

2.1 Detailed one-dimensional computer modeling of HIT solar cells:-

Pioneering work in detailed electrical modeling of a-Si:H solar cells was done by Hack and Schur (1985). Other notable models in this respect are the model AMPS (McElheny et al, 1988, Arch et al, 1991) by S. J. Fonash's group at the Pennsylvania State University, USA, the model of Guha's group (Guha et al, 1989), the ASDMP program by P. Chatterjee (Chatterjee, 1992, 1994, 1996), the ASPIN program of Smole and Furlan (1992) and the ASA program by von der Linden et al (1992). Regarding detailed electrical-optical models, which include textured surfaces and light-trapping kinetics to some extent, the first global electrical-optical model developed in the world was when ASDMP was integrated (Chatterjee et al, 1996) to a semi-empirical optical model by Leblanc et al (1994). This program also takes account of specular interference effects for cells with flat surfaces. Later the developed AMPS program (D-AMPS – Plà et al, 2003) and the ASA package, developed at the Delft University of Technology (Zeman et al, 2000) also introduced light trapping effects.

Modeling of HIT cells was started by van Cleef et al (1998 a,b) using the AMPS computer code (McElheny et al, 1988), which however does not have a proper built-in optical model; and the derivative of the AMPS program (D-AMPS), where a fairly good optical model has been introduced (Plà et al, 2003). The numerical PC program AFORS-HET (Stangl et al, 2001, Froitzheim et al, 2002) has been developed especially for simulating HIT solar cells. The latter has recently also been extended to include light-trapping effects. The ASA program in its later version (Zeman et al, 2000) models both the electrical and optical properties of HIT cells. The PC-1D program (Basore, 1990, Basore et al, 1997), developed at the University of News South Wales, Australia for modeling textured mono-crystalline silicon solar cells, has also been fairly successful in modeling HIT cells. The program ASDMP by Chatterjee et al (1994,1996), has also been extended to model N-a-Si:H/P-c-Si type front (with a heterojunction only on the emitter side) (Nath et al, 2008) HIT cells and subsequently used to model double hetreojunction solar cells both on N- and P-type substrates (Datta et al, 2008, 2009, Rahmouni et al, 2010).

2.1.1 Simulation model ASDMP

We will discuss this model in a little more detail, since it has been used in all simulations in this chapter. The "Amorphous Semiconductor Device Modeling Program (ASDMP) " (Chatterjee et al, 1996, Palit et al, 1998), originally conceived to model amorphous silicon based devices, has been extended to also model c-Si and "HIT" cells (Nath et al, 2008). This one-dimensional program solves the Poisson's equation and the two carrier continuity equations under steady state conditions for the given device structure, without any simplifying assumptions, and yields the dark and illuminated current density - voltage (J-V), the quantum efficiency (QE) and the photo- and electro-luminescence characteristics of HIT cells. Its electrical part is described in P. Chatterjee (1994, 1996). The gap state model used in these calculations for the amorphous layers, consists of the tail states and the two Gaussian distribution functions to simulate the deep dangling bond states, while in the c-Si part, the tail states absent. The lifetime of the minority carriers inside the N(P) -c-Si wafer may be estimated using the formula:

$$\tau_p \approx \frac{p - p_0}{R} \ \text{ or } \ \tau_n \approx \frac{n - n_0}{R} \, , \tag{1}$$

where $\tau_p(\tau_n)$, $p(n)$ and $p_0(n_0)$ are the minority carrier lifetime, its density under the given experimental conditions (in this case under 100 mW cm^{-2} of AM1.5 light), and at thermodynamic equilibrium respectively; while R is the recombination rate in the c-Si wafer. The lifetime, calculated in this manner, is in general, position-dependent; however over a large region inside the c-Si wafer, away from the edges, it is a constant and it is this value that is taken to be the minority carrier lifetime in the wafer. van Cleef et al (1998a,b) and Kanevce et al (2009) have also used the DOS model to simulate their HIT cells.

The generation term in the continuity equations has been calculated using a semi-empirical model (F. Leblanc et al, 1994) that has been integrated into the ASDMP modeling program (Chatterjee et al, 1996, Palit et al, 1998). Both specular interference effects and diffused reflectance and transmittance due to interface roughness can be taken into account. The complex refractive indices for each layer of the structure, required as input to the modeling program, have been measured by spectroscopic ellipsometry. In all cases studied in this article, experimentally or by modeling, light enters through the transparent conducting oxide (TCO)/emitter window, which is taken as x = 0 on the position and referred to as the front contact. Voltage is also applied at x = 0. The BSF/ metal contact at the back of the c-Si wafer is taken as x = L on the position scale, where L is the total thickness of all the semiconductor layers of the device. This back contact is assumed to be at ground potential.
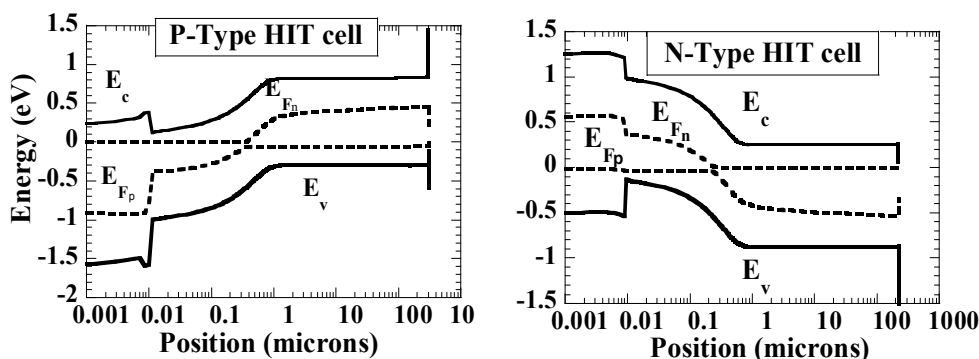
Fig. 2. Energy band diagram for HIT solar cells on P and N type wafers under 100 mW of AM1.5 light and short-circuit conditions.

The calculated energy band diagrams for typical HIT cells on P- and N-type wafers, with passivated surface defects and under 100 mW of AM1.5 light, 0 volts, are shown in Fig. 2.

4. Modeling of HIT solar cells on P-type wafer

4.1 Simulation of experimental results of P-type HIT cells

We have studied both front and double "HIT" structure solar cells on P-type c-Si wafers. These have the structure: N-a-Si:H emitter/ P-c-Si/ aluminum diffused BSF (front HIT) and N-a-Si:H emitter/ P-c-Si/ P$^+$-a-Si:H BSF (double HIT). The experimental data were obtained from the Laboratoire de Physique des Interfaces et des Couches Minces (LPICM), Ecole Polytechnique, Palaiseau, France. Table 2 compares our modeling results to the measured output parameters for front and double HIT structures. Two thicknesses of the N-a-Si:H layer are employed for the front HIT structures, while results are given for two types of

double HIT cells having the following structures: (A) 8 nm N-a-Si:H/ 3 nm pm-Si:H intrinsic layer/ P-c-Si wafer/ 23 nm P$^+$-a-Si:H/ 1.5 μm Al, and (B) the above structure, but with a 4 nm P$^+$-a-SiC:H layer sandwiched between the P-c-Si wafer and a 19 nm P$^+$-a-Si:H layer. The pm-Si:H intrinsic layer on the front surface (FS) of the c-Si wafer is there to passivate the defects on this surface. However, no such passivating layer has been deposited on the rear surface (RS) of the c-Si wafer. The defect density on FS was deduced by modeling to be 10^{11} cm^{-2}. Cell B, which has a 4 nm P-type a-SiC:H layer on the rear c-Si wafer surface, has a slightly higher V$_{oc}$ but a lower FF relative to case A, leading to a better efficiency. However, we could not replicate these results in our modeling calculations by the introduction of a P$^+$-a-SiC:H layer of the given properties alone (case B1 in Table 2). In fact, the defect density on the rear wafer surface had to be slightly reduced (case B2, Table 2) to match the experimental results.

Table 2 indicates good agreement between experiments and modeling, except that our modeling results appear to overestimate the FF and hence the efficiency of front HIT cells. In reality this is because screen-printed contacts with low temperature silver paint was used for these cells; resulting in high series resistance and low FF experimentally, which cannot be accounted for by modeling. For double HIT structures, developed later, improved contact formation resulted in very low series resistance and high fill factors experimentally, which agree well with model calculations (Table 2).

HIT type	Sample	N-a-Si:H (nm)	N$_{ss}$ on the DL (cm^{-2})	V$_{oc}$ (mV)	J$_{sc}$ (mA cm^{-2})	FF	η(%)
Front	X1 (E)	12		634	31.90	0.711	14.38
	X1 (M)	12	FS- 4x10^{11}	636	31.85	0.823	16.67
	X2 (E)	8		640	32.54	0.730	15.20
	X2 (M)	8	FS- 4x10^{11}	640	32.57	0.824	17.18
Double	A (E)	8		650	32.90	0.790	16.90
	A (M)	8	FS-10^{11} RS-8x10^{11}	660	32.84	0.781	16.93
	B (E)	8		664	33.10	0.779	17.12
	B1(M)		FS-10^{11} RS-8x10^{11}	653	33.17	0.749	16.24
	B2 (M)	8	FS-10^{11} RS- 3x10^{11}	667	33.21	0.773	17.12

Table 2. Comparison between measured (E) and modeled (M) solar cell output parameters of front and double P-c-Si HIT cells with a flat ITO front contact. DL refers to the defective layer on the wafer surface.

In Fig. 3 (a), we compare the experimentally measured external and internal quantum efficiency (EQE and IQE respectively) curves of the solar cell B to modeling results, while in Fig. 3 (b) we compare the measured IQE curves of a front HIT and the above-mentioned double HIT solar cells, both deposited in the same reactor and under approximately the same conditions of RF power and pressure as solar cells A and B above. The IQE is obtained from the EQE using the formula:

$$IQE(\lambda) = EQE(\lambda) / (1 - R(\lambda) - ITOabs(\lambda)) , \tag{2}$$

where $R(\lambda)$ is the reflectivity of the HIT cell and *ITOabs(λ)* is the fraction of the light that is absorbed in the transparent conducting oxide, that is indium tin oxide (ITO) in this case.
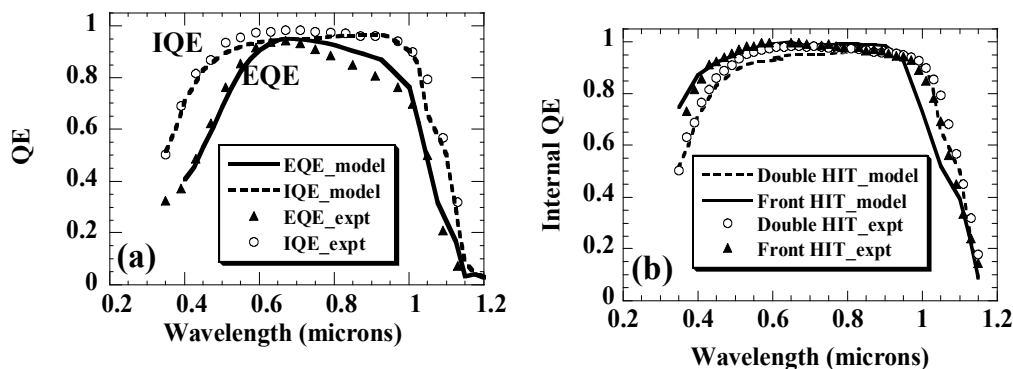
Fig. 3. Comparison of the experimentally measured external and internal QE curves of (a) a double heterojunction cell (case B2 of Table 2); and (b) of a front and the above double HIT solar cell, to modeling results, indicating a higher long wavelength IQE for the double HIT case, both experimentally and in the modeling calculations. The ITO layer is different for the two cases resulting in the difference in the short wave length QE. The lines represent the calculated results, experimental measurements are shown as symbols.

We have used the above simulations to extract the parameters that characterize different layers of the double HIT cells A and B on P-type wafers. These are given in Table 3, together with the extracted parameters of double HIT cells on N-type wafers. The experimental results used to extract the latter and comments thereon, will be discussed in section 5.1. The data in Table 3 includes some measured data: the thickness and doping density of each layer/ wafer, the band gaps of the layers and the electron and hole mobility in the c-Si wafer (Sze, 1981). We also found that a higher value of N_{ss} (as indicated in Case B2 in Table 2 and Table 3) was necessary at the RS to simulate the experimental results. No layer was intentionally deposited to passivate these defects in cells A and B.

Since the 4-nm P+-a-SiC:H layer on the RS of the c-Si wafer (part of the highly doped thin film BSF layer) produces a small but reproducible improvement in the overall device performance, we have tried to understand the basic reasons for this improvement. To realize the role of the thin P-a-SiC:H layer on the RS in case B2 we have made the P+-a-SiC:H layer thicker than in case B2 and adjusted the thickness of following P+-a-Si:H layer to yield a total BSF thickness of 23 nm. We found an all-round deterioration of the solar cell output for the thicker P+-a-SiC:H layers, including a striking fall in the fill factor. We have thus concluded that the introduction of the thin carbide layer as such is not responsible for the observed improvement in cell efficiency of case B2 relative to case A (Table 2). Rather, it appears likely that this wider band gap material helps in passivating the defects on the RS of the c-Si wafer (for which a very thin layer is sufficient) and thereby improves cell performance. In the next section we will discuss how solar cell performance is affected by the defects on the FS and RS of the c-Si wafer.

Parameters	N-a-Si:H/P-a-Si:H emitter	I-pm Si:H buffer	I-a-Si:H buffer	DL on P-c-Si/ N-c-Si on emitter side	P-c-Si/N-c-si wafer	P+-a-Si :H / N+-a-Si : H BSF
Layer thickness (µm)	0.008/ 0.0065	0.003	0.003	0.003	300/220	0.019
Electron affinity (eV)	4	3.95	4	4.22	4.22	4
Mobility gap (eV)	1.80	1.96	1.80	1.12	1.12	1.78/1.80
Don (accep)doping (cm^{-3})	10^{19}/ 1.41×10^{19}	0	0	9×10^{14}	9×10^{14}	1.4×10^{19}/ 1.45×10^{19}
Eff. DOS in CB (cm^{-3})	2×10^{20}	2×10^{20}	2×10^{20}	2.8×10^{19}	2.8×10^{19}	2×10^{20}
Eff. DOS in VB (cm^{-3})	2×10^{20}	2×10^{20}	2×10^{20}	1.04×10^{19}	1.04×10^{19}	2×10^{20}
Exp.tail prefact. -cm^{-3}eV^{-1}	4×10^{21}	4×10^{21}	4×10^{21}	——	——	4×10^{21}
Charac.energy – VB tail (ED) (eV)	0.05	0.05	0.07	——	—	0.05
Charac.energy – CB tail (EA) (eV)	0.03	0.03	0.04	—	—	0.03
Elec.mobility (cm^2/V-s)	20/25	30	25	1000/1500	1000/1500	20
Hole mobility (cm^2/V-s)	6/5	12	5	450/500	450/500	6/4
Gaussian defect density (cm^{-3})	9×10^{18}	7×10^{14}	9×10^{16}	2.6×10^{18}/ 4.5×10^{18}	10^{12}	8×10^{18}/ 9×10^{18}

Table 3. Input parameters, extracted by modeling, that characterize the above HIT cells. The defect density of 3.3×10^{17} cm^{-3} on the front wafer surface corresponds to a defect density of 10^{11} cm^{-2} (FS) and 3.5×10^{18} cm^{-3} to 8×10^{11} cm^{-2} on the rear surface (RS). The P+-a-SiC:H BSF layer in P-type HIT cells has a larger band gap (1.84 eV), and broader band tails: ED=0.7 eV, EA=0.5 eV

4.2 Influence of the defect density on the front surface of the c-Si wafer:

The effect on the solar cell output parameters of varying the defect density, N_{ss}, on front surface of the P-type c-Si wafer (that which faces the incoming light) is shown in Table 4, using as the base case the double HIT cell B2, but with an assumed textured wafer to reproduce state-of-the-art currents obtainable in HIT cells. The defect density on the RS is held at 10^{11} cm^{-2} for all cases. The results indicate a sharp fall in V_{oc}, and FF.

To understand the sensitivity, we turn to Fig. 4. We note that the electric field is higher at the amorphous - crystalline interface, when $N_{ss} = 3 \times 10^{13}$ cm^{-2} than when $N_{ss} = 10^{11}$ cm^{-2} (Fig. 4a). This is because when the N-a-Si:H layer is joined to a P-c-Si wafer, with a high defect density on its surface, most of the electrons that flow from the N-side to the P-side during junction formation, to bring the thermodynamic equilibrium Fermi levels on either side to the same level, are trapped in these states. The space charge region on the P-c-Si wafer side is therefore localized near the surface and does not extend appreciably into the c-Si wafer. We therefore have a huge density of trapped electrons, a very high interface field (Fig. 4a),

N_{ss} on FS (cm^{-2})	J_{sc} (mA cm^{-2})	V_{oc} (mV)	FF	$\eta(\%)$
10^{11}	37.50	672	0.770	19.40
2×10^{12}	38.33	586	0.658	14.79
3×10^{13}	38.14	463	0.545	9.65

Table 4. Calculated values of the solar cell output parameters J_{sc}, V_{oc}, FF and η, for different values of the defect density (N_{ss}) on that (front) surface of the crystalline silicon wafer through which light enters, indicating high sensitivity to the V_{oc} and FF. The defect density at the rear surface of the c-Si wafer is 10^{11} cm^{-2}.
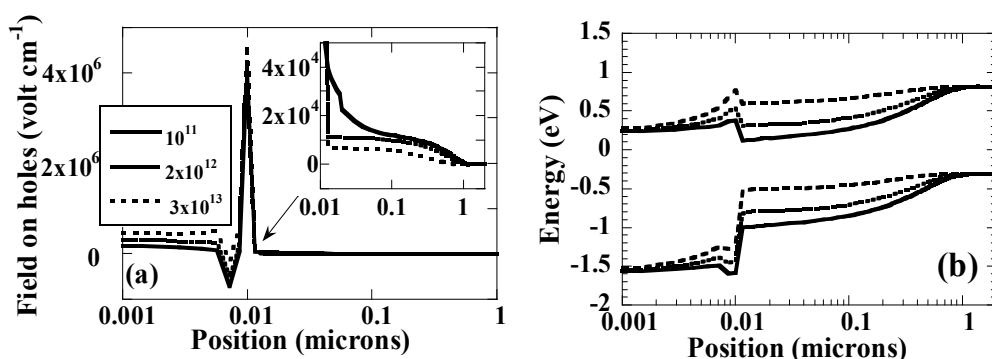
Fig. 4. Effect of changing the defect density (shown in units of cm^{-2}) on the front surface of the c-Si wafer under 100 mW cm^{-2} of AM1.5 light and 0 volts, on (a) the electric field (the inset shows the electric field on an expanded scale over the depletion region) and (b) the band diagram over the front part of the device.

and a collapse of the field over the adjacent depletion region of the c-Si wafer (Fig. 4a inset) for the case with N_{ss} = 3×10^{13} cm^{-2}. This results in the flattening of the energy bands in the totality of the P-type crystalline silicon wafer (Fig. 4b, dashed lines), and a consequent fall in V_{oc} and FF (Table 4). For the case of low N_{ss}, the space charge region on the P-c-Si wafer is not localized and more field exists up to the neutral zone of the c-Si wafer (Fig. 4a inset and band diagram in Fig. 5b, solid lines); resulting in higher V_{oc} and FF (Table 4).

4.3 Influence of the defect density on the rear surface of the c-Si wafer

Table 5 gives the calculated solar cell output parameters J_{sc}, V_{oc}, FF and efficiency for different values of the defect density (N_{ss}) on the rear surface of the c-Si wafer (away from the side where light enters). We have again varied N_{ss} between 10^{11} cm^{-2} and 3×10^{13} cm^{-2}, but this time the largest effect is on the fill factor and the short-circuit current density, as seen from Table 5 and Fig. 5 (a). In order to understand why, we have traced the band diagrams for different N_{ss} on the RS, with the N_{ss} at the FS held at 10^{11} cm^{-2} (Fig. 5b). We find that the band bending over the depletion region has completely disappeared for the highest value of N_{ss} (3×10^{13} cm^{-2}) at RS. From our modeling calculations we also note that up to a defect density of ~10^{12} cm^{-2} at RS, the solar cell output parameters do not deteriorate appreciably. For higher values of N_{ss} the decrease in J_{sc} and FF in particular, is extremely rapid, the sensitivity to V_{oc} being relatively small. Experimentally also it has been found that whether or not an intrinsic passivating layer is deposited on the rear face of the P-type c-Si wafer, the

solar cell output is little affected. From this we may conclude that the defect density on the back wafer surface in the experimental as-deposited condition is probably ≤ 10^{12} cm^{-2}, as also obtained by modeling the experimental characteristics (Table 2).

N_{ss} on RS (cm^{-2})	J_{sc} (mA cm^{-2})	V_{oc} (mV)	FF	η(%)
10^{11}	37.50	672	0.770	19.40
10^{12}	37.48	662	0.752	18.66
2×10^{12}	37.34	625	0.666	15.54
3×10^{13}	5.47	572	0.156	0.49

Table 5. Calculated values of the solar cell output parameters for different values of the defect density (N_{ss}) on that (rear) surface of the crystalline silicon wafer that is away from the incoming light, indicating that the maximum sensitivity is to the short circuit current density and fill factor. The defect density at the front surface of the c-Si wafer is 10^{11} cm^{-2}.

In order to understand the sensitivity of the solar cell output to N_{ss} on the RS, we turn to Fig. 6. We note that when N_{ss} on the rear c-Si wafer surface is highest (3×10^{13} cm^{-2}), there is a huge concentration of trapped holes at the crystalline- amorphous interface on the c-Si wafer side where the high surface defect density exists (dashed line, Fig. 6a). The hole pile-up at the crystalline-amorphous interface slows down the arrival of holes to the back contact (the collector of holes), and encourages the back diffusion of photo-generated electrons in the absorber c-Si wafer. The result is that the electron current is negative over most of the device (Fig. 6b – electron current towards the back contact is negative according to our sign convention). Thus little electron current is collected at the front contact (the collector of electrons, Fig. 6b). In addition, the back-diffusing electrons recombine with the photo-generated holes over most of the absorber c-Si, resulting in poor hole current collection at the back contact. Thus J_{sc} and FF fall sharply for very high values of N_{ss} at RS. More details can be found in Datta et al (2008).
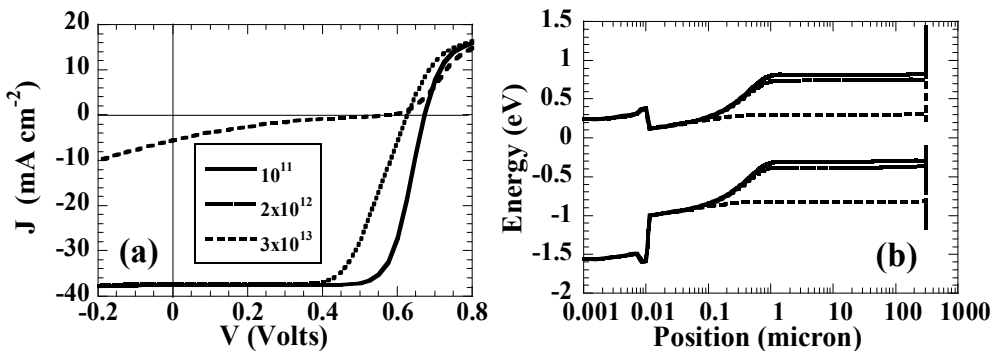
Fig. 5. Effect of changing the defect density (shown in units of cm^{-2}) on the rear surface of the c-Si wafer on (a) the illuminated current density versus voltage characteristics and (b) the band diagram at 0 volts as a function of position in the device under 100 mW cm^{-2} AM1.5 light. Results are shown for double heterojunction solar cells having a 4 nm P$^+$-a-SiC:H/ 19 nm P$^+$-a-Si:H BSF structure. The defect density on the front surface is 10^{11} cm^{-2} for all cases.
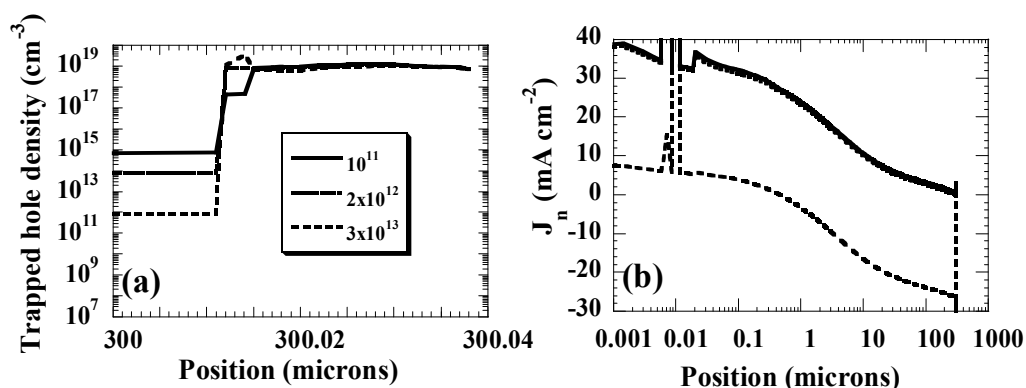
Fig. 6. Effect of changing the defect density (shown in units of cm^{-2}) on the rear surface of the c-Si wafer on (a) the trapped hole density, (b) the electron current density, J_n, and (c) the electric field on the holes. Results are shown for 100 mW cm^{-2} of AM1.5 light under short-circuit conditions.

5. Simulation of N-type HIT solar cells

5.1 Simulation of experimental results

Simulation of a range of experimental results on HIT cells developed by the Sanyo group and available in the literature (Maruyama et al, 2006, Takahama et al, 1992, Sawada et al, 1994, Taguchi et al, 2008) has been undertaken to extract typical parameters that characterize state-of-the-art HIT cells on N-type c-Si substrates, as well as to gain an insight into carrier transport and the general functioning of these cells. Both "front" HIT cells having an amorphous/ crystalline heterojunction on the emitter side only - where the light enters (Takahama et al, 1992), and "double" HIT cells having heterojunctions on both ends of the c-Si wafer (Maruyama et al, 2006, Sawada et al, 1994, Taguchi et al, 2008) have been simulated. The cells have the structure: ITO/ P-a-Si:H/ I-a-Si:H/ textured N-c-Si/ N-c-Si BSF/ metal (front HIT) (Takahama et al, 1992) and ITO/ P-a-Si:H/ I-a-Si:H/ textured N-c-Si/ I-a-Si:H/ N^{++}-a-Si:H/ metal (double HIT) (Maruyama et al, 2006, Sawada et al, 1994, Taguchi et al, 2008). In Taguchi et al (2008), after depositing the undoped and doped a-Si:H layers on both ends of the c-Si wafer, ITO films were sputtered on both sides, followed by screen-printed silver grid electrodes. Simulation of these cells (Maruyama et al, 2006, Takahama et al, 1992, Sawada et al, 1994) gives us an insight into the parameters that play a crucial role in improving HIT cell performance. On the other hand, the article by Taguchi et al (2008) gives the temperature dependence of the dark current density - voltage characteristics and the solar cell output parameters as a function of the thickness of the intrinsic amorphous layer sandwiched between the emitter P-a-Si:H and the main absorber N-c-Si. A study of the temperature dependence of the dark J-V characteristics is particularly important to understand the carrier transport mechanism in these devices. The parameters extracted by such modeling (Table 3) will be used in the following sections to calculate the sensitivity of the solar cell performance to various controlling factors.

In Table 6 we compare our simulation and experimental results of various HIT cells on N-type c-Si substrates (Takahama et al, 1992, Sawada et al, 1994, Maruyama et al, 2006). Modeling indicates that improvements in V$_{oc}$ could be brought about (a) by going from a

HIT	Reference		N_{ss} (cm^{-2}) in defective layers	τ ms	V_{oc} **mV**	J_{sc} mA cm^{-2}	FF	η %
F	Takahama et al, 1992	E	— —	—	638	37.90	0.775	18.74
		M	FS- 4x10^{11}	0.23	643	37.89	0.775	18.88
D-I	Swada et al, 1994	E	— —	—	644	39.40	0.790	20.05
		M	FS-4x10^{11} RS -10^{11}	0.5	658	39.03	0.783	20.11
D-II	Maruyama et al, 2006	E	— —	1.20	718	38.52	0.790	21.85
		M	FS & RS - 10^{11}	2.00	713	38.60	0.797	21.93

Table 6. Comparison between measured (E): and modeled (M) solar cell output of front (F) and double (D) N-c-Si HIT cells with textured ITO front contact, developed by Sanyo over the years. "τ" is the lifetime of the minority carriers in the c-Si wafer.

front HIT to a double HIT structure, (b) by decreasing the defects on the front surface of the c-Si wafer that faces the emitter layer and (c) by improving the lifetime of the minority carriers in crystalline silicon. Results indicate that it is by decreasing N_{ss} on the front surface of the c-Si wafer, that the largest increase in V_{oc} could be achieved, without any fall in FF.

We next used ASDMP to simulate the experimental results of Taguchi et al (2008). Here we have concentrated on the effect of varying the thickness of the intrinsic amorphous silicon layer at the P-amorphous emitter/ N-c-Si heterojunction. The terminology "normal" has been used to represent the thickness of the front I-a-Si:H buffer layer in the cell that yields the highest efficiency (Table 7). Modeling reveals that the I-a-Si:H thickness for this case is 3 nm. The I-a-Si:H buffer layers (front) in the cells named "Half", "Double" and "Triple" by Taguchi et al (2008) have therefore been assigned thicknesses of 1.5 nm, 6 nm and 9 nm respectively in the simulations. Results of our simulation of the experimental light J-V characteristics (Taguchi et al, 2008) as a function of this I-a-Si:H layer thickness are given in Table 7 and the input parameters extracted by such modeling, and also of the dark J-V characteristics (Figs. 7a and 7b) and typical internal quantum efficiencies of Sanyo N-c-Si HIT cells (Fig. 7c, Maruyama et al, 2006), are given in Table 3 (the same table that contains the extracted parameters of P-type HIT cells). Since modeling does not consider the resistance of the contacts; these results had to be modified by taking into account the series resistance of the contacts. The addition of the series resistance did not modify V_{oc} and J_{sc} but allowed to perfectly match the experimental fill factor and therefore the efficiency of the Sanyo HIT solar cells (Taguchi et al, 2008). In Table 7 we show the solar cell output parameters as obtained directly by modeling, without resistive losses (which gives an upper limit for the FF and therefore the efficiency) and the values of the FF and efficiency after considering the constant series resistance (marked by astericks). This resistance, comprising resistive losses in the TCO, the silver grid and the contacts, was estimated by Taguchi et al (2008) to be ~2.8 mΩ.

Cell name	μ_n (μ_p) cm²/volt-sec	I-a-Si:H thickness(nm)	N_{ss} (cm^{-2})		J_{sc} (mA cm^{-2})	V_{oc} (volts)	FF	η(%)
Half	30 (6)	1.5	4×10^{11}	E	37.4	0.699	0.776	20.3
				M	37.2	0.702	0.803 0.775*	21.0 20.2*
Normal	25 (5)	3.0	1.5×10^{11}	E	37.2	0.711	0.773	20.4
				M	37.0	0.712	0.799 0.774*	21.0 20.4*
Double	15 (3)	6.0	10^{10}	E	36.5	0.718	0.747	19.6
				M	36.7	0.717	0.766 0.747*	20.2 19.7*
Triple	15 (3)	9.0	10^{10}	E	36.4	0.715	0.717	18.7
				M	36.6	0.714	0.750 0.718*	19.6 18.8*

Table 7. Modeling (M) of the experimental (E) results of N-type HIT solar cells, having different thickness of the I-a-Si:H layer on the emitter side. N_{ss} is the defect density on that surface of the c-Si wafer that faces the emitter. The quantities given with astericks are the calculated values of FF and efficiency corrected for the series resistance of the contacts (2.8 m mΩ) (Taguchi et al, 2008).
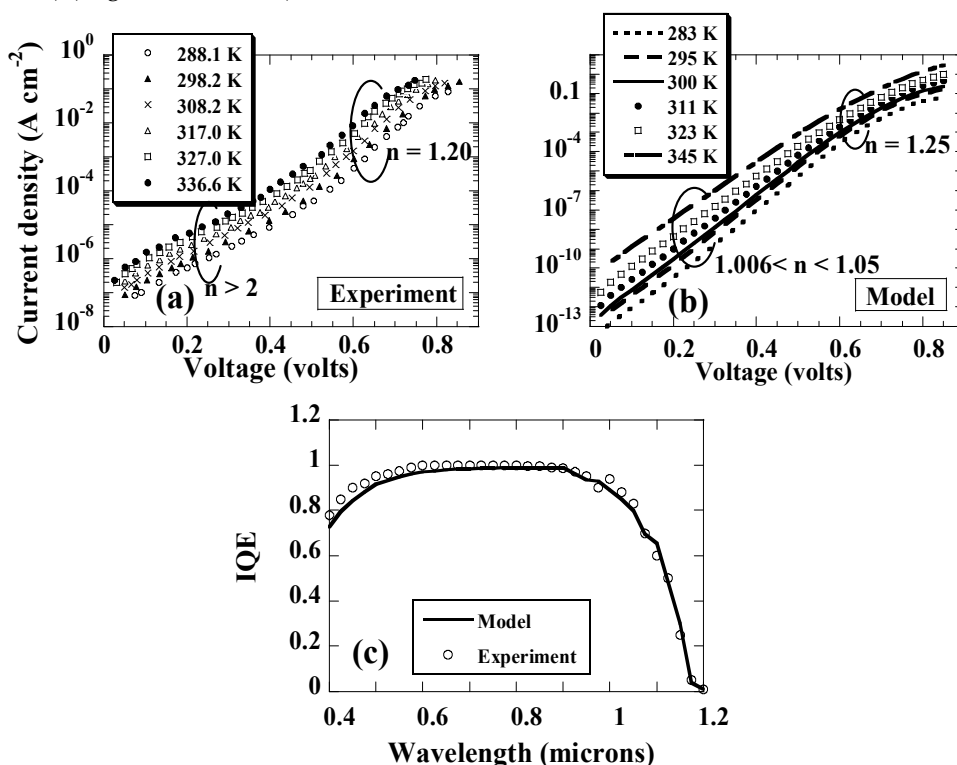
Fig. 7. (a) Experimental (Taguchi et al, 2008) and (b) simulated dark J-V characteristics of the cell with "Normal" thickness I-a-Si:H layer at the P-a-Si:H/ N-c-Si interface at various temperatures, and (c) the IQE of the same cell under AM1.5 illumination and 0 volts compared to the experimental IQE of a typical Sanyo cell (Maruyama et al,2004).

The dangling bond defect density in the I-a-Si:H layer, as extracted from modeling, is 9×10^{16} cm^{-3} and its Urbach enegy is 70 meV (Table 8). We have assumed the same values for these quantities, as well as of the capture cross-sections of the defect states inside the I-a-Si:H layer in all the cases of Table 7. Modeling indicates that in order to simulate the lower V_{oc}'s of the Taguchi et al (2008) cells "Normal" and "Half", the defect density on the surface of the c-Si wafer itself in these cases, must be higher (Table 7). We may justify this fact by assuming that a very thin buffer layer may not be as effective in passivating the defects on the surface of the c-Si wafer as a thicker buffer layer. In Table 7, we also had to assume higher carrier motilies in the front amorphous layers for the cases Half and Normal to match both the higher FF and lower V_{oc} for these cases.   Increasing carrier mobilities over the front amorphous layers improves hole collection and therefore the FF. However, higher electron mobility allows more electrons to recto-diffuse towards the front contact (collector of photo-generated holes) and recombine with holes, thus reducing V_{oc}. However the main reason for the lower V_{oc} for thinner I-a-Si:H layers (Half and Normal) is our assumption of higher surface defect density on the c-Si wafer in these cases (Table 7).

The experimental dark J-V characteristics of the cell "Normal" is shown in Fig. 7 (a) and the model curves in Fig. 7 (b). The diode ideality factor, n, calculated in the voltage range 0.4 volts$\leq$ V< 0.8 volts, from the model dark characteristics is 1.25 and compares well with the experimental value of 1.2. This value of "n" indicates that it is the diffusion current that dominates transport in this voltage range for N-c-Si HIT cells, as is also the case for homojunction c-Si solar cells. On the other hand, in the voltage range 0.1 volts< V< 0.4 volts, "n" calculated from the modeling data (Fig. 7b) is ~1, which indicates that the conductivity continues to be dominated by diffusion. The value of the slope, calculated from the experimental curves of Taguchi et al (2008) in the voltage range 0.1 volts < V < 0.4 is smaller than that of the recombination current model and remained almost constant for each temperature. The corresponding value of "n" derived from the experimental curves is greater than 2 (Fig. 7a). Taguchi et al (2008) therefore assumed that this is tunneling-limited current. If the value of "n" extracted from the experimental curves, had been due to current dominated by recombination, ASDMP would also have been able to reproduce this value of 'n', since the recombination current model is included in ASDMP. In fact ASDMP has already been used to successfully model forward and dark reverse bias characteristics of a-Si:H based PIN solar cells, where recombination plays a dominant role (Tchakarov et al, 2003). The fact that the value of "n" calculated from the ASDMP-generated dark J-V curves is ~1, while that from experiments is different, indicates that the current over this region is dominated by a phenomenon *not* taken account of by ASDMP (e.g. tunneling). Over this voltage region therefore the current could be dominated by the tunneling of electrons. However, as pointed out by Taguchi et al (2008), "the current density in this region is sufficiently low compared to the levels of short-circuit current density and does not affect solar cell performance". It therefore appears that cell performance under AM1 or AM1.5 light is not affected by tunnelling of electrons, although this phenomenon probably exists for V< 0.4 volts.

Fig. 8 shows the temperature dependence of the solar cell output parameters. We have made the comparison between experiments (Taguchi et al, 2008) and modeling, after taking account of the series resistance of the contacts that is independent of temperature. As the temperature decreases, carrier density decreases. It means less carrier recombination and therefore a higher V_{oc} at lower temperatures (Fig. 8a). However lower carrier density at
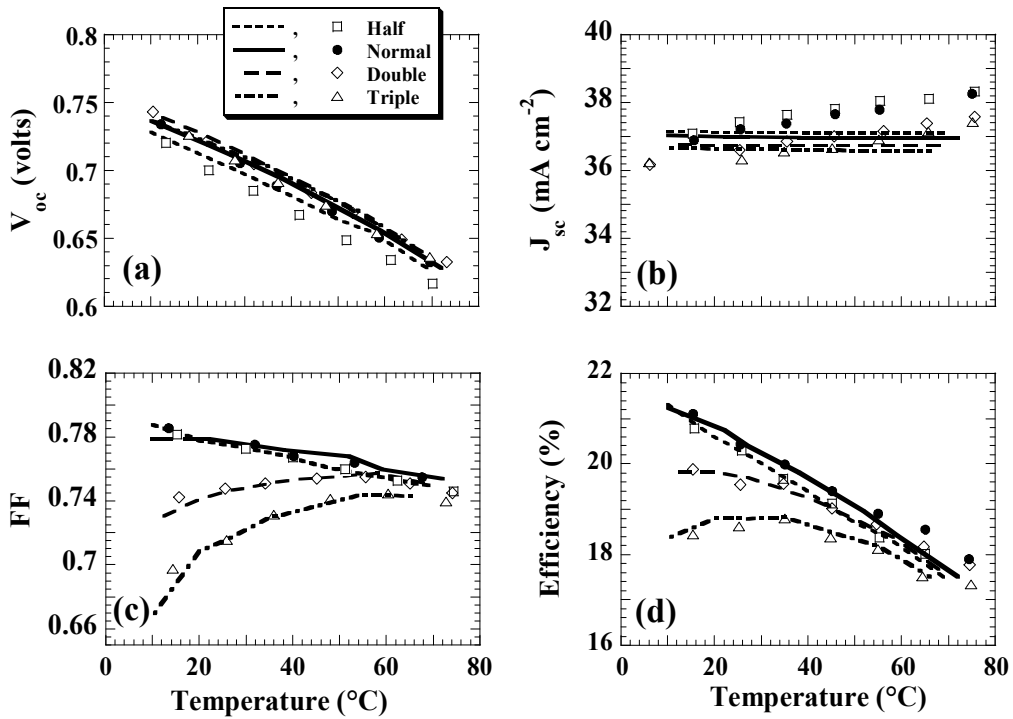
Fig. 8. Variation of (a) V_{oc}, (b) J_{sc}, (c) FF and (d) Efficiency as a function of temperature in N-c-Si HIT solar cells having different thickness of the undoped a-Si:H layer (half, normal, double, triple) at the P-a-Si:H/ N-c-Si interface. The lines are modeling results, while symbols correspond to measured data.

lower temperatures, also means that the cell is now more resistive, resulting in a fall in the FF for the cells "double" and "triple" (Fig. 8c), where performance is dominated by the undoped a-Si:H layer. Also, for the value of the band gap assumed for the I-a-Si:H layer (Table 8), the holes are able to overcome the positive field barrier at the a-Si/ c-Si interface by thermionic emission to get collected at the front contact. Thermionic emission decreases at lower temperatures, resulting in a loss of FF for cells "double" and "triple". For cells "Normal" and "Half", performance is dominated by the temperature-independent resistance of the contacts; therefore no fall in FF is seen. Finally Fig. 8 (b), indicates that the calculated J_{sc} is constant with temperature, while the measured J_{sc} increases slightly. This is because the model does not take account of the temperature dependence of the band gap and absorption coefficient of the materials.

5.2 Effect of I-a-Si:H buffer layers on the performance of N- type HIT solar cells

HIT solar cells give efficiencies comparable to those of c-Si cells because of the amazing passivating properties of the intrinsic a-Si:H layers. In fact it is this layer that gives this group of solar cells its name – "HIT". We have already discussed that it is very effective in passivating the defects on the surface the c-Si wafer. However, it must be kept as thin as possible, as it reduces the fill factor when thick (Table 7). We have next studied the effect on

solar cell performance of varying the defect density in this layer itself. For this purpose, we have assumed its thickness to be 6 nm (as in case "Double") where the best passivation of N_{ss} has been attained (Table 7). An increase in the defect density in the I-a-Si:H layer may affect the defect density (N_{ss}) on c-Si, but in this study we assume N_{ss} to be constant. We have found (Rahmouni et al, 2010) that unless the defect density of this intrinsic layer is greater than 3×10^{17} cm^{-3}, no significant loss of cell performance occurs. Similar conclusions have been reached in the case of HIT cells on P-type c-Si wafers.

5.3 Effect of the defect density on the front and rear faces of the N-type c-Si wafer

The sensitivity of the solar cell output of HIT cells on N-type wafers to the surface defect density (N_{ss}) at the amorphous/crystalline interface is given in Table 9. All aspects of the solar cell output appear to be highly sensitive to the N_{ss} on the front surface (on the side of the emitter layer) of the N-type c-Si wafer; however the sensitivity to N_{ss} on the rear face is weak and is limited to the condition when these defects are very high. We have also given in Table 8, the values of the corresponding recombination speeds at the a-Si:H /c-Si front and the c-Si/a-Si:H rear heterojunctions, as calculated by ASDMP, under AM1.5 illumination and short circuit condition. We find that for a well-passivated front interface ($N_{ss} \leq \sim 3 \times 10^{11}$ cm^{-2}) the recombination speed at this heterojunction is less than 10 cm/sec (Table 8), in good agreement with measured interface recombination speeds (Dauwe et al, 2002).

N_{ss} at front (DL) (cm^{-2})	S_p at front (DL) (cm/s)	N_{ss} at back (DL) (cm^{-2})	S_n at back (DL) (cm/s)	Jsc (mA cm^{-2})	V_{oc} (volts)	FF	η(%)
10^{10}	3.62			36.96	0.720	0.801	21.32
1.5×10^{11}	4.20			37.00	0.712	0.799	21.03
10^{12}	24.73	10^{10}	2.89×10^4	37.24	0.636	0.695	16.46
2×10^{12}	202.62			37.37	0.596	0.470	10.47
10^{13}	1.16×10^3			18.83	0.544	0.160	1.64
		10^{10}	2.89×10^4	37.00	0.712	0.799	21.03
1.5×10^{11}	4.20	10^{11}	2.37×10^4	36.99	0.711	0.799	21.01
		10^{12}	1.95×10^4	36.98	0.696	0.797	20.51
		10^{13}	1.00×10^4	35.45	0.609	0.779	16.82

Table 8. Sensitivity of the solar cell output to the defect density (N_{ss}) in thin surface layers (DL) on the front and rear faces of the c-Si wafer in N type double HIT solar cells. The P-layer thickness is 6.5 nm. The recombination speeds of holes (S_p - at the front DL) and electrons (S_n – at the rear DL), calculated under AM 1.5 light and 0 volts, are also shown.

In Fig.9 (a) we plot the light J-V characteristics and in Fig. 9 (b) the band diagram for various values of N_{ss} on the front face of the c-Si wafer. We find that for a very high defect density on the surface of the c-Si wafer, the depletion region in the N-c-Si wafer completely vanishes, while the emitter P-layer is depleted (Fig. 9b). With a high N_{ss} on the c-Si wafer, the holes left behind by the electrons flowing into the P-layer during junction formation, are localized on its surface, leading to a high negative field on the wafer surface and little field penetration into its bulk (Fig. 10a). Hence the near absence of the depletion zone in N-c-Si and a strong fall in V_{oc} for the highest N_{ss} (10^{13} cm^{-2}).
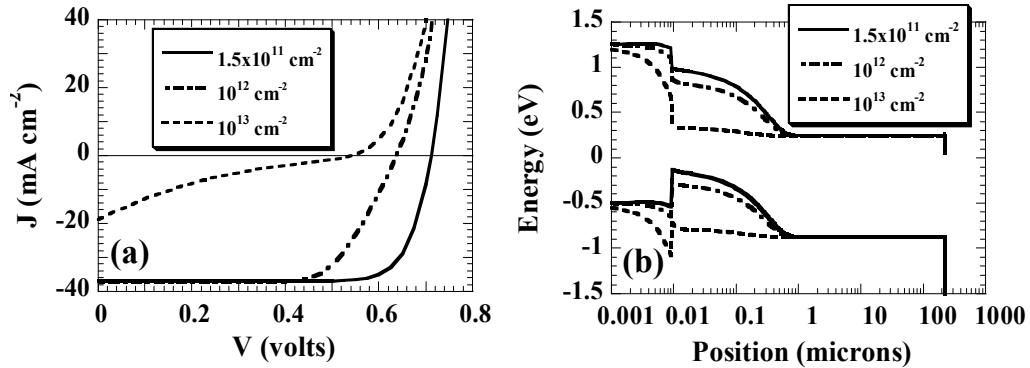
Fig. 9. (a) The light J-V characteristics and (b) the band diagram under AM1.5 light bias and 0 volts for different values of N_{ss} on the front face of the N type c-Si wafer.

In Fig. 10 (b) we plot the trapped hole population over the front part in N-c-Si double HIT cells under AM1.5 bias light at 0 volts. We note that when N_{ss} on the front c-Si wafer surface is the highest (10^{13} cm^{-2}), there is a huge concentration of holes at the amorphous / crystalline (a-c) interface on the c-Si wafer side, where the high surface defect density exists (dashed line, Fig. 10b).
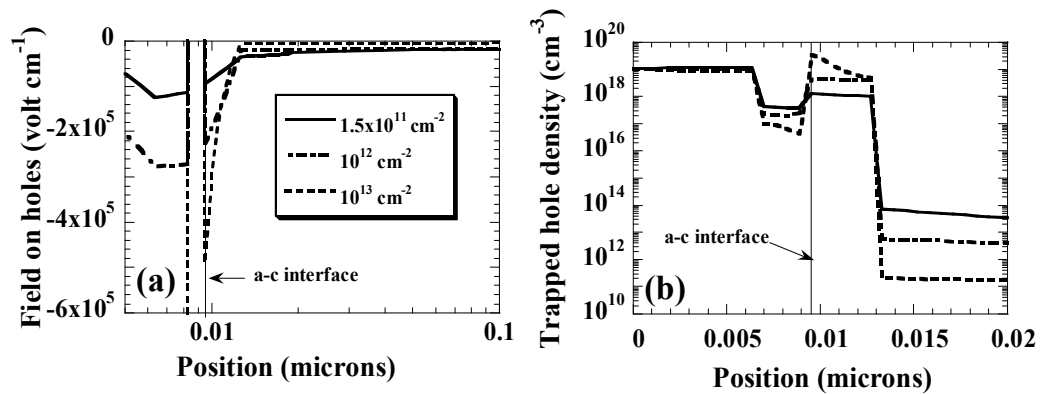
Fig. 10. Plots of (a) the electric field on the holes and (b) the trapped hole density over the front part of the device as a function of position in the entire device under illumination and short-circuit conditions, in N-c-Si HIT cells for different densities of defects on the front face of the c-Si wafer. The amorphous/crystalline (a-c) interface is indicated on (a) and (b).

The hole pile-up at the amorphous / crystalline interface slows down the arrival of holes to the front contact (the collector of holes), and attracts photo-generated electrons, i.e., encourages their back diffusion towards the front contact. The result is that the electrns back-diffuse towards the front contact and recombine with the photo-generated holes resulting in poor carrier collection (Rahmouni et al, 2010). Thus J_{sc} and FF fall sharply for high values of N_{ss} on the front surface of c-Si (Table 8). In fact we may arrive at the same conclusion also from Fig. 9 (b), which shows that for N_{ss} = 10^{13} cm^{-2}, there is almost no band bending or electric field in the c-Si wafer (the main absorber layer) so that carriers cannot be collected, resulting in the general degradation of all aspects of solar cell performance.

On the other hand Table 8 indicates that there is little sensitivity of the solar cell output to the defect states on the rear face of the wafer, except at the highest value of N_{ss}. To explain this fact, we note that the recombination over the rear region is determined by the number of holes (minority carriers) that can back diffuse to reach the defective layer. Not many succeed in doing so, since the high negative field due to the large valence band discontinuity at the c-Si/ a-Si rear interface pushes the holes in the right direction, in other words, towards the front contact. Therefore the defects over this region cannot serve as efficient channels for recombination, and there is no large difference between the recombination through these states for different values of N_{ss} (Table 8). Moreover the conduction band discontinuity at the c-Si/ a-Si interface is about half that of the valence band discontinuity. Since the mobility of electrons, relative to that of holes, is also much higher, clearly this reverse field due to the conduction band discontinuity poses little difficulty for electron collection even when the defect density at this point is high, except when $N_{ss} \geq 10^{13}$ cm^{-2}, from which point the solar cell performance deteriorates.

6. Comparative study of the performances of HIT solar cells on P- and N-type c-Si wafers

Using parameters extracted by our modeling (given in Tables 3), we have made a comparative study between the performances of HIT solar cells on 300 µm thick textured P- and N-type c-Si wafers (for more details refer to Datta et al, 2010).

6.1 Sensitivity of amorphous/crystalline band discontinuity in the performances of HIT solar cells

Since the band gap, activation energy of the amorphous layers and the band discontinuities at the amorphous/crystalline interface are interlinked, we treat these sensitivity calculations together. For HIT cells on P-c-Si, the large valence band discontinuity (ΔE_v) on the emitter side prevents the back-diffusion of holes and has a beneficial effect. Keeping this constant, we varied the mobility gap and therefore the conduction band discontinuity (ΔE_c) on the emitter side. We find that a ΔE_c upto 0.3 eV, does not impede electron collection, but instead brings up both J_{sc} and V_{oc}, due to an improved built in ptential (V_{bi}).

However high ΔE_v at the crystalline/amorphous (c-a) interface on the BSF side of P-c-Si double HIT cells (Table 9), impedes hole collection, resulting in a pile up of holes on the c-Si side of this band discontinuity (Fig. 11a) and a consequent sharp fall in the FF and S-shaped J-V characteristics for high ΔE_v, especially when the activation energy of the P-a-Si:H layer is also high (Fig. 11b).

E_μ (P) (eV)	E_{ac} (eV)	ΔE_v (eV)	J_{sc} (mA cm^{-2})	V_{oc} (mV)	FF	η %
1.75	0.3	0.41	36.70	649	0.810	19.28
1.75	0.4	0.41	36.69	647	0.688	16.34
1.80	0.3	0.46	36.70	649	0.807	19.21
1.90	0.3	0.56	36.70	649	0.762	18.14
1.90	0.4	0.56	36.68	649	0.484	11.51
1.98	0.4	0.64	27.45	649	0.171	3.04

Table 9. Variation of solar cell output with mobility gap (E_μ), activation energy (E_{ac}) and ΔE_v (P-c-Si/P-a-Si:H BSF interface) in double P-c-Si HIT solar cells. ΔE_c is held constant at 0.22eV.

It is for this reason that a transition from a front to a double HIT structure does not appreciably improve cell performance for P-c-Si HIT cells. The accumulated holes at the c-a interface, furthermore, repel the approaching holes and encourage photo-generated electron back diffusion, resulting in increased recombination, that reduces even J_{sc} for the highest ΔE_v (Table 9, Fig. 11b). Finally, for high hole pile-up, the amorphous BSF is screened from the rest of the device, so that the large variation of its band gap and activation energy (Table 9) fails to alter the V_{oc} of the device. The best double HIT performance is attained when the mobility gap (ΔE_{μ}) of the amorphous BSF P-layer is ≤ 1.80 eV and $E_{ac} = 0.3$ eV (Table 9).
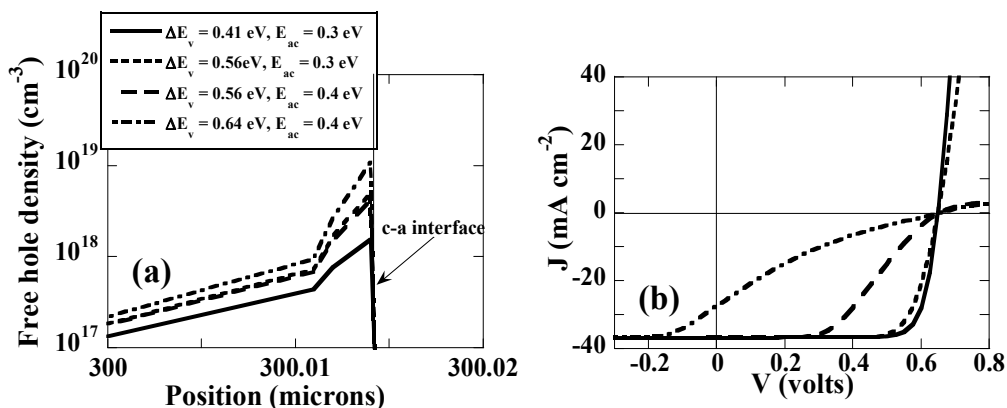
Fig. 11. Variation of (a) the free hole population near the c-Si/ amorphous BSF interface and (b) the light J-V characteristics for different valence band discontinuities (ΔE_v) and activation energies (E_{ac}) of the P-BSF layer in double P-c-Si HIT solar cells. $\Delta E_c = 0.22$eV in all cases.

Table 10 shows the effect of the variation of the emitter P-layer mobility gap, activation energy and the valence band discontinuity at the a-c interface on N-c-Si double HIT cell performance.

E_{μ} (P) (eV)	E_{ac} (eV)	ΔE_v (eV)	J_{sc} (mA cm⁻²)	V_{oc} (mV)	FF	η (%)
1.75	0.3	0.41	38.06	670	0.818	20.86
1.75	0.4	0.41	38.14	652	0.681	16.93
1.80	0.3	0.46	38.10	671	0.811	20.75
1.90	0.3	0.56	38.22	677	0.705	18.25
1.90	0.4	0.56	38.38	674	0.463	11.98
1.98	0.4	0.64	28.18	732	0.184	3.79

Table 10. Variation of solar cell output parameters with mobility gap (E_{μ}), activation energy (E_{ac}), and ΔE_v at the emitter P-a-Si:H/c-Si interface in double N-c-Si HIT solar cells. ΔE_c is held constant at 0.22eV.

Table 10 indicates that for valence band offsets up to 0.51 eV, and E_{ac} (P) ≤ 0.3 eV, the FF is high, indicating that the majority of the holes photo-generated inside the c-Si wafer, can surmount the positive field barrier due to the a-Si/ c-Si valence band discontinuity by

thermionic emission and get collected at the front ITO/ P-a-Si:H contact. However solar cell performance deteriorates both with increasing band gap and increasing E_{ac} of the P-layer. The latter is only to be expected as it reduces the built-in potential.

Fig. 12 (a) shows the effect on the energy band diagram of increasing the P-layer band gap (therefore of increasing ΔE_v, since ΔE_c is held constant) and the activation energy. Increasing ΔE_v at the P-a-Si:H/N-c-Si interface results in hole accumulation and therefore a fall in FF for $\Delta E_v \geq 0.56$ eV, for a P-layer activation energy of ~0.3 eV, due to the reverse field it generates; that is further accentuated when E_{ac} is high (Table 10). van Cleef et al (1998 a,b) have also shown that for a P-layer doping density of 9×10^{18} cm^{-3} (same as ours – Table 3, giving $E_{ac} = 0.3$ eV) and for $\Delta E_v = 0.43$ eV, normal J-V characteristics are achieved at room temperature and AM1.5 illumination, and that "S-shaped" characteristics begin to develop at higher ΔE_v and E_{ac}. In our case, for $\Delta E_v \geq 0.60$ eV, Fig. 12(c) indicates that free holes accumulate over the entire c-Si wafer, resulting in a sharp reduction of the electric field and flat bands over the depletion region, on the side of the N-type c-Si wafer (Fig. 12b). This fact results in a sharp fall in the FF and conversion efficiency (Table 10). In fact under this condition, the strong accumulation of holes on c-Si, can partially deplete even the highly defective P-layer, resulting in a shift of the depletion region from c-Si to the amorphous emitter layer (Fig. 12a). This also means that the carriers can no longer be fully extracted at 0 volts, resulting in a fall in J_{sc} (Table 10). We have found that the current recovers to the normal value of ~36 mA cm^{-2} only at a reverse bias of 0.3volts (Datta et al, 2010). Modeling indicates that for improved performance of N-c-Si HIT cells, the valence band offset has to be reduced by a lower emitter band gap, unless the tunneling of holes exists.
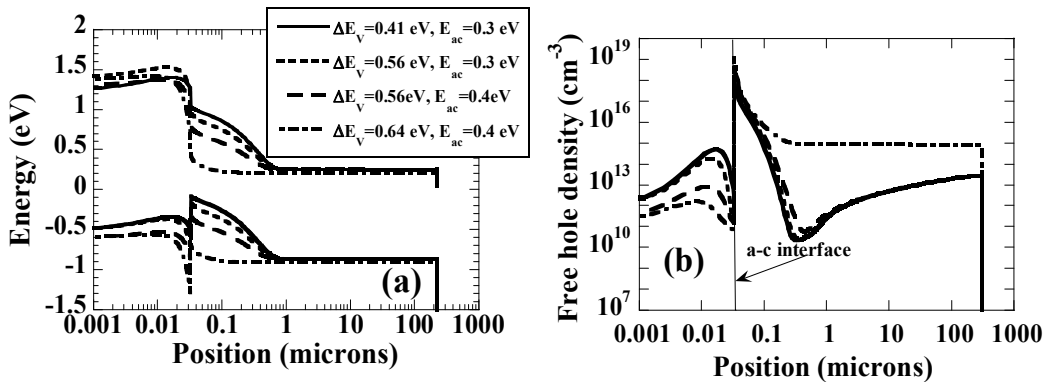
Fig. 12. Variation of (a) the band diagram under AM1.5 light and 0 volts and (b) the free hole population under the same conditions, as a function of position in the N-c-Si HIT device for different valence band discontinuities (ΔE_v) and activation energies (E_{ac}) of the emitter layer.

6.2 Sensitivity of the solar cell output to the front contact barrier height.

The front TCO/P-a-Si:H contact barrier height, ϕ_{b0} in N-type HIT cells is determined by the following expression:-

$$\phi_{b0} = E_\mu(P) - E_{ac}(P) - sbb ,\qquad\qquad (3)$$

where $E_\mu(P)$ and $E_{ac}(P)$ represent respectively the mobility band gap and the activation energy of the P-layer, and 'sbb' is the surface band bending due to a Schottky barrier at the TCO/P interface. With a change of the work function of the TCO, it is this 'sbb' that varies. In this section we study the dependence of the solar cell output to changes in this surface band bending. We hold the band gap and the activation energies of the P-layer constant at 1.75 eV and 0.3 eV respectively, so that the TCO work function has a direct effect on the front contact barrier height. The results are summarized in Fig. 15. For these sensitivity calculations we have chosen the thickness of the P-layer to be 15 nm (Rahmouni et al, 2010). Fig. 13 indicates that both V_{oc} and FF fall off for $\Phi_{b0} \leq 1.05$ eV.

We have also studied the effect of changing the rear P-a-Si:H BSF/TCO barrier height, ϕ_{bL}, in P-c-Si HIT cells. The variation in the current-density – voltage characteristics follow a similar pattern as Fig. 15.
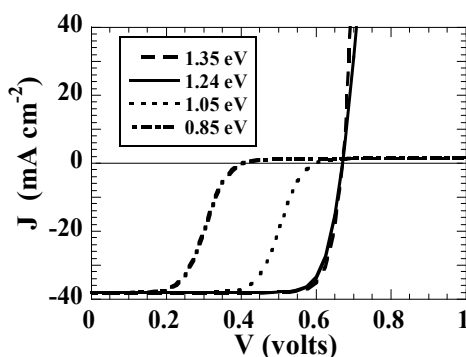
Fig. 13. The current density - voltage characteristics under AM1.5 light and 0 volts for different front contact barrier heights. The band gap, the activation energy and the thickness of the P-layer are held constant at 1.75 eV, 15 nm and 0.3 eV respectively, so that only surface band bending changes.

6.3 Relative influence of different parameters on the performance of HIT cells

In this section we make a comparative study of the influence on HIT cell performance, of the N_{ss} on the surface of the c-Si wafer, the lifetime (τ) of the minority carriers in c-Si, and the surface recombination speeds (SRS) of free carriers at the contacts. The sensitivity to the first two is shown in Table 11. For all the cases studied here, the P layer has an activation energy of 0.3 eV and a surface band bending 0.21 eV.

We note that when the defect density on the surfaces of the c-Si wafer is low, there is some sensitivity of the solar cell output to τ. In fact the conversion efficiency increases by ~3.22% and ~2.47% in double P-c-Si and N-c-Si HIT cells respectively as τ varies from 0.1 ms to 2.5 ms. By contrast there is a huge sensitivity to N_{ss}, as already noted in sections 4.2, 4.3 and 5.3; the performance of the HIT cell depending entirely on this quantity when it is high, with no sensitivity to τ (Table 11). The lone exception is the N_{ss} on the rear face of N-c-Si, to which solar cell output is relatively insensitive as already noted

Finally, the minority carrier SRS at the contacts, that regulates the back diffusion of carriers, has only a small influence in these double HIT cells. The majority carrier SRS does not affect cell performance up to a value of 10^3 cm/s, except the SRS of holes at the contact that is the

| Type | N_{ss} (cm^{-2}) | | τ | J_{sc} | V_{oc} | FF | η |
	Front	Rear	(ms)	(mA cm^{-2})	(mV)		(%)
P-c-Si	4×10^{11}	10^{11}	0.1	36.22	604	0.794	17.37
			0.5	36.61	649	0.808	19.19
			2.5	36.68	687	0.817	20.59
	3×10^{13}	10^{11}	0.5	37.24	472	0.626	11.00
			2.5	37.17	471	0.626	10.96
	4×10^{11}	3×10^{13}	0.5	5.68	572	0.154	0.50
			2.5	5.59	572	0.153	0.49
N-c-Si	4×10^{11}	10^{11}	0.1	38.39	631	0.767	18.58
			0.5	39.03	658	0.783	20.13
			2.5	39.20	678	0.792	21.05
	3×10^{13}	10^{11}	0.5	11.54	537	0.208	1.29
			2.5	11.58	537	0.207	1.29
	4×10^{11}	3×10^{13}	0.5	37.04	615	0.763	17.39
			2.5	37.08	616	0.763	17.44

Table 11. Sensitivity of double HIT solar cell output parameters to N_{ss} on the front and rear surfaces of the c-Si wafer and minority carrier life-time (τ).

hole-collector. Hole collection (at the rear contact in P-c-Si HIT and at the front in N-c-Si HIT) is already somewhat impeded by the large valence band discontinuity at the amorphous/ crystalline interface and the lower mobility of holes relative to electrons; hence a low value of SRS of holes at the contacts is expected to have a disastrous influence on hole collection. The effect of lowering S_{p0} for N-c-Si HIT cells is shown in Fig. 14, and is seen to lead to S-shaped J-V characteristics with a sharp fall in the FF when reduced to $\leq 10^4$ cm/sec. In fact when sputtering ITO onto c-Si substrates coated with a-Si:H (intrinsic and doped) films, we sometimes obtain a rather degraded P/ITO interface, where the surface recombination speed is probably reduced. Therefore, Fig. 14 indicates that ITO deposition conditions can also be critical for good solar cell performance.
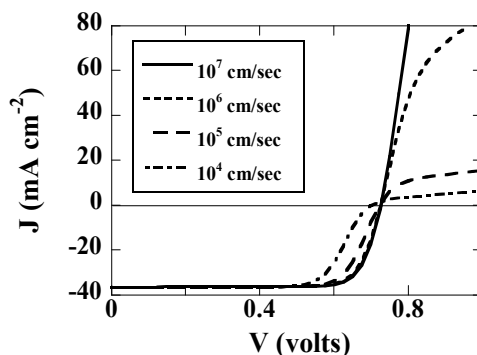
Fig. 14. The sensitivity of the illuminated J-V characteristic under AM1.5 light and short-circuit condition, to the surface recombination speed of the holes at the ITO/P front contact.

7. Conclusions

We have studied the performance of HIT cells on P-and N-type c-Si wafers, using detailed computer modeling. In order to arrive at a realistic set of parameters that characterize these cells, we have modeled several experimental results. We find that the major breakthroughs in improving the performance of these cells having textured N-type c-Si as the absorber layer, come from the introduction of an amorphous BSF layer, by passivating the defects on the c-Si wafer surface and, to a lesser extent, by improving the lifetime of the minority carriers in the c-Si wafer (Table 6).

Modeling indicates that both types of HIT cell output is very sensitive to the defects on the surface of the c-Si wafer, and good passivation of these defects is the key to attaining high efficiency in these structures. An exception to this rule is the defects on the rear face of c-Si in N-type HIT cells, to which there is not much sensitivity. The amorphous/crystalline valence band discontinuity also has a strong impact. In particular, large ΔE_v at the emitter P-a-Si:H/N-c-Si contact leads to S-shaped J-V characteristics, unless tunneling of holes takes place; while that at the P-c-Si/P-BSF contact reduces the FF in double P-c-Si HIT cells. It is for this reason that a transition from a front to double HIT structure on P-c-Si does not produce the spectacular improvement observed for N-type HIT cells (Table 6). Solar cell output is also influenced to some extent by the minority carrier lifetime in c-Si. In Table 12 we compare the performance of a P-type and an N-type HIT cell, with low N_{ss} on the wafer surface, and realistic input parameters. We find that the N-type HIT cell shows better performance than a P-c-Si HIT cell with a higher V_{oc} and conversion efficiency, because of a higher built-in potential in the former. However, the fill factor of N-c-Si HIT cells is lower than in P-type HIT cells due to the assumption of $\Delta E_v > \Delta E_c$, resulting in the holes facing more difficulty in getting collected at the front contact in the former case. This fact has also been pointed out by other workers (Stangl et al, 2001, Froitzheim et al, 2002). In P-type HIT cells, the electrons are collected at the front contact and have to overcome the relatively low ΔE_c at the crystalline/amorphous interface so that its FF is higher than in N-c-Si HIT.

Type	J_{sc} (mA cm^{-2})	V_{oc} (mV)	FF	η (%)
Double HIT on P-c-Si	37.76	694	0.828	21.72
Double HIT on N-c-Si	38.89	701	0.814	22.21

Table 12. Comparison of the performance of P-type and N-type double HIT cells, with optimized parameters. The life time of minority carriers in the c-Si wafer in both cases is 2.5 ms and its doping 10^{16} cm^{-3}.

8. Acknowledgements

9. References

Arch, J. K.; Rubinelli, F. A.; Hou, J. Y. and Fonash, S. (1991) Computer analysis of the role of p-layer quality, thickness, transport mechanisms, and contact barrier height in the performance of hydrogenated amorphous silicon p-i-n solar cells, *Journal of Applied Physics* Vol.69, No. 10(May, 1991) pp 7057 -7066, ISSN 0021-9979.

Basore, P. A. (1990), Numerical modeling of textured silicon solar cells using PC-1D IEEE Transaction on Electron Devices, Vol 37, No. 2 (February, 1990) pp. 337 – 343, ISSN 0018-9383 .

Clugston, D.A and Basore P. A. (1997), PC1D version 5: 32-bit solar cell modeling on personal computers, *Proceedings of 26th IEEE Photovoltaic Specialists Conference,* pp. 207- 201, ISBN: 0-7803-3767-0, Anaheim, USA, 1997, September 29-October 3.

Chatterjee, P. (1992), Computer modeling of the dependence of the J-V characteristics of a-Si:H solar cells on the front contact barrier height and gap state density, Technical Digest of International PVSEC-6, New Delhi, India, Feb. 10-14 (1992) pp 329-334.

Chatterjee P. (1994), Photovoltaic performance of a-Si:H homojunction p-i-n solar cells: A computer simulation study, *Journal of Applied Physics* , Vol 76 No.2 (July, 1994) pp 1301-1313, ISSN 0021-9979.

Chatterjee, P. (1996), A computer analysis of the effect of a wide-band-gap emitter layer on the performance of a-Si:H-based heterojunction solar cells, *Journal of Applied Physics*, Vol 79, No 9 (May, 1996) pp 7339-7347, ISSN (print) 0021-9979.

Chatterjee, P.; Leblanc, F.;Favre; M. and Perrin, J. (1996), A global electrical-optical model of thin film solar cells on textured substrates, *Mat. Res. Soc. Symp. Proc.* 426 (1996) pp 593-598.

Datta A., Damon-Lacoste J., Roca i Cabarrocas P., Chatterjee P. (2008), Defect states on the surfaces of a P-type c-Si wafer and how they control the performance of a double heterojunction solar cell, *Solar energy Materials and Solar Cells*, Vol 92 (August, 2008) pp 1500-1507, ISSN 0927-0248.

Datta, A.; Damon-Lacoste, J.; Nath, M.; Roca i Cabarrocas, P. andChatterjee P. (2009), Dominant role of interfaces in solar cells with N-a-Si:H/P-c-Si heterojunction with intrinsic thin layer, *Materials Science and Engineering B,* Vol 15-160 (2009), 10-13.

Datta, A.; Rahmouni, M.; Nath, M.; Boubekri, R.; RocaiCabarrocas, P. and Chatterjee, P. (2010) , Insights gained from computer modeling of heterojunction with instrinsic thin layer ''HIT'' solar cells, *Solar energy Materials and Solar Cells,* Vol 94, (April, 2010) pp 1457-1462, ISSN 0927-0248.

Damon-Lacoste J., Ph. D Thesis, Ecole Polytechnique Paris, 2007.

Dauwe, S; Schmidt, J. and Hezel, R.,2002, Very low surface recombination velocities on p- and n-type silicon wafers passivated with hydrogenated amorphous silicon films, *Proceedings of 29th IEEE Photovoltaic Specialists Conference*, pp.1246 – 1249, ISBN 0-7803-7471-1, New Orleans, USA, 2002, May 19-24.

Froitzheim, A.; Stangl, R.; Elstner, L.; Schmidt, M. and Fuhs, W. (2002), Interface recombination in amorphous/crystalline silicon solar cells, a simulation study, Proceedings *of 29th IEEE Photovoltaic Specialists' Conf.*,19-24 May (2002), New Orleans, USA, pp. 1238-1241.

Fuhs, W.; Niemann, K. and Stuke, J. (1994), Heterojunctions of amorphous silicon and silicon single crystals, *AIP Conference Proceedings,* Vol 20 (May 1974) pp 345-350.

Fujiwara, H.; Sai, H. and Kondo M. (2009), Crystalline Si Heterojunction Solar Cells with the Double Heterostructure of Hydrogenated Amorphous Silicon Oxide, *Japanese Journal of Applied Physics* Vol 48 (June 2009) pp 064506 -1-4, ISSN 0021-4922.

Guha, S.; Yang, J.; Pawlikiewicz, A.; Glatfelter, T., Ross, R. and Ovshinsky, S. R . (1989), Band-gap profiling for Improving the efficiency of amorphous silicon alloy solar cells Applied Physics Letters Vol 54, No 23 (June 1989) pp 2330-2332, ISSN 0021-8979.

Hack, M. and Schur, M (1985)., Physics of amorphous silicon alloy p-I-n solar cells, *Journal of Applied Physics,* Vol 58 (1985) pp 997-1020, ISSN 0021-8979.

Kanevce, A. and Metzger W. K. (2009), The role of amorphous silicon and tunneling in heterojunction with intrinsic thin layer (HIT) solar cells, *Journal of Applied Physics*, Vol 105, No. 9, (May,2009), pp. 094507-1-7, ISSN 0021-8979.

Leblanc, F.; Perrin, J. and Schmitt, J. (1994), Numerical modeling of the optical properties of hydrogenated amorphous-silicon-based p-i-n solar cells deposited on rough transparent conducting oxide substrate, *Journal of Applied Physics* Vol 75, No.2 (January 1994) pp 1074-1087, ISSN 0021-8979.

Maruyama, E.; Terakawa, A.; Taguchi, M.; Yoshimine, Y.; Ide, D.; Baba, T.; Shima, M.; Sakata, H. and Tanaka, M. (2006), *Sanyo's Challenges to the Development of High-efficiency HIT Solar Cells and the Expansion of HIT Business, Proceedings 4th World Conf. on Photovoltais Solar Energy Conversion,* Hawaii, USA, 9-12 May (2006).

McElheny, P.; Arch, J. K.; Lin, H.-S. and Fonash, S., Range of validity of the surface-photovoltage diffusion length measurement: A computer simulation *Journal of Applied Physics*, Vol 64 No. 3 (August 1988) pp 1254-1265, ISSN 0021-8979.

Meier, D.L.; Page, M.R.; Iwaniczko, E.; Xu, Y.; Wang, Q. and Branz, H.M. (2007), Determination of surface recombination velocities for thermal oxide and amorphous silicon on float zone silicon, *Proceedings of the 17th Workshop on Crystalline Silicon Solar Cells and Modules*, pp.214-217, Vail, CO, USA, 2007.

Nath, M; Chatterjee, P.; Damon-Lacoste, J. and Roca i Cabarrocas, P. (2008), Criteria for improved open-circuit voltage in *a*-Si:H(*N*)/*c*-Si(*P*) front heterojunction with intrinsic thin layer solar cells, *Journal of Applied Physics* , Vol 103 (February, 2008) pp 034506-1-9, ISSN 0021-8979.

Olibet, S.; Vallat-Sauvain E.; Fesquet, L.; Monachon, C.; Hessler-Wyser, A.; Damon-Lacoste, J.; De Wolf, S. and Ballif, C. (2010), Properties of Interfaces in Amorphous/Crystalline Silicon Heterojunctions, *Physics Status Solidi A,* Vol 207, No. 3 (January, 2010)pp 651–656, ISSN 1862-6300.

Olibet, S.; Vallat-Sauvain, E. and Ballif, C. (2007), Model for a-Si:H/c-Si interface recombination based on the amphoteric nature of silicon dangling bonds, *Physical Review B*, Vol 76, No 3, (July, 2007), pp 035326-1 – 14, ISSN 1098-0121.

Osuda, K.; Okamoto, H. and Hamakawa, Y. (1983), Amorphous Si/Polycrystalline Si stacked solar cells having more than 12% conversion efficiency,*Japanese Journal of Applied Physics*, Vol 22, No.9 (September, 1983), pp. L605-L607, ISSN 0021-4922

Palit, N.; and Chatterjee, P. (1998), A computer analysis of double junction solar cells with a-Si : H absorber layers, *Solar Energy Materials & Solar Cells* , Vol 53 (1998), pp. 235-245, ISSN 0927-0248.

Plá, J.; Tamasi, M.; Rizzoli, R.; Losurdo, M.; Centurioni, E.; Summonte, C. and Rubinelli, F.(2003), Optimization of ITO layers for applications in a-Si/c-Si heterojunction

solar cells , *Thin Solid Films,* Vol 425, No 1-2, (February 2003) pp. 185-192, ISSN 0040-6090.

Rahmouni, M.; Datta, A.; Chatterjee, P.; Damon-Lacoste, J.; Ballif, C. and Roca i Cabarrocas, P. (2010), Carrier transport and sensitivity issues in heterojunction with intrinsic thin layer solar cells on N-type crystalline silicon: A computer simulation study *Journal of Applied Physics,* Vol 107, No 5, (March, 2010) pp. 054521-1-14, ISSN 0021-8979.

Sakata, H.; Nakai, T.; Baba, T.; Taguchi, M.; Tsuge, S.; Uchihashi, K. and S. Kyama (2000), 20.7% highest efficiency large area (100.5 cm²) HITTᴹ cell, *Proceedings 28th IEEE Photovoltaic Spealist conference*, pp. 7-12, ISBN 0-7803-5772-8, Anchoorage, Alaska, 2000 September 15 -22.

Sawada, T.; Terada, N.; Tsuge, S.; Baba, T.; Takahama, T.; Wakisaka, K.; Tsuda, S. and Nakano S. (1994), High-efficiency a-Si/c-Si heterojunction solar cell, *Proceedings 1st World Conference on Photovoltaic Solar Energy Conversion*, pp.1219-1226, ISBN 0-7803-1460-3, Hawaii, USA, 1994, December 5-9.

Schmidt, M.; Korte, L.; Laades, A.; Stangl, R.; Schubert, Ch.; Angermann, H.; Conrad, E. and Maydell, K. V. (2007), Physical aspects of a-Si:H/c-Si hetero-junction solar cells , *Thin Solid Films*, Vol 515, No. 19 (July, 2007) pp. 7475-7480, ISSN 0040-6090.

Schmidt, M.; Angermann, H.; Conrad, E.; Korte, L.; Laades, A.; Maydell, K. V.; Schubert, Ch. and Strangl, R. (2006), Physical and Technological Aspects of a-Si:H/c-Si Hetero-Junction Solar Cells, *Proceedings of 4th World Conference on Photovoltaic Energy Conversion*, pp. 1433-1438, ISBN 1-4244-0017-1, Hawaii, USA, 2006, May, 7-12.

Sritharathikhun, J.; Yamamoto, H.; Miyajima, S.; Yamada, A. and Konagai, M. (2008), Optimization of Amorphous Silicon Oxide Buffer Layer for High-Efficiency p-Type Hydrogenated Microcrystalline Silicon Oxide/n-Type Crystalline Silicon Heterojunction Solar Cells, *Japanese Journal of Applied Physics*, Vol 47, No. 11, (November, 2008) pp. 8452-8455, ISSN 1347-4065.

Smole, F. and Furlan J. (1992), Effects of abrupt and graded a-Si:C:H/a-Si:H interface on internalproperties and external characteristics of p-i-n a-Si:H solar cells, *Journal of Applied Physics*, Vol 72, No. 12, (September, 1992) pp. 5964-5969, ISSN 0021-8979.

Stangl, R.; Froitzheim, A.; Elstner, L. and Fuhs, W. (2001), Amorphous/crystalline silicon heterojunction solar cells, a simulation study, *Proceedings of 17th European Photovoltaic Solar Energy Conference*, pp. 1387-1390, ISBN 3-936338-07-8, Munich, Germany, 2001, October 22-26.

Sze, S.M. (1981), *Physics of Semiconductor Devices* (2nd Edition),John Wiley & Sons, ISBN 9971-51-266-1.

Taguchi, M., Sakata, H.; Yoshihiro, Y.; Maruyama, E.; Terakawa, A.; Tanaka, M. and Kiyama, S. (2005), An approach for the higher efficiency in the HIT cells, *Proceedings of 31st IEEE Photovoltaic Specialists Conference*, pp.866 – 871, ISBN 0-7803-8707-4, Lake Buena Vista, FL, 2005, January 3-7.

Taguchi, M.; Maruyama, E. and Tanaka, M., Temperature Dependence of Amorphous/Crystalline Silicon Heterojunction Solar Cells, *Japanese Journal of Applied Physics* , Vol 47, (February, 2008), pp. 814-817, ISSN 0021-4922.

Takahama, T.; Taguchi, M.; Kuroda, S., Matsuyama, T.; Tanaka, M.; Tsuda, S.; Nakano, S. and Kuwano, Y. (1992), High efficiency single- and polycrystalline silicon solar cells

using ACJ-HIT structure,*Procdings of 11th European Photovoltaic Solar Energy Conference*, pp. 1057-1062, Montreux, Switzerland, 1992, October 12-16.

Tanaka, M.; Taguchi, M.; Matsuyama, T.; Sawada, T.; Tsuda, S.; Nakano, S.; Hanafusa, H. and Kuwano, Y. (1992), Development of New a-Si/c-Si Heterojunction Solar Cells: ACJ-HIT (Artificially Constructed Junction-Heterojunction with Intrinsic Thin-Layer), *Japanese Journal of Applied Physics*, Vol 31, (November 1992), pp. 3518-3522, ISSN 0021-4922.

Tanaka, M.; Okamoto, S.; Tsuge, S. and Kiyama, S. (2003), Development of hit solar cells with more than 21% conversion efficiency and commercialization of highest performance hit modules, *Proceedings of 3rd World Conference on Photovoltaic Energy Conversion*, Vol 1, pp. 955–958, ISBN 4-9901816-0-3, Osaka. Japan, 2003, May 11-18.

Tchakarov S., Roca i Cabarrocas P., Dutta U., Chatterjee P. and Equer B., Experimental study and modeling of reverse-bias dark currents in PIN structures using amorphous and polymorphous silicon, *Journal of Applied Physics*, Vol 94, No. 11, (December, 2003) , pp. 7317-7327. ISSN (print) 0021-8979.

van Cleef, M. W. M.; Schropp, R. E. I. and Rubinelli, F. A. (1998a), Significance of tunneling in *p+* amorphous silicon carbide *n* crystalline silicon heterojunction solar cells, *Applied Physics Letters,* Vol 73, No 18, (November, 1998), pp. 2609-2611, ISSN 0003-6951.

van Cleef, M. W. M.; Rubinelli, F. A.; Rizzoli, R.; Pinghini, R.; Schropp, R. E. I. and. van der Weg, W. F. (1998b), Amorphous Silicon Carbide/Crystalline Silicon Heterojunction Solar Cells: A Comprehensive Study of the Photocarrier Collection, *Japanese Journal Applied Physics*, Vol 37, (July, 1998), pp. 3926-3932, ISSN 1347-4065.

Veschetti, Y.; Muller, J.-C.; Damon-Lacoste, J.; Roca i Cabarrocas, P.; Gudovskikh, A. S.; Kleider, J.-P.; Ribeyron, P.-J and Rolland, E. (2006), Optimisation of amorphous and polymorphous thin silicon layers for the formation of the front-side of heterojunction solar cells on p-type crystalline silicon substrates, *Thin Solid Films*, Vol 511-512, (July, 2006), pp. 543-547, ISSN 0040-6090.

von der Linden M. B., Schropp R. E. I., van Sark W. G. J. H. M., Zeman M., Tao G. and Metselaar J. W., The influence of TCO texture on the spectral response of a-Si:H solar cells, *Proceedings of 11th European Photovoltaic Solar Energy Conference*, pp. 647 Montreux, Switzerland, 1992, October 12-16.

Wang, Q.; Page, M.; Yan, Y. and Wang, T. (2005), High-throughput approaches to optimization of crystal silicon surface passivation and heterojunction solar cells, *Proceedings of the 31st IEEE Photovoltaic Specialists Conference*, pp.1233-1236, ISBN 0-7803-8707-4, Orlando, FL, USA, 2005, January 3-7.

Wang, Q.; Page, M.R.; Iwaniczko, E.; Xu, Y.Q.; Roybal, L.; Bauer, R.; To, B.; Yuan, H.C.; Duda, A. and Yan, Y.F., Crystal silicon heterojunction solar cells by hot-wire CVD, *Proceedings of the 33rd IEEE Photovoltaic Specialists Conference*,pp 1-5, ISBN: 978-1-4244-1640-0, San Diego, CA, USA, 2008, May 11-16.

Wang, Q.; Page, M. R.; Iwaniczko, E.; Xu, Y.; Roybal, L.; Bauer, R.; To, B.; Yuan, H.-C.; Duda, A.; Hasoon, F.; Yan, Y. F.; Levi, D.; Meier, D.; Branz Howard, M. and Wang, T. H. (2010), Efficient heterojunction solar cells on *p*-type crystal silicon wafers, *Applied Physics Letters*, Vol 96, No. 1, (January, 2010), pp. 013507-1-3, ISSN 0003-6951.

Zeman, M.; van Swaaij, R. A. C. M. M.; Metselaar, J. W. and Schropp, R. E. I. (2000), Optical modeling of *a*-Si:H solar cells with rough interfaces: Effect of back contact and

interface roughness, *Journal Applied Physics* , Vol 88, No. 11 (December, 2000) pp. 6436-6443, ISSN 0021-8979.

News release by SANYO on 22nd May, 2009, SANYO Develops HIT Solar Cells with World's Highest Energy Conversion Efficiency of 23.0%.
< http://panasonic.net/sanyo/news/2009/05/22-1.html>.

Fabrication of the Hydrogenated Amorphous Silicon Films Exhibiting High Stability Against Light Soaking

Satoshi Shimizu[1,2], Michio Kondo[1] and Akihisa Matsuda[3]
[1]Research Center for Photovoltaics, National Institute of Advanced Industrial Science and Technology
[2]Max-Planck-Institut für extraterrestrische Physik
[3]Graduate School of Engineering Science, Osaka University
[1,3]Japan
[2]Germany

1. Introduction

A hygrogenated amorphous silicon (a-Si:H) thin film solar cell was first reported in 1976 [Carlson, & Wronski, 1976]. Since then, intensive works have been carried out for the improvement of its performances. Attempt to increase the conversion efficiencies of the thin film solar cells, a multi junction solar cell structure was proposed and has been investigated [Yang et al., 1997; Shah et al., 1999; Green, 2003; Shah et al., 2004]. It consists of the intrinsic layers having different optical bandgaps in order to absorb the sunlight efficiently in a wide spectrum range.

The density of photo-generated carriers is determined by the light absorption coefficient and the defect density of a material. The absorption coefficient of a-Si:H in a visible light region is one order magnitude higher than that of μc-Si:H due to the direct transition phenomenon. Therefore, a thin a-Si:H layer absorbs sufficient photons. This is a huge advantage for the thin film based solar cell technology in which mass production should be definitely taken into account.

However, a-Si:H has another aspect known as a Staebler-Wronski effect, i.e., the number of unpaired Si dangling bonds increases with light soaking, which lowers photocarrier density by decreasing carrier lifetime [Staebler & Wronski, 1977]. Indeed, conversion efficiencies of a-Si:H based solar cells deteriorate generally by 15-20 % due to this phenomenon. On the other hand, it is possible to suppress this deterioration to some extent by reducing a film thickness of a-Si:H with efficient light-trapping structures [e.g., Müller et al., 2004]. Indeed, the fabrication of the highly stabilized a-Si:H single junction solar cell by the precise optimizations of the optical properties and the i-layer thickness has been reported [Borrello et al., 2011]. Besides those intensive efforts, establishing the technique for fabricating highly stable a-Si:H films is essentially very important to extract its maximum potential for the solar cell applications.

Phenomenologically, a good correlation is observed between degradation ratio of a-Si:H and its hydrogen concentration, namely Si-H$_2$ bond density where a low Si-H$_2$ bond density film exhibits high stability [Takai et el., 2000]. Although the detailed microscopic model for explaining this correlation has not been revealed yet, the tendency is observed in the films prepared under the wide range of fabrication conditions [Nishimoto et al., 2002]. One of the methods to reduce a hydrogen concentration is to increase a substrate temperature. However, a high processing temperature results in increasing initial defect density. Additionally, it is preferable to use the processing temperature of around or less than 200 ^{o}C from the viewpoint of low cost fabrications. Reducing Si-H$_2$ bond density without increasing a substrate temperature is one of the key issues for the fabrication of stable a-Si:H films.

In a chemical vapor deposition process, there are mainly two steps to be considered, i.e., 1) gas phase reactions and 2) surface reactions. In the first step, depending on the electron temperature in a silane plasma, several types of precursors are generated, and they play an important role on the properties of resulting films [Matsuda, 2004]. For example, the a-Si:H films prepared under a powder rich gas condition have very high initial defect densities, namely at the low substrate temperatures [e.g., Roca i Cabarrocas, 2000]. Those powders or so-called higher-ordered silane radicals are created by the insertion reactions of SiH$_2$ radicals produced generally under a high electron temperature condition in a silane plasma. This insertion reaction is a rapid process. The SiH$_2$ radicals are created even under a relatively low electron temperature condition because it is statistically difficult to eliminate only high energy electrons from the system. A higher-ordered silane radical causes a steric hindrance and inhibits short range-ordered sp^3 bond formations on the film growing surface. For example, it is observed that the Si-H$_2$ bond density in the film, which has correlation with light-induced degradation of a-Si:H, increases when the density of the higher-ordered silane radicals in a gas phase is high [Takai et al., 2000].

In this work, to study the effect of precursors in a gas phase on the properties of the resulting film, a triode deposition system is applied for the growth of a-Si:H films where a mesh is installed between a cathode and a substrate. With such a configuration, a long lifetime radical such as SiH$_3$ mainly contributes to the film growth [Matsuda & Tanaka, 1986]. The properties and the stabilities of the resulting films are evaluated.

2. Fabrication and evaluation methods

The preparations of a-Si:H films were performed using a triode deposition system. Figure 1 shows the schematic of the system. A mesh is placed between the cathode and the substrate scepter in which a heater is mounted. VHF (100 MHz) voltage is applied on the cathode with the 20 sccm of SiH$_4$ gas flow, and a silane plasma is generated between the cathode and the negatively dc-biased mesh. All the films were prepared at 100 mTorr (13.3 Pa). The deposition precursors pass through the mesh and reach to the substrate. The substrate scepter is movable, and the distance between the mesh and the substrate (d_{ms}) is one of the important deposition parameters. The distance between the cathode and the mesh is fixed at 2 cm. In some cases, an additional mesh is installed behind the pre-existing mesh with the distance of 1.5 mm at which no plasma is generated between the two mesh under our conditions. The volume of the chamber is c.a. 1.1×10^4 cm^3, and its base pressure is c.a. 3×10^{-8} Torr. The diameters of the electrodes are 10 cm. As a comparison, a-Si:H films were also

prepared with a conventional diode system where no mesh is installed. In this case, the distance between the cathode and the substrate is fixed at 2 cm.
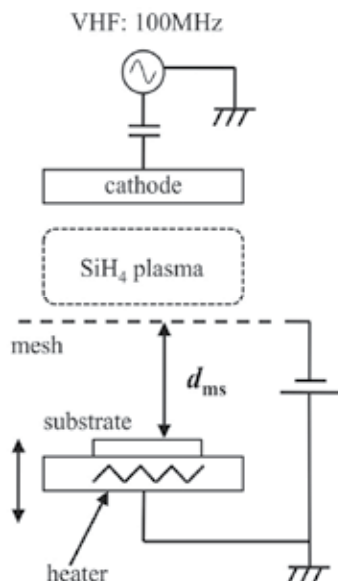
Fig. 1. Schematic of the a-Si:H growth chamber used in this study. A negatively dc-biased mesh is installed between the cathode and the substrate. The distance between the mesh and the substrate (d_{ms}) is adjustable.

The densities of Si–H and Si–H_2 bonds in the resulting film deposited on a intrinsic Si substrate were calculated from the integrated intensities of the stretching modes in a Fourier transform infrared spectroscopy (FTIR) spectrum, where the proportional constants are 9.0×10^{19} cm^2 for Si–H and 2.2×10^{20} cm^2 for Si–H_2, respectively [Langford et al., 1992]. The neutral spin density of the film deposited on a quartz substrate was measured by electron paramagnetic resonance (EPR). To study light-soaking stability of the film, a Schottky diode was fabricated on a phosphorous doped n+Si substrate (0.03 Ωcm) with a half transparent Ni electrode on the top (n+Si/a-Si:H/Ni). The native surface oxide layer on the n+Si substrate was etched with diluted HF solution before the growth of a-Si:H.

A p-i-n structured solar cell (5×5 mm^2) was fabricated in a multi-chamber system. The doped layers were prepared in conventional diode system chambers, and the i-layer was fabricated in a triode system chamber at 180 °C. The distance between the mesh and the substrate is 1.5 cm. The other detailed conditions for the solar cell fabrication are described elsewhere [Sonobe et al., 2006]. The I–V characteristics of the solar cells were measured under an illumination of AM 1.5, 100 mW/cm^2 white light. In every case, the light degradation was performed by illuminating intense 300 mW/cm^2 white light for 6 h at 60 °C.

3. Properties and stabilities of the triode-deposited a-Si:H

3.1 Properties of the a-Si:H films prepared by the triode system
3.1.1 Hydrogen concentration
The hydrogen concentrations of the a-Si:H films prepared by the triode system were measured by FTIR. Figure 2 (a) shows the spectrum of the film prepared at 250 °C with the

distance between the mesh and the substrate, d_{ms}, of 3 cm [Shimizu et al., 2005]. As a comparison, that of the conventionally prepared a-Si:H film at the same substrate temperature is shown in figure 2 (b) [Shimizu et al., 2005]. One can see that the Si-H$_2$ bond density is low in the case of the triode deposition.
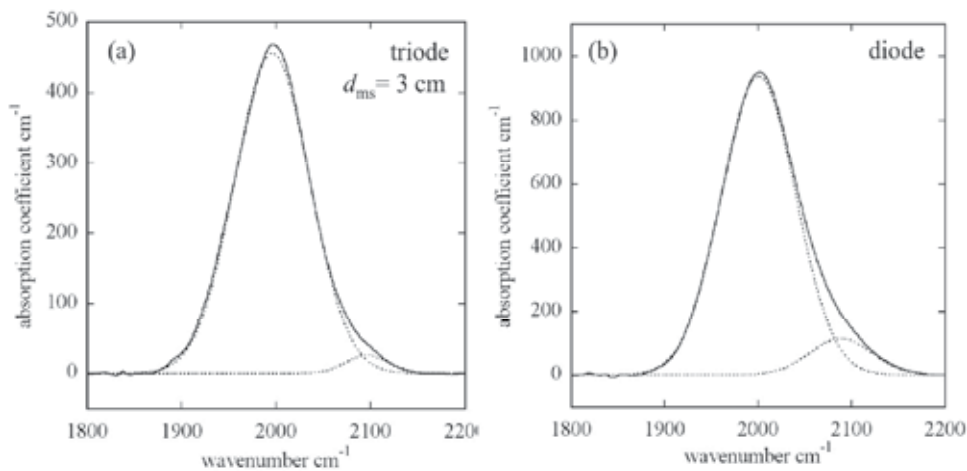
Fig. 2. Si-H and Si-H$_2$ stretching mode absorption spectra obtained in the FTIR measurement. The films were prepared by the: (a) triode system at the d_{ms} of 3 cm, and the (b) conventional diode system. In both cases, the substrate temperatures are 250 ᵒC. [Shimizu et al., 2005]

Furthermore, the a-Si:H films were fabricated with changing d_{ms}, and the results are summarized in figure 3. One can see that, as d_{ms} is increased, both Si-H and Si-H$_2$ densities decrease. The a-Si:H film prepared at d_{ms} = 4 cm contains the Si-H bond density of 4.0 at.% and less than 0.1 at.% (close to the detection limit of FTIR) of Si-H$_2$ bond density. On the other hand, the film prepared by the conventional diode method contains 9.0 at.% of Si-H bonds and 1.5 at.% of Si-H$_2$ bonds at the same substrate temperature. The similar reductions of Si-H and Si-H$_2$ bond densities with the triode system are observed in the films prepared under the several substrate temperatures as shown in figure 3.

3.1.2 Growth of a-Si:H with double mesh

With installing a mesh and increasing d_{ms}, the growth rate is reduced. To see the effect of growth rate on the resulting hydrogen concentration, the films were prepared with installing a second mesh at a fixed VHF input power and d_{ms}. With such a configuration, one can control the growth rate without changing the gas phase conditions, whereas it is not the case if the VHF power or d_{ms} is changed to control the growth rate, because the generation rate of precursors changes with the input power, and as discussed later, d_{ms} affects the flux of the precursors reaching to the substrate. Thus, to see the effect of the growth rate, the double mesh configuration was used.

Here, the films were prepared with or without the second mesh, which is represented as double or a single mesh, respectively. All the films were prepared at 250 ᵒC. The results are summarized in table 1 and figure 4 [Shimizu et al., 2007]. At the VHF power of 10 W, almost the same hydrogen concentrations are observed both in the single and the double mesh
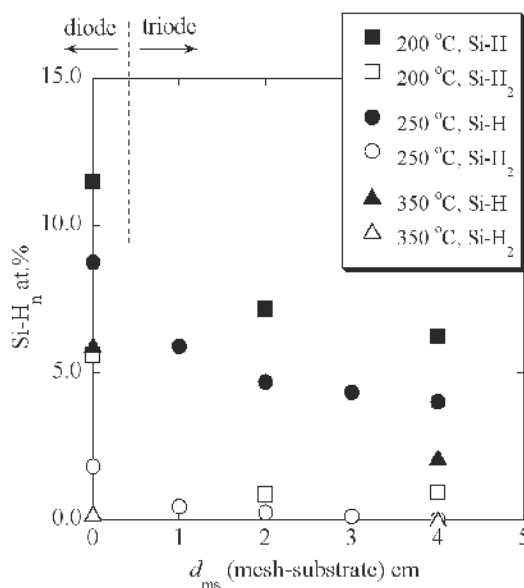
Fig. 3. Si-H and Si-H$_2$ bond densities in the a-Si:H films fabricated with the triode deposition system (triode) under the various distances between the mesh and the substrate (d_{ms}). As a comparison, those of the conventionally prepared films without the mesh are also shown (diode, d_{ms} = 0 cm). The films were prepared at the substrate temperatures of 200, 250 and 350 ºC, respectively.

cases, but the growth rates are different each other where very low growth rate is observed with the double mesh. The growth rate with the double mesh at 10 W is c.a. 0.1 Å/s which is close to the value observed at the VHF power of 2 W with the single mesh. However, the observed Si-H and Si-H$_2$ bond densities are lower in the case of 2 W with the single mesh. The similar trend is observed under the different conditions as shown in figure 4.

input power (W)	mesh	growth rate (Å/s)	Si-H (at.%)	Si-H$_2$ (at.%)
2	single	0.18	4.0	< 0.1
10	double	0.12	6.1	0.9
10	single	0.80	6.6	1.0

Table 1. Si-H and Si-H$_2$ bond densities and the observed growth rate of the films prepared under the several conditions with fixing d_{ms} (= 4 cm) and the substrate temperature (= 250 ºC).

3.1.3 Microscopic structure
In figures 5 (a) and (b), the FWHM of the Si-H and Si-H$_2$ stretching mode peaks in the FTIR spectra are platted against the density of Si-H and Si-H$_2$, respectively. The films were prepared at the VHF input power of 2 or 10 W using the each electrode configuration i.e., triode or diode system as indicated in the figure. The substrate temperature is 250 ºC in every case. While the scattered relation is observed in the Si-H bond case, one can see the good correlation between the Si-H$_2$ bond densities and their FWHMs. Moreover, while
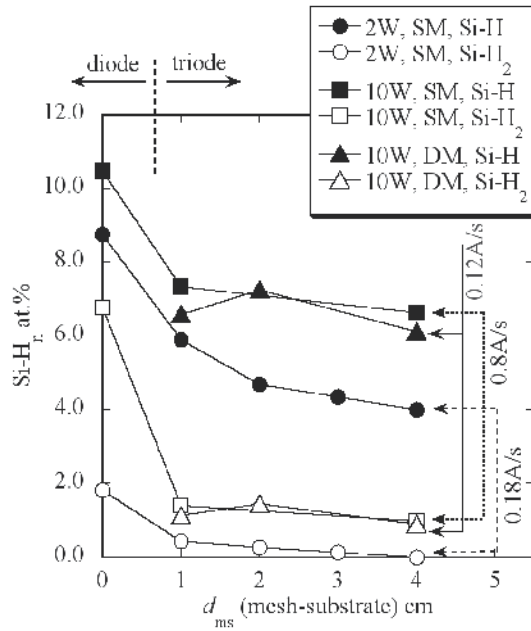
Fig. 4. Si-H and Si-H$_2$ bond densities in the a-Si:H films fabricated under the various conditions. Open and closed circle: VHF = 2 W, with a single mesh (2 W, SM), open and closed square: VHF = 10 W, with a single mesh (10 W, SM), open and closed triangle: VHF = 10 W, with double mesh (10 W, DM). As a comparison, those of the conventionally prepared films without the mesh are also shown (diode, d_{ms} = 0 cm). [Shimizu et al., 2007]
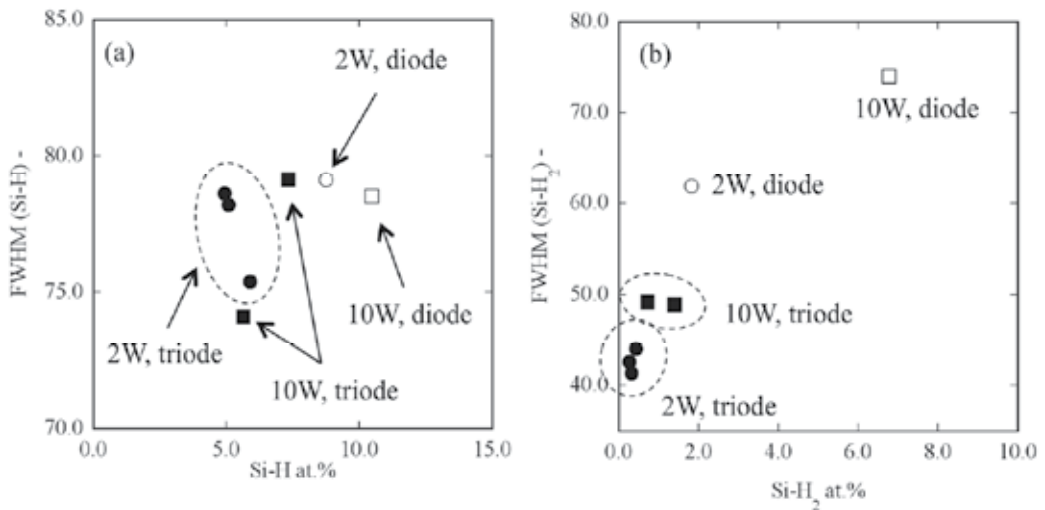
Fig. 5. FWHM of the Si-H and Si-H$_2$ stretching mode peaks in the FTIR spectra platted against the density of Si-H and Si-H$_2$, respectively. The films were prepared at the VHF input power of 2 or 10 W using the each electrode configuration (triode or diode) as indicated.

the FWHM values of the S-H peaks are more or less in the same range, the narrower FWHMs of the Si-H$_2$ peaks are observed in the triode-deposited films. Furthermore, when the electrode configuration is the same (triode or diode), the films prepared at the lower VHF input power exhibit narrower FWHMs of the Si-H$_2$ peaks.

3.1.4 Conductivity

The conductivities of the a-Si:H films fabricated using the triode system are measured. Figure 6 shows the dark and photoconductivities of the films. The photoconductivity was measured under the illumination of 100 mW/cm^2 white light. The observed dark-conductivities are of the order of 10^{-11} S/cm. The deposition rate of the triode system is typically less than 1 Å/s, which may cause unfavorable impurity incorporations during the film growth, causing the reduction of photosensitivity due to the increase of dark-conductivity. The dark-conductivity of the triode-deposited a-Si:H is, however, in the range equivalent to that observed in the diode-deposited film grown at 7.3 Å/s, and the photoconductivities of those films are of the order of 10^{-5} S/cm. The result indicates that the triode-deposited a-Si:H films do not contain substantial number of impurities which deteriorates photosensitivity.
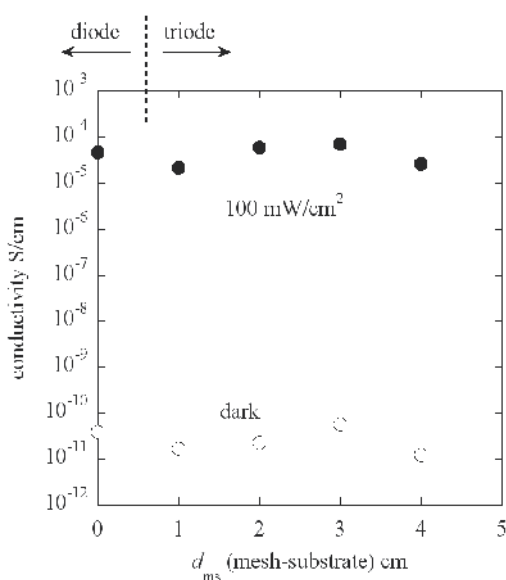
Fig. 6. The dark and photoconductivities of the a-Si:H films prepared either by a triode or a diode deposition system (d_{ms} = 0 cm).

3.2 Stabilities of the triode-deposited a-Si:H films
3.2.1 Spin density

Degradation of the film prepare by the triode system is checked by measuring the change of neutral spin density by light soaking. Figure 7 shows the result [Shimizu et al., 2008]. All the films were prepared at 250 ^{o}C, and as a comparison, the results of the diode-deposited films are also shown. The spin density is plotted against Si-H$_2$ bond density. The initial defect densities are almost the same throughout the samples ($\approx 2 \times 10^{15}$ cm^{-3}). On the other hand,

more stable behaviors are observed in the triode-deposited a-Si:H films in the degraded states. The trend is best seen in the film prepared at the d_{ms} of 4 cm where the lowest Si-H$_2$ bond density is observed as shown in figure 3.
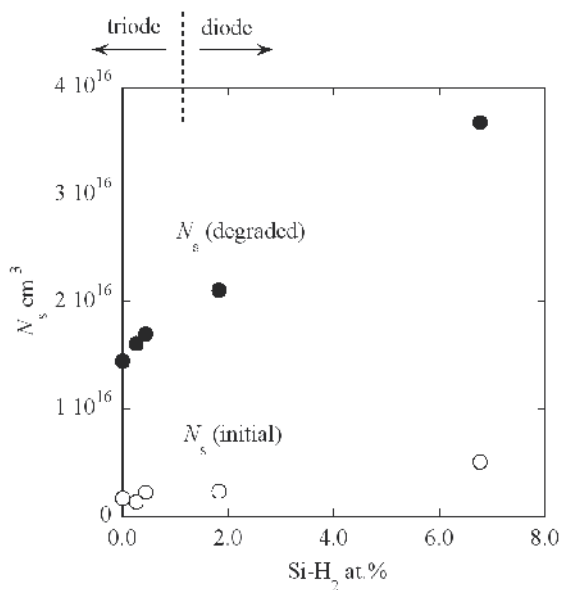
Fig. 7. Change in the neutral spin density (N_s) due to light soaking as a function of Si-H$_2$ bond density in the film. [Shimizu et al., 2008]
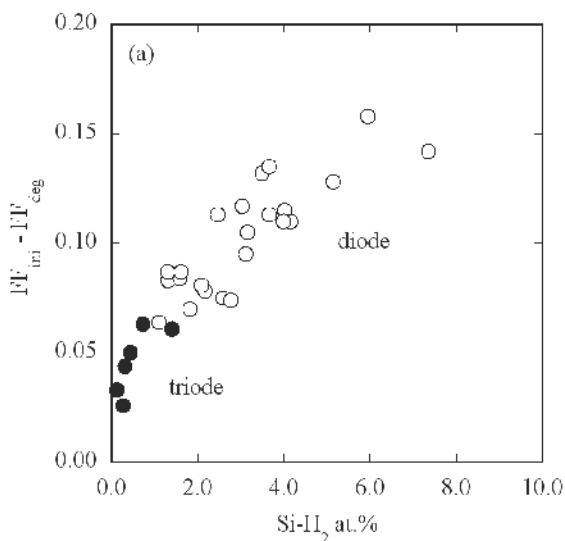
Fig. 8. Light-induced change in the fill-factor ($\Delta FF = FF_{ini} - FF_{deg}$) of the Schottky diode having the intrinsic layer produced at the each condition. Closed circle: triode-deposited film (triode), open circle: conventionally prepared film (diode). [Shimizu et al., 2005]

3.2.2 Schottky diode

Furthermore, the stabilities of the triode-deposited a-Si:H films were studied with fabricating the Schottky diodes where their fill-factor (*FF*) changes were evaluated as a measure of degradation. The intrinsic layer of the Schottky diode was fabricated either by a triode or a diode system under the various conditions. The fill-factors in the initial state (FF_{ini}) are almost the same throughout the samples: 52 - 54 %. On the other hand, the fill-factors in the degraded state (FF_{deg}) are different each other. In figure 8, the change in the fill-factor ($\Delta FF = FF_{ini} – FF_{deg}$) is plotted against Si-H$_2$ bond density [Shimizu et al., 2005]. For comparison, those of the films prepared with the diode system under the various conditions are also shown [Nishimoto et el., 2002]. One can see that the triode-deposited a-Si:H films contain low Si-H$_2$ bond densities, and correspondingly, the observed ΔFFs are low. Note that, the scattered correlation is observed when ΔFFs are plotted against the Si-H densities of the films [Shimizu et al., 2005].

3.2.3 Solar cell

The stability of the triode-deposited a-Si:H is checked with fabricating a p-i-n solar cell where the i-layer is deposited with a triode system. Since a multi chamber was used to prepare the solar cell, the i-layer fabrication conditions including the chamber geometry are different from those used in the previous sections. Especially, the distance between the mesh and the substrate is short as 1.5 cm which lowers the effect of Si-H$_2$ bond elimination than that achieved at larger distances as shown in figure 3. Additionally, the i-layer growth temperature of 180 °C was chosen. Therefore, the Si-H$_2$ bond density in the i-layer is slightly high as indicated in figure 3. On the other hand, we chose this temperature from the viewpoint of the device applications in which low temperature operations are preferable. The i-layer thickness is 250 nm. The I-V characteristic of the solar cell is shown in figure 9 [Sonobe et al., 2006].
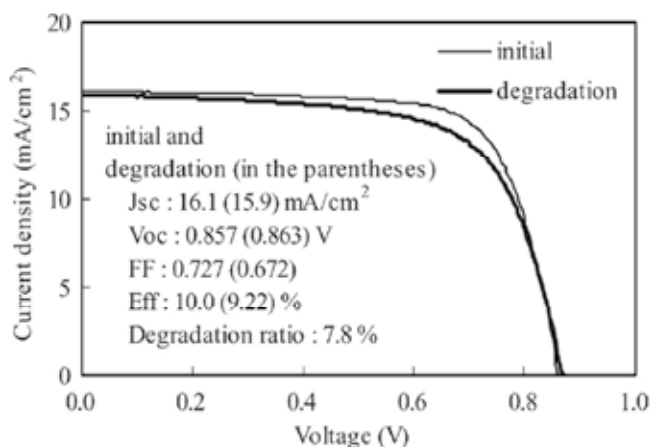
Fig. 9. The I-V characteristic of the p-i-n solar cell. The i-layer was prepared with the triode system at the substrate temperature of 180 °C. The distance between the mesh and the substrate is 1.5 cm. [Sonobe et al., 2006]

The initial conversion efficiency is 10.0 %, and after the light soaking, the stabilized efficiency of 9.2 % is achieved. The degradation ratio is 7.8 % which is the lower value compared with that generally observed in the a-Si:H solar cell prepared by a conventional

method with the same i-layer thickness. While further optimization is necessary to achieve higher stabilized efficiency, the result demonstrates the low degradation ratio of the a-Si:H solar cell with improving the stability of the i-layer itself, which is one of the essential solutions to obtain a stable a-Si:H solar cell.

4. Hydrogen elimination process

4.1 Hydrogen elimination process – post annealing

It is observed that the films grown by the triode system contain very low hydrogen concentrations, namely Si-H_2 bond densities. Those values change with the distance between the mesh and the substrate where the lowest hydrogen concentration is observed at the largest distance between the mesh and the substrate. In this section, we will discuss the possible mechanism for the reduction of Si-H and Si-H_2 bond densities in the triode deposition system.
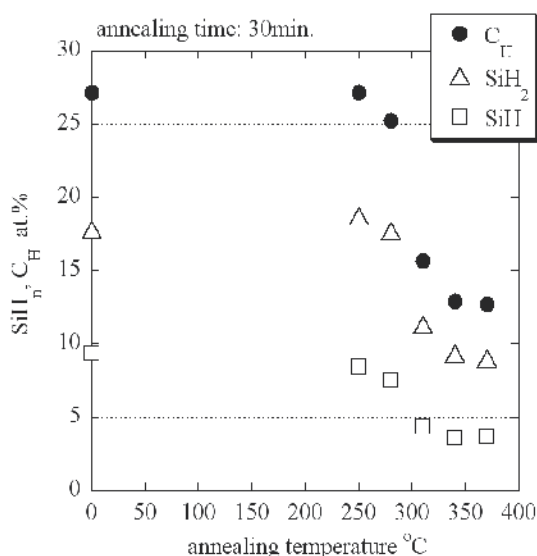
Fig. 10. Thermal effusion of hydrogen from the a-Si:H films deposited at 110 ^{o}C. The C_H is the sum of the Si-H and the Si-H_2 bond densities [Shimizu et al., 2007].

Hydrogen elimination takes place both in a film growth state and in a post annealing state when a substrate temperature is high. To distinguish it in our case, at first, the thermal annealing tests were performed on the a-Si:H films prepared at the low substrate temperature of 110 ^{o}C using the diode system. The as-deposited films contain the large initial hydrogen concentrations (C_H) of c.a. 27 at.%. After the growth, the individual film was kept in the deposition chamber and was annealed for 30 minutes at the certain temperature. The result is shown in figure 10 [Shimizu et al., 2007]. One can see that the hydrogen concentration is reduced at the high annealing temperatures. On the other hand, at the temperature of 250 ^{o}C, which is the substrate temperature used in our triode deposition system, no C_H reduction takes place at least from the bulk. The result shows that under the substrate temperature of 250 ^{o}C, the hydrogen elimination process takes place during the film growth, i.e., most likely with gas reactions.

4.2 Hydrogen elimination process during film growth

The possible hydrogen elimination processes during the a-Si:H film growth are the following and are schematically shown in figure 11.

a.   hydrogen abstraction reaction by an atomic hydrogen
b.   spontaneous thermal desorption of surface hydrogen
c.   hydrogen abstraction reaction by a SiH$_3$ radical
d.   hydrogen elimination process through a cross-linking reaction
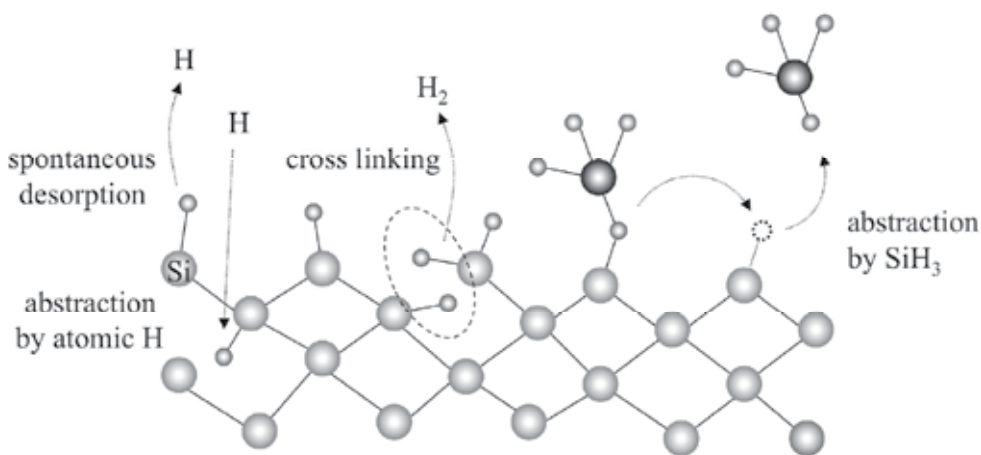
Fig. 11. Schematic of the hydrogen elimination processes during the growth of a-Si:H.

a.   Hydrogen abstraction reaction by an atomic hydrogen

Atomic hydrogen exists in an silane plasma [e.g., Matsuda, 2004]. It reacts with a bonded hydrogen of a film and forms H$_2$ molecule, resulting in a hydrogen elimination. The probability of this reaction should be proportional to the flux of atomic hydrogen. In a silane plasma, generated radicals and ions collide with SiH$_4$ molecule of which density is high in the gas phase. When the atomic hydrogen reacts with SiH$_4$, SiH$_3$ radical and H$_2$ molecule are generated at the rate constant of ~ 3×10^{-12} cm^3/s [Kushner, 1988; Perrin et al., 1996]:

$$H + SiH_4 \rightarrow SiH_3 + H_2. \tag{1}$$

The stable H$_2$ molecule does not contribute to the abstraction of the bonded hydrogen. In the triode system, basically no atomic hydrogen is generated but only the collisions take place in the region between the mesh and the substrate, indicating that the density of atomic hydrogen near the substrate is low. Therefore, it is natural to say that the hydrogen elimination process is not dominated by atomic hydrogen in the triode system.

b.   Spontaneous thermal desorption of surface hydrogen

The hydrogen desorption process from Si-H bond has been studied elsewhere [Toyoshima et al., 1991]. The activation energy of this reaction is estimated as 2 - 3 eV, and the reaction takes place only in the temperature range higher than 400 °C [Beyer & Wagner, 1983]. Therefore, it is unlikely that the spontaneous hydrogen desorption takes place under the substrate temperature of 250 °C as in our case.

c.   Hydrogen abstraction reaction by a SiH$_3$ radical

It is reported that the dominant deposition precursor for a-Si:H growth is a SiH$_3$ radical [Matsuda, 2004]. When a SiH$_3$ radical reaches to a growing surface, it physisorbs to one of the surface hydrogen atoms under a certain probability [Perrin et al., 1989; Matsuda et al., 1990].

$$\equiv \text{SiH} + \text{SiH}_3 \rightarrow \ \equiv \text{SiHSiH}_3. \tag{2}$$
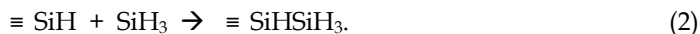
The physisorbed SiH$_3$ radical diffuses on the surface with changing the physisorption spot, and it finally captures one of the surface hydrogen, forming SiH$_4$ and it leaves from the surface. As a result, hydrogen is abstracted and a surface Si dangling bond is created. When another surface diffusing SiH$_3$ radical reaches to the surface dangling bond, it is chemisorbed and a Si-Si bond is formed [Perrin et al., 1989; Matsuda et al., 1990]. Note that, if this dangling bond is not terminated with some radicals, defect density is increased in the resulting film. As one can see, as long as a SiH$_3$ radical is supplied to the dangling bond site after the hydrogen elimination by another SiH$_3$, the density of the surface hydrogen does not decrease through the process since the chemisorped SiH$_3$ also contains hydrogen.

d.   Hydrogen elimination process through a cross-linking reaction

A cross-linking hydrogen elimination reaction takes place with a pair of Si-H bonds facing each other. Hydrogen is eliminated with forming a H$_2$ molecule and a Si-Si bond [Matsuda & Tanaka 1986; Perrin et al., 1989],

$$\equiv \text{Si-H} + \text{H-Si} \equiv \rightarrow \ \equiv \text{Si-Si} \equiv + \ \text{H}_2. \tag{3}$$
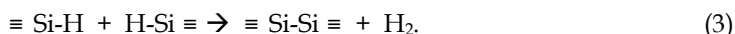
Different from the other cases (a)–(c), a dangling bond does not remain after this reaction, therefore, an atomic hydrogen or a SiH$_3$ radical which contains hydrogen atom(s) does not stick to this site, resulting in a reduction of hydrogen concentration. As described above, a Si-Si bond is formed through this process, therefore, before the reaction, the both Si atoms should be located at the configuration of five or six members of ring to form a stable Si-Si bond. On the other hand, if two Si atoms are located apart from each other where the free energy of the resulting Si-Si bond including its surrounding structures after the reaction is higher than that of before, it is unlikely that the cross-linking reaction takes place. Such an inhabitation can occur when a higher-ordered silane radical sticks to a growing surface as discussed in the next section.

4.3 Effect of deposition precursors on hydrogen elimination

For the growth of a-Si:H film, a SiH$_3$ radical is a dominant species. On the other hand, higher-ordered silane radicals are also generated in a plasma through insertion reactions of SiH$_2$ [Takai et al., 2000]. It has been reported that when the higher-ordered silane radicals such as Si$_4$H$_9$ are incorporated into the film, Si-H$_2$ bond density increases [Takai et al., 2000; Nishimoto et al., 2002]. Therefore, the flux of those species toward the substrate determines the property of the resulting film. The diffusion length (L) of a species is

$$L = (D\tau)^{1/2}, \tag{4}$$

$$D \propto 1/m. \tag{5}$$

where D is a diffusion coefficient, t is a lifetime and m is a mass of a species.

First of all, the diffusion coefficient of a SiH_3 radical is larger than that of a higher-ordered silane radical due to the difference of their mass. The ratio of the mass of a Si_nH_{2n+1} radical ($m_{SinH2n+1}$) and that of a SiH_3 radical (m_{SiH3}) is

$$m_{SinH2n+1} / m_{SiH3} \approx n. \tag{6}$$

Therefore, the diffusion coefficient of a SiH_3 radical is n-times larger than that of a Si_nH_{2n+1} radical.

Second, the lifetime of a SiH_3 radical is especially long in a SiH_4 gas phase. The density of SiH_4 molecule under the condition used in this study (0.1 Torr, 250 ${}^oC$) is ~ 10^{15} cm^{-3}. The density of SiH_3 radicals is the highest among the other generated species, and the value is ~ 10^{12} cm^{-3} in an RF silane plasma [Matsuda, 2004]. In the case of VHF plasma, as in our case, the value changes due to a high electron density and a low electron temperature effects. Estimating from the deposition rate, SiH_3 density can be one order of magnitude higher than that in an RF plasma, but in any cases, the density is still very low with respect to that of SiH_4 molecule. Therefore, most of the generated species collide with SiH_4. Here, the SiH_3 radical does not disappear due to the collision, resulting in its long lifetime:

$$SiH_3 + SiH_4 \rightarrow SiH_4 + SiH_3. \tag{7}$$

After all, the diffusion length of SiH_3 radical is very long according to equations (4) and (5). Under a certain gas flow rate condition, the radicals having small diffusion lengths are pumped out, but a large diffusion length species can still reach to the substrate. Thus, larger the distance between the mesh and the substrate, stronger the diffusion length effect. Therefore, we would like to propose that in the triode configuration, a long lifetime SiH_3 radical mainly contribute to the film growth than that in a diode system. If a SiH_3 radical sticks to a film surface, a cross-linking reaction takes place because the configuration of a five or six members of ring is easily formed with the SiH_3. On the other hand, when a higher-ordered silane radical sticks to the surface, not all of the Si atoms are located in such a configuration due to its steric-hindrance. Thus, the cross-linking reaction can take place partially, resulting in the remaining of hydrogen in the film. Once hydrogen is incorporated into the bulk of a film, it cannot be thermally eliminated at 250 ${}^oC$ as shown in figure 10.

Indeed, under the low SiH_4 flow rate condition, the higher Si-H and Si-H_2 bond densities are observed in the triode system [Shimizu et al., 2007].

4.4 Effect of growth rate

In the case of the triode system, the growth rate is low compared to that observed in a conventional diode system. In our VHF plasma case, the growth rate observed with the diode system is 7.3 Å/s, and that observed in the triode system is 0.7 Å/s at d_{ms} = 1 cm, and is 0.2 Å/s at d_{ms} = 4 cm. When the growth rate is low, hydrogen concentration of the resulting film can be low when thermal desorption from the surface and the bulk are the dominant hydrogen elimination processes. However, such elimination processes at the substrate temperature of 250 ${}^oC$ are unlikely as discussed in the previous sections.

To confirm the effect of the growth rate furthermore, the experiments were performed with installing a second mesh as described in section 3.1.2. Installing the second mesh reduces the growth rate drastically. As shown in Table 1, the observed growth rate with the double mesh at the VHF power of 10 W is c.a. 0.1 Å/s and that with the single mesh at the same VHF power is 0.8 Å/s. Under those conditions, however, almost the same Si-H and Si-H_2 bond densities are observed. Since the VHF power is fixed at the same value, the densities of the generated

radicals and ions in the plasma are basically the same in the both cases. When the VHF power is reduced to 2 W with a single mesh, the observed growth rate is 0.2 Å/s which is the similar value observed at the VHF power of 10 W with the double mesh (0.1 Å/s). On the other hand, the observed Si-H and Si-H$_2$ bond densities are different each other where lower values are observed in the low power case in which less higher-ordered silane radicals are produced due to a low electron temperature effect [Matsuda, 2004]. The results indicate that the gas phase condition is very important for determining a hydrogen concentration in the resulting film. Note that, when a plasma is unstable even in the triode case due to the lack of electrical matching, the observed Si-H and Si-H$_2$ densities are higher than the expected values shown in figure 3 (the higher value date are not presented).

5. Prospects for the future applications

The properties and the stabilities of the a-Si:H films prepared by the triode deposition system have been demonstrated in this study. The quality of the film is very good, and it exhibits very high stability against light soaking. Although the triode method reduces a growth rate of a film due to its configuration, which is a disadvantage for mass productions, we used this system to study the fundamental features. Several results indicate that the control of the gas phase condition is one of the essential factors to obtain a stable a-Si:H film. Based on this knowledge, one could establish the alternative fabrication methods which can produce the preferable gas phase condition for a stable a-Si:H fabrication.

In our result, the degree of degradation correlates well with Si-H$_2$ bond density in the film, which also corresponds to the former works. Beside the possibility of micro-void structure formation, one can propose the existence of chain-like Si-Si structures when the film contains large Si-H$_2$ bond density. Since it is a flexible structure, it can cause instability against light soaking. In figure 12 the ΔFF (= FF_{ini} – FF_{deg}) of the Schottky diode is plotted against the Si-H$_2$ bond density. It is a re-plot of figure 8 in a semi-log scale. The extrapolated line shows that the ΔFF value is zero at the Si-H$_2$ bond density of c.a. 1.3×10^{19} cm^{-3} (≈ 0.03 at.%). Although it is a hypothesis, the correlation indicates the guideline for the fabrication of stable a-Si:H films.
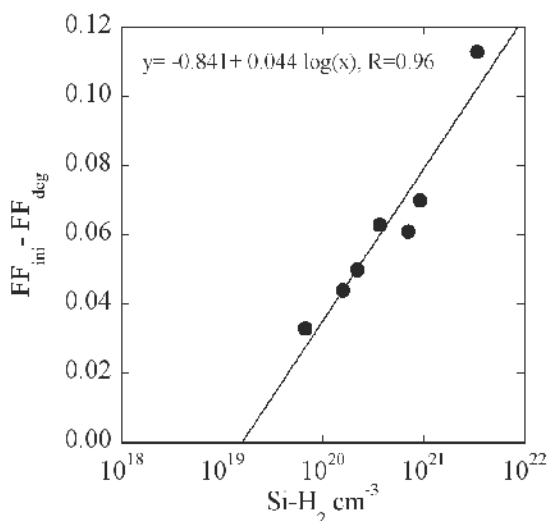
Fig. 12. Light-induced change in the fill-factor ($\Delta FF = FF_{ini}-FF_{deg}$) of the Schottky diode as a function of the Si-H$_2$ bond density (re-plot of fig. 8 in a semi-log scale).

6. Conclusions

Stable a-Si:H films against light soaking are prepared with adopting a triode deposition method where a mesh is placed between a cathode and a substrate. The resulting films contain very low Si-H and Si-H_2 bond densities compared with those observed in the films prepared by a conventional diode electrode method at the same substrate temperature. The hydrogen reduction effect is higher when the distance between the mesh and the substrate is increased. The films exhibit low initial defect densities and high photosensitivities. After the light soaking, high stabilities are observed in the films prepared by the triode system. The high stabilities of the films are also confirmed with the device configurations. It is most likely that the density of the precursors that reach to the growing surface is different each other in the triode and the diode systems. Control of gas phase condition is one of the key issues to fabricate stable a-Si:H films and related solar cells.

7. Acknowledgement

8. References

Beyer, W. & Wagner, H. (1983). The role of hydrogen in a-Si:H - Results of evolution and annealing studies. J. Non-Cryst Solids, Vol. 59-60, pp. 161-168.

Borrello, D., Vallat-Sauvain, E., Bailat, J., Kroll, U., Meier, J., Benagli, S., Marmelo, M., Monteduro, G., Hoetzel, J., Steinhauser & J., Lucie, C. (2011). High-efficiency amorphous silicon photovoltaic devices. WIPO Patent: WO/2011/033072.

Carlson, D. E. & Wronski, C. R. (1976). Amorphous silicon solar cell. Appl. Phys. Lett. Vol. 28, pp. 671-673.

Drevillon, B. & Toulemonde, M. (1985). Hydrogen content of amorphous silicon films deposited in a multipole plasma. J. Appl. Phys., Vol. 58, pp. 535-540.

Green, M. A. (2003). Crystalline and thin-film silicon solar cells: state of the art and future potential. Solar Energy, Vol. 74, pp. 181-192.

Kushner, M. J. (1988). A model for the discharge kinetics and plasma chemistry during plasma enhanced chemical vapor deposition of amorphous silicon. J. Appl. Phys., Vol. 63, pp 2532-2551.

Langford, A. A., Fleet, M. L., Nelson, B. P., Lanford, W. A. & Maley, N. (1992). Infrared absorption strength and hydrogen content of hydrogenated amorphous silicon. Phys. Rev. B, Vol. 45, pp. 13367-13377.

Matsuda, A. & Tanaka, K. (1986). Investigation of the growth kinetics of glow-discharge hydrogenated amorphous silicon using a radical separation technique. J. Appl. Phys., Vol. 60, pp. 2351-2356.

Matsuda, A., Nomoto, K., Takeuchi, Y., Suzuki, A., Yuuki, A. & Perrin, J. (1990). Temperature dependence of the sticking and loss probabilities of silyl radicals on hydrogenated amorphous silicon. Surf. Sci., Vol. 227, pp. 50-56.

Matsuda, A. (2004). Microcrystalline silicon. Growth and device application. J. Non-Cryst. Solids. Vol. 338–340, pp. 1–12.

Müller, J., Rech B., Springer, J. & Vanecek, M. (2004). TCO and light trapping in silicon thin film solar cells. Solar Energy, Vol. 77, pp. 917–930.

Nishimoto, T., Takai, M., Miyahara, H., Kondo, M. & Matsuda, A. (2002). Amorphous silicon solar cells deposited at high growth rate. J. Non-Cryst. Solids, Vol. 299-302, pp. 1116-1122.

Perrin, J., Takeda, Y., Hirano, N., Takeuchi, Y. & Matsuda, A. (1989). Sticking and recombination of the SiH_3 radical on hydrogenated amorphous silicon: The catalytic effect of diborane. Surf. Sci., Vol. 210, pp. 114-128.

Perrin, J., Leroy, O. & Bordage, M. C. (1996). Cross-sections, rate constants and transport coefficients in silane plasma chemistry. Contrib. Plasma Phys., Vol. 36, pp. 3-49.

Roca i Cabarrocas., P. (2000). Plasma enhanced chemical vapor deposition of amorphous, polymorphous and microcrystalline silicon films. J. Non-Cryst. Solids, Vol. 266-269, pp. 31-37.

Shah, A., Torres, P., Tscharner, R., Wyrsch, N. & Keppner, H. (1999). Photovoltaic Technology: The Case for Thin-Film Solar Cells., Science, Vol. 285, pp. 692-698.

Shah, A. V., Schade, H., Vanecek, M., Meier, J., Vallat-Sauvain, E., Wyrsch, N., Kroll, U., Droz, C. & Bailat, J. (2004). Thin-film Silicon Solar Cell Technology. Prog. Photovolt: Res. Appl., Vol. 12, pp. 113–142.

Shimizu, S., Kondo, M. & Matsuda, A. (2005). A highly stabilized hydrogenated amorphous silicon film having very low hydrogen concentration and an improved Si bond network. J. Appl. Phys., Vol. 97, pp. 033522 1-4.

Shimizu, S., Matsuda, A. & Kondo, M. (2007). The determinants of hydrogen concentrations in hydrogenated amorphous silicon films prepared using a triode deposition system. J. Appl. Phys., Vol. 101, pp. 064911 1-5.

Shimizu, S., Matsuda, A. & Kondo, M. (2008). Stability of thin film solar cells having less-hydrogenated amorphous silicon i-layers. Solar Energy Mater. & Solar Cells, Vol. 92, pp. 1241-1244.

Sonobe, H., Sato, A., Shimizu, S., Matsui, T., Kondo, M. & Matsuda, A. (2006). Highly stabilized hydrogenated amorphous silicon solar cells fabricated by triode-plasma CVD. Thin Solid Films, Vol. 502, pp. 306–310.

Staebler, D. L. & Wronski, C. R. (1977). Reversible conductivity changes in discharge-produced amorphous Si. Appl. Phys. Lett., Vol. 31, pp. 292-294.

Takai, M., Nishimoto, T., Takagi, T., Kondo, M. & Matsuda, A. (2000). Guiding principles for obtaining stabilized amorphous silicon at larger growth rates. J. Non-Cryst. Solids., Vol. 266-269, pp. 90-94.

Toyoshima, Y., Arai, K., Matsuda, A. & Tanaka, K. (1991). In situ characterization of the growing a-Si:H surface by IR spectroscopy. J. Non-Cryst. Solids, Vol. 137-138, pp. 765-770.

Yang, J., Banerjee, A. & Guha, S. (1997). Triple-junction amorphous silicon alloy solar cell with 14.6% initial and 13.0% stable conversion efficiencies. Appl. Phys. Lett., Vol. 70, pp. 2975-2977.

Analysis of CZTSSe
Monograin Layer Solar Cells

Gregor Černivec, Andri Jagomägi and Koen Decock
[1]University of Ljubljana, Faculty of Electrical Engineering,
[2]Department of Materials Science, Tallinn University of Technology,
[3]Solar Cells Department, Ghent University – ELIS,
[1]Slovenia
[2]Estonia
[3]Belgium

1. Introduction

Monograin layer (MGL) solar cell combines the features of a monocrystalline solar cell and a thin film solar cell. The photoactive layer is formed from the kesterite-stannite semiconductor $Cu_2SnZn(S,Se)_4$ (CZTSSe) material with the single-crystalline grains embedded into the epoxy resin (Altosaar et al., 2003). With the graphite back contact, cadmium sulphide (CdS) buffer layer, and zinc oxide (ZnO:Al/i-ZnO) window layer, the remainder of the structure resembles a thin film CIS solar cell in the superstrate configuration (Fig. 1).
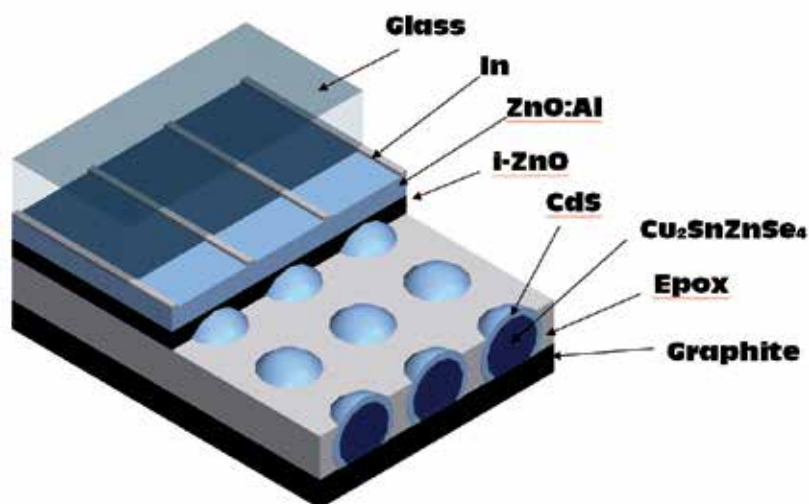
Fig. 1. The MGL solar cell. The photoactive $Cu_2SnZnSe_4$ monograins are covered with CdS, and embedded into the epoxy resin. The thin layer of the intrinsic ZnO serves as the CdS surface passivation and as the barrier for the ZnO:Al impurities. The front contact comprises indium fingers while the back contact is made of the graphite paste.

The main advantage of this cell over the thin film CIGS solar cell are the low production costs – using a relatively simple powder technology (Altosaar et al., 2005), and the replacement of the expensive indium (In) by the less expensive tin (Sn) and zinc (Zn) metals. The photovoltaic properties of this new structure are very promising: the AM1.5 spectrum conversion efficiency reaches up to 5.9% along with the open-circuit voltage (V_{oc}) up to 660 mV and the fill-factor (FF) up to 65%. The short-circuit current (J_{sc}) has its maximal value at the room temperature and then decreases with the lowering temperature. Along with the low FF, these output parameters point to some specific charge transport properties.

In order to discover the origin of the charge transport limiting mechanism we employed the numerical semiconductor simulator Aspin (Topič et al.,1996), based on the drift-diffusion equations (Selberherr, 1984) and coupled to the SRH (Schockley & Read, 1952) recombination statistics. The optical generation rate profile was calculated with the ray tracing simulator Sun*Shine* (Krč et al., 2003), which is able to determine the absorption profile in the illuminated one-dimensional (1D) structure that comprises a stack of layers with flat and/or rough adjacent interfaces. The input semiconductor material parameters were determined from the temperature resolved admittance spectroscopy measurements (Walter et al.,1996): capacitance-voltage (C-V) and capacitance-frequency (C-f), the van der Pauw measurement (Van der Pauw, 1958) and the dark current density-voltage (J-V) characteristics measurements (Sah et al., 1957). The numerical model was implemented in a similar way as in (Černivec et al., 2008) where the measured parameters were used as the input and the J-V and the external quantum efficiency (QE) characteristics were the result of the simulation. By comparing the temperature dependent output characteristics of the AM1.5 illuminated solar cell to the measurements, and additional fine tuning of the input parameters, we assumed the plausible efficiency-limiting mechanism, and by that also revealed the region in the structure that could be responsible for the charge transport limitations.

2. Input parameters measurements

In order to extract material parameters which will be further on used in the numerical analysis, following measurements were conducted: the dark J-V measurement to get insight into the recombination and transport properties of the solar cell, the C-V measurement which indicates the width and the shape of the junction, and the C-f measurement which results the information of the defect properties of the semiconductor material. The common assumption in the analyses of the measurements is a single-junction model of the solar cell. In the interpretation of the Van der Pauw measurement results we assumed a similar morphology of the annealed tablet of the CZTSSe material as it is one in the solar cell's monograin absorber.

2.1 One-diode model

Calibration of the parameters of the one-diode model does not yield any input parameters for our numerical model, but it rather gives us initial insight into the transport properties of the MGL solar cell. Table I contains the extracted temperature dependent parameters of the fitted one-diode model (Sze & Ng, 2007). The high ideality factors (n_{id}) of the temperature dependent dark J-V measurement indicate the CdS/CZTSSe heterointerfacial limited transport.

T [K]	J_0 [mA/cm²]	n_{id} [/]	R_s [Ωcm²]	G_{sh} [mS/cm²]
310	1.08×10^{-3}	2.68	2.10	0.23
290	4.85×10^{-4}	2.78	2.36	0.17
270	2.50×10^{-4}	2.99	2.66	0.12
250	8.93×10^{-5}	3.19	3.44	0.083
230	3.30×10^{-5}	3.37	4.37	0.061
210	1.44×10^{-5}	3.78	6.65	0.033

Table 1. Parameters of the fitted one-diode model.

The ideality factors above 2 deviate from the standard Sah-Noyce-Shockley theory (Sah et al., 1957) and point either to the tunnelling enhanced recombination in the space charge region (SCR) (Dumin & Pearson, 1965) or to the multilevel recombination (Breitenstein et al., 2006; Schenk et al., 1995) occurring in the highly defective interfacial regions.

Fig. 2 shows the Arrhenius plot of the dark saturation current (J_0) and its extracted activation energy ($E_{A, J0}$). The activation energy is the distance between the Fermi level and the edge of the minority carrier energy band, since these are responsible for the recombination current. In the case of the MGL solar cell, at the CdS/CZTSSe heterointerface the inverted surface makes holes to be the minority carriers, Fig. 8. Thus the $E_{A, J0}$ represents the energy distance between the CZTSSe absorber's valence band and the Fermi level near the heterointerface.
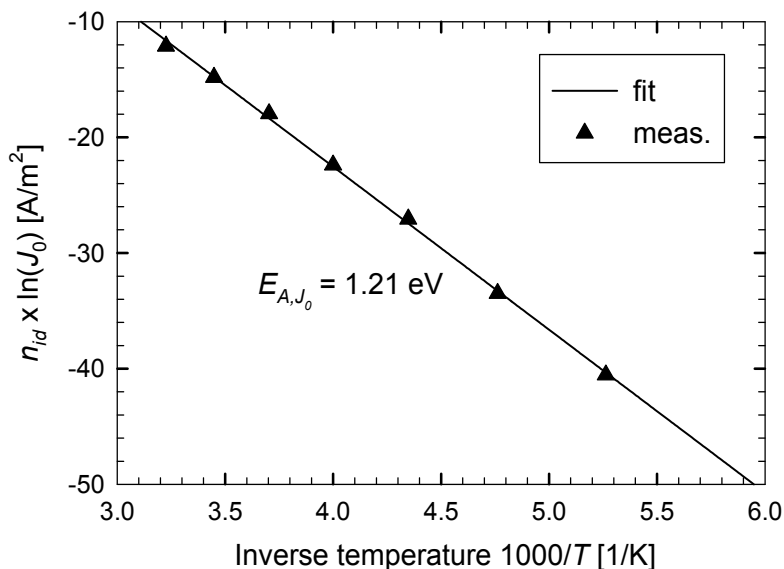
Fig. 2. Arrhenius plot of the dark saturation current as obtained from the one-diode model. The slope of the ideality factor weighted logarithm of the dark saturation current versus the inverse absolute temperature, results the activation energy $E_{A, J0}$. T is temperature in Kelvin.

Comparing the value of the $E_{A, J0}$ (Fig. 2) to the absorber's band-gap energy as extracted from the QE measurement (Fig. 13, $E_{g,CZTSSe}$ = 1.49 eV), this indicates the position of the recombination peak near the heterointerface and inside the SCR – as depicted in Fig. 8.

2.2 Capacitance-voltage measurement

To obtain the approximate values of the concentration of the uncompensated acceptors (Kosyachenko, 2010) at the edge of the SCR, and the hole mobility ($\mu_{h,CZTSSe}$) of the CZTSSe absorber layer, we combined the temperature resolved *C-V* and the van der Pauw measurements. Since the concentration of the uncompensated acceptors at the edge of the SCR corresponds to the density of free holes, we will further on introduce this as new parameter called the "apparent doping" – p_{SCR}.

Fig. 3 shows the temperature and the bias voltage dependent capacitance plot – the Mott-Schottky plot, where the capacitance results from the admittance measurement at 10 kHz. The nonlinear curves in the Mott-Schottky plot indicate a spatially non-uniform p_{SCR}, while their temperature trend points to the temperature decreasing capacitance. The slope of the curves at $V = 0$ V indicates that, in dark conditions, the apparent doping at the edge of the SCR gradually increases with the decreasing temperature.
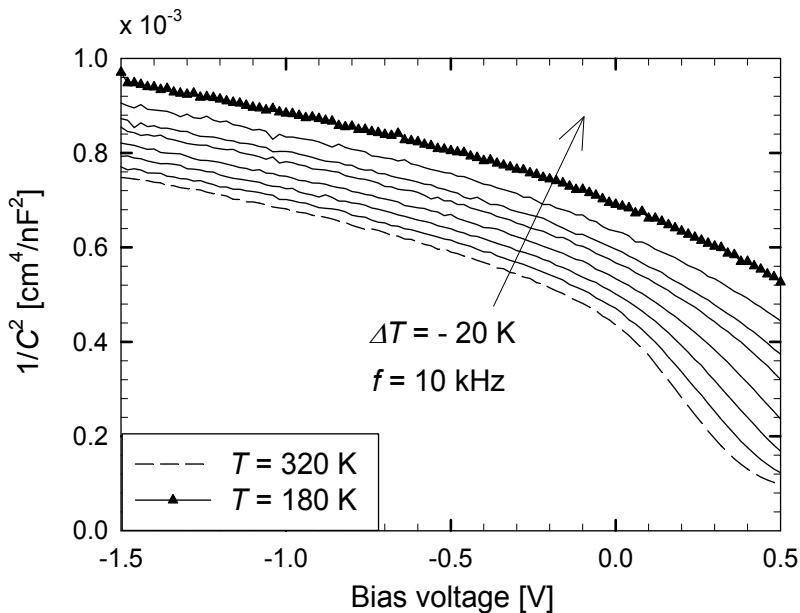
Fig. 3. The Mott-Schottky plot at 10 kHz. The dashed curve correlates to the temperature at 320 K. Arrow indicates the trend of the temperature decrement. The temperature step equals to 20 K. All curves are measured with a small signal of 10 kHz.

When we observe the 0V bias points as depicted in Fig. 4 by the triangles, we can see that p_{SCR} decreases when moving from the quasi-neutral region towards the SCR. However, for the higher temperatures (320 K, 300 K) p_{SCR} seems to be increasing towards the heterointerface after it has reached its minimum value. We are not able to explain this trend properly, but since the increasing p_{SCR} towards the heterointerface would produce only a poor photovoltaic junction, in the modelling we use the p_{SCR} values as obtained at 0 V bias. The trend of the increasing SCR width along with the increasing p_{SCR} could results from the influences of the non-ideally asymmetrical n^+/p (CdS/CZTSSe) junction in which the SCR extends also into the n^+ buffer region (CdS).
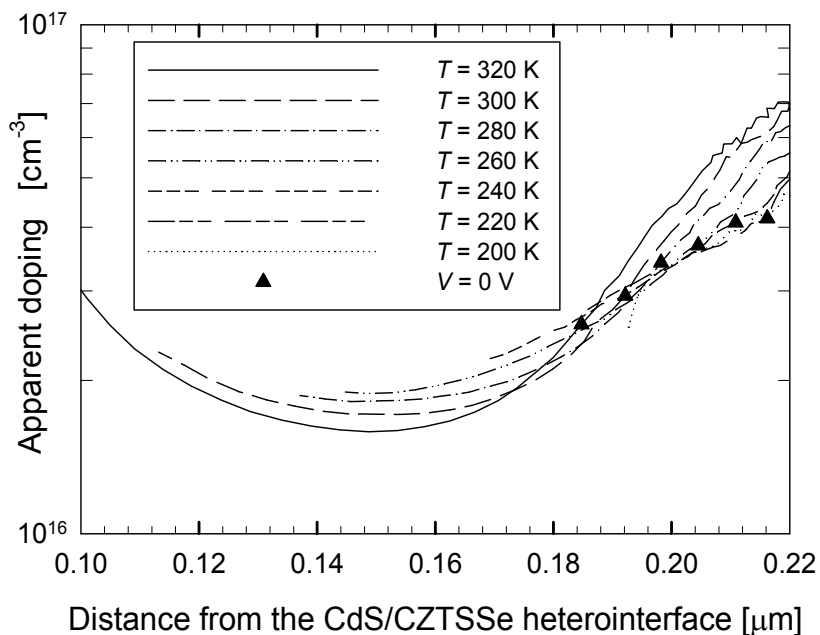
Fig. 4. The apparent doping density p_{SCR} obtained from the bias voltage derivative of the Mott-Schottky plot. The distance from the junction is calculated from the space charge region capacitance. Triangles depict the 0 V bias conditions.
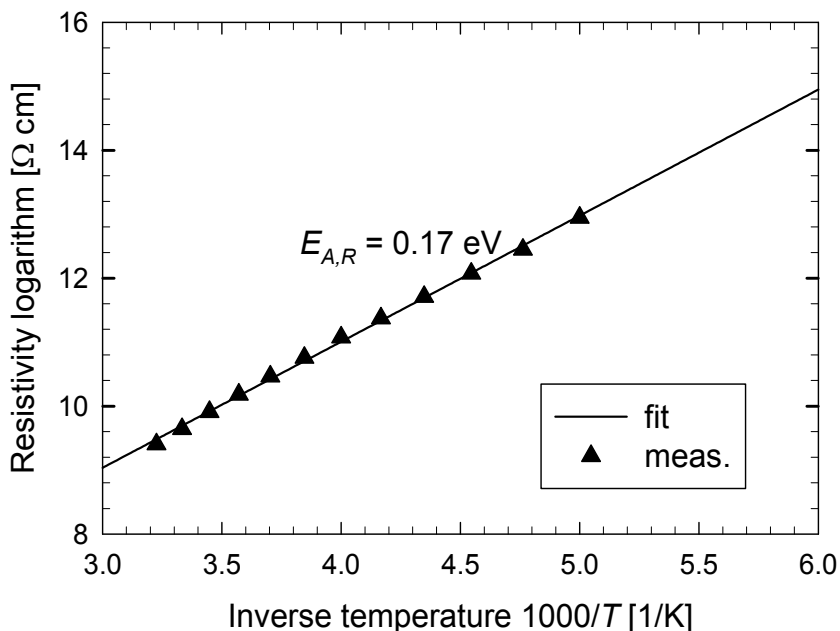
Fig. 5. Arrhenius plot of the van der Pauw measurement conducted on the annealed CZTSSe tablet. $E_{A,R}$ is the extracted activation energy. T is temperature in Kelvin.

2.3 Van der Pauw measurement

The van der Pauw measurements were conducted on the tablet of the annealed CZTSSe monograin material. The Arrhenius plot of the resistivity (ρ) of the monograin material tablet (Fig. 5) reveals the thermal activation energy ($E_{A,R}$) equal to 0.17 eV, and a very low hole mobility $\mu_{h,CZTSSe}$ equal to 0.02 cm²/Vs at 310 K. The latter was calculated according to (1) and using the p_{SCR} as obtained from the *C-V* profiling:

$$\mu_{h.CZTSSe} = \frac{1}{q \cdot p_{SCR} \cdot \rho} . \tag{1}$$

2.4 Capacitance-frequency measurement

Plotting the capacitance as a function of the measurement frequency on a semi-logarithmic scale can reveal some defects present in the energy gap of the CZTSSe absorber layer of the MGL solar cell. A gradually decaying capacitance indicates a defect with a broad energy band, while a steep transition indicates a single level defect (Burgelman & Nollet, 2005). The temperature resolved *C-f* plot shown in Fig. 6 reveals both types of transitions: a gradually decreasing capacitance at the high temperature limit (indicated with triangles), and a characteristic inflection point at the frequency equal to 10 kHz in the low temperature limit (indicated with circles).
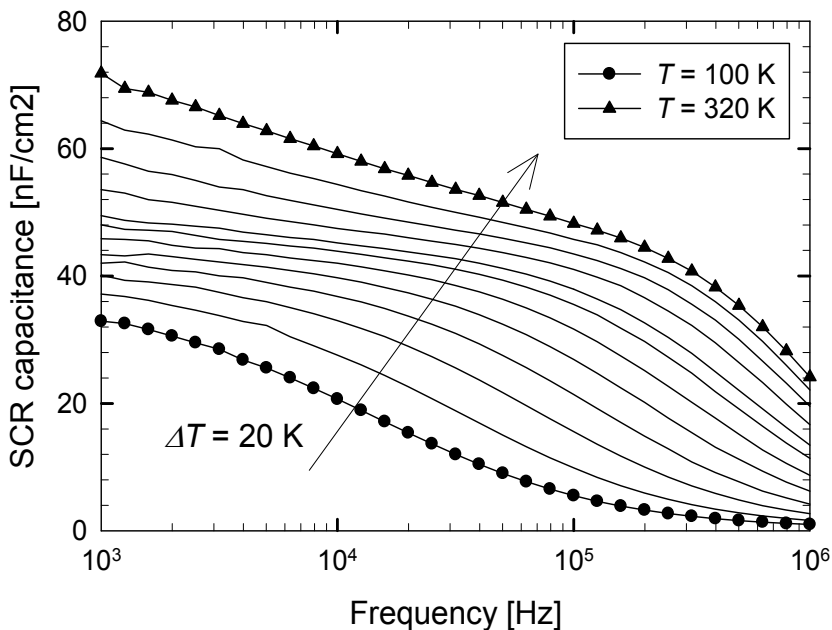
Fig. 6. Frequency dependent space charge region's capacitance measured at 0.2 V of forward bias. Solid curve with circles depicts the relation at 100 K. The arrow indicates the trend of the curves with the increasing temperature. The temperature step equals to 20 K. The curves at lower temperatures exhibit pronounced inflection points thus indicate emission from shallow traps.

The decreasing capacitance going from the high temperature towards the low temperature indicates the 'freeze out' of the carriers located in the deep traps: the temperature shrinking of the Fermi distribution tail makes the deep trapped charge less sensitive to the small perturbations of the Fermi level (the applied ac signal). The analysis according to (Walter et al.,1996) reveals two trap distributions which are shown in Fig. 7. Measurement at room temperature senses a broad trap distribution extending at least 0.3 eV deep into the energy gap from the valence band, while the measurement at low temperature fingers a very narrow distribution with its maximum at 0.05 eV. Since this maximum remains present also at high reverse biases (not shown here), we believe that this trap extends throughout the whole CZTSSe absorber layer and acts as the intrinsic acceptor doping level. However we can not draw any strong conclusions on the type of the deep trap distribution, but since this could be responsible for the compensating effect; we postulated it to be the donor-like.
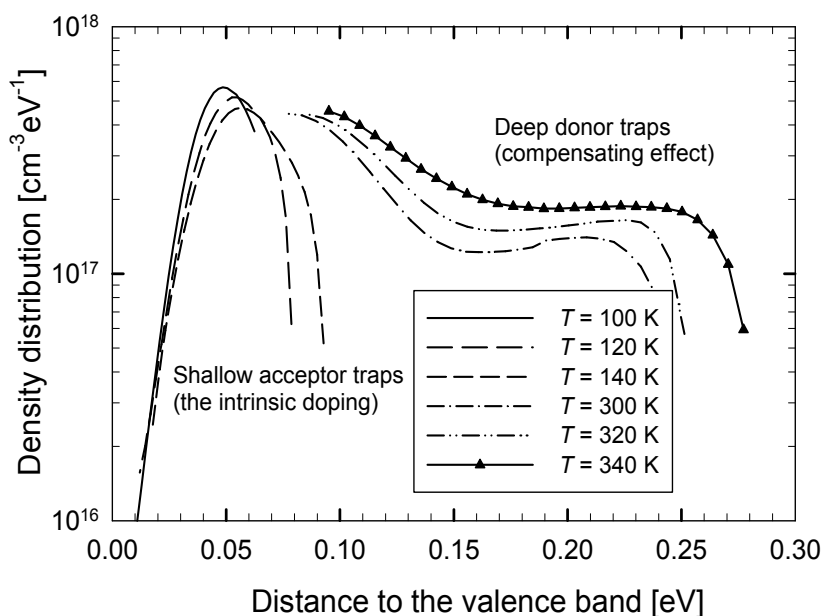
Fig. 7. Trap density distributions extracted at 0.2 V of forward bias calculated as the frequency derivative of the space charge region's capacitance. Calibration parameters were chosen according to (Walter et al.,1996): U_d = 0.8 V (built-in voltage), $\beta_p N_V$ = 5x10^7 Hz (trap emission coefficient), E_{fp} = 0.7 eV (the Fermi level position relating the valence band), 1x10^3 ≤ f ≤ 1x10^6 Hz (frequency range).

In Fig. 7 the pronounced narrow distribution at 0.05 eV above the valence band indicates the shallow acceptor traps responsible for the intrinsic doping, while the deeper and wider donor distribution (marked with triangles) results the compensation effect.

3. Modelling

From the measurements we obtained a certain insight into the recombination and transport properties (the dark *J-V* and the Van der Pauw measurements), the doping profile (*C-V* measurement) and the indication of the shallow traps (*C-f* measurement). These will be used as the guidelines to define the numerical model of the CZTSSe MGL solar cell.

The 1D carrier transport model can accurately describe the current flow only in the direction vertical to the layered structure (the direction orthogonal to the solar cell plane) therefore following assumptions are made: i) current flow in the matrix plane between the adjacent monograins is neglected, ii) all the semiconductor parameters are meant as the "effective parameters", thus neglecting the morphology by transforming a single spherical monograin solar cell into the 1D rod, and iii) the "spatial fill-factor" (S_{FF}) is introduced, which is the ratio of the grain covered area to the whole contact area. It is important to note that the S_{FF} affects only the extensive solar cell parameters (J_{sc}) while the intensive parameters (V_{oc}, FF and QE) remain intact. In our case the S_{FF} equals to 0.78.

The most important semiconductor parameters which have to be defined for each layer of the MGL solar cell prior to simulation are the band-gap energy (E_g), the electron affinity (E_χ), the acceptor and/or donor doping (N_A, N_D), the hole and electron low-field mobility (μ_h, μ_e), the hole and electron effective masses (m_h, m_e), and the parameters of the traps and/or the recombination centres (N_t – distribution density, E_t – distance to the valence band, σ – trap cross section, e_t – characteristic energy). By analyzing the conducted measurements (C-V, van der Pauw, C-f) we extracted the initial values of these parameters, relating to the CZTSSe absorber and/or to the CdS/CZTSSe heterointerface. These were further on subjected to the calibration procedure in order to fit the dark structure and the illuminated structure output characteristics to the measurements (J-V and QE). The rest of the absorber and heterointerface parameters, and those relating to the window (ZnO:Al/ZnO) and buffer (CdS) layers of the MGL solar cell, were taken similar to those used in (Černivec et al., 2008).

3.1 Dark structure *J-V* characteristics

Fig. 8 shows the CZTSSe MGL solar cell structure in its thermodynamic equilibrium. The complete solar cell comprises glass(2 mm)/ZnO:Al(1.6 µm)/i-ZnO(200 nm)/CdS(50 nm)/CZTSSe(60 µm)/graphite(500 nm) layers with the additional 100 nm thick surface
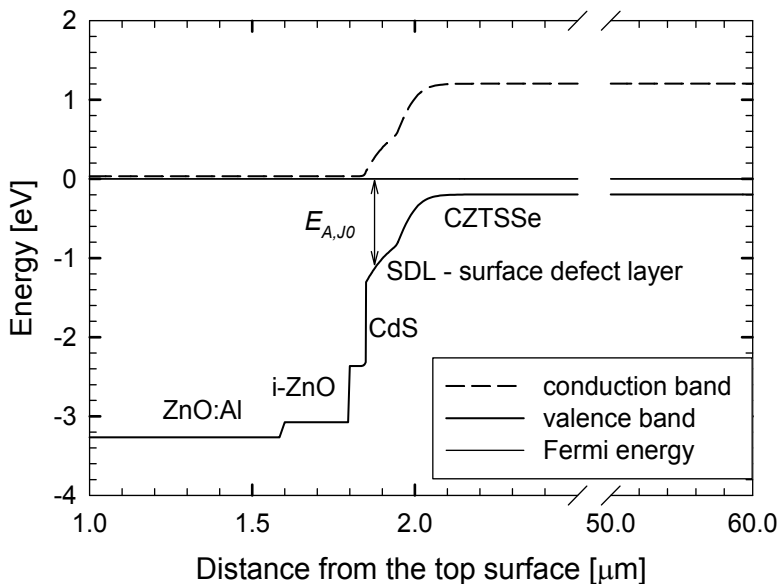
Fig. 8. Energy band diagram of CZTSSe solar cell in thermodynamic equilibrium at 310 K. $E_{A,J0}$ indicates the recombination activation energy as obtained from the Arrhenius plot from Fig. 2.

defect layer (SDL) between the CdS and the CZTSSe to account for the interfacial defects. Because of the degenerate position of the Fermi level in the ZnO:Al, i-ZnO and CdS layers, we assume these will act as the emitter contact, while the graphite at the back acts as the ohmic base contact. Further on in the structure we introduce the SDL which has an increased concentration of the mid-gap defects of the donor ($N_{tD,SDL}$) and the acceptor ($N_{tA,SDL}$) types. $N_{tD,SDL}$ will be responsible for the recombination current while the $N_{tA,SDL}$ will set the Fermi level position in the SDL layer and thus activate the $N_{tD,SDL}$.

The van der Pauw measurements of the sole CZTSSe tablets exhibit unusual high resistances, thus we assume that $\mu_{h,CZTSSe}$ will have an important impact to the series resistance – R_s (Table I). The Arrhenius plot in Fig. 5 shows the latter's exponential dependence on temperature, revealing the activation energy of 0.17 eV. We believe that the high R_s originates from the compensation of the shallow acceptor doping ($N_{tA,CZTSSe}$) by the broader distribution of deeper donor levels ($N_{tD,CZTSSe}$). This agrees well with the C-f measurement results shown in Fig. 7. Therefore, rather than calculating the mobility from the van der Pauw measurement, we will use a numerical fitting procedure to calibrate the $\mu_{h,CZTSSe}$ and the $N_{tD,SDL}$ for the preselected values of the $N_{tA,CZTSSe}$ and the $N_{tD,CZTSSe}$. The initial values for the latter two were calculated from the C-f measurement (Fig. 7).

Fig. 9 shows the calibration procedure of the measured and the simulated dark J-V characteristics at 310 K. By increasing the total concentration of the SDL mid-gap donor defects ($N_{tD,SDL}$) the dark saturation current increases, as shows the inset of Fig. 9. In the voltage range from 0.4 V to 0.6 V a good J-V fit can be found for the $N_{tD,SDL}$ equal to 10^{18} cm^{-3}, but still expressing a deviation in the slope as the result of the non-matching ideality factors: with this model it is not possible to obtain such a high ideality factor as yielded the measurement-calibration in Table I. For the lower applied voltages ($V < 0.4$ V) there is a significant deviation in characteristics which can be attributed to the shunt conductance. To compensate this difference the external shunting element can be added in the model, using the value equal to the G_{sh} at 310 K (Table I). A very good fit is found in the voltage range $V >$ 0.5 V by setting the value of the $\mu_{h,CZTSSe}$ to 1.5 cm^2/Vs – indicated by the solid line in Fig. 9.
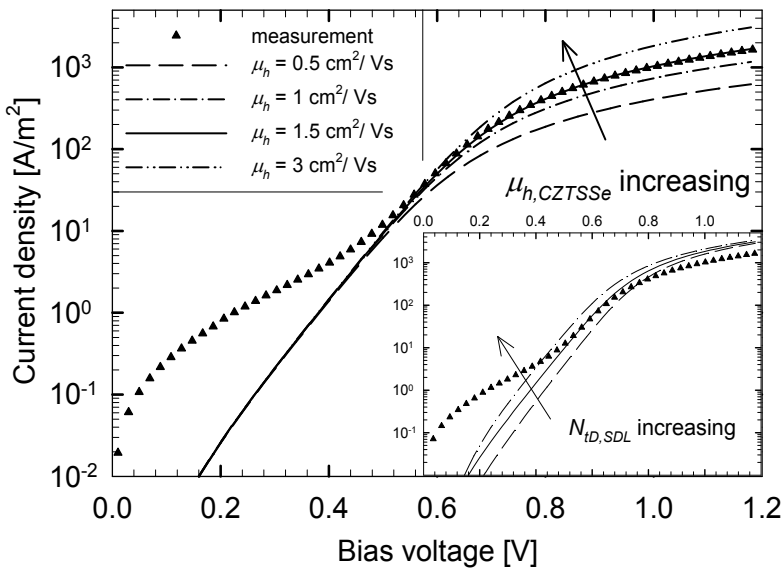
Fig. 9. Calibration of the CZTSSe monograin layer's and of the SDL's transport parameters.

In Fig. 9 the calibrated value of the CZTSSe hole mobility equals to 1.5 cm^2(Vs)$^{-1}$ and the corresponding electron mobility equals to 8 cm^2(Vs)$^{-1}$. The inset of Fig 9 shows calibration of the SDL defect concentration. The calibrated defect concentration ($N_{tD,SDL}$ = 8x10^{19} cm^{-3}/eV) corresponds to the solid J-V curve of the three simulated characteristics. The J-V curve above (dash-dotted) and the J-V curve below (dashed) correspond to one order of magnitude higher and to one order of magnitude lower SDL defect concentration, respectively.

To summarize the dark model, this is valid for the bias voltages higher than 0.5 V. When the solar cell is illuminated, this usually happens to be the range at which the recombination current starts to compensate the photogenerated current, and therefore important to match the correct V_{oc} value. For the bias voltages lower than 0.5 V the recombination current is rather low and the photogenerated current will dominate the J-V characteristics. Thus the external G_{sh} might be of lesser importance when observing the illuminated solar cell structure.

3.2 Illuminated structure characteristics

In order to calibrate the CZTSSe solar cell model under illumination, we choose to observe the temperature behaviour of the J_{sc}. This is mainly determined by the collection efficiency of the photogenerated carriers in the SCR. The collection efficiency in a large extend depends on the width of the SCR (Fig. 4), determined by the shallow acceptor traps in the CZTSSe - $N_{tA,CZTSSe}$, while its temperature dependence governs the occupation function F of the deeper donor traps $N_{tD,CZTSSe}$ (Fig. 10). Fig. 10 shows the $N_{tA,CZTSSe}$ and $N_{tD,CZTSSe}$ distributions similar to the measured trap densities from Fig. 7, and the occupation function F at 310 K and 210 K. The peak values of the trap distributions are not the same as the measured traps, but were rather subjected to the calibration procedure of fitting the J-V and QE measured and simulated characteristics. At the edge of the SCR the apparent doping p_{SCR} is a result of the compensatory effect of the density of the occupied $N_{tA,CZTSSe}$ and the density of the unoccupied $N_{tD,CZTSSe}$:

$$p_{SCR} = N_{tA,CSZSSe} - (1 - F) \cdot N_{tD,CSZSSe} . \tag{2}$$

When temperature decreases the E_{fp} moves towards the valence band, what creates more deep donors unoccupied (f_B decreases), and lowers the p_{SCR}.

In Fig. 10 the trap distributions of the model are calibrated to fit the measured short-circuit current density at 310 K. The distributions correlate well with the calculated distributions shown in Fig. 7. On the right axis the occupation functions at two different temperatures are shown in order to explain the temperature dependent collection efficiency and its influence to the short-circuit current.

The temperature decreasing p_{SCR} decreases the SCR width, leading into the lower collection efficiency and lower J_{sc}. Fig. 11 shows the SCR narrowing as the result of the Fermi redistribution according to Fig. 10. The decreased p_{SCR} would normally lead into the wider SCR, if the net charge of the SDL remained constant. This would be the case with the ideal asymmetrical n^+/p junction, resulting from the shallow doping levels. But since the net charge in the SDL originates also from the deep defects, these are then affected by the change of the charge in the CZTSSe layer. Therefore in order to satisfy the Poisson's balance, the lower temperature also leads into the charge redistribution in the SDL layer (omitted for clarity in Fig. 11): the decrement of the negative charge resulting from the less occupied acceptor traps in the CZTSSe layer is balanced by the decrement of the positive charge from the deep defects in the SDL. In the SDL the temperature shift of the Fermi level towards the conduction band makes the deep donor defects less ionized and increases the ionization of the deep acceptors.
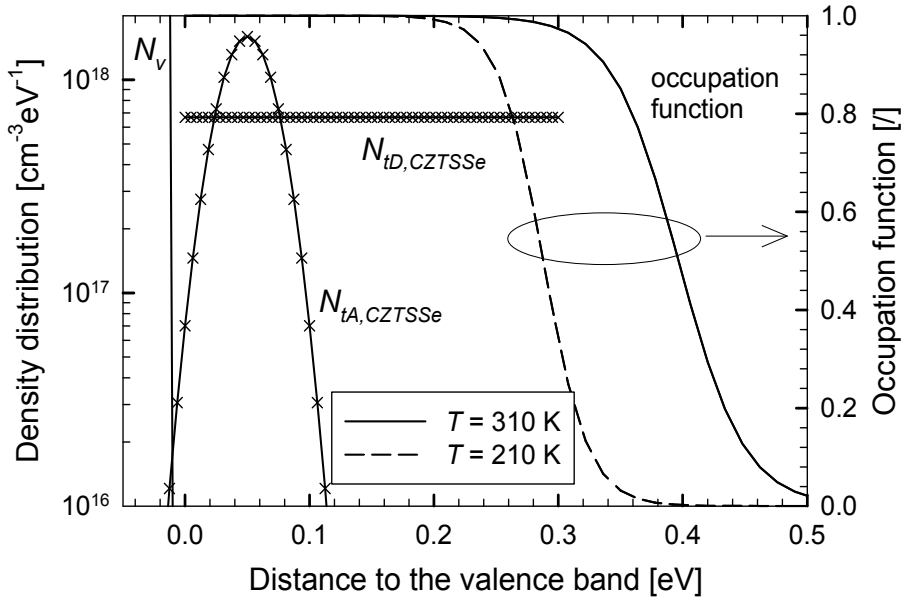
Fig. 10. Trap distributions of the CZTSSe monograin layer 50 nm deep in the SCR from the SDL/CZTSSe heterointerface.
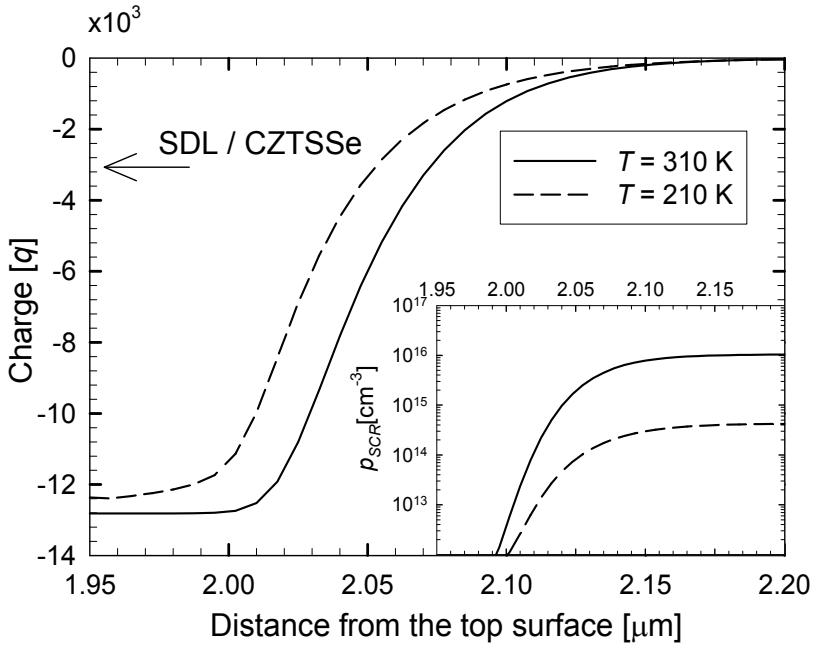
Fig. 11. Space charge region of the CZTSSe layer (q is the electron's charge) and its temperature dependence resulting from the occupation function variation (shown in Fig. 10). On the left, the interface to the SDL is indicated. The inset shows the temperature variation of the apparent doping p_{SCR}.

The modelled SCR width of approximately 0.2 μm and the p_{SCR} concentration of 10^{16} cm^{-3} at 310 K agree well with the respective measured values which equal to 0.18 μm and 2.6x10^{16} cm^{-3}, as observed from Fig. 4. Similarly well agrees the temperature correlation between the p_{SCR} and the SCR width: with the increasing p_{SCR} also the increasing SCR width is observed. In the measurement this correlation is indicated with the triangles (Fig. 4). However the corresponding temperatures do not comply: in the measurement the 320 K triangle corresponds to the lowest p_{SCR} and the 220 K triangle corresponds to the highest p_{SCR}. One should indeed always take care about the width of the SCR calculated in the apparent doping density analysis. There, the following formula is used to calculate the SCR width:

$$W_{SCR} = \frac{\varepsilon}{C} , \qquad (3)$$

where ε is the permittivity and C is the capacitance. This formula however only holds if the capacitance is governed by the depletion, and not by filling and emptying of deep states. As can be seen in Fig. 6 the capacitance is indeed governed by defects rather than depletion at f=10kHz.

Table 2 summarizes the calibrated material parameters. The parameters which were the subject of calibration are denoted bold, while the dash corresponds to the parameter for which we used the value 0. In the reality this would correspond to a very low value. Other material parameters are similar as in (Černivec et al., 2008). The effective density of states is calculated from the corresponding effective masses (Sze & Ng, 2007).

	ZnO:Al	i-ZnO	CdS	SDL	CZTSSe
W [μm]	1.6	0.2	0.05	0.1	60
m_e [m_0]	0.27	0.27	0.27	0.09	0.09
m_h [m_0]	0.78	0.78	0.78	0.73	0.73
N_D [cm^{-3}]	10^{18}	10^{18}	10^{18}	-	-
N_A [cm^{-3}]	-	-	-	-	-
E_g [eV]	3.3	3.1	2.4	1.4	1.4
E_χ [eV]	4.0	4.0	4.0	4.0	4.0
E [ε_0]	9.0	9.0	9.0	13.6	13.6
μ_e [cm^2/Vs]	100	100	100	**40**	**8**
μ_h [cm^2/Vs]	25	25	25	**15**	**1.5**
N_{tA} [cm^{-3}/eV]	-	-	-	**4x10^{17}**	**8x10^{16}**
E_{tA} [eV]	-	-	-	**0.7**	**0.05**
σ_{nA} [cm^2]	-	-	-	**2x10^{-15}**	**2x10^{-15}**
σ_{pA} [cm^2]	-	-	-	**8x10^{-13}**	**8x10^{-13}**
e_{tA} [eV]	-	-	-	**0.1 (step)**	**0.02 (gauss)**
N_{tD} [cm^{-3}/eV]	-	-	-	**8x10^{19}**	**7x10^{17}**
E_{tD} [eV]	-	-	-	**0.7**	**0.15**
σ_{nD} [cm^2]	-	-	-	**8x10^{-14}**	**10^{-14}**
σ_{pD} [cm^2]	-	-	-	**2x10^{-15}**	**10^{-15}**
e_{tD} [eV]	-	-	-	**0.1 (step)**	**0.3 (step)**

Table 2. Material parameters of the CZTSSe MGL monograin layer solar cell.

4. Analysis of the model

Fig. 12 shows the measured and simulated *J-V* characteristics of the CZTSSe MGL solar cell. The measured characteristics were obtained from the *I-V* characteristics normalized to the contacting area of the solar cell equal to $A = 4.81$ mm². Here we used the assumptions i) and ii) as defined in 3. Since the CZTSSe monograins shape in the spherical forms this means that the real current density varies throughout the structure. In the simulated *J-V* characteristics at 310 K we also took into account the S_{FF} as the assumption iii). This means that the J_{sc} obtained by using the parameters from Table 2 would in fact be larger by this factor.

In Fig. 12 we can observe a very good agreement of the measured and simulated *J-V* characteristics at 310 K while the simulation at 210 K exhibits a discrepancy in all solar cell output parameters. A possible reason for the non-matched J_{sc} at 210 K could be that in the modelling we did not account for the temperature dependent mobility, which could be the case as seen from the van der Pauw measurement of the monograin tablet (Fig. 5).
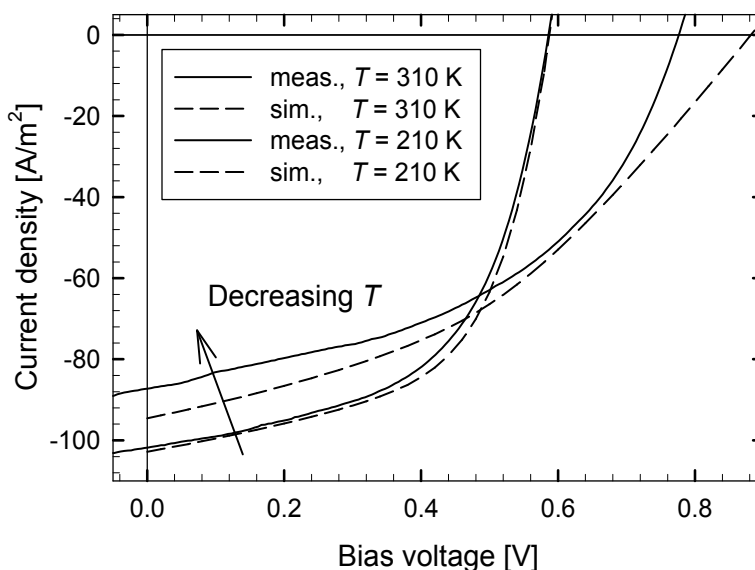
Fig. 12. Comparison of the measured and simulated *J-V* characteristics of the AM1.5 illuminated CZTSSe monograin solar cell.

Dashed lines in Fig. 12 represent the simulation and the arrow indicates temperature decrement. The short-circuit current and the open-circuit voltage trends are well correlated while their absolute value deviation at the low temperature indicate the necessity to include the temperature dependent mobility and the tunnelling enhanced recombination, respectively. At 210 K a significant mismatch also occurs with the V_{oc}. This leads us to the conclusion that it is not merely the SRH recombination (Sze & Ng, 2007) in the SDL layer that limits the V_{oc}, but there should also be present other recombination mechanisms which are less thermodynamically affected, namely the tunnelling enhanced recombination (Dumin & Pearson, 1965). The tunnelling enhanced recombination would reduce the rate of the V_{oc}-T change.

The optical simulations were performed using the Sun*Shine* simulator (Krč et al., 2003) which takes as an input a layered structure with the wavelength dependent complex refraction index coefficients, which comprise the real part $n(\lambda)$, called refractive index, and the complex part $k(\lambda)$ known as the extinction coefficient. Both are defined in for each layer. For the monograin material we used the complex refraction index coefficients as obtained by Paulson (Paulson et al., 2003) for the thin film $Cu(In_{1-x}Ga_x)Se_2$ alloy with the $x = 0.66$. This corresponds to the energy gap of 1.41 eV. The layer's interfaces were described using the roughness coefficient – σ_{rms}. In our case we set the σ_{rms} equal to 100 nm at all interfaces. Simulation of the external quantum efficiency (Fig. 13) shows a good agreement between the measured QE and the simulated QE in the shorter wavelengths region, while in the middle wavelengths there seems to exist some discrepancy – most probably due to the discrepancy between the measured and modelled $\mu_{h,CZTSSe}$. The cut-off wavelengths are well pronounced at both temperatures and correspond to the band-gap of 1.4 eV. In the long wavelength region ($\lambda > 900$ nm) the non-vanishing plateau of the simulated QE points to a mismatch in the absorption properties of the thin film CIGS and the monograin layer CZTSSe materials.
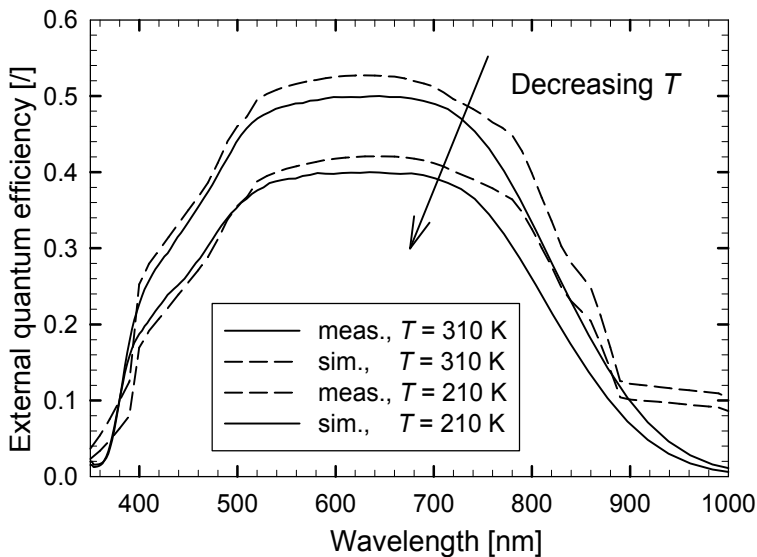
Fig. 13. Comparison of the measured and simulated external quantum efficiency of the AM1.5 illuminated CZTSSe monograin solar cell.

In Fig. 13 dashed lines represent the simulation and the arrow indicates temperature decrement. The non-vanishing plateau of the simulation originates from the mismatch in the absorption properties of the thin film CIGS (used in the simulation) and the monograin layer CZTSSe materials.

Both, measured and simulated QE show that the temperature change does not affect their shape, which inclines us to a conclusion that most of the photogenerated carriers recombine in the SDL and at the SDL/CZTSSe interface. This fact can as well be observed from the cumulative recombination profile (not shown here).

The absorptance simulations show that if all photogenerated carriers originating from the photon flux absorbed in the CZTSSe layer were extracted, the J_{sc} would equal to 37.7 mA/cm². Taking into account the S_{FF} the latter would reduce to a 29.4 mA/cm². This value

is still about 3 times larger than the measured (simulated) J_{sc} at 310 K, showing tremendous possibilities in improvement of the collection efficiency of the monograin CZTSSe absorber.

5. Conclusion

We have set up the baseline model of the $Cu_2SnZn(Se,S)_4$ monograin layer solar cell, which is able to predict the *J-V* characteristics and the external *QE* of the AM1.5 illuminated MGL solar cell in the temperature range from 310 K to 210 K. The model comprises following material properties:

i) in between the CdS and CZTSSe layers, the highly defective region called the surface defect layer – SDL, comprising a high concentrations of the mid-gap donor defects and a lower concentration of the mid-gap acceptor defects;

ii) in the CZTSSe monograin layer the narrow Gaussian distribution of shallow acceptor traps at 0.05 eV above the valence band and the wider distribution of the compensatory donor traps extending at least 0.3 eV deep into the energy band, relative to the valence band;

iii) energy gap of the CZTSSe monograin material equals to 1.4 eV, width of the SCR at 310 K equals to 180–200 nm and the concentration of the apparent doping p_{SCR} is in the range from 1×10^{16} cm^{-3} to 2×10^{16} cm^{-3}.

Low *FF* can be attributed to the low CZTSSe hole mobility, which equals to 1.5 cm²/Vs, and to the low apparent doping p_{SCR}, which originates from the compensatory effect of the shallow acceptors and deeper donors. Comparison of the flux absorbed in the CZTSSe monograin absorber and the three times lower actual current density of the extracted carriers shows us that further possibilities may reside in the shaping of the collection efficiency of the monograin absorber and/or in the additional passivation of the CdS/CZTSSe interface. Since the former is mainly attributed to the SCR this might not be an easy technological task. Whether these limiting properties are the result of the necessary surface engineering prior to the formation of the CdS/CZTSSe monograin heterojunction or they simply originate from the physical properties of the structure's materials, we were be not able to determine at this point.

6. Acknowledgments

7. References

Altosaar, M.; Jagomägi, A.; Kauk, M.; Krunks, M.; Krustok, J.; Mellikov, E.; Raudoja, A. & Varema, T. (2003). Monograin layer solar cells. *Thin Solid Films*, Vol. 431-432, pp. 466-469, ISSN 0040.6090

Altosaar, M.; Danilson, M.; Kauk, M.; Krustok, J.; Mellikov, E.; Raudoja, J.; Timmo, K. & Varema, T. (2005). Further development in CIS monograin layer solar cells technology. *Solar Energy Materials & Solar Cells*, Vol. 87, pp. 25-32, ISSN 0927.0248

Breitenstein, O.; Altermatt, P.; Ramspeck, K. & Schenk, A. (2006). The origin of ideality factors N>2 of shunt and surfaces in the dark I-V curves of SI solar cells, *Proceedings*

of the 21st European Photovoltaic Solar Energy Conference, pp. 625-628, Dresden, Germany.

Burgelman, M. & Nollet, P. (2005). Admittance spectroscopy of thin film solar cells. *Solid State Ionics*, Vol. 176, pp. 2171-2175, ISSN 0167.2738

Černivec, G.; Jagomägi, A.; Smole, F. & Topič, M. (2008). Numerical and experimental indication of thermally activated tunnelling transport in CIS monograin layer solar cells. *Solid State Electronics*, Vol. 52, pp. 78-85, ISSN 0038.1101

Dumin, D.J. & Pearson, G.L. (1965). Properties of gallium arsenide diodes between 4.2 and 300 K. *Journal of Applied Physics*, Vol. 36, No. 11, pp. 3418-3426, ISSN 0021.8979

Kosyachenko, L. (2010). Efficiency of thin film CdS/CdTe Solar Cells, In: *Solar Energy,* R.D. Rugescu, (Ed.), 105-130, InTech, ISBN 978-953-307-052-0, Vukovar, Croatia.

Krč, J.; Smole, F. & Topič M. (2003). Analysis of light scattering in amorphous Si:H solar cells by one-dimensional semi-coherent optical model. *Progress in Photovoltaics: Research and Applications*, Vol. 11, pp. 15-26, ISSN 1062.7995

Paulson, P.D.; Birkmire, R.W. & Shafarman, W.N. (2003). Optical characterization of $CuIn_{1-x}Ga_xSe_2$ alloy thin films by spectroscopic ellipsometry. *Journal of Applied Physics*, Vol. 94, No. 2, pp. 879-888, ISSN 0021.8979

Sah, C.T.; Noyce, R.N. & Shockley, W. (1957). Carrier generation and recombination in p-n junctions and p-n junction characteristics. *Proceedings of the Institute of Radio Engineers*, Vol. 45, No. 9, pp. 1228-1243, ISSN 0731.5996

Schenk, A. & Krumbein, U. (1995). Coupled defect-level recombination: Theory and application to anomalous diode characteristics. *Journal of Applied Physics*, Vol. 78, No. 5, pp. 3185-3192, ISSN 0021.8979

Schockley, W.; Read, W.T. (1952). Statistics of the recombination of holes and electrons. *Physical Review*, Vol. 87, pp. 835-842

Selberherr, S. (1984). *Analysis and simulation of semiconductor devices*, Springer Verlag, ISBN 978.0387818009, Vienna, Austria

Sze, S.M. and Ng, K.K. (2007). *Physics of semiconductor devices*, John Wiley & Sons, ISBN 9971.51.266.1 , New Jersey, USA

Topič, M.; Smole, F. & Furlan, J. (1996). Band-gap engineering in $CdS/Cu(In,Ga)Se_2$ solar cells. *Journal of Applied Physics*, Vol. 79, No. 11, pp. 8537-8540, ISSN 0021.8979

Van der Pauw, L.J. (1958). A method of measuring specific resistivity and Hall effect of discs of arbitrary shape. *Phillips Research Reports*, Vol. 13, pp. 1-9, ISSN 0031.7918

Walter, T.; Herberholz, R.; Müller, C. & Schock H.W. (1996). Determination of defect distributions from admittance measurements and application to $Cu(In,Ga)Se_2$ based heterojunctions. *Journal of Applied Physics*, Vol. 80, No. 8, pp. 4411-4420, ISSN 0021.8979

Large Area a-Si/μc-Si Thin Film Solar Cells

Fan Yang
Qualcomm MEMS Technologies, Inc.
United States

1. Introduction

Providing a sustainable and environment friendly energy source, photovoltaic (PV) power is becoming ever-increasingly important, as it decreases the nation's reliance on fossil-fuel generated electricity. Though widely regarded as a clean and renewable energy source, large scale deployment of PV is still impeded by the fact that the cost of PV energy is generally higher compared to grid electricity. Current development of PV technology is focused on two aspects: 1) improving the efficiency of PV modules and systems and 2) lowering the cost of delivered electricity through decreasing the manufacturing and installation cost. The merit of commercial solar cells aiming at terrestrial application is justified by the cost of unit PV power generation, dollar per watt ($/Wp), where Wp stands for the peak power generated by the cells.

Since the first practical PV cell grown on Si wafer at the Bell Laboratory in 1954, PV technology has been developed for more than five decades and evolved three "generations" based on different PV materials. The first generation of solar cells use crystalline materials, where the cost of the bulk materials has hit the point that further cost reduction is very difficult (Green 2007). In contrast, the second generation cells use thin film materials, where the required amount of materials is merely a few percent of that of bulk materials, significantly reducing the fabrication cost of this type of cells. The emerging, third generation of PV technology applies new materials and novel device concepts aiming at even higher efficiency and lower cost. At this moment, the commercial PV market is dominated by the first and second generation PV modules, and the third generation cells are still under lab research. As shown in Fig. 1, the efficiency of thin film PV system has improved from ~4 % in 1995 to >11 % in 2010, and will keep increasing to ~12% by 2020, a three-fold improvement compared to the system efficiency back in 1995. During the same timeframe, the cost of thin film PV system drops from ~4 $/Wp to ~0.5 $/Wp. Crystalline PV systems, though with higher efficiencies, have higher cost, i.e. 2.5 times the cost of thin film PV system. From the cost and material supply point of view, thin film solar cells will have a long-term development and gradually take more market share from the crystalline cells.

Many thin film materials can be used for PV cells, e.g., Si, CdTe, CIGS or the emerging organic/polymeric materials. Comparing to other materials, thin film Si, including amorphous Si (a-Si) and microcrystalline Si (μc-Si), have the following characters:

1. The PV active Si is the most abundant solid state element on the earth's shell, allowing for practically unlimited production of Si cells.
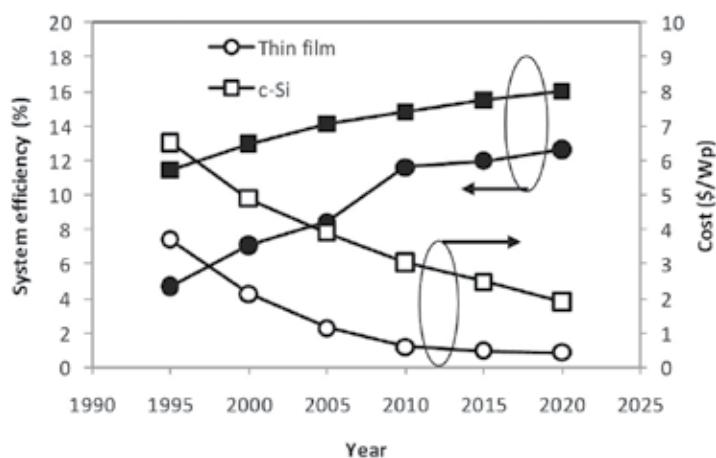
Fig. 1. Photovoltaic (PV) system efficiency and cost. Data from the U.S. Department of Energy.

2. Si has no toxicity and is environmental friendly.
3. Process of a-Si/µc-Si thin films takes the advantage of the highly mature semiconductor and display industries.
4. a-Si is a metastable material, and the initial cell performance of a-Si based cells degrades under illumination and then stabilizes, known as the Staebler–Wronski effect (Kolodziej 2004).

In addition, production of a-Si/µc-Si solar panels has a low entry barrier, thus making it more acceptable for the emerging PV manufactures. The first thin film Si solar cells were put into production in the 1980's when they were used as power sources for small electronic gadgets. Volume production of a-Si based solar panels started after the year 2000 with the introduction of large-area chemical vapor deposition (CVD) process at these companies: Sharp Corporation, United Solar Ovonic, Kaneka, Mitsubishi Heavy Industries, Ltd, etc. The true burst of Si thin film solar cells, on the other hand, came after 2007 with the "turnkey" (ready to use) thin-film solar manufacturing equipments introduced by Unaxis SPTec (later Oerlikon Solar) (Meier et al. 2007) and Applied Films Gmbh & Co. (later part of Applied Materials Inc.) (Repmann et al. 2007). The idea is that instead of developing the film deposition and module manufacturing technologies by self, the would-be solar maker can buy the full set of equipments together with the process recipes, and start manufacturing panels with relative ease. Each having a designed capacity of 40 – 60 MW, over twenty "turnkey" systems were sold to solar module makers world wide by Oerlikon and Applied Materials by 2010. The fast expansion of production capacity directly induced the drop of a-Si/µc-Si panel cost from around 5 $/Wp to less than 2 $/Wp.

At the moment thin film Si cells, including a-Si and µc-Si, take the largest market share (more than half of total production volume) among all types of thin film cells. Close to 5 GW of a-Si/µc-Si panels were manufactured in 2010, and will keep similarly large market share to at least 2013 (Fig. 2) (Young 2010). It is also noted from the same figure that the production volume of a-Si panels has an impressive compound annual growth rate (CAGR) of 42%, highest among all thin film PV technologies. Currently a significant amount of Si thin film panels are single-junction a-Si panels, whose efficiency will gradually increase to 8% - 8.5%. By adopting the a-Si/µc-Si multi-junction cells, panel efficiency will move up to
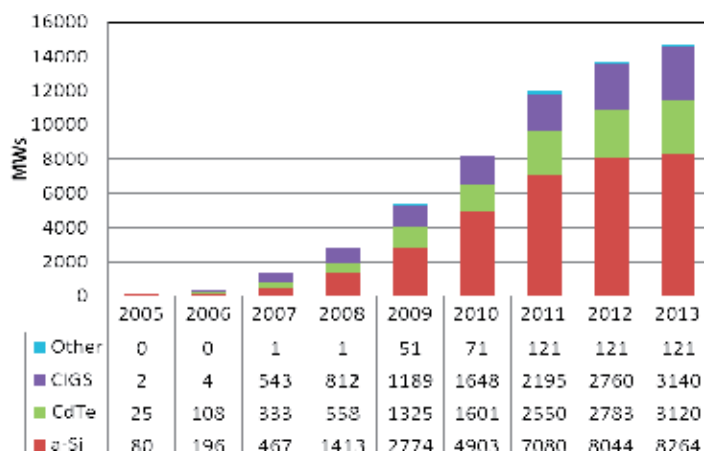
Fig. 2. Global thin film solar panel manufacturing capacity and compound annual growth rate (CAGR) by technology, 2006-2013 (estimate) (Young 2010).

around 10% after 2012. Costs for these technologies are expected to range from 0.80 to 1.20 $/Wp (Mehta 2010). Consequently, the energy cost pay-back time of these panels will be shortened to 0.5-2 years.

For the above mentioned reasons, a-Si/μc-Si solar panels are the mostly produced among all thin film technologies and will stay in large volume production the foreseeable future. This chapter introduces the fundamental thin film PV solar cell structure, the energy conversion physics, and state-of-the-art large scale solar panel manufacturing. Various methods of performance enhancement and cost reduction of large area thin film Si solar cells are focuses of this chapter.

This chapter is organized as follows. Section 1 briefly introduces the history and current production status of a-Si and μc-Si solar panels. Section 2 analyzes the cost structure of typical thin film solar panels and systems. The basic solar cell structures, including the PV active Si p-i-n junction layers and the front and back contact layers, are discussed in Section 3. Next, we describe in details the panel production process in Section 4 and 5. The front end of line (FEOL) processis first introduced, with discussions on CVD deposition of Si layers, physical vapor deposition (PVD) process of transparent conductive oxide (TCO) layers and back contacts, and laser scribing steps. The back end of line (BEOL) process is then described with the introduction of module fabrication, bus line wiring and panel encapsulation. Different process flow configurations are also compared in this part. We summary the chapter in Section 5.

2. Cost structure of PV system

To begin the discussion of the cost of solar panels, we split the cost of thin film PV system into four major parts:

1. Planning and financing: 15%
2. Inverter: 9-10%
3. Balance of system (BOS) and installation: 10-30%
4. Module: 40-66%

Sharing similar cost percentage of the first three parts with crystalline Si PV systems, the much lower module cost gives thin film PV system lower overall cost and a higher development potential. An increase or decrease of the efficiency of the module implies an increment or a reduction of the BOS and installation costs, respectively. Nevertheless, the financing and inverter cost remain always the same. Therefore, the use of lower efficiency thin film modules are financially more favorable in those cases in which the value of the installed area is not relevant. Thin film panels are thus more applicable to the PV electricity power plants built in remote areas like deserts. Large volume production and deployment is the key factor to fully demonstrate the financial benefit of thin film solar modules.

The cost of thin film modules, in turn is composed of five major components (Jäger-Waldau 2007):

1. Material cost (40%). The material consumption is determined by the film growth technology (e.g., PVD vs. CVD), and is also dominated by the module packaging and assembly technology. Special, TCO-coated glass substrates take a significant portion of the direct material cost (25-40%). Assuming similar technology used, the materials cost is inversely proportional to the production volume and panel efficiency.

2. Equipment related (capital) spending (20%). Initial investment on equipment on a-Si/µc-Si thin film panel manufactures is generally expensive. Upon fixed initial equipment investment, the annual depreciation of equipments is dominated by the deposition materials. The equipment depreciation rate is inversely proportional to the process throughput and module efficiency.

3. Labor cost (15-17%). The layered, monolithically integrated panel structure minimizes human operation, and the highly automated production methods used in the state-of-the art thin film PV panel manufactures reduce the labor cost. For a given total production volume, the labor cost is inversely proportional to the process throughput, extent of automation, and production module efficiency.

4. Energy consumption (15%). Modern PV manufactures use a significant amount of energy to run the factory, including machinery power consumption used for manipulating the substrate, controlling of substrate temperatures, RF power generators, film deposition system, vacuum system, exhaust handling, laser tool, lighting, air conditioning, etc. Once a factory is set up, a large amount of the overhead energy consumption is fixed, and the energy consumption per module is inversely proportional to the process throughput.

5. Freight (7-9%). The logistics of shipping and handling of the raw material as well as the assembled module panels take a larger portion of cost in thin film solar panels compared to their crystalline counter parts due to their greater size and weight. Unlike the other factors, freight cost is relatively constant for each panel.

As seen from the relationship of the thin film PV module cost structure summarized in Fig. 3, the process technology determines the direct material and energy consumption, equipment depreciation and ultimately the panel efficiency, which in turn affect the panel cost. In another word, more advanced module process technology leads to both higher panel efficiency and lower panel cost. Thus in this chapter, we put our focus on the process details of the manufacturing of modern, large-area a-Si/µc-Si solar panels.

3. Basic thin film Si solar cell structure

Typical a-Si single junction solar cells are composed of five principal layers: Si p-i-n diode sandwiched between two conductive layers. The front TCO forms the front contact, and the
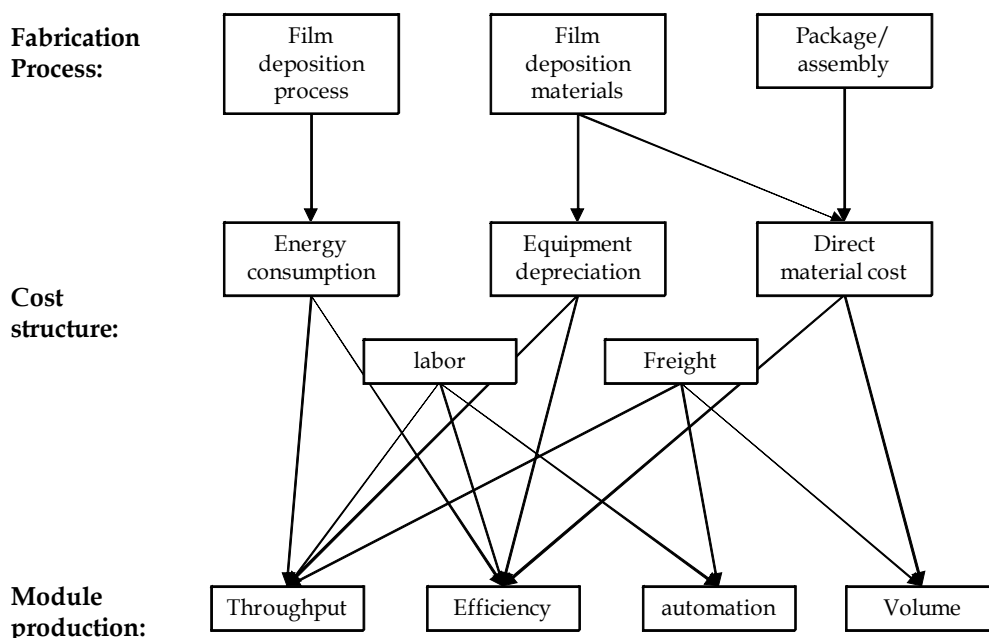
Fig. 3. Relationship between fabrication process, cost structure, and production of thin film PV modules.

back TCO and the reflector form the back contact (Fig. 4). The Si p-i-n junction absorbs sun light and generates photocarriers, which are collected by the conductive, front and back contacts. The substrate (e.g., glass) provides mechanical support for all the layers. Stacking two a-Si/µc-Si cells on top of each other forms the tandem junction structure, which is also sandwiched between the front and back TCOs.

Depends on the type of substrates on which the films are grown, there are basically two kinds of cell structures. 1) "Substrate" structure, where none-transparent substrates, i.e., metal foils, are used for growing the film stack. Sun light enters the cell from the top of the film stack by going through the top TCO. 2) "Superstrate" structure, where transparent substrates like glass or plastic films are used. Sun light enters the cell through the transparent glass/plastics and the TCO layer. The growth order of the Si p-i-n diodes are reversed in the two structures. The monolithically integrated superstrate type solar cells have superb encapsulation and compatibility with conventional electrical and safety regulations, thus holding a dominant market share.

3.1 PV active Si p-i-n layers

The Si p-i-n junction is where the sun light is absorbed and converted to charge carriers, i.e., electrons and holes. Differs from crystalline Si (c-Si), a-Si for PV and other applications (e.g., thin film transistor, TFT) are actually hydrogenated amorphous silicon alloy (a-Si:H, here noted as a-Si for simplicity), in which the H atoms passivate the otherwise high-density Si dangling bonds in pure amorphous Si film that introduce trap states and severely affect the film electrical properties. Normally the H content can be as high as a few percent. The a-Si completely loses the periodical atomic lattice structure; instead, the Si atoms randomly
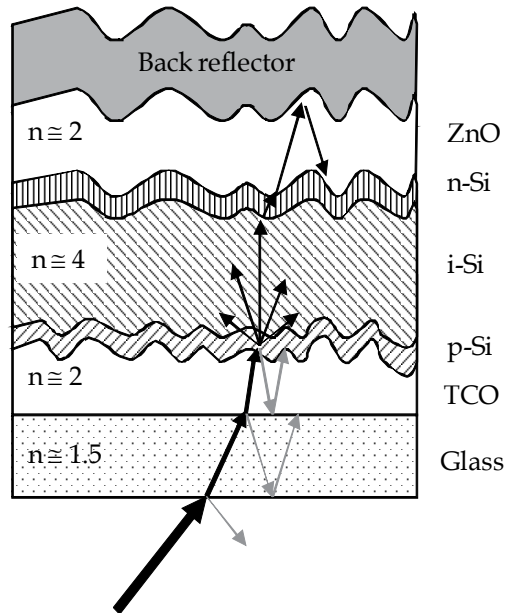
Fig. 4. Schematic single junction p-i-n a-Si solar cell. *n* stands for the index of refraction.

arrange in space. The lack of lattice structure makes a-Si a direct band gap semiconductor with a band gap of 1.8-1.9 eV at room temperature.

Hydrogenated microcrystalline Si (μc-Si:H, noted as μc-Si for simplicity) has a more complex, phase-mixed structure that consists of the crystalline phase made of silicon nanocrystallites and the amorphous Si matrix. The nanocrystallites grow into conglomerate clusters perpendicular to the film surface, whose diameters are typically between 10 and 50 nm. Embedded in amorphous silicon, the conglomerates are separated by a-Si, grain boundaries and micro-cracks. The band gap of μc-Si is 1.11 eV at room temperature, roughly the same as crystalline Si.

Photon absorption is proportional to the wavelength-dependent absorption coefficient, α, of the film. For typical a-Si and μc-Si, α is between 10^2 and 10^5 cm^{-1} in the visible range (Shah et al. 2004), which is 10-50 times larger than that of c-Si. Large α naturally allows for thinner absorber in solar cells. In the a-Si/μc-Si i-layer, an absorbed photon excites an electron from the valance band to the conduction band, creating a free electron and leaving a hole in the valance band. Due to the amorphous nature of a-Si and μc-Si films, the electrons and holes haves limited diffusion length and short life time. Electronic carrier transport properties are normally characterized by the mobility × lifetime product (μτ-product), which is the physical characteristic of both carrier drift and diffusion processes. The measured products of the electron mobility and lifetime, $\mu^0\tau^0$, is 2×10^{-8} cm^2/Vs for a-Si and 1×10^{-7} cm^2/Vs for μc-Si, respectively, much lower than those measured in c-Si wafers (Beck et al. 1996; Droz et al. 2000). The low μτ-product in a-Si or μc-Si makes the p-n diode configuration that is widely used in c-Si solar cells unsuitable with these materials, as the photocarrier collection in a p-n diode is diffusion limited. To avoid electron and hole recombination, p-i-n junction is used, where the built-in field drifts electrons towards the n-layer and holes towards the p-layer. The measured electron diffusion length is 2 μm in a-Si and 10 μm in μc-Si under the filed of

10^4 V/cm, comparable to or larger than the thickness of the solar cell film stack. As a result, the p-i-n type cells have efficient carrier collection efficiency.

Photons absorbed in the heavily doped n- and p- layers, however, don't contribute to the photocurrent as there is no net electric field in the doped layers. As a result, the n- and p-layers are usually less than 20 nm thick to limit photon absorption in these "window" layers. Further reduction of photon absorption in realized by increasing the band gaps of the n- and p-layers, e.g., doping the a-Si or µc-Si window layers with carbon so that they are transparent to the portion of the solar spectrum to be harvested in the i-layer. Total thickness of a typical single or tandem junction cell is less than 2 µm, which is only a few percent thick of a c-Si cell.

3.2 Front and back contacts

Though not PV active, the front and back contact layers play important roles on the cell performance. Optical wise, the transparent TCO layers scatter the incident sun light and enhance the optical absorption inside the i-layer. Electrical wise, since the lateral conductance of thin, doped p/n silicon layers is insufficient to prevent resistive losses, the TCO contact layers conduct the photocurrent in the lateral direction to the panel bus lines. The TCO layers used for thin film solar cells are doped wide band gap semiconducting oxides.

For efficient material usage and fast film deposition, the a-Si/µc-Si absorbers are so thin that the incoming light will not be completely absorbed during one single pass for normal incident rays. Hence, for all absorber materials, optical absorption inside the silicon layers has to be enhanced by increasing the optical absorption path. The difference of index of refraction between the TCO layers and the Si layers, plus the rough interface induce diffusive refraction of incoming light at oblique angles, thus increasing the optical path of solar radiation (Fig. 4). This is typically done by nano-texturing the front TCO electrode to a typical root-mean-square (rms) surface roughness of 40–150 nm and/or nano-textured back reflectors. In the ideal case, these rough layers can introduce nearly completely diffusive transmission or reflection of light (Müller et al. 2004).

When applied at the front contact, TCO has to possess a high transparency in the spectral region where the solar cell is operating (transmittance > 90% in 350 – 1000 nm), strong scattering of the incoming light, and a high electrical conductivity (sheet resistance < 20 Ω/sq.) (Fortunato et al. 2007). For the superstrate configuration where the Si layers are deposited onto a transparent substrate (e.g., glass) covered by TCO, it has to have at the same time favorable physicochemical properties for the growth of the silicon. For example, the TCO has to be inert to hydrogen-rich plasmas, and act as a good nucleation layer for the growth of the a-Si/µc-Si films. For all thin-film silicon solar cells, scattering at interfaces between neighboring layers with different refractive indices and subsequent trapping of the incident light within the silicon absorber layers is crucial to high efficiency.

TCO is also used between silicon and the metallic contact as a part of the back reflector to improve its optical properties and act as a dopant diffusion barrier. The back TCO layer also prevents reaction between the metal and the a-Si/µc-Si underlayers. Furthermore, applied in a-Si:H/µc-Si:H tandem solar cells, TCO can be used as an intermediate reflector between top and bottom cells to increase the current in the thin amorphous silicon top cell (Yamamoto et al. 2006). Finally, nano-rough TCO front contacts act as an efficient antireflection coating due to the refractive index grading at the TCO/Si interface.

The front and back TCO layers are at the same time electrodes that collect photogenerated carriers. As a semiconductor, the optical transparency and the electrical conductivity are closely related to the band gap structure of the TCO. The short-wavelength cutoff of the transmission spectrum corresponds to the oxide band gap, whereas the long-wavelength transmission edge corresponds to the free carrier plasma resonance frequency. On the other hand, electron conduction in TCO is achieved by degenerate doping that increases the free carrier density and moves the Fermi level into the conduction band. High carrier density and carrier mobility are thus required for TCO layers. There is, however, a tradeoff between high optical transmittance and low electrical resistance. Increasing electron carrier density decreases resistivity but also increases the plasma oscillation frequency of free carriers, thus shifting the IR absorption edge towards the visible. The transmission window is thus narrowed as a result of improved conductivity.

TCO type	ITO	ZnO:Al	SnO$_2$:F
Optical transmission (350-1000 nm)	95%	90-95%	90%
Resistivity ($\Omega \cdot$cm)	1-5×10^{-4}	3-8×10^{-4}	6-10×10^{-4}
Work function (eV)	4.7	4.5	4.8
Band gap (eV)	~3.7	~3.4	4.1-4.3
Deposition methods	RF sputtering	RF sputtering, LPCVD	APCVD, spray pyrolysis
Surface roughness	Flat	Excellent	Excellent
Plasma stability	Low	Excellent	Good
Relative cost	High	Middle	Low

Table 1. Different TCOs employed in Si thin film solar cells. RF, radio frequency. LPCVD, low-pressure chemical vapor deposition. APCVD, atmosphere-pressure CVD.

The most-widely used TCOs in Si thin film solar cells are doped SnO$_2$ (i.e., SnO$_2$:F) and ZnO (i.e., ZnO:Al) due to their temperature and chemical stabilities. Compared to the more conductive alternative indium-tin-oxide (ITO), they offer a much lower cost by avoiding the use of the costly In. At the same time, surface roughness induced by the crystalline texture of SnO$_2$ and ZnO is widely applied for increasing the optical absorption. These three typical TCOs are compared in Table 1.

The reflector layer on top of the back TCO can be Ag, Al, or white paint in a "superstrate" cell, and is the metal foil itself or another Ag/Al coating on the foil in a 'substrate' type cell. Ag is typically used in laboratory research work, while Al is more often used in mass production modules due to its lower cost and better properties in removing module shunts. Back contacts of Oerlikon's thin film panels, on the other hand, use proprietary white paint as the reflector (Meier et al. 2005). The white paint can be rolled on or screen printed directly onto the TCO. At the same time, it offers the following advantages (Berger et al. 2007): 1) high optical reflectance over a broad wavelength band, 2) optimal light scattering pattern which is generally beneficial for solar cells because this maximizes the fraction of photons that are trapped inside the solar cell due to total internal reflection at both cell surfaces, 3) pigmented materials have the potential of low cost. In certain instances, the white paint is a better surface reflector than Al, or TCO/Al reflector.

4. Factory panel production

As previously discussed (c.f., Section 2), manufacturing of the solar panels directly determines the cost of modules, which takes 40-66% of the overall PV system cost. This section focuses on the factory panel production, and addresses various methods of panel efficiency improvement and cost reduction.

FEOL   BEOL
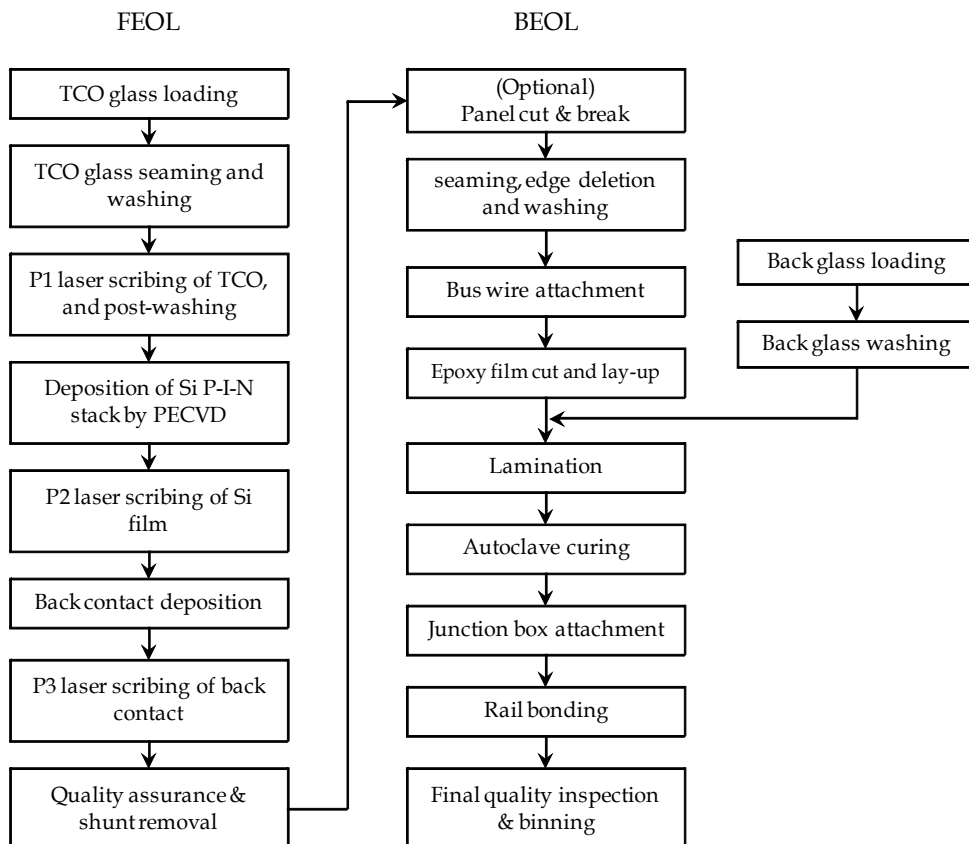
Fig. 5. Flow diagram of typical thin film solar panel production, comprising of both the front end of line (FEOL) and back end of line (BEOL) technologies and processes (Bhan et al. 2010).

Development in the a-Si and µc-Si thin film process technology combined with the booming PV market resulted in the fast expansion of a-Si/µc-Si based solar panel manufacturing after 2007. This industry largely benefits from the lab demonstration of thin film solar cells on small size substrates, as well as the large-area thin film deposition techniques developed for thin-film transistor liquid crystal display (TFT-LCD) industry. The growth of high-quality Si thin films for PV applications shares many of the skill sets required for growing Si TFT films, and using similar large-area thin film deposition chambers (Yang et al. 2007). In fact, both thin film solar "turnkey" equipment providers, Oerlikon and Applied Materials, have been manufacturing large-scale TFT-LCD deposition systems for years before becoming thin film solar equipment providers.

The general process flow of thin film panel fabrication is shown in the diagram of Fig. 5. This is a typical Applied Materials Sunfab process configuration (Bhan et al. 2010), though that of Oerlikon (Sun et al. 2009) and other 'superstrate' type panel makers are similar. The entire process is divided into the FEOL steps where the front glass substrate is deposited with active layers, and BEOL steps where the module is encapsulated. The FEOL mainly involves several film deposition and patterning steps, including the growth of Si p-i-n junctions by CVD and the growth of TCOs and metal layers by PVD. Laser scribing steps are used in between film depositions to form monolithically interconnected cells across the entire substrate. In the BEOL steps, the front glass with blanket film deposited during FEOL is cut, shaped and encapsulated to make solar panels. Optical and electrical inspections are taken upon finishing of FEOL for quality control purposes. Process of the 'substrate' type module shares many of the FEOL and BEOL steps, and the differences are discussed later in Section 4.3.

4.1 Front end of line (FEOL) process

The first step of module deposition involves loading of substrates in FEOL. Either float glass or TCO-coated glass is used, though an extra TCO growth step is required for the former case (Kroll et al. 2007; Sun et al. 2009). To prevent the glass from chipping and cracking during the following thermal cycle steps, as the film deposition steps require substrate temperatures ranging from 150 to 250 °C, the glass edge is seamed and reinforced. Then the glass goes through washing and drying steps to thoroughly remove debris, particles and organic contaminants. Laser-scribing step P1 follows to form isolated TCO contact strips. After a second washing step, the TCO glass is loaded into the film deposition chambers for the growth of PV active layers.

4.1.1 Growth of a-Si/μc-Si layers

The PV active Si p-i-n film stack is normally grown by CVD from gaseous precursors. Several CVD deposition techniques have been developed for the deposition of a-Si/μc-Si layers, including plasma-enhanced CVD (PECVD) (Schropp and Zeman 1998), remote plasma enhanced CVD (RPECVD) (Kessels et al. 2001), and hotwire CVD (Schroeder 2003). Though efficient lab-size solar cells are made with various CVD techniques, PECVD is prevailingly used for current industrial, high-throughput thin film PV module fabrication, as it possesses advantages like high deposition rate, in-situ chamber cleaning, good control over film quality, and requires lowest substrate temperature.

A typical PECVD chamber is structured like the schematics in Fig. 6. The substrate is supported by a susceptor, directly facing a gas diffuser. Process gases (SiH_4, H_2 and dopant gases) are fed into the chamber and dispersed by the diffuser. The diffuser and the susceptor are charged at opposite radio frequency (RF) voltages, thus exciting plasma within the chamber. Commonly used RF plasma is excited at 13.56 MHZ or 40 MHz, while higher RF frequencies are also used (Nishimiya et al. 2008). Higher RF frequencies are reported to deposit Si film faster due to higher plasmornic excitation energy. On the other hand, higher frequency means shorter RF wavelength, potentially forming standing wave inside the chamber that can cause non-uniform plasma distribution and reduce the a-Si/μc-Si film uniformity.

Using silane (SiH_4) as the precursor gas, the deposition of a-Si/μc-Si films can be described as a four-step process (Schropp and Zeman 1998):

1. Primary gas phase SiH_4 decomposition. The plasma excites and decomposes the SiH_4 molecules into neutral radicals and molecules, positively and negatively charged ions, and electrons.

2. Secondary gas phase reaction. The reaction between molecules, ions and radicals (product of the previous step) generates reactive species and eventually large Si-H clusters, which are also called dust or power particles. The neutral species diffuse to the substrate, while the positive ions bombard the growing film and the negative ions are constrained within the plasma.

3. Film deposition. The radicals diffusing to the substrate interact with the substrate surface in various ways, like radical diffusion, chemical bonding, hydrogen sticking to the surface or desorption from the surface.

4. Formation of a-Si film. The actively growing film then releases hydrogen and relaxes into the Si network.
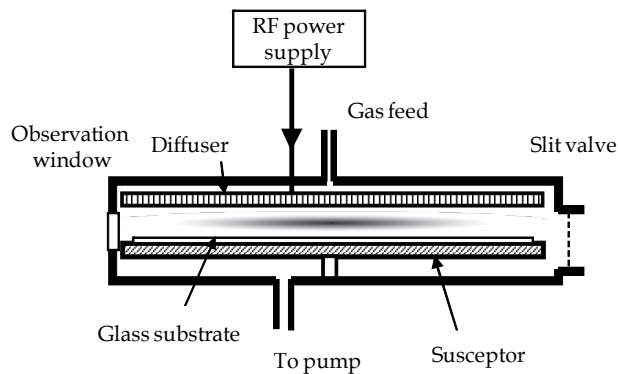
Fig. 6. Schematics of a PECVD process chamber.
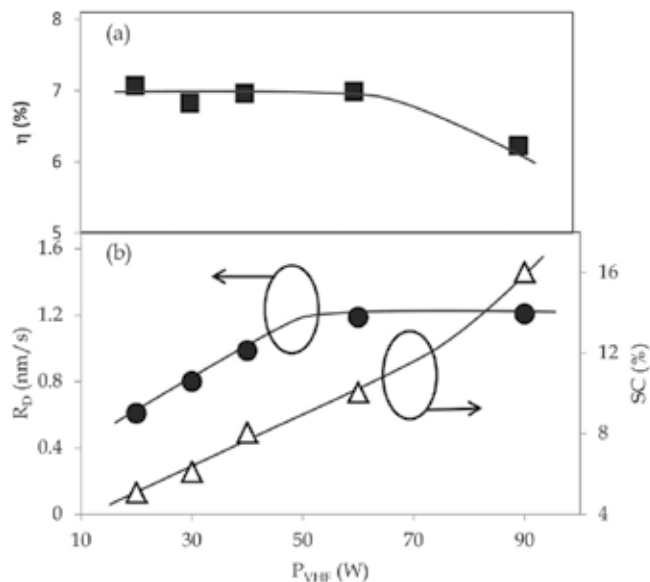
Fig. 7. Challenges met with high deposition rate (R_D) for PECVD grown µc-Si films. (a) Efficiencies of the optimal µc-Si single junction solar cell at different very-high frequency radio-frequency power (P_{VHF}). (b) Corresponding deposition rates RD and SiH_4 dilution concentration (SC) (Mai et al. 2005).

The overall film deposition is a complex process of gas and surface reactions, and is controlled by many deposition parameters, including gas composition, flow rate, chamber pressure, RF power density, RF frequency, substrate temperature, and the chamber size and geometry. Extensive studies are carried out to study the influence of those controlling parameters on the a-Si/μc-Si film properties, and are summarized in review papers (Luft and Tsuo 1993; Bruno et al. 1995). Perusing high solar energy conversion efficiency requires high quality, PECVD grown a-Si/μc-Si films, like high optical absorption, low dangling bond density, wide band gap for optical transmission of the p- and n- window layers (Schropp 2006).

Transferring the lab-developed process to solar panel production, however, has its own challenges. The PECVD steps take a significant portion of the cost in energy consumption and equipment depreciation (c.f., Fig. 3), thus substantial changes must be made to the lab-developed PECVD processes in panel manufacturing to fit the goal of lowering the panel cost. While maintaining the optimal panel performance, the widely adapted strategies are high rate of deposition (R_D) and large substrate size for high-throughput panel growth.

As previously discussed in Section 2, fast film deposition can lower the energy consumption, facilitating the throughput and process efficiency, thus effectively lower the cost of solar modules. The major obstacle to throughput increase is the μc-Si deposition, which has to be thick (> 1.5 μm) as limited by the finite absorption coefficient, thus requiring appreciably long deposition time. In fact, deposition of the μc-Si bottom cell in a-Si/μc-Si tandem junction solar panels takes the longest process time in the Oerlikon and Applied Materials process lines. To shorten the μc-Si deposition time and improve the overall throughput, research has been focused on increasing the deposition rate of μc-Si films.

Generally, increasing the density of SiH radicals promotes the growth of a-Si/μc-Si, thus increasing SiH_4 flow rate, applying higher RF power density, or using a higher RF excitation frequency all lead to higher R_D. For the simpler case of a-Si, higher RF power and higher gas flow rate result in faster film growth. As for the case of μc-Si, changing these deposition parameters at the same time affects the film crystallization in addition to increasing R_D. Since a good performed μc-Si solar cell needs to keep at the transition from microcrystalline to amorphous growth, increasing the film deposition rate should not be compromised by the film crystallinity. It is observed that increase of RF power requires higher SiH_4 concentration to keep the same crystallinity, which at the same time leads to higher deposition rate. In one example, Fig. 7 compared the high R_D achieved with increasing very high frequency (VHF) 94.7 MHz RF power (Mai et al. 2005). To maintain the maximum PV efficiency (Fig. 7a) at different VHF power (P_{VHF}), the silence concentration (SC) in the mixed gas has to increase with P_{VHF} (Fig. 7b). At small P_{VHF}, R_D increases linearly with P_{VHF}, and saturates around 1.2 nm/s when P_{VHF} is > 60 W. The solar cell efficiency, η stays constant for the same region since the μc-Si crystallinity remains unchanged. Further increase of P_{VHF} doesn't lead to higher RD, and the optimal cell efficiency drops at this region. It is important to note that higher deposition rate greatly improves the throughput of the panel manufacturing, and lowers the panel cost.

Since the merit of solar cell, $/Wp, is inversely proportional to the total solar module production (Hegedus and Luque 2003), growing solar cells over large-area substrates is one of the most efficient ways of lowering solar cell cost. For constant direct materials and labor cost, growing films over larger area substrates effectively lowers the module cost per unit area. The major challenge when scaling up the substrate is to maintain uniform film growth over large

area. Since various PECVD parameters directly affect the growth rate of a-Si / μc-Si film, the non-uniform distribution of these growth parameters induces local film thickness variation. For typical p-i-n type a-Si or μc-Si cells, the open circuit voltage (V_{OC}) and fill factor (*FF*) decrease upon increasing i-layer thickness, while J_{SC} increases as a result of the higher absorption in the thicker cells (Klein et al. 2002). Other than thickness, the RF power distribution affects the crystallinity of the as-grown μc-Si, which in turn changes the solar cell performance. For example, slight deviation of RF intensity resulted in unbalanced μc-Si crystallization in a Gen 8.5 PECVD chamber, as shown by the smaller fraction of crystallinity (FC) on the left side of chamber before adjusting the RF power supply feed (Fig. 8a), though such deviation could be too small to affect the a-Si and μc-Si film thicknesses (Yang et al. 2009). Small size a-Si/μc-Si tandem junction solar cells cut from the solar panels at corresponding locations, had non-uniform performance distribution. Sample cells from the low RF intensity side (left) had smaller short circuit current density (J_{SC}) (Fig. 8b) and higher V_{OC} (Fig. 8c) than those from the other side, while *FF* had a uniform distribution despite the RF influence (Fig. 8d). After modifying the RF feed of the PECVD chamber, balanced FC distribution was obtained, and the sample cells showed uniform distribution of J_{SC}, V_{OC} and *FF*. It is thus important to keep the uniform distribution of all process parameters in large scale process, and special attention must be paid to the RF power distribution across the whole chamber.
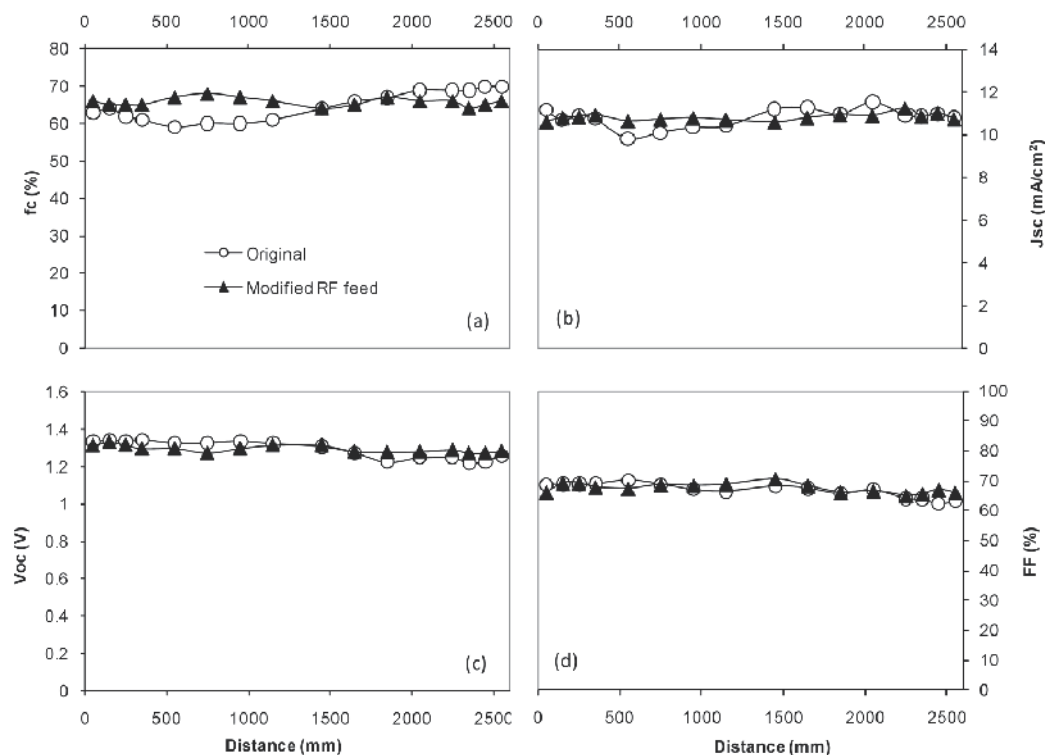
Fig. 8. μc-Si film uniformity and its impact to solar cell performance (a) Crystalline fraction (fc) change along substrate diagonal with original and modified RF feed. (b) J_{SC}, (c) V_{OC}, and (d) FF profiles along substrate diagonals. The two substrates were grown before and after modifying the RF feed location.

4.1.2 Growth of TCO layers

The TCO layers are typically grown by either CVD or PVD on industrial size substrates. Used as the front TCO layer, SnO_2:F layer are normally grown by CVD using $SnCl_4$ precursor gas on glass substrates (Rath et al. 2010). The finished SnO_2:F-coated glass is provided as substrates for later PECVD deposition of a-Si/μc-Si layers. Another front TCO candidate is AZO, which is usually grown by CVD processes using precursors like $Zn(C_2H_5)_2$ or sputter deposition (Agashe et al. 2004). Substrate temperatures are near 150 °C for the CVD deposition, and can go as high as 300 °C for sputtering.

For many solar panel manufactures, control of the front TCO properties, especially the surface roughness, can be financially unfeasible, thus purchasing glass substrate pre-coated with TCO becomes a good choice. For a-Si absorber layers a high transparency for visible light (wavelength λ = 400–750 nm) is sufficient, while for solar cells incorporating μc-Si the TCO has to be highly transparent up to the near infrared (NIR) region (400–1100 nm) to accommodate for the wider absorption spectrum of μc-Si. This imposes certain restrictions on the carrier density, n, of the TCO material, as increased free carrier absorption leads to a reduction of IR transmission (Agashe et al. 2004). SnO_2:F films fulfilling these requirements to a large extent, have been developed by Asahi Glass (Asahi Type U) (Sato et al. 1992). The ZnO crystallite facets imposes diffusive light scattering to the incident sun light, thus enhances the optical absorption with minimal absorbing layer. Further light trapping for long-wavelength light is also achieved in the Asahi high haze, HU-TCO glass, where the TCO surface has two types of textures of different characteristic length thus scattering different portions of light (Kambe et al. 2009).

The back TCO is typically AZO (c.f., Table 1), which is grown in-line with other in-house process steps. In addition, AZO provides excellent long-term stability as the back contact material. Since the back contact is grown on top of finished Si p-i-n stack, the substrate temperature should be kept low (<300 °C) to prevent the dopant diffusion from the a-Si/μc-Si n layers. The back AZO contact is typically grown by RF sputtering (Beyer et al. 2007) or low pressure (LP)-CVD (Meier et al. 2010) at temperatures < 150 °C.

4.1.3 Laser scribing

A big advantage of the superstrate type a-Si/μc-Si thin film solar panels lies in the monolithically integrated structure, which greatly reduces operational cost and increases production throughput and panel yield by eliminating connection of wafers in the fabrication of crystalline Si PV panels. The thin film panel is scribed into numerous small cells, which are interconnected in series for a high voltage output, which at the same time improves panel yield and lowers the resistive energy loss. The monolithically integrated series connection is realized by a three step patterning process that selectively removes the individual layers, i.e., TCO front contact, thin-film silicon layer stack, and back contact of the solar cell. Highly automated laser scribing patterning is widely used for all patterning steps (c.f., Fig. 5) as it provides precise positioning, high throughput and minimum area losses.

Scribing thin film layers into sections with laser has developed a mature technology applied to large-area superstrate-type module fabrication, where laser beam incidents through the glass substrate. As depicted in Fig. 9, laser scribing mechanism can be described as a four-step process (Shinohara et al. 2006).

1. Absorption of laser beam. By choosing appropriate laser energy/wavelength, the layer to be scribed absorbs the laser energy following Lambert's law, with more heat created

at the glass-side of the film (Fig. 9a). Typical laser energy is $>1\times10^6$ W/cm^2, and calculation shows more than 80% of that energy is absorbed and converted to heat building up in the film.

2. Decomposition of H from a-Si:H. The absorbed heat induces the decomposition of a-Si:H, and releases hydrogen at a temperature of > 600 °C (Fig. 9b). In fact, the local temperature in the film can be heated up to 700 °C by the laser.

3. Destruction of the PV layers and back contact. The gaseous H$_2$ quickly expends its volume and pressure under the high temperature. The pressure of the H$_2$ gas can amount to $>1\times10^7$ Pa, inducing enormous shear stress on the layers above the heated zone. In one estimation, applying a 532 nm, 12 kHz and 9.5×10^6 W/cm^2 laser beam on a-Si single junction module created shear stress of 3.9×10^8 Pa, enough to break the layers on top of the heating zone, among which the most ductile Ag layer has a shear strength of $10^7 - 10^8$ Pa (Fig. 9c).

4. Formation of heat affected zone (HAZ). Along with the H$_2$ volume expansion, the film cracks quickly followed by blasting off, effectively removing the a-Si/μc-Si layers and the back contact layers above the local, heated zone. The laser heating also damages the film around the removed region, creating a HAZ with high density of defects and poor electrical properties (Fig. 9d). By using high-frequency pulsed laser, the HAZ is limited to less than a few tens of nm wide.

It is important to note that the laser scribing removal is not a true thermal process but the mechanical blasting off of the film. By applying different wavelengths of lasers, the laser energy is absorbed by different layers, thus selectively removes those layers without affecting other, underlying layers.
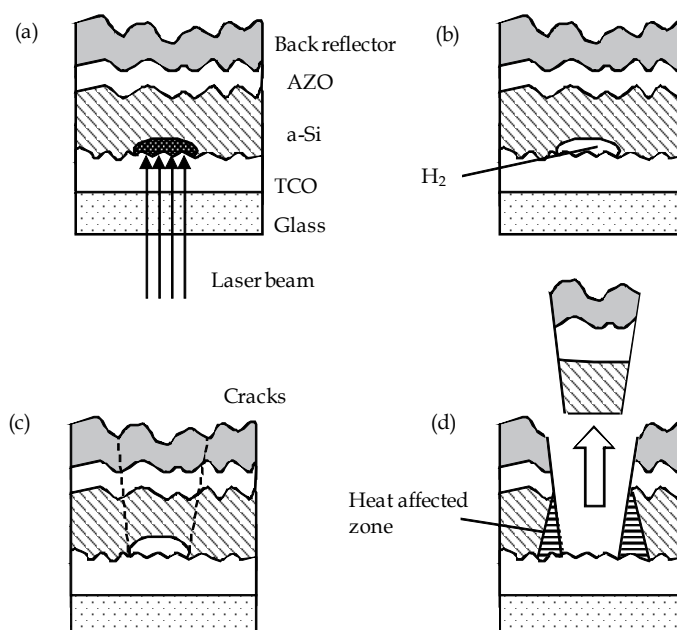
Fig. 9. Laser-scribing mechanism. (a) absorption of laser beam incidents through the glass, (b) decomposition of H from a-Si:H, (c) destruction of the photovoltaic layer and back electrode, (d) film blasted off and formation of heat affected zone (Shinohara et al. 2006).

Combination of several laser-scribed layers is used to create interconnection in Si thin-film modules (Fig. 10a). The cell strips are defined by selective ablation of individual layer stacks, and the interconnection between neighboring strip cells are provided by the overlap of conductive layers. In the microscope view of a typical interconnection area (Fig. 10b), P1 is the first laser scribing step that cuts through the front TCO layer, P2 is the second scribing step that cuts through the p-i-n junction layers, P3 is the last step that cuts through the junction layers and the back reflector. The dead-area, i.e., the narrow area between P1 and P3 lines including the HAZ, makes up the interconnection junction but doesn't contribute to photocurrent generation. State-of-the-art laser process can limit the interconnection width to < 350 µm to minimize the dead-area. For a-Si/µc-Si module production, the scribing laser is typically powerful Nd:YVO$_4$ solid-state laser with primary emission at 1064 nm and second harmonic generation at 532 nm. P1 is scribed by the 1064 nm irradiation, in which the strong absorption in TCO results in intensive local heating and explosive TCO evaporation (ablation); the glass that doesn't absorb in this wavelength keeps cool and is free from damage. P2 and P3 are similarly scribed by the 532 nm irradiation. As shown in Fig. 10c, the P3 laser cuts abrupt edges on the a-Si film without leaving any observable damage to the underlying TCO layer. The three laser scribing steps combining the subsequent film deposition steps form differences in the depths of different layers and conductive channels, forming the interconnection region of the cell strips' series connection. Power optimized, high-speed laser scribing technique is already applied in making 5.7 m^2 solar panels with exceptional performance (Borrajo et al. 2009).
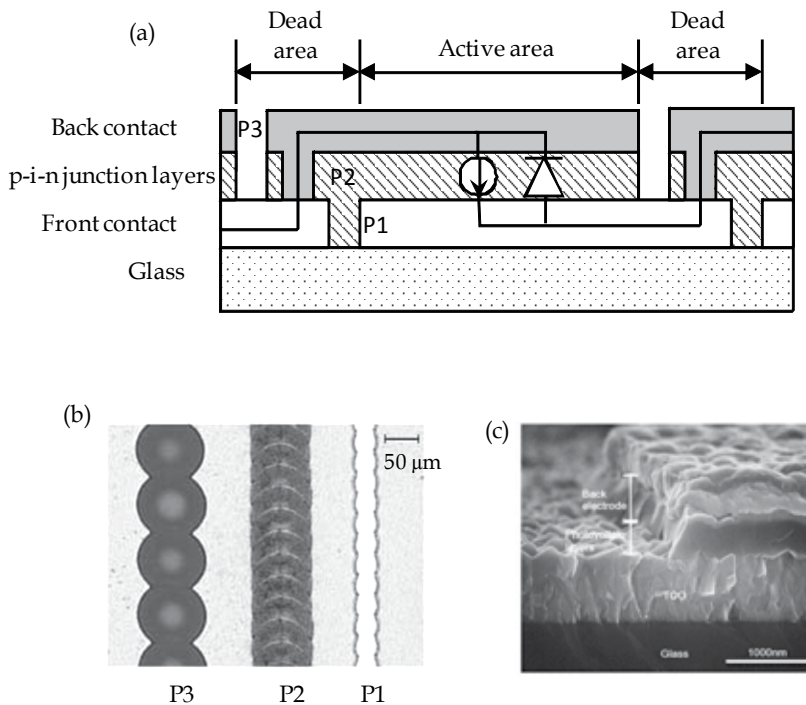
Fig. 10. (a) Schematic cross-sectional view of Si thin film solar panel showing the sectioned film and laser scribing lines (P1, P2 and P3). (b) Optical microscope image of the laser scribed lines. (c) Scanning electron microscope image of P3 scribed PV layer (Shinohara et al. 2006).

Making up the interconnection of cell strips, the laser scribing pattern is decisive to the assembled panel performance. Since the total panel area is fixed, the width of cell strips determined by the laser scribing pattern is inversely proportional to the number of cell strips. Laser scribing pattern also affects the number of junctions and total dead area, which both contribute to losses in panel power output. Thus design of the laser scribing pattern is optimized with the width of strip cells and the sheet resistance of the front and back contacts.

Precisely scribing fine lines that defines the monolithically integrated thin film solar module, laser scribing technology greatly enhanced the overall panel performance and improves the automation of the process flow. It is an important step in improving the module efficiency and driving down the module cost independent of the film deposition processes.

4.1.4 Rest of FEOL steps

After all film deposition and laser scribing steps conclude, the central PV active region is isolated from the panel edge to avoid electrical shock. In one way, the outside edge of the entire film stack is removed by 10-20 mm of width, called edge deletion. This is typically done by mechanical grinding or laser scribing (same as P2 laser).

To burn out the defects and improve panel yield, the final FEOL step involves removing cell shunts by reverse biasing the cells, or shunt busting. Shunting in Si thin film solar cells refers to high leakage current in reverse bias, which leads to a loss of power and efficiency. In large scale deposition, pinholes or locally thinner Si layer could form, which allow a connection between the top and bottom contacts, forming partially shorted PV diodes. When applying a reverse bias, larger current is focused at these shunt regions, resulting in local heat generation and consequent burning out of the low resistance pathway. Microscopic observation confirms the change of film morphology and its connection to the curing of the solar cells (Johnson et al. 2003).

As all cells are readily formed at this stage, electrical and optical inspection of individual cell strips are taken after the shunt busting for quality assurance purposes. This completes the FEOL processing of the solar panel.

4.2 Back end of line (BEOL) process

Panels fabricated at FEOL have to be further shaped and encapsulated to complete the solar panel module at the BEOL steps. Though no more film is deposited in the BEOL steps, these are important processes to ensure high quality solar panel production.

4.2.1 Module fabrication and bus line wiring

If the module size is smaller than the substrate, glass with deposited film is first scored and broken into the final panel size, and goes through edge deletion. Then the panel is thoroughly washed for another time and ready for final bus line soldering.

According to the laser scribing layout, the two terminal segments of the series connected cell strips are each soldered to a bus line. These two terminal segments serve as the beginning and ending of the series connection of all cell strips on the panel. The cross bus bars are then attached to the terminal bus line and leaves out the final electrical connection to the external circuit.

4.2.2 Module encapsulation

To stand for extreme weather conditions in field usage, the functional films, i.e., TCO layers, a-Si/μc-Si films, metal coatings, and bus lines need good encapsulation to achieve

for long panel lifetime. The most common encapsulation method for panels with the glass substrate is to use another piece of glass to cover the functional films. The gap between the two glass plates is filled with an epoxy (ethylene vinyl acetate, EVA, or polyvinyl butyral, PVB) film, which not only insulates the functional films against reactants like oxygen and moisture, but also mechanically strengthens the rigidness of the finished panel. Quality of the module encapsulation is directly associated with the failures of panels in the field. Judgment of the encapsulation properties includes low-interface conductivity, adequate adhesion of encapsulants to glass as a function of in-service exposure conditions, and low moisture permeation at all operation temperatures (Jorgensen et al. 2006).

The panel then passes through a laminator where a combination of heated nip rollers removes the air and seals the edges. The lamination film at the same time provides electrical insulation against any electric shock hazard. At the exit of the laminator conveyer, the modules are collected and stacked together on a rack for batch processing through the autoclave where they are subjected to an anneal/pressure cycle to remove the residual air and completely cure the epoxy. Finally, a junction box is attached to the cross bus wire and sealed on top of the hole of the back glass and is filled with the pottant to achieve a complete module integrity.

The fully processed module is then tested for output power, I_{SC}, V_{OC}, and other characteristics under a solar simulator. Then it is labeled, glued to the supporting bars, and packaged. At this point, the full panel assembly is finished.

4.3 Production process flow

Multiple chambers are used for deposition of different functional layers in the module production process. Optimizing the arrangement of chambers and controlling of the process flow are crucial to the production throughput and directly affect the panel production cost. There are mainly three types of process flows: batch process, continuous process and hybrid process. Characteristics of the three processes are compared in Table 2.

Batch process of film deposition is the most intuitive way of arranging deposition chambers. In this configuration, functional layers are deposited consequently onto batches of substrates. The typical batch processes are seen in Oerlikon's thin film production lines. An example is the Oerlikon KAI-20 1200 production system (Fig. 11a), which consists of two PECVD process towers, two load-locks, one transfer chamber and an external robot for glass loading from cassettes (Kroll et al. 2007). Each process tower is equipped with a stack of ten plasma-box-reactors where ten substrates are deposited simultaneously. The layers are processed in parallel at the same time in both stacks (2×10 reactors). The whole KAI-20 1200 PECVD production system shares one common gas delivery system including the mass flow controllers and one common process pump system. Engineering work has been put to ensure small box-to-box variations of deposition rates, layer thickness uniformities. The batch process normally requires small footprint, and is suitable for slow deposition that requires long process time (e.g., the absorbing i-layers). In fact the PECVD deposition of different p-, i-, and n- layers can be combined within the same chamber as long as dopant diffusion from the process chamber can be minimized. In most cases more than one chambers are used for the entire film stack, thus when they are moved between separate chambers the substrate manipulation and heating / cooling time has to be minimized to increase the process throughput.

Process flow types	Batch Process	Continuous Process	Hybrid Process
Schematics	Fig. 12a	Fig. 12b	Fig. 12c
Examples	Oerlikon Solar customers	United Solar, ECD, Xunlight	Applied Materials customers
Production volume	20 MW/yr	30 MW/yr	40-55 MW/yr
System footprint	6 m × 8.6 m (KAI 1200)	6 m × 90 m	Variable sizes
Substrate	Glass, 1.1 m × 1.25 m	Stainless steel roll, 36 cm x 2.6 km	Glass, 2.2 m × 2.6 m
Operational flexibility	Same equipment can be used for multiple depositions	Moderate operational flexibility but often leads to inefficient capital use.	Same equipment can be used for multiple depositions
Standardized equipment	Easily modified to produce different solar cell structures	Recipe of the entire line is fixed. Equipments are optimized for minimal operating conditions	Easily modified to produce different solar cell structures.
Rate of deposition affects throughput	Favors slow depositions that require long residence time.	Slow depositions require large equipments and slow process flow.	Slow process is shared by parallel chambers for high throughput.
Processing efficiency	Requires strict scheduling and control. Minimal energy integration.	Reduces fugitive energy losses by avoiding multiple heating and cooling cycles	Scheduling and synchronization of chambers are optimized by artificial intelligence.
Product demand	Changing demand for products can be easily accommodated. Possible of making multiple solar panels with different structures.	Difficult to make changes as the process recipes are fixed for the entire line.	Changing demand for products can be easily accommodated. Possible of making multiple solar panels with different structures at the same time.
Equipment fouling	Tolerable to significant equipment fouling because cleaning / fixing of equipment is a standard operating procedure. Throughput can be affected when individual plasma-box fails in the process tower.	Significant fouling in continuous operations is a serious problem and difficult to handle. Sometimes significant fouling requires shutting down of the entire production line.	Fouling chamber can be by-passed or replaced with similar chambers, thus minimizing the adverse effect to the throughput.

Table 2. Comparison of three thin film solar module process flow types

Continuous deposition of the multilayer structure is realized in a roll-to-roll manner, which ensures stable chamber conditions for consistent film growth for large volume production. United Solar, Energy Conversion Devices (ECD), and Xunlight took this type of growth configuration. For example, the ECD 30 MW a-Si process line consists of nine series-connected chambers with gas gates that isolate dopant gases between chambers (Fig. 11b)

(Izu and Ellison 2003). The film deposition substrates are 2.6 km long, 36 cm wide, 127 μm thick stainless-steel rolls fed into the deposition system at constant speed. For quality assurance, online diagnostic systems are installed allowing for continuous monitoring of the layer thickness and characterization of the PV properties of the manufactured solar cells. A big advantage of the continuous process is that the substrate does not see the atmosphere during the process, and needs to be heated and cooled only at the beginning and last chamber, thus greatly saving the pumping time and energy cost. At the same time, all chambers continuously run at the optimized, stable states, thus depositing films with uniform and consistent properties. On the other hand, Since the deposition rate and thickness of each layer varies a lot (e.g., typical p-layers are < 20 nm while the μc-i layer is normally 1-2 μm), the deposition time in each chamber are very different. Limited by a constant substrate roll feeding speed, the chamber for growing i-layers are much longer than the doped layer chamber. In fact, this 30 MW system is 90 m long.
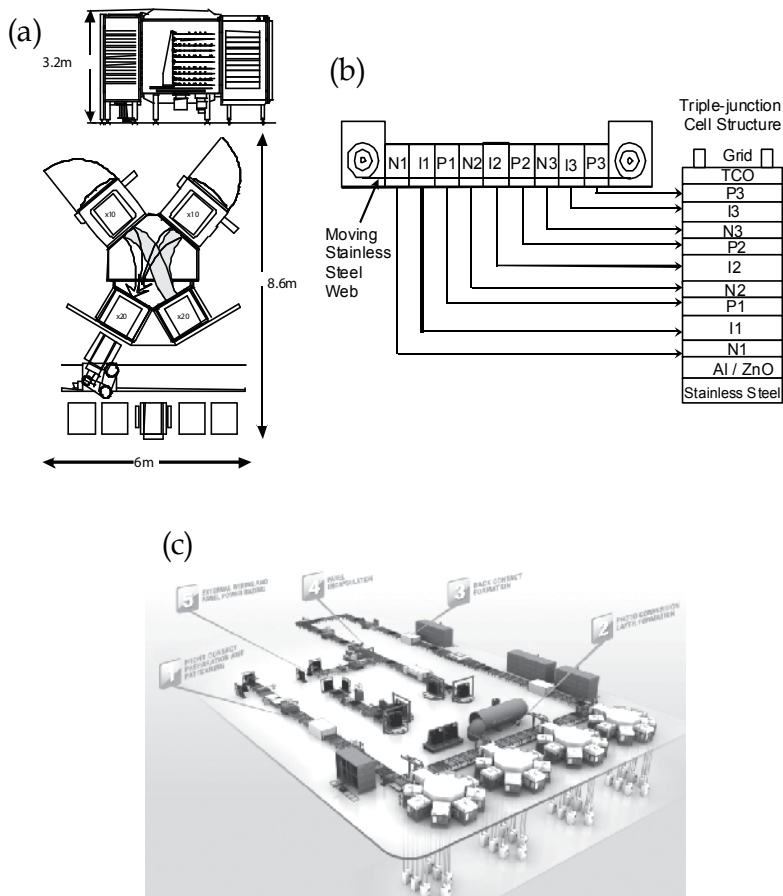
Fig. 11. Typical process systems used for Si thin film solar cell manufacturing. a) Batch process. Schematic side and top view of an Oerlikon KAI-20 1200 PECVD process system for a-Si deposition (Kroll et al. 2007). b) Linear Process. Schematic diagram of a United Solar Ovonic Corporation roll-to-roll a-Si:H alloy triple-junction solar cell processor (Yang et al. 2005). c) Hybrid (batch plus linear) process. Schematics of a Applied Materials SunFab thin film production line (Applied Materials 2010).

The hybrid-process system is designed to combine the advantages of batch and continuous processes. In this configuration, separated chambers are used like those in batch process, but individual substrates are fed into different chambers for optimal chamber utilization. Each substrate sees a queue of different process chambers like that in continuous process. Applied Materials configured its SunFab in the hybrid mode, where a group of several process chambers construct a functional cluster unit sharing a heating chamber and a center transfer robot (Fig. 11c). Each cluster is focused on a group of related functional layers (e.g., layers comprising a subcell in a multi-junction structure), and deposition of the multi-junction stack is realized by going through clusters. In this configuration, each chamber can have flexible deposition time, and the flow of substrates and synchronization of chambers are controlled by artificial intelligence algorithm for optimal system throughput (Applied Materials 2010; Bourzac 2010). This process flow combines the advantages of small footprint, easy maintenance and high production throughput, and provides flexible system configuration for versatile panel fabrication.

There are a number of considerations to weigh when deciding among batch, continuous or hybrid processes, and some of the major reasons are listed in Table 2. Generally, small production volumes favor the batch process type while continuous process is more suitable for high volume production. Capital investment cost of a batch or hybrid process system is also usually lower than the continuous process because the same equipment can be used for multiple unit operations and can be reconfigured easily for a wide variety of panel structures, though the operating labor costs and utility costs tend to be high for the former two systems (Turton et al. 2008). The continuous configuration is also more favored for 'substrate' type solar cells on metal foil substrates in a roll-to-roll deposition (Izu and Ellison 2003). Though the comparisons in Table 2 generally holds true, it is also possible that the configuration works for one solar plant may not be the best choice of another, as each plant differs at production scale, materials supply, geological confinement and many other practical characters.

5. Conclusion

In this chapter, the cost structures of a-Si/μc-Si solar modules has been described with analysis of the multilayer cell structure and module production. The monolithically integrated structure is described with explanations of layer functions. The industrial fabrication of large-area modules are introduced, including FEOL and BEOL process steps.

Module costs around half of the total thin film PV system. We analyzed the factors affecting the module efficiency and cost in terms of energy consumption, equipment investment, spending on direct material, labor and freight cost. To probe strategies of efficiency improvement, we started from the introduction of the Si p-i-n junction structure and the front/back contacts, and discussed the light absorption and its enhancement with light trapping. The photocurrent generation is achieved by effective capture of the incident solar photons, and conversion into free electrons and holes by the build-in field of the p-i-n junction. Resistance loss during photocurrent collections is minimized by the conductive front and back contact layers. At the meantime, enhancing the light absorption within thin layers is achieved using band gap engineering of the absorbing layer and optical trapping of the front/back contact layers.

Fabrication of large-area tin film solar panels are the key to increasing the production volume and reducing the $/Wp of modules. State-of-the-art fabrication includes FEOL and

BEOL process steps. In the FEOL processes, glass substrates are subsequently coated with functional layers, i.e., the a-Si/µc-Si layers by PECVD, TCO and reflector layers are grown by PVD or CVD. The monolithically integrated module structure is achieved by laser scribing of individual layers. In the BEOL processes, the panels are cut and encapsulated. Electrical wiring are also finished in the BEOL steps. The batch, linear, and hybrid process flow schemes are compared with actual factory examples.

Thin film a-Si/µc-Si solar panels have been holding the largest market share among all produced thin film panels. The power conversion efficiency of these panels is likely to increase to above 12% in the near future, but not exceed that achieved in crystalline cells. Advantages such as large-area, low-cost fabrication, and demonstrated field performance, nevertheless, render a-Si/µc-Si thin film technology attractive for large-area deployment like in solar power plants. In particular with the uncertain elemental supply becomes an issue for CdTe and CIS cells that might impair the sustainability of those PV products (Fthenakis 2009), thin film a-Si/µc-Si is likely to have long-term potential for providing energy supply in an even larger scale. Improvements on efficiency and stability would continue to drive the research in this area, while panel manufacturing will continue to be optimized for achieving lower production cost and optimal $/Wp.

6. References

Agashe, C., et al. (2004). Efforts to improve carrier mobility in radio frequency sputtered aluminum doped zinc oxide films. *Journal of Applied Physics* Vol. 95, No. 4: pp. 1911-1917, ISSN 2158-3226

Applied Materials, Inc. (2010). Applied Materials Solar, Last accessed 2011, Available from http://www.appliedmaterials.com/technologies/solar

Beck, N., et al. (1996). Mobility lifetime product---A tool for correlating a-Si:H film properties and solar cell performances. *Journal of Applied Physics* Vol. 79, No. 12: pp. 9361-9368, ISSN 2158-3226

Berger, O., et al. (2007). Commercial white paint as back surface reflector for thin-film solar cells. *Solar Energy Materials and Solar Cells* Vol. 91, No. 13: pp. 1215-1221, ISSN 0927-0248

Beyer, W., et al. (2007). Transparent conducting oxide films for thin film silicon photovoltaics. *Thin Solid Films* Vol. 516, No. 2-4: pp. 147-154, ISSN 0040-6090

Bhan, M. K., et al. (2010). Scaling single-junction a-Si thin-film PV technology to the next level. *Photovoltaics International* Vol. 7: pp. 101-106, ISSN 1757-1197

Borrajo, J. P., et al. (2009). Laser scribing of very large 2,6m x 2,2m a-Si: H thin film photovoltaic modules. *Processings of Spanish Conference on Electron Devices, 2009*, pp. 402-405, 11-13 Feb. 2009

Bourzac, K. (2010). Scaling Up Solar Power. *Technology Review* Vol. 113, No. 2: pp. 84-86, ISSN 1099274X

Bruno, G., et al. (1995). *Plasma Deposition of Amorphous Silicon-Based Materials (Plasma-Materials Interactions)*. Academic Press ISBN 978-0121379407

Droz, C., et al. (2000). Electronic transport in hydrogenated microcrystalline silicon: similarities with amorphous silicon. *Journal of Non-Crystalline Solids* Vol. 266-269, No. Part 1: pp. 319-324, ISSN 0022-3093

Fortunato, E., et al. (2007). Transparent Conducting Oxides for Photovoltaics. *MRS BULLETIN* Vol. 32, No. 3: pp. 242-247, ISSN 0883-7694

Fthenakis, V. (2009). Sustainability of photovoltaics: The case for thin-film solar cells. *Renewable and Sustainable Energy Reviews* Vol. 13, No. 9: pp. 2746-2750, ISSN 1364-0321

Green, M. A. (2007). *Third Generation Photovoltaics: Advanced Solar Energy Conversion* Springer, ISBN 978-3540265627, New York

Hegedus, S. S. & Luque, A., Eds. (2003). *Status, Trends, Challenges and the Bright Future of Solar Electricity from Photovoltaics*. John Wiley & Sons Inc., ISBN 0-471-49196-9, Chippenham, Great Britain

Izu, M. & Ellison, T. (2003). Roll-to-roll manufacturing of amorphous silicon alloy solar cells with in situ cell performance diagnostics. *Solar Energy Materials and Solar Cells* Vol. 78, No. 1-4: pp. 613-626, ISSN 0927-0248

Jäger-Waldau, A. (2007). Status and Perspectives of Thin Film Solar Cell Production. *Processings of 3rd International Photovoltaic Industry Workshop on Thin Films*, EC JRC Ispra, November 22-23, 2007

Johnson, T. R., et al. (2003). Investigation of the Causes and Variation of Leakage Currents in Amorphous Silicon P-I-N Diodes. *Materials Research Society Symposium - Proceedings* Vol. 762: pp. A7.7.1-A7.7.6, ISSN 0272-9172

Jorgensen, G. J., et al. (2006). Moisture transport, adhesion, and corrosion protection of PV module packaging materials. *Solar Energy Materials and Solar Cells* Vol. 90, No. 16: pp. 2739-2775, ISSN 0927-0248

Kambe, M., et al. (2009). Improved light-trapping effect in a-Si:H / µc-Si:H tandem solar cells by using high haze SnO_2:F thin films. *Processings of Photovoltaic Specialists Conference (PVSC), 2009 34th IEEE*, pp. 001663-001666, Philadelphia, USA, June 2009

Kessels, W. M. M., et al. (2001). Hydrogenated amorphous silicon deposited at very high growth rates by an expanding Ar-H2-SiH4 plasma. *Journal of Applied Physics* Vol. 89, No. 4: pp. 2404-2413, ISSN 2158-3226

Klein, S., et al. (2002). High Efficiency Thin Film Solar Cells with Intrinsic Microcrystalline Silicon Prepared by Hot Wire CVD. *Materials Research Society Symposia Proceedings* Vol. 715: pp. A26.22, ISSN 0272-9172

Kolodziej, A. (2004). Staebler-Wronski effect in amorphous silicon and its alloys. *Opto-Electronics Review* Vol. 12, No. 1: pp. 21-32, ISSN 1230-3402

Kroll, U., et al. (2007). Status of thin film silicon PV developments at Oerlikon solar. *Processings of 22nd European Photovoltaic Solar Energy Conference*, pp. 1795-1800, Milan, Italy

Luft, W. & Tsuo, Y. S. (1993). *Hydrogenated amorphous silicon alloy deposition processes*. CRC Press, ISBN 978-0824791469, New York

Mai, Y., et al. (2005). Microcrystalline silicon solar cells deposited at high rates. *Journal of Applied Physics* Vol. 97, No. 11: pp. 114913-114912, ISSN 2158-3226

Mehta, S. (2010). Thin film 2010: market outlook to 2015

Meier, J., et al. (2010). From R&D to Large-Area Modules at Oerlikon Solar. *Materials Research Society Symposia Proceedings* Vol. 1245: pp. 1245-A01-02, ISSN 0272-9172

Meier, J., et al. (2007). UP-scaling process of thin film silicon solar cells and modules in industrial pecvd kai systems. *Conference Record of the 2006 IEEE 4th World Conference on Photovoltaic Energy Conversion, WCPEC-4*, pp. 1720-1723

Meier, J., et al. (2005). Progress in up-scaling of thin film silicon solar cells by large-area PECVD KAI systems. *Conference Record of the Thirty-first IEEE Photovoltaic Specialists Conference, 2005*, pp. 1464-1467

Müller, J., et al. (2004). TCO and light trapping in silicon thin film solar cells. *Solar Energy* Vol. 77, No. 6: pp. 917-930, ISSN 0038-092X

Nishimiya, T., et al. (2008). Large area VHF plasma production by a balanced power feeding method. *Thin Solid Films* Vol. 516, No. 13: pp. 4430-4434, ISSN 0040-6090

Rath, J. K., et al. (2010). Transparent conducting oxide layers for thin film silicon solar cells. *Thin Solid Films* Vol. 518, No. 24 SUPPL.: pp. e129-e135, ISSN 0040-6090

Repmann, T., et al. (2007). Production equipment for large area deposition of amorphous and microcrystalline silicon thin-film solar cells. *Conference Record of the 2006 IEEE 4th World Conference on Photovoltaic Energy Conversion, WCPEC-4*, pp. 1724-1727

Sato, K., et al. (1992). Highly textured SnO_2:F TCO films for a-Si solar cells. *Reports of the Research Laboratory, Asahi Glass Co., Ltd.* Vol. 42, No.: pp. 129-137, ISSN 0004-4210

Schroeder, B. (2003). Status report: Solar cell related research and development using amorphous and microcrystalline silicon deposited by HW(Cat)CVD. *Thin Solid Films* Vol. 430, No. 1-2: pp. 1-6, ISSN 0040-6090

Schropp, R. E. I. (2006). *Amorphous (Protocrystalline) and Microcrystalline Thin Film Silicon Solar Cells*. Elsevier B. V., ISBN 9780444528445

Schropp, R. E. I. & Zeman, M. (1998). *Amorphous and Microcrystalline Silicon Solar Cells*. Kluwer Academic Publishers, ISBN 978-0792383178 Boston

Shah, A. V., et al. (2004). Thin-film silicon solar cell technology. *Progress in Photovoltaics: Research and Applications* Vol. 12, No. 2-3: pp. 113-142, ISSN 1099-159X

Shinohara, W., et al. (2006). Applications of laser patterning to fabricate innovative thin-film silicon solar cells. *Processings of SPIE*, Vol. 6107, pp. 61070J-1-18

Sun, H., et al. (2009). End-To-End Turn-Key Large Scale Mass Production Solution for Generation 1 & 2 Thin Film Silicon Solar Module. *Proceedings of ISES World Congress 2007 (Vol. I – Vol. V)*, pp. 1220-1223

Turton, R., et al. (2008). *Analysis, Synthesis, and Design of Chemical Processes*. Prentice Hall, ISBN 0-13-512966-4, Westford, MA

Yamamoto, K., et al. (2006). High Efficiency Thin Film Silicon Hybrid Cell and Module with Newly Developed Innovative Interlayer. *Conference Record of the 2006 IEEE 4th World Conference on Photovoltaic Energy Conversion*, pp. 1489-1492

Yang, F., et al. (2009). Uniform growth of a-Si:H / µc-Si:H tandem junction solar cells over 5.7m² substrates. *Processings of 34th IEEE Photovoltaic Specialists Conference*, pp. 1541-1545, Philadelphia, PA

Yang, J., et al. (2005). Amorphous and nanocrystalline silicon-based multi-junction solar cells. *Thin Solid Films* Vol. 487, No. 1-2: pp. 162-169, ISSN 0040-6090

Yang, Y.-T., et al. (2007). The Latest Plasma-Enhanced Chemical-Vapor Deposition Technology for Large-Size Processing. *Journal of Display Technology* Vol. 3, No. 4: pp. 386-391, ISSN 1551-319X

Young, R. (2010). PV Cell Capacity, Shipment and Company Profile Report, IMS Research

Novel Deposition Technique for Fast Growth of Hydrogenated Microcrystalline Silicon Thin-Film for Thin-Film Silicon Solar Cells

Jhantu Kumar Saha[1,2] and Hajime Shirai[1]
[1]Department of Functional Material Science & Engineering,
Faculty of Engineering,
Saitama University,
[2]Current address: Advanced Photovoltaics and Devices,(APD) Group,
Edward S. Rogers Sr. Department of Electrical and
Computer Engineering, University of Toronto,
[1]Japan
[2]Canada

1. Introduction

The microcrystalline silicon material is reported to be a quite complex material consisting of an amorphous matrix with embedded crystallites plus grain boundaries. Although this material has a complex microstructure, its optical properties have a marked crystalline characteristic: an optical gap at 1.12 eV like c-Si. This implies the spectral absorption of μc-Si:H covers a much larger range than a-Si:H which posses an optical gap between 1.6 and 1.75eV[i]. Compared to a-Si:H that absorbs light up to 800 nm, μc-Si:H absorbs light coming from a wider spectral range, extending up to 1100 nm . On the other hand, within its range of absorption, the absorption of a-Si:H is higher than that of μc-Si:H –due to the indirect gap of the latter. Therefore, the optical combination of these two materials takes advantage of a larger part of the solar spectrum (compared to a single-junction cell) and the conversion efficiency of the incident light into electricity can be consequently improved. Furthermore, the μc-Si:H solar cell is reported to be largely stable against light induced degradation and enhanced carrier mobility in contrast to amorphous silicon films counterpart. Consequently hydrogenated microcrystalline silicon is one of the promising materials for application to thin-film silicon solar cells.

2. Growth techniques of hydrogenated microcrystalline silicon

The growth of μc-Si:H material uses silane (SiH_4) and hydrogen as source-gas. It is currently admitted that free radical precursors (SiH_x)-SiH_3 is suspected to favor the μc-Si:H growth- and H-enhances crystalline growth by etching of looser a-Si:H tissue-were needed to attain microcrystalline growth. In order to obtain such reactive species, decomposition of the source-gases is necessary. At first, this was obtained by using PE-CVD at high temperatures (600°C). The use of low deposition temperatures of 200-300°C with a plasma present in the

deposition chamber, the so called Plasma-Enhanced Chemical Vapor Deposition technique (PE-CVD) was developed later on and allowed the low-temperature deposition of µc-Si:H films, and rapid progresses have been achieved. Unfortunately, "state-of-the-art" microcrystalline silicon solar cells consist of intrinsic µc-Si:H layers that are deposited by rf and VHF PE-CVD at deposition rates of only 1-5 Å/s. On the other hand, a µc-Si:H film with a 2-µm- thickness intrinsic absorption layer is required for application to Si thin-film solar cells because of the low optical absorption in the visible region. The µc-Si:H i-layer deposition step is the most time consuming step in the deposition sequence of the solar cell. Therefore, a novel fast deposition technique of µc-Si:H is required.

3. Novel fast deposition techniques of microcrystalline silicon

Now-a- days, for the high throughput of high-efficiency µc-Si solar cells in PV industry, one of the most crucial requirements is fast deposition of µc-Si without deteriorating the optical, structural and electronic properties of the film. To overcome the difficulty, several high-density plasma sources have been developed, such as very high frequency (VHF) plasma, inductive coupling plasma (ICP) and surface wave plasma (SWP). As it has been reported, the excitation frequency of a plasma source has an important effect on the electron acceleration in the plasma, and a high excitation frequency is expected to result in a high electron density and a low electron temperature. Therefore two new microwave plasma sources have been developed i.e. Low-pressure high-density microwave plasma source utilizing the spoke antenna and the remote-type high-pressure microwave plasma using a quartz tube having an inner diameter of 10 mm and applied those for the fast deposition of µc-Si films for Si thin-film solar cells. The remote-type high-pressure microwave plasma will be discussed in elsewhere.

3.1 Low-pressure high-density microwave plasma source utilizing the spoke antenna

The microwave plasma source is shown schematically in Fig. 1, which is composed of the combination of a conventional microwave discharge and a spoke antenna. Its chamber size is 22 cm in diameter, which enables large-scale film processing. The spoke antenna is located on a 15 mm-thick quartz plate, which is not inside of the vacuum chamber. The antenna system is shown in Fig. 2 more in detail. The length of each spoke is 4 cm, which is about 1/4 of the wavelength of a 2.45 GHz wave. The design of the spoke antenna assembly

Fig. 1. A schematic illustration of the microwave plasma source

is based on an inter-digital filter composed of parallel cylindrical rods (spokes) arranged between parallel-grounded plates. The spokes are resonantly coupled by the stray capacitance between adjacent spokes and the inductance of the spokes themselves. The resonance condition of an introduced angular frequency is given by $\omega = 2\pi f = 1/(C \times L)^{1/2}$, where f is the introduced frequency, C is the array capacitance, and L is the antenna inductance. Thus, the antenna operates as a band-pass filter. The spokes are arranged like those in a wheel, and the plasma serves as one of the grounded plates. The electromagnetic wave propagates through the spokes consecutively with a phase difference of 90°, and microwave current flows in every spoke. The current in the spokes couples inductively and capacitively to the plasma ("CM coupling"), and the induction current in the plasma accelerates the electrons to sustain the plasma, as shown in Fig. 2 & 3. The power is supplied from the center of the antenna, and the plasma under the spoke antenna is radially discharged because induction current flows near every spoke. As a result, uniform microwave plasma over an area of diameter greater than 20 cm can be generated efficiently. As well, since no magnetic field is required to generate the high-density microwave plasma, it is possible to design a simple source yielding high-density and low-temperature plasma.

(a) Microwave current   (b) Electric field

Fig. 2. The newly developed spoke antenna for introduction of microwave power (a) Microwave current, (b) Electric field.

From a material processing standpoint, large-area microwave plasmas (MWPs) have several advantages in comparison with other types of high-density sources. First, MWPs, being no magnetized sources, are free from such magnetic field induced problems as inhomogeneous density profile and charge-up damage, which is often, experienced in electron cyclotron resonance (ECR) or helicon plasma sources. Second, MWPs can be enlarged to diameters

Power supply

Fig. 3. The coupling of the spoke antenna with microwave plasma [x]

(a)   (b)

Fig. 4. Images of Ar plasma at a) 80 mTorr and b) 20 Torr. The plasma maintains uniform state under a wide pressure regime.

longer than 1 m more easily than inductively coupled plasmas (ICPs). Thus, the application of MWPs to giant electronic devices such as solar cells is promising. Third, MWPs have lower bulk-electron temperature. Fourth, MWPs can be operated stably from atomic pressure down to below 10 mTorr. Fig. 4. demonstrates that Ar plasma maintains a uniform state over 22 cm in diameter up to 20 Torr. The schematic diagram of the low-pressure high-density microwave plasma utilizing the spoke antenna is shown in Fig. 5.
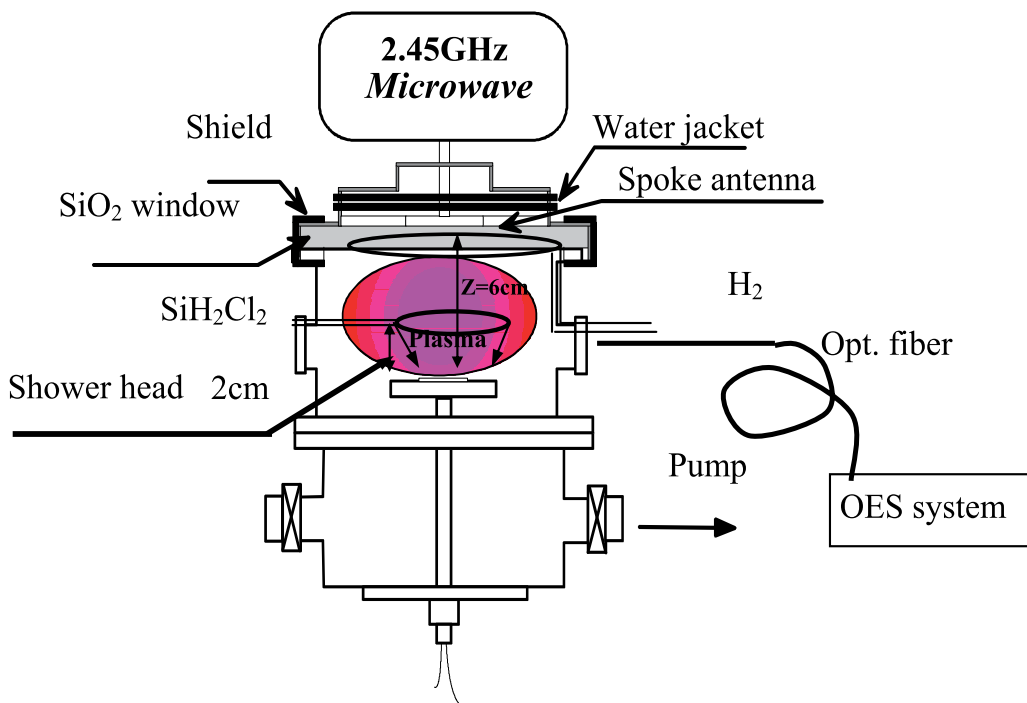
Fig. 5. The schematic diagram of the low-pressure high-density microwave plasma utilizing the spoke antenna
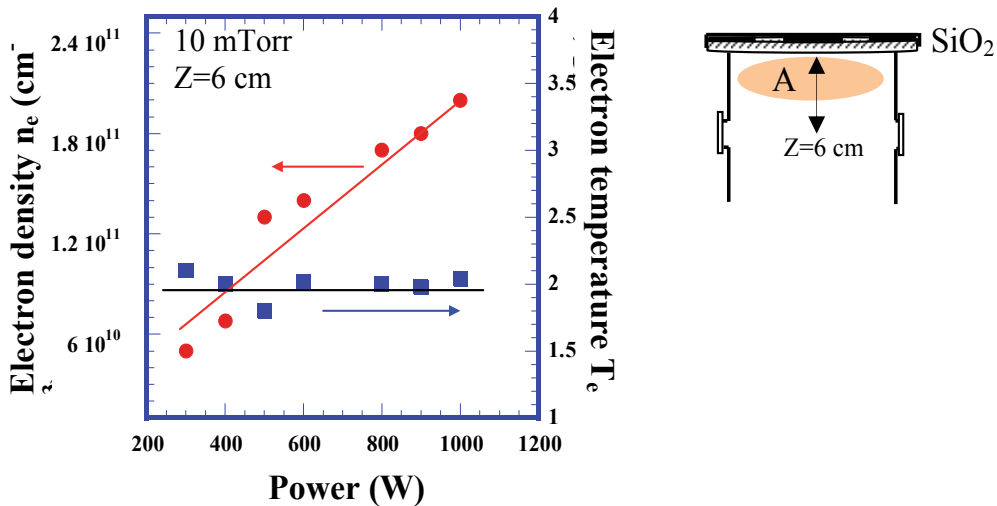
Fig. 6. Electron density, n_e, and electron temperature, T_e, measured as a function of input microwave power.

A uniform, high-density (electron density, n_e: >10^{11} cm^{-3}) and low-temperature (electron temperature, T_e:1~2 eV) plasma can be generated by the microwave plasma source utilizing a spoke antenna without using complex components such as magnetic coil as shown in Figures 6 & 7 . The T_e is almost independent of working pressure up to ~150 mTorr as shown Figure 8, which is suitable for the large area thin film processing.
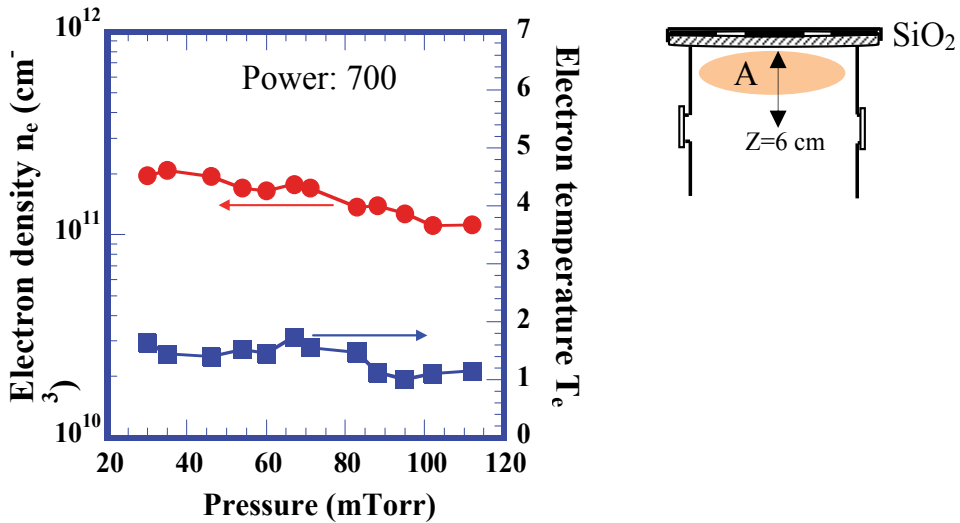
Fig. 7. Electron density and electron temperature plotted against working pressure.
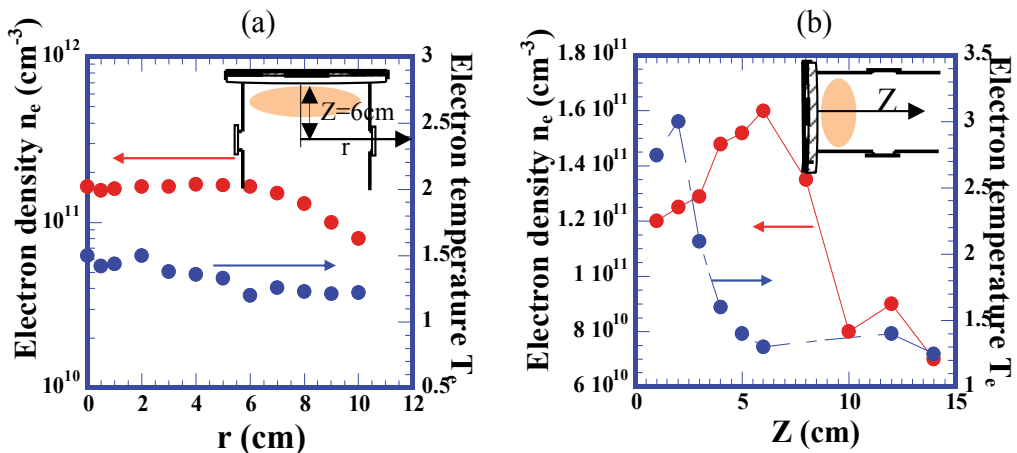
Fig. 8. The radial and axial distributions of n_e and T_e in microwave Ar plasma under microwave power of 700 W at 80 mTorr with Ar flow rate of 20 sccm.

3.2 Fast deposition of highly crystallized µc-Si:H films with low defect density from SiH$_4$ using low-pressure high-density microwave plasma

In this study, a new source gas supply method was introduced, i.e., the SiH$_4$ was introduced using a shower head placed 2 cm above the substrate holder under a steady flow of the H$_2$ plasma supplied by the ring. The results from these gas supply method were compared with the results from the another gas supply method, i.e. a SiH$_4$-H$_2$ mixture was fed into the chamber using a ring just beneath the quartz plate. Figure 9 shows the schematic of the two different gas supply methods. The film deposition parameters were included the SiH$_4$ concentration R=Fr(SiH$_4$)/[Fr(SiH$_4$)+Fr(H$_2$)] (Fr is the flow rate). The SiH$_4$ concentration was varied in a range from 5% to 67% by increasing Fr(SiH$_4$) from 3 to 30 sccm with a constant H$_2$ flow rate of 15 sccm. The film depositions were performed at the distance (Z) between the quartz plate and the substrate holder of 6 cm and the working pressure of 80 mTorr. The microwave power was fixed at 700W.
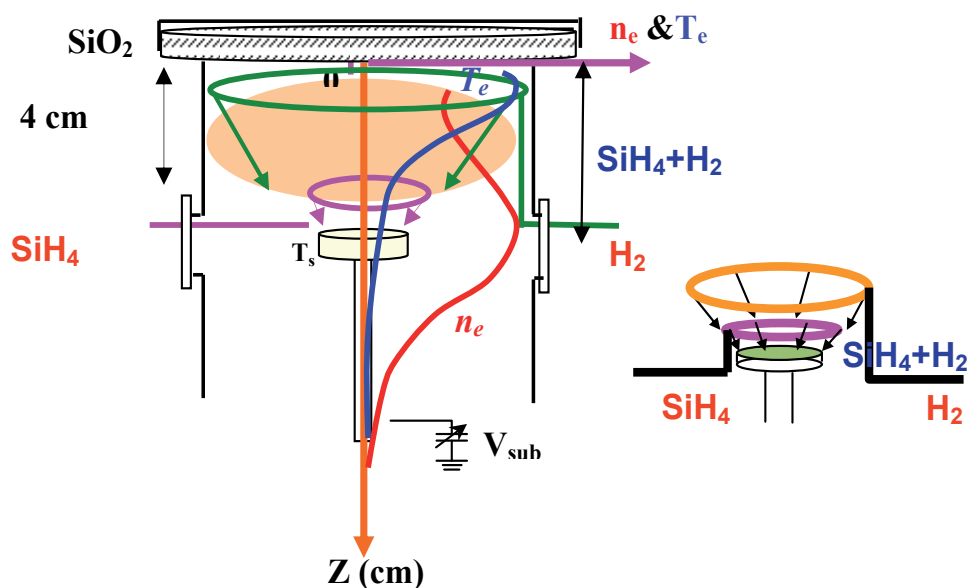
Fig. 9. Schematic of the two different gas supply methods used in this study. The distance (Z) between the quartz plate and substrate holder was 6 cm.

Fig. 10 shows the deposition rate dependence of ESR spin density, N$_s$ for the corresponding µc-Si films fabricated using two different SiH$_4$ gas supply methods at T$_s$ of 150 and 250°C. Here, the film deposition rate was controlled by varying Fr(SiH$_4$) from 3 to 30 sccm under constant Fr(H$_2$) of 15 sccm and working pressure of 80 mTorr. For all samples, the film thickness was ~ 1.5 µm and the ESR measurements were performed directly on these films. It is to be noted that N$_s$ was decreased by about one order of magnitude when the shower head was used for both T$_s$ conditions despite the other deposition conditions being the same. However, N$_s$ was almost independent of Fr(SiH$_4$) on the order of (3-4)×10^{16} cm^{-3}, which was still one order of magnitude larger than that of high quality µc-Si films reported elsewhere.
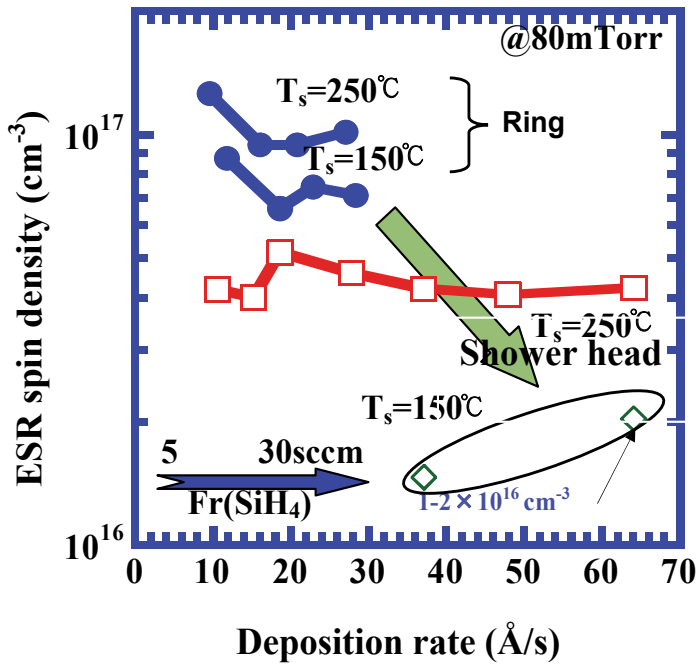
Fig. 10. ESR spin density, N_s for corresponding μc-Si films fabricated using different gas supply method as well as that for samples prepared at T_s=150˚C are plotted as a function of film deposition rate R_d.
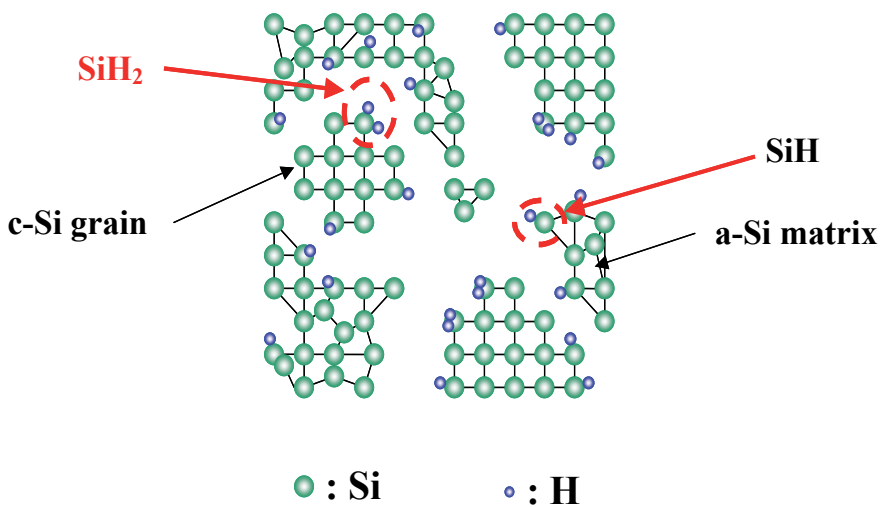
Fig. 11. μc-Si:H film microstructure

A very fast deposition rate of 65Å/s has been realized for μc-Si:H films with a Raman crystallinity ratio of Ic/Ia of about 3.5 under very low H_2 dilution (i.e. with high SiH4 concentration of 67%) as shown in Fig. 12 and low defect density of (1-2) ×10^{16} cm^{-3} using high-density and low-temperature microwave plasma. The imaginary part of the dielectric function <ε_2> spectra of μc-Si:H films fabricated from SiH_4 using high-density and low-temperature microwave plasma is shown in Fig. 13 along with that using rf PE-CVD methods. Using the optical model the best fitted volume fraction of c-Si and void i.e. *f*c-Si and *f*void in the bulk layer and void in surface layer, f_{void}, with SiH_4 concentration R for the corresponding μc-Si films is shown in Fig. 14.
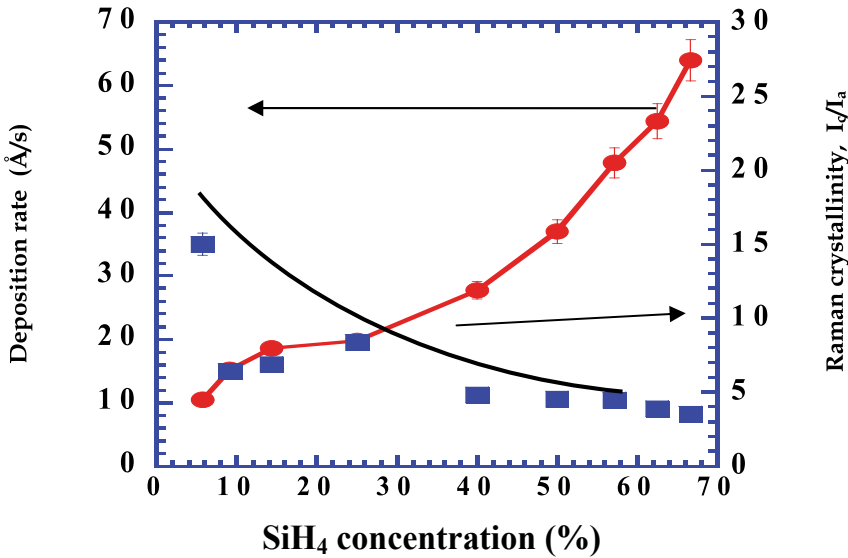
Fig. 12. Film deposition rate and Raman crystallinity, I_c/I_a as a function of SiH_4 concentration R: Fr(SiH_4)/Fr(SiH_4)+Fr(H_2).
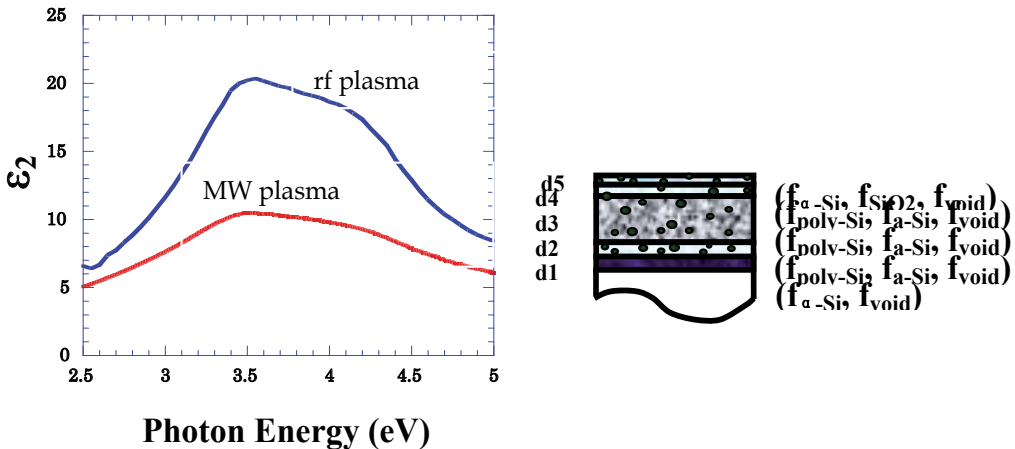
Fig. 13. Imaginary part of the pseudo dielectric function<ε_2> spectra for the μc-Si films fabricated from SiH_4 using MW Plasma along with that using rf PECVD methods and five layers optical model.
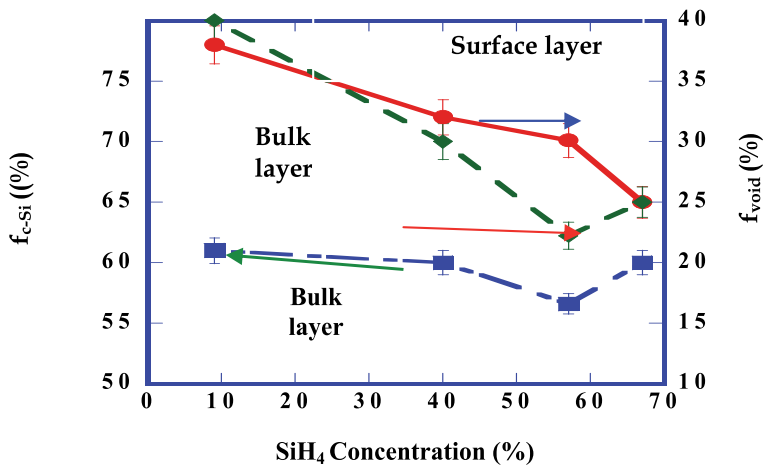
Fig. 14. Changes in f_{c-Si} and f_{void} in the bulk layer and surface layer, with SiH$_4$ concentration R for the corresponding μc-Si films shown in Fig. 11.
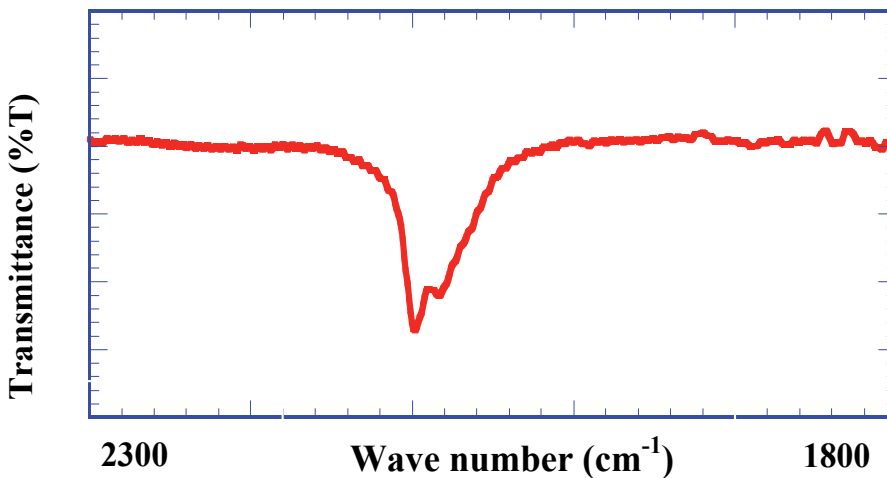
Fig. 15. The FTIR spectra for the corresponding μc-Si:H films fabricated from SiH$_4$ using MW plasma.

Highly crystallized μc-Si:H film was synthesized despite low H$_2$ dilution ratio rather than the conventional rf and VHF plasmas, because of high generation efficiency of atomic hydrogen. FTIR spectra and microstructure of μc-Si:H film and of SiH$_n$ absorption region are shown in Fig. 11 & 15 for the corresponding μc-Si film. Generally, two IR absorption peaks are observed at 2000 and 2100 cm^{-1}, which are attributed to the bulk SiH in a-Si and SiH$_2$ in μc-Si phase, respectively, in the film fabricated by the rf plasma CVD. However, no SiH absorption peak at 2000 cm^{-1} is observed in the film fabricated by high-density microwave plasma. These imply that the film crystallization is promoted extremely in the high-density plasma with negligibly small fraction of amorphous Si phase. In addition, the

IR absorption peak at 2090 cm^{-1} corresponding to the surface SiH mode in the μc-Si phase appeared as a shoulder in the high-density film. These results suggest that the c-Si phase is isolated in a-Si network as shown in Fig. 11 & 16, which is not preferable for the Si thin-film solar cells. Therefore, the suppression of the excess film crystallization is required by the selection of deposition precursor.
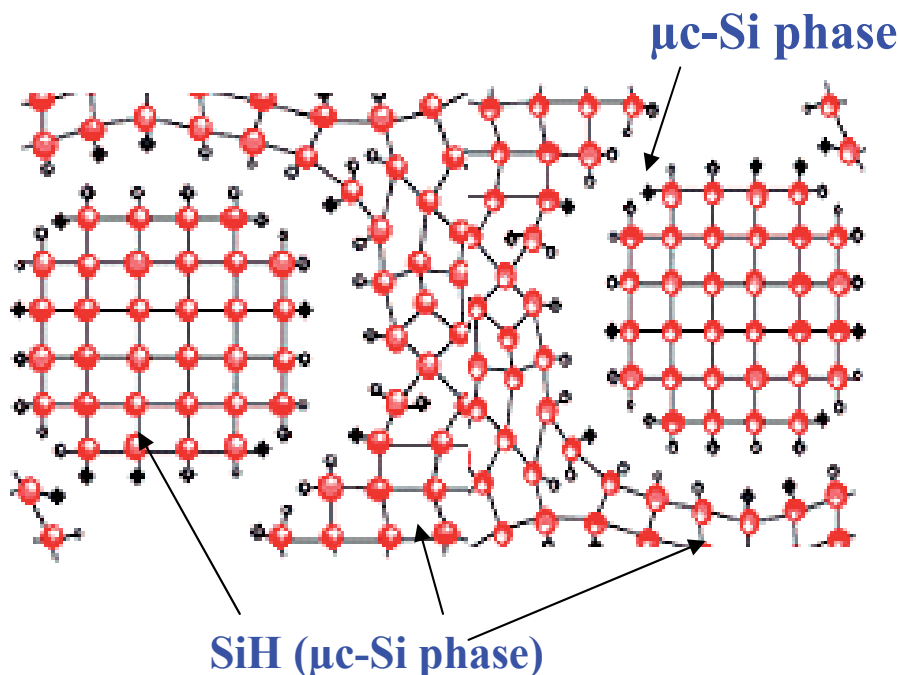
Fig. 16. μc-Si:H films fabricated from SiH$_4$ using MW plasma

Highly crystallized μc-Si:H films with a preferred (220) crystal orientation at a high deposition rate of 65 Å/s were fabricated from SiH$_4$ with a negligibly small volume fraction of amorphous Si but μc-Si network included high volume fraction of voids as shown in Fig. 15. which was hardly compatible with a device quality material. To overcome this problems, the fast deposition of highly photoconductive hydrogenated chlorinated microcrystalline Si (μc-Si:H:Cl) films with amorphous Si phase and with less volume fraction of void have been fabricated from SiH$_2$Cl$_2$ with higher threshold energy for the dissociation instead of SiH$_4$.

3.3 Fast deposition of highly crystallized μc-Si:H:Cl films with low defect density from SiH$_2$Cl$_2$ using low-pressure high-density microwave plasma
3.3.1 Fine structure of Si network of microcrystalline silicon thin-film fabricated from SiH$_2$Cl$_2$ and SiH$_4$

The typical FTIR spectra of 1-μm-thick μc-Si:H:Cl films fabricated from a SiH$_2$Cl$_2$-H$_2$ mixture, compared with those of μc-Si:H films from SiH$_4$ as shown in Fig. 17. Here, the peak assignments of SiH (bulk and surface stretching) and SiH$_2$ bulk stretching are also shown in Table 1.

Si-H (bulk stretching)	2000 cm^{-1}
Si-H (surface stretching)	2080 cm^{-1}
SiH$_2$ (bulk stretching)	2100 cm^{-1}

Table 1. Assignment of SiH, SiH$_2$ vibration modes
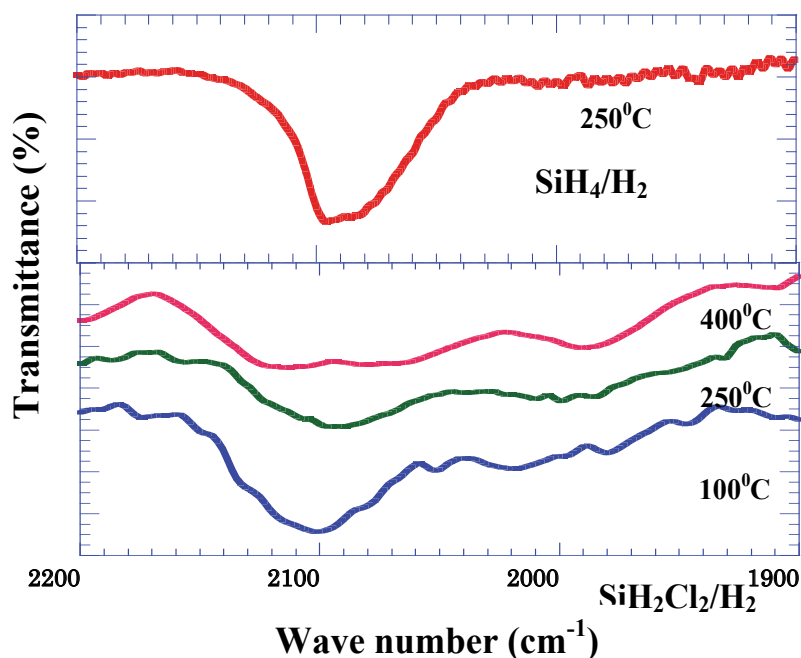
Fig. 17. FTIR spectra of μc-Si:H:Cl films at different T_ss. The typical FTIR Spectrum for the SiH$_x$ stretching absorption region in the μc- Si:H film from SiH$_4$ is also shown as a reference.

However, marked differences were observed in the fine structure between μc-Si:H:Cl and μc-Si:H. In the μc-Si:H films from SiH$_4$, the absorption peaks at 2080 cm^{-1} and 2100 cm^{-1} attributable to surface and bulk SiH$_x$ stretching absorption modes, respectively, in the nanocrystalline Si phase were dominant with a negligibly small peak of SiH absorption in the bulk a-Si phase at 2000 cm^{-1}. Thus, the film is highly crystallized with a negligibly small fraction of the amorphous Si phase. In addition, the IR absorption peak at 2080cm^{-1} corresponding to the surface SiH mode in the μc-Si phase appeared as a shoulder in the μc-Si:H film. These results suggest that the c-Si phase is isolated in a-Si network, which is not preferable for the Si thin-film solar cells. Moreover, because of excess dissociation of SiH$_4$, the μc-Si:H network showed a porous structure, which resulted in a poor carrier transport property of photo-generated carriers.

On the other hand, both SiH and SiH$_2$ absorption peaks were observed at 2000 and 2100 cm^{-1}, respectively, in the μc-Si:H:Cl films, were similar as to the μc-Si:H films fabricated using conventional rf and VHF PE-CVDs of SiH$_4$. No SiH at the surface of μc-Si phase was

observed. Moreover, the inclusion Cl in the microcrystalline Si network produces a new absorption band, which is assigned to Si-Cl bonds centered at 530cm^{-1} as described in ref. These suggest that film structure is a continuous Si network including a mixture of amorphous and crystalline Si phase, although the crystalline size is smaller. The film deposition rate reached 20 Å/s for the film synthesized from 5sccm SiH_2Cl_2, which was almost same as that for the film synthesized from SiH_4. Therefore, the fine structure of the μc-Si network from SiH_4 and SiH_2Cl_2 is different from each other.

The spectroscopy ellipsometry (SE) characterization was performed for the μc-Si:H:Cl films fabricated from a SiH_2Cl_2-H_2 mixture at different T_ss. Figure 17 shows the imaginary part of pseudo-dielectric function $<\varepsilon_2>$ spectra of μc-Si:H:Cl films fabricated from a SiH_2Cl_2-H_2 mixture at different T_ss with that of μc-Si:H from SiH_4 with a thickness of 1 μm.
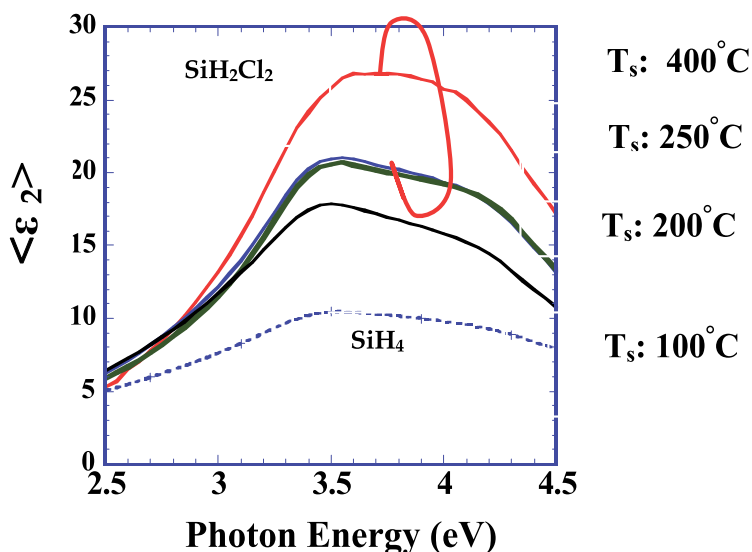
Fig. 18. Imaginary part of pseudodielectric function $<\varepsilon_2>$ spectra of μc-Si:H:Cl films fabricated from a SiH_2Cl_2-H_2 mixture at different T_ss with that of μc-Si:H from SiH_4 with a thickness of 1 μm.

In both μc-Si:H:Cl and μc-Si:H films, the fine structures were observed clearly at 3.4 and 4.2 eV, which are attributed to the E_1 and E_2 optical band transitions, respectively, in the crystalline Si (c-Si) band structure. However, the magnitude of $<\varepsilon_2>$ was much smaller in the μc-Si:H films from SiH_4 than in the μc-Si:H:Cl films from SiH_2Cl_2. Here, the magnitude of $<\varepsilon_2>$ presents qualitatively the degrees of homogeneity and the surface roughness of μc-Si films.

The $<\varepsilon_2>$ spectra were analyzed to understand the micro-structural properties of   μc-Si:H:Cl films as described in section 3.2 above. The reflective index n at 2.2 eV determined by SE analysis also increased with T_s as determined using the reference poly-Si given by Jellison as shown in Fig. 19. It was higher for the μc-Si:H:Cl films in all T_s regions than that for μc-Si:H films. Thus, the rigidity of the Si-network is greater in the μc-Si:H:Cl films from SiH_2Cl_2 than in μc-Si:H films from SiH_4 using the high-density microwave plasma source.
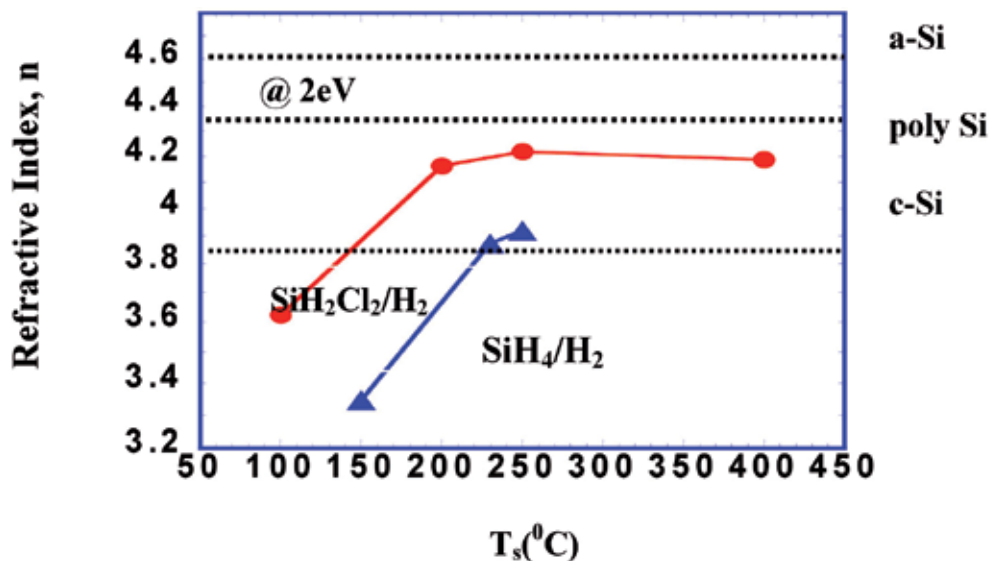
Fig. 19. The refractive index at 2.2eV in the bulk layer for µc-Si:H:Cl films plotted as a function of T_s

$f_{c\text{-}Si}$, $f_{a\text{-}Si}$ and f_{void} in the µc-Si:H:Cl films, corresponding to the bulk component, are shown in Fig.20 as a function of T_s together with those in the films synthesized from SiH_4. Notably, f_{void} in the µc-Si:H:Cl films is less than 5% despite that being 10-15% in µc-Si:H.

The differences in the fine structure of the µc-Si network between µc-Si:H:Cl films and µc-Si:H films is shown in Fig.21. The degree of the excess dissociation of SiH_2Cl_2 is considered to be suppressed rather than that of SiH_4, because the threshold energy of SiH_2Cl_2 is higher than that of SiH_4, although the high energy part of electron energy distribution (EED) also depends on the feed gas. Film crystallization was promoted efficiently in the high-density and low-temperature microwave plasma of SiH_4. However, the resulting Si film structure was still porous with much f_{void}, although $f_{c\text{-}Si}$ was over 80%. These findings originated from the excessive dissociation of both SiH_4 and H_2 in the plasma, which promoted the generation rate of not only of SiH_3 but also short life-time radicals, i.e., SiH and Si. On the other hand, $f_{a\text{-}Si}$ was still more in the µc-Si:H:Cl films than in the µc-Si:H films with less f_{void}.

3.4 Defect density of microcrystalline silicon thin-film fabricated from SiH_2Cl_2 and SiH_4

In the case of MW SiH_4 plasma, film deposition rate 65 Å/s was achieved while maintaining the low defect density but that µc-Si:H film was not available for solar cell application because of film structure was porous as described above. Similar study was performed using SiH_2Cl_2 to realize the fast deposition of µc-Si:H:Cl films with no creating additional defects, higher flux of SiH_xCl_y generated by the primary reaction in the gas phase was supplied to the depleted growing surface by increasing flow rate of SiH_2Cl_2 at a constant pressure of 120 mTorr and T_s of 250˚C. Here, the deposition precursor SiH_xCl_y generated by the primary reaction in the plasma is expected to be supplied at the growing surface efficiently by increasing a flux of SiH_2Cl_2 at a constant pressure. Thus, the fast deposition of highly crystallized µc-Si:H:Cl film with lower defect density is expected because the efficient
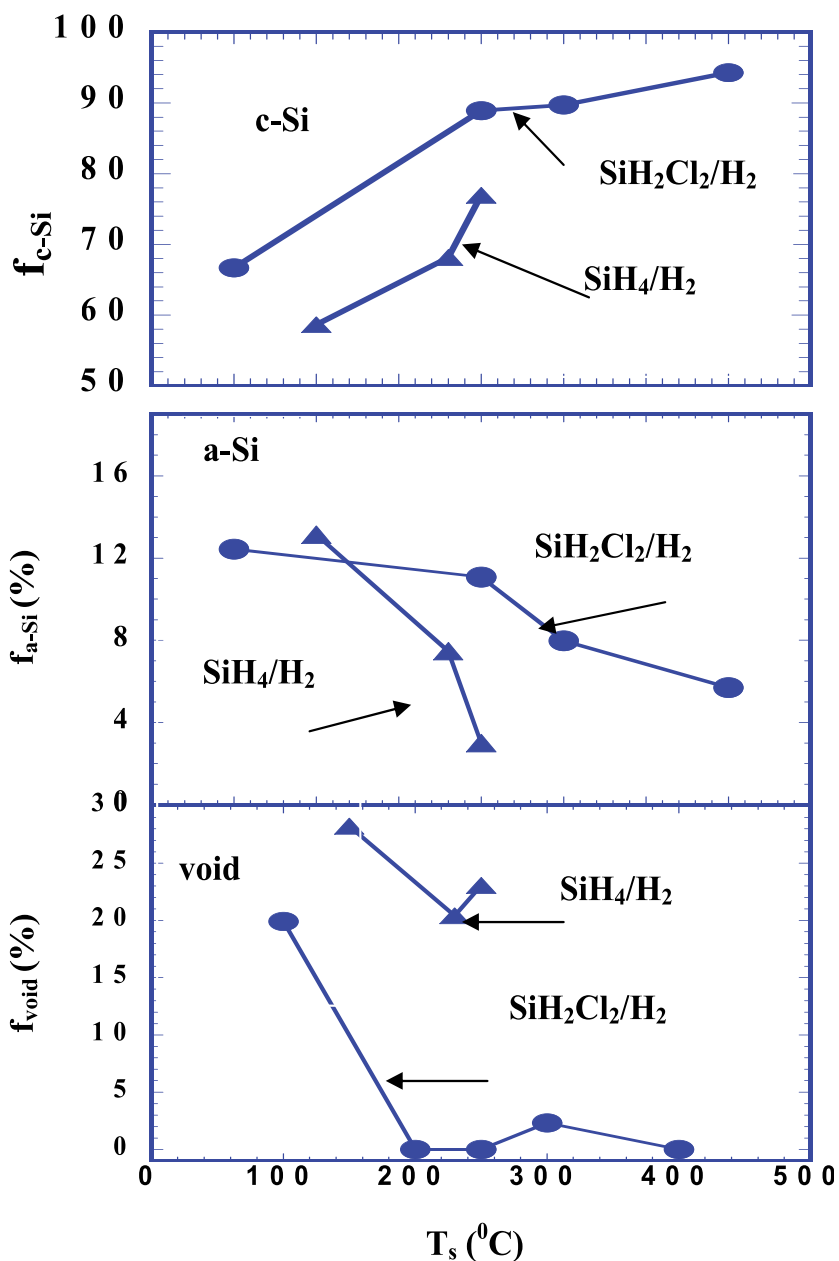
Fig. 20. The f_{c-Si}, f_{a-Si}, f_{voids} in the bulk (layer 3) of µc-Si:H:Cl films plotted as a function of T_ss. The results of µc-Si:H are also shown as a triangles symbol
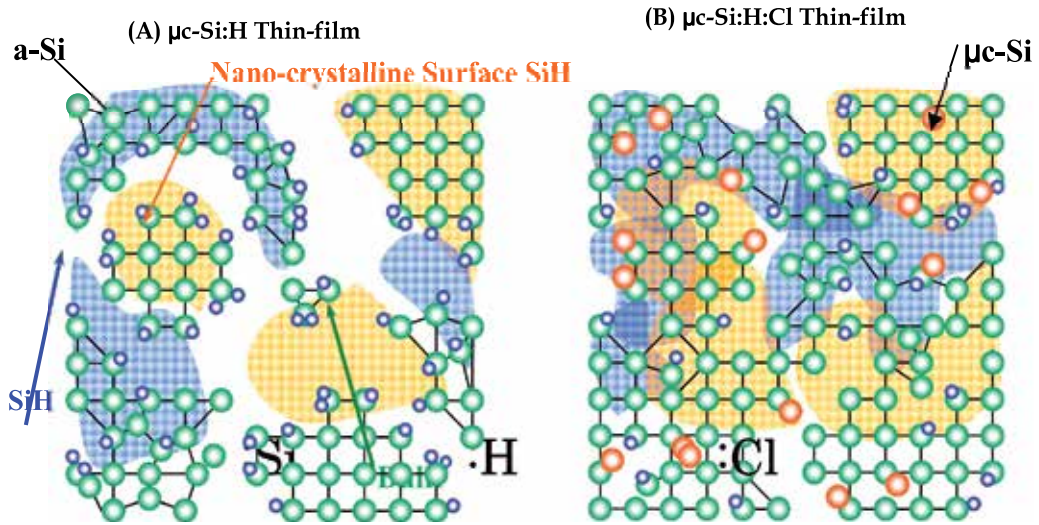
Fig. 21. Schematic of μc-Si:H and μc-Si:H:Cl network

termination of dangling bond by efficient supply of SiH_xCl_y is accelerated with the abstraction of H and Cl as HCl at the depleted growing surface. The deposition study was performed at two different T_ss of 250 and 400˚C. Figure 22 demonstrates N_ss and deposition rates of μc-Si:H:Cl films fabricated at different $Fr(SiH_2Cl_2)$ at T_ss of 250 and 400˚C, respectively. The high deposition rate of 40 Å/s has been achieved with increasing $Fr(SiH_2Cl_2)$ up to 20 sccm at T_ss of 400˚C and 250⁰C respectively. The N_s was almost independent of $Fr(SiH_2Cl_2)$ at T_s of 250˚C, whereas the N_s was markedly decreased at T_s of 400˚C. These are considered because of the efficient abstraction of H and Cl at the growing surface. The film crystallization was enhanced up to flow rate of 20 sccm of SiH_2Cl_2 at T_s of 400˚C. The N_ss were decreased systematically with increasing SiH_2Cl_2 at both T_ss to $4x10^{15}$ cm⁻³ at 15 sccm of SiH_2Cl_2.
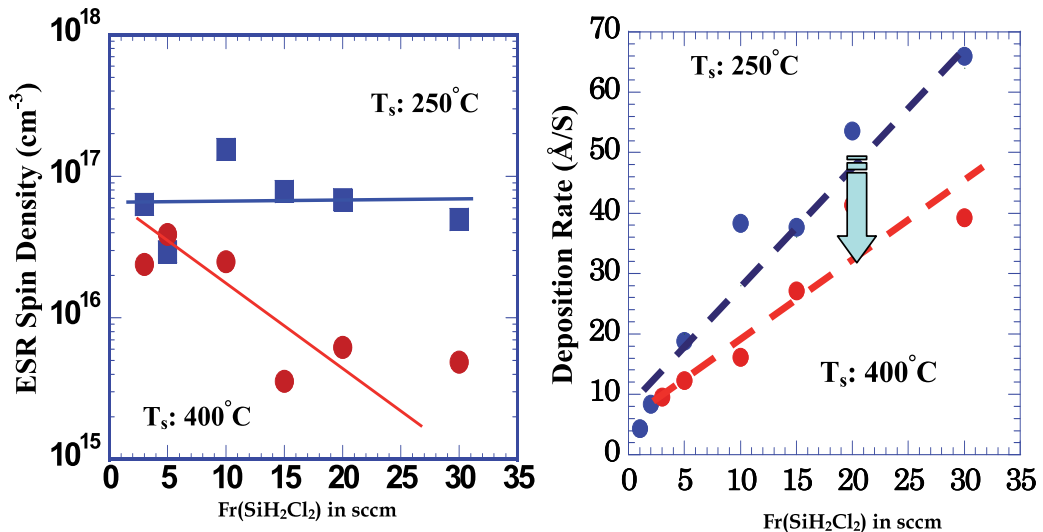
Fig. 22. ESR spin density and deposition rates of the μc-Si:H:Cl films fabricated at different flow rates of SiH_2Cl_2 at T_s of 250 and 400˚C.

By supplying the sufficient flux of SiH_xCl_y at a high T_s of 400°C, the termination of dangling bond is accelerated with enhancing the abstraction of H and Cl. These findings are effective to form a rigid Si network with less void fractions. In fact, the defect density N_s was almost constant of $4-5×10^{16}$ cm^{-3} at T_s up to 250°C, whereas it decreased markedly to $3-4x10^{15}$ cm^{-3} with $Fr(SiH_2Cl_2)$ at T_s of 400°C. Therefore, highly crystallized μc-Si:H:Cl film with low defect density was formed from a $SiH_2Cl_2-H_2$ mixture.

3.5 XRD and Raman spectra of microcrystalline silicon thin-film fabricated from SiH_2Cl_2 and SiH_4

The XRD diffraction patterns and the Raman spectrum of the μc-Si:H:Cl film fabricated at T_s of 250°C and 400°C with increasing SiH_2Cl_2 flow rates are shown in Fig 23 and Fig. 24. The XRD and Raman study of μc-Si:H:Cl films fabricated at T_s of 400°C revealed that high film crystallinities with diffraction intensities ratio of $I_{(220)}/I_{(111)}$ of 1.5-8.75 and with Raman crystallinity of I_c/I_a:5-6 were obtained.

As a consequence, highly crystallized μc-Si:H:Cl film with low defect densities of $3-4x10^{15}$ cm^{-3} was fabricated at fast deposition rate of 27Å/s. These findings suggest that the efficient abstraction of H- and Cl- terminated growing surface.
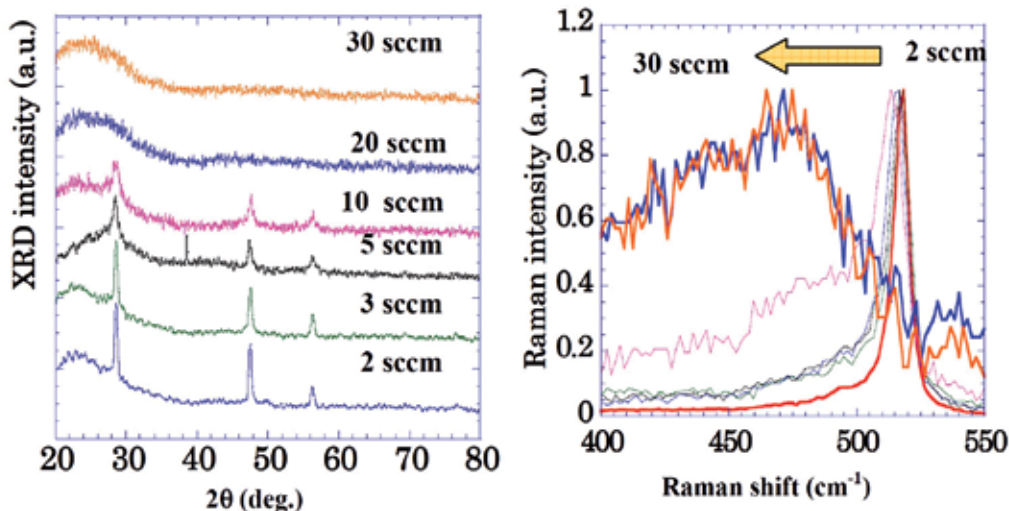
Fig. 23. XRD and Raman spectra of the μc-Si:H:Cl films fabricated at different flow rate of SiH_2Cl_2 at T_s of 250°C.

3.6 Photoelectrical properties of a-Si:H:Cl and μc-Si:H:Cl films

Fig. 25 shows the relation between the dark and photo conductivities for the μc-Si:H:Cl films fabricated by increasing the SiH_2Cl_2 flow rate at the substrate temperatures of 250°C and 400°C. The photosensitivity reached at 5-6 orders of magnitude at room temperature. The level of photoconductivity was 10^{-5} S/cm under 100 mW/cm^2 white light exposure. The dark and photo-conductivities were the order of 10^{-12} and 10^{-5} S/cm, respectively, which shows highly photosensitive films. Fig.26 shows the activation energies for the μc-Si:H:Cl films fabricated by increasing the SiH_2Cl_2 flow rate at the substrate temperatures of 250°C and 400°C The activation energies of electrical conductivity were 0.40-0.80 eV, suggesting that both a-Si:H:Cl and μc-Si:H:Cl films were intrinsic semiconductor films.
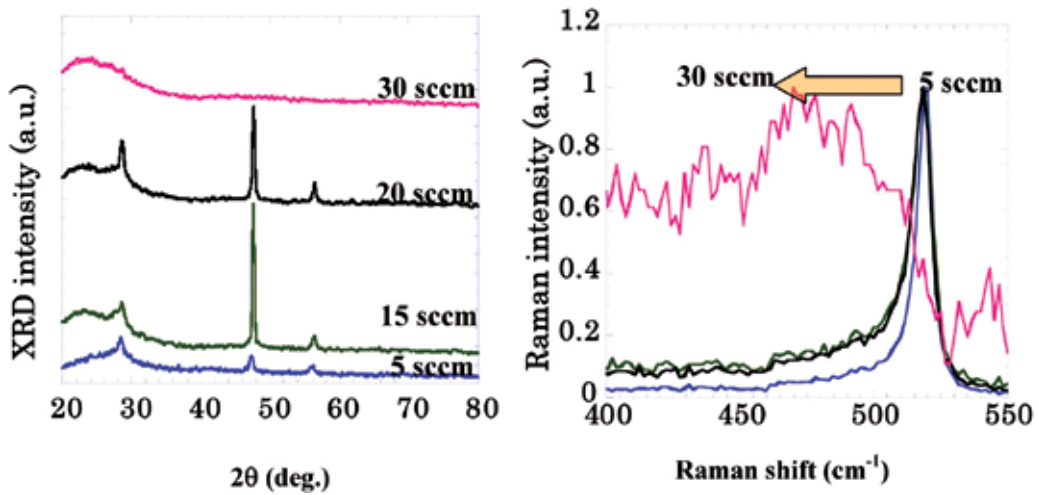
Fig. 24. XRD and Raman spectra of the µc-Si:H:Cl films fabricated at different flow rate of SiH_2Cl_2 at T_s of 250 and 400°C.
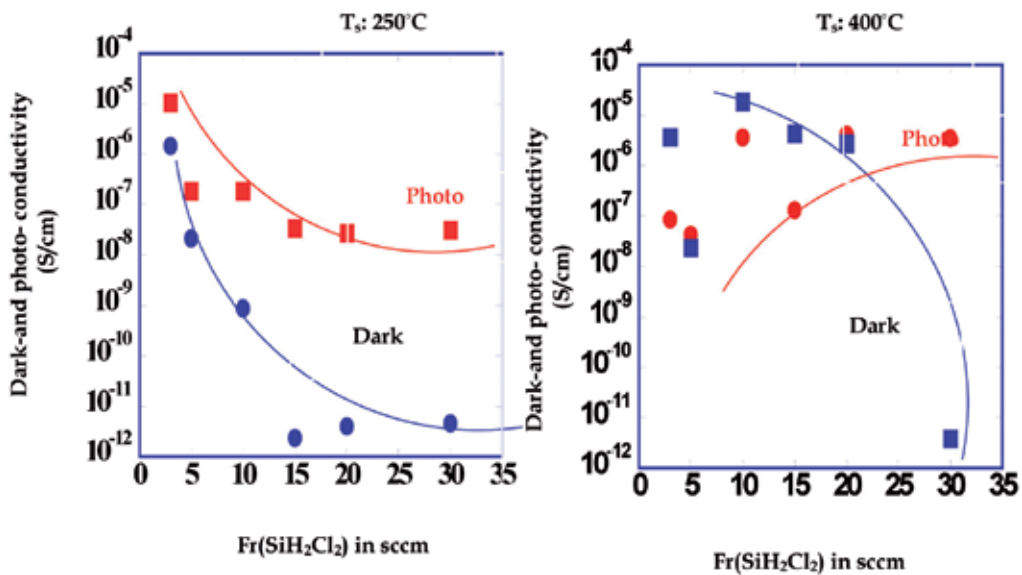
Fig. 25. Dark and photo conductivities for the µc-Si:H:Cl films as a function of SiH_2Cl_2 flow rate at the substrate temperatures of 250°C and 400°C

4. Preliminary results of p-i-n structure µc-Si:H:Cl thin-film solar cells

The preliminary result of Si thin-film solar cells using µc-Si:H:Cl thin-film fabricated by the high-density microwave plasma (MWP) of a SiH_2Cl_2-H_2 mixture are shown here. High-rate grown µc-Si:H:Cl thin-films were applied to p-i-n structure Si thin-film solar cells as intrinsic absorption layer. The solar cell was fabricated using a single chamber system. The structure of the solar cell TCO/ZnO:Al/p-i-n/ZnO:Al/Ag is as shown in Fig. 27. After the
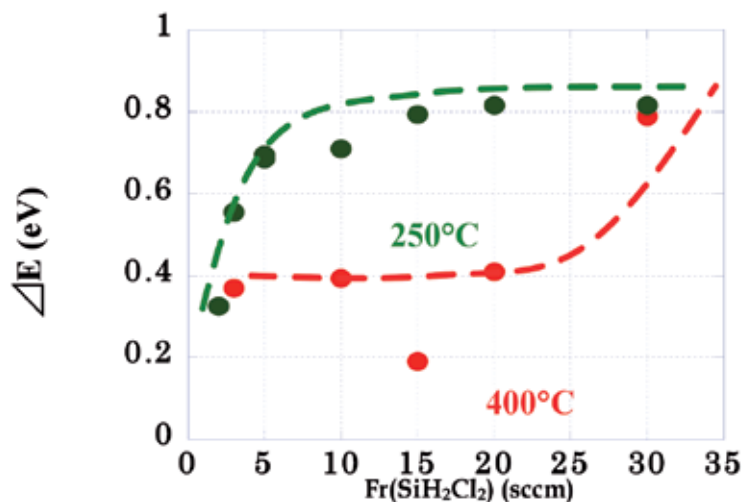
Fig. 26. Activation Energies, $\triangle$E for the µc-Si:H:Cl films as a function of SiH_2Cl_2 flow rate at the substrate temperatures of 250℃ and 400℃.

deposition of ZnO:Al and p-type Si layers on SnO_2 coated glass, respectively by rf magnetron sputtering and plasma CVD methods, µc-Si:H:Cl film with a 2-µm-thickness is fabricated using a high-density microwave plasma as a photovoltaic layer and n-type Si layer was fabricated using conventional rf plasma CVD method. When the samples were being transported between the rf chamber and MWP chamber, they were exposed to air. Subsequently, ZnO:Al and Ag layers were deposited as a top electrode using a shadow mask with a 5×5 mm² holes. Table 3 shows the typical deposition conditions for p, i and n layers, respectively. Table 4 shows the typical deposition conditions for ZnO:Al, Ag layers fabricated by rf magnetron sputtering. The photocurrent-voltage, I-V characteristics under AM 1.5, 100mW/cm² exposure condition are measured and the performance of solar cell is characterized with open circuit voltage, V_{oc}, short circuit current, I_{sc}, fill factor, FF and conversion efficiency, η. The collection efficiency was also measured from 300 to 1200 nm under bias light conditions.
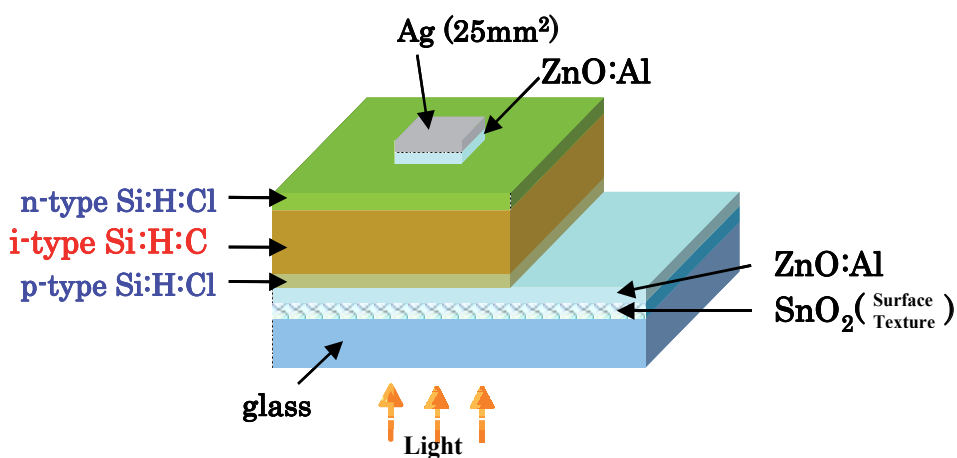
Fig. 27. The structure of the p-i-n solar cell
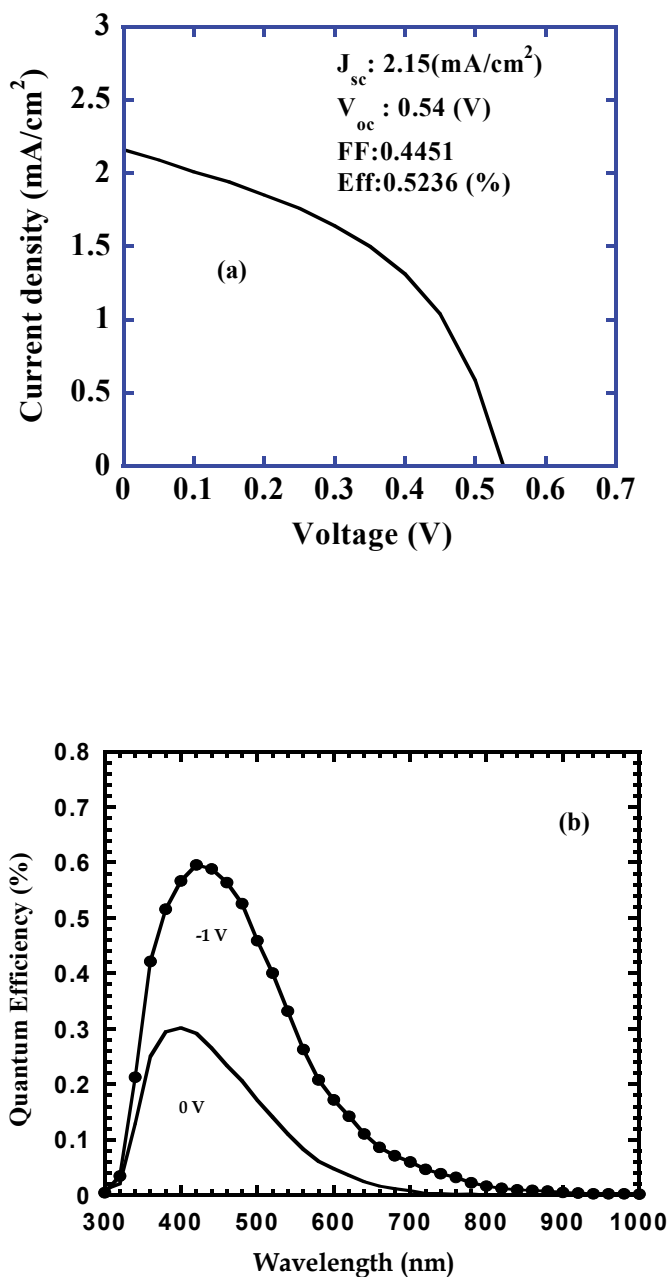
Fig. 28. (a) Photocurrent-voltage characteristics under AM 1.5 exposure condition and (b) QE spectra under -1V biased conditions of Si thin-film solar cells using a 1μm-thick μc-Si:H:Cl layer by high-density microwave plasma source.

	p(RF)	i(MW)	n(RF)
Substrate Distance (mm)	20	60	20
Substrate Temperature (○○C)	250	250	250
Power (W)	5	700	5
Pressure (mTorr)	200	120	200
H_2 (sccm)	61	15	55
SiH_2Cl_2 (sccm)	3	3	3
PH_3 (sccm)			15
B_2H_6 (sccm)	9		

Table 3. Typical deposition conditions for p, i and n layers

	ZnO:Al(front side)	ZnO:Al(back side)	Ag
Substrate Position (cm)	6	6	6
Substrate Temperature (°C)	350	250	250
RF Power (W)	100	100	50
Pressure (Pa)	2.5	2.5	2.5
thickness (Å)	2500	2500	1500

Table 4. Typical deposition condition for ZnO:Al and Ag layers

Fig.28 illustrates photocurrent –voltage characteristics for Si:H:Cl thin-film solar cells under 100 mW/cm² white light exposure. Fig. 28a shows the I-V characteristics for the cell using μc-Si:H:Cl films fabricated at 20 Å/s by the high-density microwave plasma CVD of SiH_2Cl_2. The 5-6% efficiencies have been achieved for the cells fabricated by the conventional rf plasma-CVD method. However, the performance is still poor and the open circuit voltage, (Voc):0.54 V, short circuit density, (Jsc):2.15 mA/cm², Fill Factor, FF:0.5236 and the conversion efficiency was 0.5236% in the cell made by the high-density microwave plasma from SiH_2Cl_2 but solar cell performance is confirmed by the high-density microwave plasma from SiH_2Cl_2 for the first time. The diffusion of Boron and Chlorine happens easily in i-layer by the high-density microwave plasma. Moreover, the etching reaction of p layer has occurred because of the hydrogen plasma. It is required to evaluate not only a single film but it is also necessary to evaluate the each interface i.e. AZO/p, p/i and i/n in order to improve the solar cell performance. More over   precise control of p/i, i/n, AZO/p interface formation is needed for obtaining the further high performance.

5. Conclusion

The highly photoconductive and crystallized μc-Si:H:Cl films with less volume fraction of void and defect density were synthesized using the high-density and low-temperature microwave plasma source of a SiH_2Cl_2-H_2 mixture rather than those from SiH_4 while maintaining a high deposition rate of 27 Å/s. The μc-Si:H:Cl film possesses a μc-Si and a-Si mixture structure with less volume fraction of voids. The role of chlorine in the growth of μc-Si:H:Cl films is the suppression of the excess film crystallization at the growing surface. H termination of growing surface is more effective to suppress the defect density rather than that of Cl termination. The fast deposition of the μc-Si:H:Cl film with low defect density of 3-4 ×10¹⁵ cm⁻³ is achieved with reducing Cl concentration during the film growth. Both a-Si:H:Cl and μc-Si:H:Cl films show

high photoconductivity of 10^{-5} S/cm under 100 mW/cm^{-2} exposure, are the possible materials for Si thin-film solar cells. The performance of p-i-n solar cell from µc-Si:H:Cl films using the high-density microwave plasma source was confirmed for the first time.

6. References

Ziegler, Y. (2001),More stable low gap a-Si:H layers deposited byPE-CVD at moderately high temperature with hydrogen dilution". *Solar Energy Materials & Solar Cells, 2001.* 66: p. 413- 419.

Graf S. (2005). "*Single-chamber process development of microcrystalline Silicon solar cells and high-rate deposited intrinsic layers*", in institute de Microtechnique, Universite de Neuchatel: Neuchatel.

Meillaud, F.(2005). "Light-induced degradation of thin-film microcrystalline silicon solar cells". in *31th IEEE Photovoltaic Specialist Conference*. 2005, Lake Buena Vista, FL, USA

Veprek, S. and V. Marecek (1968). "The preparation of thin layers of Ge and Si by chemical hydrogen plasma transport", *Solid State Electronics, 1968,* Vol. 11: p. 683-684.

LeComber, P.G. and W.E. Spear (1970). "*PECVD: plasma enhanced chemical vapor deposition*". *Physical Review Letters*, 1970. Vol. 25: p. 509.

A. Madan, S. R. Ovshinsky and E. Benn (1979). *Phil Mag*. B 40 (1979) 259

B. Chapman: Glow Discharge Processes. *Sputtering and Plasma Etching*, Chapter 9, John Wiley

A. Bogaerts, E. Neyts, R. Gijbels, J. van der Mullen(2002). *Spectrochimica Acta* B 57 (2002) 609J.K. Saha, N. Ohse, H. Kazu, Tomohiro Kobayshi and Hajime Shirai (2007). "18th *International Symposium on Plasma Chemistry proceedings*", Kyoto, Japan, Aug 26-31, 2007.

J. K. Saha, Naoyuki Ohse, Hamada Kazu, Tomohiro Kobayshi and Hajime Shirai (2007). *Japan Society of Applied Physics and Related Societies (the 54th Spring Meeting)*, Aoyama Gakuin University, March 27-March, 30,2007, 27p-M-2

S. Samukawa, V. M. Donnelly and M. V. Malyshev (2000). *Jpn. J. Appl. Phys*. 39 (2000) 1583

I. Ganachev and H. Sugai (2007). *Surface and Coating Technology* 174-175 (2003) 15.

J. K. Saha, H. Jia, N. Ohse and H. Shirai(2007). *Thin Solid Films* 515 (2007) 4098.

Y.Nasuno, M.Kondo and A. Matsuda (001). *Tech. Digest of PVSEC-12*. Jeju, Korea, 2001,791.

L. Guo, Y. Toyoshima, M.Kondo and A. Matsuda (1999). *Appl. Phys. Lett*. 75 (1999) 3515

G. E. Jellison, Jr. (1992). Opt. Mater. 1 (1992) 41

S. Kalem, R. Mostefaoui, J. Chevallier (1986). *Philos. Mag*. B 53 (1986) 509-513.

J.K. Saha, N. Ohse, K. Hamada, T. Kobayshi, H.Jia and H. Shirai (2010). *Solar Energy Materials & Solar Cells* 94 (2010) 524– 530.

J. K. Saha, N. Ohse, K. Hamada, K. Haruta, T.Kobayshi, T. Ishikawa, Y. Takemura and H. Shirai (2007). *Jpn. J. Appl. Phys*. 46 (2007) L696.

D.E. Aspnes (1976). Spectroscopic ellipsometry of solids, in: B.O. Seraphin (Ed.), *Optical Properties of Solids: New Developments*, North-Holland, Amsterdam, 1976, pp. 801–846 (Chapter 15).

Hiroyuki Fujiwara (2007). *Spectroscopic Ellipsometry: Principles and Applications*, John Wiley & Sons, Ltd., 2007, pp. 189–191.

H. Kokura and H. Sugai (2000). *Jpn. J. Appl. Phys*. 39 (2000) 2847

J. K. Saha, N. Ohse, K. Hamada, T.Kobayshi and H. Shirai(2007). *Tech. Digest of PVSEC-17*. Fukuoka, Japan, 2007, 6P-P5-68.

Y. Li, Y. Ikeda, T. Saito and H. Shirai (2006). *Thin Solid Films,* 511-512(2006) 46

Chemical Surface Deposition of CdS Ultra Thin Films from Aqueous Solutions

H. Il'chuk, P. Shapoval and V. Kusnezh
Lviv Polytechnic National University
Ukraine

1. Introduction

Solar cells (SC) are the most effective devices that allow direct one-stage conversion solar energy into electricity from the view of energy. The last yers tendency in traditional energetic forced to direct a significant part of research on the establishment of modern technology for production available and effective thin film SC that would not require the use of high temperature and pressure, a large number of rare and expensive materials. At the same time, to find ways for increase the conversion efficiency of solar energy it is necessary to understand the processes that occur in the elements. Therefore it is necessary to establish a correspondence between characteristics of elements and main structural, electronic and optical properties of initial semiconductor films. Therefore, the investigation of CdS thin films deposition process with desire photoelectric properties and fabrication on their base thin-film SC have great significance.

CdS is the main material for buffer layer in thin-film CdTe and Cu(In, Ga)Se$_2$ solar cells. It has a high photosensitivity and absorption, favorable energy band gap (Eg) 2,4 eV and photoconductivity (σ) 10^2 Om^{-1}cm^{-1} and does not change the properties with SC surface temperature increase during the work. One more peculiarity of this material is absence of the hole conduction due the acceptor additives and point defects recombination. Effective lifetime of the main carriers is very large (10...100 ms), that causes a initial photocurrent increase up to 10^5 times (Hamakawa, 2002). An important advantage of CdS thin films use in SC is possibility of their synthesis by different methods, including chemical deposition from solution which has significant preference over others: 1) grown nanocrystalites with a form close to spherical, while the electrochemical deposition - non-spherical (Jager-Waldau, 2004); 2) CdS thin films deposited from solution have structural, optical and electrical parameters thet do not inferior parameters of films received by other methods, but used equipment is available, simple, does not require use of the high temperatures and pressures compared, for example, with the vacuum evaporation or ion (sputtering or pulverization, spraying) methods; 3) the method is not explosive and low-toxic, compared with the vapor deposition methods; 4) enable control of the film growth and dynamically change the fabrication conditions for polycrystalline or smooth solid films.

2. Deposition of CdS thin films and structures based on

2.1 Fabrication methods

The thin film semiconductor properties largely depend on fabrication technology. Therefore development of actual methods, which would allow an influence on material parameters in the synthesis process and to obtain coating with the set properties, is an important scientific and technological problem. Recently the methods based on chemical processes dominate in the technology of metal sulfides thin films semiconductor. The semiconductor films with a thickness from several tenth of nanometers to hundreds of microns can be fabricated by a large number of so-called thin-film and thick-film methods. For large area in ground conditions aplication of thin-film solar cells crucial are not only their energy characteristics, but also their economic indicators. This causes use of bough thin film and thick-film technology methods for satisfying of such requirements as: fabrication simplicity, low cost, ability to create homogeneous films with a large area, controlling the deposition process, and ability to obtain the films with preferred structural, physical, chemical and electrooptical properties.

The deposition methods for wide range of semiconductors in detail are considered in literature (Aven & Prener, 1967, Chopra & Das, 1983, Green, 1998, Möller, 1993, Sze, 1981, Vossen & Kern, 1978,). We will consider only those methods that are used for cadmium sulfide films fabrication and are the best for solar cells producing. Thin film deposition process consists of three stages: 1) obtaining of substance in the form of atoms, molecules or ions; 2) transfer of these particles through an intermediate medium; 3) condensation of the particles on substrate. The methods of thin films fabrication are classified in several ways. Depending on the film grown phase are four methods of films deposition: 1) from the vapor phase; 2) from the liquid phase; 3) from the hydrothermal solutions; 4) from the solid phase. Depending on which way the vapour particle were obtained: using physical (thermal or ion sputtering), chemical or electrochemical processes, it is possible to classify deposition methods: physical vapor deposition; chemical vapor deposition; chemical deposition from the solution; electrochemical deposition. On the basis of physical and chemical vapor deposition were developed combined methods, such as: reactive evaporation, reactive ion sputtering and plasma deposition. Among the nonvacuum deposition methods of cadmium sulfide thin films for inexpensive solar cells with a large area perspective are: chemical deposition from baths (CBD), electrochemical deposition, mesh-screen printing, pyrolysis and pulverization followed by pyrolysis. Selection of the films deposition method first of all are specified by structural, mechanical and physical parameters, which should have thin-film sample.

Although, cadmium sulfide is the most widely studied thin film semiconductor material, interest of researchers to it is stable, and the number of scientific publications increasing all the time. Changing the deposition conditions drastically alter electrical properties of CdS thin films. CdS films, obtained by vacuum evaporation have specific resistance $1 \cdot 10^3$ Om·cm and carrier concentration of 10^{16}-10^{18} cm^{-3}. Films always have n-type conductivity, that explains their structure deviation from stoichiometry, by sulfur vacancies and cadmium excess. Electrical properties of the films are largely depended from the concentration ratio of Cd and S atoms in the evaporation process and the presence of doping impurities. Electrical properties of CdS films, fabricated by pulverization followed by pyrolysis, are determined mainly by the peculiarities the chemisorption process of oxygen on grain boundaries, which accompanied by concentration decreaseing and charge carriers mobility. Due to presence of

the sulfur vacancies such films always have n-type conductivity, and their resistance can vary widely, differing by the amount of eighth order. Epitaxial CdS films are characteristic due to carrier high mobility. With the increase of substrate temperature concentration of carriers grows by an exponential law. This increase the electron mobility. Optical properties of CdS films are strongly dependent on their microstructure and thus on the method and conditions of deposition. For example, evaporation of CdS results in smooth mirror reflective films, but increasing their thickness leads to a predominance of diffuse reflection. The CdS films, obtained by ion sputtering have the area with rapid change of transmission at 520 nm, corresponding CdS band gap. In the same time in the long-wave spectral range films have high transparency.

2.2 Use of the CdS films in photovoltaic cells

Edmund Becquerel, a French experimental physicist, discovered the photo-voltaic efect in 1839 while experimenting with an electrolytic cell, made up of two metal electrodes placed in an electricity-conducting solution. He observed that current increased when the electrolytic cell was exposed to light (Becquerel, 1839). Then in 1873 Willoughby Smith discovered the photoconductivity of selenium. The first selenium cell was made in 1877 (Adams, 1877), and five years later Fritts (Fahrenbruch & Bube, 1983) described the first solar cell made from selenium wafers. By 1914 solar conversion eficiencies of about 1 % were achieved with the selenium cell after it was finally realized that an energy barrier was involved both in this cell and in the copper/copper oxide cell.

The modern era of photovoltaics started in 1954. In that year was reported a solar conversion efficiency of 6 % (Chapin at al., 1954) for a silicon single-crystal cell. In 1955 Western Electric began to sell commercial licenses for silicon PV technologies. Already in 1958 silicon cell efficiency under terrestrial sunlight had reached 14 %. At present, available in the market SC are mainly represented of monocrystalline silicon SC. Through high-temperature process of their formation, crystal (from ingots grown from melt by Czochralski method) and polycrystalline silicon solar cells have too high price, to be seen as a significant competitor to the formation of energy from solid fuels. Polycrystalline silicon provides lower expenses and increase production, rather than crystalline silicon. In 1998, approximately 30 % photovoltaic world production was based on the polycrystalline silicon wafers. Nowadays solar cells conversion efficiency based on monocrystalline silicon is 25 %, polycrystalline – 20 % (Green at al., 2011).

In 1954 reported 6 % solar conversion efficiency (Reynolds at al., 1954) in what later came to be understood as the cuprous sulfide/cadmium sulfide heterojunction (HJ). This was the first all-thin-film photovoltaic system to receive significant attention. In following years the efficiency of Cu_xS/CdS increased up to 10 % and a number of pilot production plants were installed, but after several years of research it was realized that these solar cells have unsolvable problems of stability owing to the diffusion of copper from Cu_xS to CdS layers. By taking advantage of new technology, work out on Cu_xS/CdS, researchers have rapidly raised the effciency of the gallium arsenide based cell with 4 % efficiency (Jenny at al., 1956) to present eficiencies exceeding 27 % (Green at al., 2011).

However in the last 20 years other thin films solar cells have taken the place of the cuprous sulfide/cadmium sulfide, and their eficiency have raised up to almost 20 %. The most predominant are two: copper indium gallium diselenide/cadmium sulfide $(Cu(In,Ga)Se_2/CdS)$ and cadmium telluride/cadmium sulfide (CdTe/CdS). The first CdTe heterojunctions were constructed from a thin film of n-type CdTe material and a layer of p-

type copper telluride (Cu$_{2-x}$Te), producing ~7 % eficient CdTe-based thin-film solar cell (Basol, 1990). However, these devices showed stability problems similar to those encountered with the analogous Cu$_{2-x}$S/CdS solar cell, as a result of the difuusion of copper from the p layer. The lack of suitable materials with which to form heterojunctions on n-type CdTe, and the stability problems of the Cu$_{2-x}$S/CdS device, stimulated investigations into p-CdTe/n-CdS junctions since the early 1970s. Adirovich (Adirovich at al., 1969) first deposited these films on TCO-coated glass; this is now used almost universally for CdTe/CdS cells, and is referred to as the superstrate configuration. In 1972 5-6 % eficiencies were reported (Bonnet & Rabenhorst, 1972) for a graded band gap CdS$_x$Te$_{1-x}$ solar cell.

The research for CuInSe$_2$/CdS started in the seventies, a 12 % efficiency single-crystal heterojunction p-CuInSe$_2$/n-CdS cells were made by in 1974 (Wagner, 1975) and in 1976 was presented the first thin film solar cells with 4-5 % eficiency (Kazmerski at al., 1976). In the last 30 years a big development of these cells was given by the National Renewable Energy Laboratories (NREL) in U.S.A. and by the EuroCIS consortium in Europe.

Nowadays CdS among Si, Ge, CdTe, Cu(In, Ga)Se$_2$, ZnO belongs to the widespread group of semiconductors. Beyond the attention of researchers are still many issues associated with cadmium sulfide as componenet of thin-film semiconductor devices, although the CdS is one of the most studied semiconductor materials.

2.3 Peculiarities of chemical bath deposition (CBD)

CBD technology consist of the deposition of semiconductor films on a substrate immersed in solution containing metal ions and hydroxide, sulfide or selenide ions source. The first work on CBD is dated 1910 and concerns to the PbS thin films deposition (Houser & Beisalski, 1910). Basic principles underlying the CBD of semiconductor films and earlier studies in this field were presented in the review article (Hass at al., 1982), which encouraged many researchers to begin work in this direction. Further progress in this area is presented in review article (Lokhande, 1991), where references are given for 35 compounds produced by the mentioned method, and other related links. Chemical reactions and CBD details for many compounds were listed in the next paper (Grozdanov, 1994). The number of materials which can be produce by CBD, greatly increased, partly due to the possibility of producing multilayer film structures by this method with subsequent annealing, which stimulates crosboundary diffusion of metal ions and thereby motivates fabrication of new materials with high thermal stability. For example, crossboundary diffusion of CBD coatings PbS/CuS and ZnS/CuS leads to materials such as Pb$_x$Cu$_y$S$_z$ and Zn$_x$Cu$_y$S$_z$ with *p*-type conductivity and thermal stability up to 573 K (Huang at al., 1994). Annealing of Bi$_2$S$_3$/CuS coatings at temperatures 523-573 K leads to formation of new Cu$_3$BiS$_3$ compounds with *p*-type conductivity (Nair at al., 1997). In recent years we counted approximately 120 CBD semiconductor compouns.

Among the first applications of CBD semiconductor films were photodetectors based on PbS and PbSe (Bode at al., 1996). Although the chemically precipitated CdS films were made back in the 60's of last century, for photodetectors were used CdS layers, obtained by screen printing and sintering (Wolf, 1975). Chemically deposited CdSe films are fully suitable for use in photodetectors (Svechnikov & Kaganovich, 1980). At late 70's and early 80-ies the main direction in chemical bath deposition technology was deposition of thin films for use in solar energy conversion. One of the first developments in this area was the coating producing that absorbs sunlight (Reddy at al., 1987), and its use in glass vacuum tube collectors (Estrada-Gasca at al., 1992). Application of the chemically deposited films in

coatings for controlling the flow of sunlight was first proposed in 1989 (Nair at al., 1989). The efficiency improving of such coatings in glass vacuum tube collectors were presented in (Estrada-Gasca at al., 1993). One of the main applications of chemically deposited semiconductor films has been their use in photoelectrochemical SC, mostly CdS and CdSe films (Hass at al., 1982, Boudreau & Rauh, 1983, Rincon at al., 1998). The use of chemically deposited semiconductor films in thin SC has a short history. In the structure Mo/CuInSe$_2$/CdS/ZnO, which showed 11% efficiency (Basol & Kapur, 1990), was by the first time used chemically deposited CdS thin film. Further structure improvement allowed to reach 17% efficiency (Tuttle at al., 1995). Chemically deposited CdS film with thickness of 50 nm has been an essential element of this structure. The biggest, confirmed today for SC based on CdS/CdTe, is 16,5% efficiency in which CdS film was chemically deposited in bath (Green at al., 2011). Entering highly resistive CdS film in p-CuInSe$_2$/CdS/n-CdS solar cell structure deemed necessary step towards improving of the solar cells stability (Mickelsen & Chen, 1980). Performed theoretical calculations (Rothwarf, 1982) showed that the thickness of CBD CdS films should be as small as possible to increase efficiency of solar cells with its use. Therefore, chemical deposition technology, which allows to fully cover the substrate at small film thickness was selected for the fabrication of thin films and showed significantly better results (Basol at al., 1991). Efficiency of n-CdSe or n-Sb$_2$S$_3$ chemically deposited films with WO$_3$ inclusions as absorber material in solar cells based on the Schottky barrier has been proved in practice. For example, elements on the Schottky barrier ITO/n-CdSe(5 μm)/Pt/Ni/Au (13 nm) shows U$_{xx}$=0,72 V, I$_{к3}$=14,1 mA·cm^{-2}, fill factor 0,7, and 5,5% efficiency (Savadogo & Mandal, 1993 & 1994). Abovementioned possible applications of chemical bath deposition, particularly in solar energy conversion, provided the growing interest to chemical deposition of semiconductor thin films. Chemical deposition is perfect for producing thin films on large areas and at low temperatures, which is one of the main requirements for the mass use of solar energy.

2.4 The advantages of chemical surface deposition (CSD) over CBD

In the CBD process, the heat necessary to activate chemical reaction is transferred from the bath to the sample surface, inducing a heterogeneous growth of CdS on the surface and homogeneous CdS formation in the bath volume. The reaction is better in the hottest region of the bath. Therefore, for baths heated with thermal cover deposition also occurs on the walls, and bath, which heat up immersed heater, significant deposition occurs on heating element. Additionally, the solution in the bath should be actively mixed to ensure uniform thermal and chemical homogeneity and to minimize adhesion of homogeneously produced particles to the surface of CdS film. The disproportion of bath volume and that which is necessary for the formation of CdS film, leads to significant proportion of wastes with high cadmium content. Different groups of researchers put efforts for decreasing the ratio of volumes bath/surface through use of overlays. However the clear way for unification of large areas deposition with high cadmium utilization and high speed of growth, to achieve high efficiency of transformation is not represented.

The chemical surface deposition (CSD) technology demonstrated in this paper overcomes these limitations through use of the sample surface as a heat source and use of solution surface tension to minimize the liquid volume. The combination of heat delivery method to surface and small volume of solution leads to high utilization of cadmium and its compounds.

This paper describes CSD technology of CdS thin films from aqueous solutions of cadmium salts CdSO$_4$, CdCl$_2$, CdI$_2$. The properties of CdS films deposited on glass and ITO/glass from the nature of the initial salt and solar cells based on CdTe/CdS with CSD CdS films as windows was investigated.

3. Chemical surface deposition of CdS thin films from CdSO$_4$, CdCl$_2$, CdI$_2$ aqueus solutions

3.1 Introduction

One of the methods to increase SC efficiency based on CdS/CdTe, CdS/CuIn$_{1-x}$Ga$_x$Se$_2$, with the CdS film as the window is increasing the current density value (Stevenson, 2008). This can be achieved by reducing losses in the photons optical absorption from $\lambda > 500$ nm by reducing CdS film thickness. To provide a spatially homogeneous work of the device the CdS films should not only be thin, but solid, durable and resistant to further technology of SC production. To produce ultra-thin (from 30 to 100 nm) and homogeneous CdS films the technology of bath chemical deposition is widely used (Estela Calixto at al., 2008, Mugdur at al., 2007).

Chemical deposition technology is quite simple, inexpensive and suitable for the deposition of polycrystalline CdS films on large areas. Deposition of thin CdS films from aqueous solutions is a reaction between cadmium salt and thiocarbamid (thiourea) in alkaline medium. Mostly are used simple cadmium salts: CdSO$_4$ (Chaisitsak at al., 2002, Contreras at al., 2002, Tiwari & Tiwari, 2006, Chen at al., 2008), CdI$_2$ (Nakada & Kunioka, 1999, Hashimoto at al., 1998), Cd(CH3COO)$_2$ (Granath at al., 2000, Rau & Scmidt, 2001) and CdCl$_2$ (Qiu at al., 1997, Aguilar-Hernández at al., 2006). Thiourea (TM) is used as sulfide agent in the reactions of sulfide deposition, as has a high affinity to metal cations and decomposes at low temperatures. Deposition process can be described by two mechanisms (Oladeji, 1997, Soubane, 2007). Homogeneous mechanism involves formation of layer with the CdS colloidal particles, which are formed in solution and consists of several stages.

1. Ammonium dissociation:

$$NH_4^+ + OH^- \rightleftarrows NH_3 + H_2O \tag{1}$$

In alkaline medium due to interaction Cd^{2+} ions with the OH$^-$ environment ions is possible formation of undesirable product - Cd(OH)$_2$:

$$Cd^{2+} + OH^- \rightarrow Cd(OH)_2 \downarrow \tag{2}$$

2. Thiourea hydrolysis (NH$_2$)$_2$CS with the the formation of sulfide ions

$$(NH_2)_2CS + H_2O \rightleftarrows HS^- + H^+ + (NH_2)_2CO \tag{3}$$

$$HS^- + OH^- \rightleftarrows S^{2-} + H_2O \tag{4}$$
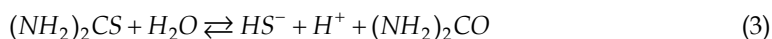
3. Final product formation

$$Cd^{2+} + S^{2-} \rightleftarrows CdS \downarrow \tag{5}$$

Deposition of thin CdS films from the aqueous solutions through the stage of cadmium tetramin $[Cd(NH_3)_4]^{2+}$ complex ion formation, which reduces the overall speed of reaction and prevents Cd(OH)$_2$ formation by the heterogeneous mechanism.

$$Cd^{2+} + 4NH_4OH \rightarrow [Cd(NH_3)_4]^{2+} + 4H_2O \qquad (6)$$

$$[Cd(NH_3)_4]^{2+} + S^{2-} \rightarrow CdS \downarrow +4NH_3 \qquad (7)$$

In general form:

$$[Cd(NH_3)_4]^{2+} + (NH_2)_2 CS + OH^- \rightarrow CdS \downarrow +4NH_3 + H^+ + (NH_2)_2 CO \qquad (8)$$
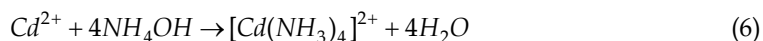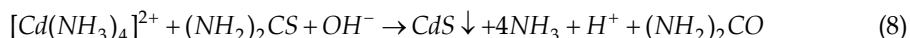
The sulphides films deposition from thiocarbamid coordination compounds has some chemical peculiarities. Depending on the nature and the salt solution composition may be dominated different coordination forms, and with thiourea molecules in complex inner sphere may contain anions Cl$^-$, Br$^-$, J$^-$, and SO$_4^{2-}$ under certain conditions. Thus, the cadmium atoms close environment are atoms of sulfur, halogens and oxygen, and at the thermal decomposition part of the Cd-Hal or Cd-O bonds are stored and in the sulfide lattice are formed Hal$_S$• and O$_S$•defects. In conjunction with the substrate the thiocarbamid complexes orientation on active centers of its surface is observed. The complex particles that can interact with active centers on the substrate are the link that provides sulfide link with the substrate. The nature of this interaction determines the nature of film adhesion. In the case of cadmium sulfide deposition on quartz or glass substrates the active centers are sylanolane groups (≡Si–OH) which interact with halide or mixed hydroxide complexes. In result of such interaction the Cd–O–Si oxygen bridges are created. This explains the good adhesion of the cadmium sulfide films deposited from thiocarbamid coordination compounds to glass substrates (Palatnik & Sorokin, 1978).

3.2 Chemical surfact deposition of CdS thin films

In CSD, a solution at ambient temperature containing the desired reactants is applied to a pretreated surface. Glass or ITO/glass (16×20 mm) substrates, CdTe (10×10 mm) and Si (30×20 mm) wafers were used in the entire work. After that sample with working solution is heated and endured for a given temperature (Fig. 1). To ensure uniformity of heating plate

$$[Cd(NH_3)_4]^{2+} + CS(NH_2)_2 + OH^- \leftrightarrow CdS\downarrow + 4N_3 + H^+ +(NH_2)CO$$
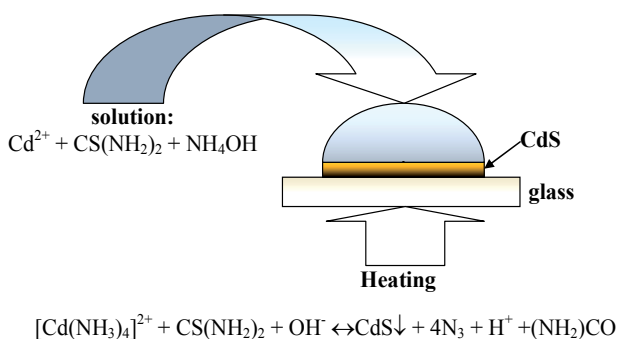
Fig. 1. Scheme of CdS films thin chemical surface deposition

with working solution is previously placed on thermostated (343 K) surface. Surface tension of the solution provides a minimum volume of reaction mixture and its maintenance on the substrate. Film deposition occurs through the heterogeneous growth of compounds on the substrate surface by transfer of heat to the work solution. Heterogeneous growth is preferred over homogeneous loss due to thermal stimulation of chemical activity on warmer surface. At a result we receive a high proportion of cadmium from a solution in film and depending on the substrate, the heteroepitaxial film growth. The outflow of heat from the solution to environment helps to keep the favorable conditions for the film heterogeneous growth in time required for film deposition. After heating the plate was removed, the surface was rinsed with distilled water and dried in the air.

The combination of factors of the heat delivery to phase division surface (substrate-solution) and small volume of working solution in the CSD allows to receive coverage with satisfactory performance, increase the efficiency of the reagents, and therefore simplify their utilization. For deposition of CdS films were used freshlyprepared aqueous solutions of one of three cadmium salts: $CdSO_4$, $CdCl_2$, CdI_2. Solution ingredients and the corresponding concentrations are presented in Table. 1.

salt	C(cadmium salt), mol/l	C(CS(NH$_2$)$_2$), mol/l	C(NH$_4$OH), mol/l
$CdSO_4$			
$CdCl_2$	0,001; 0,0001	0,1; 0,01	1,8; 1,2
CdI_2			

Table 1. Ingredients and concentrations of solutions for CSD of CdS films, T=343 K, pH=12

Several modifications of films CSD were used. First modification (A) includes single applying of working solution and it different time exposure (5 to 12 min.) on the substrate. The second modification (B) provided repeated addition (3 min intervals.) of fresh working solution on the substrate surface. The difference of the third modification (C) consistent in applying (with 3 min. time exposure) and subsequent flushing of working solution on the substrate surface, ie in layer deposition. In such way we achieved increase and regulation of CdS film thickness.

	modifications		
	A	B	C
maximum thickness, nm	62	65	105
deposition rate, nm/min.	≤6	4–6	≥8

Table 2. The CdS films maximum thickness and deposition rate depending on the CSD modification

Aplying of A modification results in the smallest CdS film thickness, as seen from Table. 2. This is because the main part of the film (80-90 % thickness) is deposited in 2-3 min. Further time exposure of the working solution-substrate system is not accompanied by visible changes in the appearance of the formed film, apparently due to exhaustion of working solution. Therefore, during the multistage (CSD modifications B and C) CdS films deposition the duration of elementary expositions deposition was 3 min. Based on the structural studies results for further work modification B was selected.

3.3 Properties of CSD CdS thin films

The film thickness was determined by ellipsometric measurement of light polarization change after light reflection from an air-film interface on the LEF-3M instrument, allowing precision from 5 to 10 nm, for film thickness less then 100 nm. Morphology of the film surface and the elemental composition were investigated using the scanning electron microscopes REMMA-102-02 with EDS and WEDS and JSM-6490LV. Crystallinity of the CdS film structure was investigated using the automated X-ray diffractometer HZG-4A (with CuK_α radiation, $\lambda=0,15406$ nm). The optical transmission measurements have been done at room temperature with unpolarized light at normal incidence in the wavelength range from 300 to 1000 nm using Shimadzu UV-3600 double beam UV/VIS spectrophotometer. The optical absorption coefficient α was calculated for each film using the equation

$$I_t = I_0 \exp(-\alpha t) \tag{9}$$

where t is the film thickness, I_t and I_o are the intensity of transmitted light and initial light, respectively. The absorption coefficient α is related to the incident photon energy $h\nu$ as:

$$\alpha \cdot h\nu = A\left(h\nu - E_g\right)^{n/2} \tag{10}$$

where A is a constant dependent on electron and hole effective mass and interband transition, E_g is the optical band gap, and n is equal to 1 for direct band gap material such as CdS. The band gap E_g was determined for each film by plotting $(\alpha h\nu)^2$ vs $h\nu$ and then extrapolating the straight line to the energy axis.

3.3.1 Thickness and deposition rate

The peculiarity of the CSD method is that after the first deposition the function of the substrate is performed not by glass, but by formed CdS film. All subsequent depositions are conducted on the same substrate. Through this growth rate of successive layers is approximately the same, and the total film thickness increases in equal size. The data of film thickness measurements and calculated average growth rate is shown on Fig. 2. The accuracy of ellipsometric measurements of thickness increased as the total thickness of the film growth, so that the absolute error varied from ± 10 nm to ± 5 nm. The highest thickness obtained was in the case of $CdSO_4$, and the least thickness in the CdI_2 case.

Apparently, among all other Cd salts, CdI_2 always results in a much thinner film. This observation was in agreement with what was reported earlier (Kitaev at al., 1965, Ortega-Borges & Lincot, 1993). This can be explained by different values of stability constant of Cd complexes complementary (Khallaf at al., 2008).While using for CSD the $CdCl_2$ (Fig. 2, a) were obtain almost linear dependence increase of film thickness on the deposition time. For films deposited with $CdSO_4$ and CdJ_2 (Fig. 2, b and c, respectively), the dependence of film thickness on deposition time was more complicated, but also had a character close to linear. This fact can be used for CdS films thickness control with high precision in the CdS/SdTe HJ fabrication. The differences in the nature of layer growth of thin CdS films can be explained by the process stages. When solution is applied to the substrate and heated, thiocarbamid complexes start to orient on active centers of the substrate surface and form CdS growth centers. The maximum possible number of growth centers is determined by the number of active centers on the substrate surface, which is considerably less than reactive particles in solution. Under the influence of continuous solution flow the grow centers increases and turn into islands. After a surface filling the islands are merging and form netted
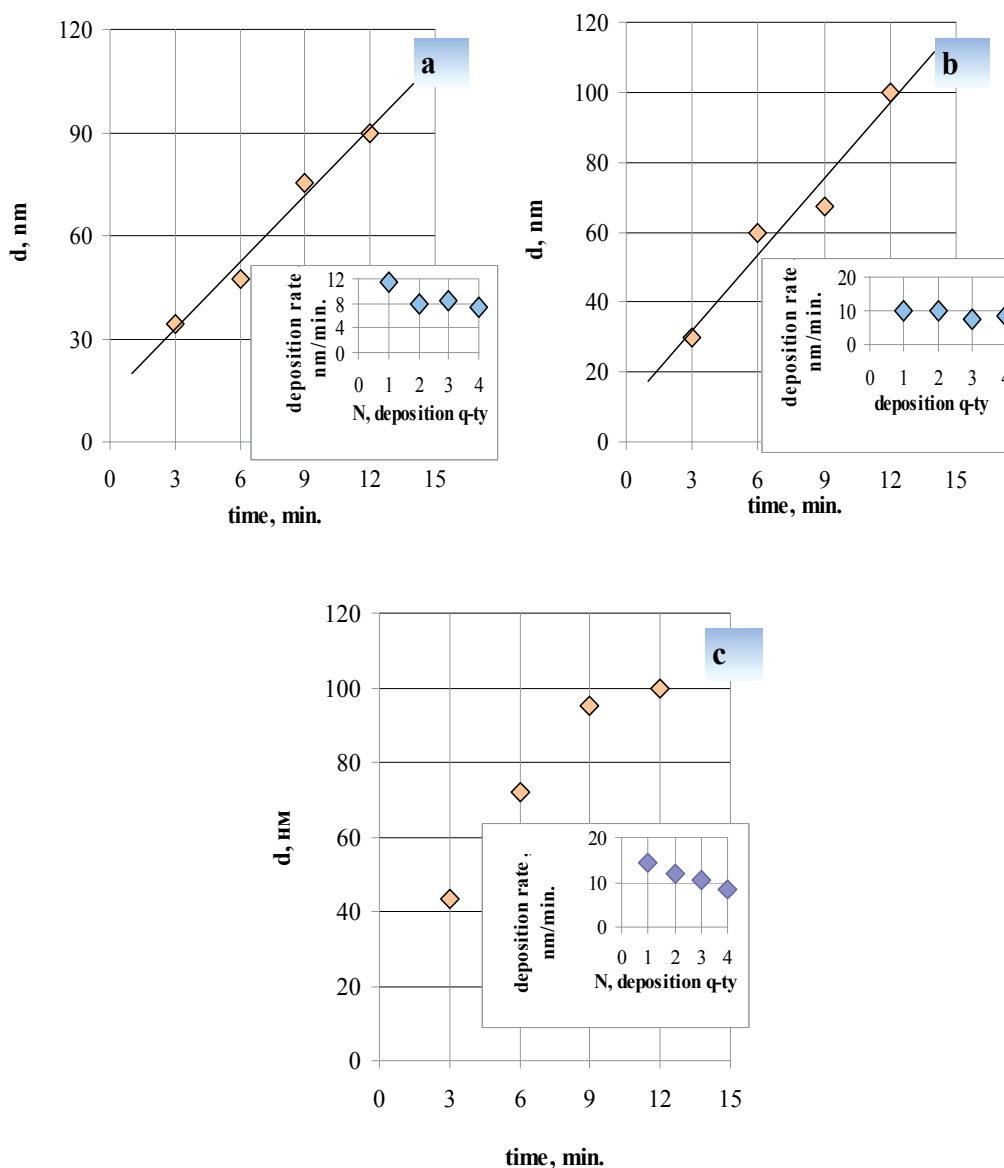
Fig. 2. The CdS thin film thickness dependence on time and quantity of deposition from aqueus solution: $CdCl_2$ (a); $CdSO_4$ (b); CdJ_2 (c). The mean deposition rate of CdS thin films on figure inset.

structures that consist of pores and channels. Further film growth is, in fact, filling the pores and channels. It slows the increase of film thickness, but does not alter the film weight gain. At later stages of the growth occurs reflection of the particles stream from the surface that leads to film growth rate decrease, and in the future - to its almost complete stop. Maximum growth rate of CSD at 343 K had films deposited from CdI_2 solution. Big deposition rates cause to the significant film defections, which confirm the results of their structural studies.

3.3.2 Surface morphology

The results of the CdS films investigation by scanning electron microscopy, deposited from diferent aqueous salt solutions are shown in Fig. 3-7, in the reflected and secondary electrons mode.
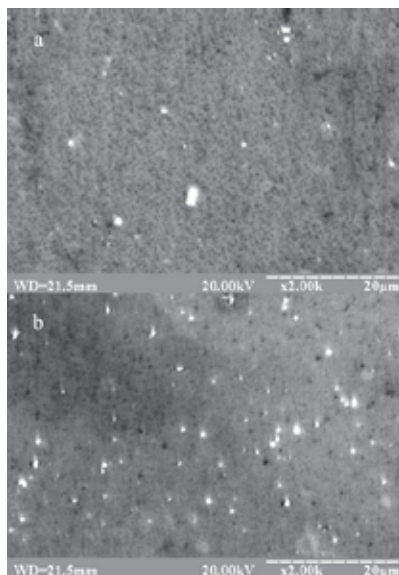
Fig. 3. Surface morphology of CdS film deposited from $CdSO_4$ aqueus solution, A modification (a) and C modification (b). REMMA-102-02, accelerating voltage 20 kV, scale 1:2000
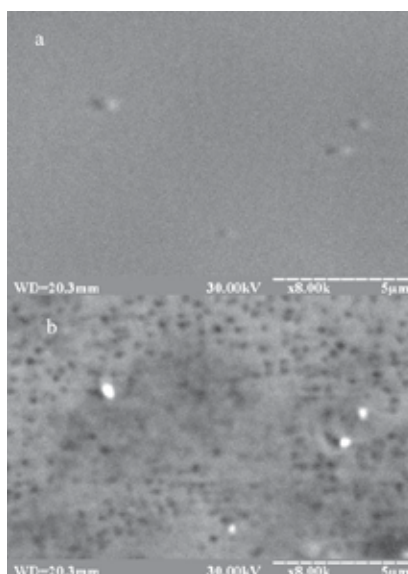
Fig. 4. Surface morphology of CdS film deposited from $CdSO_4$ aqueus solution on ITO coated glass in the secondary-electron mode (a) and reflected-electron mode (b). REMMA-102-02, accelerating voltage 30 kV, scale 1:8000
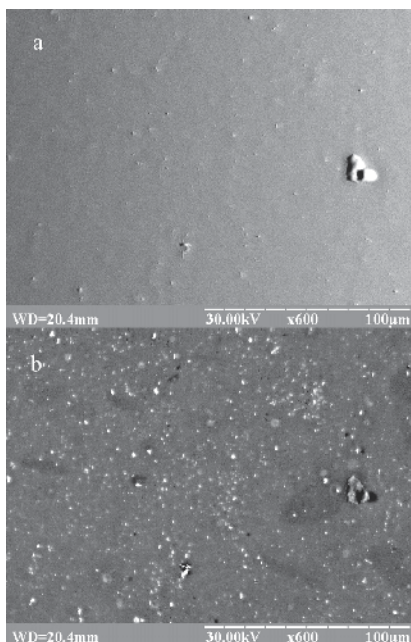
Fig. 5. Surface morphology of CdS film deposited from $CdCl_2$ aqueus solution in the secondary-electron mode (a) and reflected-electron mode (b). REMMA-102-02, accelerating voltage 30 kV, scale 1:600
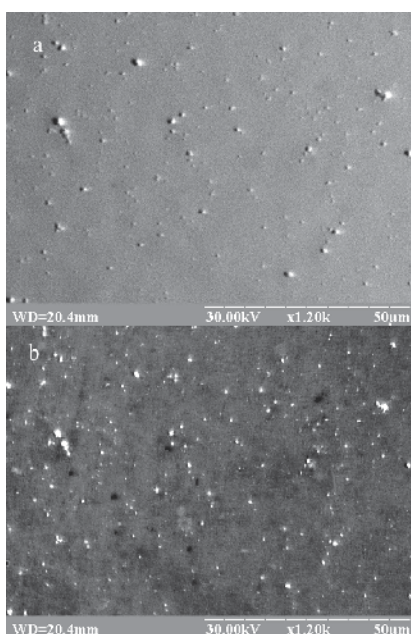
Fig. 6. Surface morphology of CdS film deposited from CdI_2 aqueus solution in the secondary-electron mode (a) and reflected-electron mode (b). REMMA-102-02, accelerating voltage 30 kV, scale 1:1200

In reflected electron mode the photo qualitatively displays the surface composition (the lighter point, the heavier elements), and in secondary electron mode - the surface morfology. As seen all CdS film fabricated by C modification completely covers the substrate across the sample area, are homogeneous and solid. In reflected electrons mode are observed white dots indicating the localization heavier compared to the film phase. Comparison of CdS film images, obtained in both reflected and secondary electrons (Fig. 4-6), indicates that the heavier phase inclusions are on the film surface.

So, these heavier phase inclusions are particles on the surface (surface macrodefects) and most likely were formed in the final phase of deposition. The concentration of macrodefects on the surface in the investigated CdS films deposited from varus cadmium salts are presented in table 3. Regardles of applied salt surface macrodefects concentration is almost the same and is 100 times smaler than for CBD films (Romeo at al., 2003). Using EDS and WDS measurements, the stoichiometry of all films were studied. The generalized results of the surface morphology and X-ray microanalysis investigation of thin CdS films, deposited from various cadmium salts are given in Table 3. We determined that the particles on the CdS films surface (macrodefects) are CdS particles with a different stoichiometry than the film. The stoichiometry deviation towards sulfur is quite unexpected because in most nonvacuum deposition methods the lack of sulfur is observed.
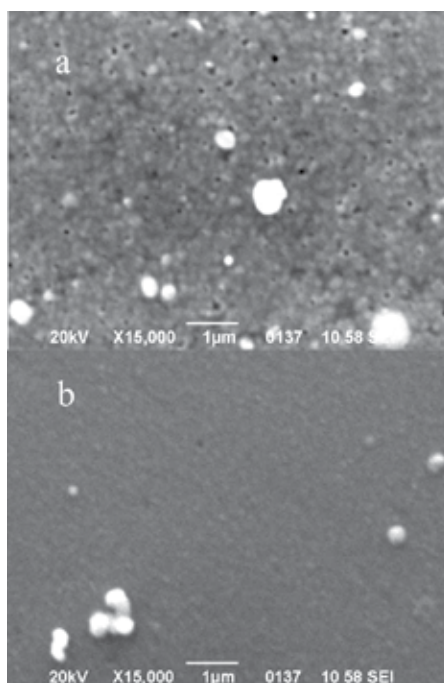
Fig. 7. Surface morphology of CdS film deposited from CdI_2 aqueus solution before (a) and after annealing (b). JSM-6490LV, accelerating voltage 20 kV, scale 1:15000

The CdI_2-based films had composition close to stoichiometric while the $CdSO_4$-based films showed the biggest deviation from stoichiometric composition that agre with results of CBD (Ortega-Borges & Lincot, 1993) (Table 3). Sulfur excess in CSD CdS films gives us the opportunity to perform annealing in the normal (air), not sulfur medium because they do

not need to enter in film extra amount of sulfur to ensure stoichiometry. Analysis of CdS films surface morphology, obtained by AFM (Fig. 8) shows that the method of deposition and the nature of the initial cadmium-containing salt have significant affect on the CdS film surface structures. Using the deposition B modification ensure much more evenly cover over the sample area than A modification. The best results were obtained by C modification. The CdS films deposited from $CdSO_4$ aqueous solution by B and C (Fig. 8, a and b, respectively) have different surface morphology. The surface of all films obtained in the C modifications, is completely packed with crystalline grains. The exception is the film obtained from cadmium iodide aqueous solution. Along with the films surface morphology the results of surface roughness analysis are presented.

salt	surface macrodefects concentration, cm^{-2}	Cd/S rate on film surface	Cd/S rate of surface macrodefects
$CdSO_4$	10^6–10^7	0,880	0,800
$CdCl_2$	10^7	0,898	0,908
CdI_2	10^6–10^7, the pineholes are observed, for films deposited from two other salts the pinholes are almost absent	0,911	1,061

Table 3. Summarized results of surface morphology and X-ray microanalysis investigation of CdS thin films, deposited from various cadmium salts

3.3.3 Crystal structure

Experimental diffraction intensities of CdS films, obtained by B and C modification of (curves 2 and 3), respectively, are shown in Fig. 9. In all tested samples polycrystallinity of CdS films is expressed with the noticeable presence of cubic phase. The curves 2 and 4 on fig. 9. indicates that the samples are almost completely polycrystalline.

The first $26,45^0$ peak of cubic phase (curves 2 and 4) is slightly expressed and shifted compered to the corresponding XRD peak from single CdS crystal (curve 1), which can be explained by the small size of grains as the probability of mechanical stress in films is very small because of low speed growth (Table 2).

In addition to the $26,45^0$ peak on curve 3 (Fig. 9) are present two more – $43,90^0$ and $52,00^0$, corresponding to the cubic phase. Implemented sample heat treatment does not result in a significant increase in the intensity of any of the three peaks, and even the intensity of first one decreases (curve 4). The shift of the first ($26,45^0$) peak (curves 3 and 4) related with a decrease after annealing of mechanical tensions in the film, and intensity decrease of this peak indicates a simultaneous transition in polycrystalline cubic phase. Size grains expected increase by recrystallization has not occurred. Thus, annealing conditions to improve crystallinity of films need correction. Based on the data diffraction pattern most of the cubic phase is contained in the films deposited by C modification $C(CdSO_4) = 0,001$ mol/l. The transition to the hexagonal phase after annealing is not observed, unlike CBD CdS film (Archbold at al., 2005, Romeo at al., 2000).

Fig. 10 shows the experimental diffraction intensities obtained from CdS films, deposited from aqueous solutions of $CdSO_4$, $CdCl_2$, CdI_2 salts on glass substrates before and after annealing. In all tested samples polycrystallinity of CdS films is expressed with the noticeable presence of cubic phase. From the curves 2 (Fig. 10, a, b, c) can be seen that as deposited samples are almost entirely polycrystalline. The first peak of 26,45 ° for the cubic
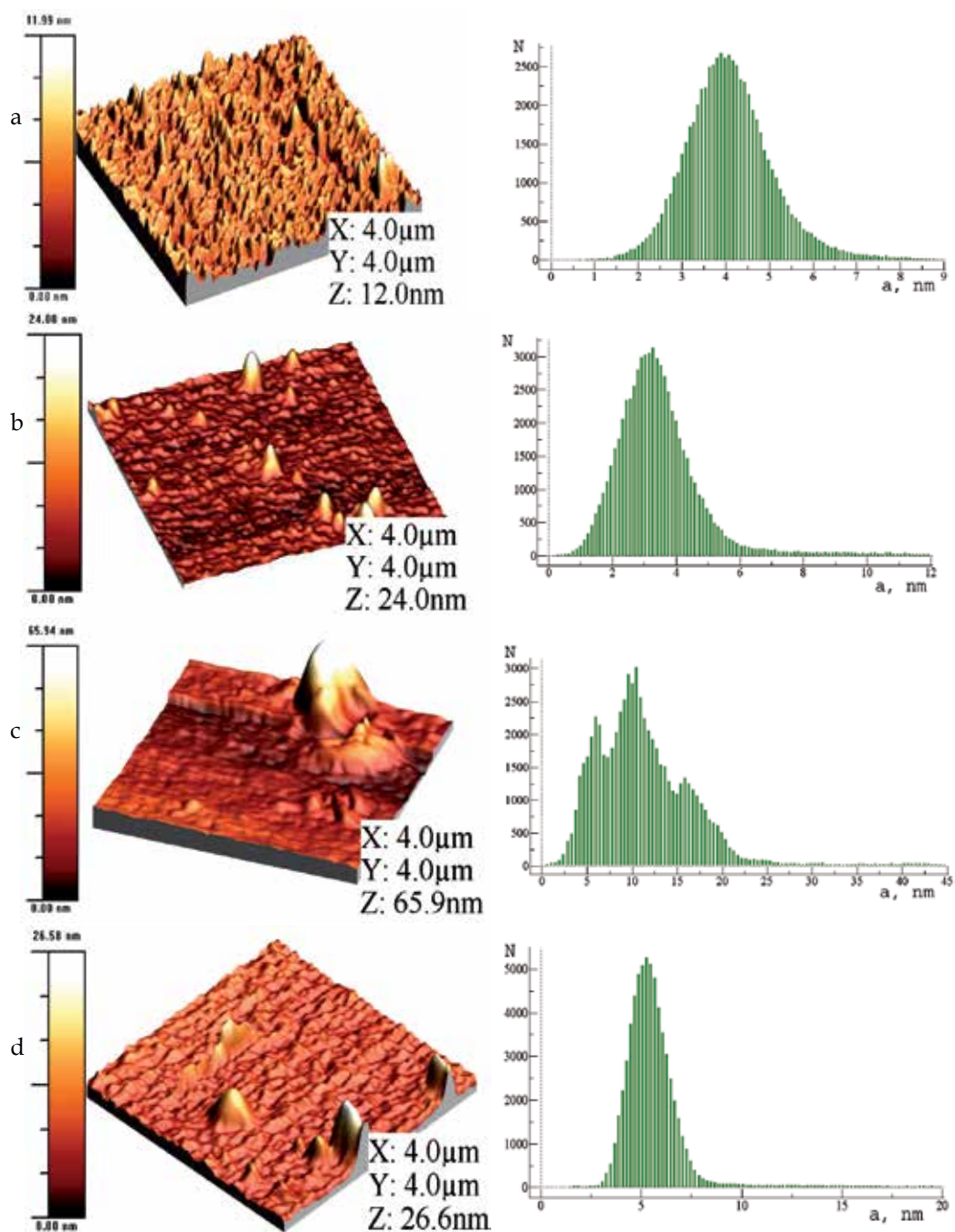
Fig. 8. AFM images and mean roughness distribution of CdS thin films grown from aqueus solution: $CdSO_4$, B modification (a); $CdSO_4$, C modification (b); $CdCl_2$, C modification (c); CdJ_2, C modification (d)
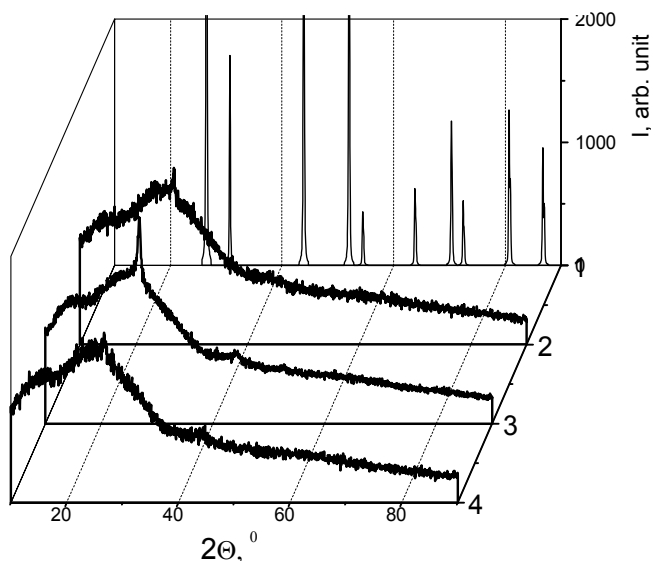
Fig. 9. XRD pattern of CdS film deposited on glass substrate from $CdSO_4$ aqueous solution with $C(CdSO_4)$=0,001 mol/l by B and C modification (curves 2 and 3); $C(CdSO_4)$=0,001 mol/l by C modification, after annealing (curve 4); with $C(CdSO_4)$=0,0001 mol/l C modification (curve 5); CdS cubic monocrystal reference pattern (curve 1).

phase have low intensitivity and is slightly shifted against the corresponding peak of CdS single crystal. This can be explained by the small size of grains as the probability of mechanical tensions in films deposited from $CdSO_4$, $CdCl_2$ salts solutions is neglectible due too low growth speed. Besides peak 26,45°, on curve 2 (Fig. 10 b) are present two more - 43,90° and 52,00° corresponding to the cubic phase. The heat treatment of samples leads to a significant increase in the intensity of the first two peaks for films deposited from $CdSO_4$, CdI_2. For films deposited from $CdCl_2$ aqueous solutions, the nature of XRD curve practically unchanges due to annealing. For CdS films, deposited from CdI_2 aqueous solution (fig. 10c curve 1) after annealing were observed intensity increases of 26,45°, 52,00° peaks and the appearance of third peak 43,90°. This indicates a reduction of disordered polycrystalline phase which transforms into crystalline phase and a rather significant restructure of CSD film, that cinsides with the results of the surface morphology investigations (Fig. 7).

Experimental diffraction intensities of CdS films deposited on Si and CdTe substrates are presented in Fig. 11. As seen, the results for various substrates were different, but both express polycrystallinity of CdS films. Besides the peaks of Si (Fig. 11 a, № 3) and CdTe (Fig. 11 b, № 5, 8) substrates are present a significant number of peaks corresponding to different phases of CdS compound. These results indicate the existence of a mixture of two structural phases (cubic and hexagonal) that is often observed for CdS films fabricated by nonvacuum methods (Calixto & Sebastian, 1999). The X-ray diffraction peaks N 1, 2, 7, 4, 9 (Fig. 11a) on silicon corespond to hexagonal structure, cubic may respond only the peak number 1. For films on CdTe substrate peaks intensity of hexagonal and cubic phases is much higher.
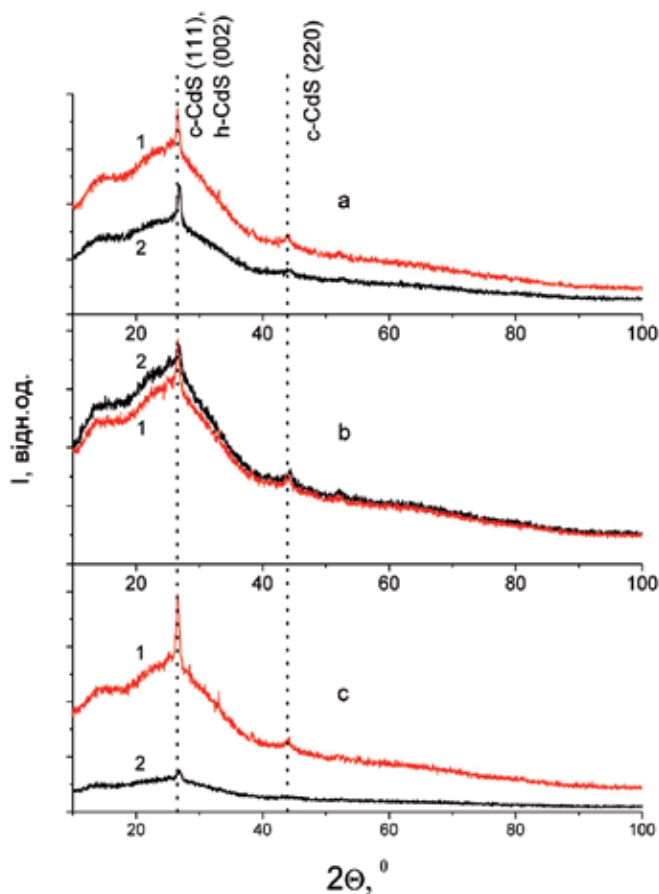
Fig. 10. XRD pattern of CdS film deposited on glass substrate from aqueus solution: CdSO₄ (a); CdCl₂ (b); CdJ₂ (c); as deposited (2); after annealing (1).

3.3.4 Optical properties

Absorption coefficient in the fundamental absorption area for all CdS samples was 10^5 cm^{-1}.The absorption spectra of samples (Fig. 12.) clearly shows the existence of the CdS compounds in all films deposited from aqueous solutions of cadmium-containing salts. Spectral dependence of CdS films absorption in the coordinates $(\alpha*h\nu)^2$ vs hν demonstrate the presence of fundamental absorption edge (Fig. 12), localized in the region 2,5 eV. The calculated band gaps of the films are in good agreement with the reported values (Landolt-Börnstein, 1999, Aven & Prener, 1967) and correspond to the direct allowed band transition. We do not observe a straight-line behaviour on graphs of $(\alpha h\nu)^{2/3}$ vs hν (direct forbidden), $(\alpha h\nu)^{1/2}$ vs hν (indirect allowed) $(\alpha h\nu)^{1/3}$ vs hν (indirect forbidden). These plots (not shown) reveal that the type of transition is neither direct forbidden nor indirect. For films deposited in the same technological modes on glass and ITO coated glass substrates, the location of fundamental absorption edge are olmost the same. A small (0,01 eV) difference between the fundamental absorption edge values for films on glass and ITO/glass are caused by the difference of substrates surface roughness.
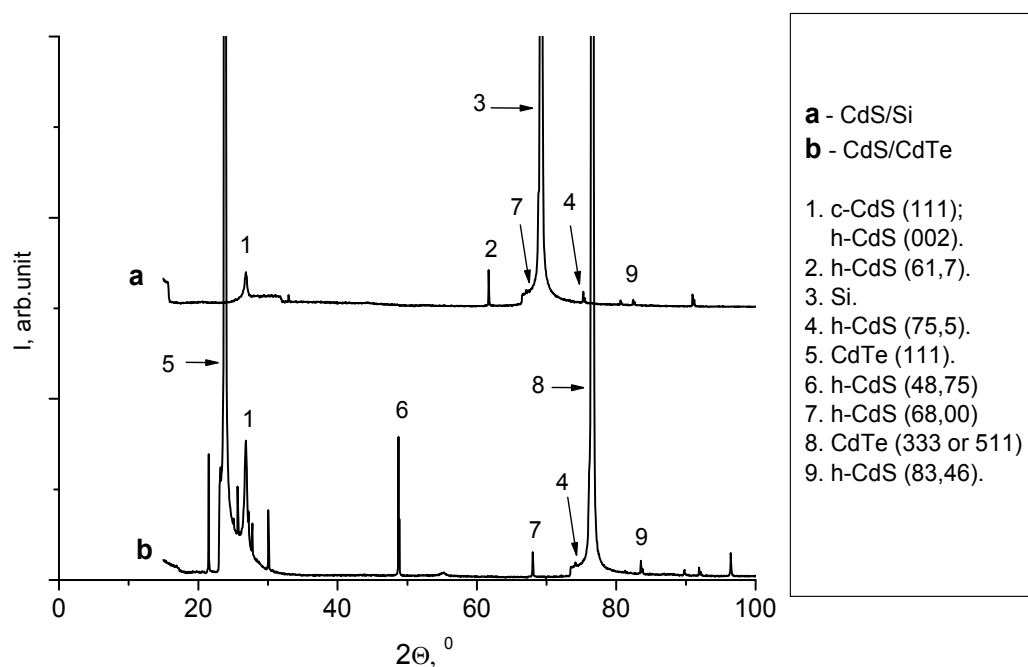
Fig. 11. XRD pattern of CdS films deposited from $CdCl_2$ aqueus solution on Si (a) and CdTe (b) substrates

The fundamental absorption edge localization feature in CdS films, in comparison with CdS monocrystal, is that in films it is shifted to higher energy region (2,537 eV and 2,547 eV for films on glass and ITO/glass, respectively).
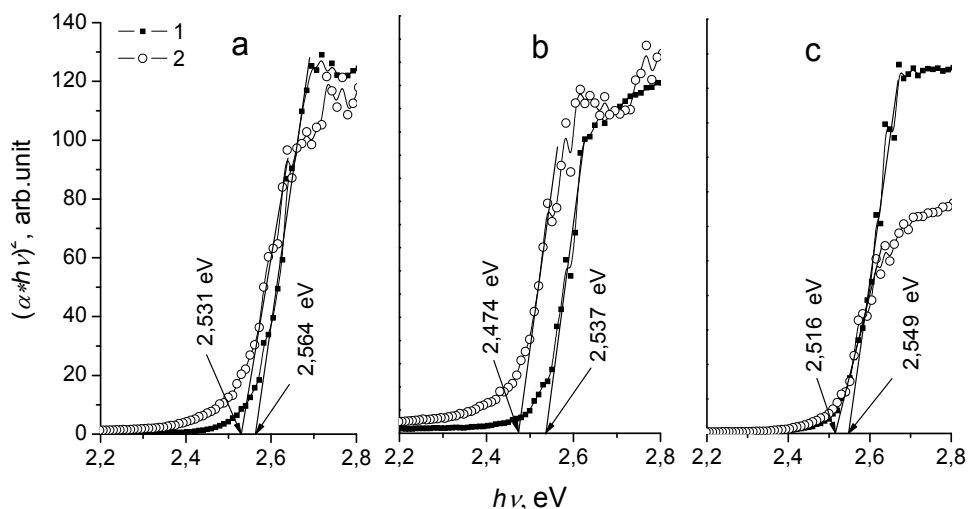
Fig. 12. Optical absorbance spectra of CdS film deposited on glass substrate from aqueus solution: $CdSO_4$ (a); $CdCl_2$ (b); CdJ_2 (c); as deposited (1); after annealing (2).

This allows to expand CdS/CdTe solar cells phototransformation area and increase their efficiency. Reducing energy fundamental absorption edge of CdS films after annealing (Fig. 12, curves 2) can be coused by grain growth (Nair at al., 2001). Sharpest edge of fundamental absorption have CdS films, deposited on glass substrate. This indicates a smaller number of macro defects in these films compared with annealed. Energy levels of this defects are lying near the edge zones. The increase long-wave "tail" of the absorption curve for annealed film (Fig. 12, a, b, curve 2) is caused by increase of absorption near the CdS film surface, where in the process of annealing in air CdO can be formed.

All films have high transmission, with the transmission in the CdI_2 case being better than that of the other three films. This was expected, since the SEM micrographs, showed the pinholes on CdI_2-based film. The lowered transmission of our films is caused by their surface roughness, due to coverage by surface macrodefects which are overgrowth crystallite, causes light scattering. Spectral dependence of optical transmission in the visible region of CSD CdS films before and after annealing are shown in Fig. 13. The main feature of the annealed CdS films spectra is small (0.033 eV) shift of fundamental absorption edge in the longwave region and reducing the optical transmission more than 20%. Reducing the transmission is determined not only by absorption and reflection from the film surface, but olso by quite significant changes in the film structure after annealing. From the SEM holes were observed (Fig. 7) after annealing they completely disappeared. X-ray pattern (Fig. 10, c, curve 1) also confirm a significant increase in the film's crystallinity structure as a result of annealing, despite indifferent directing effect of the glass substrate.
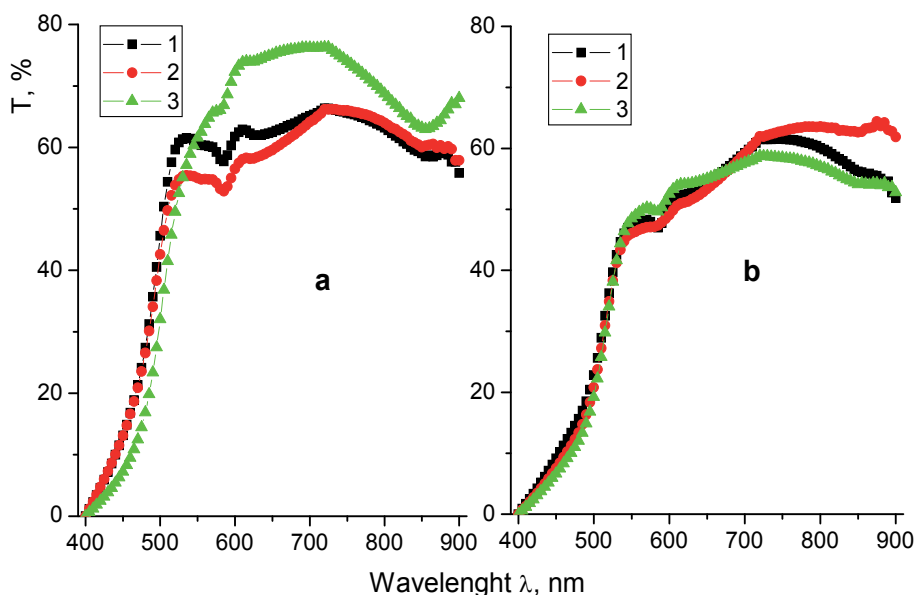
Fig. 13. Optical transmittance spectra of CSD CdS films deposited from aqueus solution: $CdCl_2$ (1); $CdSO_4$ (2), CdJ_2 (3) as deposited (a) and after annealing (b).

4. Solar cell performance

The n-CdS/p-CdTe HJ was fabricated and their electrical and photoelectric properties were investigated. The CdS thin films with 100 nm thickness were deposited by CSD using $CdCl_2$

cadmium chloride solution. Thin polycrystalline CdS films completely covered the substrate across the sample area, hade stoichiometric composition, was solid with a small surface macrodefects concentration (10^7sm^{-2}). Typical spectral dependence of transmission of CSD CdS film is shown on Fig. 13. Resistance of is fabricated n-CdS/p-CdTe SC $R_0 \approx 10^4$-10^5 Ω at T= 300 K and was determined by the electrical properties of the p-CdTe substrates. This is coused by the resistivity of used substrates which is 2-3 orders of magnitude greater than the similar parameter for n-CdS films ($R_{CdS} \approx 10^3$ Ω). Voltage cutoff in n-CdS/p-CdTe structures, as seen in Fig. 14 is $U_0 \approx 1,4$ V and its value is close to CdTe bandgap (Landolt-Börnstein, 1999). Inverse branches of curent-voltage characteristic for anisotropic structures are well described by power dependence $I_R \sim U^m$, where the m ≈ 1 to U> 2, which is typical for charge carriers tunneling or inherent space charge limited currents in velocity saturation mode (Hernandez, 1998, Lamperg & Mark, 1973). Reverse current increase observed in the investigated anisotropic heterojunction with increasing voltage bias can also be caused by imperfections in their periphery.

Fig. 15 shows relative quantum efficiency of photoconversion (ratio of short circuit current to number of incident photons) η(hv) spectra of CdS/CdTe heterojunction fabricated by CSD of CdS film on CdTe wafer. The η(hv) spectra find out to be similar for structures fabricated on different substrates what indicate high local homogeneity of substrates and reproducibility of the CSD films properties. The sharp long wave increase of η(hv) in narrow spectral range 1.4–1.5 eV for CdS/CdTe structure illumination from CdS film side is observed. Its value reach maximum in region $hv^m \approx 1.5$ eV what correspond to energy of direct band transitions in CdTe (Landolt-Börnstein, 1999, Aven & Prener, 1967).
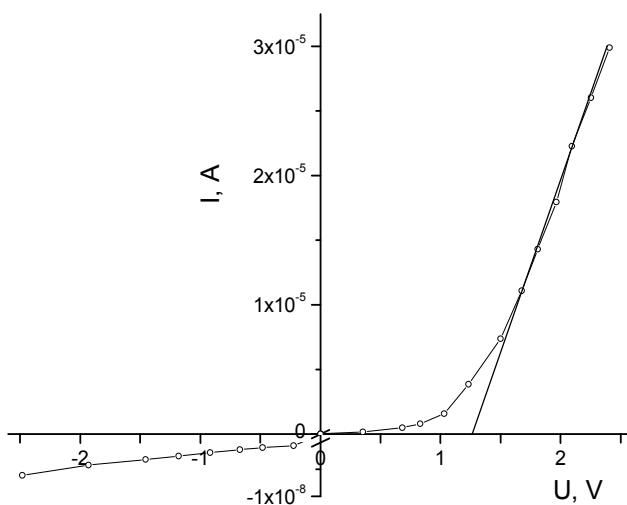
Fig. 14. Curent-voltage characteristic of *n*-CdS/*p*-CdTe HJ at 300 K

It should be notice that photosensitivity of the fabricated CdS/CdTe heterostructures maintain on high level (fig. 15, curve 1, 2) in vide region of incident photons energy. The table like part of η(hv) curve confirm fabrication of the CdS/CdTe high quality heterojunction. The observed η(hv) curve decrease at hv≥2.3 eV is similar to specular transmission spectra of CdS film used for CdS/CdTe heterostructure fabrication. The full wide on half of the maximum (FWHM) of η(hv) spectra δ≈1.1–1.2 eV in our structures is more bigger then FWHM of Ox/CdTe heterostructure (Il'chuk at al., 2000) and indicate higher quality of fabricated structures compared to known.
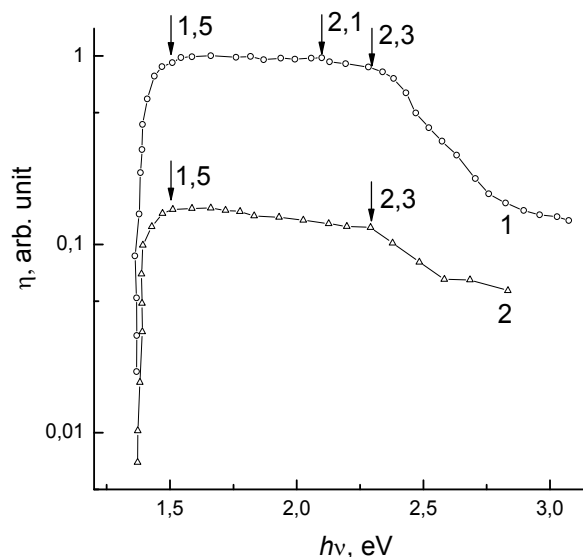
Fig. 15. Spectral distribution of the quantum efficiency of n-CdS/p-CdTe heterojunction at 300 K. Ilumination form CdS film side. The 1 and 2 curves coorespond to samples with diferet thickness of CdS film.

5. Conclusions

The II-VI binary CdS compound semiconductor thin films (30–100 nm) has been successfully deposited from aqueous solutions of $CdCl_2$, $CdSO_4$, CdI_2 salts using Chemical Surface Deposition and employing the direct heating of the substrate.

The linear dependence increase of film thickness on the deposition time was experimentally demonstrated for CSD $CdCl_2$ based films. For the two other salts of the film thickness dependence on deposition time is more complex, but has a character close to linear.

Established that for growth rate <15 nm/min. chemical deposition method allows to growth solid polycrystalline CdS films with 10^6-10^7 cm^{-2} surface macrodefects concentration.

It is proved that CdI_2 based CdS film composition was close to stoichiometric, compared to films deposited from solutions of two ather salts under identical conditions.

The possibility of n-CdS/p-CdTe high quality solar cell fabrication by CSD of CdS thin film is demonstrated. High value of CdS/CdTe heterojunction photoconversion, in region limited by CdS and CdTe band gaps, in our opinion was provided by CdS deposition method.

6. References

Adams, W.G. (1877). The action of light on selenium. *Proceedings of the Royal Society,* No.25, pp. 113–117

Adirovich, E.I., Yuabov, Y.M., & Yagudaev, G.R. (1969). CdTe thin film deposition on transparent substrates. *Fiz. Tekh. Poluprovodnikov,* Vol.3, No.1, pp. 81–85

Aguilar-Hernández, J., Sastre-Hernández, J., Ximello-Quiebras, N., Mendoza-Pérez, R., Vigil-Galán, O., Contreras-Puente, G., & Cárdenas-García, M. (2006). Influence of the S/Cd ratio on the luminescent properties of chemical bath deposited CdS films. *Solar Energy Materials & Solar Cells*, Vol.90, pp. 2305–2311

Archbold, M.D., Halliday, D.P., Durose, K., Hase, T.P.A., Smyth-Boyle, D., & Govender, K. (2005). Characterization of thin film cadmium sulfide grown using a modified chemical bath deposition process. *Conference record of the thirty-first ieee photovoltaic specialists conference*, 3-7 Januery 2005. – USA, 2005, pp.476–479

Aspects of Heterojunction Formation. *Thin Solid Films*, Vol.387, pp.141-146

Aven, M., & Prener, J.S. (Ed(s).). (1967). *Physics and Chemistry of II-VI Compounds*, North-Holland, Amsterdam

Basol, B., & Kapur, V. (1990). Deposition of $CuInSe_2$ films by a two-stage process utilizing E-beam evaporation. IEEE Trans. Electron Dev, No.37, pp. 418–421

Basol, B.M. (1990) Thin film CdTe solar cells-a review. *Proceedings of 21st IEEE Photovoltaic Specialists Conference*, pp. 588–594, Kissimimee, USA, 21–25 May, 1990

Basol, B.M., Kapur, V.K., Halani, A., & Leidholm, C. (1991). *Annual Report, Photovoltaic Subcontract Program FY*, pp. 50

Becquerel, E. (1839). Mémoire sur les effets électriques produits sous l'influence des rayons solaires. *Comptes Rendues*, No.9, pp. 561–567

Bode, D.E., Hass, G., & Thun, R.E. (1966). *Physics of Thin Films vol. 3*, Academic Press, New York

Bonnet, D., & Rabenhorst, H. (1972) 6 % efficient CdS/CdTe solat cell. *Proceedings of 9th IEEE Photovoltaic Specialists Conference*, pp. 129–131, Silver Spring, USA

Boudreau, R.A., & Rauh, R.D. (1983). Chemical bath deposition of thin film cadmium selenide for photoelectrochemical cells. *J. Elctrochem. Soc.*, No.130, pp. 513

Calixto, M.E., & Sebastian, P.J. (1999). A comparison of the properties of chemical vapor transport deposited CdS thin films using different precursors. *Solar Energy Materials & Solar Cells*, No.59, pp. 65-74

Chaisitsak, S., Yamada, A., & Konagai, M. (2002). Preferred Orientation Control of $Cu(In_{1-x}Ga_x)Se_2$ ($x \approx 0.28$) Thin Films and Its Influence on Solar Cell Characteristics. *Jpn. J. Appl. Phys*, Vol.41, pp. 1347-4065

Chapin, D.M., Fuller C.S., & Pearson, G.L. (1954). A new silicon p-n junction photocell for converting solar radiation into electrical power. *Journal of Applied Physics*, No.25, pp. 676–678

Chen, F., & et all. (2008). Effects of supersaturation on CdS film growth from dilute solutions on glass substrate in chemical bath deposition process. *Thin Solid Films*, Vol.516, pp. 2823–2828

Chopra, K. L., & Das, S. R. (1983). *Thin Film Solar Cells*, Plenum Press, New York

Contreras, M. A., Romero, M. J., To, B., & at all. (2002). Optimization of CBD CdS process in high-efficiency $Cu(In,Ga)Se_2$-based solar cells. *Thin Solid Films, Vol.* 403–404, pp. 204-211

Estela Calixto, M., Tufiño-Velázquez, M., Contreras-Puente, G., & at all. (2008). Study of chemical bath deposited CdS bi-layers and their performance in CdS/CdTe solar cell applications. Thin Solid Films, No.516, pp. 7004–7007

Estrada-Gasca, C., Alvarez-Garcia, G., & Nair, P.K. (1993). Theoretical analysis of the thermal performance of chemically deposited solar control coatings. *J. Phys. D*, No.26, pp. 1304–1309

Estrada-Gasca, C., Alvarez-Garcia, G., Cabanillas, R.E., & Nair, P.K. (1992). Theoretical efficiency of an all-glass tubular solar collector using a chemically deposited SnS-Cu_xS absorber inside the inner tube. *J. Phys. D*, No.25, pp. 1142–1147

Fahrenbruch, A.L., & Bube, H. (1983). *Fundamentals of Solar Cells*, Academic Press, London

Granath, K., Bodegard, M., & Stolt L. (2000). The effect of NaF on $Cu(In, Ga)Se_2$ thin film solar cells. *Sol. Energy Mater. Sol. Cells*, Vol. 60, pp. 279-293

Green, M. (1998). *Solar Cells – Operating Principles, Technology and System Applications*, The University of South Wales

Green, M.A., Keith, E., Hishikawa, Y., & Warta, W. (2011). Solar cell efficiency tables (Version 37). *Progress in Photovoltaics: Research and Application*, No.19, pp. 84–92

Grozdanov, I. (1994). A simple and low-cost technique for electroless deposition of chalcogenide thin films. *Semicond. Sci. Technol.*, No.9. pp. 1234–1241

Hamakawa, Y. (2002). Solar PV energy conversion and the 21st century's civilization. *Solar Energy Materials and Solar Cells*, Vol.74, No.4, pp. 13-22

Hashimoto, Y., Kohara, N., Negami, T., Nishitani, N., & Wada, T. (1998). Chemical bath deposition of Cds buffer layer for GIGS solar cells. *Sol. Energy Mater. Sol. Cells*, Vol.50, pp. 71-77

Hass, G., Francombe, M.H., & Vossen, J.L. (Eds.). (1982). *Physics of Thin Films vol. 12*, Academic Press, New York

Hernandez, E. (1998). Space-charge-limited current effects in p-type $CuIn_{0.8}Ga_{0.2}Se_2$/In Schottky diodes. *Cryst. Res. Technol*, No.33, pp. 285–289

Houser, O., & Beisalski, E. (1910). PbS film fabrication. *Chem-Ztg*, No.34, pp. 1079–1081

Huang, L., Nair, P.K., Nair, M.T.S., Zingaro, R.A., & Meyers, E.A. (1994). Interfacial diffusion of metal atoms during air annealing of chemically deposited ZnS-CuS and PbS-CuS thin films. *J. Electrochem. Soc*, No.141, pp. 2536

Il'chuk, G.A., Ivanov-Omski, V.I., Rud', V.Yu., Rud', Yu.V., Bekimbetov, R.N., & Ukrainets, N.A. (2000). Fabrication and photoelectric properties of Oxide/CdTe structures. Semiconductor structures, interfaces, and surfaces, Vol.34, No.9, pp. 1099-1102

Jager-Waldau, A. (2004). R&D roadmap for PV. *Thin Solid Films*, Vol.451-452, pp. 448-454

Jenny, D.A., Lofersky, J.J., & Rappaport, P. (1956). Photovoltaic Effect in GaAs p-n Junctions and Solar Energy Conversion. *Physical Review*, No.101, pp. 1208–1209

Kazmerski, L.L., White, F.R., & Morgan, G.K. (1976). Thin-film $CuInSe_2$/CdS heterojunction solar cells. *Applied Physics Letters*, No.29, pp. 268–270

Khallaf, H., Oladeji, I. O., Chai, G., & Chow, L. (2008). Characterization of CdS thin films grown by chemical bath deposition using four different cadmium sources. *Thin Solid Films*, No.516**,** pp. 7306

Kitaev, G., Mokrushin, S., & Uritskaya, A. (1965). *Kolloidn. Z.***,** No.27**,** pp. 51

Lamperg, G., & Mark, P. (1973). *Injection curents in solids*, Mir, Moscov

Landolt-Börnstein. Semiconductors; II-VI and I-VII Compounds; Semimagnetic Compounds. Landolt-Börnstein. – Berlin·Heidelberg·New York: Springer-Verlag, 1999. – Group III, Vol. 41b

Lokhande, C.D. (1991). Chemical deposition of metal chalcogenide thin films. *Mater. Chem. Phys*, No.27, pp. 1–43

Mickelsen, M.A., & Chen, W.S. (1980). High photocurrent polycrystalline thin-film $CdS/CuInSe_2$ solar cell. *Appl. Phys. Lett.*, No.36, pp. 371

Möller, H. J. (1993). *Semiconductors for Solar Cells*, Artech House, London

Mugdur, P.H., Chang, Y.-J., Han, S-.Y., & at all. (2007). A Comparison of Chemical Bath Deposition of CdS from a Batch Reactor and a Continuous-Flow Microreactor. *J. Electrochem. Soc.*, No.154, pp. D482–D488

Nair, P.K., Garcia, V.M., Comer-Daza, 0., & Nair, M.T.S. (2001). High thin-film yield achieved at small substrate separation in chemical bath deposition of semiconductor thin films. *Semicond. Sci. Tcchnol*, Vol.10, No.16, pp. 855–863

Nair, P.K., Huang, L., Nair, M.T.S., Hu, H., & at all. (1997). Formation of p-type Cu_3BiS_3 absorber thin films by annealing chemically deposited Bi_2S_3-CuS thin films. *J. Mater. Res.*, No.12, pp. 651–656

Nair, P.K., Nair, M.T.S., Fernandez, A., & Ocampo, M. (1989). Prospects of chemically deposited metal chalcogenide thin films for solar control applications. *J. Phys. D*, No.22, pp. 829–836

Nakada, T., & Kunioka, A. (1999). Direct evidence of Cd diffusion into Cu.In,Ga.Se2 thin films during chemical-bath deposition process of CdS films. *Appl. Phys. Lett*, Vol.**74**, pp. 2444-2446

Oladeji, I.0., & Chow, L. (1997). Optimization of Chemical Bath Deposited Cadmium Sulfide Thin Films. *J. Electrochem. Soc.*, Vol.144, No.7, pp. 2342-2346

Ortega-Borges, R., & Lincot, D. (1993). Mechanism of chemical bath deposition of cadmium sulfide thin films in the ammonia-thiourea system. *J. Electrochem. Soc.*, No.140**,** pp. 3464-3473

Palatnik, L.S., & Sorokin, V.K. (1978). *Materialovedenie v mikroelektronike*, Energia, Moscov

Qiu, S. N., Lam, W. W., Qiu, C. X., & Shih, I. (1997). ZnO/CdS/CuInSe2 photovoltaic cells fabricated using chemical bath deposited CdS buffer layer. *Appl. Surf. Sci.*, Vol.113/114, pp. 764-767

Rau, U., & Scmidt, M. (2001). Electronic Properties of ZnO/CdS/Cu(In, Ga)Se2 Solar Cells -

Reddy, T.A., Gordon, J.M., &. de Silva, I.P.D. (1987). Mira: A one-repetitive day method for predicting the long-term performance of solar energy systems. *Sol. Energy*, No.39, pp. 123–133

Reynolds, D.C., Leies, G., Antes, L.L., & Marburger, R.E. (1954). Photovoltaic effect in cadmium sulfide. *Physical Review*, No.96, pp. 533–534

Rincon, M.E., Sanchez, M., Olea, A., Ayala, I., & Nair, P.K. (1998). Photoelectrochemical behavior of thin CdS, coupled CdS/CdSe semiconductor thin films. *Solar Energy Mater. & Solar Cells*, No.52, pp. 399–411

Romeo, N., Bosio, A., & Canevari, V. (2003). The role of CdS preparation method in the performance of CdTe/CdS thin film solar cell. *3rd World Conference on Photovoltaic Energy Conversion*, 11–18 May 2003, Osaka, Japan, pp. 469–470

Romeo, N., Bosio, A., Tedeschi, R., & Canevari, V. (2000). Back contacts to CSS CdS/CdTe solar cells and stability of performances. *Thin Solid Films*, No.361-362, pp. 327–329

Rothwarf, A. (1982). *Proc. 16th IEEE Photovoltaic Specialists Conf.*, San Diego, 1982, CA, IEEE, New York, pp. 791

Savadogo, O., & Mandal, K.C. (1993). Low-cost technique for preparing n-Sb2S3/p-Si heterojunction solar cells. Appl. Phys. Lett., No.63, pp. 228

Savadogo, O., & Mandal, K.C. (1994). Low cost schottky barrier solar cells fabricated on CdSe and Sb2S3 films chemically deposited with silicotungstic acid. *J. Electrochem. Soc.*, No.141, pp. 2871

Soubane, D., Ihlal, A., & Nouet, G., (2007). *M. J. Condensed Matter*, Vol.9**,** pp. 32-35

Stevenson, R. (2008). First Solar: Quest for $1 Watt. *Spectrum*, Vol.45, No.8, pp. 22–33

Svechnikov, S.V., & Kaganovich, E.B. (1980). CdSxSe1−x photosensitive films: Preparation, properties and use for photodetectors in optoelectronics. *Thin Solid Films*, No. 66, pp. 41–54

Sze, S. M. (1981). *Physics of semiconductor devices (2nd edn.)*, John Wiley & Sons Inc., New York

Tiwari, S., & Tiwari, S. (2006). Development of CdS based stable thin film photo electrochemical solar cells. *Solar Energy Materials & Solar Cells*, Vol.90, pp. 1621–1628

Tuttle T.R., Contreras M.A., et al. (1995). *Proc. SPIE*, Vol.2531, SPIE, Bellingham, pp. 194

Vossen J.L., & Kern W. (1978). *Thin Film Processes*, Academic Press, New York

Wagner, S. (1975). Epitaxy in solar cells. *Journal of Crystal Growth*, No.31, pp. 113–121

Wolf, R. (Ed). (1975). *Cadmium Sulphede Solar Cells.* Applied Solid State Sciences, vol. 5, Nev York

Development of Flexible Cu(In,Ga)Se$_2$ Thin Film Solar Cell by Lift-Off Process

Yasuhiro Abe, Takashi Minemoto and Hideyuki Takakura
Ritsumeikan University
Japan

1. Introduction

Clean energy resources as an alternative to fossil fuels has been required. Photovoltaics is the most promising among renewable energy technologies. On the other hand, the cost of the electrical energy generated by the solar cells was higher than that generated by fossil fuels. The cost reduction of the solar cell is therefore required.

Since high-conversion efficiencies have been demonstrated for solar cells using GaAs substrates in 1977 (Kamath et al., 1977; Woodall et al., 1977), a critical problem is how to reduce power generation cost. The characters required to solar cells strongly depend on its applications. In particular, thin film solar cells are promising for terrestrial applications, because thin film solar cells are more advantageous than bulk type solar cells in terms of consumption of raw materials. Konagai et al. fabricated the thin film solar cells on a single crystalline GaAs substrate by the liquid phase epitaxy mehtod, and focused on the reuse of GaAs substrates by detaching these thin film solar cells from the GaAs substrates (Konagai et al., 1978). Konagai et al. named this separation technique the Peeled Film Technology (PFT). This is the invention of the lift-off method in solar cell development. A specific explanation of the PFT is as follows. An Al$_{1-x}$Ga$_x$As layer was introduced between the thin film solar cell and the GaAs substrate as a release layer. The thin film solar cell was separated from the GaAs substrate by etching the Al$_{1-x}$Ga$_x$As layer by the HF solution, because Al$_{1-x}$Ga$_x$As was readily dissolved by the HF solution compared to GaAs. Since a chemical technique was mainly used for the peeling, this method is defined as a chemical lift-off process. Recently, this has been researched as the epitaxial lift-off (ELO) method (Geelen et al., 1997; Schemer et al., 2000, 2005a; Voncken et al., 2002; Yablonovitch et al., 1987).

On the other hand, the cleavage of lateral epitaxial films for transfer (CLEFT) process, where the thin film was mechanically peeled, was developed as a transfer method of a single crystalline GaAs thin film (McClelland et al., 1980). A specific explanation of the CLEFT process is as follows. A photoresist was applied to a surface of a GaAs substrate. The photoresist was patterned with equally-spaced stripe openings by standard photolithographic techniques. Next, a GaAs layer was grown on this patterned substrate surface. In this case, a GaAs layer was grown on only the openings of the photoresist. The lateral growth of a GaAs layer occurs during the GaAs deposition. A single crystalline GaAs layer is therefore formed on the photoresist. Alternative substrate was bonded onto this

surface with epoxy glue. The single crystalline thin film was transferred to the alternative substrate by applying tensile strain. The CLEFT process is theorefore defined as a mechanical lift-off process.

Unfortunately, the conversion efficiency of the GaAs thin film solar cell using the lift-off process was lower than that of the GaAs bulk solar cell (Schermer et al., 2006). Recently, comparable conversion efficiencies have been demonstrated (Bauhuis et al., 2009).

On the other hand, the energy:weight ratio of the photovoltaic module is a very important index for space applications. Integration of high-efficiency III-V solar cells with light weight substrates is required. Schermer et al. developed high-efficiency III-V solar cells with light-weight by the ELO process using the GaAs substrate (Schermer et al., 2005b).

In addition, the lift-off process was applied to reuse Si substrates (Bergmann et al., 2002; Brendel, 2001). Moreover, the lift-off process was applied to fabricate flexible solar cells in the developments of II-VI and I-III-VI$_2$ semiconductor thin film solar cells (Marrón et al., 2005; Minemoto et al., 2010; Romeo et al., 2006; Tiwari et al., 1999).

Here, we focus on advantages of the lift-off process in fabrication of flexible Cu(In,Ga)Se$_2$ (CIGS) thin film solar cells. For example, for the fabrication process where CIGS layers were directly grown on flexible substrates, Ti foils (Hartmann et al., 2000; Herz et al., 2003; Ishizuka et al., 2009a; Kapur et al., 2002; Kessler et al., 2005; Yagioka & Nakada, 2009), Cu steel sheets (Herz et al., 2003), Mo foils (Kapur et al., 2002, 2003), stainless steel sheets (Britt et al., 2008; Gedhill et al., 2011; Hashimoto et al., 2003 ; Kessler et al., 2005; Khelifi et al., 2010; Pinarbasi et al., 2010; Satoh et al., 2000, 2003; Shi et al., 2009; Wuerz et al., 2009), Al foils (Brémaud et al., 2007), Fe/Ni alloy foils (Hartmann et al., 2000), ZrO$_2$ sheets (Ishizuka et al., 2008a, 2008b, 2009b, 2010), and polyimide (PI) films (Brémaud et al., 2005; Caballero et al., 2009; Hartmann et al., 2000; Ishizuka et al., 2008c; Kapur et al., 2003; Kessler et al., 2005; Rudmann et al., 2005; Zachmann et al., 2009;), are used as flexible substrates. Since these materials do not include Na, other processes to introduce Na are required (Caballero et al., 2009; Ishizuka et al., 2008a; Keyes et al., 1997). Since the thermal tolerance temperature of a PI film is ~450°C, the low temperature growth of a CIGS layer is required. The first of the advantages of the lift-off process is to enable to use a high quality CIGS layer grown on a conventional Mo/soda-lime glass (SLG) substrate in the flexible solar cell fabrication. Consequently, the low temperature growth technology for high quality CIGS layer formation and novel processes for a Na source are not required. The second is to enable to use low thermal tolerance films as the flexible substrate of a CIGS solar cell, because in the CIGS solar cell fabrication process, the highest temperature process is the growth of a CIGS layer and the process temperature after the growth of a CIGS layer is less than 100°C.

2. Experimental

2.1 Flexible Cu(In,Ga)Se$_2$ solar cell fabrication procedure

A schematic illustration of the fabrication procedure of our flexible CIGS solar cell using the lift-off process is shown in Fig. 1 (Minemoto et al., 2010). A 0.8-μm-thick Mo layer was deposited on an SLG substrate without intentional substrate heating by the radio frequency (RF) magnetron sputtering method. A 2.5-μm-thick CIGS layer was deposited on the Mo/SLG substrate by the three-stage deposition process at the highest substrate temperature of approximately 550°C (Contreras et al., 1994a; Negami et al., 2002). From energy dispersive x-ray spectrometry measurements, the Cu, In, Ga, and Se composition ratios of this CIGS layer were approxymately 23, 18, 8, and 51%, respectively. The

[Cu]/[Ga+In] and [Ga]/[Ga+In] ratios of the CIGS layer were therefore calclated to be ~0.88 and ~0.31, respectively. After CIGS surface cleaning by a KCN solution, a 0.2-μm-thick Au layer was deposited on the CIGS surface by a resistive evaporation method as a back electrode. The samples were annealed for 30 min at 250˚C in N_2 ambient. Flexible films were bonded onto support SLG substrates with a silicone adhesion bond for preparation of the alternative substrates. These alternative substrates were also bonded onto the Au/CIGS/Mo/SLG structure with conductive epoxy glue. To dry the conductive epoxy glue, the samples were annealed on a hot plate at 100˚C for 10 min in the atmosphere. Then, the alternative-sub./epoxy/Au/CIGS stacked structures were detached from the primary Mo/SLG substrates by applying tensile strain. In this detachment, the CIGS layer was transferred to the alternative substrate side (Marrón et al., 2005). The lift-off flexible CIGS solar cells were fabricated using this peeled CIGS layer. After cleaning of the CIGS rear surface by a KCN solution, a 0.1-μm-thick CdS layer was deposited on the CIGS rear surface by the chemical bath deposition method. 0.1-μm-thick i-ZnO and 0.1-μm-thick In_2O_3:Sn layers were deposited by the RF magnetron sputtering method. Al/NiCr grids were formed. Finally, the flexible CIGS solar cells using the lift-off process were completed by detaching the flexible films from the support SLG substrates. For comparison, we also prepared a standard solar cell where the lift-off process was not carried out (the Al/NiCr/In_2O_3:Sn/ZnO/CdS/CIGS/Mo/SLG structure). The properties of the films used in this study are summarized in Table 1. Figure 2 shows a photograph of the flexible solar cells using the PI film.

Material	PI	PTFE	Polyester
Thermal tolerance temperature (˚C)	450	260	120
Thickness (μm)	55	120	25

Table 1. Properties of PI, polytetrafluoroethylene (PTFE) and polyester films used in this study are summarized.

2.2 Characterization methods

Current density-voltage (*J-V*) measurements were performed under standard air mass 1.5 global conditions (100 mW/cm²) at 25˚C. External quantum efficiency (EQE) measurements of the AC mode were performed at 25˚C under white light bias (~0.3 sun) conditions. The laser-beam-induced current (LBIC) method using the laser diode (λ: 783 nm, laser power: 0.3 mW) was performed to investigate a spatial distribution of an EQE (Minemoto et al., 2005). In LBIC measurements, a nominal spot size is less than 50 μm and a scan step is 53 μm. The surfaces of the fabricated flexible solar cells were observed with an optical microscope. The *J-V*, EQE, and LBIC measurements were performed after light soaking.

3. Results and discussion

3.1 Characterization of flexible Cu(In,Ga)Se₂ solar cells fabricated using lift-off process

The *J-V* characteristics of the fabricated flexible solar cells are shown in Fig. 3. For comparison, the *J-V* characteristic of the standard solar cell is also shown. Solar cell parameters such as the short-circuit current density (J_{sc}), the open-circuit voltage (V_{oc}), the
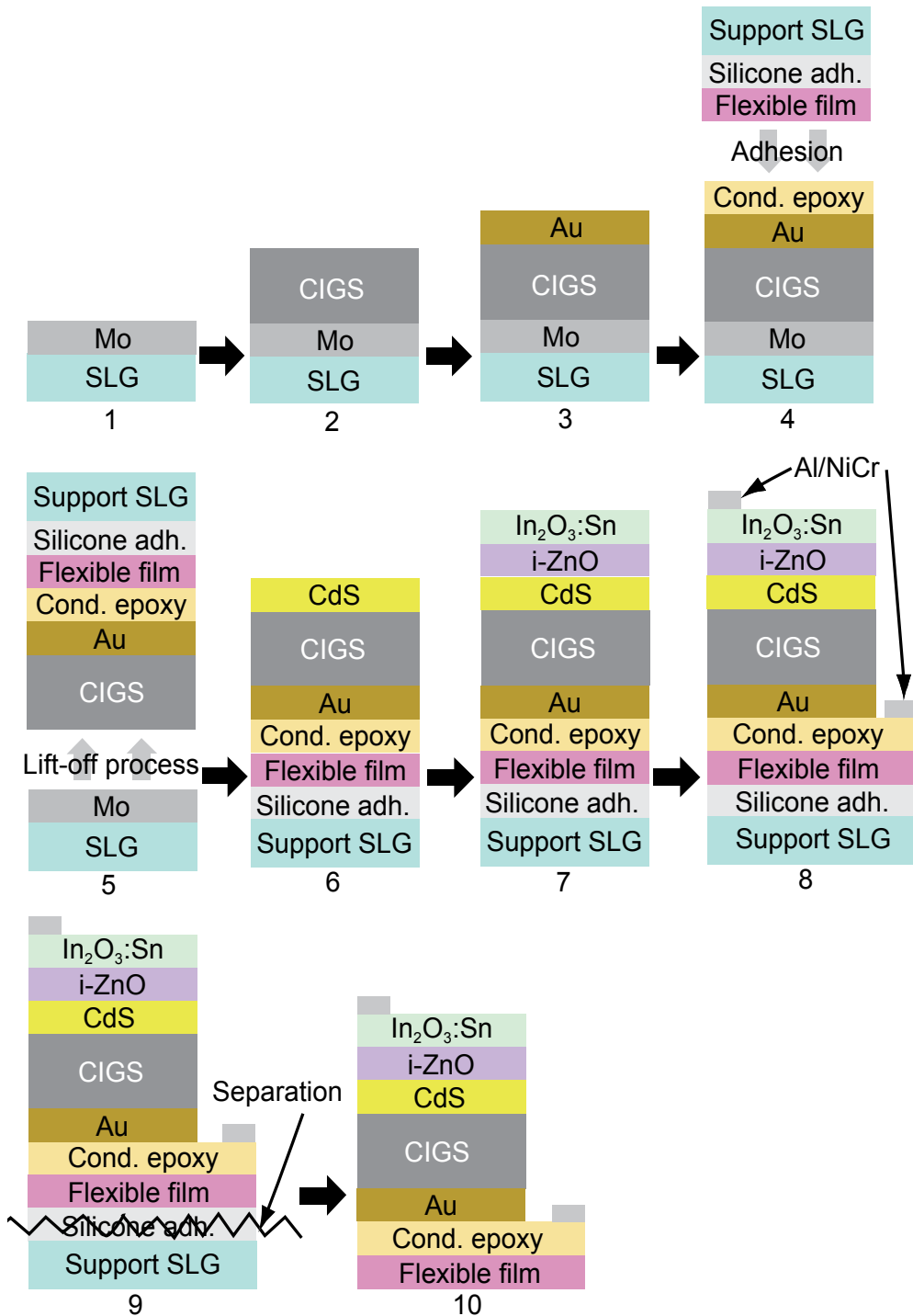
Fig. 1. Schematic illustration of fabrication procedure of flexible CIGS solar cell using lift-off process.
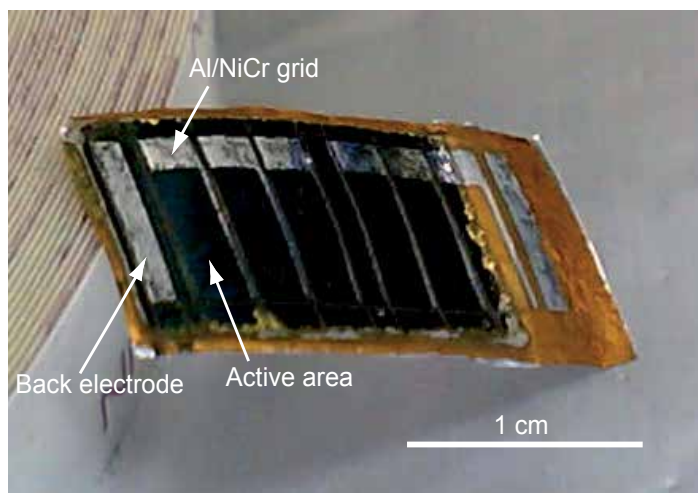
Fig. 2. Photograph of flexible CIGS solar cells using PI film.
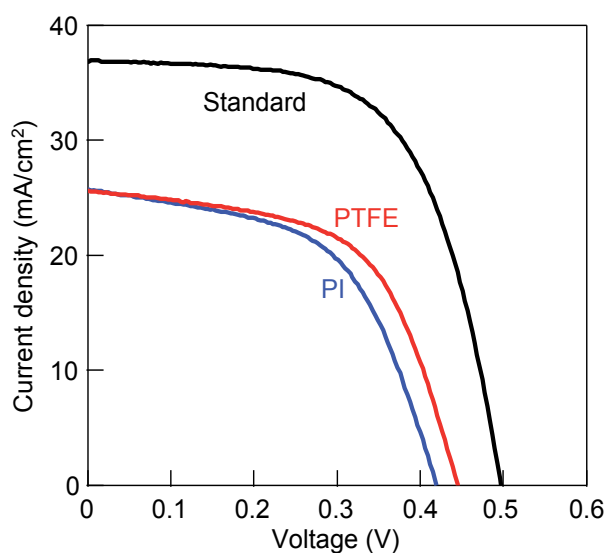
Fig. 3. Photo *J-V* curves of flexible solar cells using PTFE (red) and PI (blue) films. Photo *J-V* curve of standard solar cell without lift-off process (brack) is also shown for comparison.

Sample structure	*Eff.* (%)	J_{sc} (mA/cm²)	V_{oc} (V)	*FF* (%)
PI flexible	5.9	25.7	0.420	54.9
PTFE flexible	6.6	25.6	0.445	57.9
Standard	11.4	36.9	0.497	62.4

Table 2. Solar cell parameters obtain from flexible solar cells using PI and PTFE films. Solar cell parameters of standard solar cell are also shown for comparison.

conversion efficiency (*Eff.*), and the fill factor (*FF*) are summarized in Table 2. The conversion efficiencies of the flexible solar cells are an approximately half conversion efficiency of the standard solar cell. EQE spectra of these solar cells are shown in Fig. 4. EQEs of the flexible solar cells remarkably decrease in the long wavelength region from 700 to 1200 nm compared to the standard solar cell. We discuss this cause as below.
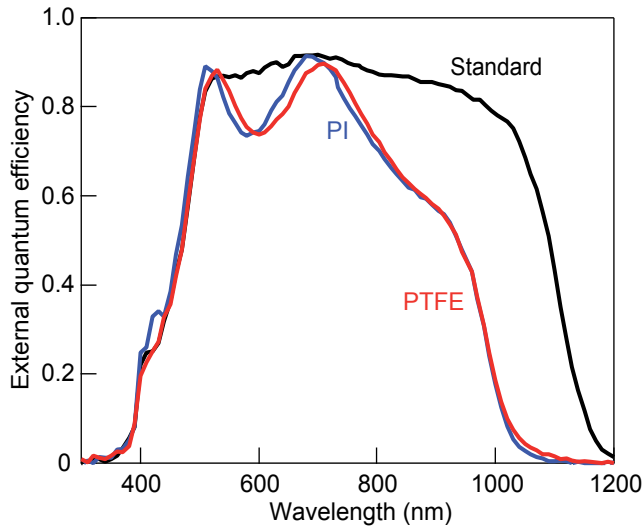
Fig. 4. EQE spectra of flexible solar cells using PTFE (red) and PI films (blue). EQE spectrum of standard solar cell without lift-off process (black) is also shown for comparison. EQE spectra of flexible solar cells are similar irrespective of substrate materials.

As shown in Fig. 5(a), the band gap profile of the standard solar cell consists of the graded band gap structure because of the three-stage deposition process. The diffusion length of electrons generated by the long wavelength light near the back electrode is improved due to the quasi-electric field in which the CIGS layer forms (Contreras et al., 1994b). The graded band gap structure is therefore beneficial for collecting the photogenerated carriers. On the other hand, as shown in Fig. 5(b), the band gap profile of the CIGS layer is inverted due to
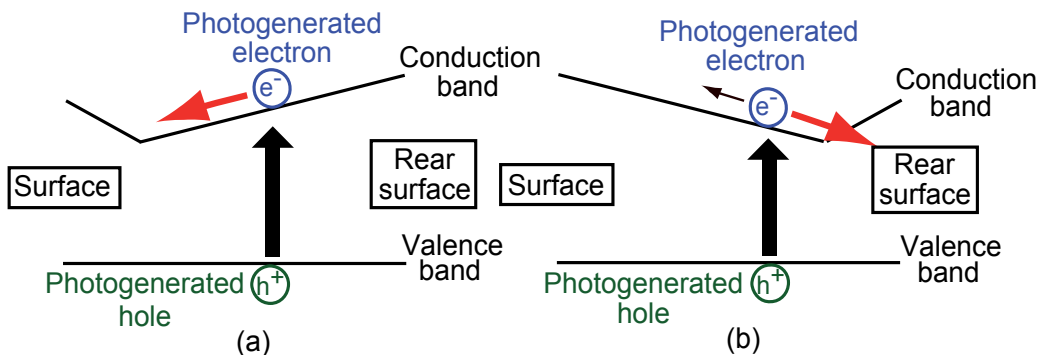
Fig. 5. Schematic illustrations of band gap profiles of CIGS layers. CIGS absorber layers with (a) double geraded band gap and (b) inverted double graded band gap structures are shown.

the lift-off process for the flexible solar cells. We speculate that the band gap profile of the inverted graded band gap structure is not beneficial for collecting the photogenerated carriers by long wavelength light. We conclude that the EQE reductions observed for the flexible solar cells are attributed to the influence of the inverted graded band gap structure.

We describe an interesting point of our flexible solar cells as below. Different materials with different thermal tolerance temperatures are used as the flexible substrates of these flexible solar cells, as shown in Table 1. These flexible solar cells, however, show the similar characteristics irrespective of the flexible film materials from Fig. 3 and Fig. 4.

LBIC and optical microscope images of the flexible solar cell using the PTFE film are shown in Figs. 6(a) and 6(b), respectively. There is a low EQE region on the lower side of the solar cell from Fig. 6(a). This low EQE region corresponds approximately to the flexurelike region from a comparison between Figs. 6(a) and 6(b). This result therefore suggests that this flexure cause reduction of an EQE. LBIC and optical microscope images of the standard solar cell are shown in Figs. 6(c) and 6(d), respectively. In contrast, the LBIC and optical microscope images are uniform for the standard solar cell.
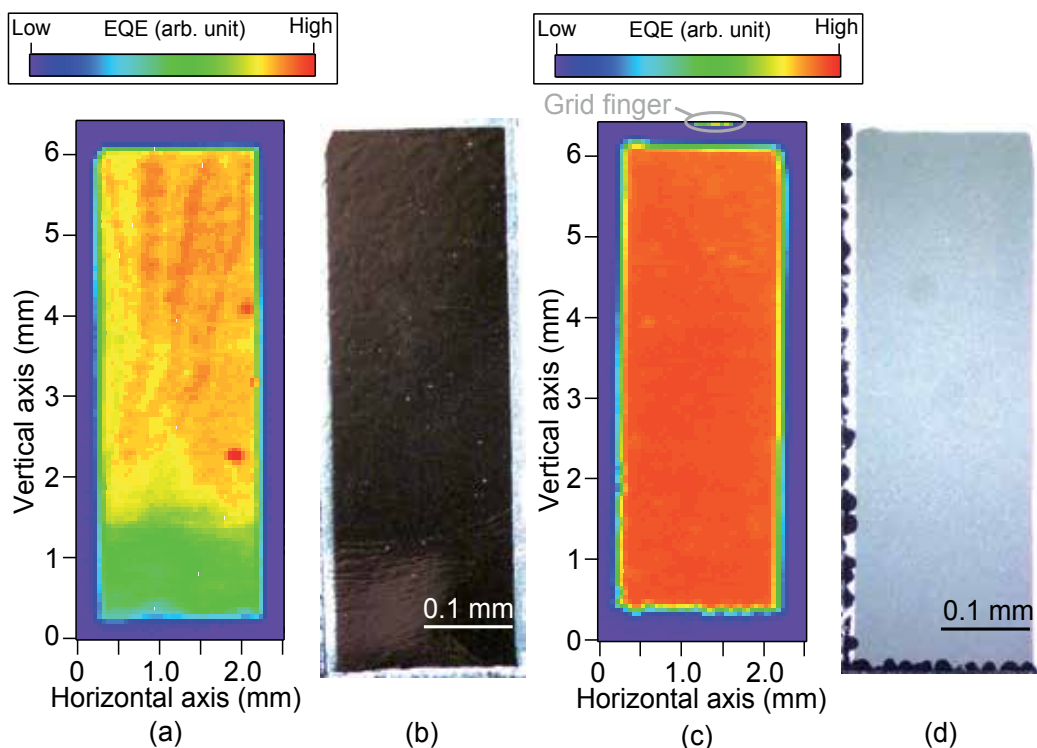
Fig. 6. (a) LBIC and (b) optical microscope images of flexible solar cell using PI film. (c) LBIC and (d) optical microscope images of standard solar cell. Indicators of EQE intensity are shown next to LBIC images.
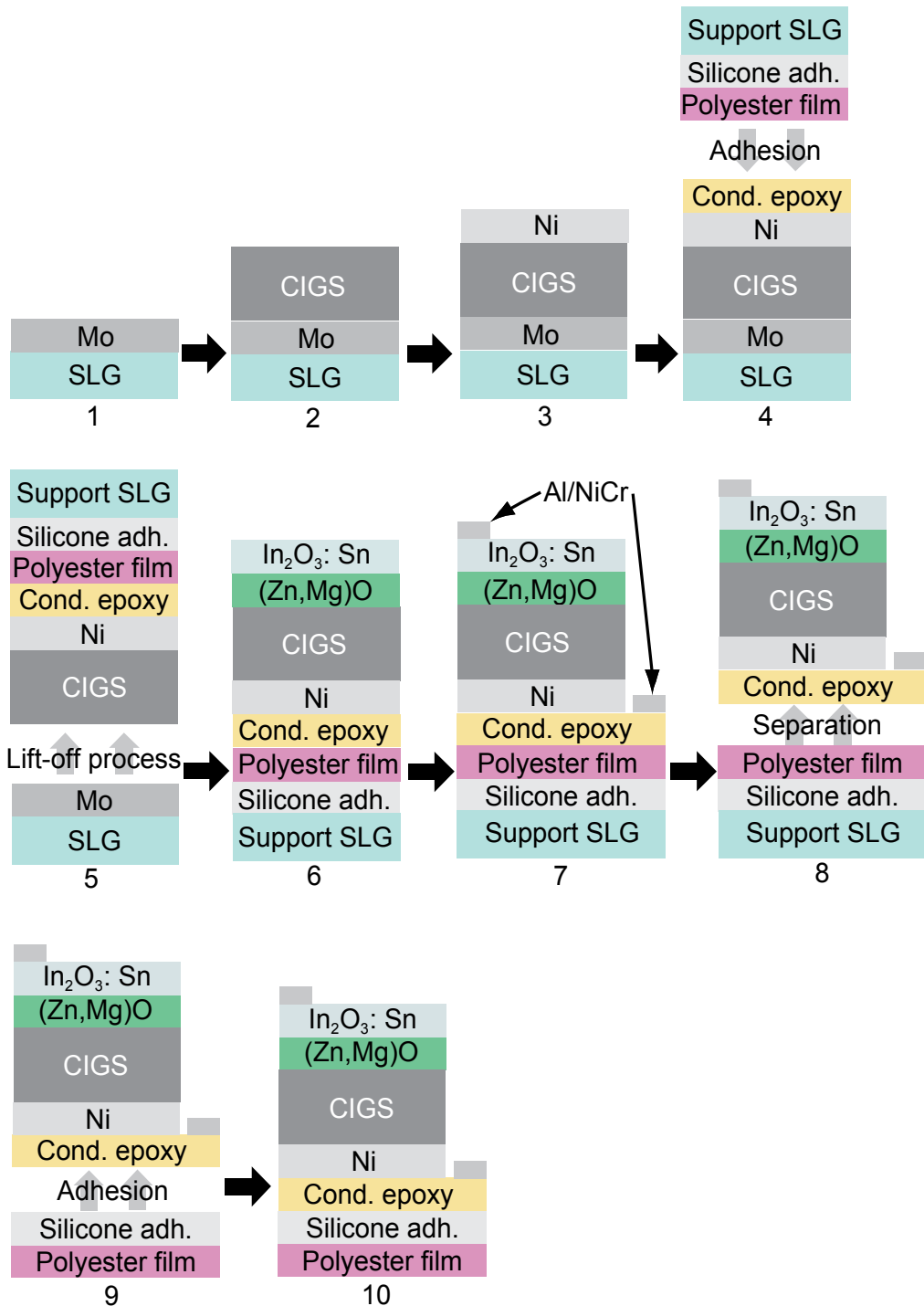
Fig. 7. Schematic illustration of fabrication procedure of flexible CIGS solar cell using $(Zn_{0.83},Mg_{0.17})O$ window layer and lift-off process.

3.2 Development of Cd-free flexible Cu(In,Ga)Se₂ solar cells

We developed a new Cd-free flexible CIGS solar cell using a (Zn,Mg)O window layer. The fabrication procedure is shown in Fig. 7. This process is basically similar to Fig. 1. We deposited a 0.1-μm-thick $(Zn_{0.83},Mg_{0.17})O$ window layer in stead of the ZnO window/CdS buffer layers. The RF magnetron cosputtering method using ZnO and MgO targets was used as the deposition technique (Minemoto et al., 2000, 2001). We also deposited a 0.2-μm-thick Ni layer by the resistive evaporation method as the back electrode in stead of the Au layer. In this subsection, a 55-μm-thick polyester film was used as a flexible substrate. Interestingly, when the flexible solar cell using the polyester film was separated from the support SLG substrate, the detachment occurred not at the support SLG/polyester interface but at the polyester/epoxy interface due to the weaker adhesion at the polyester/epoxy interface. After the substrate-free structure was once, the polyester film was therefore bonded onto the rear surface of the solar cell with a silicone adhesion bond. The photograph of the flexible solar cells fabricated via the above procedure is shown in Fig. 8. We also prepared not only the flexible solar cells using the conventional ZnO window/CdS buffer layers but also the solar cells without the lift-off process for comparison.
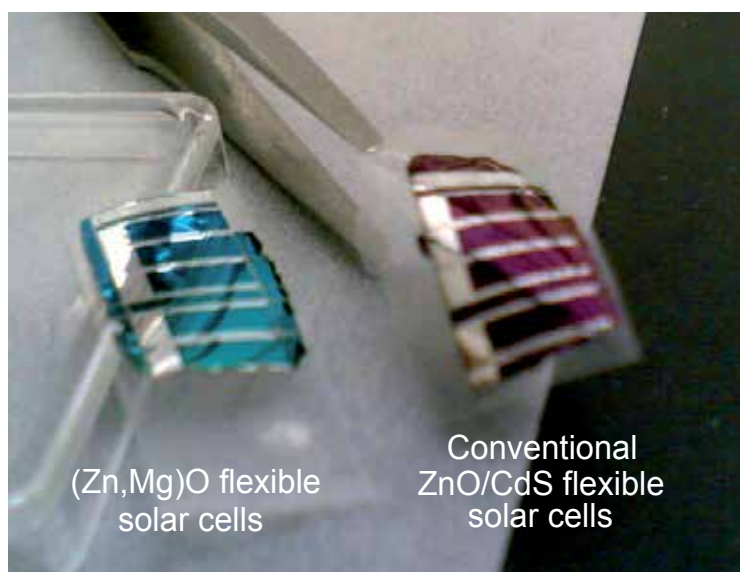
Fig. 8. Photograph of flexible solar cells using polyester film. Left solar cells are Cd-free solar cells using (Zn,Mg)O window layer. Right solar cells consist of conventional ZnO window/CdS buffer layers structure.

The *J-V* characteristics of the flexible solar cells are shown in Fig. 9. The results of the standard solar cells without the lift-off process are also shown in Fig. 9. Solar cell parameters obtained from the *J-V* characteristics are summarized in Table 3. All parameters of the ZnO/CdS solar cell is higher than those of the (Zn,Mg)O solar cell for the standard solar cells. On the other hand, although there are the differences in the window layer/ buffer layer structures for the flexible solar cells, these flexible solar cells show the similar properties.
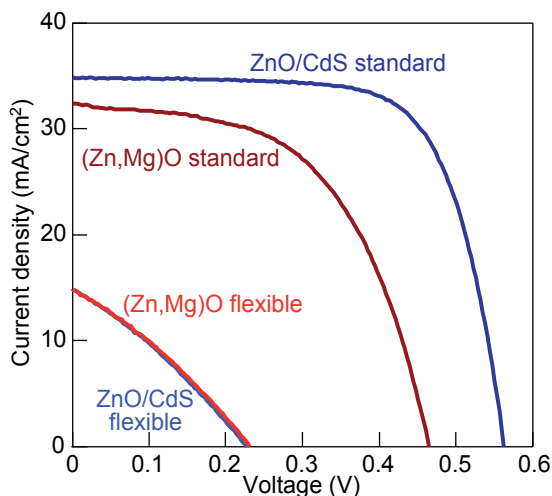
Fig. 9. Photo *J-V* curves of flexible solar cells using (Zn,Mg)O window layer and conventional ZnO window/CdS buffer layers. Photo *J-V* curves of standard solar cells without lift-off process are also shown for comparison.

EQE spectra of these solar cells are shown in Fig. 9. EQEs of the (Zn,Mg)O standard solar cell are higher than those of the ZnO/CdS standard solar cell in the region from 300 to 480 nm, because the band gap of $(Zn_{0.83}, Mg_{0.17})O$ is higher than those of CdS and ZnO (Minemoto et al., 2000). These high EQEs in this region is therefore attributed to a low transmission loss of the short wavelength light. Moreover, the tendency of this result is also observed for the flexible solar cells. We found that the (Zn,Mg)O window layer structure was effective for reducing a transmission loss of the short wavelength light even in our flexible solar cells.

Sample structure	*Eff.* (%)	J_{sc} (mA/cm^2)	V_{oc} (V)	*FF* (%)
(Zn,Mg)O flexible	1.0	14.8	0.231	30.5
ZnO/CdS flexible	1.0	14.8	0.227	30.2
(Zn,Mg)O standard	8.3	32.4	0.465	54.9
ZnO/CdS standard	13.7	34.9	0.562	70.0

Table 3. Summary of solar cell parameters obtained from flexible solar cells using (Zn,Mg)O window layer and conventional ZnO window/CdS buffer layers. For comparison, solar cell parametaers otained from standard solar cells using (Zn,Mg)O window layer and ZnO window/CdS buffer layers are also summarized.
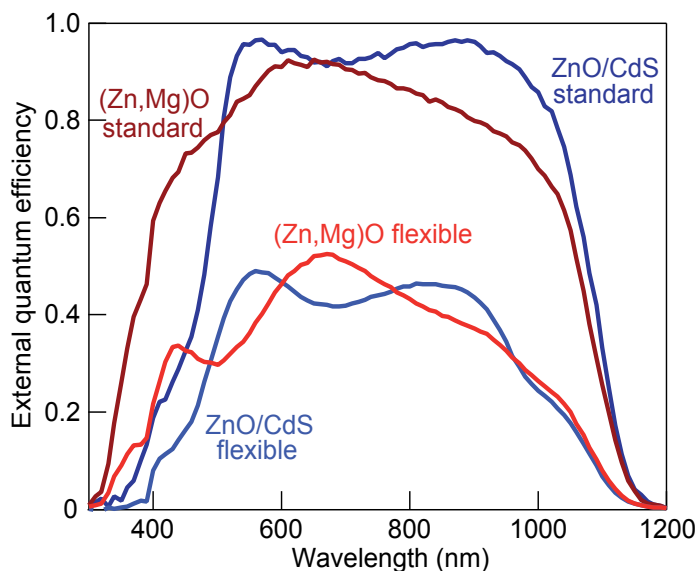
Fig. 10. EQE spectra of flexible solar cells using (Zn,Mg)O window layer (red) and conventional ZnO window/CdS buffer layers (blue). EQE spectra of standard solar cells using (Zn,Mg)O window layer (dark red) and ZnO window/CdS buffer layers (dark blue) are also shown for comparison.

Here, we discuss why these flexible solar cells showed the similar solar cell parameters. In this subsection, we used Ni in stead of Au as a back electrode material. In subsection 3.1, the ZnO/CdS flexible solar cells with the Au back electrode showed a conversion efficiency of ~6%. We think that the Ni back electrode may limit performance of these solar cells. We therefore speculate that the Ni atoms, which diffused into the CIGS layer from the back side due to the low temperature annealing, behave as recombination centers for electrons.

4. Conclusion

After we described the review of the lift-off process, we also described the advantages of the lift-off process in the flexible CIGS solar cell fabrication. We developed the fabrication procedure of the flexible CIGS solar cells using the lift-off process. The characteristics of the flexible solar cells were shown compared to the standard solar cell. Although the conversion efficiencies of the flexible solar cells using the lift-off process are an approximately half conversion efficiency of the standard solar cell, the flexible solar cells showed the similar characteristics irrespective of the substrate materials. Moreover, we attempted the concept of a Cd-free solar cell. We found that the choice of back electrode materials is a crucial problem rather than the window layer/buffer layer structure. We expect that the lift-off process further advances through our results.

5. Acknowledgment

6. References

Kamath, G. S.; Ewan, J. & Knechtli R. C. (1977). Large-Area High-Efficiency (AlGa)As-GaAs Solar Cells. *IEEE Transactions on Electron Devices*, Vol. ED-24, No. 4, (April 1977), pp. 473-475, ISSN 0018-9383

Woodall, J. M. & Hovel, H. J. (1977). An isothermal etchback-regrowth method for high efficiency $Ga_{1-x}Al_xAs$-GaAs solar cells. *Applied Physics Letters*, Vol. 30, No. 9, (February 1977), pp. 492-494, ISSN 0003-6951

Konagai, M.; Sugimoto, M. & Takahashi, K. (1978). HIGH EFFICIENCY GaAs THIN FILM SOLAR CELLS BY PEELED FILM TECHNOLOGY. *Journal of Crystal Growth*, Vol. 45, (December 1978), pp. 277-280, ISSN 0022-0248

Geelen, A. V.; Hageman, P. R. Bauhuis, G. J. Rijsingen, P. C. V. Schmidt, P. & Giling, L. J. (1997). Epitaxial life-off GaAs solar cell from a reusable GaAs substrate. *Material Science and Engineering B*, Vol. 45, (March 1997), pp. 162-171, ISSN 0921-5107

Schermer, J. J.; Bauhuis, G. J. Mulder, P. Meulemeesters, W. J. Haverkamp, E. Voncken, M. M. A. J. & Larsen, P. K. (2000). High rate epitaxial lift-off on InGaP films from GaAs substrate. *Applied Physics Letters*, Vol. 76, No. 15, (April 2000), pp. 2131-2133, ISSN 0003-6951

Schermer, J. J.; Mulder, P. Bauhuis, G. J. Voncken, M. M. A. J. Deelen, J. V. Haverkamp, E. & Larsen, P. K. (2005a). Epitaxial Lift-Off for large area thin film III/V devices. *Physica Status Solidi A*, Vol. 202, (Febrary 2005), pp. 501-508, ISSN 1862-6300

Voncken, M. M. A. J.; Schermer, J. J. Maduro, G. Bauhuis, G. J. Mulder, P. & Larsen. P. K. (2002). Influence of radius of curvature on the lateral etch rate of the weight induced epitaxial lift-off process. *Materials Science and Engineering B*, Vol. 95, (September 2002) pp. 242-248, ISSN 0921-5107

Yablonovitch, E.; Gmitter, T. Harbison, J. P. & Bhant, R. (1987). Extreme selectivity in the lift-off epitaxial GaAs films. *Applied Physics Letters*, (December 1987), pp. 2222-2224, ISSN 0003-6951

McClelland, R. W.; Bozler, C. O. & Fan, J. C. C. (1980). A technique for producing epitaxial films on reusable substrate. *Applied Physics Letters*, Vol. 37, No. 6, (September 1980), pp. 560-562, ISSN 0003-6951

Schermer, J. J.; Bauhuis, G. J. Mulder, P. Haverkamp, E. J. Deelen, J. V. Niftrik, A. T. J. V. & Larsen, P. K. (2006). Photon confinement in high-efficiency thin-film III-V solar cells obtained by epitaxial lift-off. *Thin Solid Films*, Vol. 511-512, (January 2006), pp. 645-653, ISSN 0040-6090

Bauhuis, G. J.; Mulder, P. Haverkamp, E. J. Huijben, J. C. C. M. & Schermer, J. J. 26.1% thin-film GaAs solar cell using epitaxial lift-off. *Solar Energy Materials and Solar Cells*, Vol. 93, (May 2009), pp. 1488-1491, ISSN 0927-0248

Schermer, J. J.; Mulder, P. Bauhuis, G. J. Larsen, P. K. Oomen G. & Bongers E. (2005b) Thin-film GaAs Epitaxial Lift-off Solar Cells for Space Applications. *Progress in Photovoltaics: Research and Applications*, Vol. 13, (April 2005), pp. 587-596, ISSN 1062-7995

Bergmann, R. B.; Berge, C. Rinke, T. J. Schmidt, J. & Werner, J. H. (2002). Advances in monocrystalline Si thin film solar cells by layer transfer. *Solar Energy Materials and Solar Cells*, Vol. 74, (October 2002), pp. 213-218, ISSN 0927-0248

Brendel, R. (2001). Review of Layer Transfer Processes for Crystalline Thin-Film Silicon Solar Cells. *Japanese Journal of Applied Physics*, Vol. 40, No. 7, (July 2001), pp. 4431-4439, ISSN 0021-4922

Marrón, D. F.; Meeder, A. Sadewasser, S. Würz, R. Kaufmann, C. A. Glatzel, T. Schedel-Niedrig, T. & Lux-Steiner, M. C. Lift-off process and rear-side characterization of CuGaSe₂ chalcopyrite thin films and solar cells. *Journal of Applied Physics*, Vol. 97, (April 2005), pp. 094915-1-094915-7, ISSN 0021-8979

Minemoto, T.; Abe, Y. Anegawa, T. Osada, S. & Takakura, H. (2010). Lift-Off Process for Flexible Cu(In,Ga)Se₂ Solar Cells. *Japanese Journal of Applied Physics*, Vol. 49, No. 4, (April 2010), pp. 04DP06-1-04DP06-3, ISSN 0021-4922

Romeo, A.; Khrypunov, G. Kurdesau, F. Arnold, M. Bätzner, D. L. Zogg, H. & Tiwari, A. N. High-efficiency flexible CdTe solar cells on polymer substrates. *Solar Energy Materials and Solar Cells*, Vol. 90, (November 2006), pp. 3407-3415, ISSN 0927-0248

Tiwari, A. N.; Krejci, M. Haung, F.-J. & Zogg, H. (1999). 12.8% Efficiency Cu(In,Ga)Se₂ Solar Cell on a Flexible Polymer Sheet. *Progress in Photovoltaics: Research and Applications*, Vol. 7, (October 1999), pp. 393-397, ISSN 1062-7995

Hartmann, M.; Schmidt, M. Jasenek, A. Schock, H. W. Kessler, F. Herz, K. & Powalla, M. Flexible and light weight substrates for Cu(In,Ga)Se₂ solar cells and modules, *Conference Record of the Twenty-Eighth IEEE Photovoltaic Specialists Conference 2000*, pp. 638-641, ISBN 0-7803-5772-8, Anchorage, Alaska, USA, September 15-22, 2000

Herz, K.; Eicke, A. Kessler, F. Wächter, R. & Powalla, M. (2003). Diffusion barriers for CIGS solar cells on metallic substrates. *Thin Solid Films*, Vol. 431-432, (May 2003), pp. 392-397, ISSN 0040-6090

Ishizuka, S.; Yamada, A. & Niki, S. (2009a). Efficiency enhancement of flexible CIGS solar cells using alkali-silicate glass thin layers as an alkali source material, *Conference Record of the Thirty-Forth IEEE Photovoltaic Specialists Conference 2009*, pp. 002349-002353, ISBN 978-1-4244-2949-3, Philadelphia, Pennsylvania, USA, June 7-12, 2009

Kapur, V. K.; Bansal, A. Phucan L. & Asensio, O. I. (2002). Non-vacuum printing process for CIGS solar cells on rigid and flexible substrates, *Conference Record of the Twenty-Ninth IEEE Photovoltaic Specialists Conference 2002*, pp. 688-691, ISBN 0-7803-7471-1, New Orleans, Louisiana, USA, May 19-24, 2002

Kessler, F.; Herrmann, D. & Powalla, M. (2005). Approaches to flexible CIGS thin-film solar cells. *Thin Solid Films*, Vol. 480-481, (December 2005), pp. 491-498, ISSN 0040-6090

Yagioka, T. & Nakada, T. (2009). Cd-Free Flexible Cu(In,Ga)Se₂ Thin Film Solar Cells with ZnS(O,OH) Buffer Layers on Ti Foils. *Applied Physics Express*, Vol. 2, No. 7, (June 2009), pp. 072201-1-072201-3, ISSN 1882-0778

Kapur, V. K.; Bansal, A. Le, P. & Asensio, O. I. (2003). Non-vacuum processing of CuIn₁₋ₓGaₓSe₂ solar cells on rigid and flexible substrates using nanoparticle precursor inks. *Thin Solid Films*, Vol. 431-432, (May 2003), pp 53-57, ISSN 0040-6090

Britt, J. S.; Wiedeman, S. Schoop, U. & Verebelyi, D. (2008). High-volume manufacturing of flexible and lightweight CIGS solar cells, *Conference Record of the Thirty-Thirdth IEEE*

Photovoltaic Specialists Conference 2008, pp. 574-577, ISBN 978-1-4244-2949-3, San Diego, California, USA, May 11-16, 2008

Gledhill, S.; Zykov, A. Allsop, N. Rissom, T. Schniebs, J. Kaufmann, C. A. Lux-Steiner, M. & Fischer, Ch-H. (2011). Spray pyrolysis of barrier layers for flexible thin film solar cells on steel. *Solar Energy Material and Solar Cells*, Vol. 95, (Febrary 2011) pp. 504-509, ISSN 0927-0248

Hashimoto, Y.; Satoh, T. Shimakawa, S. & Negami, T. (2003). High efficiency CIGS solar cell on flexible stainless steel, *Proceedings of third World Conference on Photovoltaic Energy Conversion 2003*, pp. 574-577, ISBN 4-9901816-0-3, Osaka, Japan, May 11-18, 2003

Khelifi, S.; Belghachi, A. Lauwaert, J. Decock, K. Wienke, J. Caballero, R. Kaufmann, C. A. & Burgelman, M. (2010). Characterization of flexible thin film CIGSe solar cells grown on different metallic foil substrates. *Energy Procedia*, Vol. 2, (August 2010), pp. 109-117, ISSN 1876-6102

Pinarbasi, M.; Aksu, S. Freitag, J. Boone, T. Zolla, H. Vasquez, J. Nayak, D. Lee, E. Wang, T. Abushama, J. & Metin, B. (2001). FLEXIBLE CELLS AND MODULES PRODUCED USING ROLL-TO-ROLL ELECTROPLATING APPROACH, *Conference Record of the Thirty-Fivth IEEE Photovoltaic Specialists Conference 2010*, pp. 000169-000174, ISBN 978-1-4244-5890-5, Honolulu, Hawaii, USA, June 20-25, 2010

Satoh, T.; Hashimoto, Y. Shimakawa, S. Hayashi, S. & Negami, T. (2000). CIGS solar cells on flexible stainless steel substrates, *Conference Record of the Twenty-Eighth IEEE Photovoltaic Specialists Conference 2000*, pp. 567-570, ISBN 0-7803-5772-8, Anchorage, Alaska, USA, September 15-22, 2000

Satoh, T.; Hashimoto, Y. Shimakawa, S. Hayashi, S. & Negami, T. (2003). Cu(In,Ga)Se$_2$ solar cells on stainless steel substrates covered with insulating layers. *Solar Energy Materials and Solar Cells*, Vol. 75, (January 2003), pp. 65-71, ISSN 0927-0248

Shi, C. Y.; Sun, Y. He, Q. Li, F. Y. & Zhao, J. C. (2009). Cu(In,Ga)Se$_2$ solar cells on stainless-steel substrates covered with ZnO diffusion barriers. *Solar Energy Materials and Solar Cells*, Vol. 93, (May 2009), pp. 654-656, ISSN 0927-0248

Wuerz, R.; Eicke, A. Frankenfeld, M. Kessler, F. Powalla, M. Rogin, P. & Yazdani-Assl, O. (2009). CIGS thin-film solar cells on steel substrates. *Thin Solid Films*, Vol. 517, (Febrary 2009), pp. 2415-2418, ISSN 0040-6090

Brémaud, D.; Rudmann, D. Kaelin, M. Ernits, K. Bilger, G. Döbeli, M. Zogg, H. & Tiwari, A. N. (2007). Flexible Cu(In,Ga)Se$_2$ on Al foils and the effects of Al during chemical bath deposition. *Thin Solid Films*, Vol. 515, (May 2007), pp. 5857-5861, ISSN 0040-6090

Ishizuka, S.; Yamada, A. Matsubara, K. Fons, P. Sakurai, K. & Niki, S. (2008a). Alkali incorporation control in Cu(In,Ga)Se$_2$ thin films using silicate thin layers and applications in enhancing flexible solar cell efficiency. *Applied Physics Letters*, Vol. 93, (September 2008), pp. 124105-1-124105-3, ISSN 0003-6951

Ishizuka, S.; Yamada, A. Fons, P. & Niki, S. (2008b). Flexible Cu(In,Ga)Se$_2$ solar cells fabricated using alkali-silicate glass thin layers as an alkali source material. *Journal of Renewable and Sustainable Energy*, Vol. 1, (Novenber 2008), pp. 013102-1-013102-8, ISSN 1941-7012

Ishizuka, S.; Yamada, A. Matsubara, K. Fons, P. Sakurai, K. & Niki, S. (2009b). Development of high-efficiency flexible Cu(In,Ga)Se$_2$ solar cells: A study of alkali doping effects

on CIS, CIGS, and CGS using alkali-silicate glass thin layers. *Current Applied Physics*, Vol. 10, (November 2009), pp. S154-S156, ISSN 1567-1739

Ishizuka, S.; Yoshiyama, T. Mizukoshi, K. Yamada, A. & Niki, S. (2010). Monolithically integrated flexible Cu(In,Ga)Se₂ solar cell submodules. *Solar Energy Materials and Solar Cells*, Vol. 94, (July 2010), pp. 2052-2056, ISSN 0927-0248

Kapur, V. K.; Bansal, A. Le, P. Asensio, O. & Shigeoka, N. (2003). Non-vacuum processing of CIGS solar cells on flexible polymeric substrates, *Proceedings of third World Conference on Photovoltaic Energy Conversion 2003*, pp. 465-468, ISBN 4-9901816-0-3, Osaka, Japan, May 11-18, 2003

Brémaud, D.; Rudmann, D. Bilger, G. Zogg, H. & Tiwari, A. N. (2005). Towards the development of flexible CIGS solar cells on polymer films with efficiency exceeding 15%, *Conference Record of the Thirty-first IEEE Photovoltaic Specialists Conference 2005*, pp. 223-226, ISBN 0-7803-8707-4, Orlando, Florid, USA, January 3-7, 2005

Caballero, R.; Kaufmann, C. A. Eisenbarth, T. Unold, T. Schorr, S. Hesse, R. Klenk, R. & Schock, H.-W. (2009). The effect of NaF precursors on low temperature growth of CIGS thin film solar cells on polyimide substrates. *Physica Status Solidi A*, Vol. 206, (May 2009), pp. 1049-1053, ISSN 1862-6300

Ishizuka, S.; Hommoto, H. Kido, N. Hashimoto, K. Yamada, A. & Niki, S. (2008c). Efficiency Enhancement of Cu(In,Ga)Se₂ Solar Cells Fabricated on Flexible Polyimide Substrates using Alkali-Silicate Glass Thin Layers. *Applied Physics Express*, Vol. 1, No. 9, (September 2008), pp. 092303-1-092303-3, ISSN 1882-0778

Rudmann, D.; Brémaud, D. Zogg, H. & Tiwari, A. N. (2005). Na incorporation into Cu(In,Ga)Se₂ for high-efficiency flexible solar cells on polymer foils. *Journal of Applied Physics*, Vol. 97, (August 2005), pp. 084903-1-084903-5, ISSN 0021-8979

Zachmann, H.; Heinker, S. Braun, A. Mudryi, A. V. Gremenok, V. F. Ivaniukovich, A. V. & Yakushev, M. V. (2009). Characterisation of Cu(In,Ga)Se₂-based thin film solar cells on polyimide. *Thin Solid Films*, Vol. 517, (Febrary 2009), pp. 2209-2212, ISSN 0040-6090

Keyes, B. M.; Hasoon, F. Dippo, P. Balcioglu, A. & Abulfotuh, F. (1997). INFLUENCE OF Na ON THE ELECTRO-OPTICAL PROPERTIES OF Cu(In,Ga)Se₂, *Conference Record of the Twenty-Sixth IEEE Photovoltaic Specialists Conference*, pp. 479-482 , ISBN 0-7803-3767-0, Anaheim, California, USA, September 29-October 3, 1997

Contreras, M. A.; Gabor, A. M. Tennant, A. Asher, S. Tuttle, J. & Noufi, R. (1994a). Accelerated publication 16.4% total-area conversion efficiency thin-film polycrystalline MgF₂/ZnO/CdS/Cu(In,Ga)Se₂/Mo solar cell. *Progress in Photovoltaics: Research and Applications*, Vol. 2, (October 1994) pp. 287-292, ISSN 1062-7995

Negami, T.; Satoh, T. Hashimoto, Y. Shimakawa, S. Hayashi, S. Muro, M. Inoue, H. & Kitagawa, M. (2002). Production technology for CIGS thin film solar cells. *Thin Solid Films*, Vol. 403-404, (January 2002), pp. 197-203, ISSN 0040-6090

Minemoto, T.; Okamoto, C. Omae, S. Murozono, M. Takakura, H. Hamakawa, Y. (2005). Fabrication of Spherical Silicon Solar Cells with Semi-Light-Concentration System. *Japanese Journal of Applied Physics*, Vol. 44, No. 7A, (July 2005), pp. 4820-4824, ISSN 0021-4922

Contreras, M. A.; Tuttle, J. Gabor, A. Tennant, A. Ramanathan, K. Asher, S. Franz, A. Keane, J. Wang, L. Scofield, J. & Noufi, R. (1994b). HIGH EFFICIENCY Cu(In,Ga)Se₂-

BASED SOLAR CELLS: PROCESSIMG OF NOVEL ABSORBER STRUCTURES, *Proceedings of the First World Conference on Photovoltaic Energy Conversion 1994*, pp. 68-75, ISBN 0-7803-1460-3, Waikoloa, Hawaii, USA, December 5-9, 1994

Minemoto, T.; Negami, T. Nishiwaki, S. Takakura, H. & Hamawaka, Y. (2000). Preparation of $Zn_{1-x}Mg_xO$ films by radio frequency magnetron sputtering. *Thin Solid Films*, Vol. 372, (August 2000), pp. 173-176, ISSN 0003-6951

Minemoto, T.; Hashimoto, Y. Satoh, T. Negami, T. Takakura, H. & Hamakawa, Y. (2001). $Cu(In,Ga)Se_2$ solar cells with controlled conduction band offset of window/ $Cu(In,Ga)Se_2$ layers. *Journal of Applied Physics*, Vol. 89, (June 2001), pp. 8327-8330, ISSN 0021-8979

What is Happening with Regards to Thin-Film Photovoltaics?

Bolko von Roedern
National Renewable Energy Laboratory
United States of America

1. Introduction

The advances and promises of thin-film photovoltaics (PV) are much discussed these days, typically using the viewpoint that a picked technology and process approach would provide "the" solution to many problems experienced implementing PV commercialization. In 2009, a thin-film PV company, First Solar, garnered world-leadership as a PV company, being the first company to produce or ship more than 1 GW of PV modules in a single year. This makes it timely to discuss the advantages and limitations of thin-film PV technology, as compared to the currently prevailing crystalline Si PV industry. Traditionally, the following technologies are considered constituting "thin-film PV:"
1. CdTe PV
2. CIGS PV (or copper-indium-gallium diselenide)
3. a-Si:H (and nc-Si:H nanocrystalline or "micromorph" silicon films)
4. less than 50 micron thick crystalline Si films

In the amorphous silicon (a-Si:H) based category, several approaches are pursued, ranging from amorphous silicon single junction modules to spectrum splitting multijunction cell structures using either a-SiGe:H cell absorbers or a-Si:H/nc-Si:H multijunctions. Pros and cons will be given for these different approaches that lead to this multitude of device structures. It is argued that as long as the advantages of the aforementioned materials are not understood, it would be difficult to "design" materials for more efficient solar cell operation.

This review will recap what is currently known about these materials and solar cell devices, keeping in mind that there will always be some unexpected "surprises," while there were many other approaches that did not result in anticipated cell/module performance improvements. This knowledge leads the author to ask the following question: "Was improper implementation or inadequate process choice responsible for the lack of solar cell/module performance improvement, or was the expectation for improved device performance or decreased device cost simply not warranted?"

The chapter of this book is written such as to not prejudge an outcome, i.e., an a priori assumption that a given measure would result in a commensurate expected performance improvement. The impact (i) of an improvement is broken down into probability (p) of achieving a projected improvement times the effectiveness (e) of such improvement, where

$$i=p*e$$

It is of interest to note that while impact is costed and/or priced by many companies, the right hand side of the above equation also has associated cost elements associated with effectiveness e plus an estimated probability p. Probabilities (p between 0 and 1 or 0% and 100%) are often assumed to be either 0% (for an unsuccessful project) or 100% (for a successful project), with the benefit of hindsight. This is true only with the benefit of hindsight, forward looking probabilities should be estimated and accounted for as accurately as possible. In financial terms, a probability between 0 and 1 should be accounted for by applying appropriate financial discounts to probabilities falling outside the extreme values, 0 or 1. Instead, often p=1 is being "assumed," but strictly speaking, this is inadmissible in forward-looking situations. Whenever p is increased at the expense of e, the total benefit for i may not be achieved as planned. Typically, p has to be empirically assessed, which is important for appropriate financial "discounting" leaving much room for discussion as to what value (between 0% and 100%) to assign to p. The foregoing statement is valid for all PV technologies (not just thin-film PV), but in the following, mainly elucidated picking thin-film PV examples. This chapter does not want to chime in on a debate about what appropriate probabilities or discount factors should be used, but rather serve as a reminder to the fact that projected probabilities occur with less than 100% probability.

2. Status and challenges for CdTe based solar cells and modules

In the year 2009, a company relying on producing CdTe based PV modules, First Solar Inc., became the World's largest photovoltaic (PV) company, producing about 1,100 MW of PV modules. Its production costs per Watt were quite low by industry standards. In 2010, direct manufacturing costs of less than $0.8/W were reported by First Solar. First Solar modules are 120 cm x 60 cm in size and were reported in 2010 to generate between 70 and 82.5 Watts under standard testing conditions, resulting in commercial module efficiency levels on the order of 10% to 11.5%. Time will tell how much room there is to further enhance power ratings and commercial module efficiency. It can be expected that in the foreseeable future, First Solar will remain among the top World Producers of PV modules. The CdTe device is a true thin-film device consisting of a TCO-coated (typically, SnO_2) glass superstrate, a CdS junction partner layer, an active CdTe layer, an often proprietary back contact, packaged in a hermetically sealed package. First Solar buys SnO_2-coated superstrates, uses vapor transport deposition (VTD) for the CdS and CdTe layers, and applies a proprietary back contact and cell series interconnect to the device structure.

Champion CdTe cells have achieved in excess of 16% efficiency (Green et al, 2011). It is of concern to some researchers that this champion cell was reported already some 10 years ago and has not improved since. The compound semiconductor CdTe has a tendency to grow and sublime stoichiometrically when exposed to high temperature. Instead of using vapor transport deposition used by First Solar, many R&D efforts use "Close-Space Sublimation" (or CSS) to deposit the CdTe layer. It appears that the deposition method for the CdS junction partner layer is not of as great importance as in the case of CIGS solar cells, where frequently chemical wet deposition schemes are used for depositing the CdS layer which is only about 100 nm thick, because that deposition method produces the greatest and most reproducible performance. CdTe layers deposited at the highest temperature compatible with the soda-lime glass superstrates typically result in the greatest device efficiency. However, other CdTe deposition schemes, most notably electro-deposition, also resulted in PV modules exhibiting substantial efficiency and performance (Cunningham et al, 2002). It

was, however, found that a critical $CdCl_2$-anneal step is crucial to achieve best solar cell or module performance (McCandless, 2001). Anneal temperatures on the order of 400 °C are typically used after the $CdCl_2$ exposure. For industrial production rates, it is important to limit the time for such anneal step in order to achieve an appropriate throughput. Looking at current commercial throughput rates, one has to conclude that this is possible. It was also attempted to substitute this $CdCl_2$ anneal step (where $CdCl_2$ is often applied as an aqueous solution] with a gaseous anneal step using HCl dry gas (McCandless, 2001). While this approach resulted in similar results as the aqueous $CdCl_2$ anneal step, a superiority using this "dry" process could not be established .

CdTe cells can be made stable and lasting, but not all production schemes result in stable cells. It was reported that excessive reliance on the $CdCl_2$-anneal step to obtain the highest cell or module efficiencies often led to less stable devices (Enzenroth et al., 2005), with processes leading to the highest pre-anneal efficiency often resulted in the most stable manufacturing recipes. It is now known that Cu, applied to many back-contacting schemes, is correlated with the stability of CdTe cells. While it has been established that "too much" Cu results in unstable cells, some rather stable cell deposition schemes were developed that use Cu-doped back contact recipes. The degradation process shows a mixture of diffusive and electromigration behavior (Townsend et al., 2001). Alternatives to using Cu for the back contact were developed (e.g., P-doping, N-doping) (Dobson et al. 2000). These 'Cu-free' recipes also showed instabilities and did so far not improve cell performance over that achieved with stable Cu-containing back-contact recipes. Perhaps, it is a flaw to ask: "Is Cu in the back contact good or bad for cell stability?" The appropriate question may well be: "When is Cu good, when is it bad, and when is it irrelevant for cell performance and stability?"

While all commercial CdTe solar modules are currently fabricated in a superstrate configuration (using a glass superstrate), the question has been posed whether such process could be inverted and/or be applied to flexible substrates. Flexible substrates (like polyimide foil) limit the temperature that can be applied during the position process. Also, the issue of low-cost hermetic packaging of such transparent foils has to be addressed in greater detail in a cost-effective manner. Because glass-encapsulated PV works, the cost of glass (on the order of $10/m² for a single sheet) can often be used as a cost-guideline for terrestrial flexible packaging schemes for power modules. It is clear at this juncture that CdTe PV and CIGS PV have greater moisture sensitivity than many Si PV schemes, requiring a more hermetic seal than Si PV might require. A point of research continues to be the "edge delete" for modules. Typically, SnO_2 coated superstrates are coated with all layers of the entire glass surface. A fast removal of such films, including the SnO_2-layer, along the module edges is required. For CdTe modules, often rather crude methods (like bead-blasting or using grinding wheels) are employed for this "edge delete" step were employed. The drawback of employing these methods is that glass surfaces are damaged using such processes, resulting in greater water penetration rates from the module edges. Also, such processes tend to weaken the glass. However, less damaging edge delete techniques like laser ablation methods are rapidly becoming feasible and more cost effective.

In order to make a monolithically interconnected module, cell "strips" have to be created that carry CdTe currents through the SnO_2. Typically, 1 cm-wide cell strips are used for CdTe modules. These strips require 3 scribes sometimes labeled P1 (SnO_2), P2 (semiconductor layer), and P3 (back-contact) scribe line. The area including and between scribes P1 and P3 is electrically "dead" and does not contribute to module power, hence reducing the total area module efficiency. Therefore, scribe lines should be narrow and close

to each other, which requires a good parallel alignment of the scribe lines with each other. With the advancement of laser technology, all of these scribes are often achieved by laser scribing. CdTe (and CIGS) cells can also be scribed with a mechanical stylus, and sometimes, lift-off techniques were used for the P3 scribe by printing a lift-off paste to segment the cell's back contact. CdTe modules can be scribed in a picture frame or landscape format. First Solar scribes in a picture frame format, arguing that high module voltages would reduce resistive (I^2R) losses in the dc module wiring. However, it was also discovered that modules are installed with a maximum string voltage of 600V (dc, in North America, 1000V in Europe), leading to relatively short strings for high-voltage modules. Realizing this, for its series 3 modules, First Solar has reduced the voltage, resulting in lower voltage (and greater current) PV modules. Other CdTe companies have elected to scribe in a landscape format.

Research activities for CdTe cells and processes concern themselves with achieving a greater open-circuit voltage (V_{OC}), greater stability, and more repeatable solar cell processing. While the CdTe semiconductor possess nearly the ideal band gap for absorbing the solar spectrum in a single junction device (about 1.5 eV), V_{OC} is limited to approximately less than 900 mV for champion cells,(about 750 - 800 mV per cell for commercial devices), well below values that were achieved for high efficiency GaAs solar cells (V_{OC} of about 1200mV in "champion" cells) where the semiconductor absorber has a very similar band gap near 1.5eV. Investigation of back contacts and device stability is sometimes hampered by the proprietary nature used by industry for these processes. Also, the role of impurities (oxygen, water vapor) and the process when and how these impurities are added are currently poorly understood.

Long-term concerns for CdTe PV are a perceived toxicity (Cd-containing compounds) and the availability of Te. While Te availability is not a problem now, it may become so after multiple terra-Watts of CdTe PV have been produced. A known mitigation scheme for incorporating less Te (and Cd) into a cell would be to make the absorber layer thinner. Unfortunately, as the absorber thickness is reduced to values below 1.5 microns, an often precipitous decrease in cell fill factor and V_{OC} were observed. For some solar cell processes, a more gradual decrease of these cell parameters is observed even as thicker absorber layers are thinned. Because absorber material costs are not a significant manufacturing cost factor, manufacturers are reluctant to sacrifice performance by making thinner absorbers, hence the development of thin absorber cells is currently only infrequently pursued. There comes a point when very thin absorber cells would also loose current density due to incomplete light absorption, but in a direct band gap thin-film semiconductor this would only happen for absorber thicknesses below 1 micrometer. Further, as the a-Si:H and nc-Si:H PV communities have shown, it may be possible to mitigate such current loss by employing optical enhancement techniques (Platz et al. 1997).

3. Status and challenges for CIGS based devices

Champion CIGS Cells have been reported near 20% cell efficiency (Green et al, 2011). It is remarkable that (a) 2 different groups on two continents (National Renewable Energy Laboratory, NREL and Center for Solar Hydrogen, ZSW) have achieved this efficiency level, and that (b) different material compositions all can achieve high efficiency cells (Noufi 2010). The record cells were mostly made by a process call co-evaporation. Typically, this process has multiple "stages" involved, finishing devices with a Cu-poor (or In-rich) surface

layer (Gabor et al. 1994). This process has also been adopted for CIGS module manufacturing. Other processes used for commercial module fabrication are sputtering and (time-consuming!) selenization using H_2Se gas, various hybrid processes, electro-deposition, and nano-particle precursor inks. Only time will tell if the latter deposition processes can achieve the same performance as the co-evaporation process can? There are currently different schools of thought as to why best solar cell results are obtained using these multi-stage processes. Some people argue that the Cu-poor surface phase is a perfect ordered vacancy compound (Schmid et al. 1993), while other researchers believe that a non-perfect Cu-deficient surface layer can enhance CIGS solar cell performance (It may be instructive to compare this issue to the crystalline Si PV case. Traditionally, this PV technology has used monocrystalline and multicrystalline Si wafers. While several promoters have some understanding that there is an efficiency difference between mono-Si and multi-Si based technologies, some Si advocates say that all Si cells "should" have the same efficiency potential.)

Nano-particle approaches have been promoted based of the promise that the absorber properties could be fixed in the ink precursor. Nevertheless, the scale-up of nano-particle precursor deposition approaches has also shown significant variation in output power. Researchers typically have the uniformity of a semiconductor absorber layer in mind when looking at enhanced control scheme, thereby neglecting the "junction-uniformity" upon scale up, which can be observed in any commercial manufacturing process even when the absorber properties remain constant upon deposition area scale-up and/or throughput.

This author ranks the probability as quite low that Se could be added in a "fast" process to metallic precursor layers. Past work was carried out along these lines (Attar et al. 1994) . Similarly, advantages of CuSe or InSe precursors have not as yet been demonstrated to lead to high solar cell efficiencies (Anderson et al. 2003). In addition to films made by the former process having problematic mechanical film properties (flaking), rapid post-deposition selenization approaches have also not yet lead to great solar cell efficiency. This observation currently necessitates handling a high vapor pressure Se (relative low temperature) Se evaporation source and low vapor pressure Cu evaporation source (relative high evaporation temperature) in the same vacuum system.

CIGS PV showed the last significant "win-win" situation in PV when it was suggested (for reasons of lowering manufacturing cost) to change substrate material from using boro-silicate glasses to soda lime (ordinary window) glass. What was not anticipated was that such switch also increased the cell performance obtained. It is now understood that controlled addition of Na can enhance the performance seen in CIGS cells. In fact, Na addition was essential for making high-efficiency CIGS cells on metal foils a reality. The reasons for this advantage are poorly understood, but the observation is overwhelming that Na can improve CIGS solar cell performance.

The CIGS cell typically consists of the following structure: Glass/Mo-film/multi-stage-CIGS/CdS/TCO. Since a finished cell can be exposed only to moderate temperature (<200 ^{o}C, perhaps <150 ^{o}C), sputtered ITO or ZnO or LPCVD (Low Pressure Chemical Vapor deposited) ZnO are typically used as the TCO. The Mo-film and the TCO deposition processes may use more than one deposition process for fabricating such layer (e.g. sputtering condition). When using co-evaporation for the CIGS deposition process, the best performance results are obtained when substrate temperatures during the deposition process are high, approaching the softening point of glass. The CdS layer, for high

performing CIGS cells and modules, uses a wet (CBD chemical bath deposition) process for a thin (100 nm thick) CdS layer. For modules, scribing the p(1) through p(3) scribe lines can involve laser and/or mechanical methods (Tarrant & Gay, 1995). Because of a higher current density in CIGS (typically, 33 mA/cm^2 ± 15%) cell strips are typically only 5 to 6 mm wide. For such cells, scribing tolerances are particularly important for minimizing the non-contributing module area.

Many commercial CIGS modules are currently fabricated on rigid glass substrate/cover glass structures, limiting moisture ingress to the module perimeter. Even these structures initially had problems passing the damp heat (1000 hours at 85% relative humidity, 85 C) tests. This suggests that CIGS cells are more moisture sensitive than modules made using Si solar cells. Some commercial CIGS manufacturers fabricated on flexible metal foil material have therefore designed their cells as Si cell replacement to be packaged within glass sheets. The question has been posed whether such process could be inverted and/or be applied to flexible substrates. Flexible substrates (like polyimide foil) limit the temperature that can be used to deposit the CIGS films, but allow monolithic (scribed) integration of the module, while stainless steel substrates allow the use of higher deposition temperatures, but, because they are conductors, not the monolithic interconnection. Typically, PV made on metal foils is "slabbed" into individual solar cells, giving up some advantages of a roll-to-roll fabrication process.

In order to increase the humidity tolerance, it is presently not clear whether to make the solar cell more tolerant to moisture or whether to lower the water transmission rate of the module package. It is known that the ZnO layer used as the top contact by some entities deteriorates upon moisture contact. Some groups therefore work on replacing the TCO material. On the other hand, it is also known that there can be degradation for CIGS cell recipes that use an ITO instead of a ZnO contact for CIGS cells, and that other technologies (like a-Si or a-Si/nc-Si technologies) have achieved acceptable stability using ZnO for top and/or bottom solar cell contacts. It is somewhat likely that there is not a single cause or mechanism for moisture sensitivity, and that CIGS PV will be more sensitive to moisture than Si–based PV. This leaves the question how cost-competitive flexible CIGS is for power generation. Such competitiveness will require a light-weight, flexible and optically transparent low-cost moisture barrier. Acceptable barriers may exist as commercial prototypes, but commercial cost for such foils is not clear. If these foils were significantly more expensive than glass, the advantage of flexible CIGS PV could be diminished.

The long-term stability of CIGS is acceptable, depending on details of device processing and the quality of the package. Having been discovered some time ago, "transients" in CIGS-based devices are poorly understood. If finished solar cells or modules are exposed to moderate heat in the dark (<150 ^{o}C, for example when modules are laminated), a power loss is often (but not always) observed. Such behavior is currently not predictable. Often, but not always, the power loss recovers when the module is exposed to natural or artificial light. These "transients" may change as modules age and pose a problem for qualification tests, specifying a pre-and post stress power variations that could be larger than stress induced power losses. For some CIGS pilot production modules, it was found that such transient loss effects were on the same order as stress or deployment induced losses. The question is to what degree recovery can be relied upon to achieve performance predictions that on average are correct?

Some tests (like the 85/85 test) heat the modules in the dark. Because of this behavior, the qualification test for modules utilizes the manufacturer's labeled module power rather than

the measured module power as the criterion for power loss upon stressing. CIGS (and all) thin-film modules are tested using the IEC 61646 accelerated testing specifications. One manufacturer exposed CIGS modules with questionable lamination power losses to actual sunlight to ascertain the amount of recovery.

Long-term potential limitations to CIGS PV are the limited availability of In metal. The use of In could be reduced by manufacturing thinner cells than the thicknesses used today. However, experimental and commercial reality is similar to what has been said about thin CdTe solar cells above, because materials cost for the semiconductor layer currently are low, typically best performance, not minimum thickness is used for commercial activities. It is also unclear if a competing technology, flat panel displays, will continue to use In (ITO) or will switch to a different TCO material. Being limited by In availability is not expected to be a problem until terawatts of CIGS PV modules have been fabricated. Another potential problem is customer acceptance. CIGS cells use a small amount of CdS in the buffer. Several entities have therefore developed alternative buffers to CdS (Contreras et al. 2003). Such work may be successful (but no performance improvements were yet found because of using alternative buffers), and it is of interest to note that a similar wet deposition process for best alternate junction partners also uses CBD. There are also efforts to develop CIGS-solar cells using earth-abundant non-toxic materials only. This requires replacing the In (and perhaps Ga) used in CIGS solar cells. A popular candidate is currently Zn ("CZTS" cells), and efficiencies near 9% were reported for such cells (Todorov et al. 2010). Using such alternative materials suffers from the fact that the "secret" of CIGS solar cell operation is not understood (why the device optimizer has to do what he has to do in order to attain high efficiency solar cells, why In, Ga and CBD CdS work extremely well). Researchers focus on materials that have appropriate optical properties, but appear to miss out on the important relevant electronic differences between CIGS and alternative materials.

Research issues for CIGS based solar cells are: Understanding the difficulties scaling up current champion cell recipes to commercial size, understanding the befits of incorporating Na into cell, understanding the stoichiometric requirements (In to Ga to Cu to Se concentration ratios, in combination with other parameters such as solar cell thickness, chemistry of buffer layers etc.), understanding 'transients' in solar cells, understanding the 'secrets' of In, Ga, Cu, Se, and Na required for achieving champion-level efficiencies, developing alternative buffer layers, and understanding how V_{OC}, FF and J_{SC} losses could be mitigated in cell using absorbers <1 micrometer thick. There is less focus on the quality of the back contact, but unless Mo is used as the contacting layer, cell results are typically much poorer. The secret of the Mo use should be part of understanding why current champion cell recipes have to be made the way that they are being made.

4. Status and challenges for amorphous silicon and micromorph solar cells and modules

Amorphous silicon constituted the first commercial thin-film PV module product. The process of making amorphous silicon solar cells and modules was first invented by the RCA and Energy Conversion Devices (ECD) laboratories (Catalano et al. 1982, Izu et al, 1993). There was also a strong push by Japanese Companies (Sanyo, Fuji, Cannon, Sharp, to name a few) for commercializing this PV technology. At the time, both power and consumer products were being developed.

Spectrum splitting multijunction solar cells were invented in Japan (Kuwano et al. 1982) and consequently developed at ECD (later, doing business under their Uni-Solar brand name)

and Solarex (later doing business as BP Solar, but in 2002, pulling out of all thin-film PV activities), and also in Japan and Europe. For a while, it was believed that this was the easiest pathway to achieving high-efficiency low-cost solar cells and modules. While multijunctions offer a theoretical efficiency advantage, the practical advantages are of a lesser degree. This is because in case of the a-Si-based multijunction cells, the subcells of the stack are not perfect in terms of their I(V) parameters. This has a beneficial aspect for energy generation, because as long as non-ideal subcells are stacked, one cannot invoke ideal mismatch factors when calculating mismatch for the stack (Chambouleyron and Alvarez, 1985). In fact, for multijunction III-V-based solar cells, it was shown that by managing the current flow through the stack (limiting the current by the top-cell), fill factors of the stack can well exceed the fill factor of the weakest cell in the stack (Wanlass & Albin, 2004).

Fabrication of a-Si:H solar cells and modules uses plasma enhanced chemical vapor deposition (PECVD). Typically, silane gas (SiH_4) (germane gas GeH_4 for a-SiGe:H layers) is piped into a deposition chamber near 1/1000 of one atmosphere, and by applying an rf frequency, hydrogenated amorphous silicon (hydrogenated amorphous silicon germanium alloy) layers are deposited. In many instances, the frequency of 13.56 MHz set aside for such applications was used to excite such plasma, but in the 1980s, it was reported that using higher frequencies could produce a-Si:H films and solar cells with slightly improved properties and/or higher deposition rates (Shah et al. 1988). The higher frequency deposition has been adopted by a few commercial companies. Amorphous silicon can be doped, typically with phosphorus or boron, by adding a phosphorus or boron containing gas to the gas mixture. Typically phosphine (PH_3) is used for n-type doping, while for p-type doping, B_2H_6, BF_3, and $B(CH_3)_3$ have been investigated among other doping gases.

The a-Si:H cells and modules are available in both substrate and superstrate configurations. Due to the relative low deposition temperature (200 °C or less) the choice of substrate material is less driven by temperature capabilities, but rather by issues like substrate availability, cost, and commercial handling issues. Commercial cells are illuminated through the p-doped contact and are hence termed n-i-p structures in substrate configuration or p-i-n structures for superstrate configurations. For superstrate configurations, a commercial or in-house prepared TCO layer is coated with one or more p-i-n sequences. Illumination through the p-type contact is clearly enhancing cell performance. Glass superstrate modules are typically scribed and interconnected into 1 cm-wide cell strips, commonly using laser scribing and welding methods. When conductive substrates (like Uni-Solar's stainless steel) are used, individual cells are cut from the substrate. Methods have been found to contact the top-contact TCO layer in such cells to extract the substantial currents from large-area cells.

Amorphous silicon (a-Si:H) PV went to its so far highest market share in 1988, thereafter losing market share because a resurgent activity in crystalline Si PV and because a-Si:H based module efficiencies were quite low and did not achieve stabilized efficiency levels that were predicted then (15% efficient module efficiency was predicted to be achievable by the late 1990s). Amorphous silicon suffers from so called Staebler-Wronski degradation. The a-Si:H based solar cells and modules are made with greater "initial" efficiency at modest deposition temperature (say 200 °C), but when the devices are exposed to light, a reduction of power (and all parameters like V_{OC}, FF, and J_{SC}) typically occurs. The exact amount of such loss depends on the details of device fabrication, but the effect is significant (say typically for commercial devices on the order of 30%). The Staebler-Wronski degradation can mostly be removed by annealing (for one hour or so) at temperatures of 130 C, but this temperature is greater than the normal operating temperature of PV modules and could

damage module components. The strongest tool for mitigating such degradation is keeping the intrinsic-a-Si:H absorber layer thin. In 1990/1991, the US a-Si program therefore asked that only "stabilized values" for material properties and solar cell efficiencies should be reported. The stabilization procedure was specified as light-soaking under one-sun light intensity for 1000 hours at a sample temperature of 50° C (Luft et al. 1992). This change had two consequences: (1) a reduction of cell efficiency values as initial value were previously reported; (2) establishment and study of light-soaking in the major amorphous silicon laboratories. While this procedure is now followed by most commercial manufacturers, it is tempting to report better initial values, which is sometimes done. There was a debate whether or not Staebler-Wronski degradation could be entirely eliminated. To date, no elimination scheme has proven successful, but, as mentioned earlier, the magnitude of the effect can be controlled. While for many years it was believed that initial and stabilized performance scaled, it is now clear that smaller initial performance may result in greater stabilized performance and vice versa.

Large-area PECVD deposition may result in non-uniform deposition because different amounts of electric field are available on the rf cathodes of the typically capacitive coupled flat plate reactors used, because the wave length of the rf frequency and the physical dimension of the electrodes become of comparable magnitude. This problem typically becomes larger when higher frequencies (smaller wavelengths) are used to excite the rf (or vhf) plasma. Another source of non-uniformity arises from the fact that the feed-in distribution ratios of the precursor gases (SiH_4, GeH_4 and H_2) can change (because of consumption) in large area systems. It should be noted that on the other hand, such consumption can lead to desirable grading, say of the Ge-content in a-SiGe:H layers (Guha et al. 1988). These issues can all be overcome, by using the appropriate or segmented electrodes and gas feed-ins for large-area deposition. In the early 1990s, SERI (Solar Energy Research Institute, before the organization became NREL in 1991) specified attaining a certain amount of thickness uniformity (typically, ±5%) for large-area a-Si:H deposits in its subcontracts. These uniformity specifications were typically met, but what wasn't realized then is that the conditions used for meeting the uniformity criteria may not have been the same leading to the most efficient modules.

The following points may be important to assess degradation mechanisms: (1) there are interrelated "slow" and "fast" components to the solar cell degradation (Lee et al. 1996); (2) wrong fundamental degradation models could be the culprit for not being able to eliminate or minimize degradation, resulting in inadequate stabilization and "unexpected" degradation of commercial module product. High light intensity and low exposure temperature as well as process details like hydrogen dilution can favor the formation of fast (or 'easy to anneal') degradation (Lee et al. 1996, von Roedern & DelCueto, 2000)). Operating temperatures of an a-Si:H module could affect the annealing and stabilization process. Hence, a typical a-Si:H arrays show greater efficiency in the summer than in winter. This behavior is opposite to many other PV technologies, where efficiencies during summer are lower than during winter because higher operating temperatures (such temperature behavior also holds for a-Si:H modules) results in lower module voltages for the same radiation level, hence lower module power. For a-Si:H modules, the annealing effect (increasing efficiency) must be often more significant than the temperature effect (lowering efficiency). It is of importance to note that degradation and continued outdoor exposure affects the temperature coefficients observed. Typically for a-Si:H modules, T-coefficients become less negative, sometimes even positive after prolonged exposure. A detailed study

how degradation affects the amount of degradation that is observed has been published (Whitaker et al. 1991).

There was a resurgence of a-Si:H activities after the year 2005 when big companies entered the a-Si module arena by making or adapting deposition lines for a-Si:H-based PV modules. Many researchers believed that this could result in a renaissance for a-Si:H PV. However, the question should be answered: how could this be the case when these companies used the same PECVD process that was researched for over 30 years for the deposition of a-Si:H PV modules? Several a-Si:H PV companies have recently given up on this technology. Is this because the economical circumstances were not right, or is it because performance and cost expectations for such modules could not be met? The reader must draw his or her own conclusion on this.

In the 1980s, it was proposed that changing the radio-frequency (to values greater than 13.56 MHz) could change the properties of a-Si:H and also facilitate the growth of nanocrystalline thin film (nc-Si:H) layers. The nc-Si:H layers can be grown when there is a high hydrogen dilution of the gas fed into a PECVD system (typically>98% H_2). Subsequently, nc-Si:H layers were investigated as absorber layers for a-Si:H-based solar cells. For more than 10 years, it is known that layers resulting in the highest solar cell efficiency are "mixed phase" (nanocrystallites of relative small size, typically << 50 nm in size), rather than those involving the largest grains and almost no "amorphous tissue" (Luysberg et al., 2001). Like for a-SiGe:H, it was found that the properties of nc-Si were not "quite good" enough for use in single junction solar cells. Hence, these layers are typically used as a-SiGe:H replacement in spectrum slitting multijunction solar cells. One group termed the word "micromorph" for such solar cells.

The micromorph solar cell constitutes a conundrum for the solar cell optimizer. Multijunction solar cells are to be approximately 'current matched.' A common target value for the current density in champion tandem multijunction solar cells is 13 mA/cm². This value is difficult to attain in the stabilized thin a-Si:H top junction. It remains to be seen if the field, if sustained, will gravitate to optically enhanced solar cell (Platz et al., 1997) or if a triple junction solar cell structure (having a current density of 8.7 mA/cm²) will prevail. Since nc-Si:H absorber layers were developed later than a-SiGe:H, some promoters projected a greater efficiency potential for such layers than for a-SiGe:H absorbers. In reality, cell performance for multijunction cells containing a-SiGe:H and nc-Si:H is about the same (approximately 12% stabilized "total-area" efficiency). It has been suggested that the crystalline nature of the nc-Si:H layer would result in deposition rate independent properties of the nc-Si:H solar cell. Unfortunately, experimental observations could not support such prediction, nc-Si deposited at higher deposition rates (say >2 nm/sec) shows a significant loss in solar cell efficiency. Since optimum nc-Si:H cells are 1.5 to 2 microns thick (compared to 0.2 micrometer thick a-SiGe:H absorbers), deposition times for nc-Si:H absorbers are typically longer. This poses another decision for the solar module optimizer: Should one "trade" consumable cost (GeH_4 gas is expensive!) for even higher equipment capital cost ? The statement that currently a-SiGe:H and nc-Si:H solar cells and modules would have about the same efficiency is sometimes controversial (Yan et al., 2007). (An article in Photon International reported that while "micromorph" modules had a higher efficiency than a-Si:H modules, the plant size for micromorh deposition equipment was also greater than for a-Si:H module deposition. If the same amount of equipment was used, micromorph production will result in a lesser annual output than producing pure a-Si:H modules with the same deposition equipment.)

Some PV technologies have come under attack for using poisonous or harmful gases. There have also been reports that the use and release of system etching gases (NF_3 is typically used) could make Si-based PV less environmentally friendly, since etching gases like NF_3 possess a green-house gas potential about 20,000 times greater than CO_2. Photon International estimated that for an a-Si:H module factory, the greenhouse gas "pay-back" time could be twice as long as the energy pay-back time (pay-back time characterizes the avoided greenhouse gases or energy that is used to produce a PV system including the modules). The energy pay-back time for an a-Si:H PV array is on the order of 1 year. For crystalline Si PV the same issue may arise, as some PECVD systems used to deposit a "fire-through" a-SiN$_x$:H antireflection layers also use PECVD for depositing the a-SiN$_x$:H films in etch-cleaned PECVD chambers using NF_3. There are ways to mitigate the emission of NF_3; (1) avoid the use of NF_3 cleaning, or (2) use alternatives for etch-cleaning chambers like on-site generated F_2.

5. Status and challenges for crystalline silicon film solar cells and modules

It is intriguing to use crystalline Si films to make Si PV. There is a problem that when depositing such films, silicon may become loaded with impurities from the substrate material used. At one point in time, it was thought that this could be overcome by using Si as a substrate, for example, a Si ribbon material grown quickly. This approach has not proven successful, presumably because the crystalline Si films grow with different rates epitaxially on different substrate crystalline orientations. There is also the quest for using lower temperature substrate materials, but even a solid state recrystallization requires temperatures that exceeds soda-lime glass softening temperatures. Many groups using crystalline Si films have used, with some success, heavily doped mono-crystalline wafers, mullite (alumina) derivatives, pure graphite, multi-crystalline Si films, or specialty glasses to achieve deposition or recrystallization of crystalline Si films. For some of the foregoing substrate choices, differences in the thermal expansion coefficients of silicon and the substrate material can result in additional issues that need to be resolved. The Solar program of the US Department of Energy (DOE) projected that in the 1980s, Si PV would transition from wafers to films. Such transition, however, has not yet happened, because films still result in a rather low solar cell efficiency compared to wafer Si. Most people define film silicon less than 50 microns thick Si film on a foreign (non wafer Si) substrate as thin-film PV.

One device issue is the small voltage that is achievable using thin Si films. Values for V_{OC} near 600 mV have been reported, but typical values are lower than that, perhaps on the order of 500 mV or less. The low voltages and fill factors are a universal observation for thin cells, but many researchers focus on short-circuit current density (J_{SC}) for thin–absorber cells. This leads to the following question: Should one first tackle a loss of V_{OC} and FF in thin absorber cells, or should one begin tackling short-circuit current densities? In 1998, Dr. Jürgen Werner summarized Si film solar cell observations by plotting grain size on a logarithmic abscissa scale and voltage or efficiency on the ordinate. It was observed that a huge "valley" existed. For grain sizes between 10 nm and 1 millimeter, no good correlation could be observed between grain size and cell voltage or efficiency. In the 12 years following such plot, despite new experimental trials, not many new observations were added to Werner's original plot. This poses the question to what degree grain size could be an effective "driver" towards higher solar cell efficiency?

For many years, NREL had worked with the Astropower Corporation (Delaware, and its successor, GE) on developing thin crystalline Si solar cells and modules. They delivered

various cell and module prototypes. What was striking was that with about 30 micron thick absorbers, short circuit current densities (<28 mA/cm²)and QE responses were measured for such cells that were similar to champion light enhanced nanocrystalline nc-Si:H-cells were the absorber was only 1.5 to 2 microns thick. This poses the question to what degree the fall-off of the quantum efficiency red response is determined by incomplete carrier generation or by incomplete carrier collection or both? Thin Si PV is a perfect example demonstrating where reliance on the appropriate R&D assumptions will greatly affect the optimization efforts. If losses were due to incomplete carrier collection, one would gear optimization attempts towards reducing collection losses, while incomplete generation losses would be fixed by enhancing generation, typically by applying optical enhancement schemes. It is possible that measured QE responses are affected by both factors, while a majority of R&D efforts may have been conducted under the assumption to enhance generation in thin solar cells by researching optical enhancement techniques alone. It is currently not known what the potential of crystalline Si film solar cells is. The observations made during the last 30 years optimizing Si based solar cells could suggest that progress with thin Si film solar cells could be less likely and may not be attainable, if the observations rather than the expectations were correct.

A similar question should be asked for another case of crystalline Si PV, recrystallized amorphous silicon. Commercial development for crystalline Si film solar modules has occurred at Pacific Solar (later CSG, Crystalline Si on Glass, at one point in time, affiliated with Q-Cells, now belonging to Suntech Corporation). CSG modules achieved about the same performance level as amorphous silicon (a-Si:H) modules. CSG uses 2 micrometer thick layers for the absorber (a recrystallized a-Si precursor on a specialty glass substrate). This observation poses a very fundamental R&D question: "Was CSG not given enough resources to develop a better solar cell, or was the expectation erroneous that a better solar cell efficiencies would result from recrystallized 2 micrometer-thick crystalline silicon layers (recrystallized 2 micron thick amorphous silicon) than using 0.5 micron thick a-Si:H layers directly to produce a solar cell or module?" In order for fundamental science to impact technology, a more conclusive answer to this question has to be found.

6. Relating champion cell efficiencies and commercial module performance

Champion efficiencies are often used as the yardstick to gauge the PV status of a certain technology. It was found that the credibility of such numbers improves when champion results of independent testing laboratories are used, although several PV entities have developed internal procedures to obtain, within experimental uncertainty, the same results as independent testing laboratories. What is more controversial is that sometimes "unoptimized" solar cell results have been reported. In those instances, it is not clear what efficiency level might be attainable upon further cell optimization. As argued in the introduction section of this chapter and elsewhere, it is not clear if greater control and reduction in variability increases or decreases champion cell efficiencies. It is recommended that for the time being, either possibility should be considered as likely, namely that unoptimized device performance can or cannot be further improved after full optimization.

Champion solar cell efficiencies can be linked to current and future commercial module performance, based on what is known today about solar cell champion efficiency levels, which in recent years have not shown too much progress. In order to obtain current

Eff. (%)	Module	T.coeff. (power)	Technology	Current c/c performance ratio (module/cell eff.)
19.5	SunPower E19/318	-0.38 %/C	mono-Si, special junction, sp. j. (1)	78% (19.5/25.0)
17.1	Sanyo HIP-215N	-0.34 %/C	CZ-Si, "HIT," sp. J (1)	69% (17.1/25.0)
15.1	Suniva ART245-60	-0.46%/C	CZ-Si, sp. J. (2)	72% (15.1/21.0)
14.3	Kyocera KD235GX-LPB	-0.44%/C	MC-Si, standard junction (std. j.)	70% (14.3/20.4)
14.3	Solar World SW235/240	-0.45%/C	CZ-Si, std. j.	68% (14.3/21)
14.3	Solar World SW 220/240	-0.48%/C	MC-Si, std. j.	72% (14.3/20.4)
13.9	Solaria 230/210	-0.5 %/C	"standard" mono-Si cells, 2x concentration	65%* (13.9/21.5)
13.6	Suntech STP 225-20Wd	-.0.44%/C	MC or CZ-Si, std. j.	67% (13.6/20.4)
13.6	Evergreen Solar ES 195	-0.49%/C	String-ribbon-Si std. j.	65% **(13.6/20.4)
12.5	Q-Cells Q.smart UF 95	-(0.38 %+/-0.04)%/C	CIGS	62% (12.5/20.3)
11.5	First Solar FS-382	-0.25%/C	CdTe	69% (11.5/16.7)
11.9	Avancis 130 W	-0.45%/C	CIGS	59% (11.9/20.3)
10.1	Abound Solar AB62/72	-0.37 %/C	CdTe	60% (10.1/16.7)
10.0	Sharp NA-NA-V142H5/NA	-0.24%/C	a-Si/nc-Si	80% (10/12.5)
7.2	Uni-Solar PVL144	-0.21 %/C	a-Si, triple junction	60% (7.2/12.1)
6.3	Kaneka T-EC-120	n/a	a-Si single junction	62% (6.3/10.1)
1.7	Konarka Power Plastic 1140	+0.05%/C	organic	20% (1.7/8.3)

*There is no good published value for 2x concentrated cell performance. Here, the corresponding Solar cell efficiency is taken as 21.5%.
** There is some uncertainty whether or not string-ribbon Si can reach multicrystalline Si efficiencies, but this has been assumed.

Table 1. Module Efficiency from survey of manufacturers' websites and commercial module efficiency over champion cell efficiency ratios"

commercial performance, an internet survey provides some guidance as to what module products, and technologies are commercially available. Then the ratio between verified champion efficiency and module performance can be calculated. It is clear that commercially available module efficiencies have to be discounted from champion cell level efficiencies, and that module efficiencies are smaller than solar cell efficiencies. In 2006, this author used a "discount" of 20% between champion cells and commercial modules (von Roedern, 2006). Now, 5 years later, the data suggest that it would be very unlikely that average commercial module efficiencies could exceed 80% of the respective champion level solar cell efficiency. The most mature and selective technologies (wafer-Si) have not yet exceeded this (80%) value for even for their best commercial modules yet.

Table 1 shows a summary from February 2011 of commercially available PV modules. Only modules available on manufacturer's public websites for sale where the technology is identifiable are listed.

Using the 80% argument, it can then be estimated what maximum average commercial module efficiency is likely based on what is known about champion solar cells today. Table 2 provides such breakdown.

The point to be made is that there is a difference between champion cell and champion module efficiency (estimated to constitute an efficiency difference of about 20%). While some technologies may reach a high ratio earlier than others, current champion-cell efficiency numbers can be used to estimate future commercial module efficiencies. There are some claims that some modules perform better in hot environments than at low temperature. These real effects are on the order of +/- 10% in energy generation, but there are unknowns of similar magnitude like the degradation encountered over the system lifetime, the quality of the installation, the weather fluctuations, and the accuracy of the name-plate rating, to name a few factors.

Technology	Future commercial module performance (80% of current record cell efficiency)	Future Relative Performance	Future Relative-cost (using a 50% thin film cost advantage)
Silicon (non-stand)	19.8%	1.21	0.83(competitive)
Silicon (standard)	16.4%**	1.00	1.00 (reference)
Silicon (standard, 2x)	17.2%	1.05	0.71 (competitive)
CIS	16.2%	0.99	0.51 (highly competitive)
CdTe	13.2%	0.80	0.63 (highly competitive)
a-Si (1-j)	8.0%	0.49	1.02 (about the same)
a-Si (3-jj), (or a-Si/nc-Si)	9.8%	0.60	0.83 (competitive)

**Since there is only a marginal performance difference for standard cells using mono- or multi-Si wafers, an "average" champion cell performance of 20.5% was used to calculate standard Si module performance. 12.3% was used for spectrum splitting a-SiGe:H and nc-Si:H multijunctions

Table 2. Anticipated Future Module Efficiency and Relative Cost Based on Today's Demonstrated Champion Cell Performance

Low light-level efficiency values may look better for some modules then for others, but those higher low-light-level efficiencies can be lost after a module is deployed or stressed (Wohlgemuth 2010). Low light-level higher efficiency also affects the energy output differently in different climates. The more overcast the weather, the more important is lasting higher low light-level efficiency. The interactions between climate and energy output poses the question whether PV modules will get a single rating or a deployment site specific rating because modules are sold in STC Watts and revenues are received in terms of energy generated.

7. Notes on reliability and durability of thin-film modules

One of the most frequently questions asked is: How durable is this technology versus longer-established wafer-Si PV technology and whether or not Si PV would be "the

hallmark of stability" as these technologies are sometimes presented. Clearly, there are changes in all technologies, and as modules age or are stressed, transient behavior, power and temperature coefficients will change (Whitaker et al., 1991, del Cueto & von Roedern, 2006, Wohlgemuth, 2010). I sense some reluctance in the testing community to specify accelerated stress conditions, because not all effects and mechanisms for module degradation or failure are known, and because some people in that community hold out the hope that there would be better accelerated stress conditions that would better predict real world performance of modules. What is not realized is that there could also be a value for having standards, and that standard conditions will not reflect real-world conditions or energy generation. For example, the fuel economy of automobiles is based on standard tests, while the prudent driver will know that he or she may not achieve or exceed the standards because of their driving techniques and conditions differ. I advocate that it is the manufacturer's duty to assure durability, and that long-term durability depends to a large degree on whether or not an appropriate manufacturing process was used. Technology related instability problems with any PV technology are currently difficult to identify, and mistakes were made in all technologies leading to the observation of unacceptably high module failure rates. Newer technologies are apt to reveal greater failure rates for a while.

While glass to glass sealed modules are often being produced, glass breakage can lead to increased failures in thin film PV modules. Glass breakage and its mitigation are the topics of much research. Standards are sometimes helpful and sometimes misleading. For example, two sheets of annealed glass laminated with a layer of ethyl vinyl acetate (EVA) can pass the hailstone impact test (a 2.5 cm diameter hailstone impacting at terminal velocity, 23 m/s). This has led many module developers assume that if the hail test can be passed, the mechanical strength was acceptable. Yet, thermally induced glass breakage will occur. Given the observation that glass breakage is not so much a factor for crystalline Si PV modules, the use of partially strengthened or partially tempered glass is strongly recommend to be used for thin-film PV modules.

It is also well established that some forms of PV are much more moisture or oxygen sensitive than other technologies. Sensitivity to ingress of elements can be mitigated by either making the device (solar cell) less sensitive to the penetrating elements, or by better sealing the module package. In practice, both approaches may be used to result in the most cost-effective scheme to increase the durability of a PV module. Glass will not allow penetration of elements and provides a perfect seal, except for the edge glass to glass seal. This may not be the case for flexible schemes where flexible layers have to be used. While flexible opaque materials may provide neccessay low transmission rates and do not pose a glass breakage problem, other issues may become critical when there is a need to use optically transparent barrier foils for flexible PV modules. An early example that the quality of a "package" needs to accommodate the sensitivity of the device was provided when the tested packaging approach used by industry (for a-Si:H-based PV module technology) did not sufficiently protect flexible CIGS modules. In fact, it was determined that the established (a-Si:H) package should be labeled as 'breathable,' as water vapor diffuses rather quickly through Tefzel and EVA. If the device can endure such water vapor transmission, its stability may be acceptable. There are now pilot-quantity flexible transparent barrier materials for niche applications for more sensitive PV technologies (like CIGS) with much lower (and perhaps adequately low) water transmission rates. What is more difficult to evaluate is how those materials compare in terms of cost to glass.

Most systems today are assessed by their energy output. That adds a complication, because in some climates modules with cracked glass may continue to perform well for a number of months or even years. Because glass breakage is very evident, and because these broken modules are not likely to deliver guaranteed powers after many years and may present a safety problem, broken modules may get replaced before they cause a notable power loss. Similar arguments apply to the effect of delamination. If modules get replaced as soon as a visible defect appears, it may become more difficult to assess average long-term stability. An added problem is that it is hard to predict how delamination will progress. One thing to notice is that T-coefficients for power may become smaller negative (or for stabilized a-Si:H- or OPV-based PV even slightly positive) numbers as the modules are being deployed. Smaller than wafer Si PV negative temperature coefficients are typically viewed as something positive, as the derate going from an STC to a real world condition rating decreases. However, if the T-coefficient were to become a less negative number upon deployment, one has to keep in mind that the STC degradation may actually increase more rapidly than the outdoor data might suggest.

The testing community is looking to develop rapid tests that can reliably predict long-term module performance. Such development requires an understanding about all major mechanisms leading to long-term power loss. Only after individual mechanisms are known can there be an assessment how they will respond to acceleration. Then, perhaps more appropriate tests could be developed. In the mean time, much "infant mortality" of PV modules can be avoided by passing qualification tests. For example, when the "wet high potential test" (wet high pot) test was being implemented, modules having defects in the edge seal were identified and eliminated. While the wet high pot test was originally conceived out of safety concerns, it was also useful for eliminating early module failures. Further testing of leakage currents is important, and modules should perhaps be tested not only to the safety standard but rather to the lowest leakage current that can be measured for a specific module configuration. For wafer Si PV modules, much progress with respect to module durability was achieved by passing the JPL "block" tests that later resulted in the appropriate qualification test (e.g., IEC 61215, 61730). However, one should not forget that a module passing qualifications tests may fall below guaranteed (warranted) power in the field while modules that could not pass qualification tests may show acceptable durability upon long-term deployment (Wohlgemuth et al., 2006).

Further (beyond not understanding all mechanisms in detail), the accurate prediction of lifetime details is further encumbered by the statistical nature of the degradation behavior, leading to a spread in the observed data. Hence, rather than testing individual modules, statistically relevant identical module samples have to be assessed. The other issue is that outdoor conditions vary and cannot be in detail predicted. The latter observation poses the question whether module manufacturers will develop modules for specific climates, or whether there will be one product for all climates. Whether or not we will see differentiation in the modules for weather-specific sites will undoubtedly depend on the cost savings encountered if/when climate-specific modules are manufactured. Many industrial items, say automobiles or consumer electronics, are manufactured such that only a single quality standard and product exists. Customers like 'rankings' of items using standardized procedures or tests but do often not realize that if the difference between ranks is less than the uncertainty there may be statistically no difference between those ranks.

There cannot be absolute certainty about the warrantee period until such time has passed. Typical wafer Si PV guarantees given about 20 years ago correctly predicted that such modules or PV arrays would provide on average 80% or more of their initial rating. Today,

typically such power warrantee increased to 80% of minimum rated power output after 25 years. Manufactures give 'competitive' warranties, which in addition to technical reasons define the typical 25-year power warranty period. Since wafer Si PV is providing such guarantees, the competing thin-film PV companies have to do so as well. In the opinion of the author, such warranties will likely be met by many reputable manufacturers. However, the numbers are quite staggering. If in 2010 about 15 GW of PV were sold world-wide and if 1.5 GW of modules installed in 2010 required replacement before 2035 due to low power (assumption: 10% of modules require warranty replacement because of more than the guaranteed power loss has occurred), that is 5 million 300-W modules, and corresponds to the wattage manufactured in 2010 by one of the world's largest PV companies. While no predictions can be made with absolute certainty, it is somewhat likely that all enduring PV modules, including thin-film PV module technologies, will meet or exceed current limited power warranty of 80% after 25 years.

8. Outlook

Future development of PV technologies is uncertain. Table 2 provided the author's current outlook on efficiency and relative costs. It is difficult to project real PV costs far enough into the future. However, Table 2 also shows that projections are possible based on what is known today about specific PV technologies. Table 2 also provides an example of why it is important to make independently verified champion solar cells. "Champion" solar cell efficiency numbers provide historic continuity, as they have served as a "yardstick" to progress within each PV technology. Looking at crystalline Si PV, it is not clear if standard or non-standard approaches will gain or lose market share. Table 2 essentially says that if the cost reduction is proportional to an efficiency decrease, there is no net economical benefit.

Whenever observations do not confirm expectations, it is suggested to question expectations with the same scrutiny as observation (experimental results). The statistical nature of data needs to be realized; it should be always said what is being compared, best, average or worst data. For solar cell efficiencies, this requires an understanding to distinguish between best (champion) and average production efficiencies. Sometimes, advantages and disadvantages of a process change are not pointed out with the same scrutiny. Researchers have to ask themselves whether there should be further optimization of known factors, or if greater progress could be made being guided by unexpected or empirical results. Historic examples exist for new results being developed guided by a flawed theory (e.g., the invention of black powder) or the guidance of a correct theory could lead to unexpected results (Columbus discovering America while searching for a new route to India). It is especially important to keep observations and already established results in mind to avoid unnecessary repetition of experiments. Without this, unfruitful approaches to solar cell development could be tried anew.

It is important to realize the role of material science in this process. On one hand, it is known that higher quality materials can result in higher solar cell performance, while on the other hand it is also known that sometimes the incorporation of "inferior" material layers resulted in champion level efficiency cells. The use of CBD CdS, resistive TCO, and polycrystalline, non-stoichiometric, Na-laden CIGS films on glass rather than single crystal CIGS makes that point. It is well known that solar cell optimization is "interactive," i.e., when one layer in a cell is improved, other layers may need to be reoptimized. For example, when the TCO layer

in an a-Si:H-based solar cells were switched from SnO_2 to ZnO, the p-layer deposition conditions also had to be reoptimized to obtain the highest efficiency solar cell or module after such switch. A fundamental answer has to be found for the following question: Why is a high-lifetime mono-crystalline silicon wafer easily processed into a low efficiency solar cell? In addition, the following question requires an answer: "Is there a single set of parameters defining stabilized champion solar cells, or are multiple combinations of materials and solar cell parameters (V_{OC}, J_{SC}, and FF) capable of reaching champion level cell efficiencies? Recent observation in the case of CIGS solar cells suggests that there could be indeed multiple optima.

The proprietary nature sometimes hurts the development of correct models. For example, to correctly identify the stability mechanisms in solar cells or modules, all processing detail may have to be known. Often, companies do not wish to make such knowledge public. In these instances, it appears most effective to bring together researchers in a conference or workshop setting to discuss as much of a problem as is possible.

It is not clear which technologies will "win" in the long run. Thin films have a cost advantage over crystalline Si, provided the durability is comparable and the performance is high enough. Arguments were presented that the benefit from moving from wafer Si to thin film products can be calculated.

9. Acknowledgement

10. References

Anderson, T.J., Crisalle, O.D. Li, S.S. & Holloway, P.H. (2003). Future CIS Manufacturing Technology Development. NREL/SR-520-33997, see the entire report

Attar, G., Muthaiah, A., Natarajan, H., Karthikeyan, H., Zafar S., Ferekides, C. S. & Morel, D.L. (1994). Development of Manufacturable CIS Processing. *Proceedings of the First World Conference on Photovoltaic Energy*, (Waikoloa, HI, 5.-9.12.1994), pp. 182-185. ISBN 0-7803-1459-X

Catalano, A., D'Aiello, R.V., Dresner, J., Faughnan, B., Firester, A., Kane, J., Schade, H., Smith, Z.E., Swartz, G. & Triano, A. (1982). Attainment of 10% Conversion Efficiency in Amorphous Silicon Solar Cells *Conference Record of the 16th IEEE Photovoltaic Specialists Conference*, (San Diego, CA, 27-30.9.1982), pp. 1421-1422. ISSN 0160-8371

Chambouleyron, I. & Alvarez, F., (1985). Conversion Efficiency of Multiple-Gap Solar Cells under Different Irradiation Conditions. *Conference Record of the 18th IEEE Photovoltaic Specialists Conference*, (Las Vegas, NV, 21-25.10.1985), pp. 533-538. ISSN 0160-8371

Contreras, M.A., Nakada, T., Hongo, M., Pudov, A.O., & Sites, J.R., (2003). $ZnO/ZnS(O,OH)/Cu(In,Ga)Se_2$ Solar Cell with 18.6% Efficiency. *Proceedings of the. 3rd World Conference on Photovoltaic Energy Conversion*, Osaka Japan, paper 2LN-C-08

Cunningham, D.W., Frederick, Gittings, Grammond, Harrer, S., Intagliata, J., O'Connor, N.,Rubcich, M., Skinner, D., & Veluchamy, P., (2002). Progress in Apollo®

Technology. *Conference Record of the 29th IEEE Photovoltaic Specialists Conference,* (New Orleans, 5.19-24.2002), pp. 559-562. ISBN 0-7803-7471-1

Dobson, K., Visoly-Fisher, I., Hodes, G., and Cahen, D. (2000). Stability of CdTe/CdS thin-film solar cells. *Solar Energy Materials and Solar Cells*, 62 (2000) pp. 295-325. ISSN 0927-0248

del Cueto, J.A. & von Roedern, B. (2006). Long-term transient and metastable effects in cadmium telluride photovoltaic modules. *Progress in Photovoltaics: Research & Applications* 14, 615-628. ISNN 1099-159X, (an example for CdTe PV)

Enzenroth, R. A., Barth, K.L. & Sampath, W.S. (2005). Correlation of stability to varied $CdCl_2$ treatment and related defects in CdS/CdTe PV devices as measured by thermal admittance spectroscopy. *Journal of Physics and Chemistry of Solids*, 66 pp. 1883-1886. ISSN 0022-3697

Gabor, A.M., Tuttle, J., Albin, .D.S., Contreras, M.A., Noufi, R., & Hermann, A. M., (1994). High Efficiency $CuIn_xGa_{1-x}Se_2$ Solar Cells made from $In_xGa_{1-x})_2Se_2$ precursor films. *Applied Physic Letters* 65, pp. 198-200. ISSN 0003-6951

Green, M.A., Emery, K., Hishikawa, K.Y. & Warta, W. (2011). Solar Cell Efficiency Tables (version 37). *Progress in Photovoltaics: Research and Applications 19*, pp. 84-92. ISSN 1099-159X. In some instances, results from earlier such tables or results from the "notable exceptions" tables are used

Guha, S., Yang, J., Pawlikiewicz, A., Glatfelter, T., Ross, R. & Ovshinsky S.R. (1988). A Novel Design for Amorphous Silicon Solar Cells. *Conference Record of the 20th IEEE Photovoltaic Specialists Conference*, (Las Vegas, NV, 26-30.9.1988), pp. 79-84. ISSN 0160-8371

Izu, M., Deng, X., Krisko, A., Whelan, K., Young, R., Ovshinsky, H. C., Narasimhan, K. L. & Ovshinsky, S. R., (1993). Manufacturing of Triple-Junction 4 ft² a-Si Alloy PV Modules. *Conference Record of the 23rd IEEE Photovoltaic Specialists Conference*, (Louisville, KY, 10-14.5.1993), pp. 919-925. ISBN 0-7803-1220-1

Kuwano, Y., Ohniishi, Nishiwaki, H., Tsuda, S., Fukatsu, T., Enomoto, K., Nakashima, Y., and Tarui, H., (1982). Multi-Gap Amorphous Si Solar Cells Prepared by the Consecutive, Separated Reaction Chamber Method. *Conference Record of the 16th IEEE Photovoltaic Specialists Conference*, (San Diego, CA, 27-30.9.1982), pp. 1338-1343. ISSN 0160-8371

Lee, Y., Jiao, L. H., Liu, H., Lu, Z., Collins, R.W. & Wronski, C. R., (1996). Stability of a-Si :H Solar Cells and Corresponding Intrinsic Materials Fabricated Using Hydrogen Diluted Silane. *Conference Record of the 25th IEEE Photovoltaic Specialists Conference,* (Washington, DC, 13-17.5.1996), pp. 1165-1168. ISBN 0-7803-3166-4

Luft, W., Stafford, B., von Roedern, B., & DeBlasio, R. (1992). Preospects of amorphous silicon photovoltaics. *Solar Energy Materials and Solar Cells*, 26, pp. 17-26. ISSN 0927-0248

Luysberg, M., Scholten, C., Houben, L., Carius, R., Finger, F. & Vetter, O., (2001). Structural Properties of Microcrystalline Si Solar Cells. *Materials Research Society Symposia Proceedings* 664, pp. A15.2.1-6. ISBN 1-55899-600-1

McCandless, B. E., (2001). Thermochemical and Kinetic Aspects of Cadmium Telluride Solar Cell Processing. *Materials Research Society Symposia Proceedings* 668 (San Francisco, CA 16-20.4.2001), pp. H1.6.1-12. ISBN 1-55899-604-4

Noufi, R., (2010). Private communication

Platz, R., Pellaton Vaucher, N., Fischer, D., Meier, J. & Shah, A., (1997). Improved Micromorph Tandem Cell Performance through Enhanced Top Cell Currents. *Conference Record*

26th IEEE Photovoltaic Specialists Conference, (Anaheim, CA, 29.9-3.10.1997), pp. 691-694. ISBN 0-7803-3767-0

Schmid, D., Ruckh, M., Grunwald, F. & Schock, H.W. (1993). Chalcopyrite/defect chalcopyrite heterojunctions on the basis of CuInSe2. *Journal of Applied Phys*ics 73, pp. 2902-2909. ISSN 0021-8979

Shah, A., Sauvain, E., Wyrsch, N., Curtins, H., Leutz, B., Shen, D. S., Chu, V., Wagner, S., Schade, H. & Chao, H. W. A. (1988). a-Si:H Films Deposited at High Rates in 'VHF' Silane Plasma : Potential for Low-Cost Solar Cells. *Conference Record of the 20th IEEE Photovoltaic Specialists Conference,* (Las Vegas, NV 26-30.9.1988), pp. 282-287. ISSN 0160-8371

Tarrant, D.E. & Gay, R. R., (1995). Research on High-Efficiency, Large-Area CuInSe2-Based Thin-Film Modules, NREL/TP-413-8121. The fabrication sequence of Siemens Solar is shown on pages 2 & 3 in Figures 2 & 3

Todorov, T. K., Reuter, K.B. & Mitzi, (2010). High Efficiency Solar Cell with Earth-Abundant Liquid-Processed Absorber. *Advanced Materials* 22, pp. E156-159. ISSN 1121-4095.

Townsend, S.W., Ohno, T.R., Kaydanov, V., Gilmore, A.S., Beach, J.D. & Collins, R.T. (2001). The Influence of Stressing at Different Biases on the Electrical and Optical Properties of CdS/CdTe Solar Cells.. *Materials Research Society Symposia Proceedings* 668 (San Francisco, CA 16-20.4.2001), pp. H5.11.1-6. ISBN 1-55899-604-4

von Roedern, B. & del Cueto, J.A. (2000). Model for Staebler-Wronski Degradation Deduced from Long-Term, Controlled Light-Soaking Experiments. *Matarials Research Society Symposia Proceedings* 609, (San Francisco, CA24-28.4.2000), pp. A10.4.1-6. ISBN 1-55899-517-X

Wanlass, M.W. & Albin, D.S., (2004). A Rigerous Analysis of Series-Connected, Multi-Bandgap, Tandem Thermophotovoltaics (TPV) Energy Converters. *Proceedings of the 6th Conference on Thermophotovoltaic Generation of Electricity,* (Freiburg, Germany 14-16.6.2004), American *Institute of Physics Conference Proceedings* 738, pp. 462-470. ISBN 0-7354-02221

Whitaker, C.M., Townsend, T. U., Wenger, H. J., Illiceto, A., Chimento, G. & Paletta, F. (1991). Effects of Irradiance and Other Factors on PV Temperature Coefficients. *Conference Record of the 22nd IEEE Photovoltaic Specialists Conference*, (Las Vegas, NV 7-10.10.1991), pp. 608-613. ISBN 0-87942-635-7

Yan, B., Yue, G. & Guha, S., (2007). Status of nc-Si :H Solar Cells at United Solar and Roadmap for Manufacturing a-Si :H and nc-Si :H Based Solar Panels. *Materials Researchy Society Symposia Proceedings* 989 (San Francisco, CA, 9-13.4.2007), pp. 335-346. ISBN 978-1-55899-949-7

von Roedern, B. (2006). Thin Film PV Module Review. *Refocus magazine (Elsevier) (July + August 2006)* pp. 34-36. ISSN 1471-0846

Wohlgemuth, J.H. (2010). private communication

Wohlgemuth, J.H., Cunningham, D.W., Monus, P., Miller, J. & Nguyen, A., (2006). Long- term reliabilty of photovoltaic modules. *Conference Record of the 2006 IEEE 4th World Conference on Photovoltaic Energy Conversion* (Waikoloa, HI 7-12.5.2006), pp. 2050-2053. ISBN 1-4244-0017-1

Spectral Effects on CIS Modules While Deployed Outdoors

Michael Simon and Edson L. Meyer

Fort Hare Institute of Technology, University of Fort Hare
South Africa

1. Introduction

The effect of spectral distribution on the performance of photovoltaic (PV) modules is often neglected. The introduction of multi-junction devices such as Copper Indium Diselenide (CIS) necessitated a concerted investigation into the spectral response on these devices. In part this attributed to the wider spectral response resulting from a combination of different energy band gaps. This in turn implies that the device should have a relatively lower dependence on outdoor spectral content, which depends on a number of factors such as year time, location, day time and material composition in the atmosphere.

The availability of outdoor spectral data, which in most cases is not available, allows for the evaluation of the outdoor response of the CIS technology as the spectrum shifts during the course of the day, during cloud/clear sky condition and seasons. This study reports on the effect of outdoor spectrum, which is different from the reference AM 1.5, on the CIS performance parameters.

2. Different outdoor methodologies currently adopted

2.1 The concept of average photon energy

In trying to quantify the 'blueness' or 'redness' of outdoor spectrum, Christian *et. al.* adopted the concept of Average Photon Energy (APE) as an alternative (Christian et al., 2002). He defined APE as a measure of the average hue of incident radiation which is calculated using the spectral irradiance data divided by the integrated photon flux density, as in equation 1.

$$APE = \frac{\int_a^b E_i(\lambda)d\lambda}{q_e\int_a^b \Phi_i(\lambda)d\lambda} \tag{1}$$

where :
q_e	=	electronic charge
$E_i(\lambda)$	=	Spectral irradiance
$\Phi_i(\lambda)$	=	Photon flux density

As an indication of the spectral content, high values of average APE indicate a blue-shifted spectrum, whilst low values correspond to red shifted spectrum. Although this concept at

first approximation characterizes the spectral content at a particular time-of-the day, no direct feedback of the device information is obtained since it is independent of the device. The concept of Average Photon Energy (APE) has also been adopted to illustrate the seasonal variation of PV devices (Minemoto et al., 2002; Christian et al., 2002).

2.2 The Air Mass concept

The mostly commonly adopted procedure (Meyer, 2002; King et al., 1997) is to calculate the Air Mass (AM) value at a specific location and relate the module's electrical parameters. It is standard procedure for PV manufacturers to rate the module's power at a specific spectral condition, AM 1.5 which is intended to be representative of most indoor laboratories and is not a typical spectral condition of most outdoor sites. The question that one has to ask is, why then is AM 1.5 spectrum not ideal? What conditions were optimized in the modeling of AM 1.5 spectra? What are the cost implications on the customer's side when the PV module is finally deployed at spectra different from AM 1.5?

The modeled AM 1.5 spectrum commonly used for PV module rating was created using a radiative transfer model called BRITE (Riordan et al., 1990). The modeled conditions used for example the sun-facing angle, tilted 37º from the horizontal, was chosen as average latitude for the United States of America. The 1.42 cm of precipitable water vapor and 0.34 cm of ozone in a vertical column from sea level are all gathered from USA data. Ground reflectance was fixed at 0.2, a typical value for dry and bare soil. In principle this spectra is a typical USA spectrum and therefore makes sense to rate PV modules which are to be deployed in USA and the surrounding countries.

AM is simply defined as the ratio of atmospheric mass in the actual observer - sun path to the mass that would exist if the sun was directly overhead at sea level using standard barometric pressure (Meyer, 2002). Although the concept of AM is a good approximation tool for quantifying the degree of 'redness' or 'blueness' of the spectrum, the major draw back is that it is applied under specific weather conditions, i.e., clear sky, which probably is suitable for deserts conditions.

2.3 The spectral factor concept

Another notion also adopted to evaluate the effect of outdoor spectrum, is the concept of Spectral Factor. As described by Poissant (Poissant et al., 2006), Spectral Factor is defined as a coefficient of the short-circuit current (I_{sc}) at the current spectrum to the short-circuit current at STC (I_{STC}).

$$m_t = \frac{I_{sc}}{I_{STC}} \cdot \frac{\int_{\lambda_1}^{\lambda_2} E_{STC}(\lambda)d\lambda}{\int_{\lambda_1}^{\lambda_2} E(\lambda)d\lambda} \tag{2}$$

From equation 2, the I_{sc} and the I_{STC} is obtained using the equation 3 and 4 respectively.

$$I_{sc} = \int_{\lambda_1}^{\lambda_2} E(\lambda)R_t(\lambda)d\lambda \tag{3}$$

$$I_{STC} = \int_{\lambda_1}^{\lambda_2} E_{STC}(\lambda)R_t(\lambda)d\lambda \tag{4}$$

where: $E(\lambda)$ = Irradiance as function of wavelength
                $E_{STC}(\lambda)$ = Irradiance at STC
                $R(\lambda)$ = Reflectivity

The spectral factor quantifies the degree of how the solar spectrum matches the cell spectral response at any given time as compared to the AM1.5 spectrum.

2.4 The useful fraction concept

With regard to changes in the device parameters, the concept of Useful Fraction used by Gottschalg et al (Gottschalg et al., 2003) clearly demonstrates the effect of varying outdoor spectrum. Useful fraction is defined as the ratio of the irradiance within the spectrally useful range of the device to the total irradiance.

$$UF = \frac{1}{G}\int_0^{E_g} G(\lambda)S(\lambda)d\lambda \tag{5}$$

Where E_g is the band-gap of the device (normally the cut - off wavelength) and G is the total irradiance determined as:

$$G(\lambda) = \int_0^{\lambda_{cut-off}} G(\lambda)d\lambda \tag{6}$$

where $G(\lambda)$ is the spectral irradiance encountered by a PV cell.

3. Methodology used in this study

Before the CIS module was deployed outdoors, the module underwent a series of testing procedures in order to establish the baseline characteristics. Visual inspection was adopted to check for some physical defects e.g. cracks, and incomplete scribes due to manufacturing errors. Infrared thermography revealed that no hot spots were present before and after outdoor exposure. These procedures were used to isolate the spectral effects with respect to the performance parameters of the module. To establish the seasonal effects on the module's *I-V* curves, three *I-V* curves were selected. One *I-V* curve for a winter season and the 2nd *I-V* curve for summer season were measured. The 3rd *I-V* curve was used to establish whether the module did not degrade when the winter curve was measured. All curves were measured at noon on clear days so that the effect of cloud cover would be negligible. For accurate comparison purposes all *I-V* curves had to be normalized to STC conditions so that the variations in irradiance and temperature would be corrected. Firstly the I_{sc} values were STC corrected by using equation 1 (Gottschalg et al., 2005).

$$I_{sc} = \left(\frac{I_{sc}}{G} \times 100\right) + \left(25 - T_{module}\right) \times \alpha \tag{7}$$

where a is the module temperature coefficient [A/oC].

Each point on the *I-V* curve had to be adjusted according to equation 8.

$$I_2 = I_1 + I_{sc} \times \left[\left(\frac{1000}{G} \right) - 1 \right] + \alpha \left(25 - T_{module} \right) \tag{8}$$

where: I_1 =   measured current at any point
           I_2 =   new corrected current
           G =   measured irradiance

The corresponding voltage points were also corrected according to equation 9.

$$V_2 = V_1 - R_s \times \left(I_2 - I_1 \right) + \beta \times \left(25 - T_{module} \right) \tag{9}$$

where: V_1 =   measured voltage at a corresponding point for I_1
           R_s =   internal series resistance of the module [Ω]
           β =   voltage temperature coefficient of the module [V/°C]
           V_2 =   new corrected voltage

The outdoor spectrum was also measured for winter and summer periods in order to compare them for possible changes in the quality of the two spectra (figure 5). With regard to changes in the device parameters, the concept of Weighted Useful Fraction (WUF) (Simon and Meyer, 2008; Simon and Meyer, 2010) was used to clearly demonstrate the effect of varying outdoor spectrum. This concept was developed due to some limitations noted with other outdoor spectral characterization techniques (Christian et al., 2002).

The methodology used by Gottschalg et al (Gottschalg et al, 2002) makes use the assumption that the energy density (W/m²/nm) within the spectral range of the device at a specific wavelength is totally absorbed (100%). But in reality the energy density at a specific wavelength has a specific absorption percentage, which should be considered when determining the spectral response within the device range. It was therefore necessary to introduce what is referred to as the Weighted Useful Fraction (WUF) (Simon and Meyer, 2008; Simon and Meyer, 2010).

$$WUF = \frac{1}{Gtot} \int_0^{E_g} G(\lambda) d(\lambda) SR(\lambda) \tag{10}$$

where: $G(\lambda)$ is the integrated energy density within device spectral range with its corresponding absorption percentage evaluated at each wavelength.

As a quick example, at 350 nm for a-Si device, its corresponding energy density (W/m²/nm) is 20% of the irradiance (W/m²) received which contribute to the electron-hole (e-h) creation and for mc-Si at the same wavelength, 60% is used to create e-h pairs. But the concept of Useful Fraction considers that at each wavelength, all the energy received contributes to the e-h, which is one of the short comings observed from this methodology. The idea of using Weighted Useful Faction was to address these short falls which tend to over estimate the overall device spectral response.

The data obtained using the concept of Weighted Useful Fraction represents a statistical phenomenon of occurrences. Therefore the Gaussian distribution as a statistical tool was used to interpret the data simply because of a mathematical relationship (Central Limit Theorem). In this case the theorem holds because the sample is large (major condition of the theorem) and therefore the Gaussian distribution is suitable to be applied. In this study, the

3rd parameter Gaussian distribution function was used to describe the distribution pattern and to accurately determine the variance of points from the peak value (central value). The peaks of the Gaussian distribution was obtained by firstly creating frequency bins for the WUF and determine the frequency of the points in each bin expressed as a percentage. The bins were imported into SigmaPlot 10 and the peak 3rd Gaussian distribution function was used to accurately generate the peak WUF. Figure 1 illustrates the frequency distribution bins for a-Si:H module.
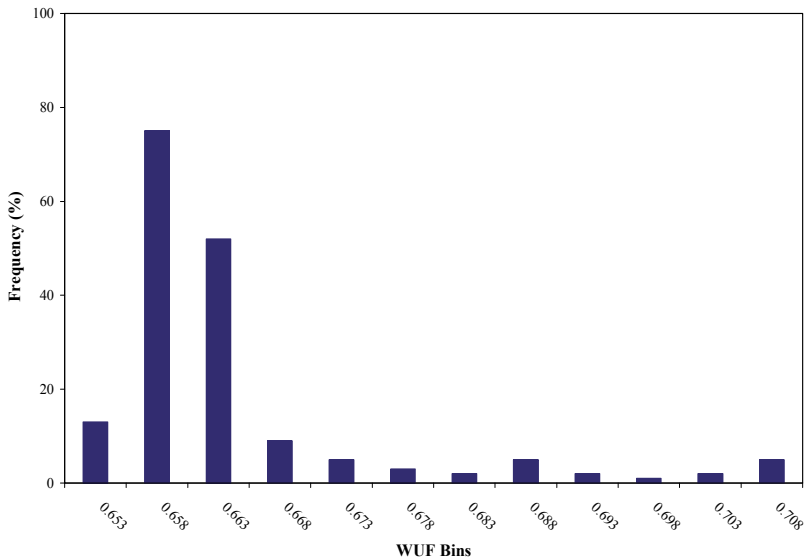

Fig. 1. Frequency distribution of WUF for a-Si:H module

Evident from figure 1 is an increase in WUF frequency at specific WUF value. This percentage frequency represents the number of data points measured at a specific WUF during the study period.

The centre of the points, which corresponds to the spectrum the device "prefers" most, was obtained using the peak Gaussian distribution of the form:

$$f = a\exp\left[-0.5\left(\left(x - x_o\right)/b\right)^2\right] \tag{11}$$

where: a = highest frequency
            x = WUF value
            x_o = WUF centre value
            b = deviation (2σ)

Figure 2 illustrates a typical Gaussian distribution used to accurately determine the mean Weighted Useful Fraction.

Also illustrated is the width of the distribution as measured by the standard deviation or variance (standard deviation squared = σ^2). In order to interpret the results generated from each Gaussian distribution, two main terminologies had to be fully understood so that the results have a physical meaning and not just a statistical meaning. The standard deviation (σ) quantifies the degree of data scatter from one another, usually it is from the mean value.

In simple statistics, the data represented by the Gaussian distribution implies that 68% of the values (on either side) lie within the 1st standard deviation (1σ) and 95% of the values lie within the 2nd standard deviation. The confidence interval level was also analyzed when determining the mean value. The confidence interval quantifies the precision of the mean, which was vital in this analysis since the mean represents the WUF spectrum from which the devices responds best during the entire period of outdoor exposure. The increase in standard deviation means that the device spends less time on the corresponding WUF spectrum. Ideally it represents the error margin from the mean value. The percentage frequency value corresponding to the mean WUF value represents the percentage of the total time of outdoor exposure to which the device was responding best to that spectrum.
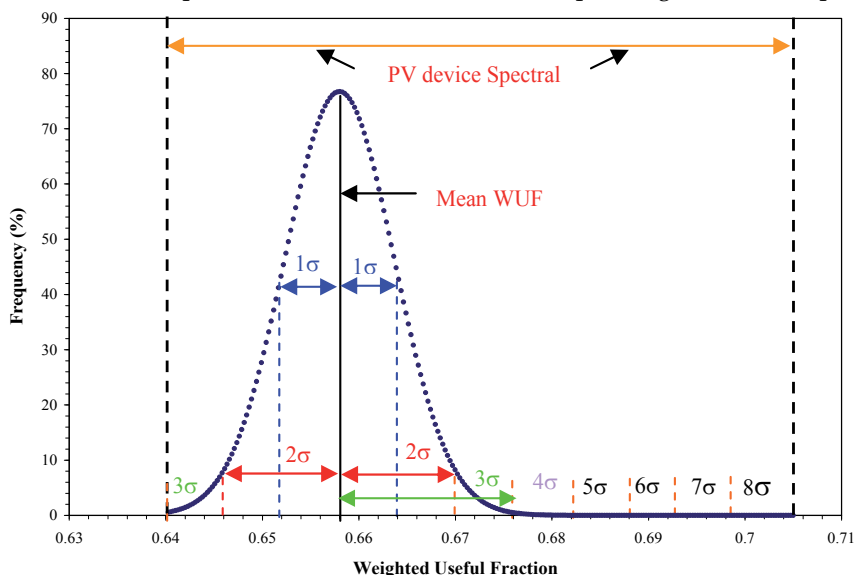

Fig. 2. Illustration of Gaussian distribution used to determine the mean WUF.

Depending on how the data is distributed, the Gaussian curve 'tails' differently from each side of the mean value. The increase in σ in this case reveals two crucial points regarding the statistical data in question. Firstly, it quantifies the total time spent at a specific spectrum as the σ increases during the entire period of monitoring. Secondly it reveals the entire spectral range to which PV devices respond. From figure 2, the standard deviation increases from 1σ to 8σ on one side of the mean WUF and from the other side varies from 1σ to 3σ. The total range of the WUF is from 0.64 to 0.7 although it spends less time from spectral range where standard deviation σ is greater than a unit. A high confidence level of each Gaussian distribution indicates the accuracy of the determined mean. All results presented in this work showed a high confidence level.

Normalization of I_{sc} was achieved by dividing the module's I_{sc} with the total irradiance within the device spectral range ($G_{Spectral\ Range}$). The commonly adopted correlation existing between the module's I_{sc} and back-of-module temperature is of the form $I_{sc} = (C_0 + C_1 T_{device}) \times G_{SpectralRange}$ (Gottschalg et al., 2004). Firstly, the relationship between $I_{sc}/G_{SpectralRange}$ (which is referred to as $\varphi_{SpectralRange}$ from this point onwards) is plotted against back-of-module temperature. The empirical coefficient C_0 and C_1 are obtained. The second

aspect is to plot $\varphi_{SpectralRange} \div (C_o + C_1 T_{device}) = f(WUF)$ versus the Weighted Useful Fraction (WUF), from which the predominant effect of the spectrum can be observed and analyzed. Due to a large number of data obtained, all results analyses were made using only data corresponding to global irradiance (G_{global}) > 100 W/m². This was done to reduce scatter without compromising the validity of the results

4. Results and discussion

Although the outdoor parameters might 'mimic' the STC conditions, the performance of the PV device will not perform to that expectation. By analyzing the effect of outdoor environment, the spectrum received is largely influenced by solar altitude and atmospheric composition, which in turn affect device performance.

Figure 3 illustrates the seasonal effects on the CIS module current-voltage *(I-V)* characteristics when deployed outdoor, first on 31 January 2008 and later on 12 June 2008.

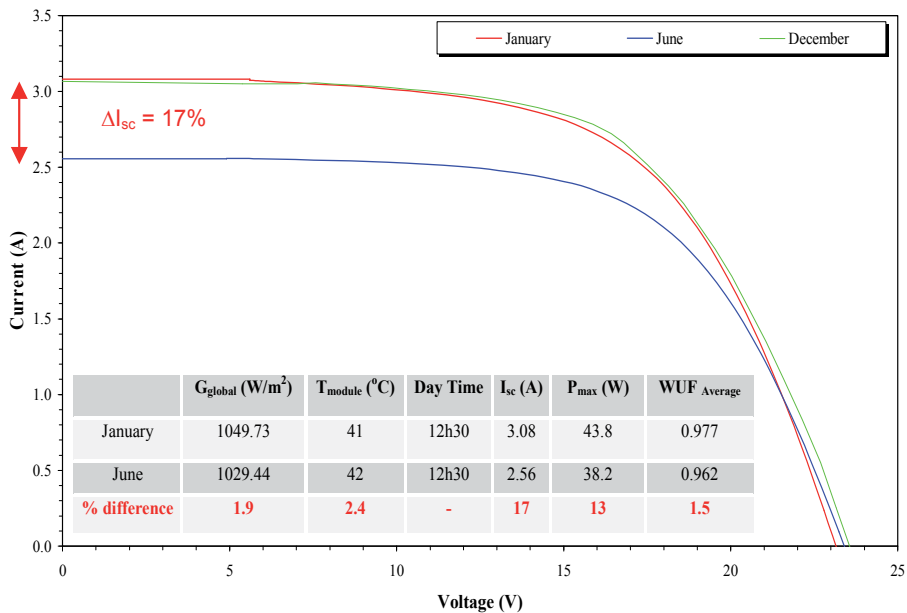|	G_{global} (W/m^2)	T_{module} (^{o}C)	Day Time	I_{sc} (A)	P_{max} (W)	WUF $_{Average}$
January	1049.73	41	12h30	3.08	43.8	0.977
June	1029.44	42	12h30	2.56	38.2	0.962
% difference	1.9	2.4	-	17	13	1.5

Fig. 3. Comparison of the CIS I-V characteristics for a typical summer clear sky and winter clear sky. The accompanying table lists the conditions before corrections to STC.

The January *I-V* curve was taken a few days after deployment of the modules while operating at outdoor conditions. Two aspects needed to be verified with this comparative analysis of the I-V curves for that time frame: Firstly the state of the module, i.e. whether it did not degrade within this time frame needed to be ascertained so that any effect on device I_{sc}, FF and efficiency would be purely attributed to spectral effects. Secondly, this was done to see the effect of seasonal changes on the *I-V* characteristics. Since the outdoor conditions are almost the same when the measurements were taken, the I-V curves were normalized to STC conditions using the procedure mentioned in section 2. Since the 3 *I-V* curves had been corrected for both temperature and irradiance, therefore any

modification or changes on the I_{sc} values is purely due to spectral effect. The difference in module's I_{sc} is largely attributed to the outdoor spectral composition, which as have been mentioned earlier on, depends on season and time of the year amongst other factors. The CIS module was also simulated using Solar Studio Design. At each AM value, the module's *I-V* curve was obtained. Figure 4 illustrates the effects on the simulated CIS *I-V* curves as the Air Mass was varied.
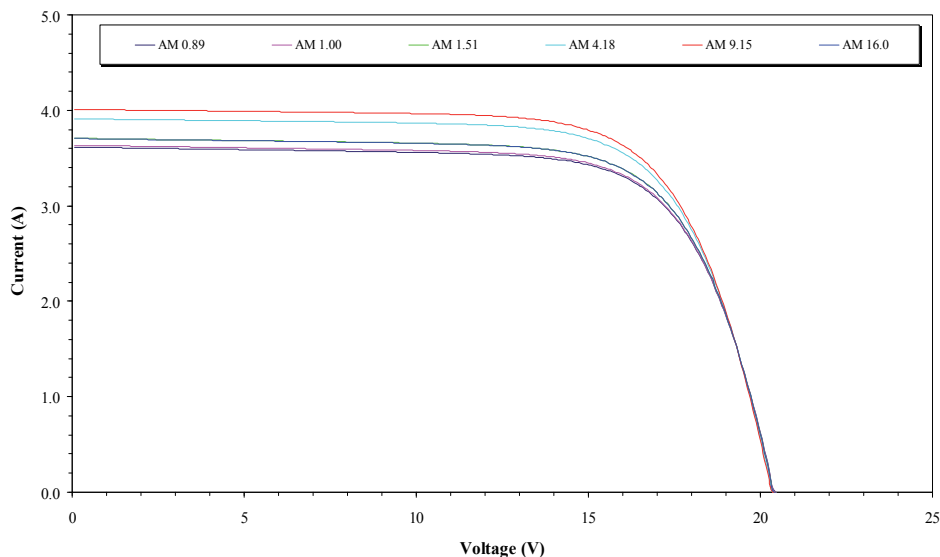

Fig. 4. The effect of varying Air mass on the simulated CIS module.

The change in outdoor spectrum as characterized by the AM values affect the module's *I-V* curves, mostly the I_{sc}. Although this module is rated at STC using the AM1.5 spectrum, the CIS module is performing less at AM1.5 as compared to AM 9.15. The *I-V* curve at AM 1.5 coincides with the *I-V* curve at AM 16.0. It should be noted that the change in AM value is an indication of the spectral content dominating. The $\Delta I_{sc} = 7.5\%$ difference between I_{sc} at AM 1.5 and I_{sc} at AM 9.15 is purely due to spectral changes. Returning back to figure 1, the difference in I_{sc} between winter and summer spectrum is due to spectral changes. The typical winter and summer spectra were compared with the view of finding any variation in the profiles. All values were divided by the highest energy density in each curve so as to normalize them. Figure 5 presents the normalized spectral distribution corresponding to the two *I-V* curves in figure 3.

Clearly there is a difference in the spectral content primarily due to the difference in solar altitude and hence air mass. In the absence of the device degradation, similar irradiance and module temperatures, the reduction in module performance is attributed to the difference in spectral distribution associated with the seasonal variation. To further verify whether indeed the reduction in the module's I_{sc} was due to spectral changes associated with seasonal changes, the device WUF for the entire year was analyzed. The monthly average WUF was considered to be sufficient to provide evidence, if any in its profile. Figure 6 shows the evolution of the monthly average WUF of the CIS module.
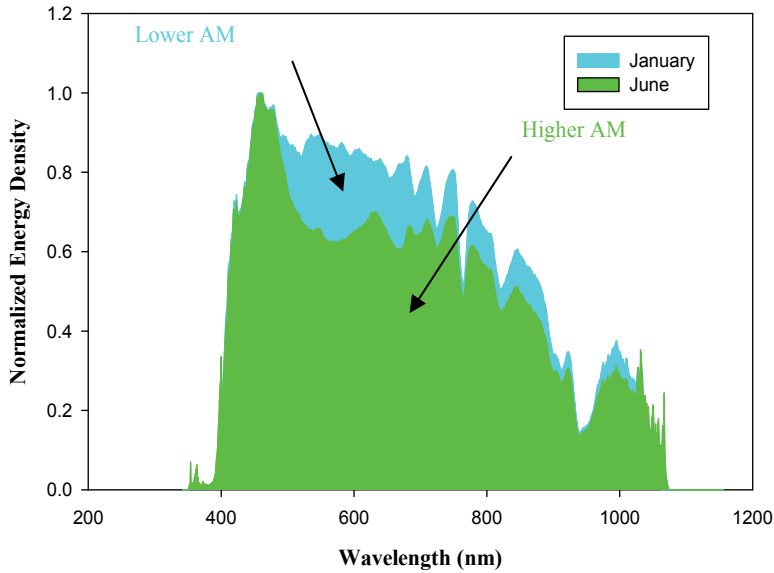
Fig. 5. Normalized spectral distribution for January and June months.
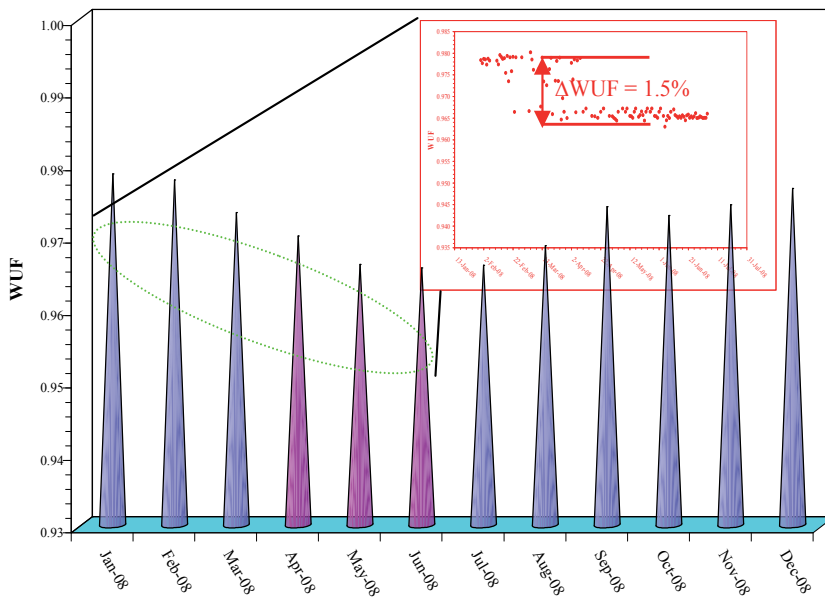

Fig. 6. Evolution of daily average Weighted Useful Fraction versus timeline. Inset is an average daily profile for the period from January to June 2008.

Evident from figure 6 is the high values of CIS WUF for the entire period which indicates that the device performs well under full spectrum. Taking the average values of the upper

(summer) and the lower for winter, a 1.5% drop in WUF is noticed (inset figure). A small change in WUF results in large change of the device's I_{sc}. In order to verify this assumption, the change in WUF versus Air Mass was established as is presented in figure 7.
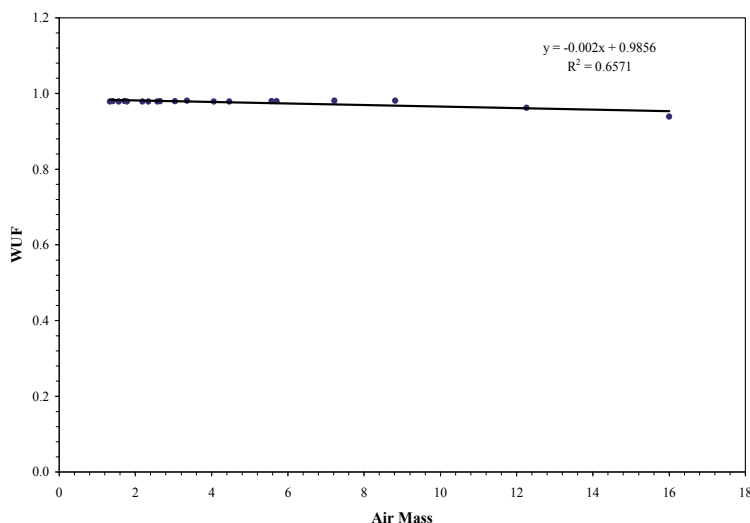

Fig. 7. Influence of the air mass on device spectral variations as characterized by WUF for CIS module.

The relationship established in figure 7 was used to calculate the change in WUF at different Air Mass values, a typical change in season. Values for low air mass (indication of a summer spectrum) and high air mass (indication of winter) were used to calculate the % change in WUF and later compared to the simulated % change in I_{sc} at different AM values, the same values that has been used in previous calculation. Equations 12 and 13 illustrate the equations used for this calculation.

$$WUF_{1.0} = -0.002 \times AM1.0 + 0.9856 \tag{12}$$

$$WUF_{9.15} = -0.002 \times AM9.15 + 0.9856 \tag{13}$$

where: $WUF_{1.0}$ is the calculated value of WUF at AM 1.0 and the $WUF_{9.15}$ is the calculated value of WUF at AM 9.15.

From figure 4 the value for I_{sc} (AM 1.0) and I_{sc} (AM 9.15) were used to calculate the % change in I_{sc} as the spectrum changes. The $\Delta WUF = WUF_{1.0} - WUF_{9.15}$ expressed as a %, was found to be 1.66%, while the $\Delta I_{sc} = 11.88\%$. From this analysis, one can conclude that a small % change in ΔWUF result in large % difference of the module's I_{sc}, which explains the 17% decrease in I_{sc} due to a ΔWUF of 1.5%. The slight difference in the two results is due to the difference in the actual operating conditions in which case the simulated conditions are different from the actual conditions when the two I-V curves in figure 4 were measured.

A 10 point moving average was applied so that a clear correlation can be seen. By fitting a 3rd order polynomial fit, a functional relationship between FF and WUF is observed. The FF of the device is an indication of the series and junction quality of the device cells; therefore

by plotting the FF with WUF a functional relationship can be established. Figure 8 shows the slight increase in FF as the WUF varies.
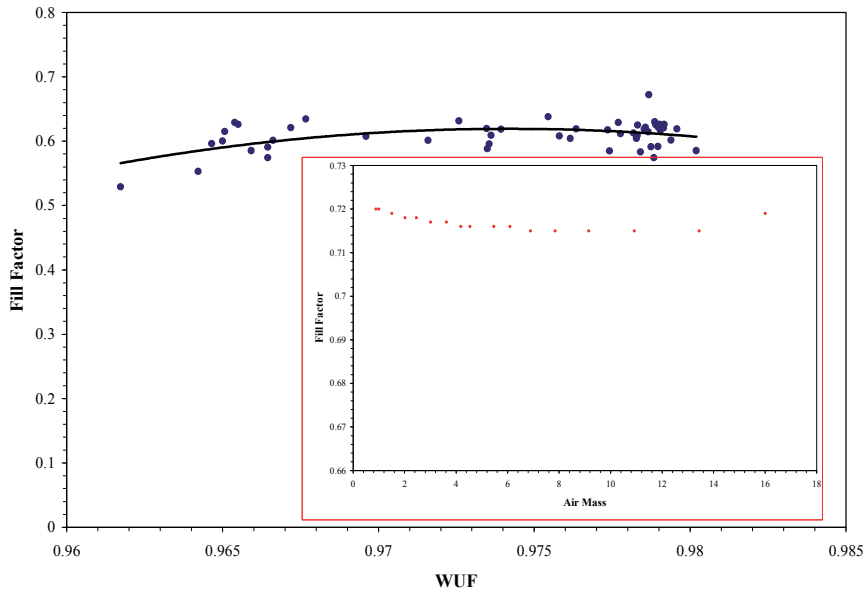

Fig. 8. Effect on CIS average Fill factor due to outdoor irradiance and spectral changes. Inset is the variation of FF vs. Air Mass for the same device.

Observed from figure 6, a 6.5% increase in FF is observed within the WUF range 0.960 - 0.983 (considering the % difference between the averages of the upper and low values of the FF). It should however be noted that this percentage increase value is just an indication of the change in FF. The increase in FF as observed is attributed to the quality of the spectrum dominating which result in 'supplying' sufficient energy for the electron-hole creation, with less energy losses, which in most cases is dissipated as heat. From the inset figure, a decrease in FF as AM values increase from AM 1.5 is evident. Closely analyzing the two graphs, the spectrum dominating under the WUF range of the CIS module is a blue rich spectrum which explains a slight increase in FF. From the inset figure, the FF is higher at AM 1.5 and decrease as the spectrum becomes longer wavelength dominated. Clearly the change in outdoor spectrum has an effect on the FF of the CIS module. Often reported is the relationship between efficiency and global irradiance as measured by the pyranometer. For CIS module, the variation of aperture efficiency with WUF is visible described by a logarithmic fit into the scattered data. Both WUF and irradiance affect device performance with the same magnitude. Gottschalg et al., (Gottschalg et al., 2004) established a relationship for device aperture efficiency and Useful Fraction (UF). The efficiency is described by $\eta \approx \frac{\alpha}{A} UF$ which when interpolated to our concept of Weighted Useful Faction (WUF) the device efficiency would be described by $\eta \approx \frac{\alpha}{A} WUF$: where $\alpha = Power(P)/Spectral \operatorname{Re} sponsiveRange(UI)$, is roughly a constant. This relationship exhibit a

linear trend of efficiency with WUF in our case. The other key performance indicator in PV analysis is the device aperture efficiency. The efficiency of CIS module was also analyzed using the same procedure for FF analysis. Figure 9 indicate the efficiency versus WUF of the CIS device.
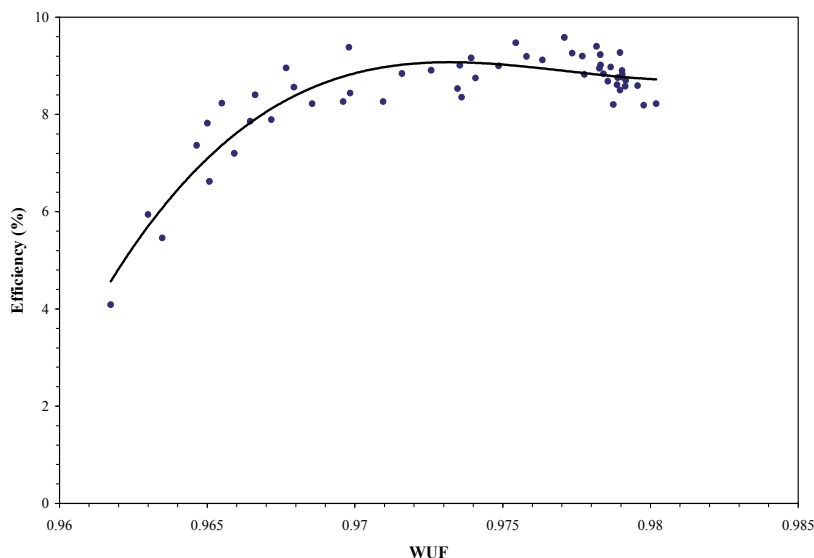

Fig. 9. Correlation between aperture efficiency versus outdoor WUF of the CIS module.

The efficiency increases logarithmically with an increase in Weighted Useful fraction (WUF > 0.960), which do not agree with the theoretical relationship illustrated in the previous section ($\eta \approx \frac{\alpha}{A} WUF$). One can attribute this discrepancy of the measured data and theory as follows: The α in the equation above is assumed to be a constant, but in actual fact it is strongly dependant on the irradiance available within the denominator function (UI). The irradiance within the Responsive Spectral Range (UI) is assumed to be a constant, a single value to be precise. In reality the irradiance does fluctuates within this range, rendering the α not to be a constant parameter. However the device efficiency exhibits a logarithmic increase as a function of WUF, due to the irradiance variations, resulting in α not to be a constant. The effect of season on device efficiency was also investigated; the results are shown in figure 10.

It is observed from figure 10 that the device efficiency is stable for both summer and winter. The PV module's performance parameters e.g. I_{sc}, V_{oc}, FF and η are characterized by what is referred to as temperature coefficients. Temperature coefficient is described as the rate of change (derivative) of the parameter with respect to the temperature of the PV device performance parameters (King et al., 1997). For PV system sizing and design, knowing the device temperature coefficient plays a very critical role. Quantifying the spectral effects on its own has proved to be a challenge; as a result no temperature coefficient with respect to outdoor spectrum has been documented. In figures 11 and 12, the relationship between outdoor spectral effects (WUF) and the average back - of module temperature is presented. Using a linear fit to the data, a spectral temperature coefficient is obtained. Figure 11 illustrates the relationship between WUF and temperature for a winter period.
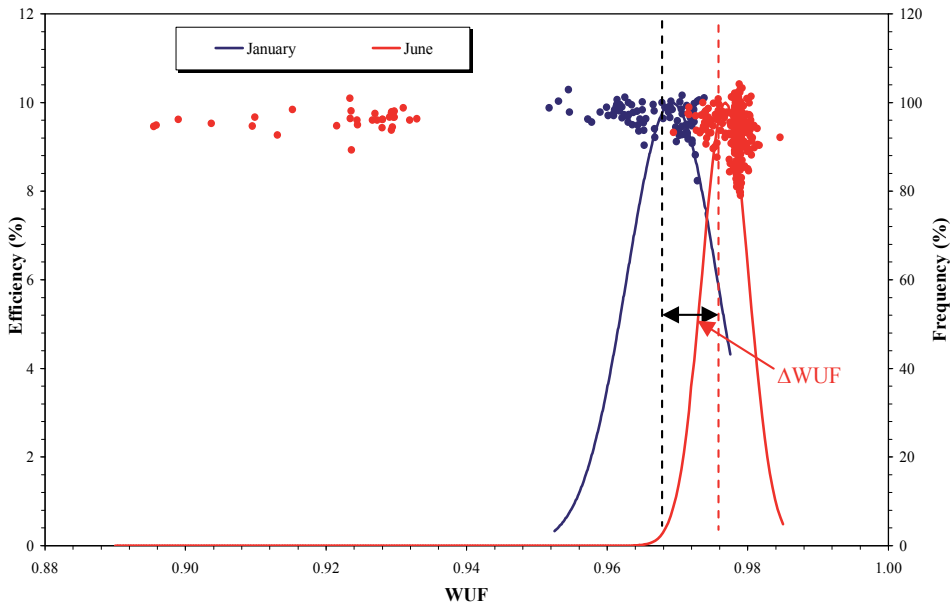
Fig. 10. Average outdoor aperture efficiency as a function of WUF of CIS module for both winter and summer period.
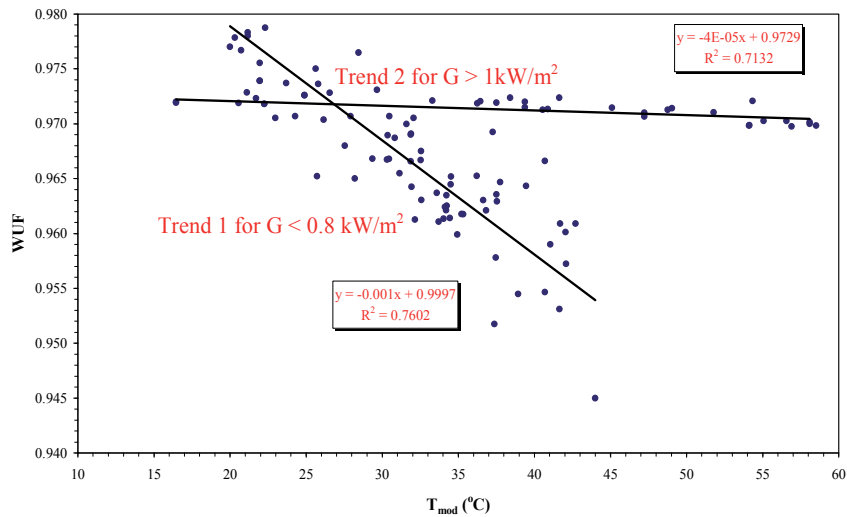

Fig. 11. Relationship between the outdoor WUF and back of module temperature of the CIS module during winter period.

Observing the results in figure 11, two temperature coefficients for WUF are obtained during the winter period. This trend in behavior could have been attributed to the different outdoor weather patterns observed for winter period. Some days even during winter, the outdoor climatic conditions would resemble a typical clear sky summer season, indicated by

very high temperature (indicated by trend 2), while the rest of the days would be for typical winter season, normally characterized by mostly low temperature. In both cases, a negative WUF temperature coefficient is observed, with trend 1 being -0.001/^{o}C and for trend 2 being -0.4×10^{-5}/^{o}C.

The same procedure was also used to find the effect of temperature on WUF for summer months of CIS module. Figure 12 shows the WUF versus temperature relationship.

Interesting to note from figure 12 is that the spectral effect temperature coefficient for summer period is the same as the one obtained during winter, clear sky (trend 2) although for summer the highest temperature reached was above 60°C while for trend 2 (figure 11), the highest was less than 60°C. From the two figures, it has been shown that temperature coefficient due to spectral effect (WUF$_\beta$) can be obtained once the outdoor spectrum data for a device is correctly calculated using the Weighted Useful Fraction (WUF) concept. Like other performance parameters, whose temperature coefficients are equally important in PV characterization and system design, the WUF should be also be considered as this might help to minimize some of the system sizing errors, which in most instances lead to under performance, unreliable and financial repercussions.
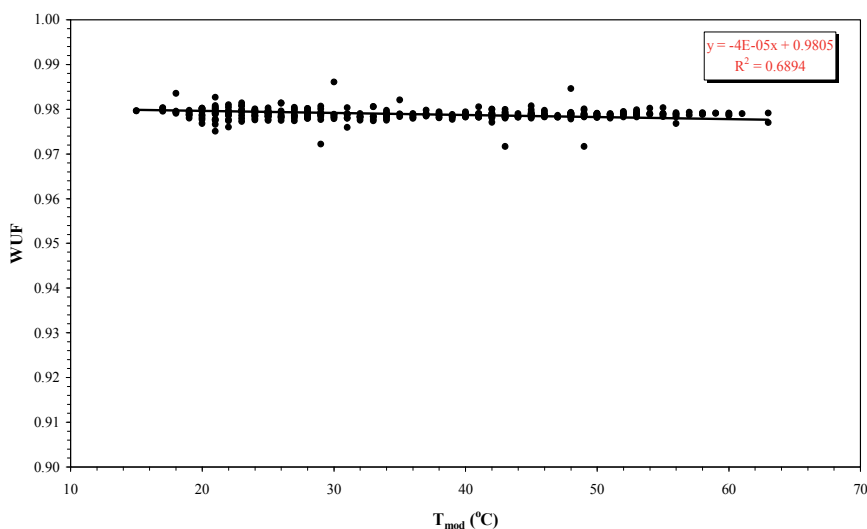

Fig. 12. Relationship between the outdoor WUF and back of module temperature of the CIS module during summer period.

5. Conclusion

The outdoor spectral effects using the Weighted Useful Fraction (WUF) of CIS module was analyzed. Observed was a 17% decrease in the device short - circuit (I_{sc}) current attributed due to a change in season. The change in season (summer/winter) result in the outdoor spectrum to vary by ΔWUF = 1.5%, result in the decrease in the device I_{sc}. From the analysis done, it was concluded that a small percentage change in ΔWUF resulted in large % difference of the module's I_{sc} as the outdoor spectrum changed during the course of the day, which confirmed that the 17% decrease in I_{sc} was due to a ΔWUF of 1.5 %. A strong correlation between FF and the WUF exists for CIS module. It is observed that the FF increases by 6.5% as WUF increases. The temperature coefficient of a device is one of the important concepts for characterizing device performance parameter. A close correlation between WUF and temperature was established. Temperature coefficients for spectral induced effect (WUF) were found to be $-0.001/^{o}C$ for winter period and $-4\times10^{-5}/^{o}C$ for summer seasons. This difference in WUF_{β} for summer and winter indicated that the temperature coefficients obtained in controlled environment (indoor procedure) can not be truly dependable for modeling purposes or system sizing since the outdoor conditions has an effect also. It should also be noted that the temperature coefficient for spectral effect is indeed an important parameter to consider.

6. References

Christian NJ, Gottschalg TR, Infield DG, Lane K (2002). Influence of spectral effects on the performance of multijunction amorphous silicon cells. *Photovoltaic Conference and Exhibition*, Rome

Gottschalg TR, Infield DG, Lane K, Kearney MJ (2003) Experimenatal study of variations of solar spectrum of relevance to thin film solar cells. *Solar Energy materials and solar cells*, vol 79, pg 527 – 537.

Minemoto T, Toda M, Nagae S, Gotoh M, Nakajima A, Yamamoto K, Takakura H, Hamakawa Y (2007). Effect of spectral irradiance distribution on the outdoor performance of amorphous Si//thin-film crystalline Si stacked photovoltaic modules., *Solar Energy Materials and Solar Cells*, Vol.91, pp. 120-122

M Simon and E.L Meyer (2008). Spectral distribution on photovoltaic module performance in South Africa. evaluation for c-Si modules", *33rd IEEE Phovoltaic Specialist Conference, San Diego,* California, USA.

Meyer, E.L, (2002). On the Reliability, Degradation and Failure of Photovoltaic Modules. *University of Port Elizabeth, PhD-Thesis*, 74-77, 34-38.

King, D.L, Kratochvil JA (1997). Measuring solar spectral and angle-of-incident effects on photovoltaic modules and solar irradiance sensors. *26th IEEE Phovoltaic Specialist Conference,Anaheim,CA,USA*

Riordan C, Hulstrom R (1990). What is an Air Mass 1.5 spectrum. *20th IEEE Phovoltaic Specialist Conference*, *New York,* pg 1085 – 1088.

Poissant Y, Lorraine C, Lisa DB (2006) (http://www.cete-vareness.nrcan.gc.ca).

Gottschalg R, Betts TR and Infield DG (2004). On the importance of considering the Incident Spectrum when measuring the outdoor performance of amorphous

silicon photovoltaic devices. *Measurement Science and Technology*, vol.15, pg 460-466.

M Simon and E.L Meyer (2010). The effects of spectral evaluation for c-Si modules", *Progress in Photovoltaic: Research and Application,* DOI:10.1002/pip.973.

Edited by Leonid A. Kosyachenko

The first book of this four-volume edition is dedicated to one of the most promising areas of photovoltaics, which has already reached a large-scale production of the second-generation thin-film solar modules and has resulted in building the powerful solar plants in several countries around the world. Thin-film technologies using direct-gap semiconductors such as CIGS and CdTe offer the lowest manufacturing costs and are becoming more prevalent in the industry allowing to improve manufacturability of the production at significantly larger scales than for wafer or ribbon Si modules. It is only a matter of time before thin films like CIGS and CdTe will replace wafer-based silicon solar cells as the dominant photovoltaic technology. Photoelectric efficiency of thin-film solar modules is still far from the theoretical limit. The scientific and technological problems of increasing this key parameter of the solar cell are discussed in several chapters of this volume.

IntechOpen

9 789535 160687